

Dissertation zur Erlangung des Doktorgrades  
der Fakultät für Chemie und Pharmazie  
der Ludwig-Maximilians-Universität München

# **From Molecular Building Blocks to Condensed Carbon Nitride Networks: Structure and Reactivity**



**Bettina Valeska Lotsch**

**aus**

**Frankenthal / Pfalz**

**2006**

## **Erklärung**

Diese Dissertation wurde im Sinne von § 13 Abs. 3 bzw. 4 der Promotionsordnung vom 29. Januar 1998 von Herrn Prof. Dr. Wolfgang Schnick betreut.

## **Ehrenwörtliche Versicherung**

Diese Dissertation wurde selbstständig, ohne unerlaubte Hilfe erarbeitet.

München, den 20. 11. 2006

---

Bettina Valeska Lotsch

Dissertation eingereicht am 20. 11. 2006

1. Gutachter: Prof. Dr. Wolfgang Schnick

2. Gutachter: Prof. Dr. Jürgen Senker

Mündliche Prüfung am 19. 12. 2006

*To my parents  
and sister*



## Acknowledgements

First of all, I would like to express my gratitude to Prof. W. Schnick for giving me the opportunity to work in his group, for the freedom of research paired with continuous advertisement and support, and for his stimulating enthusiasm. Without his professional guidance and encouragement, this thesis would not have become what it is.

I am indebted to Prof. J. Senker for introducing me into the “brave new world” of solid-state NMR, for his encouragement to never stop digging deeper, for his conviction that the time issue comes only second, and for his seemingly never ending repertoire of questions, answers, ideas and patience, as well as for being co-referee of this thesis.

I am thankful to Prof. T. Bein, Prof. D. Johrendt, Prof. K. Karaghiosoff and Prof. T. M. Klapötke for their being available as examiners in my *viva-voce*.

Special thanks go to Dr. Markus Döblinger, as well as Lena Seyfarth and Jan Sehnert for a fruitful collaboration and stimulating insights into electron diffraction, solid-state NMR, and the world of theory, respectively.

For carrying out innumerable measurements, as well as for the “postprocessing” involved, I would like to thank Sandra Albert, Dr. Sascha Correll, Dr. Markus Döblinger, Dagmar Ewald, Dr. Gerd Fischer, Helmut Hartl, Dr. Alexandra Lieb, Prof. Dr. Konstantin Karaghiosoff, Juliane Kechele, Thomas Miller, Christian Minke, Peter Mayer, Dr. Peter Mayer, Dr. Oliver Oeckler, Andreas Sattler and Wolfgang Wünschheim.

In detail, I would like to thank

- Dr. Oliver Oeckler for his invaluable advice (both in real and in reciprocal space) and for his particular “challenging” view on things in general,
- Dr. Jörn Schmedt auf der Günne and Christian Minke for their assistance and cooperation in all NMR-related matters,
- Dr. Barbara Jürgens for opening up the intriguing playground of C/N chemistry and shifting the focus to the most interesting problems,
- Andreas Sattler and Theresa Soltner for their assistance, invaluable discussions and exchange of views on C/N matters and beyond,

- my bachelor and research students Lucia Romana Lorenz and Daniel Benker for their participation and support,
- Carolin Buhtz for her creative contributions to the electron diffraction investigations and her imperturbable capability to listen and de-dramatize things,
- Dr. Alexandra Lieb for keeping company in our “night-lab”, for her unfailing nutritional backup, and for her inspiringly different world outlook – I learned a lot ...
- Dr. Ulrich Baisch and Dr. Sascha Correll for their outstanding helpfulness and guidance,
- Dr. Alexandra Lieb, Juliane Kechele, Robert Kraut, Dr. Abanti Nag, Rebecca Römer and Wolfgang Wünschheim for their collegiality and for creating a pleasant working- and “biosphere” in laboratory D 2.107,
- Wolfgang Wünschheim for technical support whenever hardware or software of all kinds quit the service,
- Richard Betz, Sebastian Braun, Dr. Markus Döblinger, Michael Göbel and Dr. Oliver Oeckler for proof-reading this thesis and for racking their brains for me ...

For providing a particularly convenient working atmosphere throughout the last years and for all sorts of technical, scientific and “personal” support, I would like to thank my – present and past – colleagues Dr. Ulrich Baisch, Constantin Beyer, Sabine Beyer, Daniel Bichler, Cordula Braun, Sascha Correll, Holger Emme, Cora Hecht, Elsbeth Hermanns, Gunther Heymann, Dr. Henning Höppe, PD Dr. Hubert Huppertz, Stefanie Jakob, Petra Jakubcová, Friedrich Karau, Juliane Kechele, Johanna Knyrim, Robert Kraut, Dr. Alexandra Lieb, Catrin Löhnert, Thomas Miller, Christian Minke, Helen Müller, Dr. Abanti Nag, Dr. Oliver Oeckler, Sandro Pagano, Dr. Regina Pocha, Florian Pucher, Stefan Rannabauer, Christoph Röhlich, Rebecca Römer, Andreas Sattler, Dr. Jörn Schmedt auf der Günne, Christian Schmolke, Stefan Sedlmaier, Jan Sehnert, Lena Seyfarth, Theresa Soltner, Florian Stadler, Dr. Johannes Weber, Wolfgang Wünschheim and Martin Zeuner.

Above all, I am indebted to my parents, my sister and Sebastian, who continuously encouraged and supported me with maximum forbearance and patience. For all what they have done and sacrificed, suffice it to say:

*Gratitude is one of the least articulate of the emotions, especially when it is deep.*

Felix Frankfurter



*Be not afraid of growing slowly, be afraid only of standing still.*  
Chinese Proverb

# Contents

<b>1</b>	<b>Introduction</b>	<b>15</b>
<b>2</b>	<b>Experimental Methods</b>	<b>22</b>
2.1	Preparative Methods . . . . .	22
2.1.1	Vacuum and Inert Gas Line . . . . .	22
2.1.2	Furnaces . . . . .	22
2.1.3	Glove Box . . . . .	23
2.1.4	Operating Techniques . . . . .	23
2.2	Analytical Methods . . . . .	24
2.2.1	Diffraction Techniques . . . . .	24
2.2.2	Spectroscopic Methods . . . . .	30
2.2.3	Elemental Analysis . . . . .	36
2.2.4	Mass Spectrometry . . . . .	37
2.2.5	Thermal Analysis . . . . .	37
<b>3</b>	<b>Theoretical Basis and Models</b>	<b>38</b>
3.1	Dynamical Processes . . . . .	38
3.2	Neutron Scattering . . . . .	41
3.2.1	Basic Principles . . . . .	41
3.2.2	Diffraction . . . . .	43
3.2.3	Quasielastic Neutron Scattering (QENS) . . . . .	44
3.2.4	Motional Models . . . . .	46
3.2.5	EISF . . . . .	47
3.3	Magnetic Resonance . . . . .	48
3.3.1	Basic Principles . . . . .	48
3.3.2	Interaction Hamiltonians and Operator Formalism . . . . .	50
3.3.3	High-Resolution NMR: General Aspects and Techniques . . . . .	63

---

<b>4 Dynamics and Reactivity</b>	<b>69</b>
4.1 Ammonium Dicyanamide . . . . .	71
4.1.1 Introduction . . . . .	71
4.1.2 Solid-State NMR . . . . .	73
4.1.3 Neutron Scattering . . . . .	90
4.2 Ammonium Cyanoureat . . . . .	105
4.2.1 Introduction . . . . .	105
4.2.2 Crystal Structure . . . . .	105
4.2.3 Thermal Reactivity . . . . .	110
4.2.4 Cyanoguanylurea . . . . .	121
<b>5 CN<sub>x</sub> Precursors</b>	<b>128</b>
5.1 Dicyanamides . . . . .	130
5.2 Guanidinium Dicyanamide . . . . .	135
5.2.1 Introduction . . . . .	135
5.2.2 Crystal Structures . . . . .	135
5.2.3 Vibrational Spectroscopy . . . . .	141
5.2.4 Thermal Behavior . . . . .	143
5.3 Melaminium Dicyanamide . . . . .	148
5.3.1 Introduction . . . . .	148
5.3.2 Crystal Structure . . . . .	148
5.3.3 Thermal Behavior . . . . .	151
5.3.4 Temperature-Dependent FTIR Spectroscopy . . . . .	153
5.3.5 Discussion . . . . .	155
5.4 Guanylurea Dicyanamide . . . . .	157
5.4.1 Introduction . . . . .	157
5.4.2 Crystal Structure . . . . .	157
5.4.3 Spectroscopic Characterization . . . . .	159
5.4.4 Thermal Behavior . . . . .	160
5.5 Tricyanomelamines . . . . .	167
5.6 Non-Metal Tricyanomelamines . . . . .	170
5.6.1 Crystal Structures and Spectroscopic Characterization . . . . .	170
5.6.2 Thermal Behavior . . . . .	185
5.6.3 DSC and <i>In Situ</i> X-Ray Diffraction . . . . .	186
5.6.4 IR Spectroscopy . . . . .	188
5.6.5 Solid-State NMR . . . . .	191

5.6.6	Discussion . . . . .	192
5.7	Preliminary Conclusion . . . . .	193
<b>6</b>	<b>Melam</b>	<b>196</b>
6.1	Introduction . . . . .	197
6.2	Thermal Behavior of Melamine . . . . .	200
6.3	Adduct Phases . . . . .	203
6.3.1	Mass Spectrometry . . . . .	203
6.3.2	Elemental Analysis . . . . .	204
6.3.3	IR Spectroscopy . . . . .	205
6.3.4	NMR Spectroscopy . . . . .	206
6.3.5	Thermal Analysis . . . . .	212
6.4	Melam . . . . .	213
6.4.1	IR Spectroscopy I: Formation . . . . .	215
6.4.2	Analytical Data . . . . .	216
6.4.3	Crystal Structure . . . . .	216
6.4.4	IR Spectroscopy II: Structure . . . . .	218
6.4.5	Solid-State NMR Spectroscopy . . . . .	218
6.4.6	Thermal Behavior . . . . .	221
6.4.7	UV/Vis Spectroscopy . . . . .	222
6.4.8	Discussion . . . . .	224
6.5	Melam Derivatives . . . . .	226
6.5.1	Melam Solvates . . . . .	227
6.5.2	Melamium Salts . . . . .	234
6.5.3	Metal-Melam Complexes . . . . .	246
6.6	Ammeline Salts . . . . .	263
6.6.1	Introduction . . . . .	263
6.6.2	Crystal Structures . . . . .	264
6.6.3	IR Spectroscopy . . . . .	270
6.6.4	Discussion . . . . .	273
6.7	Melaminium Dinitrate . . . . .	274
6.8	Preliminary Conclusion . . . . .	278
<b>7</b>	<b>Melon</b>	<b>280</b>
7.1	Introduction . . . . .	281
7.2	“Melem Oligomer” . . . . .	285

---

7.3	Synthesis and Composition	287
7.4	Reactivity	289
7.5	Morphology	291
7.6	Vibrational Spectroscopy	292
7.7	X-ray Powder Diffraction	294
7.8	Solid-State NMR Spectroscopy	295
7.8.1	CP- and CPPI-MAS Experiments	295
7.9	Electron Diffraction	303
7.9.1	Phenomenological Descripton	303
7.9.2	Structure Elucidation	306
7.9.3	Structure Description	312
7.10	Melon: Theoretical Calculations	314
7.10.1	Structural Models	314
7.10.2	<i>Ab Initio</i> NMR Calculations	319
7.11	3D Approaches	320
7.12	Side Phases	326
7.13	Models for Graphitic Carbon Nitride	329
7.13.1	Fully Condensed Structure Models	329
7.13.2	“Defect” Structure Models	331
7.13.3	“Mixed” Structure Models	333
7.14	Preliminary Conclusion	334
<b>8</b>	<b>Discussion and Outlook</b>	<b>337</b>
<b>9</b>	<b>Summary</b>	<b>345</b>
<b>10</b>	<b>Appendix</b>	<b>355</b>
10.1	Syntheses	355
10.1.1	Ammonium Dicyanamide $\text{NH}_4[\text{N}(\text{CN})_2]$	355
10.1.2	$\text{ND}_4[\text{N}(\text{CN})_2]$	355
10.1.3	Ammonium Cyanoureat NH <sub>4</sub> [H <sub>2</sub> NC(=O)NCN]	356
10.1.4	Cyanoguanylurea H <sub>2</sub> NC(=O)NHC(NH <sub>2</sub> )NCN	356
10.1.5	Guanidinium Dicyanamide $[\text{C}(\text{NH}_2)_3][\text{N}(\text{CN})_2]$	356
10.1.6	Melaminium Dicyanamide $[\text{C}_3\text{N}_3\text{H}(\text{NH}_2)_3][\text{N}(\text{CN})_2] \cdot \text{H}_2\text{O}$	357
10.1.7	Guanylurea Dicyanamide $[(\text{H}_2\text{N})\text{C}(=\text{O})\text{NHC}(\text{NH}_2)_2][\text{N}(\text{CN})_2]$	358
10.1.8	Non-Metal Tricyanomelamines	358
10.1.9	<sup>15</sup> N-Melamine $\text{C}_3^{15}\text{N}_6\text{H}_6$	360

10.1.10 Ammeline Salts . . . . .	360
10.2 Chemicals . . . . .	361
10.3 Crystal Structures . . . . .	362
10.3.1 2,4-Diamino-1,3,5-Triazine . . . . .	362
10.3.2 Guanylurea Sulfate . . . . .	364
10.4 Melon: Electron Diffraction . . . . .	366
10.5 Solid-State NMR Spectroscopy . . . . .	367
10.5.1 Line Shape Simulations . . . . .	367
10.5.2 Program Code . . . . .	368
<b>Abbreviations</b>	<b>375</b>
<b>Bibliography</b>	<b>378</b>
<b>List of Publications and CSD / CCSD Deposition Numbers</b>	<b>409</b>
<b>Curriculum Vitae</b>	<b>414</b>

# Chapter 1

## Introduction

The ongoing quest for the hypothetical binary carbon nitride  $C_3N_4$  stands for a prospering area of research in modern solid-state and materials chemistry, that has taken root at the frontiers of basic and applied research in the past 15 years. Nitridic materials constitute an exceptionally versatile group of compounds in terms of chemical bonding, ranging from salt-like over metallic to covalent, the latter one comprising both molecular representatives ( $S_4N_4$ ) and extended solids such as  $(BN)_x$  or  $P_3N_5$  [1–8]. Non-metal nitrides such as silicon nitride  $Si_3N_4$ , c-BN, or GaN have long been known for their exceptional physical and chemical properties, among which low density, high melting points, hardness, resistance and semiconducting properties are the most prominent ones [2, 5, 6]. In terms of chemical stability these high-performance ceramic materials by far outperform oxidic materials, the latter however still dominating the field of functional ceramics, represented for instance by ferroelectrics, zeolites, zirconia, or high-temperature superconductors.

However, the extension of nitride chemistry to mixed nitrides such as oxonitrides, nitridosilicates, nitridophosphates or oxonitridophosphates has produced a plethora of novel materials with interesting structures [9–20] and tunable properties, now being at the forefront of materials science: Ternary nitrides based on rare earth metal ions in a nitridosilicate framework have pioneered the rapidly growing field of inorganic LEDs [21–26], and multinary phases such as  $SiONs$  and  $SiAlONs$  represent tailor-made ceramics with outstanding material properties [21, 27–30]. Likewise, the formal introduction of boron and carbon into a silicon nitride network has recently opened up a novel class of amorphous  $Si-B-(C-N)$  high-performance polymers with unprecedented thermal stability [31–33].

The screening for novel ultrahard materials among combinations of low-weight main group elements, featuring covalent bonding and highly cross-linked structures, has become manifest in the compounds  $c-BC_2N$  [34–36] or  $\gamma-Si_3N_4$ , a novel, high-pressure silicon nitride modification

adopting a Spinel-type structure [5, 37–40].

In terms of hardness, a most promising candidate is the hypothetical binary carbon(IV)nitride alternatingly made up from carbon and nitrogen, whose existence is still a matter at issue.

For the dense,  $sp^3$ -hybridized modifications a bulk modulus larger than that of diamond is conjectured following the empirical principles by *Liu* and *Cohen* [41] according to which the bulk modulus is inversely proportional to both ionicity and interatomic distances. For a realistic estimation of the hardness of a material, however, the shear modulus has also to be taken into account, thus suggesting an overall similar, but slightly lower hardness for carbon nitride as compared to diamond [42].

Nevertheless, a promising new member of the family of ultrahard materials is to be expected, whose potential properties span a wide range of interesting features, such as high thermal conductivity and large band gaps (3 – 4 eV), or auxetic behavior of certain  $CN_x$  phases [42–45]. According to theoretical calculations, at least four metastable highly condensed, crystalline modifications may exist:  $\alpha$ - $C_3N_4$  (hexagonal),  $\beta$ - $C_3N_4$  ( $\beta$ - $Si_3N_4$ -type), pseudocubic  $C_3N_4$  (defect  $ZnS$ -type), cubic  $C_3N_4$  (Willemite-II-type), whose stabilities are similar, yet less than that of graphitic carbon nitride ( $g$ - $C_3N_4$ ) with  $sp^2$ -hybridized carbon [41–55].

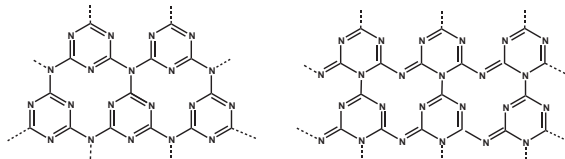


**Figure 1.1:** Hexagonal (left) and orthorhombic modification (right) of  $g$ - $C_3N_4$ , both based on nitrogen bridged 1,3,5-triazine rings as elementary building blocks.

Apart from various phases with higher or lower nitrogen content [56–58], carbodiimide-bridged structures [59, 60], and  $CN_x$ -heterofullerenes and -nanotubes [61–65], hypothetical low density 3D-networks made up from triazine building blocks with  $SrSi_2$ - or  $ThSi_2$ - type topologies have recently been presented and ranked within the stability range of the  $g$ - $C_3N_4$  phases [66].

Innumerable attempts using a broad repertoire of physicochemical methods have been undertaken to find viable synthetic pathways to carbon nitride [42–44]: Apart from chemical techniques at ambient conditions such as pyrolyses, shock-wave techniques, CVD- (HFCVD, PECVD) and PVD-processes (ion beam deposition), laser techniques [67], and sputtering processes have been utilized. The as-obtained, predominantly amorphous  $CN_x$  thin films exhibit interesting optical, electronic, or tribological properties according to their nitrogen content, and have already found applications as reactive films or coatings, as thin films in solar cells [68, 69], in sensors, MEMs (micro-electromechanical devices) [70], or transistors [71]. A rather “chemical” approach to 3D  $C_3N_4$  immediately follows from direct analogy to the system graphite-diamond: According to DFT-calculations, the conversion of graphitic carbon

nitride into  $\text{sp}^3\text{-C}_3\text{N}_4$  should be feasible with modern high-pressure techniques at pressures  $\leq 75$  GPa [51, 59, 72].

Commonly invoked structure models for graphitic carbon nitride, which can formally be derived from graphite-type  $(\text{CN})_x$  layers by introducing ordered carbon vacancies, consistently derive from triazine units that are linked up by essentially planar trigonal nitrogen atoms, building up an infinite two-dimensional array with hexagonal or orthorhombic symmetry (Fig. 1.1) [42–44, 48, 50–53, 55, 73, 74]. In addition, carbodiimide-bridged structures were discussed [59].

The triazine ring system ( $\text{C}_3\text{N}_3$ ) is found in various heterocycles as a structural building block, as is the case for the important  $\text{CN}_x$  precursor 2,4,6-triamino-*s*-triazine (melamine,  $\text{C}_3\text{N}_3(\text{NH}_2)_3$ ) (**1**) (Fig. 1.2). Despite persistent research efforts, the existence and molecular structure of the condensation products of melamine, namely the compounds melam  $[(\text{C}_3\text{N}_3)(\text{NH}_2)_2]_2\text{NH}$  (**3**), melem  $\text{C}_6\text{N}_7(\text{NH}_2)_3$  (**2**), and melon  $[\text{C}_6\text{N}_7(\text{NH})(\text{NH}_2)]_n$  (**4**), has long been subject to debate.

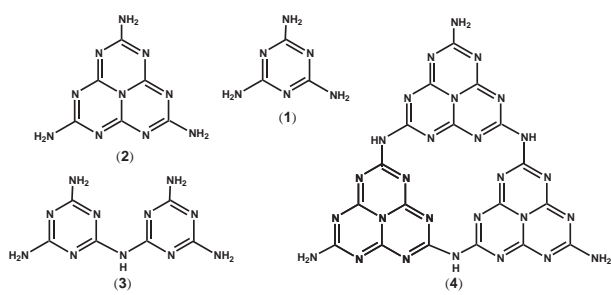


**Figure 1.2:** Known and assumed structures of potential precursor compounds for  $\text{C}_3\text{N}_4$ . (**1**) Melamine, (**2**) melem, (**3**) melam, (**4**) possible structure of “melon”.

bridged by an NH-unit [76–79]. The question as for the role of melam in the condensation process from melamine to  $\text{g-C}_3\text{N}_4$  has not been resolved as yet. The same holds true for melon, for which either an oligomeric structure (trimer of melem) or a 1D polymeric structure based on heptazine units is discussed (Fig. 1.2) [76, 80, 81].

With the structural characterization of melem (2,5,8-triamino-heptazine) the ultimate proof of the existence of a key intermediate in the condensation cascade of melamine to  $\text{g-C}_3\text{N}_4$  was accomplished [82], which as a consequence significantly extended the pool of molecular motifs for  $\text{g-C}_3\text{N}_4$  [83, 84]: DFT calculations carried out by Kroke et al. [85] suggest the existence of a graphitic  $\text{C}_3\text{N}_4$  phase based on heptazine units (Fig. 1.3), which is expected to be by  $30 \text{ kJ mol}^{-1}$  more stable than the triazine-based analogue (Fig. 1.1).

According to early investigations by Pauling and Sturdivant [75], the latter compounds exhibit the *sym-heptazine* nucleus (tri-*s*-triazin,  $\text{C}_6\text{N}_7\text{H}_3$ ) as characteristic building block, the terminology confirming a close analogy to the *cyanuric* building motive found in triazines (Fig. 1.2).

Neither for the molecular nor for the crystal structure of melam experimental evidence is available. Spectroscopic data however were interpreted on the basis of two triazine rings

Viable synthetic routes to graphitic carbon nitride have recently been subject to vivid research efforts [42–44]. The primarily employed “precursor-route” is based on the pyrolysis of molecular compounds or thermally induced two-component reactions between suitably functionalized precursors [1, 86]. Molecular compounds exhibiting an adequate scheme of atom connections (“pre-organization”) as well as the desired over-all stoichiometry, have proven to be particularly suitable precursors [87, 88].

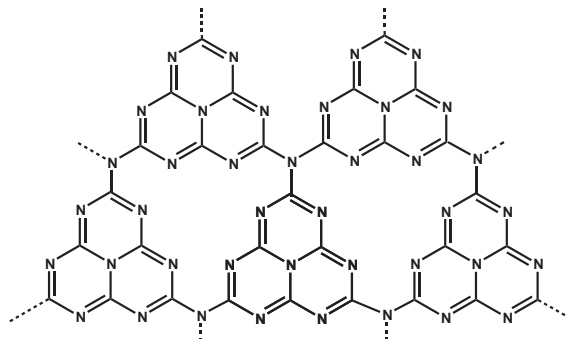


**Figure 1.3:** Structural model for  $g\text{-C}_3\text{N}_4$  based on heptazine building blocks.

According to these principles, the high-performance ceramics  $\text{Si}_3\text{B}_3\text{N}_7$  and  $\text{SiBN}_3\text{C}$  have been obtained from thermal decomposition of the single-source precursor TADB (trichlorosilylaminodichloroborane) and methylamine [31, 32]. Likewise,  $\text{Cl}_3\text{SiNPCl}_3$  with the built-in structural element of two vertex sharing  $\text{PN}_4^-$  and  $\text{SiN}_4$ -tetrahedra bridged by a nitrogen atom has been proven to be a particularly useful precursor for the synthesis of  $\text{SiPN}_3$  [89]. Analogously, the

binary non-metal nitride  $\text{P}_3\text{N}_5$  was successfully obtained by the pyrolysis of the single-source precursor tetraaminophosphonium iodide  $[\text{P}(\text{NH}_2)_4]\text{I}$  [14–16].

The synthesis of graphitic carbon nitride has been attempted using a wide range of different precursors [83, 84, 90, 91]. Pivotal starting materials used most frequently can almost exclusively be derived from the triazine, yet rarely from the heptazine core, thereby conforming to the pre-organization principle and combining the requirements of high nitrogen and low hydrogen contents. Irrespective of the synthesis conditions and the partly significant hydrogen contamination, the structures of the obtained products are commonly interpreted without conclusive argumentation on the basis of threefold N-bridged triazine systems. In doing so, solely the possible formation of spherically corrugated layers or  $\text{CN}_x$  nanotubes is being considered.

Owing to the very resistant N–H or C–H bonds and the inclusion of further heteroatoms such as oxygen into the 2D-network depending on the choice of precursor, and the overall difficulties in preparing pure  $g\text{-C}_3\text{N}_4$  phases with exact stoichiometry, ultimate proof of the existence of either pure  $g\text{-C}_3\text{N}_4$ , or  $\text{sp}^3\text{-C}_3\text{N}_4$  has not been given as yet. Similarly, no conclusive experimental evidence has been put forward for either of the structural models proposed for  $g\text{-C}_3\text{N}_4$ , which eludes conventional structural characterization due to its largely polymeric and amorphous character. Apart from solid-state NMR studies on the structure

of paracyanogene [92] and a small number of  $^{13}\text{C}$ -CP MAS experiments using poorly crystalline carbon nitride samples [93, 94], no experimental studies exist to date which are comprehensively dealing with this issue.

The lack of structural information can in principle be tackled qualitatively by gaining detailed insight into the actual species occurring during the course of the reaction and constituting the final products. Therefore, knowledge about possible intermediates and preferred reaction pathways is not only a prerequisite for a tailored synthetic approach to graphitic carbon nitride (“crystal engineering”), but can deliver vital information on the structure of the reaction products. Understanding the processes on a molecular level can thus be indispensable to rule out certain structural models in favour of others, whose formation pathways agree well with all stages of the reaction history. A prominent example for a highly relevant inconsistency in carbon nitride chemistry can be ascribed to the lack of insight into processes occurring on a molecular level: The popular concept of thermally linking triazine units via trigonal planar nitrogen atoms has been sustained, although the condensation of melamine to melem has been proven to proceed as an intermediate stage prior to the formation of g-C<sub>3</sub>N<sub>4</sub> [82]. Disregarding this fact has long hampered the heptazine-hypothesis to enter the focus of the scientific community.

“*Corpora non agunt, nisi fluida seu dissoluta*”.<sup>1</sup> A thorough understanding of molecular solid-state reactions has traditionally been suffering from the nescience of their feasibility and the predominance of mechanistic investigations in solution. Only a limited number of comprehensive studies on molecular solid-state reactions exists in the literature [95]. As apart from classical photoreactions most reactions are induced thermally, the solid compound must exhibit a sufficiently high melting point, which is rarely met in molecular crystals, leading to melting prior to the reaction onset. In addition, both the technical and the methodological realization of *in situ* monitoring of solid-phase reactions is by far more demanding as compared to the situation in solution, since comparable information is accessible in a rather indirect way and often complicated by intermolecular interactions and the impact of the crystal field, both of which being difficult to treat in a straightforward way.

Intriguing features of molecular solid-state reactions are their simple and resource-saving implementation without the necessity of using a solvent, thus providing an easy work-up, as well as increased selectivity and efficiency with diminished formation of unwanted side-products in many cases. Accordingly, asymmetric transformations with high enantioselectivity could be achieved by making use of the chiral environment of the molecules in the crystal [95, 96]. At the same time, however, reaction control is greatly reduced when considering the

---

<sup>1</sup> “Compounds that are not fluid or dissolved do not react”, by *Aristotle*

special case of thermal solid-state reactions using one-component homogeneous solids, thus requiring maximum precision in exercising thermal control. Alternatively, the strategy of crystal-engineering can be pursued by creating one- or two-component solids by intramolecular substitution, mixed-crystal formation, or host-guest complexation to selectively tailor reactivity on a molecular level.

According to the topochemical principle introduced by Kohlschütter and Hertel, and reformulated by Schmidt [97–100], reactions in the solid state occurring with a minimum of atomic or molecular movement are preferred. As a result, static lattice constraints restrict the products of a topochemical reaction to those pre-organized in the parent crystal [101–107]. This principle, however, has recently been challenged by the observation of long-range anisotropic molecular movements in typical “topochemical” photoreactions by the application of atomic force microscopy to irradiated single crystal surfaces [108–110]. Thus, differentiating seems advisable between *topochemical* reactions and the special case of *topotactic* reactions, the latter running in a single-crystal-to-single-crystal fashion without crystal disintegration and without significant geometric changes requiring far-reaching molecular movements [108, 111, 112]. According to *Lotgering* [113] topotactic reactions include “all chemical solid-state reactions that lead to a material with crystal orientations correlated with the crystal orientation of the reagent”.

Prominent examples of topochemical reactions are photoreactions such as [2+2] photodimerizations of cinnamic acid derivatives [99, 100, 114, 115] and coumarins [96, 116, 117], or the polymerization of diacetylenes [118] whose reactivity is largely governed by the packing of the reactants rather than by their intrinsic molecular reactivity.

Solid-state reactions proceeding in a non-topochemical fashion are those taking place at locally increased defect concentrations, surfaces or disordered domains, the latter imperfections being essential for the reactions to occur. Along these lines, amorphous solids or inclusion compounds may provide a reaction environment without 3D interlocking, thus allowing for easy phase rebuilding and transformation through unrestricted molecular migration [108, 117, 119, 120].

The significance of thermal solid-state reactions, particularly of the latter kind, has long been disregarded in carbon nitride chemistry (cf. above). The synthetic concept of precursor chemistry has, however, continuously shaped the awareness of the reactivity principle, which is indispensable for the directed synthesis of highly condensed networks. An appealingly simple synthetic route to extended 2D carbon nitride networks is based on the thermal treatment of suitable ternary carbon nitrides such as cyanamides [82], dicyanamides [121–124], or tricyanomelamines [125–127], thiocyanates [83] or melamine derivatives [82–84, 128],

utilizing “self-condensation” reactions initiated by unsaturated or nucleophilic moieties without the necessity of co-reactants or specifically functionalized reaction sites. However, it must be emphasized that the classification of a reaction as “solid-state reaction” is critical in many respects, as essentially all reactions – apart from topotactic reactions – exhibit some form of “molecular loosening”, which can lead to microscopic melting at the reaction front invisible or undetectable by thermal analysis. Moreover, the majority of reactions in carbon nitride chemistry has simply not been classified with respect to the type of reaction that occurs. Although it is still common practice to treat such thermal condensations as “black box” reactions, the elucidation of their mechanism and dynamic processes is a prerequisite to obtain well-defined solids with tailored connectivities.

In order to comprehensively understand and utilize processes on a molecular level, three main goals have to be pursued; their implementation will be referred to in more detail at the beginning of each chapter:

1. **Chemical Screening.** Candidates potentially exhibiting reactivity in the solid phase have to be selected according to chemical considerations, and their performance tested. Chapters 5, 6 and 7 are devoted to this issue and present examples of potential  $\text{CN}_x$  precursors. Candidates have been selected from three major groups of compounds, namely dicyanamides, tricyanomelamines, and condensation products of melamine.
2. **Reaction Pathway.** Microscopic and macroscopic processes have to be identified by a *qualitative* description of the reaction pathways and possible intermediates. As an extension of the chemical screening, the thermal behavior of the above  $\text{CN}_x$  precursors was monitored by a combination of *in situ* spectroscopic and diffraction techniques. The thermolysis pathways and their significance with respect to the formation of extended carbon nitride solids are discussed in Chapters 5 to 7. An in-depth study of the complex thermal decomposition of ammonium cyanoureatate will be presented in the second part of Chapter 4.
3. **Reaction Mechanism.** A full understanding of the reaction requires the *quantitative* description of the reaction parameters such as kinetics, thermodynamics, and the processes occurring on the submicroscopic level.

This approach provides the basis of the first part of Chapter 4, in which the thermal solid-state reactivity and  $\text{NH}_4^+$  dynamics of ammonium dicyanamide will be delineated as an example.

# Chapter 2

## Experimental Methods

### 2.1 Preparative Methods

#### 2.1.1 Vacuum and Inert Gas Line

Thermolyses and manipulations of air-sensitive compounds were carried out under an atmosphere of dry argon (purity grade 4.8, Messer) to exclude humidity and oxygen throughout the reactions. The reaction vessels (Schlenk flasks, ampules) were connected to a vacuum line *via* ground necks and dried *in vacuo* using a heat gun or fan burner. Evacuation was accomplished with a rotary vane pump (RZ 8, VAP 5, suction capacity  $8.6 \text{ m}^3 \text{ h}^{-1}$ , Vacuubrand) down to pressures of 0.1 Pa. Purification and drying of inert gas was carried out by successively passing the latter through columns filled with blue silica gel (Merck), potassium hydroxide pellets (purum, Merck), molecular sieve (porewidth 0.3 nm, Merck), and phosphorus pentoxide on an inert carrier material (Sicapent<sup>TM</sup>, Merck). To remove adherent traces of oxygen, nitrogen or hydrogen, the gas was finally passed over titanium sponge (99.5 %, Alfa) at 973 K.

#### 2.1.2 Furnaces

Reactions at elevated temperatures (typically 320 – 940 K) were conducted in tubular furnaces with electric resistance heating, a maximum continuous operating temperature of 1273 K and programmed temperature control, allowing for heating rates  $\geq 1 \text{ K min}^{-1}$ . The temperature was measured in the reaction zone with a Ni/Cr-Ni thermocouple, the reliability being  $\pm 20 \text{ K}$ . Typically, a vertical set-up was chosen, thus leading to a separation of the reaction products within the reaction tube according to their volatility. Flow tubes were placed horizontally in the tubular furnace and connected to a vacuum line for supply of a permanent reactive or inert gas atmosphere.

### 2.1.3 Glove Box

For manipulation and storage of hygroscopic or air-sensitive compounds under argon (purity grade 4.8, Messer) a glove box (MB150-Gl and UniLab,  $O_2 < 1$  ppm,  $H_2O < 1$  ppm, MBraun) was used.

### 2.1.4 Operating Techniques

#### 2.1.4.1 Ion Exchange

Ion exchange reactions were conducted according to the column principle using vertically placed glass frits (length: 26 cm,  $\varnothing_{ext.}$  12 – 24 mm, pore size: P 1 – 2). The frits were filled with an ion exchange resin ( $H^+$ -form, art. no. 4765, Merck) suspended in deionized water. In special cases (low solubility of the product, poor ion exchange capacity for certain ions), metathesis reactions were carried out by slowly combining aqueous or methanolic solutions of the reactants under heating.

#### 2.1.4.2 Thermal Conversions and Sublimation

Thermal conversions were typically carried out under counter-pressure of the evolving gases such as ammonia. The well-ground reactant mixture was directly loaded in pre-dried ampoules, which were subsequently sealed off under argon to lengths of approximately 12 cm. For temperatures below 550 K, Duran<sup>TM</sup> ampules ( $\varnothing_{ext.}$  16 mm, wall thickness: 1.5 mm) were used, for temperatures beyond 550 K thick-walled ampules made from silica glass ( $\varnothing_{ext.}$  15 mm, wall thickness: 2 mm, Vogelsberger Quarzglastechnik K. D. Kindl GmbH) were sealed with an oxyhydrogen burner. Reactions requiring pressure equalization were conducted in pre-dried Duran<sup>TM</sup> or silica glass ampules ( $\varnothing_{ext.}$  16 – 24 mm, wall thickness: 1 – 1.5 mm) equipped with a paraffin bubble counter. To preclude corrosion of the glass walls by the reactants, corundum crucibles were used as insets. Condensation reactions under dynamic vacuum were carried out using a flow tube-type set-up. The flow tube (silica glass, length: 68 cm,  $\varnothing_{ext.}$  29 mm) was loaded with the starting material contained in a combustion boat (length: 80 mm, corundum, Friatec), placed horizontally in a tubular furnace, and exposed to dynamic vacuum while heating the reactant. Evolving gases were collected in a cold trap. Crude products such as <sup>15</sup>N-enriched melamine raw material were purified by sublimation in a Duran<sup>TM</sup> flask equipped with a cold finger. The flask was evacuated (1 Pa) and heated ( $1\text{ K min}^{-1}$ ) in a tubular furnace, while the sublimate deposited at the bottom zone of the cold finger.

## 2.2 Analytical Methods

### 2.2.1 Diffraction Techniques

For a detailed disquisition on this subject, the reader is referred to standard works in the literature [129, 130], as well as to the textbook by *Zou* [131].

#### 2.2.1.1 Theory

Since its advent in 1912, X-ray crystallography, i. e. structure analysis based on X-ray diffraction, is still the most important technique for studying the structures of objects periodically ordered on an atomic length scale. Electron diffraction of single crystals was discovered fifteen years later, leading thereafter to the exploitation of the wave properties of electrons by invention of the electron microscope using magnetic lenses. By combination of electron diffraction and atomic resolution electron microscopy with crystallographic image processing, a new powerful tool for structure analysis – electron crystallography – is emerging.

The interaction of waves or particles – typically photons (such as X-rays), neutrons, or electrons – with periodically ordered objects of dimensions similar to the wavelength of the incident radiation, can to a first approximation be described using the concept of kinematical scattering theory.

The mathematical treatment of diffraction in three dimensions is given by the *Laue Equations*, which are equivalent to the condition that the vectorial momentum transfer  $\mathbf{Q}$  is equal to a reciprocal lattice vector  $2\pi\mathbf{r}^*$

$$\mathbf{Q} = 2\pi\mathbf{r}^*, \quad (2.1)$$

where  $\mathbf{Q} = \mathbf{k} - \mathbf{k}_0 = \frac{2\pi}{\lambda}(\mathbf{s} - \mathbf{s}_0)$ .

$\mathbf{r}^*$ : reciprocal lattice vector

$\mathbf{k}_0/\mathbf{s}_0$ : wave vector / unit vector of the incident radiation

$\mathbf{k}/\mathbf{s}$ : wave vector / unit vector of the scattered radiation

The correlation of the scattered intensity  $I(\mathbf{Q})$  with the arrangement of atoms  $v$  at position  $\mathbf{r}$  is then given by the *structure amplitude*  $F(\mathbf{Q})$  as a function of the momentum transfer  $\mathbf{Q}$ :

$$F(\mathbf{Q}) = \sum_v f_v^i(\mathbf{Q}) \cdot T_v(\mathbf{Q}) \cdot \exp\{i\mathbf{Q}\mathbf{r}_v\}, \quad (2.2)$$

where

$$\begin{aligned} f_v^X(\mathbf{Q}) &= \int \rho_v^0(\mathbf{r}) \cdot \exp\{i\mathbf{Q}\mathbf{r}\} d\tau && \text{for X-rays,} \\ f_v^N(\mathbf{Q}) &= b_v && \text{for neutrons,} \\ f_v^E(\mathbf{Q}) &= \frac{2\pi me}{h^2} \int_{\Omega} \varphi_j(\mathbf{r}) \exp\{i\mathbf{Q}\mathbf{r}\} d\tau && \text{for electrons,} \end{aligned}$$

and  $T_v(\mathbf{Q})$  denotes the atomic temperature factor, which represents a correction for the deflection of the atoms from their equilibrium positions due to thermal movements.

$f_v^i(\mathbf{Q})$  represents the atomic scattering factors and describes the angle-dependent atomic scattering amplitudes for the respective type of interaction. Owing to the finite expansion of the electron cloud around a nucleus, for X-rays,  $f_v^X(\mathbf{Q})$  has to be summed up over the static electron density  $\rho_v^0(\mathbf{r})$  of infinitesimal volume elements  $d\tau$ , taking into account a phase factor  $\exp\{i\mathbf{Q}\mathbf{r}\}$ . Similarly, for electrons  $f_v^E(\mathbf{Q})$  depends on the type and state of the atom, where the strength of the interaction of electrons with matter is indicated by the *interaction constant*, defined as

$$\sigma = \frac{2\pi me\lambda}{h^2}. \quad (2.3)$$

For both X-rays and electrons,  $f_v^i(\mathbf{Q})$  decreases rapidly with increasing  $|\mathbf{Q}|$ .

Neutrons interact with the atomic nuclei, which are by a factor of  $10^5$  smaller than the extension of the entire atom and can therefore be approximated as point scatterers. Therefore, the integral over the infinitesimal volume elements simplifies to a constant factor, which is given by the scattering length  $b_v$ . Thus, the atomic form factor is isotropic and does not exhibit an angle-dependent decrease with increasing momentum transfer.

For X-rays and neutrons, the scattered intensities are proportional to the square of the structure amplitude, taking into account several correction terms during data reduction:

$$I_{hkl} \propto |F_{hkl}|^2, \quad (2.4)$$

where

$I_{hkl}$ : intensity of reflection ( $hkl$ )

$F_{hkl}$ : structure amplitude.

By Fourier transformation of  $F(\mathbf{Q})$ , the scattering density functions  $\rho(\mathbf{r})$  or  $\varphi(\mathbf{r})$  can be accessed, which translate the observed structure amplitudes into electron, nuclear, or potential

distributions, respectively.

$$\rho^{X,N}(\mathbf{r}) = \int F(\mathbf{Q}) \exp^{-i\mathbf{Q}\mathbf{r}} d^3Q, \quad (2.5)$$

$$\varphi^E(\mathbf{r}) = \int F(\mathbf{Q}) \exp^{-i\mathbf{Q}\mathbf{r}} d^3Q. \quad (2.6)$$

### 2.2.1.2 X-ray Diffraction by Single Crystals

Suitable single crystals were collected using a polarization microscope MZ 6 (Leica) by covering a crop of crystals with a thin film of paraffine on a glass carrier, and fixing the selected crystal with grease on a glass stick or within a glass capillary (Hilgenberg,  $\varnothing_{ext}$ . 0.3 – 0.5 mm). Air-sensitive single crystals were collected in a glove box, the glass capillaries closed with grease and immediately sealed with pitch after locking them out of the glove box. The quality of the preselected single crystals was checked using a Laue or Precession camera in Laue mode (Buerger Precession camera 205, Huber Diffraktionstechnik GmbH) operating with white Mo–K $\alpha$  - radiation (Röntgengenerator Kristalloflex 760, Siemens). The Laue diagrams were recorded with imaging plates [132], for the readout a laserscanner (BAS 2500 Bio Imaging Analyser, Fuji Photo Film Corporation) was employed. The programs BASREADER [132] and Tina [133] were used for evaluating the diagrams.

### 2.2.1.3 Structure Solution and Refinement from Single-Crystal Data

Single crystals were measured at temperatures between 120 and 293 K on an IPDS single-crystal X-ray diffractometer (STOE & Cie GmbH) equipped with a 600 Series CRYOSTREAM Cooler (Oxford Cryosystems), or on a rotating anode Kappa CCD diffractometer (Bruker AXS / Nonius), both of which using graphite monochromated Mo–K $\alpha$  radiation ( $\lambda = 71.073$  pm). The raw data were reduced using the software specific of the respective instruments, typically accounting for Lorentz-, polarization, and isotropic extinction corrections. Analysis of the data sets, including determination of the possible space groups, was carried out with the program XPREP [134], which was also used for semi-empirical absorption corrections, if applicable.

The crystal structures were solved by direct methods using the program SHELXS-97 [135] and refined on  $F^2$  by applying the full-matrix least-squares method implemented in SHELXL-97 [136].

The quality of the structure model is evaluated by different residuals, which compare the structure amplitudes calculated according to the structure models  $F_{ci}$  with those measured experimentally  $F_{oi}$ . The function minimized during refinement is given by the  $R$  value  $wR2$

(weighted  $R$  value on  $F^2$ ), and the *goodness of fit* (GooF), which are defined as follows:

$$wR2 = \sqrt{\frac{\sum_i w(F_{oi}^2 - F_{ci}^2)^2}{\sum_i w(F_{oi}^2)^2}} \quad (2.7)$$

$w$  : weighting factor based on the measured standard deviations  $\sigma(F_o)$ ,

$F_{oi}^2$ : observed structure amplitude,

$F_{ci}^2$ : calculated structure amplitude.

$$GooF = \sqrt{\frac{\sum_i w(F_{oi}^2 - F_{ci}^2)^2}{N - P}} \quad (2.8)$$

N: number of reflections,

P: number of parameters.

However, evaluation of the structure model may more reliably be carried out based on unweighted  $R$  values, since  $wR2$  is somewhat biased by the weighting scheme. The unweighted residual  $R1$ , is defined as follows:

$$R1 = \frac{\sum_i ||F_{oi}| - |F_{ci}||}{\sum_i |F_{oi}|} \quad (2.9)$$

The statistical consistency of the data is given by the internal  $R$  value  $R_{int}$ , as well as  $R_\sigma$

$$R_{int} = \frac{\sum_i \sum_j |F_{oj}^2 - \overline{F_{oi}^2}|}{\sum_i \overline{F_{oi}^2}} \quad R_\sigma = \frac{\sum_i \sigma F_{oi}^2}{\sum_i (F_{oi}^2)} \quad (2.10)$$

Evaluation and verification of the structure models and the selected space groups was done using the program PLATON (including ADDSYM and MISSYM) [137,138], integrated into the program package WINGX [139]. Typically, no absorption corrections were carried out due to the weak absorption coefficients of the constituent atoms (C, N, H, O), and the positions of hydrogen atoms were determined from difference Fourier syntheses. For visualization of the crystal structures, the program DIAMOND was employed [140].

#### 2.2.1.4 X-ray Diffraction by Powders

X-ray diffraction experiments on powder samples were conducted on two STOE Stadi P diffractometers in focussing geometry using Ge(111)-monochromated Cu- $K\alpha_1$  radiation ( $\lambda = 154.06$  pm) or Ge(111)-monochromated Mo- $K\alpha_1$  radiation ( $\lambda = 70.093$  pm), respectively. Measurements were performed in Debye-Scherrer (capillary) or transmission geometry. The radiation diffracted by the sample was registered by a position sensitive detector with

an opening angle of  $2\theta = 5^\circ$ . Low-temperature measurements (293 K – 100 K) were carried out using Cu–K $_{\alpha 1}$  radiation by adjusting a cooling finger unit connected to a Cryostream Controller (600 series, Oxford Cryosystems) on top of the sample capillary. Evaporation of liquid nitrogen allowed for the realization of different cooling rates ( $1 - 10 \text{ K min}^{-1}$ ) and a minimum temperature of 100 K.

High-temperature *in situ* X-ray diffractometry was performed using Mo–K $_{\alpha 1}$  radiation with an integrated furnace, and unsealed silica glass capillaries (Hilgenberg,  $\varnothing_{ext.}$  0.5 mm) as sample containers. If limited pressure build-up by evolving reaction gases was desirable, the capillaries were closed according to a method developed by Rannabauer [141]. The data collection was restricted to a  $2\theta$  range of approximately  $3 - 20^\circ$  and an average scan collection time of 20 – 40 minutes. The samples were heated from 293 K to temperatures around 973 K in steps of  $10 - 15 \text{ K min}^{-1}$ , using heating rates of 20 or  $50 \text{ K min}^{-1}$  between the scans.

### 2.2.1.5 Electron Diffraction

For general aspects of electron microscopy and electron diffraction (ED), see refs. [130,131,142] and general textbooks.

**General Remarks** The interaction of electrons with matter substantially differs from that of X-rays, which gives rise to both assets and drawbacks. In the following, some general aspects distinguishing the two techniques will be highlighted in brief:

- Electrons have much shorter wavelenghts than X-rays commonly used for structure elucidation purposes.
- Electrons interact with matter much stronger than X-rays, because they interact with both the nucleus and the electrons of the scattering atoms through Coulomb forces. Therefore, crystals which are several orders of magnitude smaller than those required for single-crystal X-ray diffraction can be analyzed by electron crystallography. ED can therefore significantly extend the range of samples amenable to structure analysis by single-crystal X-ray diffraction.
- The strong interaction of electrons with matter gives rise to multiple scattering and non-linear effects due to the interference of different scattered waves, rendering the relation between diffraction images and projected potentials rather complex (see below).
- Owing to the interaction of electrons with matter *via* Coulomb interactions, they detect the electrostatic potential distribution in crystals, rather than the electron density dis-

tribution as do X-rays. Therefore, particular issues, which are related to the potential distribution, such as the oxidation states of atoms in crystals, may be addressed.

- Electron beams are easily directed and focused by magnetic lenses, as they are charged particles.

**Multiple Scattering** A serious problem in ED is incidental from dynamical scattering effects, which render kinematical diffraction theory no longer appropriate for the analysis of ED images. A possible strategy is to circumvent or at least diminish the influence of multiple scattering and non-linear effects by taking advantage of the following factors [131]:

- **Crystal thickness.** The thinner the crystal, the less multiple scattering occurs.
- **Accelerating voltage of the microscope.** Higher voltage, leading to shorter wavelengths, diminishes multiple scattering effects.
- **Crystal alignment.** Crystal tilt may prevent atoms projecting on top of each other, which also reduces multiple scattering.
- **Size of the unit cell.** Multiple scattering depends on the structure amplitude  $|F(\mathbf{Q})|$  and the magnitudes  $|F(\mathbf{Q} - \mathbf{Q}') \cdot F(\mathbf{Q}')|$  of all possible pairs summing up to  $|F(\mathbf{Q})|$  [131]. In general, larger unit cells, giving rise to more and weaker reflections than smaller ones, are less affected by multiple scattering.
- **Light atom structures.** Weak scatterers generally give rise to weaker potentials and, hence, less multiple scattering.

In the most favorable cases, where several of the above aspects are valid, the amplitude of the wave function  $\Psi_{ex}(\mathbf{Q})$  at the exit surface is roughly proportional to the amplitude of the structure factor of the crystal and, as a result, the diffracted intensity  $I^E(\mathbf{Q})$  is proportional to the square of the structure amplitude

$$I^E(\mathbf{Q}) \propto |F^E(\mathbf{Q})|^2. \quad (2.11)$$

In the above borderline case, a treatment of ED data in the *kinematical approximation* may be justified (“weak phase object approximation”).<sup>1</sup>

---

<sup>1</sup>If required, the simulation of the dynamical intensities can then subsequently be carried out by means of a *multi-slice* calculation based on the *n*-beam dynamical diffraction theory [131].

**Experimental** ED and TEM measurements were carried out on a JEOL 2011 instrument equipped with a tungsten cathode operating at 200 kV. The images were recorded using a TVIPS CCD camera (F114). The sample was finely dispersed by sonication in ethyl alcohol suspension for 30 minutes and a small amount of the suspension was subsequently dispersed on a carbon-coated copper grid in air. The grids were mounted on a single tilt holder with a maximum tilt angle of 30° and subsequently transferred into the microscope. Suitable crystallites were singled out among those yielding diffraction patterns of main poles, typically with the zone axis [001] aligned along the electron beam. The selected-area aperture was adapted in each case to the size of the selected thin crystalline domains.

Precession experiments were conducted using a FEI Tecnai 12 transmission electron microscope with a LaB<sub>6</sub> cathode, operating at 120 kV. A precession angle of approximately 1.7° was applied. The images were recorded on TVIPS 2k CCD camera (F224HD) with 16 bit dynamic range.

Reflection intensities were extracted using the ELD program package [143, 144]; for simulation of the kinematical diffraction patterns the program JSV1.08lite [145] was employed. Calculation of the electron diffraction patterns was done using the programs VEC [146] and JEMS [147]. Structure solution and refinement was carried out using the program SIR-97 [148].

## 2.2.2 Spectroscopic Methods

### 2.2.2.1 Vibrational Spectroscopy

FTIR and Raman measurements were carried out on a Bruker IFS 66v/S FTIR spectrometer (Bruker Analytik GmbH), which is equipped with a FRA 106/S Raman module operating with a Nd:YAG laser system ( $\lambda = 1064$  nm). IR spectra were recorded in an evacuated cell between 400 and 4000  $\text{cm}^{-1}$  (DLATGS detector), Raman spectra of the neat solids were acquired between 0 and 3500  $\text{cm}^{-1}$  (Ge detector). KBr pellets of samples insensitive to air were prepared by pressurizing a finely ground sample / KBr mixture (5 mg sample, 500 mg KBr, desiccator) using a hand press with a press capacity of 10 kN. Pellets of air-sensitive compounds were prepared in a glove-box (MB150-G1 and UniLab,  $\text{O}_2 < 1$  ppm,  $\text{H}_2\text{O} < 1$  ppm, MBraun) in an atmosphere of dry argon (purity grade 4.8, Messer) using dry KBr (623 K, 0.1 Pa). The program OPUS (Bruker Analytik GmbH) [149] served for evaluation of the spectra.

IR spectra of the neat solids ( $650 - 4000 \text{ cm}^{-1}$ ) were recorded in reflection geometry using a Spectrum BXII FT-IR spectrometer (Perkin Elmer) equipped with a DuraSamplIR II diamond ATR device (Smith Detection).

Temperature dependent FTIR measurements were conducted between 450 and 4000  $\text{cm}^{-1}$  on a FTIR Spectrum One spectrometer (Perkin Elmer) using a glass cell (volume approx. 50 mL) closed at each side with KBr windows ( $\mathcal{D}_{ext}$ . 15 mm) to detect the gas spectra under static vacuum (1 Pa initial pressure). Typically, 15 mg of the solid sample was filled into the tubular elongation of the gas cell, which was evacuated and subsequently closed by Young valves, then heated to 743 K ( $1 \text{ K min}^{-1}$ ) by means of a tube furnace (Carbolite) equipped with a 2132 temperature controller (Eurotherm).

### 2.2.2.2 Inelastic and Quasielastic Neutron Scattering

**Quasielastic Neutron Scattering** Quasielastic neutron scattering measurements were performed at the backscattering spectrometer (BSS) at the cold source of the medium flux reactor FRJ-2 reactor in Jülich, Germany. A powdered sample of ammonium dicyanamide  $\text{NH}_4[\text{N}(\text{CN})_2]$  was held in a thin-walled (0.5 mm), slab-shaped aluminium can with an inner spacing of about 1 mm. The spectra were recorded in backscattering geometry using single crystal diffraction of cold neutrons with Bragg angles  $2\theta = 180^\circ$  for monochromatization and energy analysis (“X-X-backscattering spectrometer”), yielding a particularly high energy resolution.

The BSS instrument is designed for inelastic scattering experiments with very small energy transfers in the order of 1  $\mu\text{eV}$ . In order to obtain sufficient intensity, the resolution of momentum transfers  $dQ$  is relaxed. The beam size at the sample approximates to 3.5 cm x 3.5 cm, the neutron flux being in the order of  $10^4 \text{ cm}^{-2} \text{ s}^{-1}$ . A schematic drawing of the BSS in-

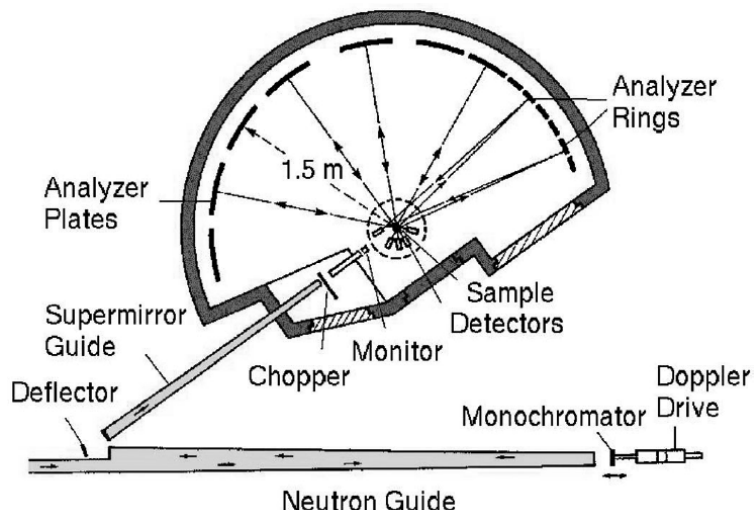


**Figure 2.1:** Schematic representation of the backscattering spectrometer BSS at FRJ-2 in Jülich. A prominent feature is the change of the incident energy by Doppler-shifting the neutron wavelength.

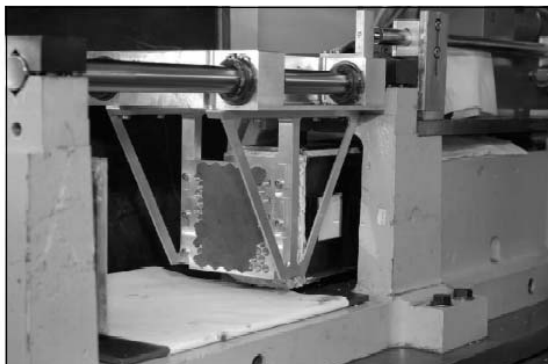
strument is shown in Figure 2.1. A Si(111) single crystal was used as monochromator, corresponding to an incident energy of 2.08 meV and an incident wavelength of 6.271 Å (Fig. 2.2, bottom). The energy transfers are scanned by varying the incident energy whilst keeping the final energy fixed. The change of the incident energy is accomplished by moving the monochromator and thus Doppler-shifting the neutron wavelength.

The backscattered neutrons are deflected by a graphite crystal to the sample. The energy of the scattered neutrons is then analyzed by spherically curved silicon analyzer crystals as shown in Figure 2.2 (top). The latter are adjusted at different scattering angles, and measurements at ten different Q-values could be performed simultaneously.

The energy transfer range for the Si(111) monochromator amounts to  $-15 \mu\text{eV} \leq E \leq 15 \mu\text{eV}$  with an energy resolution between 1.2 and 2.4  $\mu\text{eV}$  (FWHM). The Q-range accessible to the instrument ranges from 0.2 to 1.9  $\text{\AA}^{-1}$  with a Q-resolution between 0.05  $\text{\AA}^{-1}$  and 0.25  $\text{\AA}^{-1}$ . The analyzed neutrons are detected by ten helium counters simultaneously, which are adjusted close to the sample. Neutrons that are directly scattered from the sample into the detectors



Analyzer plates and rings



Monochromator mounted on doppler-drive

**Figure 2.2:** Interior view of the backscattering instrument BSS at FRJ-2 in Jülich. Top: Spherically curved silicon analyzer plates and rings, bottom: Si(111) single crystal monochromator, mounted on the Doppler-drive.

are eliminated by gating the data acquisition according to the phase of the chopper disk. Air scattering is avoided by filling the spectrometer housing with argon during the measurement. Inelastic fixed window scans were conducted between 10 and 380 K ( $\text{NH}_4dca$ ) or 80 and 320 K (transformation product) using a stationary  $\text{Si}_{0.9}\text{Ge}_{0.1}$  (111) monochromator, which in combination with the  $\text{Si}(111)$  analyzer crystals gives rise to an energy offset of  $14.47\text{ }\mu\text{eV}$ . The data fit was carried out by using a Vogel-Fulcher type peak function [150, 151] with the Vogel-Fulcher temperature set to zero. Elastic fixed window scans (stationary Doppler drive) were recorded between 15 and 320 K with the spectrometer set to the elastic position, the finite energy resolution of the spectrometer, which defines the “energy window”, amounting to  $1.3 - 1.8\text{ }\mu\text{eV}$  (FWHM).

The raw data obtained from  $\omega$ -scans between 4.6 K and 400 K were corrected for background and contamination by the sample can as well as detector efficiencies and monochromator misalignment. Multiple scattering or multiphonon corrections were not applied. During the normalization procedure for determining the resolution function, the sample scan at 4.6 K was used instead of a vanadium standard, as the latter systematically underestimated the mean squared displacement parameters of ammonium dicyanamide, yielding negative values for the Debye-Waller factors at low temperatures. Coherent scattering events due to Bragg scattering or phonons may severely deteriorate data evaluation. For most of the measurements it was not possible to exclude those detectors from the fits that were significantly contaminated by coherent scattering contributions. Therefore, the ratio of elastic and quasielastic intensity was not fixed at the theoretical value of 0.66 (cf. 3.2.4 on page 46) according to an isotropic 4-site jump model, but was used as a variable.

Fitting of the data was carried out with the program TOFSYS, which was developed and is maintained by the Institut für Festkörperforschung, Forschungszentrum Jülich GmbH, Germany [152].

**Inelastic Neutron Scattering** Inelastic neutron spectra in the energy region of phonons and librations have been collected at temperatures between 2 and 140 K using the thermal time-of-flight spectrometer SV-29 at the continuous neutron source DIDO of FRJ-2/Jülich, Germany. The scattered neutrons are detected by 500  $^3\text{He}$  counters arranged in 90 units. The range of scattering angles comprises  $10^\circ - 130^\circ$  (solid angle: 0.05 srad). The momentum transfer covered by the instrument amounts to  $\approx 1 - 10\text{ }\text{\AA}^{-1}$ , the energy resolution being  $3\text{ \%}\leq\Delta E/E\leq 8\text{ \%}$ .

The sample was held in a standard aluminum can of length 70 mm, width 30 mm and an inner diameter of  $\approx 1\text{ mm}$  (wall thickness  $\approx 0.5\text{ mm}$ ). The sample holder was oriented at  $135^\circ$  with respect to the incident neutron beam. From the range of possible wavelengths ( $1.0\text{ }\text{\AA}\leq\lambda$

$\leq 4.0 \text{ \AA}$ ), the spectra were measured at incident wavelengths of 1.59 and 1.08  $\text{\AA}$ , allowing for energy transfers up to 25 or 41 meV, respectively, and the raw data were normalized with respect to vanadium. Cooling below room temperature was achieved in all cases using a closed cycle cryostat, and heating was accomplished by using a cryofurnace.

### 2.2.2.3 Solution-state NMR

$^1H$ ,  $^{13}C$  and  $^{14}N / ^{15}N$  NMR spectra were recorded as DMSO- $d_6$  or  $D_2O$  solutions on an Eclipse EX-400 spectrometer (JEOL), the chemical shifts being referenced with respect to TMS ( $^1H$ ,  $^{13}C$ ) and nitromethane ( $^{14}N / ^{15}N$ ) as external standards.

### 2.2.2.4 Solid-State NMR

**Wide-Line NMR** Static powder spectra were obtained on a conventional impulse solid-state NMR spectrometer DSX Avance 500 (Bruker) at a resonance frequency of 76.91 MHz ( $^2H$ ) between 38 and 385 K or 36.149 MHz ( $^{14}N$ ) at 160 and 293 K. Typically, the finely powdered sample of ammonium dicyanamide (150 mg) was filled into ultra precision NMR glass tubes ( $\varnothing$  5 mm, Norell inc., Landisville) in a glove box, covered by a 4 mm glass block as spacer and subsequently sealed off using a fan burner after locking them out of the box.

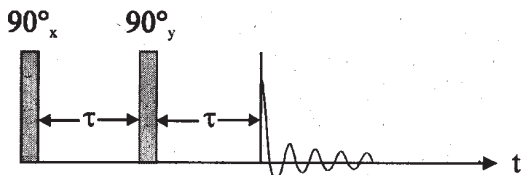


**Figure 2.3:** Pulse scheme of a typical quadrupole solid-echo sequence, composed of two successive, phase-shifted  $90^\circ$  pulses with pulse spacing  $\tau$ .

Low temperature  $^2H$  spectra between 38 K and RT were recorded using a single-resonance low-temperature probe (WB.SOL5, Bruker, Q = 60). The probe was placed in a cryostat STVP-200 (Janis Research), which was cooled with liquid nitrogen or helium below  $\approx 90$  K. For temperatures above RT, a variable temperature single resonance probe (WB.SOL5, Bruker, Q = 90) was used, the heating being effected by a continuous

stream of compressed air or dry nitrogen. The temperature stability was better than  $\pm 1$  K in the whole temperature range, the temperature being accurate to about  $\pm 2$  K. All probes were equipped with a solenoid coil with a diameter of 5 mm. For  $^{14}N$  spectra the single resonance probe (cf. above) was used (Q = 45); the cooling was effected with liquid nitrogen. Wide-line spectra were typically measured applying a standard solid-echo impulse sequence as outlined in Figure 2.3 [153], preceded by a saturation sequence. For suppression of the most frequent artefacts, the phase of the second pulse was cycled by  $\phi \pm 90^\circ$  with respect to the first, and both pulses were phase-cycled by a cycle observation, yielding an eight-step phase cycle. Typical  $90^\circ$  pulse lengths were around 2.5  $\mu\text{s}$  ( $^2H$ ) or 2.0  $\mu\text{s}$  ( $^{14}N$ ) and the

interpulse spacing  $\tau$  was fixed to 20  $\mu$ s for the low temperature spectra and 40  $\mu$ s for the high temperature spectra ( $^2H$ ) or 60  $\mu$ s for  $^{14}N$ . The dwell time was chosen between 0.1 and 2  $\mu$ s ( $^2H$ ) or 0.1  $\mu$ s ( $^{14}N$ ), attaching special attention to an accurate determination of the echo maximum. The recycle delay between the scans was adjusted to 3 – 5 times  $T_1$  as determined by the saturation-recovery method.

For the temperature-dependent studies, the sample was heated in a sealed glass tube with a heating rate of 1 K min<sup>-1</sup> to the respective target temperature between 372 and 380 K. Repeated acquisition at regular intervals was started at room temperature and spectra were typically recorded every 2.5 to 5 minutes during the first three hours after reaching the target temperature, then increasing the repetition delay to 10 minutes. The temperature was stable within  $\pm 0.7$  K, however, the tuning was slightly shifted sporadically and had to be readjusted accordingly between two data acquisitions. The recycle delay between the scans for the high temperature spectra was fixed at 5 s, typically using a total of eight scans per spectrum.

For measuring the spin-lattice relaxation time  $T_1$ , a saturation-recovery sequence was implemented into the solid-echo pulse program with the principal phase cycling being identical to that described above. In the intermediate temperature range (120 K – 160 K) two exponentials were used for fitting the magnetization recovery curves in order to account for a second minor (< 5 %) relaxation process. The data obtained from the major relaxation process were fitted by using a BPP model (cf. Eq. 3.51 in section 3.3.2.7 on page 62).

**High-Resolution NMR**  $^1H$ ,  $^{13}C$  and  $^{15}N$  CP-MAS solid-state NMR spectra were recorded on a DSX Avance 500 and DSX Avance 400 spectrometer (both Bruker) operating at proton resonance frequencies of 500 MHz and 400 MHz, respectively. The samples were contained in 4 mm ZrO<sub>2</sub> rotors, which were mounted in standard double-resonance MAS probes (Bruker). The  $^{13}C$  and  $^{15}N$  signals were referenced with respect to TMS and nitromethane. Data collection of all experiments was performed applying broadband proton decoupling using a TPPM sequence with  $^1H$  pulse lengths of 5 – 6  $\mu$ s [154] and a phase modulation angle of 7.5°.

$^1H$  direct excitation MAS spectra were recorded using three back-to-back 90° pulses to eliminate unwanted contributions from the probe and ringing effects [155]. The recycle delay employed in  $^{13}C$  and  $^{15}N$  CP-MAS or CPPI-MAS measurements was determined by a saturation recovery sequence applied to the  $^1H$  spins, using a proton 90° impulse of 3.2  $\mu$ s.

For the  $^{13}C$  and  $^{15}N$  CP-MAS spectra, a ramped cross-polarization sequence was employed where the  $^1H$  pulse amplitude was decreased linearly by 50 %; typical contact times  $\tau_c$  between 2 ms and 20 ms were chosen. For 1D CP-MAS experiments, a spinning frequency  $\nu_{rot}$  of typically 10 kHz was applied; CPPI experiments were carried out at spinning frequencies between

5 and 6 kHz. 2D CPPI experiments consisting of a sequence of 1D spectra were acquired by varying the inversion time from  $\approx 0.2$  to  $800\ \mu\text{s}$ , or 1D experiments were carried out with a single inversion time of  $100 - 160\ \mu\text{s}$ . Contact times  $\tau_s$  were chosen according to the results of the CP-MAS spectra and typically varied between 2 and 10 ms.

$^{15}\text{N}$  direct excitation spectra of a  $^{15}\text{N}$ -labelled sample of melon were acquired with three back-to-back  $90^\circ$  pulses to eliminate acoustic ringing [155]. The nutation frequency and the recycle delay were adjusted to 75 kHz and 28800 s ( $= 8$  h) – estimated from a  $^{15}\text{N}$   $T_1$  measurement – to ensure total magnetization recovery. In total, 16 scans were collected and the spinning frequency was set to 9 kHz.

To probe homonuclear  $^{15}\text{N}$  connectivities and distances, 2D *fp*-RFDR, as well as a series of modified (1D) *fp*-RFDR experiments, allowing for selective excitation, were performed using a XY-16 phase cycle [156]. For the *fp*-RFDR mixing block, active rotor synchronization was applied with  $\nu_{\text{rot}} = 15$  kHz. The length of the soft (adiabatic)  $180^\circ$  pulse in the middle of each rotor period was adjusted according to  $p(180^\circ) = 0.3 \cdot 1/\nu_{\text{rot}}$ , corresponding to a nutation frequency of 25 kHz. A CP-sequence was implemented prior to the  $180^\circ$ -pulse train, with  $\tau_c = 20$  ms. Broadband proton decoupling was applied during the evolution and acquisition periods using a TPPM sequence [154]. The evolution period was sandwiched between two  $90^\circ$  pulses to store the magnetization of the  $S$ -spins along  $z$ , and for signal detection, respectively. Prior to the last  $90^\circ$  pulse, a zero quantum filter of  $58.87\ \mu\text{s}$  was applied. In the 2D experiment,  $90^\circ$  and  $180^\circ$  pulse lengths on the  $^{15}\text{N}$  channel were  $3.4\ \mu\text{s}$  and  $20.0\ \mu\text{s}$ , respectively and a total mixing time of  $50\ \mu\text{s}$ , as well as a recycle delay of 5 s were used.

To selectively monitor the magnetization transfer from the  $\text{NH}_2$  signal to the surrounding nuclei, a modified version of the 2D experiment was carried out. For selective excitation of the  $^{15}\text{N}$  resonance of the  $\text{NH}_2$ -groups, a CP-sequence with a short CP contact time ( $90\ \mu\text{s}$ ) was used, followed by a comb of two  $90^\circ$  pulses ( $3.4\ \mu\text{s}$ ) on-resonant on the  $\text{NH}_2$ -signal, with an interpulse spacing  $\tau$  between  $280\ \mu\text{s}$  and  $340\ \mu\text{s}$  corresponding to  $\tau = 1/4(\nu(\text{NH}) - \nu(\text{NH}_2))^{-1}$ . By using short contact times, only NH and  $\text{NH}_2$  resonances are noticeably excited, whereas the tertiary nitrogen resonances are suppressed. Afterwards the comb of  $90^\circ$  pulses allows to de-phase the magnetization of the off-resonant resonances while preserving the magnetization of the on-resonant one.

### 2.2.3 Elemental Analysis

Determination of the elements H, C, N, Cl, and S was carried out by the microanalytical laboratory of the Department of Chemistry and Biochemistry, LMU Munich, by oxidative pulping using a commercial elemental analyzer system VARIO EL with He as carrier gas.

### 2.2.4 Mass Spectrometry

Mass spectra were obtained using a MStation JMS-700 spectrometer (JEOL) with a mass resolution  $\geq 1 \text{ } u/e$ . Ions were detected by using the fast atom bombardment technique (FAB). The salt was dissolved in a 3-nitrobenzyl alcohol or glycerol matrix (FAB- / FAB+) on a target and ionized by bombardment with accelerated Xe atoms (6 kV). Electrospray Ionisation (ESI) measurements were conducted on a Finnigan MAT 95Q and a Finnigan MAT 90 mass spectrometer using an API-Interface II with an ESI probe head and a capillary voltage of 2.5 kV. For electron ionization (EI) experiments the typically neutral, yet in certain cases cationic analyte was suspended in methanol and heated on a platinum filament, which is placed in the center of the evacuated ion source ( $< 10^{-4} \text{ Pa}$ ), from 293 to 1073 K ( $120 \text{ K min}^{-1}$ ; direct electron impact, DEI). The sample was subsequently ionized by collisions with energetic electrons (70 eV). Evaluation of the results was accomplished using device-specific software. Temperature dependent direct insertion probes were recorded using DEI with the sample contained in an evacuated ( $10^{-2} \text{ Pa}$ ) Schlenk tube (length 330 mm,  $\varnothing_{ext.}$  10 mm). The tube was connected with the gas inlet system of the spectrometer via connection pieces (glass) of about 200 mm total length, thus providing dynamic vacuum conditions. The Schlenk tube was placed horizontally in a tubular furnace (Carbolite) equipped with a 2132 temperature controller (Eurotherm). The sample was heated up to temperatures between 500 and 723 K in steps of  $1 \text{ K min}^{-1}$ , and mass spectra of the volatile decomposition products were acquired successively at intervals of 2 – 10 degrees.

### 2.2.5 Thermal Analysis

Differential scanning calorimetry was conducted between 250 and 873 K on a DSC 25 (Mettler-Toledo), applying heating rates of  $1 - 10 \text{ K min}^{-1}$ . The aluminum crucible used as a sample container was placed in the calorimeter under an atmosphere of dry nitrogen.

For combined DTA/TG measurements, a thermoanalyzer TGA 92-2400 (Setaram) equipped with DTA gage heads was available. The thermal events were recorded either as a function of time, using experiment times of typically 20 h, or as a function of temperature between 293 and 873 K using heating rates between 1 and  $10 \text{ K min}^{-1}$ . The samples were placed in an unsealed  $\text{Al}_2\text{O}_3$  crucible and the measurements conducted under nitrogen. Evaluation of the results was conducted using device-specific software.

# Chapter 3

## Theoretical Basis and Models

The following chapter provides the theoretical basis necessary for the evaluation of the data obtained from neutron scattering and solid-state NMR spectroscopy. Since a comprehensive treatment of the different sections is available in the literature, only a brief introduction to the essential theoretical background and the models used in this work will be provided.

### 3.1 Classification and Study of Dynamical Processes

Dynamical processes of atoms or molecules may be classified according to different principles, of which the nature of the interaction and the type of motion are the most important ones.<sup>1</sup> Considering the type of interaction, we distinguish *collective* from *non-collective* or *single particle* motion.

For collective processes a phase relationship exists between the motions of many particles contributing to the interaction, as is for instance valid for *coherent* scattering processes (Bragg-scattering) or collective excitations (vibrational modes, phonons). These processes are deterministic and may encode information about the crystal structure of solid materials. Along these lines, neutron diffraction provides access to the probability density function (*pdf*) of the scattering nuclei by tracing the time average of the nuclear density. Therefore, when studying periodic solids, diffraction techniques yield “static” structural information, including the time-average of anisotropic nuclear displacements as expressed by the Debye-Waller factor. Single particle motions comprise both translation and rotation of atoms or molecules, which are uncorrelated and proceed stochastically, such as molecular reorientations. Single particle properties, as for instance associated with the spin-incoherent scatterer hydrogen  $^1H$ , are observed if the spin-dependent scattering lengths of atoms of a given kind, but at different

---

<sup>1</sup>This topic is dealt with in detail by *Press* [157] and *Bee* [158]

positions in the crystal, are statistically independent. This gives rise to *incoherent* scattering without interference of the scattering contributions from different scattering particles.

In neutron scattering, coherent and incoherent scattering is observed simultaneously, however, in most cases with significantly different scattering cross sections, which are governed by the nature of the isotope interacting with the neutron (see below).

In a related manner,  $^2H$  NMR spectroscopy also offers a single-particle perspective on complex dynamical processes owing to the dominant effect of the local quadrupole interaction between the electric field gradient and the deuteron on the NMR spectra. In contrast,  $^1H$  NMR spectroscopy simultaneously maps the interactions between all dipolar coupled proton nuclear spins, thereby yielding typically broad and featureless spectra whose interpretation is still a non-trivial task.

As a consequence,  $^2H$  solid-state NMR is a valuable resource for gaining insight into dynamical processes in solid materials over a broad time scale. The study of fast motions ( $\tau^{-1} = 10^8 - 10^{12}$  Hz) can be addressed by  $T_1$  and  $T_{1Q}$  relaxation measurements, whereas for intermediate time scales ( $10^3 - 10^8$  Hz), line shape simulations of 1D quadrupolar spectra have proven to be exceptionally versatile tools for extracting detailed models of motion for the reorienting species involved. Processes in the slow motion limit ( $\tau^{-1} = 10^{-2} - 10^4$  Hz) can be probed by exchange spectra and stimulated echo techniques [159–162].

By its very nature,  $^2H$  line shape analysis is capable of correlating structural information – as for instance obtained from neutron diffraction – and dynamics by visualizing reorientational processes on an intermediate time scale that is not accessible *in situ* by neutron scattering. However, in and beyond the fast motion limit ( $\tau^{-1} \geq 10^{12}$  Hz) the sensitivity of solid-state NMR to line shape changes decreases, leading to motionally narrowed spectra at high jump frequencies from which no further information on the jump geometry can be extracted.

Quasielastic neutron scattering (QENS) can compensate for this loss of information as it monitors processes with small energy transfers and short correlation times ( $\tau \leq 10^{-8}$  Hz), such as quantum mechanical tunneling, fast molecular rotations or librations. QENS thus provides information complementary to  $T_1$  measurements in terms of the time scale of molecular reorientations, and even has the potential to unveil reorientational geometries in the fast motion limit. However, whereas for  $^2H$  NMR the sensitivity only depends on the value of the quadrupole-coupling constant, that of QENS decreases with a decreasing radius of rotation. QENS is therefore primarily sensitive to large angle jumps and not suited to differentiate between subtle differences in the models of motion.

By combining neutron diffraction, quasielastic neutron scattering, and  $^2H$  NMR spectroscopy, three powerful techniques are at hand by means of which essentially the whole range of re-

**Table 3.1:** Classification of single particle rotations in molecular crystals according to the rotational potential [157].

Fluctuating potential	Strong	Weak
Static potential		
<b>Strong</b>	Rotational jumps	Librations and rotational tunneling
<b>Weak</b>	Rotational diffusion	Quantum-mechanical free rotation

orientational dynamics can be covered.

In this work, the reorientation of the ammonium ion is studied, representing an example of an incoherent single-particle process. As the reorientational motion of a three-dimensional rotor is strongly influenced by its surrounding potential, a simplified classification of single particle rotations in molecular crystals may be accomplished in terms of the rotational potential as outlined in Table 3.1 [157].

Strong fluctuating potentials are effected by high temperatures and thus frequent transitions between rotational states and phonon states occur. Strong static potentials are observed predominantly in ionic compounds, whereas weak static potentials prevail in so-called van-der-Waals-type crystals.

Two important, extreme cases of stochastic dynamic disorder may be highlighted: Continuous, diffusive motion is characterized by the diffusional constant  $D_r$ . This type of motion, which is observed in the presence of weak or neglectable static potentials, is continuous in its angular variables and entirely undirected. In the limit of very strong static potentials the molecules are confined to a discrete number of equilibrium orientations which are occupied at random. Transitions across the barriers separating the equilibrium orientations occur by thermally activated jumps (*jump diffusion* or *molecular reorientation*). These jumps are characterized by their correlation time  $\tau$  and jump distance  $R$ , where the jumping time is assumed to be infinitesimally short.

## 3.2 Neutron Scattering

In this thesis, quasi- and inelastic neutron scattering experiments were carried out with the focus on the analysis of molecular reorientations. Neutron diffraction has been employed previously for a complementary characterization of the processes described in the present work [122, 163], and X-ray diffraction techniques represent the backbone of this thesis since they have become indispensable as the most important routine analytical tools in modern solid-state chemistry. Therefore, diffraction will also be briefly discussed in the context of scattering theory.<sup>2</sup>

### 3.2.1 Basic Principles

Scattering processes can either proceed under conservation of energy (*elastic*), or with a change in energy (*inelastic*). A schematic drawing of a scattering experiment is given in Figure 3.1.

<sup>2</sup>For disquisitions on neutron scattering see *Squires* [164] or *Lovesey* [165]. Theory and applications of quasielastic neutron scattering are discussed by *Bee* [158]. A comprehensive treatment of thermal vibrations and lattice dynamics has been given in the monograph by *Willis and Pryor* [166].

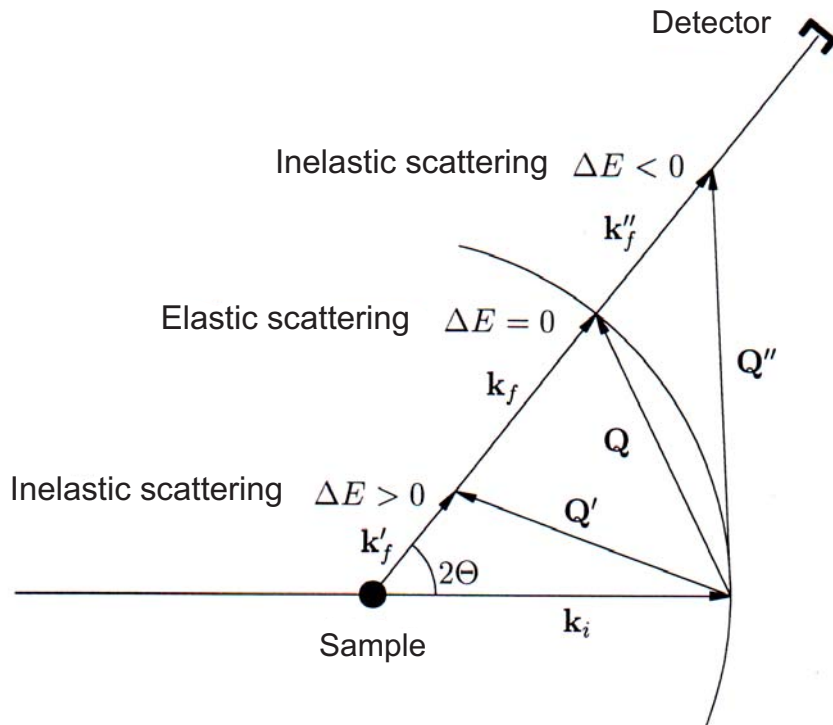


**Figure 3.1:** Schematic representation of the scattering geometry.  $k_i$  ( $i$  = “incident”) is the wave vector of an incident neutron,  $k_f$  and  $k_f'$  /  $k_f''$  ( $f$  = “final”) denote wave vectors of elastically and inelastically scattered neutrons, respectively.  $2\theta$  is the scattering angle. The figure has been adopted from ref. [167].

The relevant parameters of a scattering experiment are given by

$$\Delta E = \hbar\omega = E_f - E_i, \quad (3.1)$$

$$\mathbf{Q} = k_f - k_i, \quad (3.2)$$

where  $\Delta E$  is the energy transfer and  $\mathbf{Q}$  is the wave vector transfer from the initial state  $i$  to the final state  $f$ .

The scattering experiment gives access to the partial differential cross section  $d^2\sigma/d\Omega dE$  representing the number of neutrons of initial energy  $E_i$ , which are scattered with final energy  $E_f$  in the energy interval  $[E_f, E_f + dE]$  into a solid angle element  $d\Omega$ . The total spin state of the scattering particle and the neutron determines the type of interaction. Thus, the properties of coherent and incoherent scattering result from the spin-independent (si) and spin-dependent (sd) parts of the interaction, respectively. The scattering cross section can be divided into a coherent and an incoherent part, the sum of which is detected in a scattering experiment:

$$\sigma = \sigma_{coh} + \sigma_{inc} = 4\pi b_{si}^2 + 4\pi b_{sd}^2, \quad (3.3)$$

where  $b$  denotes the scattering length.

The partial differential cross section is proportional to the scattering function  $S(\mathbf{Q}, \omega)$  under the assumption that only a small fraction of the neutrons is scattered (first Born approximation):

$$\frac{d^2\sigma}{d\Omega dE} = \frac{k_i}{k_f} S(\mathbf{Q}, \omega), \quad (3.4)$$

where the scattering function is the sum of the coherent and incoherent parts:

$$\frac{d^2\sigma}{d\Omega dE} = \frac{N}{4\pi} \frac{k_i}{k_f} [\sigma_{coh} S_{coh}(\mathbf{Q}, \omega) + \sigma_{inc} S_{inc}(\mathbf{Q}, \omega)]. \quad (3.5)$$

Within the scope of the *van Hove* formalism [168] which is usually applied in the classical high-temperature regime ( $|\Delta E| \ll k_B T/2$  and  $\hbar^2 Q^2/(2M) \ll k_B T/2$  ( $M$  = mass of scattering particle)), the coherent and incoherent scattering functions are the Fourier transforms with respect to time and space of the classical pair- or self-correlation functions  $G(\mathbf{r}, t)$  and  $G_S(\mathbf{r}, t)$ , respectively:

$$S_{coh}(\mathbf{Q}, \omega) = \frac{1}{2\pi} \int_{-\infty}^{\infty} \int_{-\infty}^{\infty} G(\mathbf{r}, t) e^{-i\omega t} e^{i\mathbf{Q} \cdot \mathbf{r}} d\mathbf{r} dt, \quad (3.6)$$

$$S_{inc}(\mathbf{Q}, \omega) = \frac{1}{2\pi} \int_{-\infty}^{\infty} \int_{-\infty}^{\infty} G_S(\mathbf{r}, t) e^{-i\omega t} e^{i\mathbf{Q} \cdot \mathbf{r}} d\mathbf{r} dt. \quad (3.7)$$

The pair correlation function  $G(\mathbf{r}, t)$  gives the probability of finding a given particle with index  $j$  at the position  $\mathbf{r}$  at time  $t$ , if the reference particle with index  $\theta$  was at  $\mathbf{r} = 0$  (origin) at time  $t = 0$ . The self-correlation function  $G_S(\mathbf{r}, t)$  encodes the probability of finding a given particle at the position  $\mathbf{r}$  at time  $t$ , if it was at  $\mathbf{r} = 0$  at  $t = 0$ .

### 3.2.2 Diffraction

Diffraction experiments provide information on the crystal structure of a compound by delivering the time and space average of the structure. The latter includes the three-dimensional periodicity as well as the thermal displacement of the atoms from their equilibrium positions. Information is obtained by the interference of the waves scattered by the constituent atoms and is thus given by the coherent scattering length  $b_{coh}$ , which is specific of a given isotope. The coherent scattering cross section of deuterium is significantly larger than that of hydrogen, the high (spin-)incoherent scattering cross section of the latter yielding a high, poorly structured background.

Neutron diffraction is therefore preferably conducted with deuterated samples; only the coherent scattering function is discussed in the following. Neutron scattering lengths as well as scattering cross sections of the isotopes relevant to this thesis are listed in Table 3.2.

In neutron diffraction measurements no energy analysis is carried out, rendering the

*Table 3.2: Coherent scattering lengths and scattering cross sections of selected elements according to Bee [158].*

Element or Isotope	$b_{coh}$ / fm <sup>a</sup>	$\sigma_{coh}$ / barn <sup>b</sup>	$\sigma_{inc}$ / barn <sup>b</sup>
H	-3.74	1.76	79.91
D	6.67	5.60	2.04
N	9.36	11.01	0.49

<sup>a</sup> 1 fm =  $10^{-15}$  m

<sup>b</sup> 1 barn =  $10^{-24}$  cm<sup>2</sup>

differential cross section

$$\frac{d^2\sigma}{d\Omega} = \int_{-\infty}^{\infty} \frac{d^2\sigma}{d\Omega dE} dE = S_c(\mathbf{Q}) + S_d(\mathbf{Q}), \quad (3.8)$$

where  $\mathbf{Q} = 2k_i \sin[(2\theta)/2]$  is the wave vector transfer of the elastic scattering and  $S_c(\mathbf{Q})$  is the *elastic* coherent part of the scattering function, representing the Bragg scattering of a sample. The *inelastic* coherent portion  $S_d(\mathbf{Q})$  describes the thermal diffuse scattering and will not be considered further.

The reflection intensity  $I(\mathbf{Q})$  of a diffraction experiment is proportional to the scattering function  $S_c(\mathbf{Q})$ , which is equal to the squared structure factor  $|F(\mathbf{Q})|^2$ .

$$S_c(\mathbf{Q}) = |F(\mathbf{Q})|^2 \propto I(\mathbf{Q}), \quad (3.9)$$

$$F(\mathbf{Q}) = \sum_{\kappa=1}^N b_{\kappa} T_{\kappa}(\mathbf{Q}) \cdot \exp[i\mathbf{Q} \cdot \mathbf{r}(\kappa)]. \quad (3.10)$$

In fractional coordinates (xyz) of the atoms in the unit cell, the structure factor reads

$$F_{hkl} = \sum_{\kappa=1}^N b_{\kappa} T_{\kappa}(\mathbf{Q}) \cdot \exp[2\pi i(hx(\kappa) + ky(\kappa) + lz(\kappa))], \quad (3.11)$$

where  $b_{\kappa}$  denotes the coherent scattering length of atom  $\kappa$  and  $(hkl)$  the Miller indices. The temperature factor  $T_{\kappa}(\mathbf{Q})$  describes the attenuation of the scattering intensity by thermal movements of the atoms.<sup>3</sup>

### 3.2.3 Quasielastic Neutron Scattering (QENS)

The study of molecular reorientations and translations is a major domain of incoherent quasielastic neutron scattering, involving energy transfers in an energy interval of approximately  $-2 \text{ meV} \leq \Delta E \leq 2 \text{ meV}$ , which corresponds to a temperature of  $T \approx 23 \text{ K}$ . If the measurements are conducted at higher temperatures as in the present work, the scattering function can be calculated in the *van Hove* approximation (3.2.1). QENS allows for the characterization of the time and spatial dependence of a motional process.

If the neutron scattering experiments are carried out by using hydrogen-containing samples, all coherent and also incoherent contributions of isotopes other than hydrogen are significantly smaller (Table 3.2).

<sup>3</sup>For a detailed treatment of thermal vibrations in crystallography, see the monograph by *Willis and Pryor* [166].

Assuming that the energies due to internal molecular vibrations, translational movements of the center of mass, and molecular reorientations are entirely uncorrelated and thus separable, the incoherent structure factor can be divided into two parts:

$$S_{inc}(\mathbf{Q}, \omega) = S_{inc}^{rot}(\mathbf{Q}, \omega) + S_{inc}^i(\mathbf{Q}, \omega). \quad (3.12)$$

The inelastic part  $S_{inc}^i(\mathbf{Q}, \omega)$  contains contributions of internal excitations which are usually not located in the energy range of quasielastic scattering. It therefore contributes to the measured spectra at larger energy transfers. However, acoustic phonons typically give a sloping background in the region  $\omega \approx 0$ , which can cause substantial problems for large widths of the quasielastic distribution.  $S_{inc}^{rot}(\mathbf{Q}, \omega)$  only includes the rotational part of the motional process. The latter can further be subdivided into elastic and quasielastic components, yielding

$$S_{inc}^{rot}(\mathbf{Q}, \omega) = \exp[-\langle u^2 \rangle_H \cdot Q^2] \left( EISF(\mathbf{Q})\delta(\omega) + S_{inc}^{quasi}(\mathbf{Q}, \omega) \right), \quad (3.13)$$

where the *elastic incoherent structure factor*, EISF, has been introduced. The EISF contains spatial information and gives rise to an elastic line ( $\hbar\omega = 0$ ) in the spectra.  $\langle u^2 \rangle_H$  is the mean square displacement of the hydrogen atoms and  $\exp[-\langle u^2 \rangle_H \cdot Q^2]$  represents the Debye-Waller factor.

The quasielastic part  $S_{inc}^{quasi}(\mathbf{Q}, \omega)$  encodes both spatial and time information about the system and contributes a broad distribution of excitation energies, given by a  $Q$ -independent sum of Lorentzians. The sum of the EISF( $\mathbf{Q}$ ) and  $S_{inc}^{quasi}(\mathbf{Q})$  is independent of the model of motion. The signal intensity is attenuated by action of the Debye-Waller factor due to the thermal movements of the atoms. The  $Q$ - and energy dependence of the structure factor provides valuable information on the geometry of the underlying motional processes. The scattering functions for some simple reorientational jump models utilized in this work will be introduced in the following section. The difference between the jump models and the models for rotational diffusion under the influence of a static potential gain significance only at large wave vector transfers ( $QR \geq 2$ ) [157, 158, 169, 170]. Since owing to the measurement geometry only a  $Q$ -range from about 0.2 to 1.9  $\text{\AA}^{-1}$  was covered by the experiments discussed in the present work, a differentiation between simple jump models and rotational diffusion was not possible. Since the vectorial properties of the scattering function are lost by the powder average, the scattering function will henceforth be referred to as  $S(Q, \omega)$  instead of  $S(\mathbf{Q}, \omega)$ .

### 3.2.4 Motional Models

For a quantitative description of incoherent scattering the scattering contributions of single particles are summed up; hence, the incoherent scattering function  $S(Q, \omega)$  for the ammonium ion can be deduced by simply considering the motion of a single hydrogen atom. On this background, the rotational motion of the ammonium group can be regarded equivalent to jumps of a hydrogen atom between equivalent sites. In the following, the jumps are assumed to be instantaneous, where  $\tau$  represents the average residence time in one of the equilibrium positions. Starting from rate equations, the *intermediate* scattering function and, by Fourier transformation, the scattering function, can be calculated directly.

For the ammonium ion in ammonium dicyanamide, only two motional models will be considered. As will be outlined in Chapter 4.1 on page 71, rotational diffusion can be neglected, as can  $90^\circ$  jumps around the  $C_2$  axes of the tetrahedron, since no evidence for more than four equilibrium positions has been found by neutron powder diffraction [122, 163]. Thus, only jumps around a *fixed* threefold or twofold axis, both yielding indistinguishable scattering functions (**model 1**), and random jumps around *any* of the two- and/or threefold axes (**model 2**) will be briefly discussed. For **model 1**, the form of the scattering function is predicted as follows [171–174]:

$$S_{inc}^{rot}(Q, \omega) = \exp(-2W) \left\{ \frac{1}{2} [1 + j_0(QR_H)] \delta(\omega) + \frac{1}{2\pi} [1 - j_0(QR_H)] \frac{3/2\tau}{(3/2\tau)^2 + \omega^2} \right\}. \quad (3.14)$$

**Model 2** reads

$$S_{inc}^{rot}(Q, \omega) = \exp(-2W) \left\{ \frac{1}{4} [1 + 3j_0(QR_H)] \delta(\omega) + \frac{3}{4\pi} [1 - j_0(QR_H)] \frac{1/\tau}{(1/\tau)^2 + \omega^2} \right\}, \quad (3.15)$$

where  $\exp(-2W)$  is the Debye-Waller factor,  $j_0(X)$  the zeroth order Bessel function of the first kind ( $j_0(X) = \sin(X)/X$ ),  $R_H$  the interproton distance and  $Q$  the wave vector transfer. On comparison with Eq. 3.13, the expressions  $\frac{1}{2} [1 + j_0(QR_H)]$  and  $\frac{1}{4} [1 + 3j_0(QR_H)]$  can be identified with the EISF.

From the above equations it gets evident that the relative intensities of the elastic and quasielastic components depend on the model for the geometry of reorientational motion. The width of the quasielastic component, on the other hand, depends both on the model and the correlation time  $\tau$ . For very small correlation times (residence times), the Lorentzian will broaden and finally merge into the background, thus placing a lower limit to the correlation times observable by the experiment. The upper limit is given by the instrumental resolution: if  $\tau$  is larger than a particular period of time (typically in the nanosecond range),

the quasielastic component will be so narrow that it merges into the instrumental resolution function, that is, the  $\text{NH}_4^+$  group will appear rigid.

### 3.2.5 EISF

The EISF, which was defined in Equation 3.13, provides a link between dynamical models introduced on the basis of QENS data and the static density distribution obtained by neutron scattering. As outlined above, the EISF corresponds to the time-independent component of the autocorrelation function and therefore represents the time averaged distribution of the scattering density of all particles in the sample [158]. For protonated samples the EISF can essentially be described in good approximation as the Fourier transform of the hydrogen density distribution. The EISF is only observed for spatially confined motions such as rotational reorientations as discussed here. For non-confined motions such as translational diffusion, the EISF vanishes.

The same time average of the density distribution of all librating and reorienting molecules is observed in neutron diffraction experiments. The corresponding parameter is known as the Fourier transform of the deuteron *pdf* (probability density function).

### 3.3 Nuclear Magnetic Resonance

Nuclear magnetic resonance spectroscopy has been utilized in this work both as a probe for dynamical processes in the solid state, and as an aid for structure elucidation in polycrystalline and semi-amorphous materials.

In the following sections, a brief outline of the basic principles encountered in solid-state NMR spectroscopy will be given, with the emphasis on those interactions relevant to deuteron magnetic resonance and typical experiments probing the magnetic response of diluted spin-1/2 nuclei (denoted  $S$  in the following; abundant spins (protons) will be termed  $I$ ) such as  $^{13}C$  or  $^{15}N$ . For a detailed treatment of the principles and potential applications of NMR spectroscopy, see for instance refs. [175–177].

#### 3.3.1 Basic Principles

NMR spectroscopy is one of the most powerful techniques for investigating the two principal “states” of solid materials, namely static structure and dynamics. The basis of this capability is the particular form of the nuclear spin Hamiltonian, which for an arbitrary spin-system is given as the sum of two parts [175–178]:

$$\hat{H} = \hat{H}_{ext} + \hat{H}_{int}. \quad (3.16)$$

$\hat{H}_{ext}$  includes interactions with external fields (Zeeman interaction  $\hat{H}_Z$ ) or with the magnetic part of radio frequency pulses ( $\hat{H}_{rf}$ ).  $\hat{H}_{int}$  accounts for interactions with internal fields, couplings with the local environment (chemical shift interaction  $\hat{H}_{CS}$ , spin-rotation interaction  $\hat{H}_{SR}$ , quadrupolar interaction  $\hat{H}_Q$ ), or couplings with other spins (homo- and heteronuclear dipolar interactions  $\hat{H}_D$ , scalar interactions  $\hat{H}_J$ ). Thus, the Hamiltonian is given by

$$\hat{H} = \hat{H}_Z + \hat{H}_{rf} + \hat{H}_{CS} + \hat{H}_{SR} + \hat{H}_Q + \hat{H}_D + \hat{H}_J. \quad (3.17)$$

The Zeeman interaction only depends on the gyromagnetic ratio  $\gamma$ , which is characteristic for each nucleus, and the external magnetic field  $\mathbf{B}_0$ . The Zeeman Hamiltonian is therefore given by

$$\hat{H}_Z = -\omega_0 \hat{I}_Z, \quad (3.18)$$

where  $\omega_0 = \gamma \mathbf{B}_0$ .

The internal terms may all be regarded as first order perturbations of the Zeeman Hamiltonian and as such are a function of the internal structure and microscopic dynamics of a sample.

Each of these anisotropic interactions can be represented by a diagonal, time independent second rank tensor  $\underline{\underline{R}}^\lambda$  in an appropriate principal axis system (PAS). A detailed discussion of the different terms of Eq. 3.17 will be given in section 3.3.2. Conveniently,  $\underline{\underline{R}}^\lambda$  is decomposed into an isotropic part  $\underline{\underline{R}}^{(0)}$ , which is invariant under rotation, as well as into an antisymmetric ( $\underline{\underline{R}}^{(1)}$ ) and a symmetric part ( $\underline{\underline{R}}^{(2)}$ ), both of which are traceless and represent the anisotropic properties of the interaction. Besides the isotropic part  $\underline{\underline{R}}^{(0)}$ , which exclusively determines the NMR spectra of liquids, only  $\underline{\underline{R}}^{(2)}$  is relevant to most solid-state NMR experiments, since  $\underline{\underline{R}}^{(1)}$  can usually be neglected as it does not contribute in first-order perturbation. In its PAS, the tensor  $\underline{\underline{R}}^{(2)}$  is characterized by a coupling constant  $\delta_\lambda$  as well as an asymmetry parameter  $\eta_\lambda$ , which encode the relative magnitudes of the principal axes and are thus given by the internal properties only.

However, the observed spectral features (signal shape and position) also depend on the orientation of the interaction tensors with respect to  $\mathbf{B}_0$ , which is expressed by rotating  $\underline{\underline{R}}^{(2)}$  into the laboratory fixed axis system (LAS) by using so-called *Euler transformations* based on the axis triple  $(\alpha, \beta, \gamma)$ .

Spectra of powdered samples are intrinsically affected by the random distribution of the orientation of each interaction tensor, which typically leads to broad line-shapes as demonstrated in Figure 3.2. Whereas many-body interactions, such as dipolar coupling, often give rise to broad, featureless spectra (Fig. 3.2, (c)), interactions with single-particle character, such as the chemical shift or quadrupole coupling, yield characteristically structured resonance lines (Fig. 3.2, (a) + (b)). In addition, dynamical processes often lead to characteristic changes of the line shape as a function of the correlation time, and at the same time may provide direct information about the orientational distribution function.

While being the key to a variety of information that can be extracted from solid-state NMR as compared to solution NMR spectra, the combined orientation dependence of the interaction tensors typically leads to poor spectral resolution on the one hand; on the other hand it necessitates a unified description using irreducible spherical tensor notation, which will be made use of in the following sections [179].

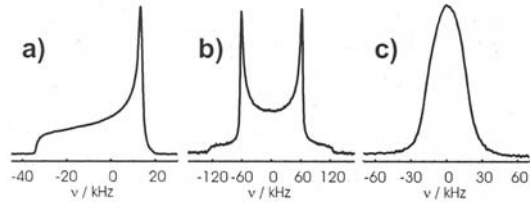


**Figure 3.2:** Typical static powder spectra, which are dominated by a single type of interaction. (a) Chemical shift anisotropy; (b) quadrupole interaction; (c) homonuclear dipolar interaction. The picture was taken from ref. [178].

### 3.3.2 Interaction Hamiltonians and Operator Formalism

The interpretation of solid-state NMR spectra may be complicated owing to the interplay of different internal interactions as well as the orientational dependence of the resonance frequency as outlined above. In convenient cases, however, the spectra are dominated by a single type of interaction, as for example in the case of quadrupolar magnetic resonance. For less abundant spins such as  $^{13}C$  or  $^{15}N$ , the chemical shift interaction typically outweighs other interactions such as the homo- or heteronuclear dipolar couplings between  $S$  spins, since owing to the low gyromagnetic ratio of these nuclei the already weak couplings can be eliminated by applying MAS using moderate spinning frequencies. The dipolar interactions with protons can be efficiently suppressed using well-established decoupling techniques, such as continuous wave or TPPM decoupling, by which the heteronuclear dipolar coupling is made time-dependent and is therefore selectively averaged out under MAS conditions.

In the following, we will therefore delineate the mathematical notation used for the different types of interactions as given by Eq. 3.17 separately. Note that the expression for the Zeeman Hamiltonian  $\hat{H}_Z$  has already been introduced by Eq. 3.18. A discussion of the spin-rotation Hamiltonian  $\hat{H}_{SR}$  will be omitted, as will a treatment of the *indirect* dipolar and scalar interactions. The strength of these couplings are usually small and are covered by the corresponding *direct* interactions. The quadrupole interaction is the one most relevant in this thesis and will therefore be given special attention.

#### 3.3.2.1 Chemical Shift Interaction

The chemical shift  $\sigma$  is based on the coupling of the nuclear spin with magnetic fields induced by the cyclic movement of the surrounding electrons. It is therefore associated with a characteristic change of the local magnetic field experienced by a nucleus and, thus, a sensitive probe of the chemical environment of each magnetically inequivalent spin. The Hamiltonian  $\hat{H}_{CS}$  can be written as

$$\hat{H}_{CS} = \gamma \cdot \hat{I} \cdot \underline{\underline{\sigma}} \cdot \mathbf{B}, \quad (3.19)$$

where  $\underline{\underline{\sigma}}$  is a second rank tensor and  $\hat{I}$  is defined as vector operator  $\mathbf{I} = (I_x I_y I_z)$ . The orientational dependence of the principal axis system of the chemical shift tensor with respect to the laboratory axis system is given by the secular part of  $\hat{H}_{CS}$  as:

$$\hat{H}_{CS} = -\omega_0 \cdot \hat{I}_z \cdot \left\{ \sigma_{iso} + \frac{1}{2} \delta (3 \cos^2 \theta_{LP} - 1 + \eta \sin^2 \theta_{LP} \cos(2\phi_{LP})) \right\}, \quad (3.20)$$

where

$$\begin{aligned}\sigma_{iso} &= \frac{1}{3}(\sigma_{xx} + \sigma_{yy} + \sigma_{zz}), \\ \delta_{CS} &= \frac{2}{3}(\sigma_{zz} - \frac{1}{2}(\sigma_{yy} + \sigma_{xx})), \\ \eta &= \frac{\sigma_{xx} - \sigma_{yy}}{\sigma_{zz}} \quad \text{where} \quad |\sigma_{zz}| > |\sigma_{yy}| > |\sigma_{xx}|.\end{aligned}$$

$\theta_{LP}$  und  $\phi_{LP}$ , which are equivalent to the Euler angles  $\beta$  and  $\alpha$ , respectively, denote the polar angles between the  $z$ -axis of the external magnetic field and the  $z$ -axis of the PAS. According to the general properties of the coupling tensors as outlined above, the chemical shift tensor  $\underline{\sigma}$  is a superposition of an isotropic part  $\sigma_{iso} = \frac{1}{3}Tr(\underline{\sigma})$ , yielding the isotropic chemical shift, and of an anisotropic part, which is a function of  $\delta_{CS}$ ,  $\eta_{CS}$ , and the orientation of the chemical shift tensor with respect to  $\mathbf{B}_0$ . The latter part is closely related to the width and symmetry of the powder spectra. For axially symmetric systems,  $\sigma_{xx} = \sigma_{yy}$  and, thus, the asymmetry parameter  $\eta$  becomes zero.

For protons in diamagnetic materials the relevant chemical shift region is rarely larger than 10 – 15 ppm, implying that effects of chemical shift anisotropy (CSA) for deuterons are usually small enough to be ignored. In contrast, significantly larger values for  $\delta$  and  $\sigma$  can be found in paramagnetic systems.

### 3.3.2.2 Dipolar Interaction

The dipolar interaction arises from the through-space coupling of nuclear spins *via* their magnetic moments. The dipolar Hamiltonian  $\hat{H}_D$  is divided into a homonuclear part, based on the interaction of spins of a single isotope, and a heteronuclear part, if nuclei of different sorts are involved. By dividing the nuclear moments into pairs of spins  $i$  and  $j$ , the dipolar Hamiltonian  $\hat{H}_D$  is given by summation over all possible combinations of spin pairs  $ij$ .  $\hat{H}_{D,ij}$  is traceless and symmetric, and is thus equal to  $\underline{\underline{R}}_{ij}^{(2)}$  according to the terminology used above. The Hamiltonian for a spin pair, using irreducible spherical tensor notation to account for any arbitrary orientations in the LAS, is given by an equation similar to that for the quadrupole Hamiltonian:

$$\hat{H}_D = \sum_{m=-2}^2 (-1)^m A_{2-m}^D T_{2m}^D. \quad (3.21)$$

The spin operators  $A_{lm}^D$  are defined as

$$\begin{aligned}
 A_{20}^D &= \frac{1}{\sqrt{6}} \left( 3\hat{I}_Z \hat{S}_Z - \hat{I} \hat{S} \right), \\
 A_{2\pm 1}^D &= \pm \frac{1}{\sqrt{2}} \left( \hat{I}_Z \hat{S}_\pm + \hat{I}_\pm \hat{S}_Z \right), \\
 A_{2\pm 2}^D &= \hat{I}_\pm \hat{S}_\pm,
 \end{aligned} \tag{3.22}$$

where  $I_\pm = \hat{I}_x \pm i\hat{I}_y$ .

The lattice variables  $T_{lm}^D$  are given as

$$T_{2m}^D(LAS) = \sum_{k=-2}^2 D_{mk}^{(2)*}(\Omega_{LP}) T_{2k}^D(PAS), \tag{3.23}$$

where

$$T_{20}^D(PAS) = -\sqrt{6}\hbar\gamma_I\gamma_S r_{IS}^{-3}, \tag{3.24}$$

$$T_{2\pm 1}^D(PAS) = T_{2\pm 2}^D(PAS) = 0,$$

and  $r_{IS}$  is the internuclear distance between spins  $I$  and  $S$ .  $\Omega_{LP}$  represents the Euler angles  $(\alpha_{LP}, \beta_{LP}, \gamma_{LP})$  by which the LAS is rotated into the PAS.  $D_{mk}^{(2)*}(\Omega_{LP})$  denotes the complex conjugated Wigner-Rotation matrices according to *Rose*, which are tabulated in ref. [180].

The combined Hamiltonian  $\hat{H}_0 = \hat{H}_Z + \hat{H}_D$  is obtained by retaining only the secular part of  $\hat{H}_D$ , i.e. the part which commutes with  $\hat{H}_Z$ . Thus, in first order perturbation theory, only the irreducible tensor operator  $A_{20}^D$  contributes to the energy correction of the Zeeman energy levels. For homonuclear dipolar interactions, the complete operator  $A_{20}^D$  commutes with the zeroth order Zeeman Hamiltonian, yielding

$$\hat{H}_D^{II'} = -\frac{1}{2} \left( \frac{\gamma_I \gamma_{I'} \hbar}{r_{II'}^3} \right) \cdot \left( \frac{\mu_0}{4\pi} \right) \cdot (3\cos^2\theta_{LP} - 1) \left( 3\hat{I}_Z \hat{I}'_Z - \hat{I} \hat{I}' \right). \tag{3.25}$$

In the heteronuclear case, the secular part of  $A_{20}^D$  reduces to  $\frac{2}{\sqrt{6}}\hat{I}_Z \hat{S}_Z$ :

$$\hat{H}_D^{IS} = -\frac{1}{2} \left( \frac{\gamma_I \gamma_S \hbar}{r_{IS}^3} \right) \cdot \left( \frac{\mu_0}{4\pi} \right) \cdot (3\cos^2\theta_{LP} - 1) \left( 2\hat{I}_Z \hat{S}_Z \right). \tag{3.26}$$

### 3.3.2.3 Quadrupole Interaction

The quadrupole interaction arises from the coupling of the nuclear quadrupole moment of a nucleus with the electric field gradient tensor of the electron density at the position of the nucleus. This type of interaction is only observed for spins with  $I > 1/2$ . The Hamiltonian of the quadrupolar interaction energy is obtained by a classical multipole expansion of the electrostatic energy of a nuclear charge in the electric field of its environment. Taking into account the quantization of the spin angular momentum, the Hamiltonian is given by the coupling of the angular momentum vector operator  $\hat{I}$  with a Cartesian second rank tensor:

$$\hat{H}_Q = \hat{I} \underline{\underline{Q}} \hat{I}^T = \frac{eQ}{2I(2I-1)\hbar} \cdot \hat{I} \underline{\underline{V}} \hat{I}^T, \quad (3.27)$$

where  $e$  is the proton charge and

$\underline{\underline{Q}}$ : quadrupole coupling tensor,

$Q$ : quadrupole moment,

$\underline{\underline{V}}$ : electric field gradient tensor.

$\underline{\underline{Q}}$  and  $\underline{\underline{V}}$  are symmetric and traceless tensors of second rank. In its PAS, the quadrupole coupling tensor is expressed in Cartesian coordinates as follows:

$$\underline{\underline{Q}} = \frac{e^2 q_{zz} Q}{2I(2I-1)\hbar} \begin{pmatrix} -\frac{1}{2}(1-\eta) & 0 & 0 \\ 0 & -\frac{1}{2}(1+\eta) & 0 \\ 0 & 0 & 1 \end{pmatrix} \quad (3.28)$$

with

$$eq_{zz} = V_{zz}, \\ \eta = \frac{V_{xx} - V_{yy}}{V_{zz}}, \quad \text{where} \quad |V_{zz}| \geq |V_{yy}| \geq |V_{xx}|.$$

It is evident that for a complete description of  $\underline{\underline{Q}}$ , two parameters, the electric field gradient  $q$  as well as the asymmetry parameter  $\eta$ , are sufficient.

To account for arbitrary orientations of the principal axis system of the interaction with respect to the laboratory frame, the quadrupole Hamiltonian can be expressed using spherical coordinates by analogy to the dipolar interaction. Expansion into irreducible tensor operators  $A_{l,m}^Q$  ( $l = 2$ ) and lattice variables  $T_{l,m}^Q$  yields

$$\hat{H}_Q = \sum_{m=-2}^2 (-1)^m A_{2-m}^Q T_{2,m}^Q. \quad (3.29)$$

The spin operators  $A_{lm}^Q$  are defined as

$$\begin{aligned} A_{20}^Q &= \frac{1}{\sqrt{6}} \left( 3\hat{I}_Z^2 - \hat{I}\hat{I} \right), \\ A_{2\pm 1}^Q &= \pm \frac{1}{\sqrt{2}} \left( \hat{I}_Z \hat{I}_\pm + \hat{I}_\pm \hat{I}_Z \right), \\ A_{2\pm 2}^D &= \hat{I}_\pm^2. \end{aligned} \quad (3.30)$$

The lattice variables are given by

$$T_{2m}^Q(LAS) = \sum_{k=-2}^2 D_{mk}^{(2)*}(\Omega_{LP}) T_{2k}^D(PAS), \quad (3.31)$$

where

$$\begin{aligned} T_{20}^D(PAS) &= \sqrt{\frac{3}{2}} \left( \frac{e^2 q_{zz} Q}{2I(2I-1)\hbar} \right), \\ T_{2\pm 1}^D(PAS) &= 0, \\ T_{2\pm 2}^D(PAS) &= \frac{1}{2} \eta \left( \frac{e^2 q_{zz} Q}{2I(2I-1)\hbar} \right). \end{aligned} \quad (3.32)$$

The asymmetry parameter  $\eta$  of the EFG tensor is defined as

$$\eta = (q_{xx} - q_{yy})/q_{zz}. \quad (3.33)$$

Equation 3.31 relates tensor components in the LAS to those in the PAS of the electric field gradient tensor by means of Wigner rotation matrix elements,  $D_{mk}^{(2)*}(\Omega_{LP})$ , with Euler angles  $(\alpha_{LP}, \beta_{LP}, \gamma_{LP})$ . Usually it is convenient to decompose this single transformation into a series of rotations. Thus, if a step-wise rotation from the PAS into an orthonormal molecular frame, the so-called crystal axis system (CAS), and subsequently into the LAS, is given by  $\Omega_{CP}$ , then

$$D_{mk}^{(2)}(\Omega_{LP}) = \sum_{l=-2}^2 D_{ml}^{(2)}(\Omega_{LC}) D_{lk}^{(2)}(\Omega_{CP}). \quad (3.34)$$

Based on the general commutation relation  $[I_Z, A_m] = mA_m$ , only the secular part of the Hamiltonian is retained and given by

$$\hat{H}_Q^{(1)} = A_{20}^Q T_{20}^Q(LAS) = \frac{\omega_Q}{4} \left( 3\cos^2\theta_{LP} - 1 + \eta\sin^2\theta_{LP}\cos 2\phi_{LP} \right) \cdot \left( 3\hat{I}_Z^2 - \hat{I}\hat{I} \right), \quad (3.35)$$

where

$$\omega_Q = \frac{e^2 q_{zz} Q}{2I(2I-1)\hbar}.$$

The quadrupolar term lifts the twofold degeneracy of transitions between the Zeeman eigenstates  $|1\ 1\rangle$ ,  $|1\ 0\rangle$  and  $|1-1\rangle$  at the Larmor frequency. Whereas by the energy correction in first order perturbation the energy levels  $|1\ 1\rangle$  and  $|1-1\rangle$  are destabilized by the same amount, the energy of the  $|1\ 0\rangle$  level is lowered by double the amount of energy. Thus, each nucleus gives rise to two resonances which are located symmetrically with respect to  $\omega_0$ :

$$\omega = \omega_0 \pm \frac{3\omega_Q}{4} (3\cos^2\theta_{LP} - 1 + \eta \sin^2\theta_{LP} \cos 2\phi_{LP}). \quad (3.36)$$

The resonance frequency  $\omega$  is thus a function of the orientation of the principal axis system (PAS) of the EFG with respect to the laboratory axis system (LAS) determined by the external magnetic field.

In the presence of motion, the quadrupole-coupling tensor of a single deuteron can switch between  $N$  different sites, whose orientations are defined with respect to the CAS for convenience. For fast site exchange ( $\omega\tau \ll 1$ ) the mean frequency  $\bar{\omega}$  of a single crystallite with orientation  $(\theta, \omega)$  with respect to  $\mathbf{B}_0$  is given by

$$\bar{\omega} = \sum_{j=1}^N p_{eq}(j) \cdot \omega_j = \pm \sqrt{\frac{3}{2}} \frac{e^2 q Q}{2\hbar} \sum_{j=1}^N \rho_{eq}(j) \sum_{m,l=-2}^2 \rho_{2m} D_{ml}^{(2)}(\Omega^{PC}) D_{l0}^{(2)}(\Omega^{CL}). \quad (3.37)$$

$N$  is the number of sites which define the jump geometry and  $p_{eq}(j)$  denote the *a priori* probabilities of finding a deuteron on site  $j$ . The Eulerian transformations  $\Omega = (\alpha_{LP}, \beta_{LP}, \gamma_{LP})$  represent the Wigner rotation matrizes rotating the PAS into the CAS ( $\Omega^{PC}$ ), and the CAS into the LAS ( $\Omega^{CL}$ ) according to the convention by *Rose* as delineated by *Spies* [180]. In the PAS, the only non-vanishing elements of the quadrupole-coupling tensor  $\rho$  are  $\rho_{20} = (3/2)^{1/2}$  and  $\rho_{2\pm 2} = 1/2 \eta$  with  $\eta$  being the asymmetry parameter ( $0 \leq \eta \leq 1$ ). The latter is defined by the Cartesian components of the coupling tensor according to  $\eta = (\rho_{XX}^{(2)} - \rho_{YY}^{(2)}/\rho_{ZZ}^{(2)})$  with  $|\rho_{ZZ}^{(2)}| \geq |\rho_{YY}^{(2)}| \geq |\rho_{XX}^{(2)}|$ .

### 3.3.2.4 Powder Spectra

A central aspect of this thesis in terms of NMR spectroscopy is the line shape analysis of  $^2H$  powder spectra. The  $^2H$  nucleus ( $I = 1$ ) exhibits a sufficiently small quadrupole coupling interaction, so that the latter can be treated in the framework given by first order perturbation theory.

The magnitude of the quadrupolar coupling nevertheless by far exceeds that of the chemical shift or dipolar interaction of the nuclei present in the sample. The influence of the latter on the deuteron NMR spectra can therefore be neglected. If the local symmetry at the nitrogen nucleus in an ammonium group is of interest,  $^{14}N$  ( $I = 1$ ) quadrupole spectra may furnish information *via* the magnitude of the quadrupole coupling constant and the asymmetry parameter  $\eta$ . Unlike the moderate coupling constants encountered in  $^2H$  NMR spectroscopy, the QCCs observed for  $^{14}N$  span a wide range from several hundred kHz up to a few MHz, depending on the symmetry at the nucleus that is probed. Thus, recording  $^{14}N$  wideline spectra poses an experimental challenge, since the large spectral widths can only be tackled with difficulties owing to the problem of uniform excitation of the whole spectral range. In the present work, several attempts to record  $^{14}N$  spectra at different temperatures were made; the interpretation of the obtained spectra however is not straightforward and will therefore be discussed only briefly in Chapter 4 on page 69. The form of Eq. 3.36 on the preceding page only allows for the interpretation of single-crystal spectra.

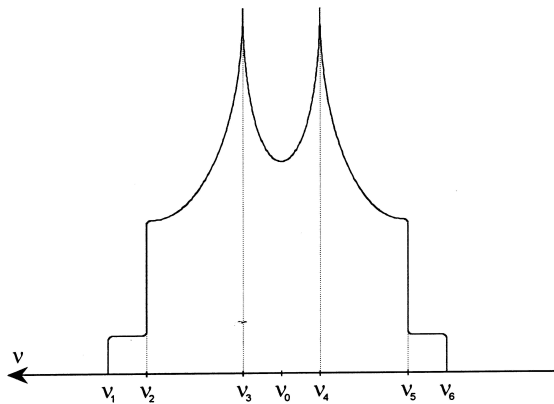


**Figure 3.3:** Schematic representation of a three-level system with an asymmetry parameter  $\eta$  of 0.5. The discontinuities observed at particular frequencies are labelled; for further discussion see text.

To analyze powder spectra, a powder averaging procedure has to be implemented which considers all orientations of the magnetic field vector  $\mathbf{B}_0$  in the PAS system, that is represented by the polar angles  $\theta_{LP}$  and  $\phi_{LP}$ . The random distribution of the crystallites is either accounted for by summation over standardized, infinitesimal surface elements  $\sin\theta_{LP} d\theta d\phi_{LP}$  of a unit sphere spanned by the angles  $\theta$  and  $\phi$ , which are associated with well-defined frequencies according to the resonance condition given by Eq. 3.36.

Alternatively, a so-called ASG-tiling can be carried out, which is implemented in the

program MXQET [181] typically used for calculation of the  $^2H$  spectra in this thesis. This procedure is based on the summation over octahedral faces which are divided into small, equilateral triangles associated with a special weighting scheme [182].

Figure 3.3 displays a typical quadrupolar powder pattern. By introducing the quadrupole coupling constant  $QCC = \frac{e^2 Qq}{h}$  and transformation of Eq. 3.36, we obtain the frequencies of the principle axes  $\nu_x$ ,  $\nu_y$  and  $\nu_z$ , which are observed if the respective axes are aligned along the direction of the magnetic field  $\mathbf{B}_0$ . Thus, three singularities occur in the spectrum,

corresponding to specific orientations: for  $\theta = \phi = 0^\circ$  at  $\pm \frac{3}{4}(e^2 q_{zz} Q/h)$ , for  $\theta = 90^\circ$ ,  $\phi = 0^\circ$  at  $\pm \frac{3}{8}(e^2 q_{zz} Q/h)(1 + \eta)$  and for  $\theta = 90^\circ$ ,  $\phi = 90^\circ$  at  $\pm \frac{3}{8}(e^2 q_{zz} Q/h)(1 - \eta)$ .

From the differences between the associated discontinuities  $\Delta\nu_i$  the asymmetry parameter  $\eta$  as well as QCC can be calculated (Eqs. 3.38 – 3.40):

$$\nu_1 - \nu_6 = \Delta\nu_z = 3 \cdot \frac{QCC}{2I(2I-1)} = 3Q_{zz}, \quad (3.38)$$

$$\nu_2 - \nu_5 = \Delta\nu_y = \frac{3}{2} \cdot \frac{QCC}{2I(2I-1)} \cdot (1 + \eta) = -3Q_{yy}, \quad (3.39)$$

$$\nu_3 - \nu_4 = \Delta\nu_x = \frac{3}{2} \cdot \frac{QCC}{2I(2I-1)} \cdot (1 - \eta) = -3Q_{xx}. \quad (3.40)$$

The two borderline cases for the asymmetry parameter, which manifest themselves in characteristic shapes of the powder spectra, are given by

$$\eta = 0 \quad \iff \quad \nu_2 = \nu_3 \quad \nu_4 = \nu_5 \quad (3.41)$$

$$\eta = 1 \quad \iff \quad \nu_1 = \nu_2 \quad \nu_5 = \nu_6 \quad \nu_3 = \nu_4 \quad (3.42)$$

### 3.3.2.5 $^2H$ NMR: Dynamics of Nuclei

Deuteron NMR spectroscopy is particularly suited for the study of dynamical processes, allowing us to monitor rotational motions over a wide range of characteristic frequencies, in particular slow and even ultraslow motions [159, 183, 184]. The following aspects of  $^2H$  NMR render this method unique among a range of NMR techniques for studying dynamics, developed during the past 30 years since the advent of high resolution solid-state NMR spectroscopy [161, 179, 183, 185].

- Deuterons represent well-defined nuclear spin labels, since  $^2H$  NMR spectra are almost exclusively governed by the quadrupole interaction with the EFG at the deuteron site. As this field gradient is intrinsically associated with the electrons in the X–D bonds, it is entirely intramolecular in nature and thus represents a unique probe of *single particle* motions by tracing the trajectories of *individual* X–D bonds. For a covalently bonded deuterium atom in an ammonium group, the EFG can therefore be treated as axially symmetric in good approximation, the symmetry axes in the case of an ammonium ion being the four N–D bonds.
- $^2H$  NMR allows for the discrimination of different *types* of motions through deuteron

line shape analysis, such as rotational diffusion, or discrete motion (rotational jumps), as well as different geometries of the latter.

- The *dynamic range* covered by deuteron NMR spectroscopy is extraordinarily high. By combining various techniques, such as the 2D exchange spectroscopy ( $10^{-2} - 10^4 \text{ s}^{-1}$ ), selective inversion ( $10^{-2} - 10^5 \text{ s}^{-1}$ ), line shape analysis ( $10^3 - 10^8 \text{ s}^{-1}$ ) and measurement of  $T_2$  ( $10^{-2} - 10^4 \text{ s}^{-1}$ ), as well as  $T_{1Z}$  ( $10^8 - 10^{12} \text{ s}^{-1}$ ) and  $T_{1Q}$  anisotropies ( $10^{-1} - 10^{12} \text{ s}^{-1}$ ), rotational motions can be monitored over many orders of magnitude of characteristic frequencies. In addition, measurements of the spin-lattice relaxation time  $T_1$  provide information about spectral densities in a wide frequency range around the NMR frequency itself.
- Based on the above wide range of correlation times that are accessible, *motional heterogeneity* associated with different degrees of mobility present in heterogeneous materials can be detected, as for instance in glasses and polymers or liquid crystals.

### 3.3.2.6 Line Shape Analysis

Molecular motion in the *slow motion limit* ( $\tau_c \gg QCC^{-1}$ ) can be assessed by 2D exchange methods or selective inversion [161, 179, 183]. In this frequency range, the line shape is largely insensitive to the motion because the extra broadening caused by slow or ultra-slow motions is by far smaller than the natural line width.

Line shape analysis is one of the most powerful probes of dynamics in the *intermediate exchange region* where correlation times are on the order of  $QCC^{-1}$  and signal intensity is spread over the whole spectral frequency range. This technique allows for the determination of the *type* of motion as well as its *geometry* and *correlation time* by analyzing changes of the spectral line shape and width. In the *fast exchange limit* where  $\tau_c \ll QCC^{-1}$  (frequency range  $\approx 10^8 - 10^{12} \text{ s}^{-1}$ ) the calculation of the Bloch-McConnel-type equation 3.43 can be reduced to a weighted spatial average over all positions of the motional process. In this frequency regime, the line width and asymmetry change according to the geometry of motion, however the principal line shape is retained and information on the exchange frequency is entirely lost.

To probe processes beyond the fast exchange limit,  $T_{1Z}$  or  $T_{1Q}$  measurements or the use of complementary techniques such as quasielastic neutron scattering, have to be employed.

For intermediate exchange frequencies, the line shapes of  $^2H$  echo spectra undergo significant changes depending on the correlation time  $\tau_c$  and the evolution time  $t_1$  of the solid-echo experiment. Analysis of the line shape changes have been carried out with a program written

by *Greenfield et al.* [181], which allows for the simulation of multi-jump processes for different jump geometries, including the use of up to four independent jump axes and up to 100 deuterium sites, as well as different *a priori* probabilities. Parameters to be entered manually include experimental parameters (pulse length of the 90° pulse, evolution time  $t_1$ ) and model-dependent variables (quadrupole coupling constant, Euler angles defining the jump sites with respect to the jump axis, exchange matrices, jump rates for each jumping frame). Artefacts arising from finite pulse power are accounted for, as is the dipolar interaction of the deuterons with their surroundings by convolution of the simulated spectra with a Gaussian function with variable FWHM. Significant distortions in the experimental spectra arising from off-resonance effects and the asymmetries caused by the probe head were typically accounted for in the simulated spectra by introducing a linear attenuation spreading over the whole spectrum.

Since MXQET only provides an interface for simulations based on one single quadrupole-coupling constant, we independently designed a program for the simulation of  $^2H$  line shapes based on the same mathematical procedure as described above (Eqs. 3.37, 3.43 – 3.50) using the C++ library Gamma [186]. Some mathematical routines were carried out with the commercial program package MATLAB [187]. Using this routine for simulating spectra with up to three QCCs it was possible to verify that this procedure gives identical results as compared to summing up three separate spectra simulated with MXQET with one single QCC each.

**Markov Equation** Molecular reorientations in the solid phase can often be treated by assuming the model of a stationary Markov process to apply. For systems in a thermodynamic equilibrium, this is equivalent to a stochastic movement of the deuterons, where the conditional probabilities of finding a deuteron at site  $\Omega_i$  at a given time  $t_i$ , if at time  $t_{i-1}$  it has been at site  $\Omega_{i-1}$ , is only dependent on the time difference  $\Delta t = t_i - t_{i-1}$  and – if applicable – on the jump site  $\Omega_{i-1}$  [161, 188]. The reorientational dynamics of an ammonium group can be treated according to the above model, where the time-dependent change of the FID  $G(t)$  is described by a Bloch-McConnel-type equation:

$$\frac{d\mathbf{G}}{dt} = \mathbf{G}(i\underline{\underline{\omega}} + \underline{\underline{\pi}}). \quad (3.43)$$

The elements of the row vector  $\mathbf{G}$  are the complex transverse magnetization vectors associated with one component of the quadrupolar doublet arising from each of the orientational sites in a static scenario.  $\underline{\underline{\omega}}$  is a diagonal matrix ( $\underline{\underline{\omega}}_{ij} = \delta_{ij}\omega_j\Omega_j$ ) representing the site frequencies associated with the jumping site  $\Omega_j$ .  $\underline{\underline{\pi}}$  denotes the exchange matrix and contains the jump frequencies  $\pi_{ij}$ . The matrix element  $\pi_{ij}$  represents the jump rate of the site exchange from site  $i$  to site  $j$ . For reasons of microreversibility, the elements  $\pi_{ij}$  must fulfill the “detailed-balance”

condition

$$p_i \pi_{ij} = p_j \pi_{ji}, \quad (3.44)$$

where  $p_j$  is the *a priori* probability of finding the deuteron on site  $j$  and  $\underline{\underline{\pi}}$  is a symmetric matrix only if all *a priori* probabilities are equal. Since the sum of the conditional probabilities over all  $i$  equals one, the diagonal elements are always the negative sum over a column, thus

$$\sum_i \pi_{ij} = 0. \quad (3.45)$$

The jump rates  $\pi_{ij}$  can be extracted from solid-echo spectra, whose line shape is calculated as the Fourier transform of the echo decay (Eq. 3.50 on page 62). The echo decay is summed up over all possible orientations of the crystals in a powdered sample, and the contributions from dipolar coupling to surrounding nuclei is accounted for by multiplication with a Gaussian or Lorentzian function. Fourier transformation from the echo maximum with respect to  $t$  then yields the spectral intensity  $I(\omega)$  and, accordingly, the line shape of the deuterium echo spectra.

**Motional Models** For the ammonium ion in  $\text{ND}_4[\text{N}(\text{C}\equiv\text{N})_2]$ ,  $180^\circ$  or  $120^\circ$  jumps about one single  $C_2$  or  $C_3$  axis of the tetrahedron, respectively, were considered, as well as an isotropic four-site exchange. The exchange matrices for the different processes are given by Eqs 3.46, 3.48, and 3.49. The *a priori* probabilities were chosen to be equal for all sites and all models. The Euler angles for each site (in degrees) are indicated, following the sequence  $(\beta, \alpha, \gamma)$ . Since  $\gamma$  could be set to zero in all cases, it is omitted for clarity.

$$\underline{\underline{\pi}}^{180^\circ} = \kappa \begin{pmatrix} -1 & 1 & 0 & 0 \\ 1 & -1 & 0 & 0 \\ 0 & 0 & -1 & 1 \\ 0 & 0 & 1 & -1 \end{pmatrix} \quad (3.46)$$

1. (54.75,0)
2. (54.75,180)
3. (125.25,90)
4. (125.25,270)

Alternatively, Eq. 3.46 was simplified taking into account the coupling between the exchange sites in the above model and using only two sites (TS) given by the tetrahedral angle:

$$\underline{\underline{\pi}}^{180^\circ, TS} = \kappa \begin{pmatrix} -1 & 1 \\ 1 & -1 \end{pmatrix} \quad (3.47) \quad \begin{array}{l} 1. (54.75,0) \\ 2. (54.75,180) \end{array}$$

$$\underline{\underline{\pi}}^{120^\circ} = \kappa \begin{pmatrix} 0 & 0 & 0 & 0 \\ 0 & -2 & 1 & 1 \\ 0 & 1 & -2 & 1 \\ 0 & 1 & 1 & -2 \end{pmatrix} \quad (3.48) \quad \begin{array}{l} 1. (0,0) \\ 2. (109.5,0) \\ 3. (109.5,120) \\ 4. (125.25,240) \end{array}$$

$$\underline{\underline{\pi}}^{Tet} = \kappa \begin{pmatrix} -3 & 1 & 1 & 1 \\ 1 & -3 & 1 & 1 \\ 1 & 1 & -3 & 1 \\ 1 & 1 & 1 & -3 \end{pmatrix} \quad (3.49) \quad \begin{array}{l} 1. (54.75,0) \\ 2. (54.75,180) \\ 3. (125.25,90) \\ 4. (125.25,270) \end{array}$$

where  $\kappa$  is the reciprocal correlation time.

**Solid-Echo** For wide-line spectra extending over a considerable spectral frequency range, the rapid decay of magnetization following the application of a  $\frac{\pi}{2}$  radiofrequency pulse precludes the use of standard FT methods, since a significant part of the signal is lost in the inevitable dead-time of the receiver. By applying a second  $\frac{\pi}{2}$  pulse, in quadrature with the first one, and with a pulse spacing of  $t_1$ , the magnetization of spin =  $I$  nuclei can, however, be refocussed, leading to the formation of a so-called “solid echo” [161,179,183]. The evolution of the transverse magnetization under the quadrupolar interaction then results from integration of Eq. 3.43 over the complete time period  $t$ , starting directly after the first pulse and including the complete echo decay. By taking the FT from the echo maximum, undistorted absorption spectra may be obtained.

Note that the resulting echo is identical with the FID only in the borderline cases of static systems or in the fast exchange limit. In the presence of motion in the intermediate frequency regime ( $\omega\tau \approx 1$ ), however, this is no longer valid, and the spectral shape is markedly dependent on the evolution time  $t_1$  [159,161]. This dependence can therefore serve as an additional

verification of the motional model [183]. The spectral line shape in the presence of exchange is calculated as a function of  $\pi_{ij}$  and the interpulse distance  $t_1$  and is given by the Fourier transform of the echo decay

$$K(t, t_1) = \mathbf{1} \exp((-i\omega + \pi)(t - t_1)) \exp((i\omega + \pi)t_1) \mathbf{G}(0), \quad (3.50)$$

where  $t > t_1$  and the column vector  $\mathbf{G}(0)$  represents the *a priori* probabilities  $p_j$ .

### 3.3.2.7 Spin Lattice Relaxation

The spin lattice relaxation rate is determined by the transitions among the Zeeman levels, i. e. the eigenstates of the Zeeman Hamiltonian. The orientation-dependent spin-lattice relaxation constant  $T_{IZ}^{-1}(\theta, \phi)$  is given by the spectral density  $J^{(\theta, \phi)}$  [189]:

$$\frac{1}{T_{IZ}(\theta, \phi)} = \frac{3}{40} QCC^2 \left[ J^{(\theta, \phi)}(\omega_0) + 4J^{(\theta, \phi)}(2\omega_0) \right], \quad (3.51)$$

where  $QCC = e^2 Q q \hbar^{-1}$  and  $QCC/2\pi = e^2 Q q h^{-1}$  is the quadrupole-coupling constant.

The above so called Bloembergen-Purcell-Pound (BPP) spectral density approach is only valid for stochastic Markovian processes with a unique correlation time and overall isotropic motion (cf. Eq. 3.43).

From the spectral density at the Larmor frequency  $\omega_0$

$$J(\omega_0) = \frac{\tau}{1 + \omega_0^2 \tau^2} \quad (3.52)$$

we can extract the correlation times  $\tau$  and – by assuming Arrhenius-type behavior – the energy of activation  $E_a(T)$  as well as the attempt frequency  $\tau_0^{-1}$ :

$$\tau = \tau_0 \exp\left(\frac{E_a}{RT}\right). \quad (3.53)$$

The spin-lattice relaxation time  $T_1$  can be readily probed by using the saturation-recovery method. The magnetization recovery  $M_z$  subsequent to a radio-frequency perturbation can be described by

$$M_z \propto \left[ \exp\left(\frac{-t}{T_1}\right)^{1-\nu} \right]. \quad (3.54)$$

The stretching parameter  $\nu$  is only relevant for heterogeneous relaxation processes, i. e. a distribution of relaxation times as for instance observed for glassy systems. A single spin-lattice

relaxation rate ( $\nu = 0$ ) leads to a monoexponential recovery behavior. In certain cases, two or more relaxational stimuli may operate, which are associated with distinct correlation times each, typically differing in more than one order of magnitude and may contribute to significantly different extents to the overall relaxation process. This situation, as was encountered for the intermediate exchange regime in ammonium dicyanamide, can be accounted for by describing the saturation recovery by two exponentials with different weighting factors.

### 3.3.3 High-Resolution NMR: General Aspects and Techniques

The properties of the various interactions relevant to solid-state NMR demonstrate that though resolution is lost and complexity is created by the interplay of isotropic and anisotropic parts of the Hamiltonians, a plethora of additional information is gained as compared to NMR of liquids, which is influenced by  $\underline{R}^{(0)}$  only.

Nevertheless, the abundance of information contained in solid-state NMR spectra requires techniques for spectral simplification, in particular line-narrowing and sensitivity enhancement, in order to extract the different components of the NMR interactions discussed above. The issue of obtaining high-resolution spectra of powdered samples despite the presence of a variety of “disturbing” interactions has been tackled by the development of selective averaging techniques based on multi-pulse sequences or magic angle spinning (MAS). Pulse sequences such as frequency switched Lee-Goldburg (FS-LG) [190, 191] or TPPM decoupling [154] have been developed to suppress the perturbing influence of the heteronuclear and homonuclear dipolar coupling caused by protons. These sequences allow for the acquisition of high-resolution spectra of less abundant spins without dispensing with polarization transfer from the abundant spin reservoir.

**Magic Angle Spinning** Another technique removes anisotropic components by manipulation of the *spatial part* of the NMR Hamiltonian, followed by a selective re-introduction of the orientation dependence, or anisotropy, into the spectrum by controlled manipulation of the spin-system using rf-pulses and the concept of multi-dimensional spectroscopy (see below). Whereas multi-pulse sequences are typically designed to average out “unwanted” interactions by removing only *particular spin operators*,<sup>4</sup> the MAS technique removes the second rank secular parts of *all* internal interactions by modulating  $\underline{R}^{(\lambda)}$ , leaving only the isotropic parts unchanged [178]. Owing to the intrinsic angle dependence of the interactions, which is encoded in the term  $(3 \cos^2 \theta_{LP} - 1)$  (cf. Eqs. 3.20 on page 50, 3.25 on page 52 and 3.35 on page 54), it is possible to eliminate all anisotropic interactions by rapidly spinning the sample about

---

<sup>4</sup>Typically, only spin operators transforming either according to  $l = 1$  or  $l = 2$  under rotation, are removed, where  $l$  is the rank of the subspace of the spherical tensor operators of the irradiated spins.

an axis tilted by the magic angle  $\beta_M = \cos^{-1}(1/\sqrt{3}) = 54^\circ 44'$  with respect to  $\mathbf{B}_0$ . The finite spinning frequency, however, leads to the appearance of spinning side bands in the spectra at frequencies given by  $\omega^* = \omega_{iso} \pm m \cdot \omega_{rot}$  ( $m = \text{integer}$ ), whose intensities are directly encoded in the static spectrum. Therefore, information about the anisotropic properties, given by  $\delta_\lambda$  and  $\eta_\lambda$ , are indirectly available by line shape analyses of the side band patterns.

**Cross-Polarization** The CP pulse sequence [192, 193] is used to enhance the polarization of low-gamma nuclei by transferring magnetization from the protons. After an initial  $\frac{\pi}{2}$ -pulse on the protons, spin-lock rf-fields are applied on both channels. If the *Hartmann-Hahn condition* is met, i. e.  $B_{1,I}\gamma_I = B_{1,S}\gamma_S \Leftrightarrow \omega_{1,I} = \omega_{1,S}$ , the two spin species experience a *common frequency* with respect to the quantization axis, hence energy-conserving “flip-flop” terms are allowed and appear in the effective dipolar Hamiltonian (Fig. 3.4 (left), (a)). As a result, the low-gamma nuclei are thermodynamically linked to the proton spin bath, and polarization transfer occurs until spin-temperature equilibration. The initial  $\frac{\pi}{2}$ -pulse ensures that the polarization of the protons at the start of the spin-lock is oriented along the toggling frame quantization axis. By varying the contact time  $\tau_c$ , the magnetization build-up at the dilute spins, which is a function of the internuclear distance  $d_{I-S}$ , can be monitored and is thus a measure of the number of protons in spatial proximity.

### 3.3.3.1 Spectral Editing

The assignment of solid-state NMR spectra of samples containing nuclei of natural abundance is often hampered by the complexity of 1D MAS spectra and the low sensitivity of the nuclei under study, such that the loss of signal intensity intrinsic to multi-quantum experiments cannot be compensated.

As an alternative, special spectral editing techniques have been designed, which enable the separation of the resonances according to their multiplicity, i. e., the number of directly attached protons. In fact, spectral editing when combined with chemical shift analysis is often sufficient to provide an unambiguous characterization in medium sized molecular systems. Apart from spectral editing techniques based on the scalar coupling, most experiments exploit the heteronuclear dipolar coupling by discriminating between different cross-polarization rates due to variable strengths of the through-space interaction between abundant (typically  $^1H$ ) and dilute spins ( $^{13}C$ ,  $^{15}N$ ). A drawback of these techniques is their sensitivity to the presence of molecular motion, as the latter modulates the dipolar couplings. They are therefore designed for rigid solids and typically work only in the slow spinning regime ( $\nu_{rot} \leq 6$  kHz).

**Cross-Polarization with Polarization Inversion (CPPI)** The CPPI sequence (also IRCP, Inversion Recovery Cross-Polarization) represents a spectral-editing technique which is directly derived from the standard CP sequence. The latter is modified by introducing a phase inversion during the contact time and changing the phase of the proton spin-lock pulse by  $180^\circ$  (Fig. 3.4 (left), (b)). The inversion dynamics is largely dominated by the  $I - S$  dipolar coupling, and is thus similar to the polarization build-up in the standard CP sequence [82, 161, 194]. The major advantage over the latter is given by the fact that the magnetization in the CPPI experiment starts from a maximum value, whereas the CP magnetization curves rapidly build up from zero, where the data sampling is difficult for small contact times. In contrast, the CPPI inversion curves associated with different proton environments can easily be distinguished by their characteristic time-dependence also for small inversion times. As

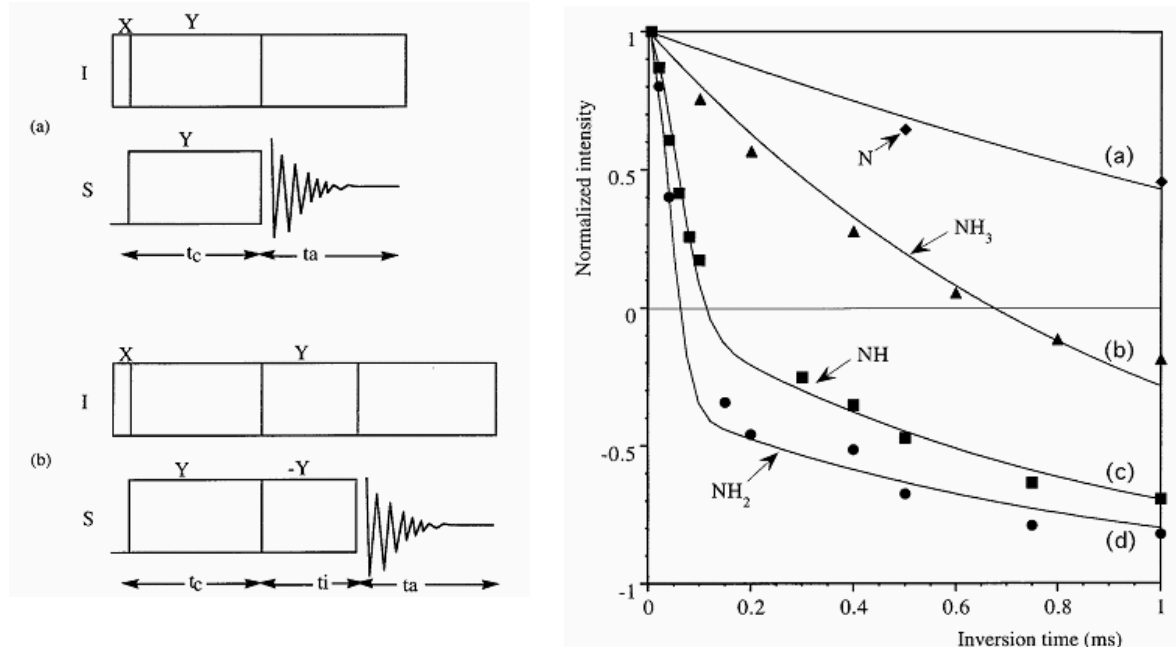


**Figure 3.4:** Left: (a) Standard CP impulse sequence; (b) modified CP sequence by applying a phase inversion to the proton spin lock pulse (CPPI).  $\tau_c$ : contact time;  $\tau_i$ : inversion time;  $\tau_a$ : acquisition time. X and Y denote the pulse phases. Right: Normalized CPPI signal intensities for different  $\text{NH}_n$  species ( $n = 0 - 3$ ), plotted against inversion time. Both figures are taken from ref. [194].

the abundant spins  $I$  are typically protons, the CPPI sequence is very sensitive to the local proton environment. As outlined in Figure 3.4 (right), the integrated normalized intensities for different  $\text{NH}_n$  species ( $n = 0, 1, 2, 3$ ) exhibit markedly different polarization inversion dynamics, which are a function of the number of covalently bonded protons.

The spin dynamics observed for different  $\text{NH}_n$  species can be classified according to two models. The first model is associated with systems exhibiting only weak dipolar couplings

(non-protonated heteronuclei), or with mobile species such as rotating ammonium groups (Fig. 3.4 (left), curves (a) and (b), respectively). In this case, the decrease in magnetization follows a single exponential [194, 195]:

$$M_S(\tau_i) = M^0(\tau_c) \left[ 2 \exp \left( -\frac{\tau_i}{T_{IS}} \right) - 1 \right], \quad (3.55)$$

assuming that the cross-polarization time  $T_{IS}$ , which is related to the strength of the  $I - S$  dipolar coupling, is significantly smaller than the relaxation time of the protons in the rotating frame  $T_{I\rho}^H$  ( $T_{IS} \ll T_{I\rho}^H$ ).  $M^0(\tau_c)$  denotes the polarized magnetization reached after the contact time  $\tau_c$ .

If strong heteronuclear dipolar coupling is present, as for instance in rigid NH or NH<sub>2</sub> groups (Fig. 3.4 (left), curves (c) and (d), respectively), the time-dependence of the magnetization inversion can be described by

$$M_S(\tau_i) = M^0(\tau_c) \left[ \frac{2}{n+1} \exp \left( -\frac{\tau_i}{T_D} \right) + \frac{2n}{n+1} \cdot \exp \left( -\frac{3\tau_i}{2T_D} \right) \exp \left( -\frac{\tau_i^2}{T_C^2} \right) - 1 \right]. \quad (3.56)$$

$T_C$  is again a time constant related to the dipolar coupling to nearby protons, leading to a coherent transfer of polarization;  $T_D$  describes the decay caused by isotropic spin diffusion ( $T_C \leq T_D$ ) and  $n$  corresponds to the number of directly bonded protons.

The polarization inversion according to Eq. 3.56 is characterized by two time-scales. The initial rapid decrease in magnetization is due to the dipolar coupling with nearby protons, whereas the equilibrium value is approached at a much slower rate due to spin diffusion. The cross-over between the two time-regimes, indicated by a “kink” in curves (c) and (d) (Fig. 3.4), is given by

$$[2/(n+1)] - 1, \quad (3.57)$$

where  $T_C \ll \tau_i \ll T_D$  and, therefore,  $\exp(-3\tau_i^2/T_C^2) \approx 0$ , and  $\exp(-\tau_i/T_D) \approx 1$ , leading to Eq. 3.57.

In the absence of motion, the CPPI sequence can therefore be used as a straightforward measure of the number of protons attached to a heteronucleus, in the present case <sup>15</sup>N, thereby greatly facilitating the interpretation of CP-MAS spectra where the chemical shift information is insufficient for a complete spectral assignment.

### 3.3.3.2 Zero- and Double-Quantum NMR

To make use of the versatility of interactions that can be addressed by solid-state NMR, pulse sequences have been developed in recent years which allow either to *separate* or to *correlate* internal interactions [178,185]. While seeking for high resolution, the focus is on the *elimination* of the anisotropic signatures of the different interactions. A next step, however, is to *retrieve* this information while keeping a high resolution spectral encoding. This is typically done in multidimensional experiments or in spectral editing pulse sequences. To this end, complex excitation sequences have been tailored so as to selectively reintroduce the different interactions through different mechanisms (such as rotary resonances) taking advantage of their different symmetry properties [175]. Among the different interactions, dipolar coupling is one of the most important as it is a direct function of the distance between the interacting spins. Experiments based on reestablishing the homo- or heteronuclear dipolar couplings through zero- and double-quantum excitations have been devised in the past [156,196–204]. Pulse sequences such as TOSSY [205], REDOR and READPOR [206–209], HETCOR [210–212], or the symmetry-based  $CN_n^\nu$  or  $RN_n^\nu$  pulse sequences [198,200,213], allow for the determination of orientations and distances *via* *through-space* couplings [156,196,197,201,202,205,213,214]. *Through-bond* connectivities can be probed by pulse sequences such as INADEQUATE [201,215] and MAS-HMQC [216] [202,205,217,218].

Based on the above experiments, the elucidation of structural motifs, as well as atom connectivities and spatial orientations of molecular fragments has increasingly entered the focus of modern solid-state NMR and is particularly promising if applied to semi-crystalline or amorphous materials [214,219–222].

***fp*-RFDR** An experiment designed to recouple homonuclear dipolar couplings between dilute spin pairs was applied in this work to a semi-crystalline carbon nitride polymer. The so called *fp*-RFDR (finite pulse radio-frequency driven dipolar recoupling) restores homonuclear dipolar interactions based on constructive usage of finite pulse-width effects in a phase- and symmetry-cycled  $\pi$ -pulse train [156,223–225]. By applying a rotor-synchronous  $\pi$  pulse of finite width every rotation period in the limit of rapid MAS (such that  $\tau_p > 0.1\tau_R$ ), non-zero effective homonuclear dipolar couplings are generated, whereas chemical shift interactions (both isotropic shifts and chemical shift anisotropy), are averaged out by the *fp*-RFDR sequence. The information contained in the restored dipolar coupling can be “read out” through dephasing of the transverse magnetization during proton decoupling, if transverse relaxation is negligible (cf. Fig. 3.5) [156, 223]. Typically, a CP sequence is implemented prior to the  $\pi$ -pulse train.

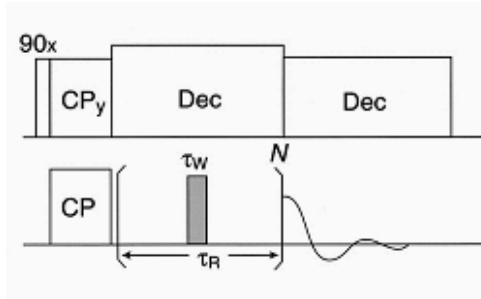


**Figure 3.5:** Pulse sequence for a fp-RFDR experiment. An XY-16 pulse sequence (repeated  $N$  times) is used so that a  $\pi$  pulse of duration  $\tau_w$  is applied at the point in every rotor cycle,  $\tau_R$ . The  $\frac{\pi}{2}$  pulses sandwiching the RFDR sequence are not shown. The picture was taken from ref. [156].

During the mixing time  $t_1$ , zero-quantum coherences (i.e. the spin part of the restored dipolar coupling has the form of zero-quantum dipolar coupling, which is identical to that for a static spin system) are created, if the nuclei are close enough for magnetization exchange to take place. Thus, the appearance of cross-peaks in the 2D spectrum obtained at sufficiently long mixing times will be a signature of the spatial proximity of the different resolved building blocks. At the same time, a qualitative measure of the distance information is at hand by recording different spectra using varying mixing times.

## Chapter 4

# Carbon(IV)Nitride Precursors I. Solid-State Dynamics and Reactivity

Chapter 4 will be concerned primarily with an in-depth study on various aspects inherent to solid-state reactions. As the study of solid-state reactions will mainly be used as a tool to characterize dynamics on a molecular level and, ultimately, optimize the selection of precursors and the synthesis strategies for graphitic carbon nitride, we will deal with the goals outlined in Chapter 1 in reverse order:

By delineating the basic principles governing typical solid-state reactions of model systems, qualitative and quantitative aspects of the reaction mechanism will be addressed. In consequence, an empirical basis will be established by which the selection of potentially reactive  $\text{CN}_x$  precursors is driven (cf. Chapter 1) and which therefore precedes the issue of “Chemical Screening” as explicated in Chapter 5. Two examples of solid-phase reactions have been selected and will be discussed in some detail in this chapter, thereby constituting the basis for the following investigation of the thermal behavior of various  $\text{CN}_x$  precursors.

In the first part, the solid-phase transformation of the model system ammonium dicyanamide into dicyandiamide will be discussed. To this end, a *quantitative* account of the temperature-dependent molecular dynamics of the ammonium ion will be given and its impact on the transformation will be outlined. In doing so, physical models of motion and their description by complementary techniques will be of major importance, thereby providing a sound basis for the discussion of thermally induced solid-state reactivity. As a next step, processes on a submicroscopic level constituting the *reaction mechanism* and their kinetics will be delineated. As this model reaction has recently been subject to a comprehensive study [122, 123, 163], we

focus here on complementary results obtained by solid-state NMR spectroscopy and quasi-as well as inelastic neutron scattering. The relevance of dicyanamides in general as potential  $\text{CN}_x$  precursors will be comprehensively addressed in Chapter 5.

In contrast, a rather complex solid-state reaction will be discussed in the second part, whose *reaction pathway* will be traced in detail with the emphasis being on the *qualitative* description of the reactants, intermediates, and products involved. Ammonium cyanoureate has been deliberately chosen as an example owing to its close relationship to ammonium dicyanamide and its accordingly similar constitution, whose influence on the basic reaction pathway will be elucidated. It can, however, not be considered as a classical  $\text{CN}_x$  precursor compound and will therefore not be discussed further in this context.

Thus, two examples of solid-state reactions will be presented in the following, which are guided by varying central questions and thus characterized by fundamentally different analytical approaches.

## 4.1 Ammonium Dicyanamide

### 4.1.1 Introduction

The need for understanding the elementary processes governing solid-state reactions in carbon nitride chemistry has stimulated the search for simple model systems providing a link between hypothesis and experience.

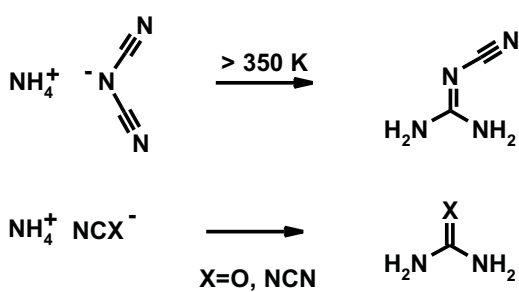


**Figure 4.1:** Concept of the isolobal analogy between ammonium cyanate and ammonium dicyanamide according to the “cyanide-displacement law”.

Historically important compound ammonium cyanate  $\text{NH}_4[\text{OCN}]$ , the two compounds being related by an isolobal analogy [226–228] according to *Grimm’s cyanide displacement law* (Fig. 4.1) [229]. At temperatures beyond 353 K, ammonium dicyanamide transforms into its molecular isomer dicyandiamide  $\text{NCN}=\text{C}(\text{NH}_2)_2$  in a topochemical reaction without passing through the melt, which can be viewed in direct analogy to the conversion of ammonium cyanate into urea  $\text{O}=\text{C}(\text{NH}_2)_2$  [121–123, 230]. Although the latter reaction, which had given birth to a new conceptual approach to modern chemistry, has been investigated thoroughly in the liquid phase, only very little attention has been directed towards the solid-phase behavior of the reactants [227, 231, 232]. Above 440 K, dicyandiamide is converted into melamine,  $\text{C}_3\text{N}_3(\text{NH}_2)_3$ , which then polymerizes forming highly condensed  $\text{CN}_x$  species [42, 73, 82].

Ammonium dicyanamide  $\text{NH}_4[\text{N}(\text{CN})_2]$  ( $\text{NH}_4\text{dca}$ , Figs. 4.1 and 4.4) has entered the focus as an ideal model system in that it intrinsically links reactivity with function: The solid-state transformation of ammonium dicyanamide involves the formation of classical  $\text{CN}_x$  precursors such as dicyandiamide and melamine, thus constituting a cornerstone in the reaction cascade towards g- $\text{C}_3\text{N}_4$ .

The thermal behavior of the molecular salt  $\text{NH}_4\text{dca}$  closely resembles that of *Wöhler’s* his-

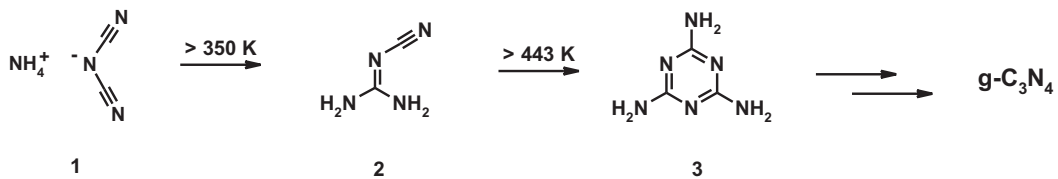


**Figure 4.2:** Transformation of ammonium dicyanamide into dicyandiamide and melamine at elevated temperatures.

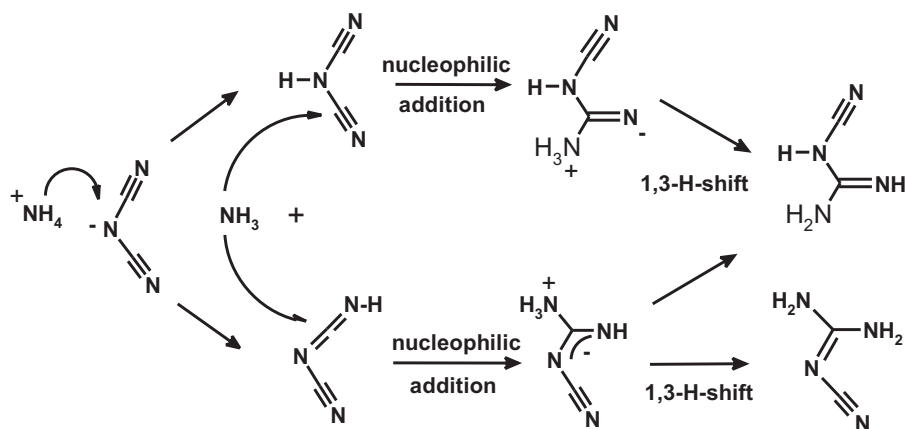


**Figure 4.3:** Possible mechanisms for the thermal transformation of ammonium dicyanamide into dicyandiamide. The bottom reaction pathway is preferred.

Both the crystal structure and the thermal conversion of  $\text{NH}_4\text{dca}$  were investigated in some depth by a broad spectrum of analytical techniques, such as *in situ* single-crystal X-ray and neutron powder diffraction,  $^{15}\text{N}$  and  $^{13}\text{C}$  solid-state NMR spectroscopy, vibrational spectroscopy, and thermal analysis. The following study is conceived as a continuation of the above preliminary results, which are summarized in the literature [122, 123, 163].

As a major result, the transformation was classified as a topochemical solid-state reaction proceeding in a non-topotactic fashion, yet with minimal molecular movement and structural changes under carefully controlled temperature conditions. The combined use of temperature programmed Raman and solid-state NMR spectroscopy afforded a comprehensive picture of the transformation mechanism on the molecular level, which can be described as an initial proton transfer from the ammonium ion to one of the terminal nitrogen atoms of the nitrile groups, followed by a nucleophilic addition of the as-formed ammonia to the adjacent electrophilic carbon (Fig. 4.3).

By tracing the time average of the nuclear density, neutron diffraction allows for the determination of the probability density function (*pdf*), therefore providing the *a priori* probabilities for the site occupation of the four deuterium nuclei. On the other hand, solid-state NMR – by offering an intriguing single-particle perspective owing to the dominant effect of the local quadrupolar interaction on the spectra – is a valuable resource for gaining insight into dynamical processes in solid materials on a large time scale.

Traditionally,  $^2\text{H}$  NMR spectroscopy is used as a powerful technique for the study of dynamics in glassy systems, liquid crystals, and polymers, with the emphasis being on structural phase and glass transitions of essentially amorphous systems [159, 160, 233–239]. As an extension, by performing  $^2\text{H}$  line-shape simulations with the symmetry restrictions imposed by

the deuteron *pdf* in mind, we are capable of correlating structural and dynamic information and, thus, may enter the realm of solid-state reactivity. As we are interested in the topochemical transformation of ammonium dicyanamide into dicyandiamide, extending the  $^2H$  NMR technique to the *in situ* study of solid-state reactions seems to be a straightforward issue, which will be discussed in some detail in the following. As a guiding theme, the dynamics of  $\text{ND}_4dca$  will be comprehensively delineated by means of wide-line  $^2H$  NMR spectroscopy, and supplemented by results from inelastic and quasielastic neutron scattering, including the pre- and post-transformation stages as well as the transformation process itself.

#### 4.1.2 Solid-State NMR

##### 4.1.2.1 Ammonium Ion Dynamics: Line-Shape Simulations

$\text{NH}_4dca$  and its deuterated analogue  $\text{ND}_4dca$  were synthesized according to a procedure described in section 10.1 on page 355 and in refs. [122, 123, 163, 240]. Wide-line  $^2H$  NMR spectra of the ammonium ion in  $\text{ND}_4dca$  were recorded in a temperature range between 38 K and 390 K; selected experimental spectra obtained by applying the solid-echo technique are displayed in Figure 4.5. Spectra recorded above RT will be discussed separately in section 4.1.2.3 on page 84.

On inspecting the line shapes, we can distinguish between four major dynamic regions: The high-temperature range ( $\geq 230$  K) is characterized by narrow ( $\text{FWHM} \approx 6$  kHz) spectra of non-Lorentzian type, whose line widths are slightly decreasing with increasing temperature. The line shapes do, however, not correspond to completely motionally averaged spectra as observed for typical liquids, which are composed of a single Lorentzian. In the upper intermediate region ( $160 < T < 190$  K) the spectral shape becomes increasingly featureless and collapses into a broadened quasi-Lorentzian line around 160 K. At even lower temperatures (100 – 150 K), a gradual crossover to a broad powder spectrum can be observed, the latter being charac-

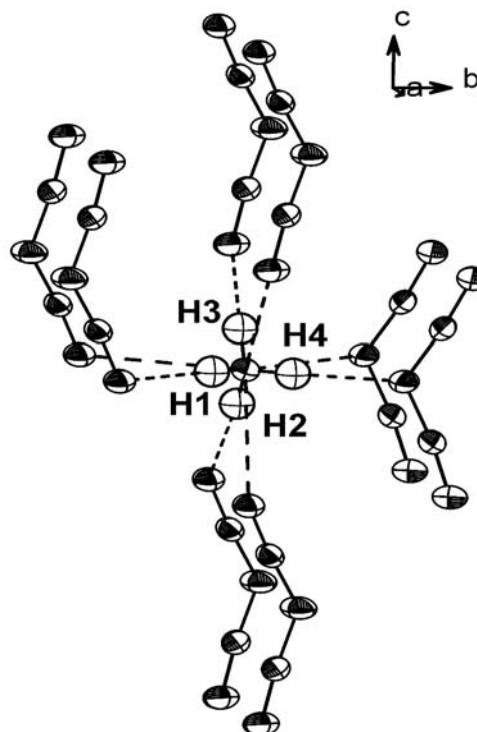


**Figure 4.4:** Coordination sphere and labelling scheme of the ammonium ions in  $\text{NH}_4[\text{N}(\text{CN})_2]$ , displacement ellipsoids are drawn at the 50 % probability level. N and C: ellipsoids, H: circles.

teristic of slow motion. Towards the lower limit of the intermediate temperature range, the spectra can best be described by a weighted superposition of a Lorentzian line and a Pake spectrum with a variable, temperature-dependent ratio of the corresponding subspectra. In the temperature range in which the line shape undergoes major changes, the motionally induced spin-spin relaxation time  $T_2$  is short, leading to a drastic attenuation of the spectral intensity of the powder spectrum due to the solid-echo acquisition, whereas the intensity of the Lorentzian remains essentially unaffected (see below). The so-called reduction factor is increasingly taking effect between 140 and 160 K in the experimental spectra. In the low-temperature range ( $< 100$  K), motion affecting the line shape is finally slowed down, leaving behind a superposition of three axially symmetric Pake spectra with slightly different QCCs and a common asymmetry parameter of essentially zero ( $\eta = 0.02(1)$ ).

Finding an appropriate model of motion for the ammonium ion can be significantly facilitated using the results of neutron diffraction as a starting basis [122, 163]: Since in the whole temperature range the nuclear density of the deuterons is essentially concentrated around the four tetrahedral sites, we can rule out models implying isotropic rotational diffusion of the  $\text{ND}_4^+$  group in a flat potential with the deuteron sites distributed over spherical trajectories. Similarly,  $90^\circ$  jumps around the  $C_2$  axes of the tetrahedron can be excluded, since this would increase the number of accessible deuteron sites to eight, which does not conform to the neutron diffraction data. Possible models are thus only those mapping all tetrahedral sites before and after the jump onto themselves.

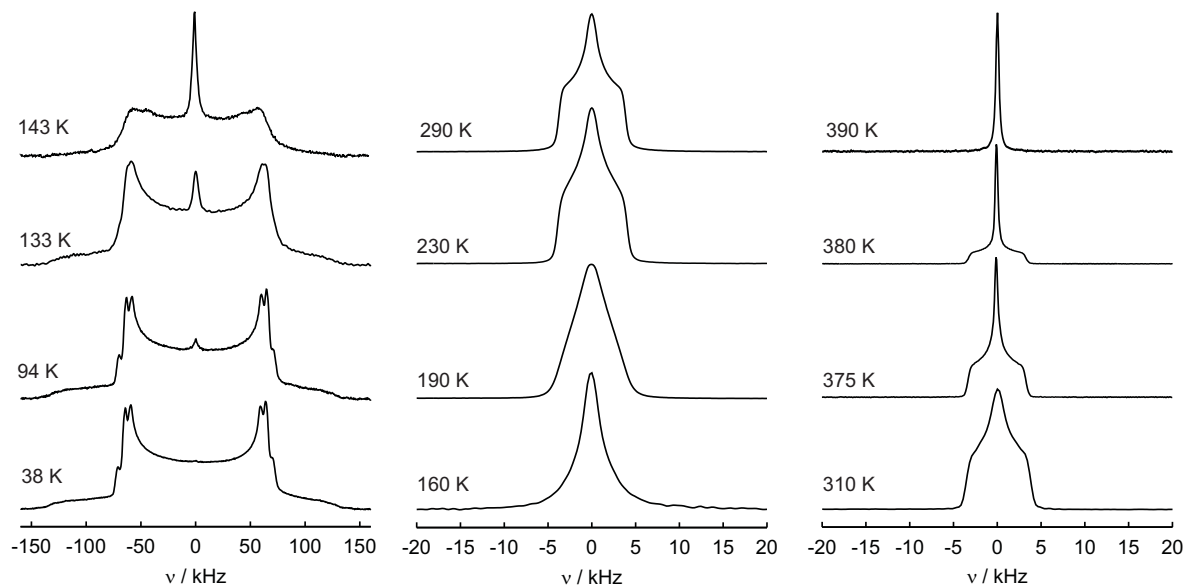


**Figure 4.5:** Representative solid-echo  $^2\text{H}$  spectra of ammonium dicyanamide as a function of temperature between 38 and 390 K.

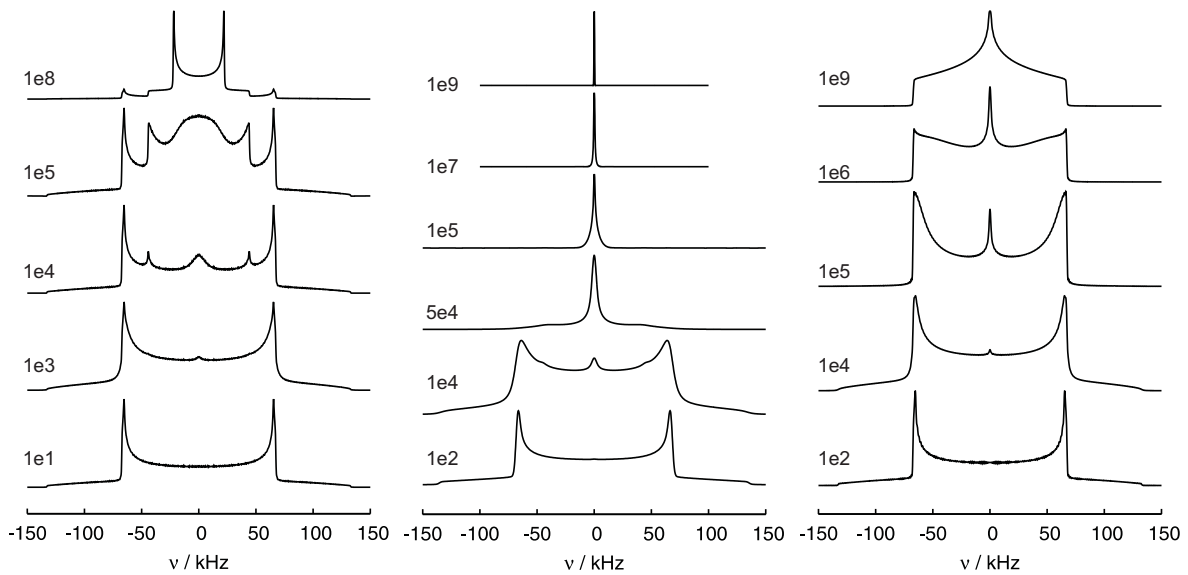


**Figure 4.6:** Line-shape simulations carried out for different jumping geometries. Left: Jumps about a single  $C_3$  axis; middle: isotropic tetrahedral jumps; right: coupled  $180^\circ$  jumps of two pairs of deuterons about a single  $C_2$  axis. Exchange frequencies are indicated.

The latter scenario would be compatible with jumps of the tetrahedron about one of its threefold ( $C_3$ ) or twofold ( $C_2$ ) axes each, which are located along the N–D bonds or bisecting the D–N–D angles, respectively. These models should be observed preferentially if site symmetry constraints or characteristic distortions of the tetrahedral symmetry apply, the latter being for instance induced by the hydrogen-bonding network. The most intuitive model if symmetry restrictions can be neglected as in the present case ( $ND_4^+$  located on a general site with symmetry 1), is represented by a random four site exchange of the deuterons, featuring an isotropic jump motion in a tetrahedral potential. This model can be equally expressed as simultaneous jumps about all  $C_2$  and  $C_3$  axes, and according line-shape simulations are depicted in Figure 4.6 (middle).

For comparison, Figure 4.6 (left and right) displays simulations carried out for jumps in a strongly distorted fourfold potential.  $120^\circ$  jumps around a single  $C_3$  axis entail the superposition of a static spectrum (one static deuteron) with that of the three exchanging deuterons, which does not collapse into a single Lorentzian, regardless of the exchange frequency (Fig. 4.6, left). As outlined in Figure 4.6 (right), for simultaneous  $180^\circ$  jumps of two coupled pairs of deuterons separated by the tetrahedral angle about a single  $C_2$  axis one would expect a narrowing of the spectra, yet not a complete motional averaging in the high-frequency limit. As the line-shape simulations for a  $C_2$  jump therefore differ significantly from those observed in the experimental spectra, this model of motion can be excluded as well.

Another scenario could be envisaged where jump motion about a fixed axis is accompanied by tumbling of the axis itself, which nevertheless has to be compatible with the tetrahedral potential. This model would however create redundancy in that it could be more easily expressed in terms of a simple four site exchange of the deuterons without any symmetry restrictions. From Figure 4.6 it gets evident that neither the two nor the three site exchange can satisfactorily reproduce the experimental spectra.

According to the above line of argument, simulations based on a tetrahedral jump geometry were performed, including all-site exchange with equal *a priori* probabilities. Three noticeable aspects affecting the strategy of the simulations will be pointed out in the following:

The first detail that has to be addressed is given by the existence of three N–D quadrupole-coupling constants in the low-temperature spectra. According to line-shape simulations carried out with a program written to accommodate more than one QCC per ammonium group, the spectra can in principle be reproduced equally well by a simple superposition of three separate Pake spectra with QCCs of 161, 177 and 193 kHz as demonstrated in Figure 4.7. Relevant fitting parameters are given in Table 4.1.

The intensity ratios obtained by the fitting procedure nicely sum up to a total of four Pake spectra corresponding to four N–D QCCs, two of which being essentially identical. Since only

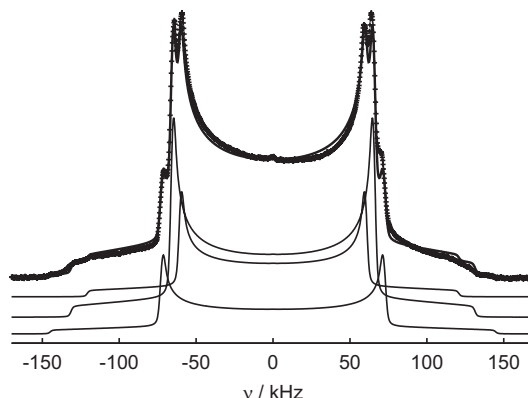


**Figure 4.7:** Deconvolution of a Pake spectrum of the ammonium group measured at 38 K. The spectrum (crosses) can be fitted (solid lines) by a superposition of three static spectra with different QCCs (161, 177, 193 kHz) and intensity ratios of 1 : 2 : 1.

**Table 4.1:** Fit results for the deconvolution of a static  $^2H$  spectrum at 38 K.

	(a)	(b)	(c)
QCC / kHz	193(2)	177(2)	161(2)
$\eta$	0.02(1)	0.02(1)	0.02(1)
intensity ratio	1	2.0(2)	1.1(2)

one crystallographically independent ammonium ion is present in the unit cell of  $\text{ND}_4\text{dca}$ , the different Pake spectra can be associated with the four N–D bonds rather than with different types of ammonium ions. Since for a covalently bound deuteron the electric field gradient is completely dominated by the electron distribution in the  $\sigma$ -bond and its orientation with respect to the external magnetic field, the magnitude of the quadrupole-coupling constant is mainly determined by the strength of the N–D bond as well as dynamical processes affecting the interaction of the deuteron with the electric field gradient.

Whereas at low temperatures the largest quadrupole-coupling constant of the spectra (193 kHz, cf. Table 4.1) corresponds to those expected for static N–D bonds of ammonium groups [176, 241, 242], we simultaneously find smaller values (161 kHz) at low temperatures as well as a continuous decrease of the quadrupole-coupling constants from temperatures  $> 133$  K (125 kHz at 370 K). A possible explanation would be the presence of a process which leads to an effective reduction of the QCCs, even if the principal reorientational process is assumed to be unchanged. In agreement with the neutron diffraction data, librational motion of the deuterons on the surface of a cone can well account for the observed phenomenon. As ammonium ion librations are expected to be fast on the NMR time scale ( $\tau^{-1} >> 3/2$  QCC), their influence on the spectra will be referred to only implicitly by starting from a reduced effective quadrupole-coupling tensor in the line-shape analyses. According to the simulations, the librational amplitudes change with temperature, and hence the resulting effective quadrupole-coupling tensor will also be a function of temperature as outlined in Figure 4.12 on page 82 below.

Provided that the N–D bond strength is similar for all N–D bonds, a marked difference of the QCCs can only result from varying hydrogen-bonding strengths and, thus, degrees of librational motion of the four N–D bonds. Evaluation of the thermal displacement parameters of the deuterons by neutron diffraction suggests deuteron D2 to exhibit less pronounced thermal motion as compared to the other deuterons D1, D3 and D4 (for nomenclature, see Figure 4.4, D labelled analogously to H [122, 123]). D2 could therefore be associated with the largest QCC, yet no satisfactory differentiation and, hence, assignment can be made for the remaining deuterons within experimental error.

Whereas in the slow motion region the experimental spectra are reproduced well by the sum of three different subspectra, this is no longer valid in the high-temperature range. Simulations performed with three effective QCCs systematically overestimate the width of the spectra above  $\approx 190$  K and do not account for the observed “shoulders” on both sides of the Lorentzian line (cf. Fig. 4.5 on page 74).

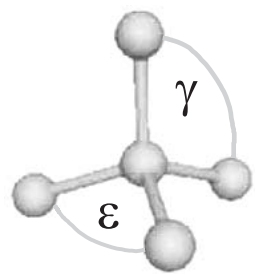
In general, one would expect the librational amplitudes of the deuterons to increase with tem-

perature, thereby inducing a large-angle tumbling of the  $\text{ND}_4^+$  group and a gradual loosening of the hydrogen-bonding network. As a consequence, the differences in the site frequencies are averaged out, and so are the quadrupole-coupling constants. Therefore, at temperatures above 160 K, a single QCC is sufficient for the simulation of the spectra.

As a second noticeable detail, the intensity in the center of the experimental spectra at intermediate temperatures (100 – 150 K) can only be satisfactorily accounted for by using a weighted superposition of a broad powder spectrum and a single Lorentzian line, although a sharp – yet weak – Lorentzian-type feature around the center frequency also arises from the simulations using a homogeneous jump process (Figure 4.6 on page 75, middle; exchange frequency 1e4). This observation also manifests itself in the bi-exponential behavior of the relaxation time between 120 and 160 K, the best fit being achieved by applying a double-exponential function accounting for two relaxational processes on a significantly different time-scale and with differing weight (cf. section 4.1.2.2 on page 82). The second relaxation process was found to be around 10 ms, which is up to four orders of magnitude faster than the main relaxational process, and to be essentially temperature independent in the small temperature window in which its relaxation time could be extracted. The noticeable increase of the Lorentzian between 120 and 160 K can be attributed to the strong attenuation of the major part of the spectrum owing to the influence of the reduction factor and simultaneous amplification of the Lorentzian by motional narrowing, thereby falsifying the true relative intensities. As the contribution of the second relaxational process is thus small ( $\approx 2 – 5\%$ ) and restricted to a limited temperature range, a separate treatment of the two different relaxational processes seems to be justified.

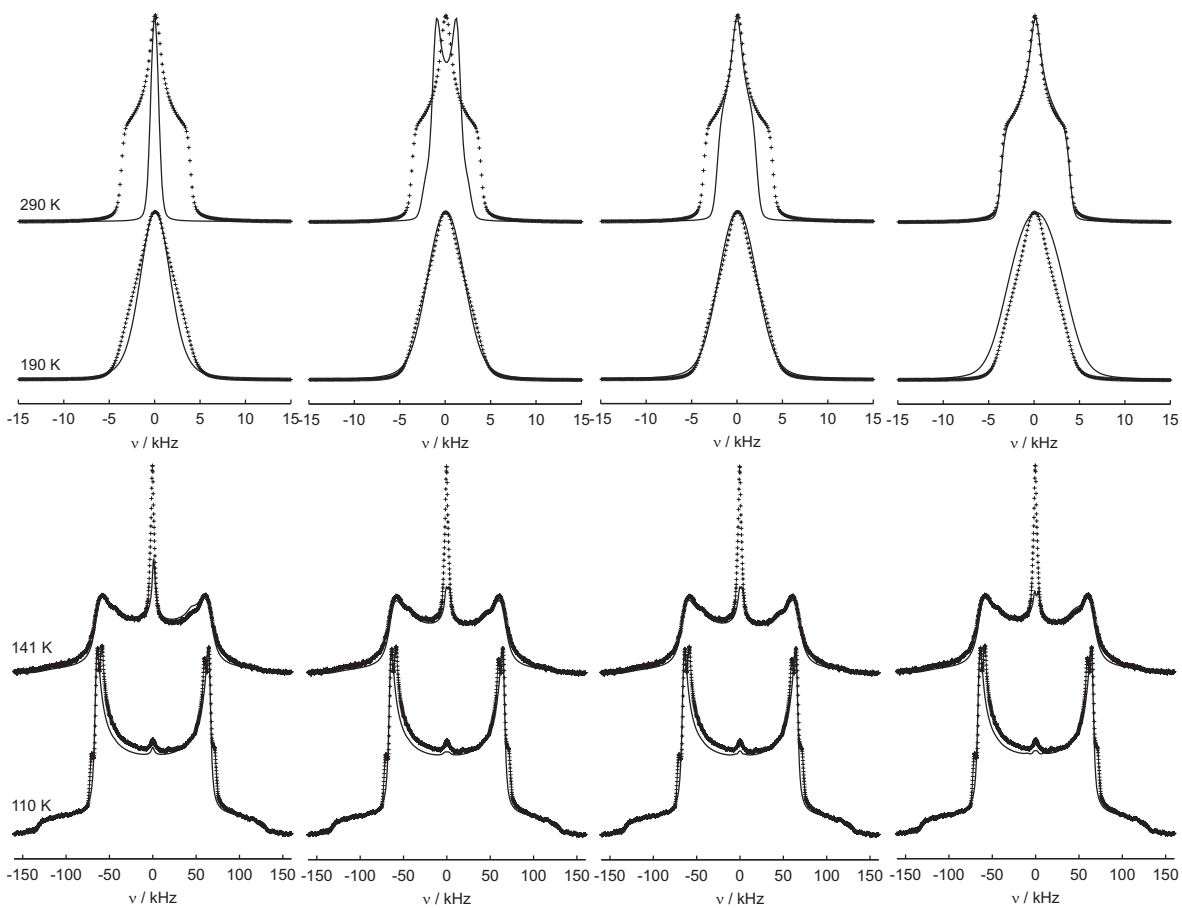
As possible sources for the observed Lorentzian, surface-adsorbed ammonium groups, volatile  $\text{ND}_3$ , or  $\text{D}_2\text{O}$  with liquid-like dynamics may be considered.

Thirdly, the high-temperature region of the experimental spectra can only be fitted accurately by using one single QCC and simultaneously introducing a distortion of the tetrahedral jump geometry. Simulations performed with the sites being located on an ideal tetrahedron are contrasted with those based on different distortions of the tetrahedral geometry in Figure 4.9. For a definition of the tetrahedral angles referred to in the following, see



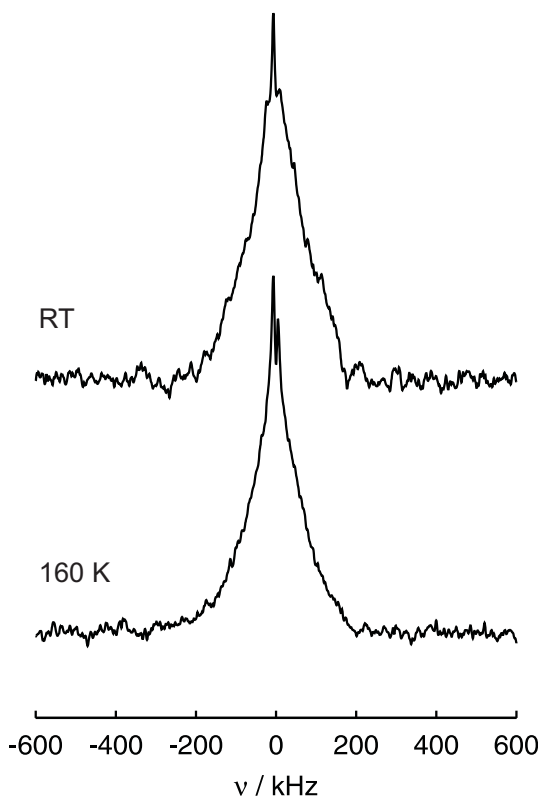
**Figure 4.8:** Definition of the tetrahedral angles  $\gamma$  and  $\epsilon$  used in the text.

Figure 4.8. The latter vary either in the magnitude or type of the distortion. A compressed tetrahedral geometry has been chosen exemplarily, which is in effect undistinguishable from an elongation of the tetrahedron in the simulations, as the line shape is only affected by the magnitudes of the respective angles. For an ideal tetrahedron with  $\Delta\gamma = \Delta\epsilon = 0^\circ$  one



**Figure 4.9:** Experimental spectra (crosses) from 110 K to 290 K (bottom to top) and simulations (solid lines) for different tetrahedral geometries with retention of at least one  $C_2$  axis. Deviations  $\Delta\gamma$  and  $\Delta\epsilon$  from the tetrahedral angle are (from left to right): Ideal tetrahedral symmetry,  $\Delta\gamma = \Delta\epsilon = 0^\circ$ ; symmetrically compressed ( $D_{2d}$  symmetry),  $\Delta\gamma = \Delta\epsilon = 1^\circ$ ; asymmetrically compressed ( $C_{2v}$  symmetry),  $\Delta\gamma = 3.5^\circ$ ;  $\Delta\epsilon = 0.5^\circ$ ; asymmetrically compressed,  $\Delta\gamma = 6.0^\circ$ ;  $\Delta\epsilon = 0.5^\circ$ .

would expect a liquid-like Lorentzian at high temperatures, whose width is about one quarter of the experimental line width; we can therefore discard ideal tetrahedral geometry for the  $\text{ND}_4^+$  ion in the high-temperature region. The same applies for a symmetrically compressed (or stretched) tetrahedron, for which we would expect a slightly broadened line with a pronounced symmetric splitting at fast reorientational frequencies. This effect is so pronounced that even distortions of as little as  $\Delta\gamma = \Delta\epsilon = 1^\circ$  would clearly show up in the spectrum. Around 190 K, a symmetrically distorted tetrahedron matches the experimental data quite well; the same holds true for an asymmetrically stretched tetrahedron, which is shown for a minor distortion of  $\Delta\gamma = 3.5^\circ$  and  $\Delta\epsilon = 0.5^\circ$  in Figure 4.9. The high-temperature spectra do, however, not satisfactorily reproduce the experimental results as the spectral width of the signal – though slightly broadened – is still too small.



**Figure 4.10:**  $^{14}\text{N}$  wide-line spectra measured at 160 K (bottom) and room temperature (top). The full width of the spectra ( $\sigma_{zz}$ ) is disguised by technical problems in realizing larger excitation widths.

The best fit is achieved when considering a significantly asymmetric distortion of the tetrahedral jump geometry at higher temperatures, which amounts to about  $\Delta\gamma = 6^\circ$  and  $\Delta\epsilon = 0.5^\circ$ . The broadening of the Lorentzian as well as the characteristic “humps” of the otherwise straight flanks are thus reproduced quite smoothly. At temperatures below  $\approx 210$  K, the simulated line shapes overestimate the size of the spectrum, which prompts us to postulate a decreasing distortion of the tetrahedron with decreasing temperature. As can be seen from Figure 4.9, the influence of the distortion diminishes below  $< 150$  K, where simulations for different degrees of tetrahedral compression essentially yield identical spectra. From a crystallographic point of view we would expect a distortion to take place at lower temperatures when rotational motion gradually freezes out and the cation no longer experiences an average crystal field. This effect could principally play a role in the case of ammonium dicyanamide as well, as we cannot distinguish between different degrees of

distortions in the low-temperature region. It does, however, not seem straightforward to assume significant distortion in the low-*and* high-temperature region, with a temporal lifting of the distortion in the intermediate temperature range. This model is therefore not considered further.

A possible source of increasing distortion of the tetrahedron could, however, be the anisotropic temperature-dependence of the lattice parameters in ammonium dicyanamide [122, 123, 163]. Possibly, the observed decrease of the *c*-axis comes along with a compression of the ammonium ion along an axis parallel to *c*, that is, roughly along the vector connecting D2 and D3 (cf. Fig. 4.4 on page 73). Therefore, the latter deuterons may approach each other with increasing temperature, thus well giving rise to the observed distortion of one tetrahedral angle ( $\Delta\gamma$ ) of  $\approx 6^\circ$ . An independent proof of the tetrahedral distortion can be expected from  $^{14}\text{N}$  ( $I = 1$ ) NMR spectroscopy, as the quadrupolar broadening at the ammonium-nitrogen would vanish in case of perfect tetrahedral symmetry. Figure 4.10 displays two wide-line  $^{14}\text{N}$  spectra ob-

tained at different temperatures, exhibiting powder spectra with widths in the 0.8 MHz range. Owing to the limited spectral width of the probe and the final excitation width determined by the pulse length, it was not possible to accurately determine both the asymmetry and width of the spectra. Nevertheless, the obvious broadening of the spectra on going from low to high temperatures clearly indicates a significant distortion of the tetrahedral symmetry to be present, thus supporting the above line of argument.

Using the above findings as increments, based on which a general picture of the ammonium ion geometry and dynamics can be established, the results from the line-shape simulations between 38 K and 390 K are outlined in Figure 4.11.

In Figure 4.12, the change of the effective quadrupole-coupling constant is contrasted with the change of the tetrahedral distortion as obtained by the simulation as a function of temperature. In order to assess the librational amplitudes for the deuterons in the observed temperature range, a common fixed QCC of 177 kHz at all temperatures as well as the respective reorientational frequencies obtained from the variable QCC-fits were used (Fig. 4.11), leaving the librational amplitudes as the fitting parameter. Taking into account neutron diffraction and quasielastic neutron scattering data (cf. section 4.1.3.3), we have to consider the presence of significant librational motion at the lowest temperatures accessible in the NMR experiment. When fixing the static QCC at 177 kHz, the corresponding librational amplitude is 5° at 38 K which seems a reasonable value at this temperature. The librational amplitudes calculated

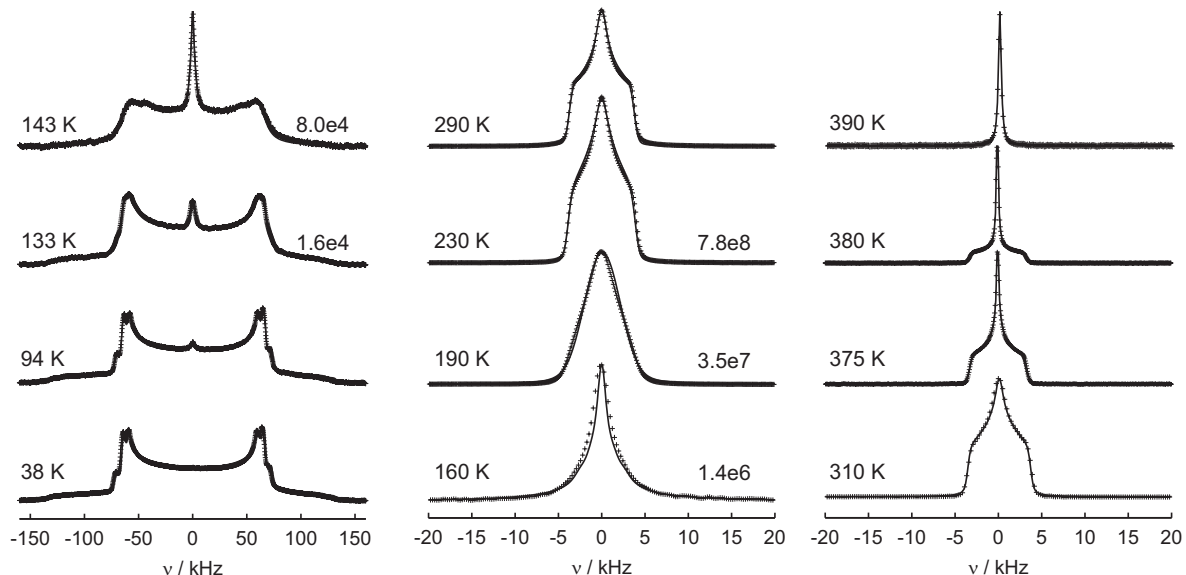


**Figure 4.11:** Experimental spectra obtained between 38 and 390 K, together with the respective line-shape simulations. Both a central Lorentzian and three QCCs at low temperatures (cf. text) were taken into account. Jump rates  $\pi_{ij}$  are given in seconds. The high-temperature solid-echo spectra at  $T \geq 375$  K already show signs of the transformation onset (increase of the central  $ND_3$  signal).

according to this procedure are displayed in Figure 4.12 (right), together with the amplitudes extracted by neutron diffraction for comparison (cf. Figure 4.25 on page 100). The librational amplitudes obtained from NMR were fitted by using an analytical function based on a simple cone-type librational model with one half of the cone opening angle being defined as the librational amplitude. Owing to the somewhat arbitrary choice of the starting parameters,

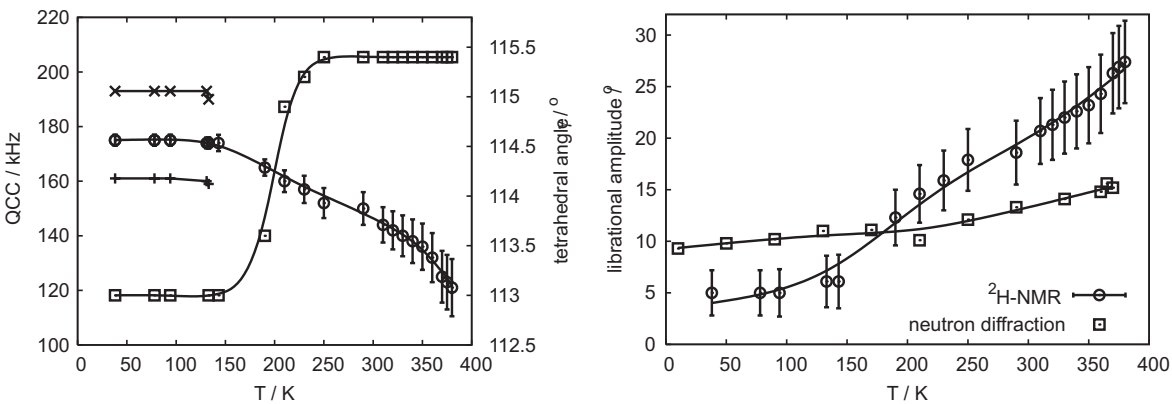


**Figure 4.12:** Left: Quadrupolar coupling constants and tetrahedral distortion ( $\Delta\gamma$ , squares) as a function of temperature. Right: Librational amplitudes for the ammonium group obtained by wide-line  $^2\text{H}$  NMR spectroscopy (circles) as a function of temperature, using a static QCC of 177 kHz and a simple cone-type librational model, and by rigid-body analysis of neutron powder diffraction data (squares).

the values obtained from  $^2\text{H}$  NMR should not be over-interpreted, the more so by considering the fact that the underlying models for librational motion are slightly different for the three experimental data sources, rendering a direct comparison critical. From inspection of both librational amplitudes and effective quadrupole-coupling constants (Fig. 4.12, left), which are intrinsically linked with each other, we can associate the temperature range between 160 and 230 K with the most prominent dynamical changes. Most likely this feature correlates directly with the onset of  $\text{ND}_4^+$ -distortion developing with a sigmoidal increase as a function of temperature.

#### 4.1.2.2 Relaxation Studies

To learn about the time scale and homogeneity of the reorientational dynamics of the ammonium group beyond the fast motion limit, which is not accessible by line-shape analysis, the temperature dependence of the  $^2\text{H}$  spin-lattice relaxation time was probed by applying a saturation-recovery sequence (Figure 4.13, left). The fast relaxational process attributable to a liquid-like reorientational behavior of a small fraction of ammonium groups (cf. above) was only taken into account at temperatures between 120 and 160 K by using a double-exponential fit function; at all other temperatures, the relaxation behavior was found to be monoexpo-

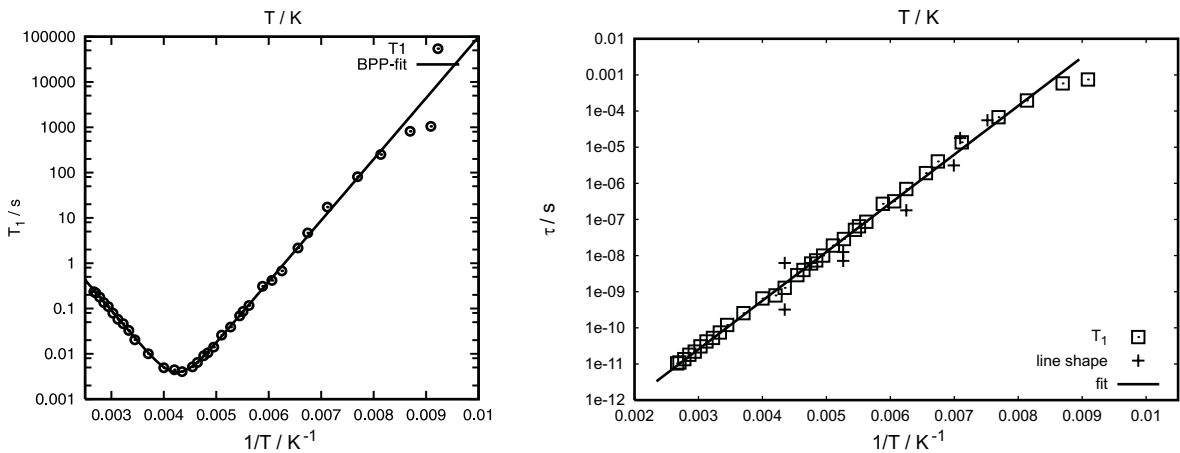


**Figure 4.13:** Left:  $T_1$  relaxation time measurements for the reorientational motion of the  $ND_4^+$  ion as a function of the inverse temperature. The experimental data (circles) are fitted by using a BPP-type model (solid line). Right: Arrhenius plot of the correlation time  $\tau$  versus inverse temperature. Synopsis of the data obtained from  $T_1$  relaxation measurements (squares) and those extracted from the line-shape analyses (crosses) by using the relation  $\tau = (4 \cdot \pi_{ij})^{-1}$ . The spin-lattice relaxation data based on Eqs. 3.51 on page 62 and 3.52 on page 62 are considered more reliable owing to the larger number of data points and the smaller estimated standard deviation.

ential. Note that this scenario is consistent with the line-shape analyses (cf. Fig. 4.11 on page 81), which in the low and lower intermediate temperature regime were carried out using a superposition of the powder spectrum and a Lorentzian line. The latter can therefore be associated with the observed fast relaxational process. A contour plot of the relaxation time measurements at 83 K is shown in Figure 4.14. The relaxation time of the central Lorentzian is roughly 10 ms, whereas the saturation recovery for the main fraction of the spectrum gives rise to  $T_1 \approx 1800$  s.

According to the above line of argument, only the data for the dominating structural relaxation process were taken into account for extracting the temperature dependence of the longitudinal relaxation time, the latter spanning a range between a minimum of  $\approx 4$  ms at 230 K to maximum values of  $> 2000$  s below 100 K. The data could be fitted by using a simple BPP-type model (Fig. 4.13, left), corresponding well to that expected for an isotropic tetrahedral jump motion and an average QCC for the four deuterons of 177 kHz (Eq. 3.51 on page 62).

By evaluating the spin-lattice relaxation rate  $T_1^{-1}$ , which is determined by the spectral density and QCC (valid for isotropic jump processes), we can derive correlation times and jump rates for the reorientational processes (Eqs. 3.52 and 3.53 on page 62). In Figure 4.13 (right) the correlation times obtained from relaxation measurements as well as such obtained from line-shape analyses are plotted against the inverse temperature, yielding an essentially straight line. From the Arrhenius-like temperature behavior and the magnitude of the attempt frequencies

we can classify the reorientational jumps as a thermally activated single-particle process.

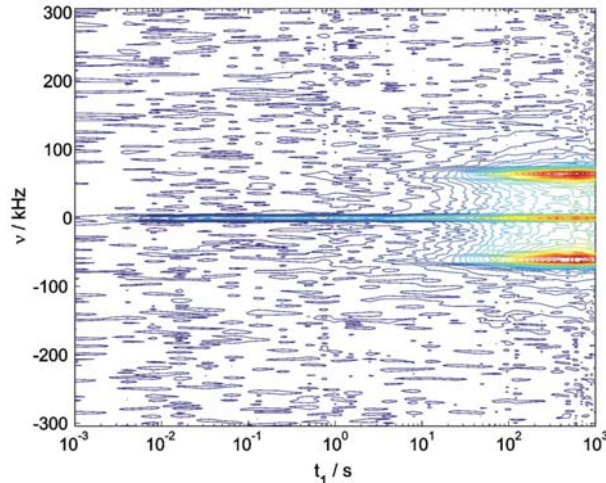


**Figure 4.14:** 2D representation of the saturation-recovery sequence applied to a solid-echo  $^2H$  experiment at 83 K. The longitudinal relaxation time of the central Lorentzian amounts to 10 ms, whereas the Pake spectrum has a relaxation time of 200 s. The intensity ratio of the two spectral features is 0.02, thus justifying a separate treatment in a heterogeneous scenario.

The slope of the straight line directly delivers the energy of activation for the jump process as  $25.8(2)$   $\text{kJ mol}^{-1}$ , and an attempt frequency  $\tau_0^{-1}$  of  $440(80)$  THz. Compared to similar simple non-deuterated ammonium salts such as  $(\text{NH}_4)_n\text{X}^{n-}$  ( $\text{X} = \text{SnCl}_6, \text{BF}_4, \text{GeF}_6, \text{PbCl}_6, \text{ClO}_4, \text{PtCl}_6, \text{PdCl}_4$ ) [243–248], which exhibit activation energies in the order of  $1.5 - 6.7$   $\text{kJ mol}^{-1}$ , this value appears to be at the upper end of the scale, which is indicative of comparatively high potential barriers for the reorientational motion of the ions due to rather strong hydrogen bonding of the ammonium group to the surrounding anions.

This finding renders the presence of rotational diffusion highly unlikely as stated above: The latter type of motion comes

along only with flat potential walls, typically occurring in the high-temperature region and displaying a non-classical temperature behavior. Similarly high activation energies were for instance reported for  $\text{NH}_4\text{Cl}$  ( $\approx 19$   $\text{kJ mol}^{-1}$ ) [249] and for  $[\text{NH}_4][\text{HF}_2]$  (25  $\text{kJ mol}^{-1}$  extracted from proton  $T_1$  measurements) [250]. The magnitude of the jump rate  $\tau^{-1}$  at the high-temperature end is in the THz region and therefore close to the frequencies of the lattice vibrations.

#### 4.1.2.3 Reactivity: High-Temperature Studies

The conversion of  $\text{ND}_4\text{dca}$  into dicyandiamide has been investigated by *in situ*  $^2H$  measurements at temperatures above 370 K (Figs. 4.5 on page 74 and 4.11 on page 81).

To record a close-to-realtime picture of the transformation process, typically a slow heating rate of the sample ( $1$   $\text{K min}^{-1}$ ) was chosen, followed by isothermal treatment at the respective reaction temperature (372 – 380 K). The onset of the reaction was clearly indicated by the gradual growth of a central Lorentzian line with a width of roughly 500 Hz (FWHM). The increase of the Lorentzian was accompanied by a decrease of the  $\text{ND}_4^+$  spectrum, which is shown at three different waiting times at 380 K in Figure 4.15 (left). An

estimate of the relative fractions of the subspectra was carried out by deconvoluting the total spectrum and extracting the relative portions of the two contributing species as shown in Figure 4.15 (right). The Lorentzian can be attributed to highly mobile  $ND_3$  being released during the reaction. Although theory and previous experiments already suggested ammonia to be a reactive intermediate during the transformation [122, 123, 163], the evolution of the latter could be proven directly for the first time by the *in situ*  $^2H$  NMR data. However, it cannot be decided on the basis of the 1D spectra alone whether the Lorentzian line originates from free  $ND_3$  in the gas phase above the solid sample, or is rather due to  $ND_3$  adsorbed on the sample surface, or even “quasi-free”  $ND_3$  diffusing through the bulk sample *in statu nascendi*. Towards the final phase of the reaction, spectra were recorded using longer recycle delays (200 s) so as to probe spectral fractions pertaining to slowly relaxing species, which were previously suppressed by applying short scan delays. By doing so, a broad Pake spectrum superposed on the narrow ammonia signal could be visualized, which most likely can be attributed to the product species dicyandiamide (Fig. 4.16).

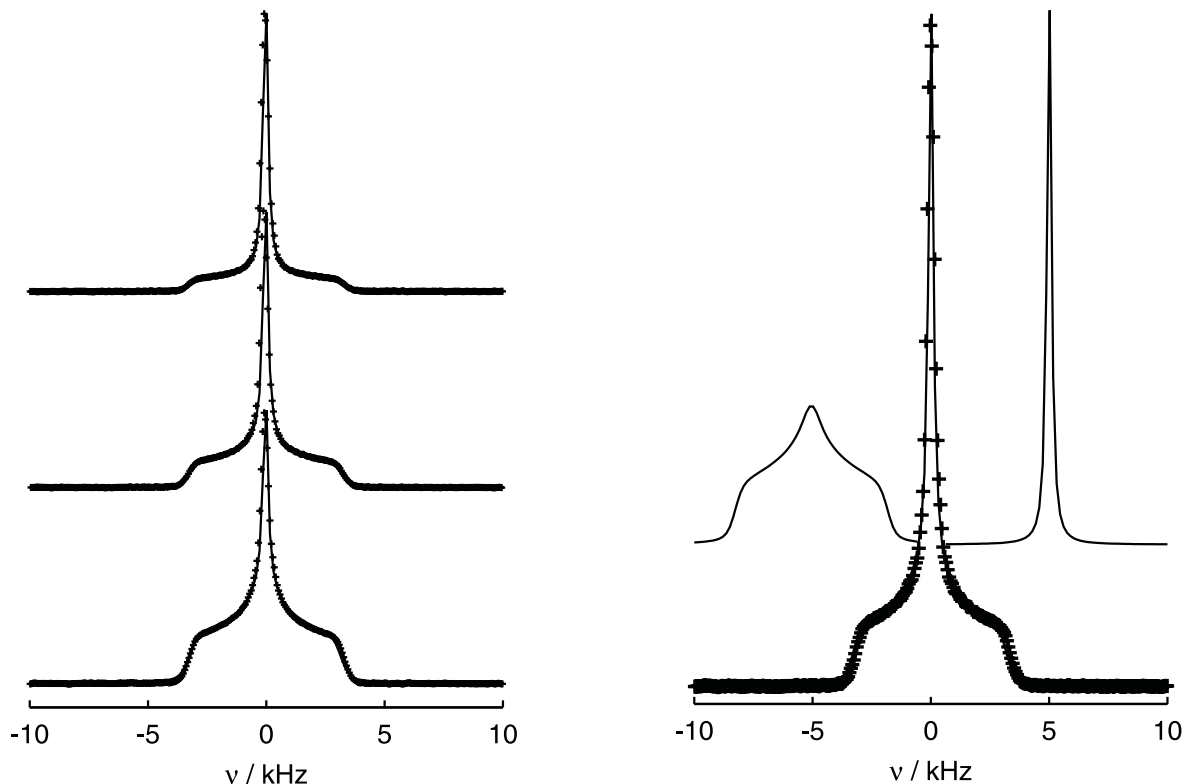


**Figure 4.15:** Left: Fits (solid lines) of the experimental spectra (crosses) recorded at 380 K for different tempering times. Right: The fit can be represented by the sum of two subspectra pertaining to  $ND_4^+$  (broad spectrum) and  $ND_3$  (Lorentzian).

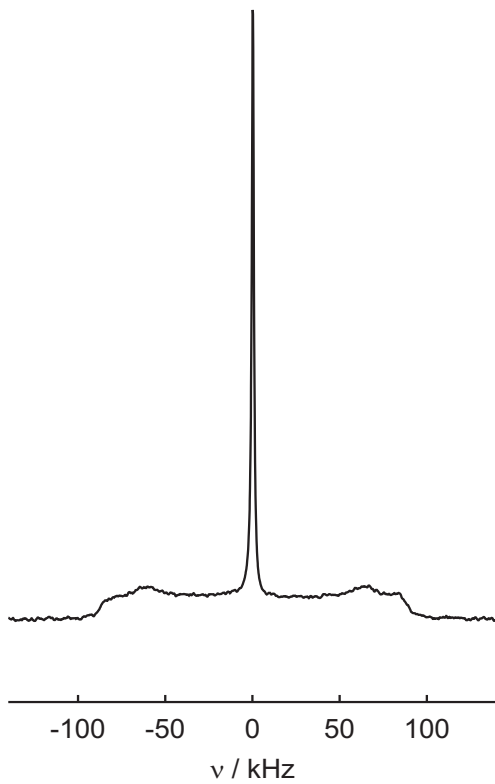


**Figure 4.16:**  $^2\text{H}$  wide-line spectrum measured after a tempering time of 360 minutes at 380 K (recycle delay 300 s). The experimental spectrum is a superposition of a broad Pake spectrum, presumably originating from dicyandiamide, and the  $\text{ND}_3$  Lorentzian.

Apart from small angle librations, the amino groups of the latter are expected to be largely static at the temperature under consideration, thus giving rise to a quasi-static powder spectrum as was observed in the experiment. The reduction of the  $\text{ND}_4^+$  portion of the spectra proceeds on different time scales depending on the chosen target temperature.

Interestingly, the evolution of ammonia does not – as could be expected – approach a limit value which is then maintained, since the reaction proceeds in a closed system. Contrarily, a gradual decrease of ammonia is observed beyond a certain point, which points to the successive “consumption” of ammonia as the reaction proceeds. The ammonia intensity is plotted in Figure 4.17 as a function of time at four different target temperatures between 372 and 380 K. The origin of the time axis is associated with the onset of heating at room temperature, which results in the release of ammonia being observed only shortly before reaching the target temperature after 80 minutes on average.

The onset and initial velocity of ammonia evolution does not vary significantly with the target temperature chosen. For the lowest temperatures (372 and 375 K), however, the rate of ammonia evaporation decelerates steadily (negative curvature), whereas at 378 and 380 K a short “induction” phase is observed, followed by an acceleration period (positive curvature) and a terminal slowing down near the maximum  $\text{ND}_3$  intensity. As a consequence, the maximum  $\text{ND}_3$  intensity is reached significantly later at lower temperatures as compared to the situation at 378 and 380 K.

Since the generated ammonia is subsequently consumed stoichiometrically as the reaction towards dicyandiamide proceeds, we deal with two independent processes characterized by differing time constants, where the formation of ammonia is typically faster than its reassembly. The latter is much more attenuated at lower temperatures, proceeding on a time scale of several hours. At 372 K the decrease in  $\text{ND}_3$  intensity apparently levels off after isothermal

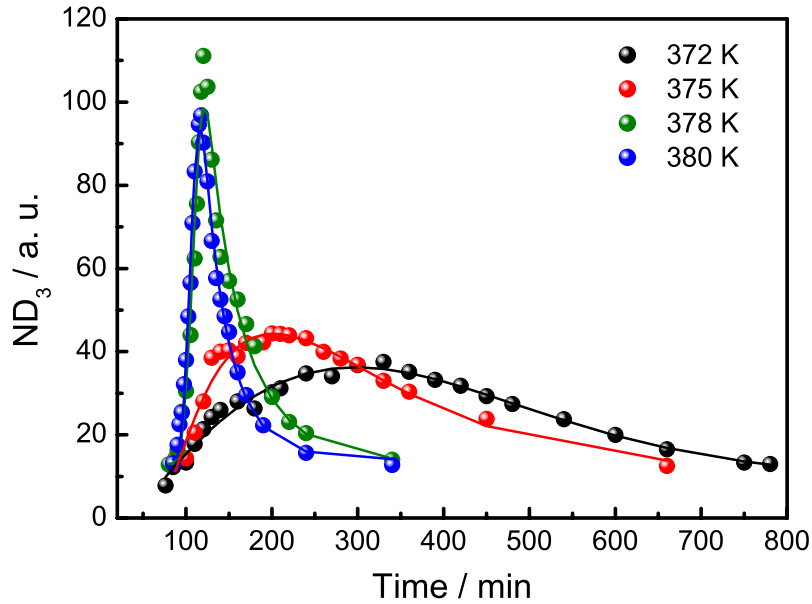


**Figure 4.17:** Time evolution of the ND<sub>3</sub> intensity, monitored at 372 K (black), 375 K (red), 378 K (green), 380 K (blue) and fitted using Eq. 4.1.

tempering for 12 hours, suggesting the transformation did not proceed quantitatively within the experimental time window.

To parameterize the time evolution of the ammonia intensity, an Avrami-type equation was modified with an exponential decay as a function of the “reaction time”  $t$ . In its original form, the Avrami-Erofeev expression was developed for nucleation and crystal growth kinetics [251–254]; in the present context, however, it is simply used to continuously fit the observed change from both sigmoidal and deceleratory growth to exponential decay. The isothermal yield-time curves are represented by

$$I(t) = I(0) + M_0 \cdot \exp - ((t - t_0)/\tau_1)^a \cdot \left\{ 1 - \exp - ((t - t_0)/\tau_2)^b \right\}, \quad (4.1)$$

where  $M_0$  is the fitting parameter for the maximum signal intensity. The most relevant fit parameters ( $t_0 \approx 76 - 85$  minutes) are listed in Table 4.2.  $\tau_2$  accounts for the rate of ammonia evolution, while  $\tau_1$  is associated with the decrease of ND<sub>3</sub>. By introducing the exponents  $a$  and  $b$  the curvature of both decay and slope can be suitably adjusted. From Table 4.2 it can be seen that  $\tau_1$  is similar for 378 and 380 K, whereas it is about ten times larger at 375 K, and almost twenty times at 372 K. Similar relations hold for  $\tau_2$ , suggesting the rate of ND<sub>3</sub> evolution and consumption to increase significantly with isothermal temperature.

Nevertheless, for temperatures  $\geq 378$  K the kinetics of both  $\text{ND}_3$  evolution as well as decrease are similar and can hardly be distinguished within experimental error.  $I(0)$  accounts for the fact that no abrupt onset, but rather a smooth increase of ammonia evolution during the heating period, i.e. already before reaching the target temperature, is observed.

**Table 4.2:** Fit results for the time dependence of ammonia evolution at 372, 375, 378, and 380 K, using Eq. 4.1. The time constants  $\tau_1$  and  $\tau_2$  are given in minutes, the initial  $\text{ND}_3$  intensity at the target temperature  $I(0)$  in arbitrary units.

Parameter	372 K	375 K	378 K	380 K
$\tau_1$	370(9)	180(11)	19(2)	16(2)
$\tau_2$	345(23)	120(10)	36(2)	26(2)
$a$	1.8(3)	1.4(3)	0.7(1)	0.8(2)
$b$	1.0(2)	1.2(2)	4.2(6)	3.6(6)
$I(0)$	10(1)	11(2)	13(2)	14(2)

As outlined above, for the two lower temperatures a deceleratory kinetics, which can be translated into a consistent reduction of the rate of ammonia evolution, is observed, while a sigmoid-type curve best describes the growth kinetics for  $T \geq 378$  K, corresponding to a change of  $b$  from  $\approx 1$  at lower temperatures (first-order kinetics) to  $b > 1$  at 378 and 380 K. In the latter temperature regime, a short “induction” time prior to the acceleratory growth is observed, which may be associated with a structural rearrangement (generation of defects, amorphization or microscopic melting) required for the release of ammonia from the former ammonium sites. After passing an acceleratory regime at  $T \geq 378$  K, the evolution of ammonia finally slows down at all temperatures, possibly induced by the  $\text{ND}_3$  equilibrium pressure reached in the gas phase, which counteracts further evaporation of ammonia. Ammonia “re-consumption” can roughly be described using a Gaussian-type decay ( $b \approx 2$ ) at lower temperatures, whereas at higher temperatures it becomes increasingly first-order ( $b \approx 1$ ), indicating the concentration of ammonia to be the rate determining factor for the conversion of the presumed intermediate “ $\text{HN}(\text{CN})_2$ ” into dicyandiamide.

Considering the entire reaction process including the initial deuteron (proton) transfer, we are now able to draw a realistic picture of the different time scales on which the transformation proceeds: According to Schotte et al. [255, 256], a coupling between the relaxational single particle motion and lattice modes is possible if both are of the same order of magnitude. We can therefore argue that in the presence of fast reorientational motion of the  $\text{ND}_4^+$  tetrahedra, the transfer of a deuteron to an adjacent anion is stimulated by the coupling of the jump motion to the lattice modes, thereby providing a mechanism for the deuteron detachment and the following transformation of the ionic ammonium dicyanamide into the molecular compound

dicyandiamide. As the jumps of the  $\text{ND}_4^+$  group can be considered to be instantaneous (cf. above), the dwell time of the deuterons (protons) on their actual sites roughly corresponds to the correlation time at temperatures above 370 K. Thus, the detachment of the deuteron (proton) is likely to proceed in a cooperative fashion upon translational-rotational coupling on a time scale in the order of  $10^{-11}$  s. As the deuteron (proton) transfer is very fast, the rate determining step of the overall reaction is not associated with the deuteron (proton) transfer, but with the separation of ammonia from the ammonium sites, its diffusion through the sample, and its subsequent nucleophilic addition to the nitrile carbon. These processes may be retarded by a temperature gradient, giving rise to a non-uniform propagation of the transformation within the powdered sample. At any rate, the velocity of the overall transformation is in the order of minutes, which corresponds to a time regime typically encountered in solid-state reactions.

It has previously been observed that conducting the reaction under the pressure of ammonia facilitates the product formation and leads to significantly higher yields [122, 123, 163]. From the  $^2\text{H}$  NMR experiments we can therefore add evidence that counter pressure of ammonia is essential for its re-uptake into the sample and stoichiometric consumption, which cannot be ensured if

- ammonia is allowed to evaporate from the sample and
- the reaction time is chosen too short with respect to the reaction temperature.

We note that prior to these investigations it has not been clear that reaction times beyond a minimum of four hours have to be chosen in order to furnish satisfactory conversion and yield. If the reaction is terminated too early, a lack of ammonia will inevitably result in the formation of a large fraction of amorphous material, presumably the polymerization product of the free acid dicyanamide  $\text{HN}(\text{CN})_2$ , which is likely formed together with ammonia in the first step of the reaction. Dicyanamide has long been known to be particularly acidic and, at the same time, highly susceptible to polymerization [230, 240]. The question to which extent ammonia is inevitably “lost” in a side reaction, accompanied by polymerization of dicyanamide, cannot be decided unambiguously. To resolve this issue, a simultaneous *in situ* screening of the  $^2\text{H}$  spectra of the starting material and the product would be necessary, which is critical owing to the long  $^2\text{H}$  relaxation time of the deuterons in dicyandiamide.

### 4.1.3 Neutron Scattering

Information on the temperature-dependent rotational dynamics of the  $\text{NH}_4^+$  ion and the vibrational states of ammonium dicyanamide as a whole, which is complementary to that obtained from  $^2\text{H}$  NMR, was furnished by quasielastic and inelastic neutron scattering experiments at the BSS and SV-29 instruments of the FRJ-2 research reactor (Forschungszentrum Jülich), respectively.

Analysis of quasielastic scattering data, in a well-defined system, is very much simplified by employing a strong incoherent scatterer, such as hydrogen. This eliminates the need to model pairwise interactions between atoms and concentrates solely on the dynamics of the individual hydrogen atoms. For an incoherent scatterer undergoing reorientational motion, the scattering function is composed of a quasielastic as well as an inelastic term and may be written as (cf. section 3.2.1 on page 41)

$$S(Q, \omega) = \exp \left[ -\langle u^2 \rangle Q^2 \right] \{ EISF(Q) \delta\omega + [1 - EISF(Q)] L(\Gamma, \omega) \} \otimes R(\omega) + S^{inel}(Q, \omega) \quad (4.2)$$

where

$$L(\Gamma, \omega) = \frac{1}{\pi} \frac{\Gamma}{\Gamma^2 + \omega^2}. \quad (4.3)$$

$\langle u^2 \rangle$  is the mean squared atomic displacement (MSD) whose  $Q$ -dependence is expressed in terms of the Debye-Waller factor  $\exp \left[ -\langle u^2 \rangle Q^2 \right]$ , and  $R(\omega)$  denotes the instrumental resolution function.

#### 4.1.3.1 QENS: Inelastic Fixed Window Scans

Inelastic fixed window scans (IFW) at an energy offset of  $\Delta E = 14.5 \mu\text{eV}$  were carried out in a large temperature range between 10 and 380 K in order to assess the compatibility of the backscattering instrument with the energy characteristics of the reorientational motion of ammonium dicyanamide. This technique allows relaxational processes to be observed by the intensity of inelastically scattered neutrons at the specified energy, thus yielding information similar to that obtained from dynamic mechanical or dielectric spectroscopies, or from  $T_1$  relaxation measurements as discussed in section 4.1.2.2.

A dynamic process is observed to enter the dynamic window accessible to the instrument at temperatures of  $\approx 230$  K, which peaks around 320 K (“low-temperature process”). The regular descent of the intensity, however, is distorted by the onset of another process

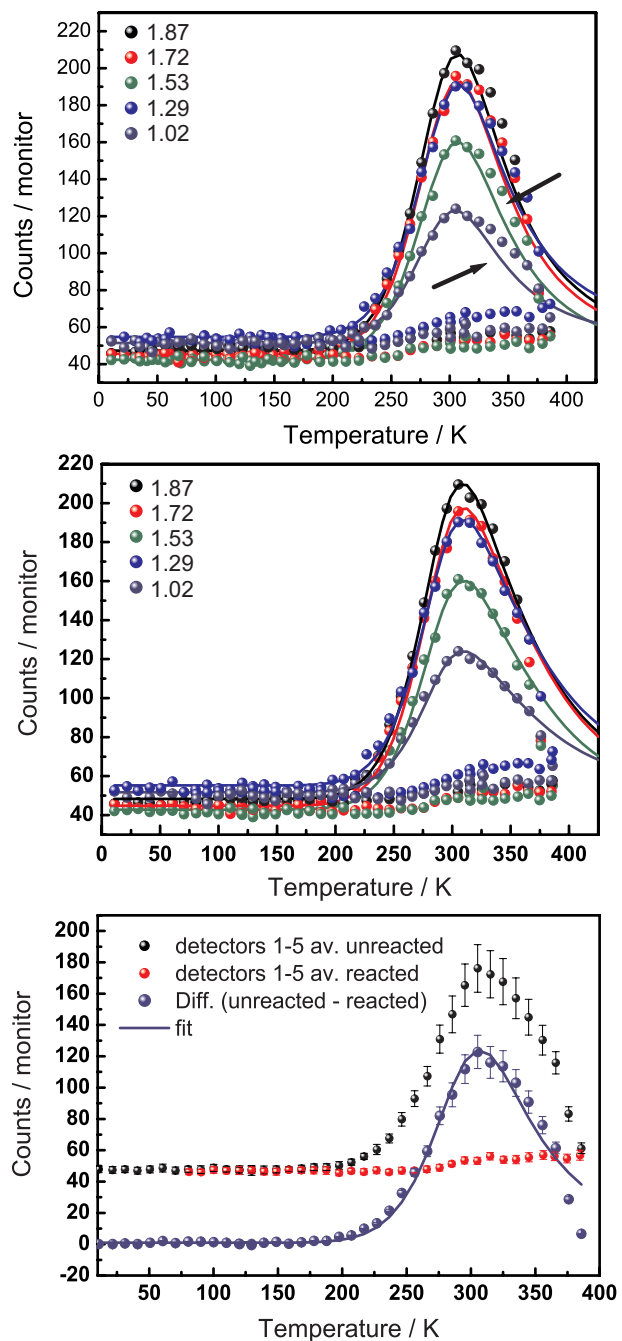


**Figure 4.18:** Inelastic fixed window scans of  $\text{NH}_4\text{dca}$  as a function of temperature at different wave vector transfers (in  $\text{\AA}^{-1}$ ). Heating of ammonium dicyanamide is associated with the high intensity curves; the low intensity curves correspond to heat treatment of the reacted sample. Color differentiation according to the scattering angle of the respective detector groups 1 to 5. Three different approaches to data evaluation are shown: Top: model A; middle: model B; bottom: model C. The discrepancy between the fit curves and the experimental data for model A is pointed out by arrows for two representative detectors. For further details see text.

(“high-temperature process”), which is either correlated with the beginning of the slow transformation of the sample, or can be interpreted in terms of changes in the energy characteristics of the actual jump process (Fig. 4.18, heating curves for  $\text{NH}_4\text{dca}$  (high intensity curves)). The effective onset of the transformation, however, can clearly be seen by the rapid drop-off in the intensity around 360 K, which is not retraced by the fitting curves. This disproportionate loss of intensity does, however, not necessarily indicate the absence of relaxational processes, but rather the intensity of the inelastic scattering to move out of the energy window  $\Delta E$  of the IFW scans, caused by a change of the characteristic time scale of the process.

In order to probe the relaxational processes present after the transformation, which may either be specific of the product, or due to unreacted sample, or indicative of reactive intermediates such as  $\text{NH}_3$  not fully consumed during the transformation, IFW-scans were performed with the reacted sample between 80 and 320 K. The slight increase in intensity at temperatures around 260 K clearly suggests a relaxation process in the appropriate energy window to operate, though detectable only with strongly attenuated intensity and a slightly different time scale as compared to the unreacted sample (Fig. 4.18, heating curves for the transformation product (low intensity curves); further discussion see below).

**Table 4.3:** Relaxation parameters obtained for the “low-temperature” relaxational process from different data evaluations. The following data were used as the data basis: (A) Average from separate fits of detectors 1-5, using a single exponential in each case; only the build-up of the curves (heating measurements, data points 1-35) were taken into account for the fits. (B) Separate fit of detectors 1-5 with a double peak function allowing for the use of two relaxational processes (heating measurements, all data points). (C) Difference plot between the detector average of the unreacted and that of the reacted sample, respectively (all data points).

	(A)	(B)	(C)	$^2\text{H}$ NMR
$E_a$ / kJ mol <sup>-1</sup>	$20.9 \pm 0.6$	$23.7 \pm 1.7$	$23.3 \pm 0.8$	$25.8 \pm 0.2$
$T_{max}$ / K	$310.3 \pm 2.0$	$306.8 \pm 3.7$	$306.9 \pm 2.8$	
$\tau_0^{-1}$ / THz	$11.6 \pm 3.1$	$38.1 \pm 8.7$	$31.9 \pm 4.3$	$435 \pm 80$

Accordingly, when comparing the temperature dependence of the relaxation time with the data from Figure 4.13 (left), which could be fitted using a BPP-type model with a single relaxation time, the scenario is different for the IFW data. Considering only a single relaxational process cannot fully account for the broadening observed in the high-temperature regime, as illustrated in Figure 4.18 (top spectrum). However, as the “low-temperature process” dominates the spectrum, the curve was fitted by using only the slope and ignoring the data points of the drop-off (model A) as a rough approximation. The relevant fit parameters corresponding to the dominant relaxational process are listed in Table 4.3 (left). A better fit is obtained when using the sum of two Vogel-Fulcher-type equations accounting for the presence of two distinct

relaxational processes with different energy characteristics (model B, Fig. 4.18 and Table 4.3, middle) [150, 151]. Owing to the very small contribution of the “high-temperature process”, its energy of activation ( $\approx 25 \text{ kJ mol}^{-1}$ ) could not be determined reliably. Considering the temperature run for the reacted sample, a possible correlation with the shoulder observed for the “high-temperature process” in the transformation region may be conjectured. Therefore, the data for  $\text{NH}_4\text{dca}$  and the product were averaged and subtracted. The resulting data set was then fitted inferring a single relaxation process, yielding a reasonable agreement with the difference plot (model C, Fig. 4.18 and Table 4.3, right).

Figure 4.19 displays the temperature dependence of the inverse correlation time obtained for models A – C. The linear correlation that arises when plotting  $\ln(\tau^{-1})$  vs.  $1/T$  clearly indicates an Arrhenius-type behavior typical of thermally activated processes.

All models used above principally furnish alternative approaches to the characterization of the *major* relaxational process observed in the IFW-scans. Although model A slightly underestimates both  $E_a$  and  $\tau_0^{-1}$ , the results of the different models are in reasonable agreement with each other.

Though being similar in terms of the principal order of magnitude, the IFW-data yield systematically smaller values for  $E_a$  and  $\tau_0^{-1}$  as compared to the  $^2\text{H}$  NMR data (Table 4.3 and Fig. 4.13 on page 83). However, two facts must be taken into account: First, the reorienta-

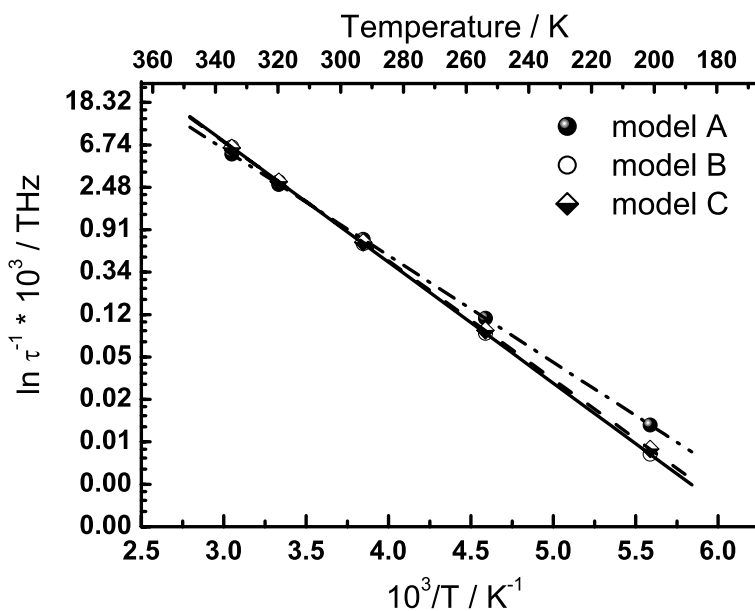


**Figure 4.19:** Arrhenius plots of the inverse correlation time  $\ln(\tau^{-1})$  versus the inverse temperature for IFW models A – C.  $\tau^{-1}$  was calculated based on the parameters obtained from the different IFW-fits as listed in Table 4.3.

tional dynamics may differ in terms of their energy characteristics for deuterated ( $^2H$  NMR) and protonated (QENS) samples. Secondly, both techniques detect reorientational relaxations with different correlation functions  $F(t)$ , where that for QENS  $\{\langle P_1(\cos\theta(t)) \rangle\}$  is associated with the first Legendre polynomial  $P_1$ , while that for NMR  $\{\langle P_2(\cos\theta(t)) \rangle\}$  is proportional to the second Legendre polynomial  $P_2$ . As a consequence, the inverse correlation times in QENS may be smaller by a factor of  $\geq 10$  [158, 257], which may explain the observed discrepancy. As for the nature of the minor relaxational process, no ultimate evidence can be given for either of the possibilities outlined above. On the one hand, reorientational dynamics of ammonia contained in the bulk sample or physisorbed on the surface during and after the transformation would presumably give rise to onset and maximum temperatures  $T_m$  in the IFW-plot significantly lower than that observed in the experiment ( $T_{onset} \approx 260$  K,  $T_m \approx 360$  K) [258]. On the other hand,  $180^\circ$  jumps of the amide protons of the transformation product dicyandiamide  $\text{NCN}=\text{C}(\text{NH}_2)_2$  are expected to give rise to inelastic scattering at significantly higher temperatures, associated with a larger energy transfer. In fact, only a limited number of  $180^\circ$  rotational jumps observed within the time scale window available to quasielastic neutron scattering have been reported [161, 162, 167, 189, 259–261]. As evidenced by  $^2H$  NMR (cf. Fig. 4.16 on page 86), the spectrum of the transformation product *dda* appears static at 380 K, which is diagnostic of slow exchange of the deuterons on a time scale  $\leq 1$  kHz. Another possible interpretation of the dynamic heterogeneity may come into play if the  $Q$ -dependence of the minor relaxation process is considered. Purely rotational and thus localized processes do not exhibit any  $Q$ -dependence of their maximum temperature  $T_m$ , whereas spatially non-restricted processes such as diffusion do. A significant  $Q$ -dependence for the “high-temperature process” cannot be unambiguously inferred, however, the latter appears to “grow out” of the low-temperature relaxation curve on going from the high- (detectors 1 and 2) to the low-angle data (Fig. 4.18). This apparent shift in  $T_m$  could be accounted for by assuming the reaction intermediate  $\text{NH}_3$  to diffuse through the sample *in statu nascendi* before being reincorporated by nucleophilic addition to the nitrile carbon atom as has been suggested in section 4.1.2.3 on page 84. It is, however, questionable whether non-consumed  $\text{NH}_3$  can still account for the intensity observed in the IFW-scans of the reacted sample as this would presuppose ammonia not to penetrate the sample holder after the reaction. In addition, measurements using the reacted sample do no longer exhibit an obvious  $Q$ -dependence and therefore have to be either associated with relaxational processes of the product *dda* as outlined above, or with slightly altered reorientational dynamics of the ammonium group in the starting material  $\text{NH}_4[\text{N}(\text{CN})_2]$ , which has not been consumed quantitatively during the reaction.

### 4.1.3.2 QENS: Elastic Fixed Window Scans

A less specific technique to study the dynamics of a material is to measure the temperature dependence of the purely elastic scattering. The neutron scattered intensity is monitored within a narrow energy range centered at  $\omega \approx 0$  as a function of temperature and scattering vector  $\mathbf{Q}$ . When the width  $\Gamma$  of the quasielastic component due to the stochastic dynamical processes (cf. Eq. 4.2) reaches the instrumental resolution with increasing temperature, intensity is lost from the energy window integrated by the resolution function. Thus, only the elastic part of the model scattering function is measured, by means of which an efficient method is provided to determine the temperature window in which relaxational processes appear in the system. After convolution with the instrumental resolution function  $R(\omega)$ , the observed intensity of the elastic line follows a  $Q$ -dependence determined by the Debye-Waller factor

$$I_{FW}(\mathbf{Q}, T, \omega \approx 0) \propto \exp \left[ -\langle u^2 \rangle Q^2 \right] \int_{-\infty}^{\infty} R(\omega) S_{inc}^{rot}(\mathbf{Q}, \omega) d\omega. \quad (4.4)$$

In harmonic approximation, we expect the logarithm of the measured elastic intensity to decrease linearly both in  $Q^2$  and in temperature due to a linear increase of the mean squared displacement with temperature. The temperature dependence of the MSD was modelled by making use of a series expansion where

$$\langle u^2(T) \rangle \approx \langle u_0^2 \rangle + (\delta \langle u_1^2 \rangle / \delta T) T + \dots \quad (4.5)$$

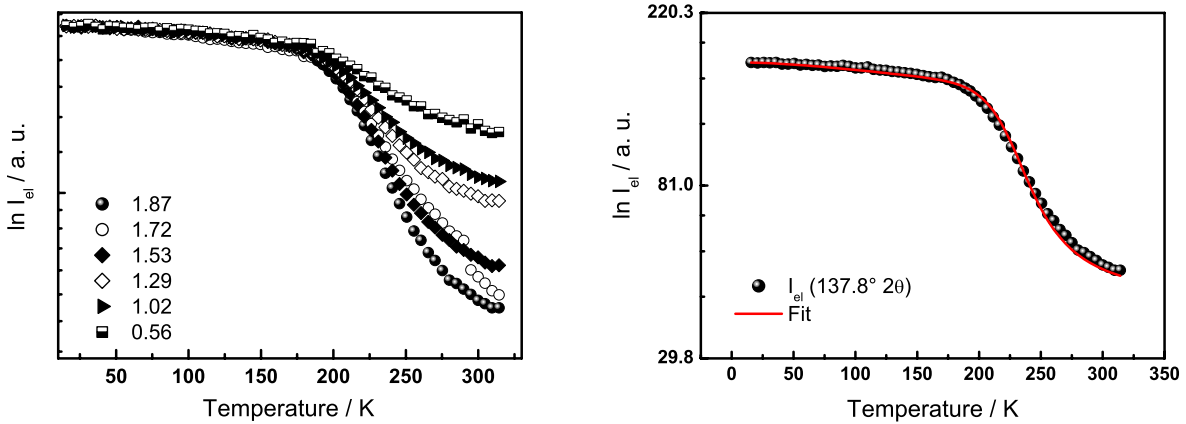


**Figure 4.20:** Left: Fixed window scans for ammonium dicyanamide, monitoring the temperature dependence of the normalized elastic intensity at different  $Q$  values. The relaxation step centered at 230 K corresponds to the reorientational dynamics of the ammonium group. Right: Model calculation for the relaxation step observed in the EFW-scan at  $Q = 1.87 \text{ \AA}^{-1}$ . The elastic part of the scattering function was calculated by assuming  $E_a = 22(2) \text{ kJ mol}^{-1}$  and  $\tau_0^{-1} = 37(3) \text{ THz}$ .

A fixed window scan taken at various wave vector transfers is shown in Figure 4.20 (left). As can clearly be seen, a linear behavior of  $\ln(I_{el})$  vs. temperature can be observed up to  $\approx 190$  K, where accordingly only the Debye-Waller factor contributes to the observed variation of the elastic intensity. At  $T \geq 190$  K the elastic intensity significantly drops, giving rise to a characteristic temperature of  $T_{1/2} \approx 230$  K for the inclination point of the intensity curves, where the quasielastic linewidth is equal to the instrumental resolution. The rapid loss of elastic intensity can be associated with the time scale of the  $\text{NH}_4^+$  reorientational dynamics entering the energy window accessible to the instrument. The EFW-scans were used as a rough estimation of the onset-temperature for quasielastic intensity to be observed in the  $I/\omega$ -scans, which will be discussed in section 4.1.3.3 on the facing page. The overall decrease of the elastic intensity was fitted by applying a hyperbolic approximation of the Debye-integral for  $\langle u^2(T) \rangle$  [262, 263], which was then used in calculating the elastic intensity according to Equation 4.4. A reasonable fit was obtained by using  $E_a = 22(2)$  kJ mol<sup>-1</sup> and an attempt frequency  $\tau_0^{-1}$  of 37(3) THz (Figure 4.20, right), which satisfactorily reproduces the parameters obtained from the IFW-scans (Table 4.3).

The low-temperature part of the above EFW-scan exhibits an almost linear intensity loss with increasing temperature, which according to Equation 4.4 can be ascribed to the growing MSD of the scattering hydrogen atoms. Therefore, the temperature dependence of the Debye-Waller

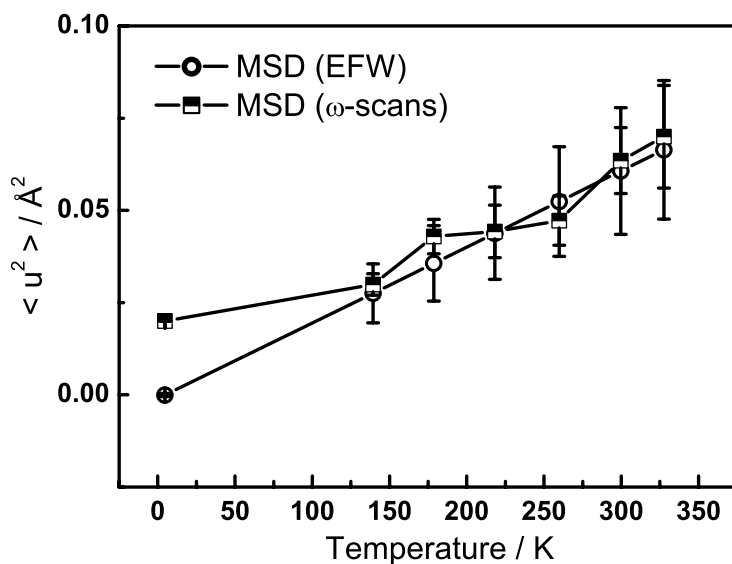


**Figure 4.21:** Mean squared displacements of hydrogen in  $\text{NH}_4^+$  as obtained from EFW- (circles) and  $\omega$ -scans (squares), respectively, as a function of temperature. The MSDs extracted from the EFW-scans do not include zero-point motion as this term cancels by normalizing.

factor was fitted by making use of Equation 4.5 and the resulting relation [264, 265]

$$\ln[I(T)] = a - [\delta \langle u^2 \rangle / \delta T] T Q^2. \quad (4.6)$$

The resulting MSDs (averaged over the data for  $Q = 1.87, 1.72, 1.53 \text{ \AA}^{-1}$ ), together with the values obtained from the  $I/\omega$ -scans (cf. section 4.1.3.3), are plotted as a function of temperature in Figure 4.21. The EFW-values are extrapolated from the straight lines obtained by using Equation 4.6 in the temperature range 15 to 170 K. According to Figure 4.21, the results agree quite well within the experimental error.<sup>1</sup> The linear increase of the MSDs up to 170 K is characterized by a slope  $\delta \langle u^2 \rangle / \delta T \approx 2.07 \cdot 10^{-4} \text{ K}^{-1} \text{ \AA}^2$ , conforming well to literature data [264–266].

#### 4.1.3.3 QENS: $\omega$ -Scans

The onset of quasielastic scattering in the accessible energy window could be estimated by evaluating the peak intensity loss in the EFW-scans. For essentially model-independent quasielastic fitting, a single elastic component at zero energy transfer of integrated area  $A_0 \equiv EISF$  was employed in combination with a broader Lorentzian  $L$ , of integrated area  $A_1 \equiv [1 - EISF]$  and width  $\Gamma$ . Both were convoluted with the resolution function,  $R(\omega)$ , appropriate for the BSS instrument, at each momentum transfer  $Q$  (Eq. 4.2). The quasielastic broadening of the incoherent elastic peak observed in the measurements is the Fourier transform of the van Hove

<sup>1</sup>Errors may for instance arise from neglecting the temperature dependence of the constant factor  $a$  in Equation 4.6, representing a  $Q$ -independent loss of elastic intensity, which could account for multiple scattering processes [264].

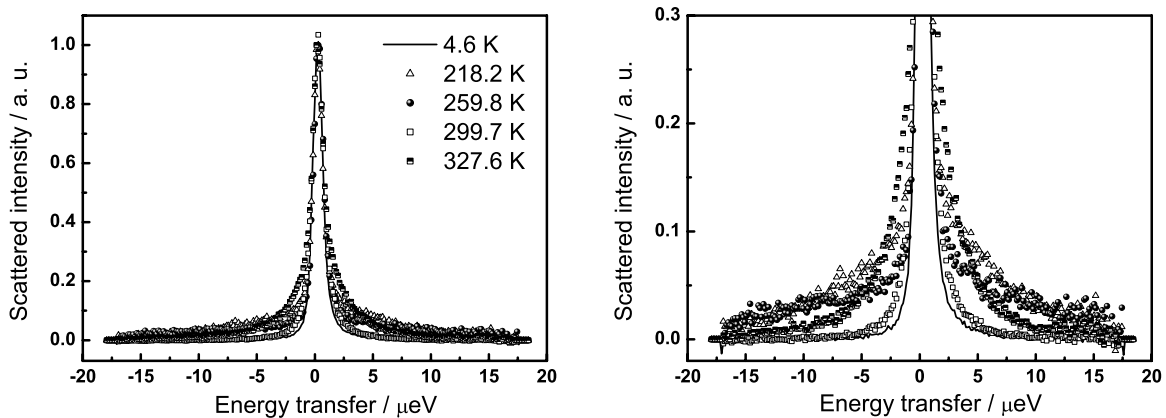


**Figure 4.22:** Left: Normalized QENS spectra of  $\text{NH}_4[\text{N}(\text{CN})_2]$  at five different temperatures. The scan at 4.6 K (solid line) only contains an elastic signal and was therefore used to determine the instrumental resolution function. Right: Magnification of the region where quasielastic broadening is observed.

self-correlation function (cf. section 3.2.1 on page 41). When this broadening has a Lorentzian dependence on the neutron energy transfer, a self-correlation function is probed that has an exponential time dependence on the observed picosecond time scale. Analysis of the spectra was carried out after background correction and convolution with the instrumental resolution function by simultaneously fitting the data of detectors 1–5 with an average scattering angle of  $2\theta = 99.3^\circ$ . For the fit a Lorentzian was employed, whose temperature-dependent width  $\Gamma(T)$  was assumed to be constant for different  $Q$  values. In addition, the intensities of the elastic and quasielastic components were extracted as a function of  $Q$  and  $T$ .

Figure 4.22 exemplarily shows the QENS spectra obtained at five different temperatures at the highest wave number transfer ( $1.87 \text{ \AA}^{-1}$ ). No quasielastic scattering was observed below 218 K, and the spectra at  $4.6 \leq T \leq 178.7$  K were accordingly fitted with a single Lorentzian. The temperature dependence of  $\Gamma$ , which is directly proportional to the inverse correlation time  $\tau^{-1}$ , is plotted in Figure 4.23. The energy of activation was determined as  $2425(72)$  K ( $20.2(6)$  kJ mol $^{-1}$ ), and  $\tau_0^{-1} \approx 24.8(8)$  meV, which is similar to the values obtained from the IFW-scans (Table 4.3). Nevertheless, it must be noted that a significant discrepancy is observed with respect to the relaxation rates, which are on average smaller by a factor of  $\approx 1.5$  when determined by the  $\omega$ -scans. This may most likely be due to deficient background correction or use of an incorrect channel width when fitting the data with TOFSYS [152]. Both multiple scattering effects and the presence of more than one quasielastic Lorentzian,

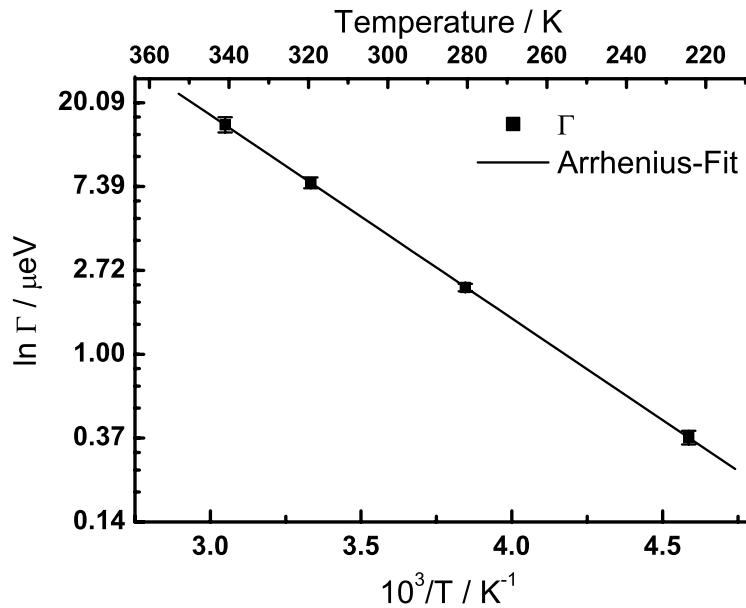


**Figure 4.23:** Arrhenius-plot of the width  $\Gamma$  of the quasielastic Lorentzian extracted from the  $I/\omega$ -scans, versus the inverse temperature. Quasielastic broadening is observed only between 218 and 328 K.

which would be diagnostic of an alternative jump model such as 90° jumps, would lead to an increase of  $\Gamma$  rather than an underestimation as observed in the experiment. Although the small width may serve as an additional evidence for the correctness of the postulated reorientational model, the relaxation rates extracted from the IFW-scans are nevertheless considered more reliable.

Owing to the fact that the incoherent neutron scattering cross section for a hydrogeneous crystal is proportional to  $\exp(-\langle u^2 \rangle Q^2)$ , as expressed by Equation 4.2, the variation of the measured scattering intensity  $S(Q, \omega)$  *vs.*  $Q^2$  yields a source for determining the mean squared atomic displacement parameters, which is complementary to both EFW-scans and  $^2H$  NMR measurements.

The significance of the MSDs obtained from this source is, however, somewhat limited in that the elastic integrals of the reference scan are calculated based on the normalization factors, which in turn depend on the choice of a “reference MSD”, since an independent vanadium standard could not be used for data normalization. Based on the NMR data, the reference parameter was chosen such that at 310 K  $\langle u^2 \rangle \approx 0.135 \text{ \AA}^2$ ; this seems to be a sensible choice if we set  $\langle u^2 \rangle$  to 0.007  $\text{\AA}^2$  at 10 K and assume a linear increase of  $\langle u^2 \rangle$  with T.

Figure 4.24 displays the plot of the total intensity *versus*  $Q^2$  for different temperatures. Despite of the high noise level, each data set can be fitted by a straight line, thus reproducing

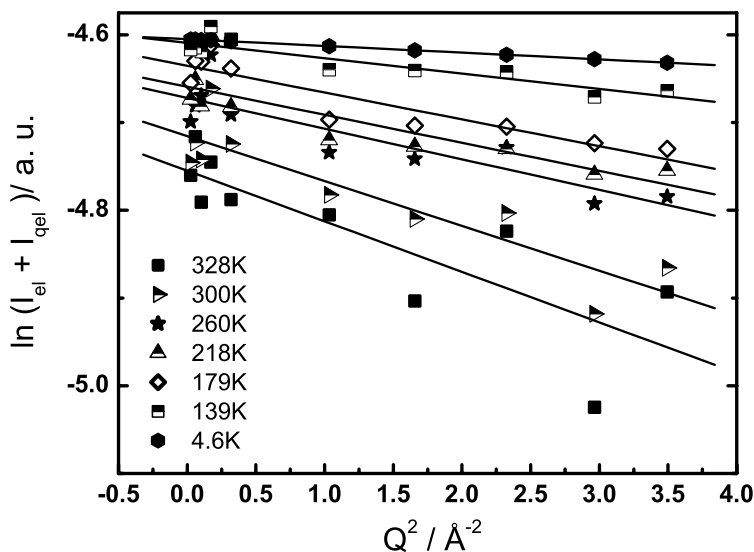


**Figure 4.24:** Elastic intensity [ $\ln(I_{el+gel})$ ] *vs.*  $Q^2$  at different temperatures as obtained from the  $\omega$ -scans. The slopes of the fitted straight lines represent the MSDs at the respective temperatures.

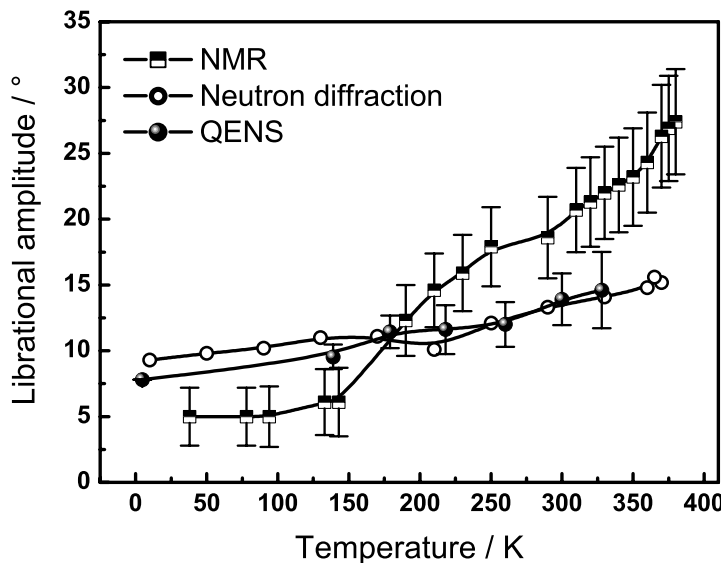


**Figure 4.25:** Librational amplitudes of the deuterons as obtained from  $^2\text{H}$  NMR and neutron powder diffraction, contrasted with those of the hydrogenated sample measured by QENS  $\omega$ -scans. Note that the differences may in part be due to different librational models used for the calculations.

the linearity in  $Q^2$  as required by Equation 4.2. Based on these results, the MSDs in the temperature range 5 – 328 K were calculated and are shown in Figure 4.21 on page 96.

However, a constant factor of 0.01235  $\text{\AA}^2$  was subsequently added to all MSDs in order to account for the significantly larger MSDs obtained from neutron powder diffraction at low temperatures [163]. This procedure may be justified by the fact that on the one hand, the librational amplitudes of deuterons as probed by neutron powder diffraction of  $\text{ND}_4[\text{N}(\text{CN})_2]$  are expected to be smaller by a factor of  $\approx \sqrt{2}$  as compared to the hydrogenated analogue. On the other hand, anisotropic thermal displacements were probed by neutron diffraction, whereas an isotropic librational model was used for the QENS data evaluation, yielding somewhat smaller values for the librational amplitudes. Thus, both effects should roughly cancel out each other, thereby rendering the librational amplitudes extracted by the different methods similar, which is implemented by adding a constant factor to the less reliable QENS data. In contrast, the  $^2\text{H}$  NMR data are calculated based on a cone-type model with the deuteron librating on the surface section of a sphere, which is expected to yield slightly larger MSD values as compared to neutron powder diffraction and QENS. Figure 4.25 shows a synopsis of the librational amplitudes obtained by  $^2\text{H}$  NMR, neutron powder diffraction, and QENS ( $\omega$ -scans) (see also Fig. 4.12 on page 82, right).

A measure of the quasielastic scattering is embodied in the *elastic incoherent structure factor*,

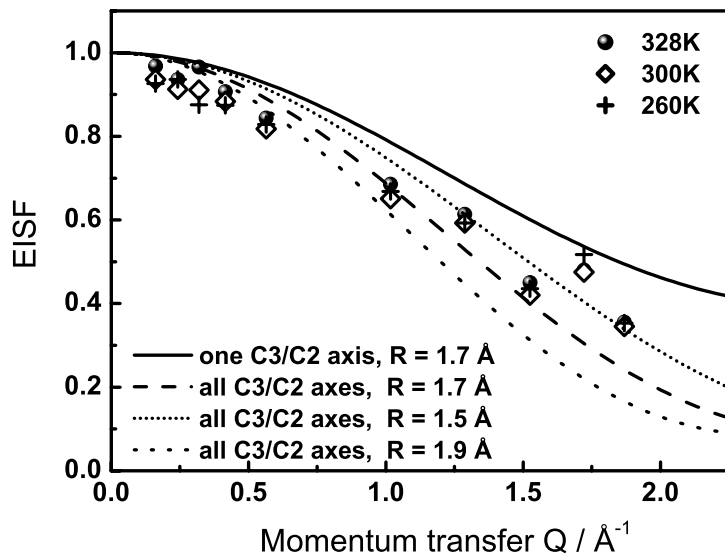


**Figure 4.26:** The form factor associated with the elastic component as a function of wave vector transfer  $Q$  at 260, 300 and 328 K. The solid and dashed lines represent simulations for a threefold jump model around one single  $C_3$  or  $C_2$  axis and all  $C_3$  or  $C_2$  axes, respectively. The dotted lines mark variations in the jump distance calculated using the multi-axis model for the lower limit 1.5 Å and the upper limit 1.9 Å.

EISF, the ratio of the elastic scattering to the total scattered intensity (cf. section 3.2.5 on page 47). From the  $Q$ -dependence of the EISF, it is possible to deduce information about the geometry of single particle hydrogen motion, while the width of the quasielastic peak gives information about the time scale of the motion. Note however, that the EISFs for different jump models significantly differ only above  $j_0(QR)$  with  $QR \approx \pi$ . Thus, the EISF is intrinsically sensitive to the reorientational geometry only for large jump distances and wave vector transfers. As outlined above, free rotation or rotational diffusion of the  $\text{NH}_4^+$  ions as well as 90° jumps can be ruled out, as it would require a fairly uniform distribution of hydrogen nuclear density on the surface of a sphere, or eight discrete hydrogen positions, respectively, which clearly contradicts the neutron diffraction data. Whereas a differentiation between 180° or 120° jumps about *any* of the  $C_2$  or  $C_3$  axes, respectively, on the basis of the rotational EISF is not possible, proof of the predominance of *single* or *multiple* axis rotation may nevertheless be furnished (cf. section 3.2.4 on page 46). Taking a jump distance of 1.7 Å, the EISF displays a minimum at a distinct  $Q$  value ( $\approx 2.6 \text{ Å}^{-1}$ ) for rotation about a single two- or threefold axis, thereby being close to one-half. This  $Q$  value is similar to that for multiaxis rotation about any of the  $C_2$  or  $C_3$  axes. However, the EISF for the multiaxis model is significantly smaller at its minimum ( $\approx 0.1$ ).

Figure 4.26 displays the experimental powder-EISF together with the theoretical EISFs for

the models outlined above, all for  $R = 1.7$  Å. In addition, to demonstrate the influence of the jump distance on the EISF,  $R$  is varied between 1.5 Å (top curve) and 1.9 Å (bottom curve) for the multi-axis model, as represented by the dotted lines. Although the data do hardly allow for *a priori* extraction of the correct jump model, the multiaxis model reproduces the experimental EISF obtained at different temperatures quite nicely and thus corroborates the isotropic jump model suggested previously by the  $^2H$  NMR data.

#### 4.1.3.4 Inelastic Neutron Scattering

Inelastic neutron scattering experiments were carried out at the thermal time-of-flight spectrometer SV-29 of FRJ-2/Jülich in order to probe the density of states in the regime of lattice and librational modes of  $\text{NH}_4[\text{N}(\text{CN})_2]$  as well as its deuterated analogue. As the intermolecular and even more so, the intramolecular vibrations extend to much larger energy transfers in the meV-domain, information on the vibrational density of states is accessible. Spectra obtained at  $T = 2$  K for two different wave vector transfers are displayed in Figure 4.27.

The energy gain spectra of  $\text{NH}_4[\text{N}(\text{CN})_2]$  at 2 K exhibit a strong band in the regime of lattice modes (acoustic and optic phonons) with maxima at 7 and 10 meV. This band – in this case with a resolved doublet structure – is found for the deuterated analogue in the same energy range and may therefore be attributed to acoustic phonons as no isotopic shift is observable. Another feature of medium intensity is seen in the range 21 – 28 meV (maximum at 23 meV) for  $\text{NH}_4[\text{N}(\text{CN})_2]$  and between 20 and 26 meV (maximum at 22 meV) for  $\text{ND}_4[\text{N}(\text{CN})_2]$  (Fig. 4.27, right), whose origin cannot be unambiguously established, since the isotopic shift is only weak. The band centered at 36 meV in the low-temperature spectra of  $\text{ND}_4[\text{N}(\text{CN})_2]$  (Fig. 4.27, bottom right) is tentatively associated with the first librational transition energies  $E_{01}$ . The analogous band is not visible in the spectrum of  $\text{NH}_4[\text{N}(\text{CN})_2]$ , which can be rationalized by the isotopic shift ( $\approx \sqrt{2}$ ) towards higher energy transfers, which are outside the energy range of the spectrometer. However, quantitative assignments of the observed bands can only be done on the basis of *ab initio* in combination with lattice dynamical calculations.

To roughly assess the consistency of the INS data with those obtained for ammonium di-cyanamide by QNS and  $^2H$  NMR, activation energies  $E_a$  were computed (M. Prager, FZ Jülich) on the basis of librational transition energies  $E_{01}$  tentatively extracted from the experimental spectra (33.9 and 38.3 meV). As a significant simplification, the ammonium ion was considered to be a one-dimensional rotor in a constant potential [157],<sup>2</sup> using the frame-

<sup>2</sup>The rotational potential is usually represented by the first two terms of a Fourier expansion in the rotational angle.

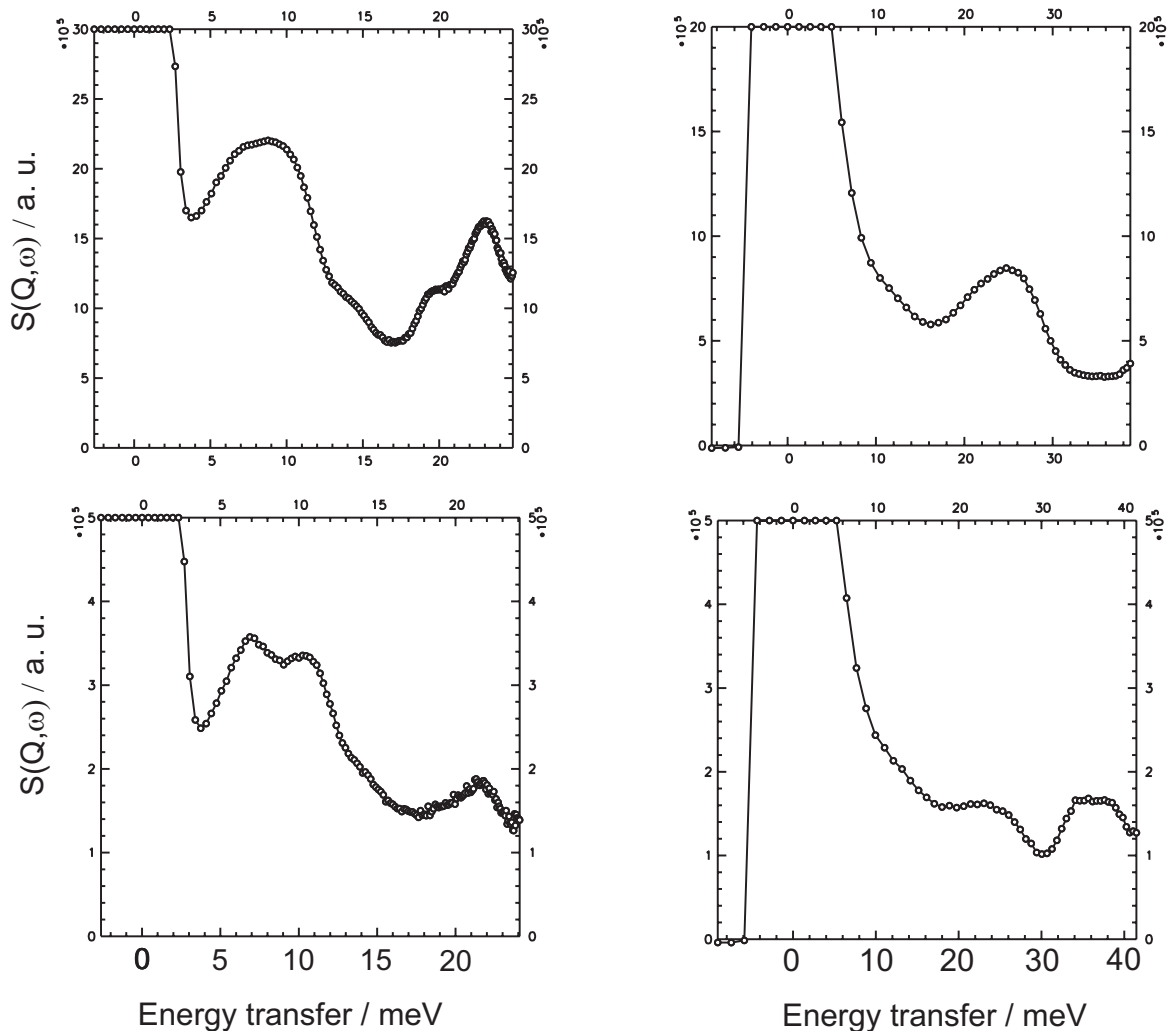


**Figure 4.27:** INS spectra for  $\text{NH}_4[\text{N}(\text{CN})_2]$  (top) and  $\text{ND}_4[\text{N}(\text{CN})_2]$  (bottom) in the regime of phonon energies at  $Q = 1.59 \text{ \AA}^{-1}$  (left), and at  $1.08 \text{ \AA}^{-1}$  (right).

work of the single particle model (SPM) [157, 267].<sup>3</sup>

The corresponding activation energies (242.6 ( $= 23.5 \text{ kJ mol}^{-1}$ ) and 240.3 meV ( $= 22.2 \text{ kJ mol}^{-1}$ ) correspond closely to those obtained from the NMR measurements. The corresponding librational amplitudes were estimated to be 14 and 13°, respectively, from the proton probability density function and were found to correspond quite well to the value obtained from neutron diffraction measurements at 10 K (10°) [163].

After the decomposition of the hydrogenated sample at 400 K, the spectrum below 25 meV recorded at 3 K has changed completely according to the expectations. The new features

<sup>3</sup>The single particle model describes the dynamics of molecular species by assuming an isolated group whose reorientations are hindered *via* interaction with the environment. The total potential energy depends on the symmetry of the rotating group and that of the environment.

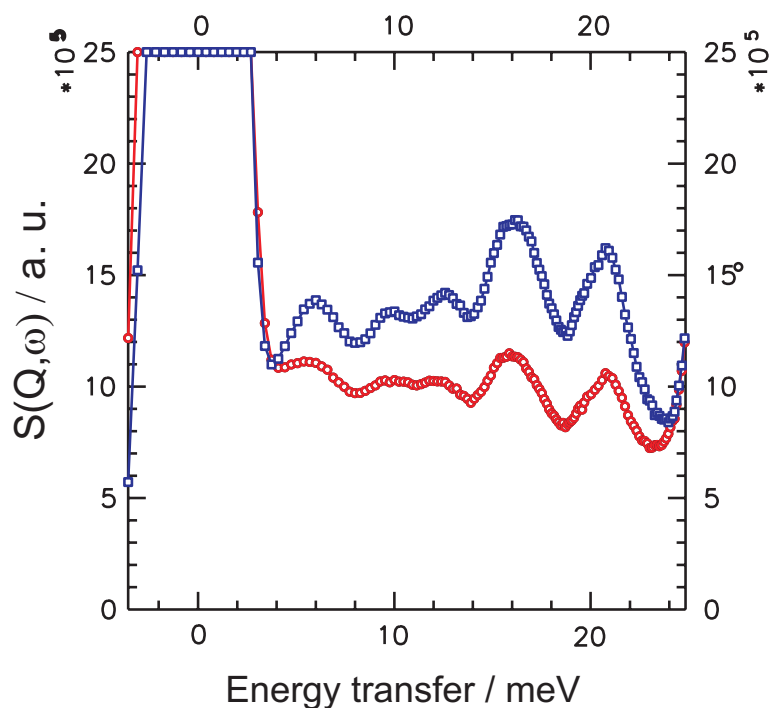


**Figure 4.28:** Synopsis of the INS spectra of pristine dicyandiamide (blue,  $T = 2\text{ K}$ ) and the transformation product of  $\text{NH}_4[\text{N}(\text{CN})_2]$ , pyrolyzed at  $400\text{ K}$  (red,  $T = 3\text{ K}$ ).  $Q = 1.59\text{ \AA}^{-1}$ .

observed can be attributed to the formation of dicyandiamide on comparison with a spectrum taken from a pure sample of commercially available dicyandiamide under identical conditions, as shown in Figure 4.28. Apart from minor intensity differences, the regimes of lattice and librational modes between 4 and 25 meV are largely identical. The better resolution of the bands in the spectrum of pure dicyandiamide may result from different degrees of crystallinity of the two samples.

In conclusion, INS spectroscopy provides yet another evidence for the identity of the transformation product and the quantitative transformation of the starting material ammonium dicyanamide.

## 4.2 Ammonium Cyanoureate

### 4.2.1 Introduction

As demonstrated in the previous section, ammonium dicyanamide, whose solid-phase reactivity is largely driven by the nature of the cation, provides a versatile model system for the study of reactions proceeding in the solid state. Due to the fundamental role of the ammonium ion and the nitrile-group of the dicyanamide anion in this transformation, comparable systems with similar reactive groups were devised in order to address the question as to whether or not a core framework of molecular and structural features may be established that govern the observed type of solid-state reactivity.

Among the potential candidates, ammonium cyanoureate (**1**) was found to be quite closely related to ammonium dicyanamide (**2**), from which it can formally be derived by hydration of one of the nitrile-groups, thereby maintaining the ammonium ion and one nitrile-group as the reactive centres (Fig. 4.29).

Although the free acid cyanourea (*N*-cyanocarbamimidic acid) (**3**) has been mentioned as early as 1870 in the literature [268] and its molecular structure and reactivity has been characterized [269–272], crystal structure information is only available for the silver and, though incomplete, for the potassium salt of cyanourea [273,274]. Studies of the behavior of cyanourea in aqueous and organic solution reveal the susceptibility of cyanourea to intermolecular addition and consecutive decomposition reactions. In neutral and organic solution, different degrees of cyanoguanylurea (**4**) and cyanobiuret (**5**) are formed [275], whereas ammeline (**6**) (2,4-amino-6-hydroxy-1,3,5-triazine) and 1,3-dicarbamoylguanidine (**7**) are the main products in alkaline and acidic solution, respectively (Figure 4.29) [276,277]. On the background of the structural similarities to ammonium dicyanamide, an investigation of the structure-reactivity relationship for ammonium cyanoureate in the solid phase seems worthwhile and will be elucidated in a step-by-step fashion in the following sections according to ref. [278].

### 4.2.2 Crystal Structure

Ammonium cyanoureate was synthesized according to the procedure outlined in section 10.1 on page 355.

The compound crystallizes in the space group  $P2_1/c$  (no. 14) with four formula units in the unit cell. Details of the crystal structure solution and refinement are summarized in Table 4.4. For comparison, the unit cell of ammonium dicyanamide is depicted in Figure 4.31; the coordination sphere of the ammonium ion is outlined in Figure 4.4 on page 73.

The cyanoureate anions are stacked in parallel chains along [001], forming a framework in

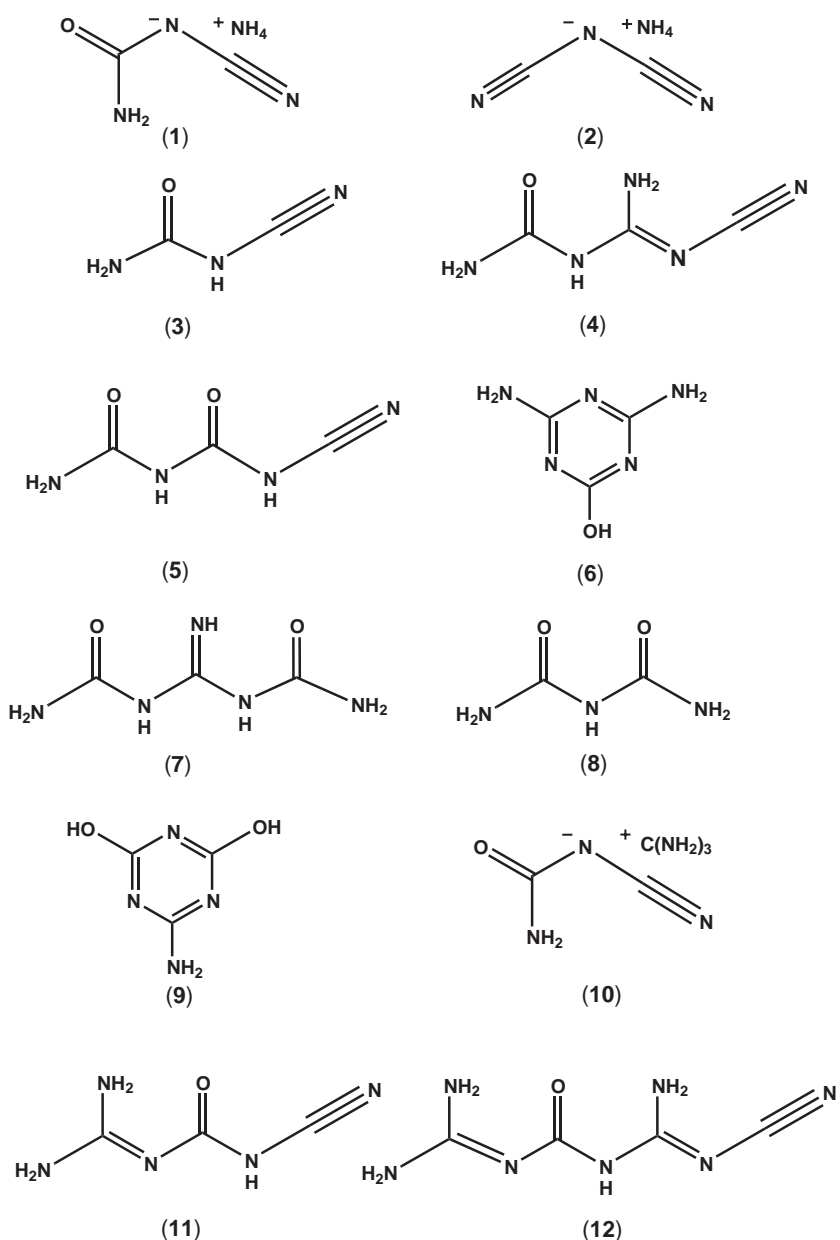


**Figure 4.29:** Molecular formulas of several compounds which are chemically or structurally related to the cyanourea structure: (1) ammonium cyanoureatate, (2) ammonium dicyanamide, (3) cyanourea, (4) cyanoguanylurea, (5) cyanobiuret, (6) ammeline, (7) 1,3-dicarbamoylguanidine, (8) biuret, (9) ammelide, (10) guanidinium cyanoureatate, (11) cyanocarbamoylguanidine, (12) [1-cyanoguanyl-3-guanyl]urea.

which pairs of ammonium ions are embedded (Fig 4.30, left).

As observed in the silver salt of cyanourea [273], the molecular structure of the essentially planar cyanourea anions exhibits a *cisoid* arrangement of the nitrile group and the oxygen atom, rendering the amide group *trans* to the nitrile moiety. The central nitrogen atom carries the negative charge without significant delocalization into the nitrile group, which is consistent

**Table 4.4:** Crystallographic data of ammonium cyanoureatate.

Formula	$\text{NH}_4[\text{H}_2\text{NC}(=\text{O})\text{NCN}]$
$M_w$ / g · mol <sup>-1</sup>	102.11
crystal system, space group	monoclinic, $P2_1/c$ (no. 14)
$T$ / K	140
diffractometer, monochromator	STOE STADI 4
radiation ( $\lambda$ / pm)	Mo-K $\alpha$ (71.073)
monochromator	graphite
$a$ / pm	388.95(8)
$b$ / pm	1121.0(2)
$c$ / pm	1096.4(2)
$\beta$ / °	92.57(3)
$V$ / $10^6$ · pm <sup>3</sup>	477.5(2)
$Z$	4
$\rho_{calcd}$ / g · cm <sup>-3</sup>	1.420
$F(000)$	216
$\mu$ / mm <sup>-1</sup>	0.115
crystal size / mm <sup>3</sup>	0.51 x 0.29 x 0.18
diffraction range	$2.60 \leq \theta \leq 28.02$
index range	$-5 \leq h \leq 5, -14 \leq k \leq 14,$ $-14 \leq l \leq 14$
total no. reflections	6513
independent reflections	1158 ( $R_{int} = 0.0360$ )
observed reflections	980
refined parameters / constraints	with $F_o^2 \geq 2\sigma(F_o^2)$
GooF on $F^2$	89 / 0
$R$ indices $ I > 2\sigma(I) $ (all data)	1.073
	$R_1 = 0.0297$ (0.0397)
	$wR_2 = 0.0769$ (0.0829)
	with $w = [\sigma^2(F_o^2) + (0.0409P)^2 + 0.1113P]^{-1}$
	where $P = (F_o^2 + 2F_c^2)/3$
min./max. residual	
electron density / $e \cdot 10^{-6}$ pm <sup>-3</sup>	-0.193 / 0.203

with the interatomic distances N2–C1 (116.5 pm) and C1–N3 (130.7 pm), corresponding to the localization of the triple bond and, hence, to the molecular formula  $\text{N}\equiv\text{C}=\text{N}=\text{C}(=\text{O})\text{NH}_2$  for the cyanoureatate anion (Table 4.5). The anions are hydrogen bonded *via* weak N2 ··· H6 contacts (241.8 pm) between adjacent amide and nitrile groups along [001], and *via* medium strong N2 ··· H5 contacts (216.1 pm) along [001], [0 $\bar{1}$ 1] and [011].

The ammonium ion exhibits slight deviations from the ideal tetrahedral symmetry with H–N–H bond angles between 108° and 113° (Table 4.5).

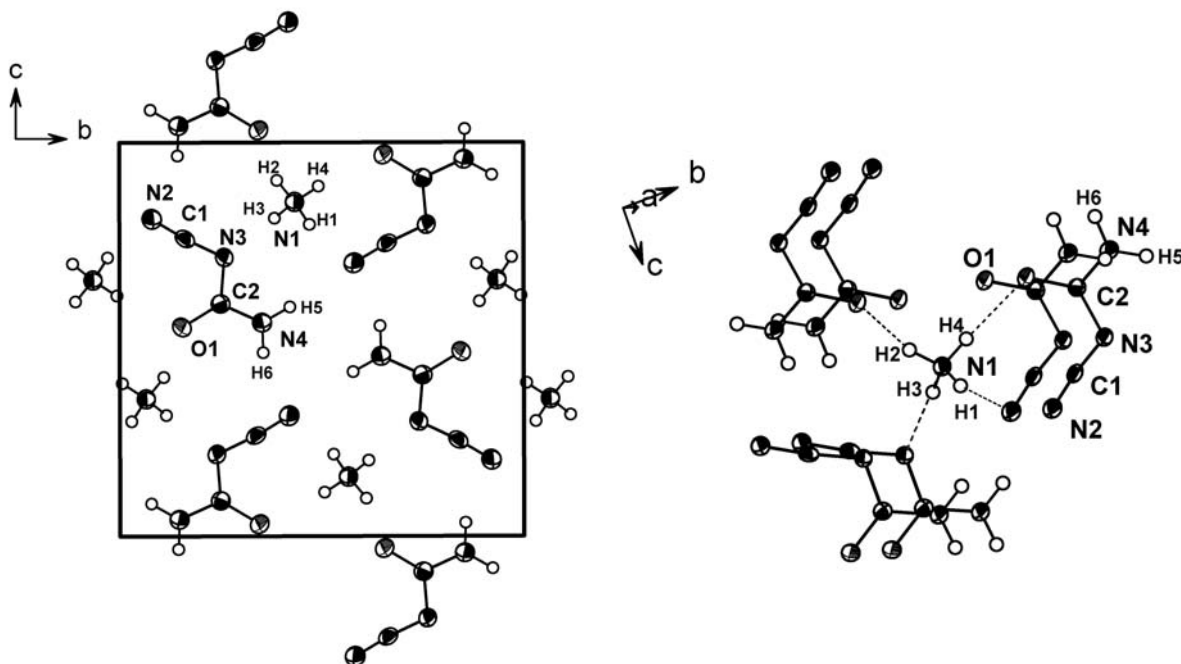


**Figure 4.30:** Left: Crystal structure of  $\text{NH}_4[\text{H}_2\text{NC}(=\text{O})\text{NCN}]$ , view along  $\bar{1}00$ . Ellipsoids are drawn at the 70 % probability level. Right: Coordination sphere of the ammonium ion in  $\text{NH}_4[\text{H}_2\text{NC}(=\text{O})\text{NCN}]$ . The hydrogen bonding network is indicated by dotted lines. Ellipsoids are drawn at the 70 % probability level.

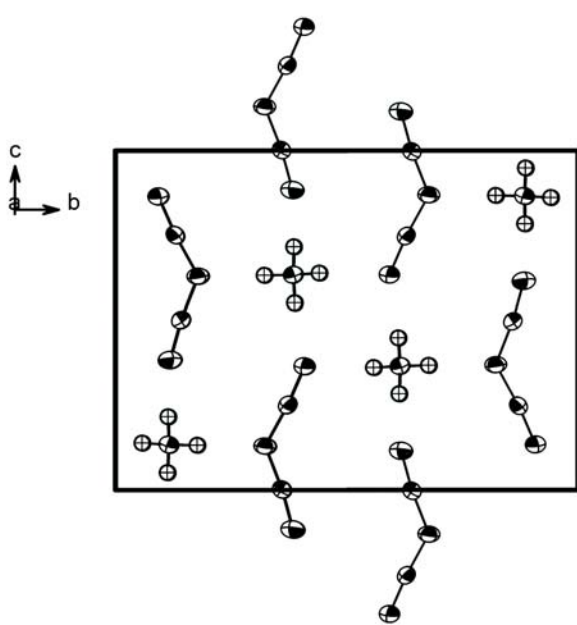


**Figure 4.31:** Unit cell of the related ammonium salt  $\text{NH}_4[\text{N}(\text{CN})_2]$ , view along  $[100]$ .

The cation is coordinated by three pairs of anions, of which one pair is doubly coordinated via  $\text{O}1$  and  $\text{N}2$ , forming an inner coordination sphere that resembles an irregular heptahedron. The six closest cation-anion contacts range between 280 and 346 pm, involving  $\text{O}1$  (3x), the central nitrogen  $\text{N}3$  (2x) and the terminal nitrogen  $\text{N}2$  (1x). The cation-anion assembly is characterized by four hydrogen bonds of medium strength in the range from 191 to 203 pm, where two donors are oxygen and two are nitrogen atoms (bridging and terminal) (Fig. 4.30, right).

The temperature behavior of the lattice parameters and the cell volume of ammonium

**Table 4.5:** Bond lengths and angles of  $\text{NH}_4[\text{H}_2\text{NC}(=\text{O})\text{NCN}]$ .

Distances / pm		Angles / $^\circ$	
O1–C2	125.7(2)	C2–N4–H5	121(1)
N4–C2	133.8(2)	C2–N4–H6	120(1)
N4–H5	90(2)	H5–N4–H6	118(2)
N4–H6	89(2)	N2–C1–N3	174.7(1)
N2–C1	116.5(2)	H1–N1–H2	109(2)
C1–N3	130.7(2)	H1–N1–H3	108(2)
N1–H1	95(2)	H2–N1–H3	109(2)
N1–H2	92(2)	H1–N1–H4	108(2)
N1–H3	91(2)	H2–N1–H4	110(2)
N1–H4	91(2)	H3–N1–H4	113(2)
N3–C2	137.5(2)	C1–N3–C2	115.61(9)
		O1–C2–N4	121.9(1)
		O1–C2–N3	123.90(9)
		N4–C2–N3	114.23(9)
Hydrogen bonding			
N1–H1 … N2	200(2)	N1–H1–N2	167(2)
N1–H2 … O1	191(2)	N1–H2–O1	163(2)
N1–H3 … N3	199(2)	N1–H3–N3	170(2)
N1–H4 … O1	203(2)	N1–H4–O1	157(2)

cyanoureatate is displayed in Figure 4.32.

As evidenced by the negative slope of the curve pertaining to the crystallographic *c*-axis, the latter exhibits a negative coefficient of expansion, resulting in an anomalous thermal behavior in the investigated temperature range. In contrast, the cell volume increases with temperature. This phenomenon can also be observed for ammonium dicyanamide [122, 123, 163], which also exhibits a contraction of the *c*-axis with rising temperature. In spite of the formal similarity considering the symmetry and temperature characteristics of the structural parameters, the inner coordination sphere and the arrangement of the ions in the unit cells of the two structures differ. The question at issue in case of a solid-state transformation is the nature of the product-determining factor. This may either be the extended solid-state arrangement of the ions as determined by the pre-organization of the molecules in the unit cell and packing effects, or the thermodynamic driving force generating the energetically most favored product (i. e. molecular structure), irrespective of the crystallographic conditions (“solution-like” conditions), or the co-action of both factors. This issue will be considered in detail in the following sections.

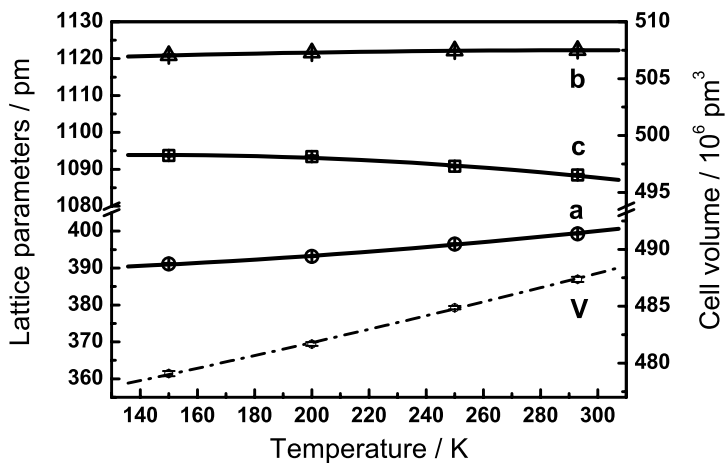


**Figure 4.32:** Temperature dependence of the lattice parameters (left *y*-axis) and cell volume (right *y*-axis) in  $\text{NH}_4[\text{H}_2\text{NC}(=\text{O})\text{NCN}]$  as determined by X-ray powder diffraction between 150 and 293 K. The contraction of the *c*-axis with rising temperature indicates a negative thermal expansion coefficient, giving rise to an anomalous temperature behavior.

### 4.2.3 Thermal Reactivity

#### 4.2.3.1 Thermal Analysis

The investigation of the thermal behavior of the title compound seems to be particularly intriguing in terms of comparison with that of the related compound ammonium dicyanamide. The first question to be addressed is whether reactivity in the solid state is likely to occur in this system, or if melting or complex decomposition are the prevailing temperature responses. As a primary step, large crystals of ammonium cyanoureat (1) were investigated under a microscope during thermal treatment of the sample up to 453 K. This procedure did not affect the bulk crystal shape, yet led to a continuous clouding of the initially clear crystal together with a keying of the surface and simultaneous softening of its consistency. This indicates the conversion into polycrystalline material or potential solid-state reactivity to occur.

DSC and DTA/TG measurements indicate significant differences in the thermal behavior of ammonium cyanoureat depending on the heating and pressure conditions, rendering the course of the thermal reactivity a complex interplay between the latter variables. The DSC curve for a sample heated continuously up to 773 K in a closed aluminium crucible (heating rate  $0.5 \text{ K min}^{-1}$ ) displays a weak and broad exothermic signal at 355 K, followed by a sharp exothermic signal (onset 385 K), which is typically preceded by an endothermic deflection of the baseline. Between 390 and 463 K, a complex series of thermal events is observable

(Fig. 4.33, left). The main product recovered after the above thermal treatment is urea together with ammeline (**6**) as proven by X-ray powder diffraction, a frequently encountered decomposition product of C/N/O materials [275, 277, 279, 280].

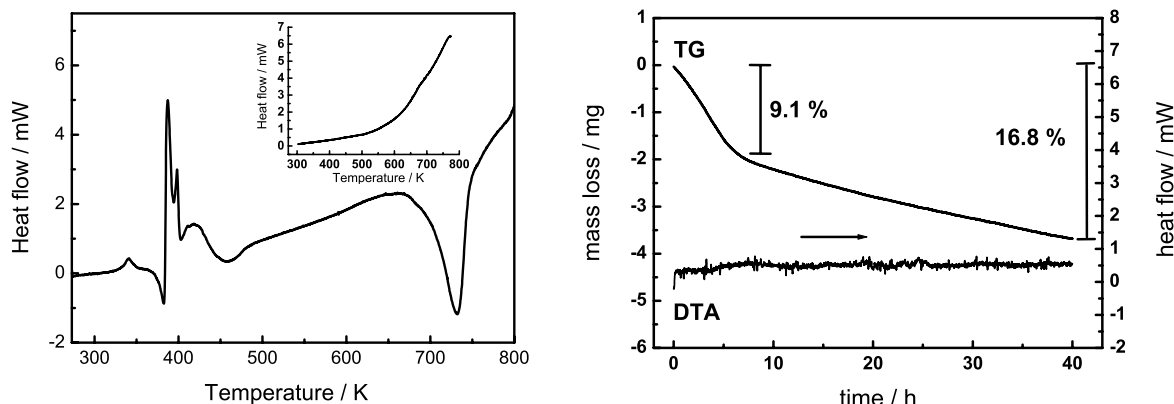


**Figure 4.33:** Left: DSC heating and cooling curve (inset) of  $\text{NH}_4[\text{H}_2\text{NC}(=\text{O})\text{NCN}]$  recorded between  $\text{RT}$  and  $800 \text{ K}$  with a heating (cooling) rate of  $0.5 \text{ K min}^{-1}$ . Right: Isothermal TG and DTA heating curves of  $\text{NH}_4[\text{H}_2\text{NC}(=\text{O})\text{NCN}]$  recorded at  $358 \text{ K}$ . The weight of the sample was  $21.97 \text{ mg}$ .

It is known from the literature that ammeline (**6**) is formed to a small extent at temperatures above  $498 \text{ K}$  as a minor decomposition product of urea besides the main products biuret (**8**), cyanuric acid, ammelide (**9**), and melamine [281]. At temperatures below  $473 \text{ K}$ , however, the formation of ammeline by urea decomposition is negligible, suggesting a different source of ammeline in the present case. If the above heating experiment is conducted in an  $\text{Al}_2\text{O}_3$  crucible open to the atmosphere ( $\leq 1 \text{ K min}^{-1}$ ), the products differ substantially from those obtained under DSC conditions. In this case, no ammeline formation is observed, whereas urea is detected in all product mixtures obtained below  $\approx 425 \text{ K}$  (at higher temperatures sublimation of urea occurs). Above  $473 \text{ K}$  the products are transformed into amorphous graphitic C–N materials.

If the sample is heated to  $358 \text{ K}$  ( $1 \text{ K min}^{-1}$ ) in unsealed  $\text{Al}_2\text{O}_3$  crucibles and annealed for  $40 \text{ h}$ , no thermal event is recorded (DTA) in spite of the ongoing transformation of the sample as evidenced by X-ray powder diffraction. The powder pattern of the product phase recovered after  $40 \text{ h}$  is largely identical to that obtained in the heating experiments. The TG curve shows a continuous mass loss, which decreases after  $5 \text{ h}$  at  $358 \text{ K}$  where it amounts to  $\approx 9.1\%$ . Most likely, the observed mass loss is due to the formation of ammonia. When annealing further the curve flattens, yet the mass loss continues beyond the end of the measurement after  $40 \text{ h}$ , where it has added up to  $16.8\%$  (Fig. 4.33, right). The number of products obtained by reaction in an open system is very sensitive to only slight variations of the reaction conditions and may in the most unfavorable case lead to a complex mixture of side phases along with the

main products. In the following, the thermal behavior under optimized isothermal conditions (358 K, pressure equalization), leading to a minimum of products, will be considered in detail.

#### 4.2.3.2 *In situ* X-ray Powder Diffraction

The *in situ* observation of the phase transformation by means of variable temperature X-ray powder diffraction further approves the absence of melting under controlled temperature conditions. When heated isothermally at 358 K for several hours, the onset of the phase transformation is observed after 8 h (Fig. 4.34). As indicated by the comparatively long coexistence of the starting material and product phases ( $> 2$  h), the reaction kinetics of the phase transformation may qualitatively be assessed as relatively slow. The transformation onset and rate both increase exponentially by raising the transformation temperature, the crystallinity of the product however being correlated inversely with the annealing temperature. When compared to ammonium dicyanamide, whose optimum transformation temperature is between 368 and 373 K, the temperature characteristics for the transformation process of the two compounds is quite similar, which may suggest the ammonium ion to play a decisive role for the solid-state reactivity in both salts.

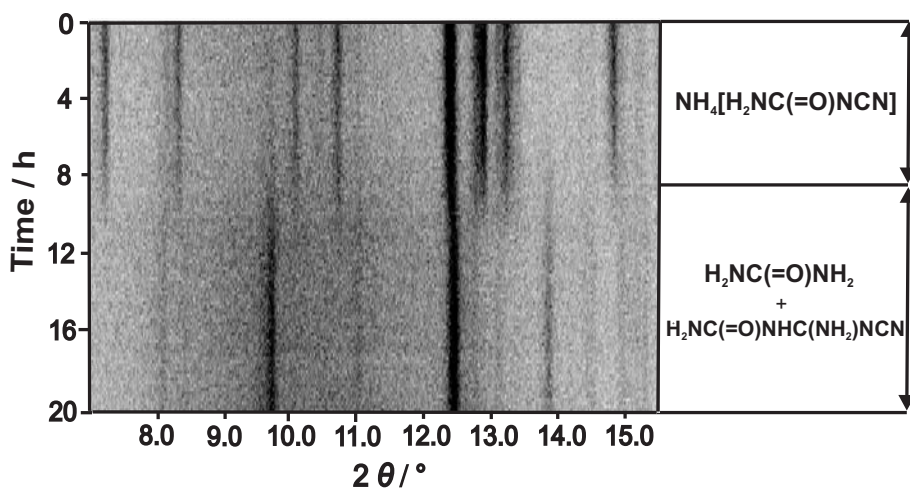


**Figure 4.34:** Isothermal X-ray powder diffraction patterns of  $\text{NH}_4[\text{H}_2\text{NC}(=\text{O})\text{NCN}]$  recorded at 358 K for 20 h. The measuring time for each diffractogram ( $7 - 15.5^\circ 2\theta$ ) was 11 minutes and the heating rate up to the starting temperature  $5 \text{ K min}^{-1}$ . The starting material and products are indicated at the right margin.

Due to the moderate crystallinity of the product phase, indexing of the powder patterns was not successful. By comparison, a part of the reflection lines could again be attributed to urea as observed in the heating experiments in a closed vessel, yet all other components could not be identified from the heterogeneous product phase by X-ray diffraction methods. Therefore, the identification of the products was attempted by complementary analytical methods, which

was, however, complicated by the poor solubility of a large fraction of the product phase in water or organic solvents apart from DMSO.

In accord with the above observations, a series of single-crystal X-ray diffraction measurements conducted isothermally at 348 – 351 K confirm the conversion of a single crystal of  $\text{NH}_4[\text{H}_2\text{NC}(=\text{O})\text{NCN}]$  into polycrystalline material after  $\approx 14$  days. The transformation is indicated by the complete disappearance of the reflections and the emergence of Debye-Scherrer rings. The transformation can also visually be confirmed on inspection of the single crystal prior to and after the heating procedure as demonstrated in Figure 4.35.

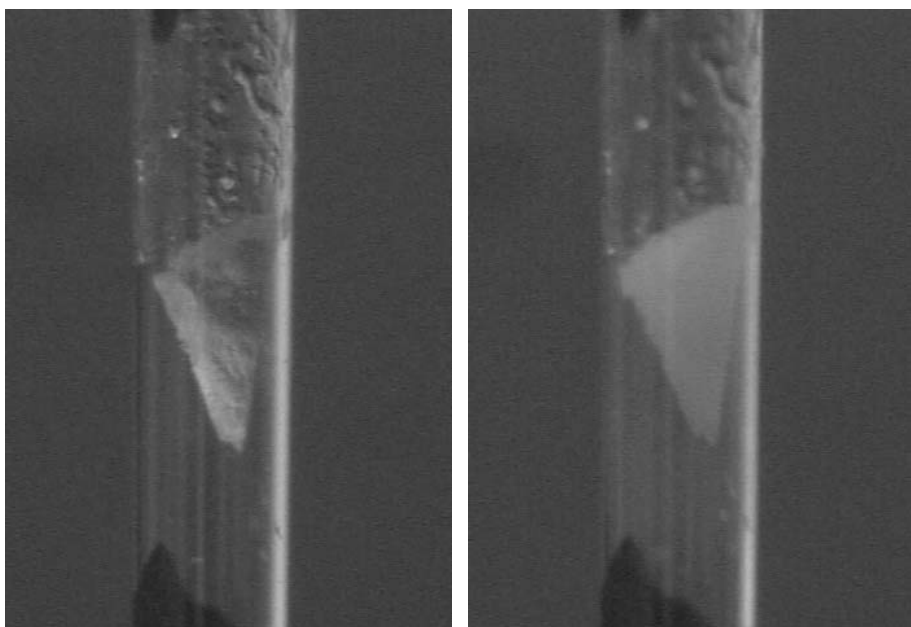


**Figure 4.35:** Micrographs of the capillary containing a single crystal of ammonium cyanourate prior to (left) and after isothermal heating at 348 – 351 K for 14 days (right).

The refinement of the data sets reveals the site occupation factor of N1 (ammonium nitrogen) to be smaller than one ( $0.89 < \text{sof}(\text{N1}) < 0.93$ ), suggesting a slight tendency towards the release of ammonia without effecting a collapse of the structure. In order to fulfill the criterion of electro-neutrality, an intermolecular proton transfer to the anion must occur, leading to a small yet undetectable fraction of the free acid cyanourea, which may be incorporated statistically into the parent structure. Allowing the site occupation factor for N1 to be smaller than 1 ( $\approx 0.944(6)$ ) for the data set collected at 140 K also slightly improved the refinement. This finding may further corroborate the occurrence of an energetically favored static disorder due to facile proton exchange reactions in the solid state even at low temperatures, which is accompanied by the loss of small amounts of ammonia.

### 4.2.3.3 Vibrational Spectroscopy

In accordance with the IR spectra of the transformation product the presence of urea in the product mixture is corroborated as indicated by the intense absorption lines around 1664, 1620 and  $1450\text{ cm}^{-1}$  (Fig. 4.36, middle). Principally, the appearance of the product spectrum suggests the conservation of the majority of molecular fragments as compared to ammonium cyanoureatate, since the presence and location of the absorption bands pertaining to the N–H, C=O and C≡N moieties are not significantly altered upon transformation.

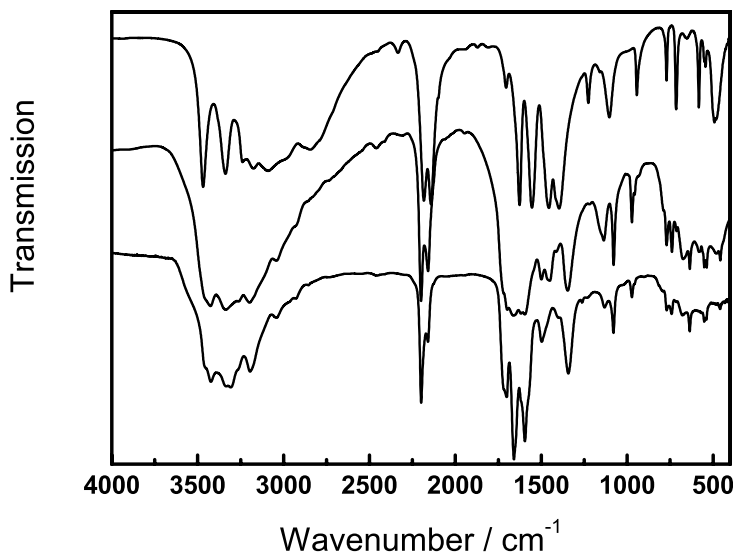


**Figure 4.36:** IR spectra of ammonium cyanoureatate (top), the decomposition product obtained at 358 K (middle) and cyanoquanylurea (bottom), recorded in the range  $4000 - 400\text{ cm}^{-1}$  at room temperature.

This is indicative of the core of the starting material staying intact. In particular, a nucleophilic attack of ammonia at the nitrile carbon as observed in ammonium dicyanamide seems to be most unlikely due to the still clearly visible nitrile band in the product spectrum. Owing to the product mixture and the appearance of several minor bands and band shifts, the complexity of the spectrum is increased. Among the newly emerged bands are signals at  $2199 / 2159\text{ cm}^{-1}$  and 1703, 1499, 1346, 1136, 1079, 972, 739, 674, 635, and  $458\text{ cm}^{-1}$ . In order to establish the identity of the missing product components, the IR data are not sufficient and need to be complemented by other spectroscopic data.

#### 4.2.3.4 NMR Spectroscopy

$^1H$  and  $^{13}C$  spectra of a range of products that were obtained under varying temperature conditions were recorded in DMSO-d<sub>6</sub> solution at ambient temperature. The  $^{13}C$  NMR spectrum of the product obtained after optimizing the reaction parameters and thus the degree of purity, shows three signals at 160.2, 156.0, and 116.8 ppm (Fig. 4.37, left). In some cases signals at 167.1, 158.6, and 124.3 ppm are also present, whose intensities strongly depend on the thermal history of the sample. When the spectral region between 150 and 170 ppm is visualised enlarged, the splitting of the signal at 160 ppm becomes evident. Comparison with the  $^{13}C$  NMR spectrum of urea permits the assignment of one of the signals at 160 ppm to urea. The signal around 117 ppm is easily attributed to a nitrile carbon atom, whereas chemical shifts of the signals at 156, 158 and 160 ppm are characteristic of amide- or amino(imino)methyl-groups with sp<sup>2</sup>-hybridized carbon atoms. The signals at 167 and 124 ppm are identical with the  $^{13}C$  chemical shifts of ammonium cyanoureat, yet are also observed when no ammonium ion is detectable by  $^{14}N/^{15}N$  NMR spectroscopy. The  $^1H$  spectrum of the product typically exhibits six signals at 5.40, 6.47, 7.13, 8.20, 8.71, 9.45 ppm and an impurity at 6.08 ppm, where the signal at 5.40 ppm can again be attributed to urea (Fig. 4.37, right). In several spectra, the signal around 7 ppm is superposed by a broad feature, indicating fast exchange of acidic N–H protons as typically observed for ammonium or guanidinium ions. Simultaneously, a medium intense signal at 5.10 ppm is present, which is close to the NH<sub>2</sub> protons

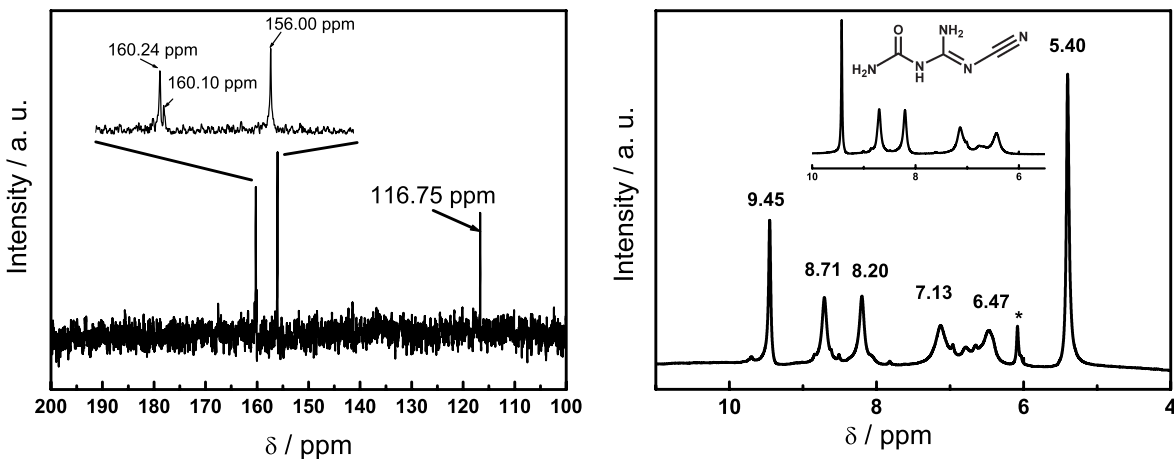


**Figure 4.37:** Left:  $^{13}C$  NMR spectrum of the solid-state decomposition product of ammonium cyanourate recorded in DMSO-d<sub>6</sub> solution at 293 K. The region between 150 and 163 ppm is shown enlarged in the inset. Right:  $^1H$  NMR spectrum of the solid-state decomposition product of ammonium cyanourate recorded in DMSO-d<sub>6</sub> solution at 293 K. The  $^1H$  spectrum of cyanoguanylurea is shown in the inset; the asterisk denotes an unknown impurity.

of ammonium cyanourea. The integrated intensities of the five major resonances, which appear in the region of both acidic and non-acidic NH and NH<sub>2</sub> groups, are approximately equal. Based on the spectroscopic information sketched above the molecular structure of the missing product components may be derived:

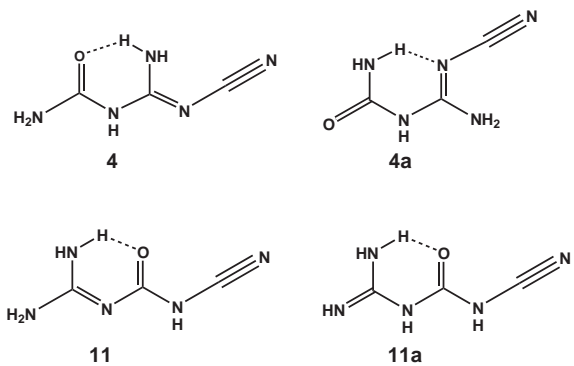


**Figure 4.38:** Conformational isomers of cyanoguanylurea (**4**), (**4a**) and cyanocarbamoylguanidine (**11**) and (**11a**). Intramolecular hydrogen bonding is indicated by dashed lines.

cyanourea (**10**) to be present in the product mixture along with the above main products. Thus, the presence of the <sup>13</sup>C signals at 158 (cation), 167 and 124 ppm (anion), as well as the sharp <sup>1</sup>H signal around 5 and the broad signal at 7 ppm can be explained without invoking the presence of small portions of unreacted starting material.

#### 4.2.3.5 Mass Spectrometry

The structural picture outlined above may be corroborated by mass spectrometry. Spectra obtained by Direct Electron Ionization (DEI+) clearly contain peaks at *m/z* 60 and 127, which can be assigned to the two main products urea and cyanoguanylurea (**4**) or cyanocarbamoylguanidine (**11**).

The molecular peaks are supplemented by peaks at *m/z* = 111 [M-NH<sub>2</sub>]<sup>+</sup>, 84 [M-HNCO]<sup>+</sup>, 44 [M<sub>urea</sub>-NH<sub>2</sub>]<sup>+</sup>, and 43 [M-(H<sub>2</sub>N)<sub>2</sub>CNCN]<sup>+</sup> / [M<sub>urea</sub>-NH<sub>3</sub>]<sup>+</sup>, belonging to molecular fragments of the parent mass peaks. DEI+ spectra of some decomposition products further contain weak peaks at *m/z* 169 and 152, which are consistent with the molecular structure of [1-cyanoguanyl-3-guanyl]urea (**12**). Although the formation of the latter as a result of thermal decomposition reactions during sample evaporation in the mass spectrometer cannot be excluded, the presence of small amounts of **12** in the initial product mixture must be assumed and may be corroborated by the observation of additional NMR signals in some

product samples. Some spectra exhibit signals at  $m/z$  126 and 85, which are larger than the expected isotope peaks of 127 and 84, respectively. These peaks may be attributed to the trimerization of the intermediately formed cyanamide  $\text{H}_2\text{NCN}$  to melamine  $\text{C}_3\text{N}_6\text{H}_6$  and to the corresponding decomposition products, or to the  $[M - H]^+$  peak of  $m/z$  127. No mass spectroscopic evidence is found for the formation of cyanobiuret (**5**), which was claimed to occur as a by-product in the decomposition of cyanourea in solution [275]. Mass spectra recorded in the  $\text{FAB}^+$  mode contain a large signal at  $m/z$  60, whereas  $\text{FAB}^-$  spectra show the presence of an anion with  $m/z$  84. These findings are fully consistent with the assumption of guanidinium cyanoureat ( $m/z$  (cation) 60,  $m/z$  (anion) 84) to be formed under certain conditions as a minor conversion product.

As for the identity of the main transformation product, several reasons can be cited as evidence for cyanoguanylurea (**4**) to represent the appropriate molecular structure, yet the formation of small fractions of **11**, depending on the temperature conditions, cannot be excluded:

Foremost, the decomposition of cyanourea or a mixture of the potassium salt of cyanourea with the parent free acid in aqueous solution was reported to entail the formation of cyanoguanylurea (**4**, **4a**) as the major product [275]. In order to compare the solid-state transformation product with that obtained in aqueous solution, a mixture of ammonium cyanoureat and cyanourea in a 3:1 ratio were reacted in water at 308 K for 7 – 10 days. Both the X-ray powder pattern as well as the  $^1\text{H}$  and  $^{13}\text{C}$  NMR spectra of the above product correspond to those of the solid-state decomposition product, neglecting the reflections/signals due to urea present in the latter (Fig. 4.37). Additionally,  $^{15}\text{N}$  spectroscopic investigations of the sample synthesized according to the above procedure give strong support for the validity of structure **4**. In the proton coupled or decoupled spectra,  $^{15}\text{N}$  signals are observed at – 181.1 (s,  $\text{C}\equiv\text{N}$ ), – 264.6 (s,  $\text{NH}$ ), – 278.0 (s,  $\text{C}=\text{N}$ ), – 291.2 (t,  $\text{NH}_2$ ), and – 295.3 ppm (t,  $\text{NH}_2$ ). For structure **11** the  $^{15}\text{N}$  signal of the bridging  $-\text{NH}-$  unit would be expected at  $\sigma < -300$  ppm by analogy with the related cyanourea or cyanoureat structures.

Moreover, the band location of the cyano-groups observed in the IR spectra ( $2200 / 2159 \text{ cm}^{-1}$ ) is very close to the nitrile signal in dicyandiamide  $(\text{H}_2\text{N})_2\text{C}=\text{N}-\text{C}\equiv\text{N}$  ( $2205 / 2165 \text{ cm}^{-1}$ ), whereas that of cyanourea  $(\text{H}_2\text{N})(\text{O}=\text{)C}-\text{HN}-\text{C}\equiv\text{N}$  is positioned at  $2254 \text{ cm}^{-1}$ , accompanied by a weak signal at  $2203 \text{ cm}^{-1}$ . The observed differences in the  $\text{C}\equiv\text{N}$  stretching frequencies owing to the isolobal substituents O and HN may further substantiate the validity of the cyanoguanylurea structure.

In addition, the mass spectra strongly corroborate the above conclusion by the presence of a fragment peak at  $m/z$  84, which equals the molecular peak of dicyandiamide. The facile fragmentation of the parent peak at  $m/z$  127 *via* a *McLafferty* type rearrangement into  $\text{HNCO}$

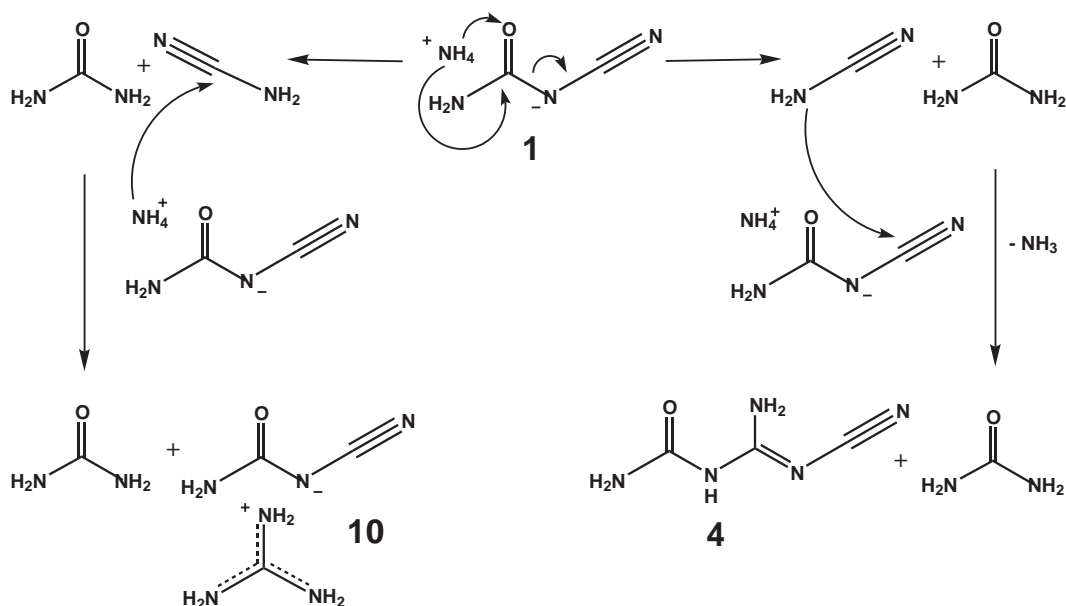


**Figure 4.39:** Two alternative mechanistic pathways of the solid-state transformation of **1**. The two-step mechanism sketched to the right is characterized by the nucleophilic attack of the intermediately formed cyanamide at the nitrile carbon of a neighboring anion, resulting in cyanoguanylurea (**4**) and urea. The alternative pathway (left) shows the nucleophilic addition of ammonia to the cyanamide carbon C1, leading to urea and the guanidinium salt of cyanourea (**10**) without evolution of one mole of ammonia.

(*m/z* 43) and dicyandiamide (*m/z* 84) is in agreement with the experimental pattern. The isomeric cyanocarbamoylguanidine structure (**11**, **11a**) would generate fragments with *m/z* 42 and 85, the latter of which however is not observed to a significant extent in most of the mass spectra.

Finally, the principal existence of cyanocarbamoylguanidine (**11**, **11a**) has not yet been established, since no data whatsoever are available for this compound in the literature. Therefore, the lack of information on the hypothetical cyanocarbamoylguanidine strongly suggests the instability of this compound, presumably with respect to the cyclization to the isomeric compound ammeline (**6**), which thus adds to the correctness of the above line of argument.

#### 4.2.3.6 Discussion

The previous section has given an outline of the tentative reaction participants and characteristics, yet no conclusive picture of the reaction mechanism has been presented. This can however only be done speculatively on the argumentative basis sketched above. In order to illuminate the potential course of the transformation, crystallographic details have to be taken into account. First of all, the product distribution strongly suggests the reaction pathway to differ substantially from that observed for ammonium dicyanamide:

Whereas in the latter case, the nucleophilic attack of the *in situ* generated ammonia occurs

at the nitrile carbon atom of the dicyanamide anion, the conservation of the nitrile moiety in ammonium cyanoureatate indicates the role of the ammonium group to be fundamentally different in the two compounds. The evolution of ammonia appears to be more pronounced in the latter case, since it is observable by a weak exothermic event around 355 K in the DSC measurements when the sample is heated gradually. In contrast, in ammonium dicyanamide the small mass loss due to evolving ammonia is not detectable by DSC. These observations suggest that ammonia is not retained in the transformation products of ammonium cyanoureatate stoichiometrically as is the case for ammonium dicyanamide. As described previously, the overall assembly of the ions shows a tendency towards  $H \cdots O$  hydrogen bonding in the present case, which is in contrast to the molecular arrangement in ammonium dicyanamide ( $H \cdots N$  bonding) and may therefore significantly alter the solid-state reactivity as compared to the latter. In ammonium dicyanamide, the trajectory of the protons during the transformation is directed towards the terminal and, to a lesser extent, to the central nitrogen atoms of the anion.

Whereas the nucleophilic attack of the *in situ* generated ammonia can only proceed at one of the chemically equivalent electrophilic carbon atoms in ammonium dicyanamide, leading finally to the molecular compound dicyandiamide in either case, the potential attack of ammonia in ammonium cyanoureatate may proceed at two different carbon atoms, leading in each case to different products. The conservation of the nitrile group in one of the products suggests the attack of ammonia to take place at the carbamoyl C2 atom, thereby inducing a breakage of the C2–N3 bond and, ultimately, the generation of urea and cyanamide  $H_2NCN$  after proton exchange. The intermediately formed cyanamide is prone to consecutive reactions, such as the nucleophilic attack at a neighboring nitrile carbon to form cyanoguanylurea (**4**) (Fig. 4.39, right).

An alternative scenario resulting in a different product distribution comes into play if ammonia is not evolved from the sample, but adds to the cyanamide intermediate to form the stable guanidinium cation, thereby blocking the nucleophilic attack of cyanamide at the parent cyanourea anion (Fig. 4.39, left). The spectroscopic data suggest the coexistence of both reaction pathways at low temperatures, which are realized by different targets of the initial

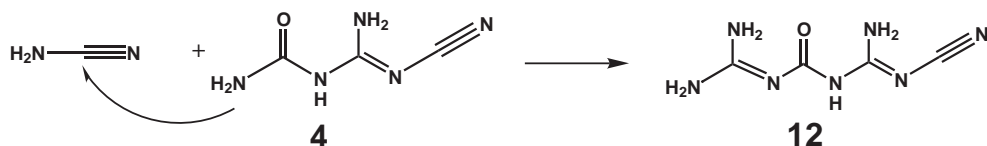


**Figure 4.40:** Mechanism of the assumed formation of [1-cyanoguanyl-3-guanyl]urea (**12**) from cyanoguanylurea (**4**) by nucleophilic addition of the latter to the intermediately formed cyanamide.

nucleophile ammonia. However, the significant mass loss observed in the isothermal DTA / TG experiments (first step 9.1 %, final mass loss 16.8 %) suggests the former reaction pathway (Fig. 4.39, right) to be the dominant one. Also, the observed exothermic event at 355 K in the DSC heating curve can be correlated with the evolution of ammonia, which at this stage does not induce significant structural changes as evidenced by X-ray powder diffraction. This may be assessed as further evidence for the facile release of ammonia, necessarily resulting in follow-up proton-transfer reactions. In a consecutive reaction, the main product cyanoguanylurea may further act as a nucleophile, attacking the intermediate cyanamide to form [1-cyanoguanyl-3-guanyl]urea (**12**), which is detected as a side phase by mass spectrometry (Fig. 4.40).

Since the reaction sequence leading to the observed products proceeds in the solid state and, hence, is dominated by little molecular freedom, the pre-orientation of the reactive centers is assumed to be such that the diffusion length necessary for the reaction to occur is minimized. Taking into account the thermal behavior of the lattice parameters, a competing reaction pathway may become increasingly favored. Since the anions are arranged in a head-to-tail manner along [001], the amide group of one anion is located close to the nitrile moiety of a neighboring anion ( $N_4 \cdots C_1$  355 pm at 140 K) (Fig. 4.30). Owing to the anomalous contraction of the *c*-axis with rising temperature, the reactive centers move closer and a nucleophilic attack of the amide  $N_4$  at  $C_1$  prior to or after breakage of the  $C_2$ – $N_3$  bond would lead to the isomeric cyanocarbamoylguanidine structure (**11**) as sketched in Figure 4.41. Although this reaction pathway seems to be facile in terms of the structural arrangement, no evidence

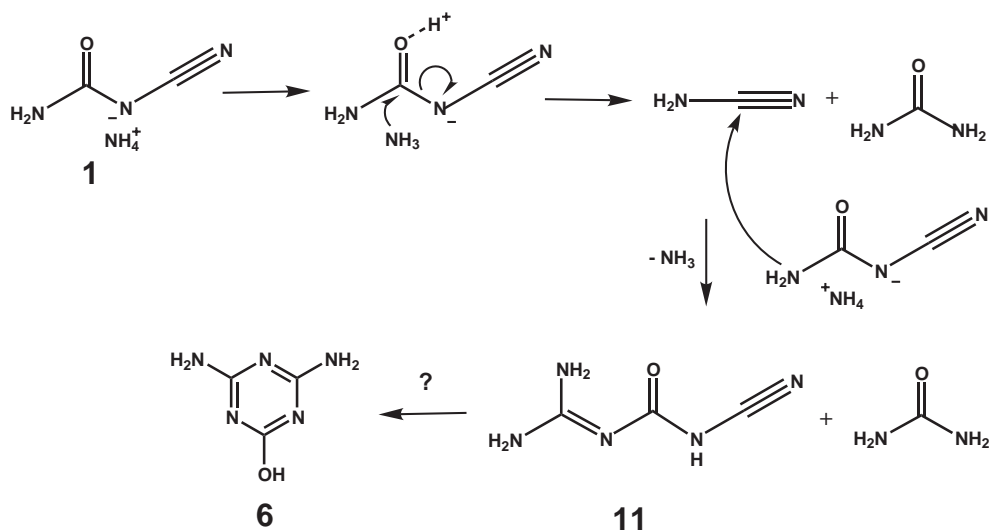


**Figure 4.41:** Tentative reaction mechanism leading to the isomeric cyanocarbamoylguanidine (**11**) and urea by the action of the amide nitrogen of **1** as nucleophile. Subsequent cyclization of cyanocarbamoylguanidine to ammeline (**6**) may be favored under certain temperature conditions.

has been found for the formation of **11** as discussed above. It may however not be excluded that under certain reaction conditions the formation of this isomer **11** is favored, presumably followed by rapid cyclization to ammeline, which is found as the major product in the DSC experiments (Fig. 4.41).

In conclusion, the observed transformation can be classified as a non-topochemical thermally induced reaction which despite its complexity proceeds in the solid phase, yielding a microcrystalline mixture of several reaction products. The thermal reactivity of ammonium cyanoureatate fundamentally differs from the related compound ammonium dicyanamide, which may tentatively be correlated with the differing hydrogen bonding network, resulting in a more facile release of ammonia, and the altered reactivity of the anion due to the presence of an electrophilic amide carbon. The above example demonstrates the interplay between the chemical functionality and the reaction conditions, leading to a variety of possible reaction pathways different from those in solution, which are not significantly limited by the rigid crystal lattice.

#### 4.2.4 Cyanoguanylurea

The above line of argument in delineating a qualitative reaction pathway has been exclusively drawn upon the evidence obtained from a combination of analytical techniques. Attempts to directly prove the correctness of the product identification and the postulated structure of the major decomposition product cyanoguanylurea ( $[(\text{cyanoamino})\text{iminomethyl}]\text{-urea}$ ,  $\text{H}_2\text{NC}(=\text{O})\text{NHC}(\text{NH}_2)\text{NCN}$  (**4**)) invariably failed in the first instance owing to the difficulties in obtaining single crystals of the main product. The presumptions made above could however be verified by establishing independent access to cyanoguanylurea, which accrued as a side product in the synthesis of zinc cyanoureatate (**5**) (cf. ref. [282]). The synthesis conditions proved suitable for the growth of single crystals, by means of which the identity and proposed structure of the main product could be confirmed.

##### 4.2.4.1 Formation of Cyanoguanylurea

Previous synthetic approaches towards cyanoguanylurea in organic solvents utilized reactions between the urea derivative carbamoyl-O-alkylisourea (**6**) [283,284] or trimethylsilylated cyanourea (**7**) with cyanamide (**8**) or cyanourea (**1**) [285], respectively. A simpler synthesis was proposed by *Iio et al.*, who obtained cyanoguanylurea from solutions containing free acid cyanourea or combinations of the latter with one of its salts [275] (Fig. 4.42).

In the present case, ammonium cyanoureatate (**2**) was added to an ion exchange resin, whose acidic sites had been loaded by an aqueous  $\text{ZnCl}_2$  solution. It is well-known that despite thorough washing small amounts of a salt solution may be adsorbed by the resin, depending on

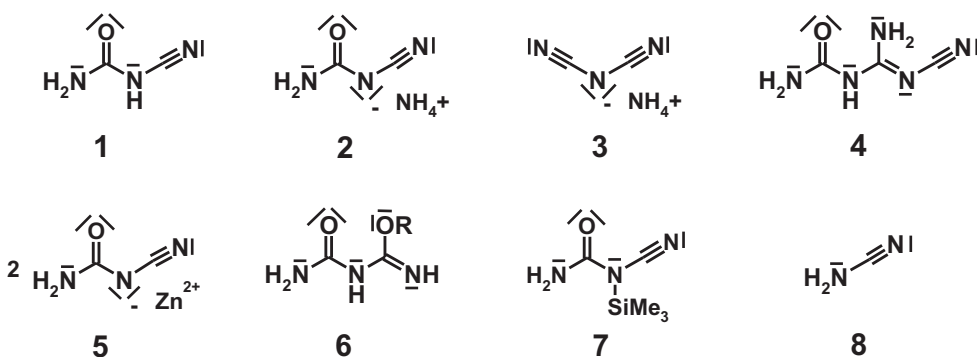


**Figure 4.42:** Molecular formulas of cyanourea and structurally related species referred to in the text: (1) cyanourea, (2) ammonium cyanoureat, (3) ammonium dicyanamide, (4) cyanoguanylurea, (5) zinc cyanoureat, (6) carbamoyl-*O*-alkylisourea, (7) *N*-cyano-*N*-(trimethylsilyl)-urea, (8) cyanamide.

the ionic interactions with the matrix, and subsequently released upon consecutive exchange steps. The latter scenario may be applicable also in this case, as evidenced by the presence of traces of  $\text{NH}_4\text{Cl}$  in the product mixture alongside cyanoguanylurea (4) and the main product zinc cyanoureat (5). This is indicative of an incomplete removal of  $\text{ZnCl}_2$  after the loading and washing procedures. A potential formation mechanism for 4 may therefore be proposed as follows:

$\text{ZnCl}_2$  is assumed to stimulate the molecular degradation pathway, which otherwise is induced thermally in a like manner as discussed above. The cleavage of the  $\text{C}(=\text{O})-\text{NCN}$  single bond, which can thermally be stimulated by a proton transfer from the ammonium ion to the oxygen atom, can be effected by  $\text{ZnCl}_2$  in two ways: By coordination of  $\text{ZnCl}_2$  to the oxygen atom, the  $\text{C}(=\text{O})-\text{NCN}$  single bond becomes strongly polarized, leading to subsequent cleavage with formation of hydrogen isocyanate, cyanamide and ammonia or related species after proton transfer reactions. A more simple explanation is invoking the Brønsted acidity of concentrated aqueous solutions containing  $\text{Zn}^{2+}$  species:

As was reported previously, cyanoguanylurea is formed in a slow reaction in aqueous and organic solutions containing the free acid cyanourea together with a cyanoureat salt [275]. In an investigation of the influence of pure Brønsted acidity on the formation of cyanoguanylurea, the attempt of a quantitative synthesis of cyanoguanylurea from ammonium cyanoureat in mildly ( $\text{pH} \approx 3$ ,  $\text{HCl}$ ) acidic aqueous solution led to the formation of cyanourea and ammonium chloride only.

In strongly acidic solution ( $\text{pH} \approx 1$ ,  $\text{HCl}$ ), cyanourea and ammonium chloride were formed together with an unknown phase. Consequently,  $\text{H}_2\text{NC}(=\text{O})\text{NHC}(\text{NH}_2)\text{NCN}$  will only be formed in the presence of Brønsted acids *via* the intermediate formation of cyanourea and subsequent reaction of the latter with unreacted ammonium cyanoureat, but not if cyanourea

is formed quantitatively. Therefore it is assumed that in the present case cyanoguanylurea is obtained by the interplay of the Brønsted and Lewis acidic character of aqueous  $Zn^{2+}$  solutions, the latter of which playing the decisive role in the decomposition reaction.

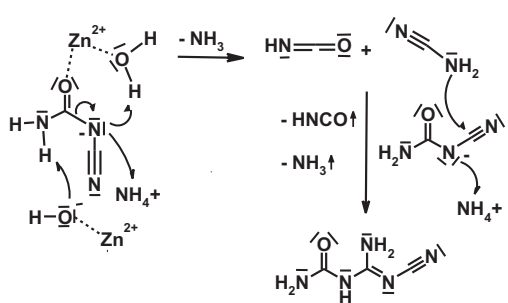


**Figure 4.43:** Tentative mechanism for the formation of cyanoguanylurea from ammonium cyanoureate in the presence of  $ZnCl_2$ . The  $Zn^{2+}$  species in aqueous solution are only drawn schematically so as to indicate their function.

Given that the formation of cyanoguanylurea only occurs as a minor side reaction, the exact stoichiometry of the overall reaction cannot be resolved. Furthermore, for the same reason the outline of the tentative reaction mechanism appears to be critical, since the nature of the species actually involved cannot be verified. However, in light of the corresponding product formation by either thermal treatment or the presence of  $ZnCl_2$  in an ammonium cyanoureate solution, the acid species  $ZnCl_2$  may be assumed to act as a catalyst in the fragmentation of the cyanoureate anion. In a subsequent

step, addition of cyanamide to another cyanoureate anion may occur, resulting in the formation of cyanoguanylurea (Fig. 4.43).

Another question to be addressed is the poor water solubility of cyanoguanylurea, and hence, the inhibited crystallization from aqueous solution observed in the above investigations (cf. 4.2). The fact that the opposite was found in the ion exchange reaction, namely the facile crystallization from aqueous solution, suggests a significant increase in water solubility, presumably owing to the different pH of the solution due to the slightly acidic character of  $ZnCl_2$ . The tendency towards crystallization may, however, also result from the presence of  $NH_4Cl$ , which has been reported in the literature to act as a mineralizer [286–290].

#### 4.2.4.2 Crystal Structure

Cyanoguanylurea crystallizes in the monoclinic crystal system, space group  $P2_1/n$  (no. 14), with four formula units in the unit cell. Details of the crystal structure solution and refinement are given in Table 4.6. As proposed in the above study on the thermally induced formation of  $H_2NC(=O)NHC(NH_2)NCN$ , the molecule has a cyanoguanylurea structure and not that of its isomer cyanocarbamoylguanidine (Fig. 4.44). All protons could be unambiguously localized at N1, N2 and N5. Thus, the “imino” tautomer ( $H_2N(HRN)C=NCN$  ( $R = H$ , organic residue)) rather than the “amino” tautomer ( $HRN(HN=)CNHCN$ ) represents the molecular structure of cyanoguanylurea as also found for dicyandiamide (cyanoguanidine) as well as for some *N*-

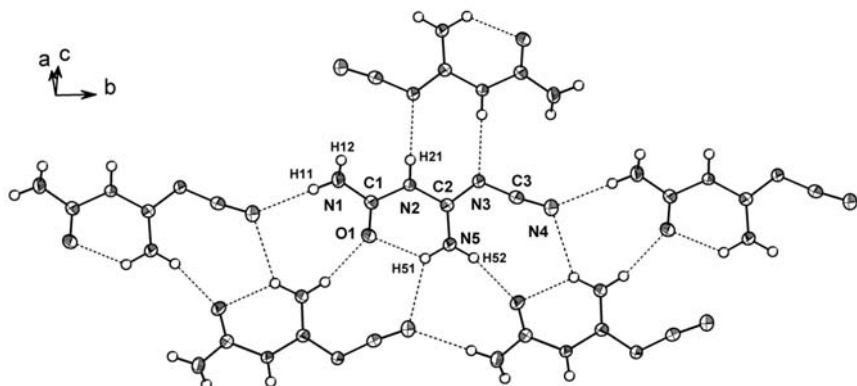


**Figure 4.44:** Environment of the cyanoguanylurea molecule in a layer formed by a hydrogen bonding network (dotted lines). The displacement ellipsoids are drawn at the 50 % probability level.

cyano-*N'*-substituted guanidines both in solution and in the solid state [291–298]. By analogy with the structural data reported for the prototype structure of dicyandiamide [291, 292], the bonding situation is not fully accounted for by assuming the prevalence of the resonance structure **a** as depicted in Figure 4.45.

Although drawing a double bond between C2 and N3 appears to be energetically reasonable in

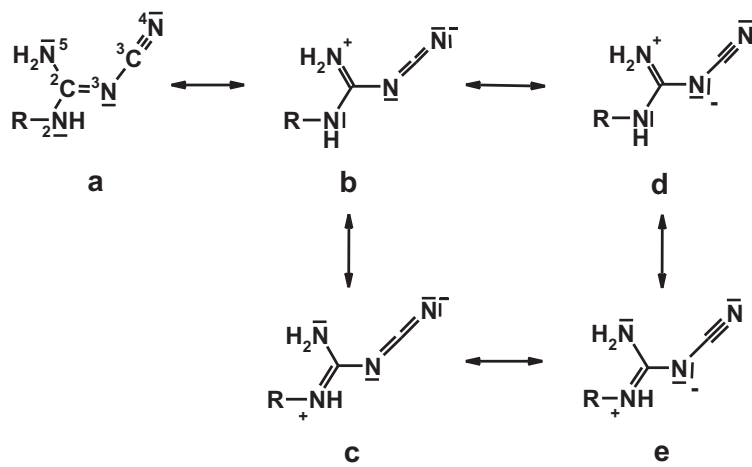


**Figure 4.45:** Resonance structures of *N*-cyano-*N'*-substituted guanidines. The “true” electronic structure may be considered as a superposition of the neutral structure **a** and the charge-separated structures **b** and **d**. Given the relatively long bond length C2–N2, structures **c** and **e** obviously contribute to a lesser extent in cyanoguanylurea.

terms of conjugation and mandatory in view of the experimentally found proton distribution, the adjacent bond distances C3–N3 (132.0(2) pm) and C2–N5 (131.5(2) pm), though formally drawn as single bonds (Fig. 4.45), are shorter than C2–N3 (133.3(2) pm); their values are all intermediate between those of a single and a double bond (Table 4.7).

This finding is indicative of the  $\pi$  electron density being equally distributed over parts of the guanidine system (N5–C2–N3) as well as the N3–C3 bond. This suggests that structures **b–e** jointly contribute as much as **a** to the total valence structure. This phenomenon is frequently encountered in structures containing the cyanoguanidine unit [291–298], indicating the conventionally reported structure for cyanoguanidine derivatives to be rather simplistic and inappropriate if the contributing charge separated forms **b – e** are neglected [291–293]. Although the C3–N4 distance of 116 pm indicates that the cyanamide and not the carbodiimide structure represents the bonding situation most appropriately, the N3–C3–N4 moiety is slightly bent ( $< 173.3^\circ$ ) and the atomic displacement ellipsoid of C3 is not elongated perpendicular to the molecular plane as observed for the adjacent atoms N3 and N4 (Table 4.7). This result may not be an artifact but truly reflect the “superposition” of structures **a**, **d** and **e** on the one hand, and **b** and **c** with two adjacent allenic double bonds on the other hand, thus dislocating the electron density of C3 along and not perpendicular to the N3–C3–N4 bond system.

The nitrile region in the IR spectrum of cyanoguanylurea showing a “doublet” at 2199 (s) / 2158  $\text{cm}^{-1}$  (w) is very similar to that of dicyandiamide ((2202 (s) / 2160  $\text{cm}^{-1}$  (w)) which may

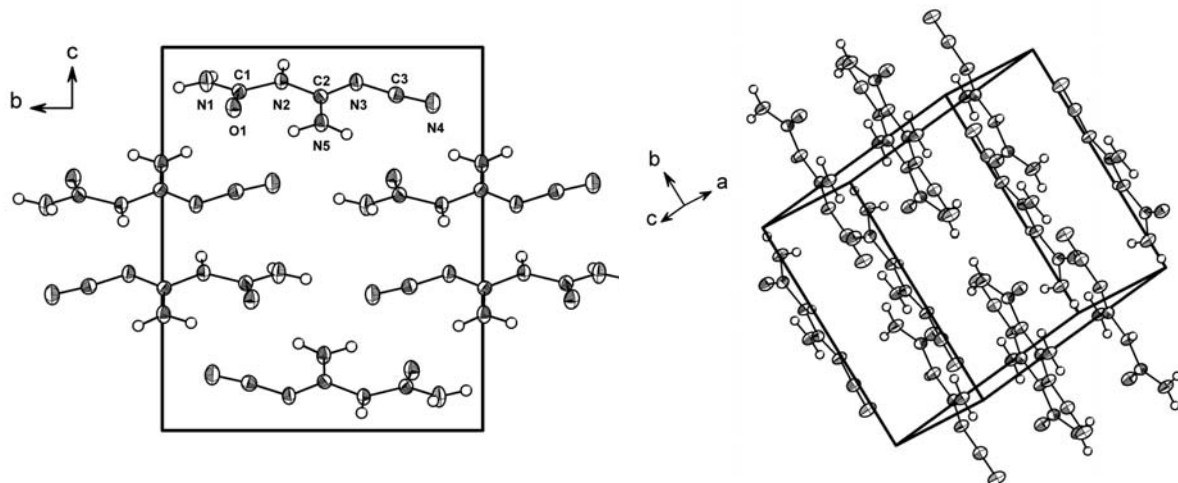


**Figure 4.46:** Left: Unit cell of cyanoguanylurea, view along [100]. Displacement ellipsoids are drawn at the 50 % probability level. Right: Layered structure of cyanoguanylurea made up from hydrogen-bonded molecules; view along the planes spanned by [010] and [301]. Displacement ellipsoids are drawn at the 50 % probability level.

also serve as evidence for a similar electron density distribution in the two related compounds (Fig. 4.36).

The molecule is embedded in a hydrogen bonding network, comprising medium strong and weak hydrogen bonds ( $H \cdots N/O \approx 210 - 240$  pm). The intramolecular contact  $N5\text{--}H51 \cdots O1$  represents the strongest hydrogen bond, resulting in a six-membered “chelate ring” reminiscent of keto-enol tautomeric systems. This interaction seems to direct the structural

**Table 4.6:** Crystallographic data for guanylurea dicyanamide.

Formula	$H_2NC(=O)NHC(NH_2)NCN$
$M_w / g \cdot mol^{-1}$	127.12
crystal system	monoclinic
space group	$P2_1/n$ (no. 14)
$T / K$	200
diffractometer	Nonius Kappa CCD
radiation ( $\lambda / pm$ )	Mo-K $\alpha$ (71.073)
monochromator	graphite
$a / pm$	476.7(1)
$b / pm$	965.3(2)
$c / pm$	1165.6(2)
$\beta / ^\circ$	97.75(3)
$V / 10^6 \cdot pm^3$	531.4(2)
$Z$	4
$\rho_{calcd} / g \cdot cm^{-3}$	1.589
$F(000)$	264
$\mu / mm^{-1}$	0.127
crystal size / $mm^3$	0.23 x 0.13 x 0.07
diffraction range	$3.53 \leq \theta \leq 27.50$
index range	$-6 \leq h \leq 6, -12 \leq k \leq 11, -15 \leq l \leq 15$
total no. reflections	9162
independent reflections	1215 ( $R_{int} = 0.0423$ )
observed reflections	1048
refined parameters	with $F_o^2 \geq 2\sigma(F_o^2)$
GooF on $F^2$	103
$R$ indices (all data)	1.081
	$R_1 = 0.0357$ (0.0429)
	$wR_2 = 0.0964$ (0.1016)
	with $w = [\sigma^2(F_o^2) + (0.0510P)^2 + 0.1677P]^{-1}$
	where $P = (F_o^2 + 2F_c^2)/3$
min./max. residual	- 0.219 / 0.193
electron density / $e \cdot 10^{-6} pm^{-3}$	

**Table 4.7:** Bond lengths and angles of  $H_2NC(=O)NHC(NH_2)NCN$ .

Distances / pm		Angles / $^\circ$	
O1–C1	123.5(2)	C2–N2–C1	126.3(2)
N1–C1	133.2(2)	C3–N3–C2	119.1(2)
N2–C2	136.7(2)	O1–C1–N1	123.8(2)
N2–C1	139.3(2)	O1–C1–N2	121.6(2)
N3–C3	132.0(2)	N1–C1–N2	114.6(2)
N3–C2	133.3(2)	N5–C2–N3	125.6(2)
N4–C3	116.4(2)	N5–C2–N3	120.7(2)
N5–C2	131.5(2)	N3–C2–N2	113.7(2)
		N4–C3–N3	173.2(2)
N1–H11	88(2)	C1–N1–H11	118(2)
N1–H12	88(2)	C1–N1–H12	120(2)
N2–H21	83(2)	H11–N1–H12	119(2)
N5–H51	95(2)	C2–N2–H21	115(2)
N5–H52	88(2)	C1–N2–H21	119(2)
		C2–N5–H51	118(1)
		C2–N5–H52	120(2)
		H51–N5–H52	122(2)
Hydrogen bonding			
N1–H11 … N4	214(2)	N1–H11–N4	179(2)
N1–H12 … O1	226(2)	N1–H12–O1	146(2)
N2–H21 … N3	215(2)	N2–H21–N3	168(2)
N5–H51 … O1	198(2)	N5–H51–O1	130(2)
N5–H51 … N4	237(2)	N5–H51–N4	134(2)
N5–H52 … O1	206(2)	N5–H52–O1	162(2)

arrangement, which significantly deviates from molecular planarity: Whereas the cyanoguanidine fragment is almost planar (torsion angle C2–N2–N3–C3 = 179°), the urea unit is twisted with respect to the former around the C1–N2 bond, thus introducing torsion angles N1–C2–N2–C3 of 164° and O1–C2–N2–C3 of 16°, thereby circumventing an eclipsed arrangement of the atoms (Fig. 4.46, left). This situation may explain the virtual absence of  $\pi$ -delocalization into the C2–N2 bond of the guanidine system (136.7(2) pm), since potential conjugation with the C1–O1 double bond is reduced by the above twisting. The molecules are stacked along the *b*-axis, forming planes extending in the [301] direction (Fig. 4.46, right). While the planes are spaced by about 470 pm, the shortest “interplanar” distances are the hydrogen bonding contacts between O1 and H12 which are as short as 230 pm. However, owing to the relatively sparse interactions between the planes, the crystal structure of cyanoguanylurea may be considered as a layered structure, the layers being made up from hydrogen bonded molecular units.

## Chapter 5

# Carbon(IV)Nitride Precursors II. Chemical Screening and Thermal Reactivity

This Chapter will be concerned with chemical principles governing the molecular precursor route towards graphitic carbon nitride, which may be considered to represent the ultimate pre-stage to the three-dimensional modifications of  $\text{C}_3\text{N}_4$ . According to Chapter 1, a vital issue is set by an adept choice of molecular precursors that combine on a molecular level all essential features crucial for the construction of extended  $\text{CN}_x$  networks. Therefore, in choosing possible precursors, a range of prerequisites have to be considered, among which the chemical composition and reactivity are the most prominent ones.

Suitable molecular systems may exhibit a simple constitution, combining an alternate arrangement of carbon and nitrogen, thereby featuring a carbon(IV)nitride core, with a minimum content of hydrogen and possibly an excess of nitrogen, such as found for instance in cyanuric azide. Whereas solid-state reactivity in the actual sense is not a crucial condition, reactivity in a general sense is an almost trivial requirement for the essential crosslinking reactions towards highly condensed  $\text{CN}_x$  systems.

However, the formation of extended carbon nitrides has long been treated as a “black-box reaction”, with no particular attention being paid to possibly general reaction principles and analogies when using different precursor sources.

Similarly, information about the exact stoichiometry and composition, as well as structural building units of the as-obtained  $\text{CN}_x$  materials is still sparse and rather speculative [73, 82–85, 124, 299–301]. Although the importance of reproducible and tailored synthesis strategies towards low-dimensional  $\text{CN}_x$  networks as well as their structural characterization

is beyond controversy, little advertence has been attached to resolving the detailed mechanism of thermal condensation reactions of molecular precursors. However, in order to compile basic principles of thermal reaction pathways and to identify the smallest structural motifs of the resulting “g- $\text{C}_3\text{N}_4$ ” structures, a broad overview over different reaction types of various substrates, the formation of intermediates and potential analogies between them is mandatory. Special emphasis is therefore placed in this work on the screening and selection of potential precursors exhibiting *solid-state* reactivity, as this non-trivial feature may afford an in-depth insight into well-defined processes on a molecular level leading to the construction of extended networks.

The molecular systems chosen comprise dicyanamides  $[\text{N}(\text{CN})_2]^-$  and tricyanomelamines  $[\text{H}_n\text{C}_3\text{N}_3(\text{NCN})_3]^{(3-n)-}$  ( $n = 1,2$ ), which are known to exhibit various types of thermally induced transformations [121–126, 302, 303]. A guiding principle has been the extension of dicyanamide and tricyanomelamine chemistry to non-metal representatives by selection of salt-like C/N/H compounds, in order to ensure facile conversion into pure, metal-free carbon nitride materials. All compounds selected have been checked for thermally induced solid-state reactivity, which clearly imposes severe limitations on the choice of possible precursor compounds, as further discussed in section 5.2.

In the following, a systematic investigation of different precursor systems is presented, both with respect to principal structural features and properties. The focus is thereby placed on possible interrelations between structure and reactivity, and common aspects entailing general trends will be emphasized.

## 5.1 Dicyanamides

According to *Franklin*, dicyanamide can be classified as a member of the series of ammonocarbonic acids, which is obtained by successive de-ammoniation of a hypothetical ortho-ammonocarbonic acid (Figure 5.1) [80]. This concept is built upon the formal analogy between carbonic acids of water / oxygen and those based on the ammonia / nitrogen system, and therefore delivers a classification scheme according to which the compositions of the familiar compounds guanidine, biguanide, cyanamide, dicyandiamide, and melamine as well as melam, melem, melon and hydromelonic acid can be traced back to a single common ancestor.

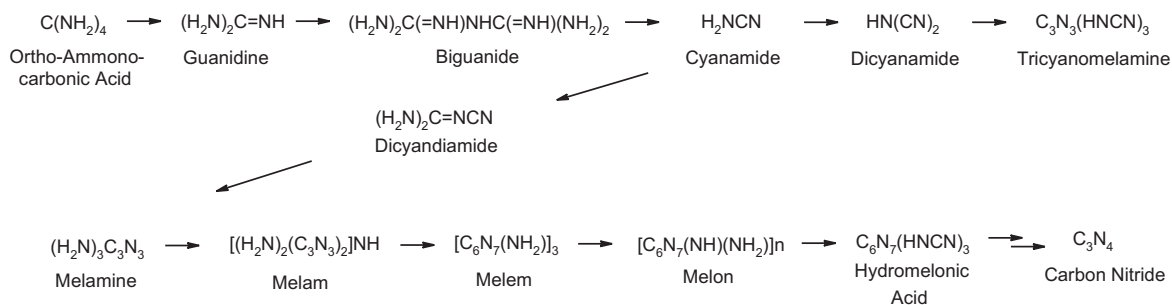
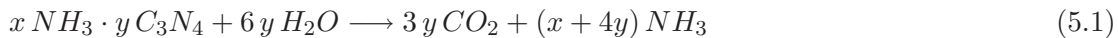


**Figure 5.1:** Formal series of the de-ammoniation products of the hypothetical ortho-ammonocarbonic acid by analogy to the well-known dehydration products of ortho-carbonic acid  $C(OH)_4$ , namely  $H_2CO_3$  and  $CO_2$ , according to *Franklin* [80].

Note, however, that this scheme only works out the *formal* relations between the above carbon nitrides, displaying in a simplified form transformations that may in principle be feasible. However, not every single transformation has been accomplished yet by the simple loss of ammonia, for instance the conversion of cyanamide into dicyanamide, which has however been achieved by dissolving melon in fused disodium cyanamide [80]. This classification scheme is additionally supported by the behavior of the ammonocarbonic acids toward water. When heated in the presence of water, all ammonocarbonic acids are hydrolyzed, usually through various mixed aquo-ammonocarbonic acids, to carbon dioxide and ammonia in accordance with the general equation



where  $x NH_3 \cdot y C_3N_4$  represents any of the known ammonocarbonic acids.

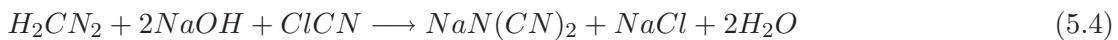
The free acid dicyanamide  $HN(C\equiv N)_2$  is unstable in its free state; it can, however, be stabilized in aqueous solution. The latter was prepared by decomposing a suspension of silver dicyanamide in water by means of hydrogen sulfide. *Madelung* and *Kern* determined the

equivalent conductance of  $HN(C\equiv N)_2$  to be as high as  $392\text{ }cm^2 \cdot \Omega^{-1} \cdot mol^{-1}$ , being indicative of a strong acid. On evaporation of the solution thus obtained, a white, flocculent, polymeric material of undetermined composition deposited [80,230]. According to *Burdick*, a crystalline solid of composition  $HC_2N_3 \cdot H_2O$  is obtained by filtering of the flocculent material, which, however, could not be reproduced by others [80,230,304,305].

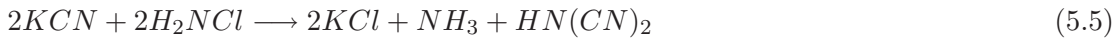
The first dicyanamide salt has been prepared as early as in the 1870s by *Bannow*, who obtained a silver salt with the sum formula “ $AgC_2N_3$ ” by addition of ammoniacal silver nitrate to the aqueous solution of a potassium salt synthesized by the reaction of potassium cyanide with mercuric cyanide [306,307]. *Franklin* optimized the synthesis procedure by heating a mixture of mercury and sodium cyanide, from which mercury is driven off, yielding dicyanogen, and sodium dicyanamide is formed according to



which is isolated as the monohydrate and finally gives off its crystal water under heating at 573 K [80]. Notably, by reaction of melon and sodium amide as described above, using appropriate portions of the reactants, a good yield of sodium dicyanamide instead of disodium cyanamide has been obtained by *Franklin* [80]. Several synthetic routes to the sodium salt of dicyanamide, which was used in this work as a convenient reagent, have been developed in the meantime. As they have been comprehensively discussed in the literature, only a short summary will be given by the following equations [80,163,230,240,304]:



An alternative approach [231] utilizes the reaction of chlorine with  $NaOH$ ,  $KCN$  and ammonia, which *via* several intermediates proceeds according to



The dicyanamide anion can be formally derived from the amide ion by replacing both hydrogen atoms by cyanide moieties. It thus possesses a planar bent structure with point group  $C_{2v}$ . Unlike the pyramidal structure of  $HN(C\equiv N)_2$ , the planar form of the anion brings about significant contributions from mesomeric resonance structures (Fig. 5.2), which is supported by the high frequency of the antisymmetric N–C stretching mode ( $\approx 1400\text{ }cm^{-1}$ ), and the considerable stability of the dicyanamide salts as compared to the free acid.

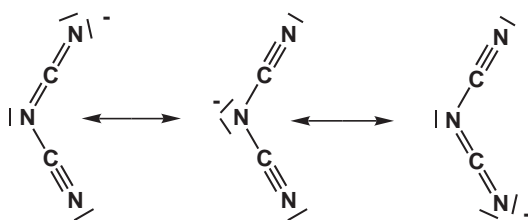


**Figure 5.2:** Mesomeric forms of the dicyanamide anion, leading to a charge delocalization and increase of the acidic character of the parent acid dicyanamide.

The  $N(CN)_2^-$  is isoelectronic to a number of 34 electron species, such as cyanazide  $NC(N_3)$  [308, 309], the polynitrogen ion  $N_5^+$  [310–313], the *N*-carbonyl-1-oxo-methaneiminium ion  $[N(CO)_2]^+$  [314] and to the neutral species malonic acid dinitrile  $CH_2(CN)_2$ , or diisocyanomethane  $CH_2(NC)_2$  (Fig. 5.3) [315].

The conformation and chemical behavior of the dicyanamide can nicely be rationalized with the concept of “pseudoelements”, which has originally been formulated in 1922 by *Madelung* and *Kern* in the so-called *cyanide displacement law*, according to which atoms adopt the properties of atoms having atomic numbers higher by  $n$  by addition of  $n$  ( $= 1, 2, 3$ ) cyanide groups [230]<sup>1</sup>. Thus, the members of the sequence  $OCN^-$ ,  $N(CN)_2^-$  and  $C(CN)_3^-$  can be considered as *pseudohalogenides* [319, 320]; likewise,  $N(CN)_2^-$  has *pseudochalkogenocyanate* character by analogy with the cyanate ion.

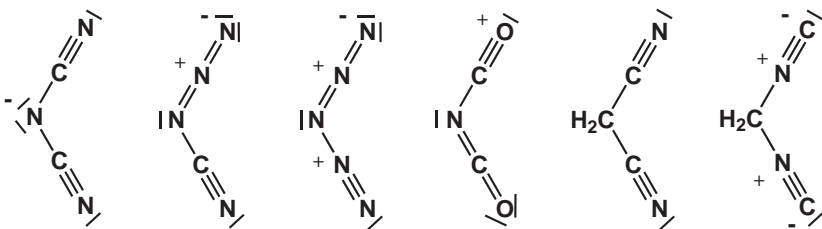


**Figure 5.3:** Neutral and charged  $34 e^-$  species, which are isoelectronic to the dicyanamide anion.

The IR and Raman spectroscopic characterization of dicyanamides has been advanced predominantly by *Kuhn* and *Mecke* (Na-, Hg-, Cu- and Pb-salts) [305], *Perkins* (Hg-, Pb- and Ba-salts) [321], and *Köhler*, by whom the first organometallic dicyanamides  $(CH_3)_2Sn[N(CN)_2]_2$ ,  $(C_6H_5)_2Sn[N(CN)_2]_2$ , and  $(C_6H_5)_3M[N(CN)_2]$  ( $M = Ge, Sn, Pb$ ) have been prepared and spectroscopically characterized [322–324].

Throughout the last decades, much progress has been done with respect to the structural characterization of dicyanamides by means of X-ray single-crystal structure analysis.

<sup>1</sup>Both the *cyanide displacement law* as well as the *hydride displacement law* developed by Grimm in 1925 [229] represent special cases of the isolobal principle [316–318].

*Britton* and *Chow* communicated the first crystal structure analyses of  $(CH_3)_2Sn[N(CN)_2]_2$ ,  $(CH_3)_3Sn[N(CN)_2]$  [325], and  $(CH_3)_2Tl[N(CN)_2]$  [326]. In recent years, *Jürgens* and others have structurally characterized a considerable number of mono- ( $M^+ = Li$  [240, 327],  $Na$  [125],  $K$ ,  $Rb$  [126],  $Cs$  [328],  $Ag$  [329, 330]) and divalent ( $M^{2+} = Mg$ ,  $Ca$ ,  $Sr$ ,  $Ba$  [331, 332],  $Pb$  [333],  $Zn$  [334, 335],  $Cd$  [336]) metal dicyanamides. The first solvent-free dicyanamides of the trivalent lanthanides ( $Ln = La$ ,  $Ce$ ,  $Pr$ ,  $Nd$ ,  $Sm$ , and  $Eu$ ) have been presented recently by *Jürgens* [337].

Transition metal dicyanamides  $M^{2+}[N(CN)_2]_2$  ( $M = Cr$ ,  $Mn$ ,  $Fe$ ,  $Co$ ,  $Ni$ ,  $Cu$ ) adopting a Rutile-type structure were found to exhibit a variety of magnetic properties [338–344]. Driven by the quest for molecular magnets based on dicyanamides, a plethora of solvated transition metal dicyanamides has been synthesized recently in which the dicyanamide anions act as terminal and bridging ligands in various bonding modes [345–351]. In this context the complex dicyanamide  $\kappa\{ (BEDT-TTF)_2Cu[N(CN)_2]Br \}$  ( $BEDT-TTF = C_{10}H_8S_8$ ) has attracted attention owing to its high transition temperature to the superconducting state  $T_c$  of 11.6 K [352]. An account of the different coordination types of the dicyanamide ion in these complexes is given by *Jürgens* [240].

In contrast, little research had been focused on the synthesis of non-metal dicyanamides, and as a consequence, only ammonium [121–123, 240], hydrazinium, as well as methyl- und  $N,N$ -dimethylhydrazinium-dicyanamide were known until recently [353]. Stimulated by the “re-discovery” of ionic liquids, the pseudohalide anions tricyanomethanide  $[C(CN)_3^-]$  and dicyanamide  $[N(CN)_2^{2-}]$  have very recently been shown to produce a range of useful ionic liquids with imidazolium, ammonium, pyrrolidinium [354–357], and trialkylsulfonium cations [358]. They are presently discussed as promising candidates for applications such as components in new solar cells. Concurrently, the anions have also been used as ligands in the synthesis of a large range of coordination polymers which display fascinating structures and long-range magnetic ordering [359]. In particular, it has been found that the structures of anionic  $M(dca)^{3-}$  networks are templated by the nature of the counter cation required for charge balance [359]. Tetramethylammonium dicyanamide was identified to form a plastic crystal phase exhibiting conductivity based on a vacancy-diffusion model [360]. Despite the newly gained interest in metal-free dicyanamides, little advertance has been attached to the crystal structure elucidation of these compounds. The following sections will focus on the study of novel non-metal dicyanamides as potential  $CN_x$  precursors, which besides the characterization of their thermal behavior will also cover aspects of their structural properties.

Structure and thermal behavior of metal-dicyanamides has been subject to previous studies reverting back to investigations by *Madelung* and *Kern* [125, 230, 240, 302, 361]. It has been

recognized that sodium dicyanamide undergoes trimerization to sodium tricyanomelamate upon heating to 595 – 695 K in a thermal solid-state reaction without passing the melt (cf. section 5.5 on page 167) [125,240]. Similarly, potassium and rubidium dicyanamide form cyclic tricyanomelamate anions between 530 and 700 K; however melting occurs prior to trimerization at 505 K (K[N(CN)<sub>2</sub>]) and 463 K (Rb[N(CN)<sub>2</sub>]) [126,240]. Whereas the dicyanamides Cs[N(CN)<sub>2</sub>] and NaCs<sub>2</sub>[N(CN)<sub>2</sub>] exhibit a thermal reactivity similar to that of potassium and rubidium dicyanamide, the product of the thermal oligomerization of Li[N(CN)<sub>2</sub>] above 565 K could not be identified unambiguously as being composed of isolated [C<sub>6</sub>N<sub>9</sub>]<sup>3-</sup> ions [240]. In contrast, di- and trivalent dicyanamides polymerize to amorphous products of yet unknown composition upon thermolysis, thus giving rise to particularly diverse modes of thermal reactivity in dicyanamide chemistry. As discussed in detail in section 4.1 on page 71, the thermally induced reactivity of NH<sub>4</sub>[N(CN)<sub>2</sub>] significantly differs from that of metal-dicyanamides in that the cation is actively involved in the observed solid-state transformation. A similar behavior has been claimed for hydrazinium dicyanamide, which was reported to be thermally unstable with respect to cyclization, forming guanazole C<sub>2</sub>N<sub>5</sub>H<sub>5</sub> in a strongly exothermic reaction at temperatures as low as 323 K [353]. Along these lines it gets evident that the nature of the cation in salt-like dicyanamides exerts a pronounced influence on the thermal reactivity of dicyanamides. Hence, dicyanamides may be tuned with respect to their thermal behavior according to the counter ions, and may thus be envisaged to represent versatile precursor compounds for the synthesis of extended carbon nitride solids, the absence of hydrogen in the anion adding to this line of argument.

## 5.2 Guanidinium Dicyanamide

### 5.2.1 Introduction

Guanidinium dicyanamide was considered an appropriate model system for the study of thermal solid-state reactivity as it shows potential to rearrange in a manner analogous to that found for ammonium dicyanamide: For instance, by nucleophilic addition of one or more of the cation  $NH_2$  groups to the nitrile carbon of the anion, carbon(IV) nitride oligomers with an alternating arrangement of C and N may be accessible. Guanidinium dicyanamide may therefore be used to validate the reaction pathway sketched for the ammonium salt and to check its transferability to other systems (cf. ref. [303]).

As yet, the only source of information about the existence of this dicyanamide has been a patent mentioning it as an air-bag component [362]. However, this reference does not furnish information on structural and spectroscopic data, nor does it explicate the thermal behavior of guanidinium dicyanamide.

The synthesis of guanidinium dicyanamide led to two polymorphic forms, which were obtained under slightly different reaction conditions, starting off from ion exchange synthesis (Fig. 5.4). The high-temperature polymorph, henceforth denoted with “ $\alpha$ ”, is easily obtained under ambient conditions, whereas the directed synthesis of the low-temperature polymorph (“ $\beta$ ”) crucially depends on the correct choice of reaction conditions (cf. section 10.1 on page 355).

### 5.2.2 Crystal Structures

In the following, the crystal structures of the products are contrasted, and their similarities evaluated. Details of the structure determination and relevant crystallographic data are summarized in Table 5.1. Interatomic distances and angles are listed in Table 5.2.

The orthorhombic unit cell of the  $\beta$ -polymorph ( $Pna2_1$ , no. 33) contains eight formula units of  $[C(NH_2)_3][N(CN)_2]$ , of which two build up the asymmetric unit. The guanidinium and dicyanamide ions are alternately stacked and about equally spaced, forming arrays of parallel

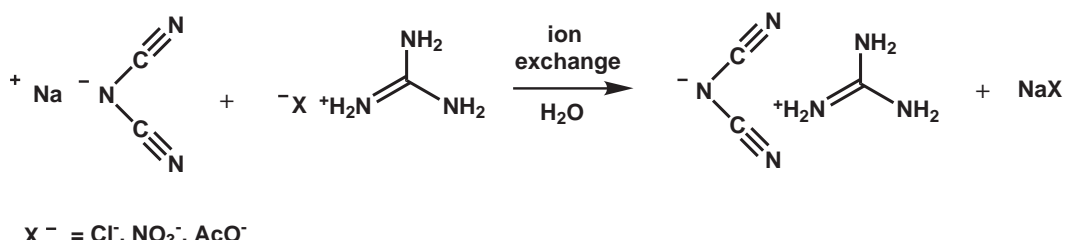


**Figure 5.4:** Synthesis of guanidinium dicyanamide by means of ion exchange in aqueous solution starting from sodium dicyanamide and a guanidinium salt.

**Table 5.1:** Crystallographic data for  $\beta$ - (left) and  $\alpha$ -guanidinium dicyanamide (right).

Formula	$\beta$ -[C(NH <sub>2</sub> ) <sub>3</sub> ][N(CN) <sub>2</sub> ]	$\alpha$ -[C(NH <sub>2</sub> ) <sub>3</sub> ][N(CN) <sub>2</sub> ]
$M_w$ / g · mol <sup>-1</sup>	126.14	126.14
crystal system	orthorhombic	monoclinic
space group	$Pna2_1$ (no. 33)	$P2_1/c$ (no. 14)
$T$ / K	200	200
diffractometer	Nonius Kappa CCD	Nonius Kappa CCD
radiation ( $\lambda$ / pm)	Mo-K $\alpha$ (71.073)	Mo-K $\alpha$ (71.073)
monochromator	graphite	graphite
$a$ / pm	1373.1(3)	1924.9(4)
$b$ / pm	495.5(1)	496.0(1)
$c$ / pm	1802.9(4)	1372.4(3)
$\beta$ / °		110.46(3)
$V$ / 10 <sup>6</sup> · pm <sup>3</sup>	1226.7(4)	1227.5(4)
$Z$	8	8
$\rho_{calcd}$ / g · cm <sup>-3</sup>	1.366	1.365
$F(000)$	528	528
$\mu$ / mm <sup>-1</sup>	0.102	0.102
crystal size / mm <sup>3</sup>	0.30 x 0.22 x 0.09	0.31 x 0.22 x 0.14
diffraction range	$3.18 \leq \theta \leq 27.47$	$3.17 \leq \theta \leq 27.50$
index range	$-17 \leq h \leq 17, -6 \leq k \leq 6,$ $-17 \leq l \leq 23$	$-23 \leq h \leq 25, -6 \leq k \leq 6,$ $-17 \leq l \leq 17$
total no. reflections	16123	14135
independent reflections	2510 ( $R_{int} = 0.0499$ )	2814 ( $R_{int} = 0.0669$ )
observed reflections	1838	1820
refined parameters	with $F_o^2 \geq 2\sigma(F_o^2)$	with $F_o^2 \geq 2\sigma(F_o^2)$
extinction coefficient $\chi$	212	212
GooF on $F^2$	0.013(2)	0.012(3)
$R$ indices (all data)	$R_1 = 0.0423$ (0.0687) $wR_2 = 0.0967$ (0.1100) with $w = [\sigma^2(F_o^2) + (0.0569P)^2 + 0.1346P]^{-1}$ where $P = (F_o^2 + 2F_c^2)/3$	$R_1 = 0.0474$ (0.0860) $wR_2 = 0.1118$ (0.1290) with $w = [\sigma^2(F_o^2) + (0.0579P)^2 + 0.1554P]^{-1}$ where $P = (F_o^2 + 2F_c^2)/3$
min./max. residual		
electron density / $e \cdot 10^{-6}$ pm <sup>-3</sup>	- 0.168 / 0.241	- 0.273 / 0.310

chains along [001] (Fig. 5.5). The cations of the chains are inclined with respect to [010], their molecular planes being tilted in two different directions while forming angles with the  $b$ -axis of about + 40° and - 40°, respectively, but being twisted relative to each other. The cations are connected by dicyanamide ions which are arranged in a screw-wise manner along

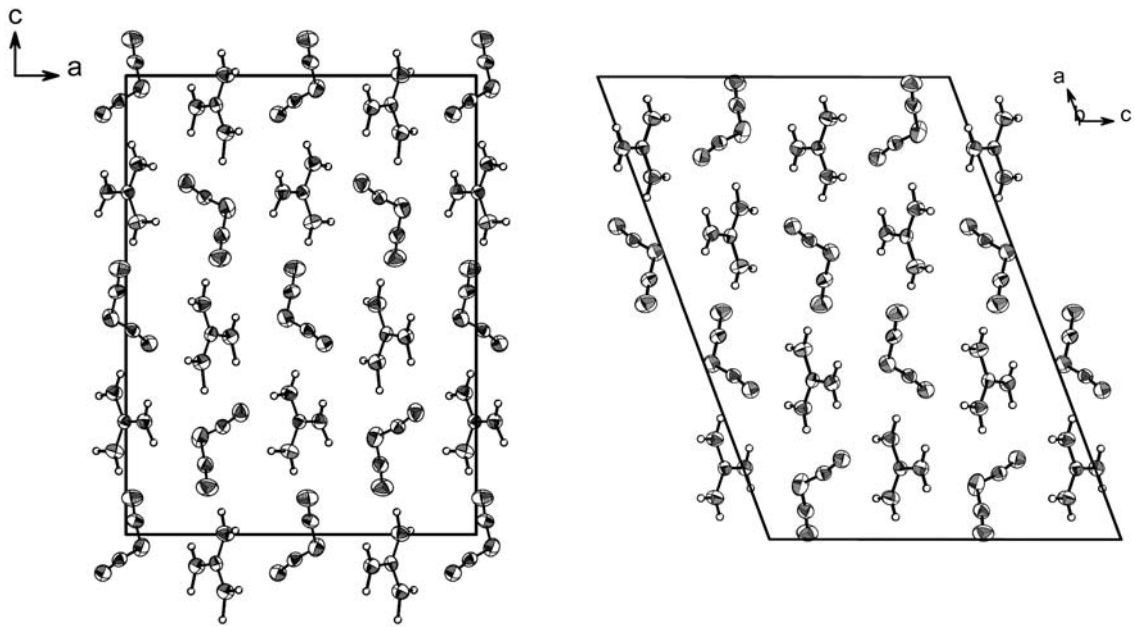


**Figure 5.5:** Left: Crystal structure of  $\beta$ -[C(NH<sub>2</sub>)<sub>3</sub>][N(CN)<sub>2</sub>], view along [010]. Right: Crystal structure of  $\alpha$ -[C(NH<sub>2</sub>)<sub>3</sub>][N(CN)<sub>2</sub>], view along [010]. Thermal displacement ellipsoids (except for H) are drawn at the 50 % probability level.

[001] and twisted around their (idealized)  $C_{2v}$  axes along [100] (Fig. 5.6).

The crystal structure of  $\alpha$ -[C(NH<sub>2</sub>)<sub>3</sub>][N(CN)<sub>2</sub>] can be described in an analogous way as that of  $\beta$ -[C(NH<sub>2</sub>)<sub>3</sub>][N(CN)<sub>2</sub>]. The polymorph crystallizes in the monoclinic space group  $P2_1/c$  (no.

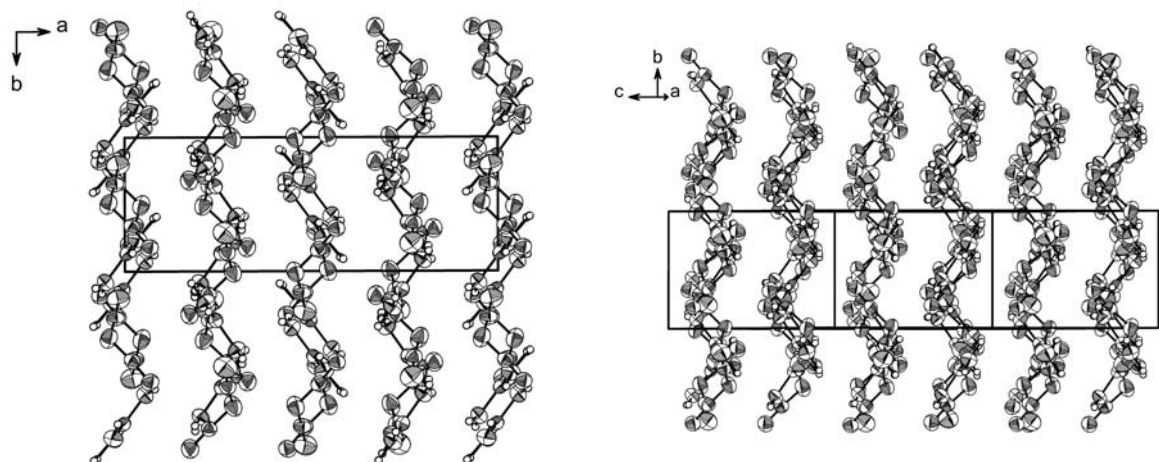


**Figure 5.6:** Left: Crystal structure of  $\beta$ -[C(NH<sub>2</sub>)<sub>3</sub>][N(CN)<sub>2</sub>], view along [001]. Right: Crystal structure of  $\alpha$ -[C(NH<sub>2</sub>)<sub>3</sub>][N(CN)<sub>2</sub>], view along [201]. Thermal displacement ellipsoids (except for H) are drawn at the 50 % probability level.

14) with lattice parameters differing only slightly from those of its orthorhombic counterpart  $\beta$ -[C(NH<sub>2</sub>)<sub>3</sub>][N(CN)<sub>2</sub>] (cf. Table 5.1).

**Table 5.2:** Selected bond lengths (in pm) and angles (in °) for  $\beta$ -[C(NH<sub>2</sub>)<sub>3</sub>][N(CN)<sub>2</sub>] (left) and  $\alpha$ -[C(NH<sub>2</sub>)<sub>3</sub>][N(CN)<sub>2</sub>] (right).

$\beta$ -[C(NH <sub>2</sub> ) <sub>3</sub> ][N(CN) <sub>2</sub> ]	$\alpha$ -[C(NH <sub>2</sub> ) <sub>3</sub> ][N(CN) <sub>2</sub> ]
C1–N1	131.9(5)
C1–N3	132.3(3)
C1–N2	133.7(5)
C2–N4	133.1(5)
C2–N5	130.3(5)
C2–N6	133.2(3)
C3–N7	115.7(4)
C3–N8	129.0(4)
C4–N9	113.1(5)
C4–N8	132.4(4)
C5–N10	114.9(4)
C5–N11	129.5(4)
C6–N12	115.3(4)
C6–N116	129.8(4)
N1–C1–N3	120.8(3)
N1–C1–N2	119.6(3)
N2–C1–N3	119.6(3)
N5–C2–N4	120.7(3)
N5–C2–N6	119.1(3)
N4–C2–N6	120.1(3)
N7–C3–N8	169.8(3)
N9–C4–N8	174.0(4)
C3–N8–C4	121.3(3)
N10–C5–N11	172.4(3)
N12–C6–N11	174.4(4)
C5–N11–C6	123.0(2)
N1–C1–N3	120.5(2)
N1–C1–N2	119.7(2)
N2–C1–N3	119.8(2)
N5–C2–N4	119.7(2)
N5–C2–N6	119.6(2)
N4–C2–N6	120.7(2)
N7–C3–N8	170.4(2)
N9–C4–N8	173.6(2)
C3–N8–C4	122.4(2)
N10–C5–N11	171.7(2)
N12–C6–N11	174.3(2)
C5–N11–C6	121.7(2)

The molecular ions are stacked alternately along [201] and assembled in an analogous manner as in the orthorhombic  $\beta$ -form (Figs. 5.5 and 5.6). The main differences between the two crystal structures, which show variations in the long range order of the molecules, may become apparent by comparing the spatial orientations of the ions along the equivalent directions [001] ( $\beta$ ) and [201] ( $\alpha$ ) (Fig. 5.6). While being tilted with respect to the *b*-axis to about the same extent (+ 40 and – 40°) and twisted relative to each other as in the  $\beta$ -form, the planes formed about parallel to (001) contain cations with tilt angles alternating in an A A B B A ... manner

along [201] in the  $\alpha$ -polymorph. In the orthorhombic form, the layers are made up alternately by cations with a uniform or with opposite tilt angles. In layers with opposite tilt angles the cations are arranged as A B A B ... along [001]. Thus, although being similar in terms of their principal arrangement, the relative orientation of the anions is different in the two modifications. This corresponds to the differing glide planes in the monoclinic as compared to the orthorhombic space group.

The first coordination spheres of the two crystallographically inequivalent guanidinium ions in  $\beta$ -[C(NH<sub>2</sub>)<sub>3</sub>][N(CN)<sub>2</sub>] and  $\alpha$ -[C(NH<sub>2</sub>)<sub>3</sub>][N(CN)<sub>2</sub>] are largely identical with respect to the arrangement of the anions. They are composed of eight dicyanamide ions each, which are grouped into pairs around the central cation with C ··· N contacts ranging from 325 to 448 pm in both polymorphs (Fig. 5.7). Thereof six (C2) or five (C1) of the closest anion-cation contacts, respectively, include terminal nitrogen atoms, whereas the remaining two or three C ··· N contacts, respectively, involve bridging amido-nitrogen atoms. The three-dimensional hydrogen-bonding network can be characterized in both modifications by the prevalence of medium strong hydrogen bridges [363] ((N–)H ··· N 194 – 260 pm ( $\beta$ ) and 204 – 270 pm ( $\alpha$ ); angles N–H ··· N 172 – 111° ( $\beta$ ) and 172 – 115° ( $\alpha$ )). In a similar way, the two crystallographically inequivalent dicyanamide anions in both polymorphs are surrounded by eight guanidinium ions each, the latter building up two sorts of layers by the spatial orientation

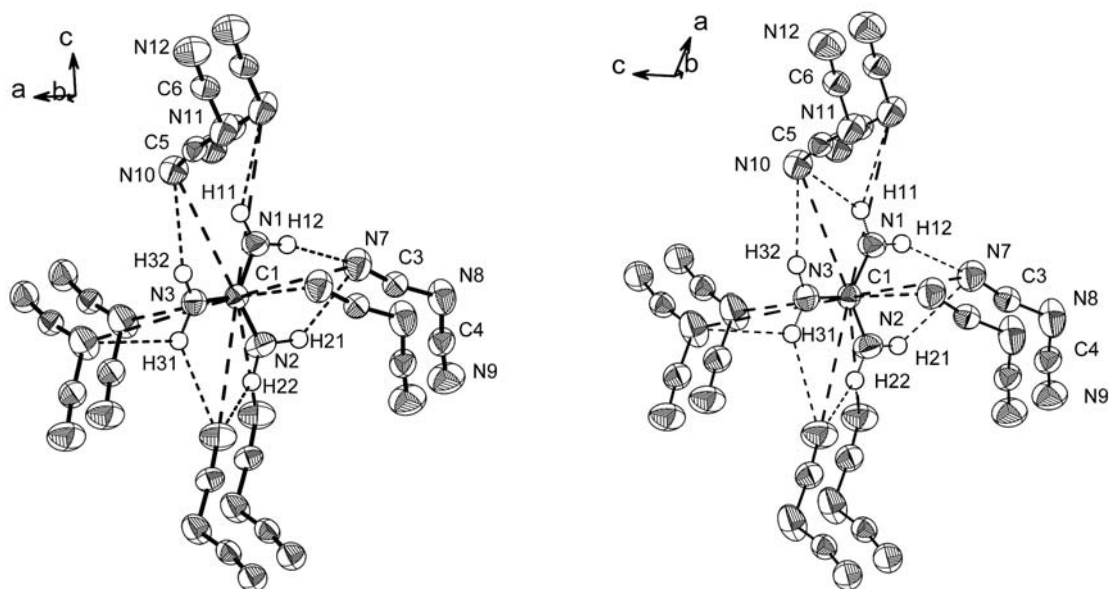


**Figure 5.7:** Left: Coordination sphere of the guanidinium cation I in  $\beta$ -[C(NH<sub>2</sub>)<sub>3</sub>][N(CN)<sub>2</sub>]. Right: Coordination sphere of the guanidinium cation I in  $\alpha$ -[C(NH<sub>2</sub>)<sub>3</sub>][N(CN)<sub>2</sub>]. The coordination sphere is indicated by dashed, hydrogen bonds by dotted lines. Thermal displacement ellipsoids (except for H) are drawn at the 50 % probability level.

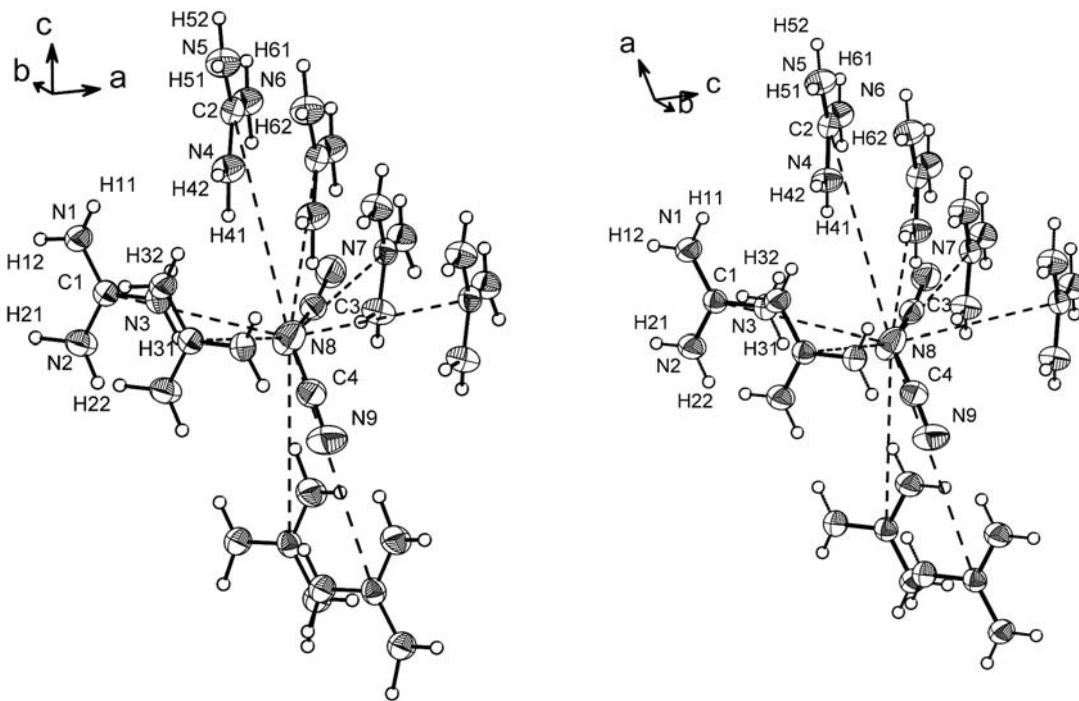


**Figure 5.8:** Left: Coordination sphere of the dicyanamide anion I in  $\beta$ - $[C(NH_2)_3][N(CN)_2]$ . Right: Coordination sphere of the dicyanamide anion I in  $\alpha$ - $[C(NH_2)_3][N(CN)_2]$ . The cations form two types of layers in a [4 + 4] manner. Thermal displacement ellipsoids (except for H) are drawn at the 50 % probability level.

of their molecular planes. These are aligned almost perpendicularly in a [4 + 4] and [6 + 2] manner, respectively (Fig. 5.8).

The angles ( $N-C\equiv N$ ) 170 – 174°, for  $\beta$  and  $\alpha$ ) and bond lengths (C–N 129 – 132 pm ( $\beta$ ) and 129 – 131 pm ( $\alpha$ ),  $C\equiv N$  113 – 116 pm ( $\beta$ ) and 114 – 116 pm ( $\alpha$ )) of the bent planar dicyanamide anions correspond to the localization of the electron density according to the formula  $[N\equiv C-N-C\equiv N]^-$ , which is in agreement with the bond lengths observed in other dicyanamides [125, 126, 287, 302, 332, 333]. The planar guanidinium ions exhibit three NCN bond angles which are very close to 120°, and all three C–N bond lengths of the guanidinium cations are essentially equal (Table 5.2). All three nitrogen atoms are associated with two protons each, corresponding to the complete delocalization of the double bond within the C–N backbones and thus, to only minor deviations from  $D_{3h}$  point symmetry.

Principally, the bond lengths and angles of the ions in the monoclinic form show less deviations from the idealized molecular geometries than in the orthorhombic modification, the significance of which should, however, not be overestimated in view of the lower data quality for the latter.

The observed X-ray powder data of both modifications could be reproduced and indexed

completely by the diffraction patterns calculated on the basis of the respective single-crystal data. Although the energy difference between the two polymorphs at room temperature was found to be extremely small (cf. section 5.2.4) and, hence, a facile reversible conversion of the two modifications may be expected in the first instance, leading to the coexistence of both phases, the powder patterns obtained were on the contrary almost exclusively single-phase.

### 5.2.3 Vibrational Spectroscopy

The vibrational spectra of both polymorphs of guanidinium dicyanamide are practically indistinguishable and resemble very much those of other ionic dicyanamides which are characterized by an intense triplet in the  $\nu(C\equiv N)$  region (Fig. 5.9) [302, 332, 333, 353]. Raman spectra were recorded *in situ* during the transformation of  $\beta$ - into  $\alpha$ -[C(NH<sub>2</sub>)<sub>3</sub>][N(CN)<sub>2</sub>], the differences of the educt and product spectra however being negligibly small. The bands observed in the IR and Raman spectra together with the respective assignments are listed in Table 5.3 [302, 333, 364–366]. A formal consideration of the theoretical number of vibrations expected for [C(NH<sub>2</sub>)<sub>3</sub>][N(CN)<sub>2</sub>] based on a factor group analysis, requires a total of 264 internal modes after subtraction of the librational and translational lattice modes [367]. However, in first approximation the internal modes of the molecular ions may be regarded as unaffected by the crystal field due to the weak interionic interactions.

Furthermore, the two inequivalent molecules building up the asymmetric unit may not lead to a systematic splitting of the bands if the molecular geometry of the molecules do not differ significantly, thereby reducing the relevant contributions to the internal modes to those from one molecular unit. In total,  $3N - 6$  internal modes per ion ( $N = 10$  and 5, respectively),

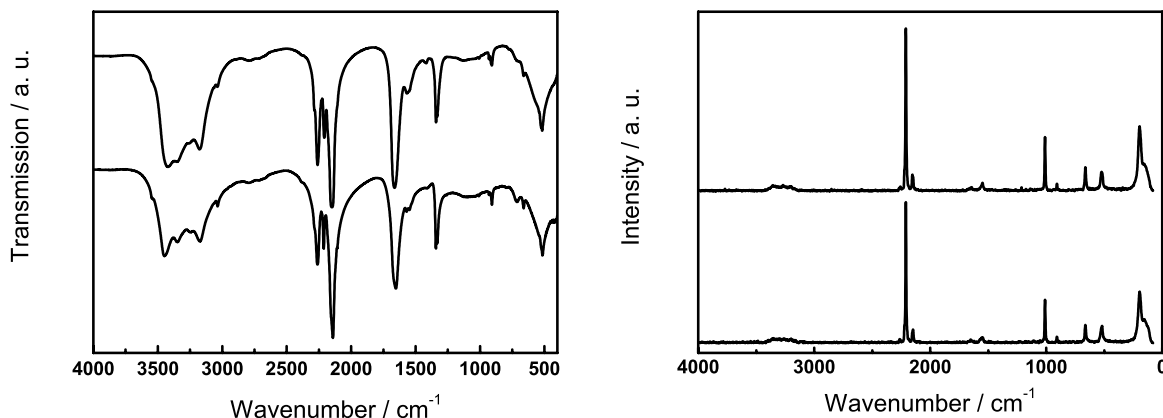


**Figure 5.9:** Left: IR spectra of  $\beta$ -[C(NH<sub>2</sub>)<sub>3</sub>][N(CN)<sub>2</sub>] (bottom) and  $\alpha$ -[C(NH<sub>2</sub>)<sub>3</sub>][N(CN)<sub>2</sub>] (top) recorded in a range from 4000 – 400  $cm^{-1}$  at room temperature. Right: Raman spectra of  $\beta$ -[C(NH<sub>2</sub>)<sub>3</sub>][N(CN)<sub>2</sub>] (bottom) and  $\alpha$ -[C(NH<sub>2</sub>)<sub>3</sub>][N(CN)<sub>2</sub>] (top) recorded between 4000 and 80  $cm^{-1}$  at room temperature.

**Table 5.3:** Vibrational frequencies (in  $cm^{-1}$ ) of  $\beta$ -[ $C(NH_2)_3$ ] $[N(CN)_2]$  (upper row) and  $\alpha$ -[ $C(NH_2)_3$ ] $[N(CN)_2]$  (lower row) as observed by FTIR and Raman spectroscopy at room temperature. The assignments are based on reference data ( $\nu$  = stretching,  $\delta$  = in-plane deformation,  $\gamma$  = out-of-plane deformation,  $\rho$  = rocking,  $\omega$  = wagging; *vs*: very strong, *s*: strong, *ms*: medium strong, *w*: weak, *vw*: very weak, *b*: broad, *sh*: sharp, *comb* = combination band/overtone).

$IR_{obs}$	$Raman_{obs}$	Assignment [302,333,364,365]
3449.8, 3348.4, 3245.9 ( <i>s, b</i> )	3349, 3199 ( <i>w, b</i> )	$\nu_{s/as}(NH_2)$
3421.3, 3347.0, 3175.3 ( <i>s, b</i> )	3356, 3268, 3200 ( <i>w, b</i> )	
3036.2, 2794.1		<i>comb</i>
3038.2, 2795.0 ( <i>w</i> )		
2261.5 ( <i>s</i> )	2262 ( <i>vw</i> )	$\nu_s(N-C)_{dca} + \nu_{as}(N-C)_{dca}$
2260.5 ( <i>s</i> )	2257 ( <i>vw</i> )	
2212.7 ( <i>ms</i> )	2210 ( <i>vs</i> )	$\nu_s(N\equiv C)_{dca}$
2208.9 ( <i>ms</i> )	2210 ( <i>vs</i> )	
2141.4 ( <i>ms</i> )	2148 ( <i>ms</i> )	$\nu_{as}(N\equiv C)_{dca}$
2148.7 ( <i>vs</i> )	2153 ( <i>ms</i> )	
1652.9 ( <i>vs</i> )	1650 ( <i>vw, b</i> )	$\nu_{as}(C-N)_{gua} + \delta(NH_2)$
1663.4 ( <i>vs</i> )	1650 ( <i>vw, b</i> )	
1570.0, 1547.1 ( <i>ms</i> )	1553 ( <i>w, b</i> )	$\delta(NH_2)$
1567.5, 1547.0 ( <i>ms</i> )	1549 ( <i>w, b</i> )	
1419.0 ( <i>vw</i> )		<i>comb</i>
1417.1 ( <i>vw</i> )		
1342.2, 1331.4 ( <i>s</i> )		$\nu_{as}(C-N)_{dca}$
1341.4, 1332.2 ( <i>s</i> )		
1110.0 ( <i>vw, b</i> )	1112 ( <i>vw</i> )	$\rho(NH_2)$
1122.8 ( <i>vw, b</i> )	1112 ( <i>vw</i> )	
1009.6 ( <i>vw</i> )	1010 ( <i>s</i> )	$\nu_s(C-N)_{gua}$
1007.6 ( <i>vw</i> )	1010 ( <i>s</i> )	
930.5, 907.7 ( <i>w, sh</i> )	907 ( <i>w</i> )	$\nu_s(C-N)_{dca}$
930.7, 908.3 ( <i>w, sh</i> )	908 ( <i>w</i> )	
714.0 ( <i>w, b</i> )		$\gamma(CN_3)_{gua} + \omega(NH_2)$
714.0 ( <i>w, b</i> )		
662.0 ( <i>w, sh</i> )	662 ( <i>ms</i> )	$\delta_s(C-N-C)_{dca}$
661.4 ( <i>w, sh</i> )	662 ( <i>ms</i> )	
545 – 525 ( <i>w, b</i> )		$\gamma_{s/as}(N-C\equiv N)_{dca}$
516.0 – 523.0 ( <i>s</i> )	518 ( <i>ms</i> )	$\delta(CN_3)_{gua} + \delta(NH_2)$
518.0 – 523.0 ( <i>s</i> )	523 ( <i>ms, b</i> )	$\delta_{as}(N-C\equiv N)_{dca}$
$\leq 500$ ( <i>w</i> )		$\gamma(NH_2)$
$\leq 500$ ( <i>w</i> )		

giving rise to  $24 + 9 = 33$  optical modes may be expected. The validity of this simplification is justified by the clarity of the vibrational spectra, where less than 33 bands are observed. A splitting of the bands due to the inequivalent sites of the molecules may be disguised

by a broadening of the absorptions which especially applies to the intense bands at 2149 and  $1663\text{ cm}^{-1}$  in the IR spectra of both polymorphs. The IR-bands at 1570 / 1568 ( $\beta$ - /  $\alpha$ -polymorph) and at  $1547\text{ cm}^{-1}$  (both polymorphs) are associated with the in-plane bending modes of  $\text{NH}_2$ , the strong absorption at  $1653 / 1663\text{ cm}^{-1}$  is attributed to a coupling of the asymmetric C–N stretching vibration with the in-plane  $\text{NH}_2$  bending of the guanidinium ion. These modes as well as the split bands assigned to the asymmetric and symmetric C–N stretching modes of the dicyanamide ions (Table 5.3) may be a manifestation of the slightly differing geometry of the two molecules in the asymmetric unit (it should be noted, however, that the absence of the mode at  $931\text{ cm}^{-1}$  in the Raman spectrum may invalidate the above assignment). The differences in the IR-spectra of the polymorphs mainly consist in slightly varying band intensities or asymmetries. Besides, minor band shifts are observed which, however, are not exactly reproducible in the Raman spectra. For instance, the high-frequency shift of the N–H stretch at  $3450\text{ cm}^{-1}$  for the  $\beta$ -form ( $\alpha$ :  $3421\text{ cm}^{-1}$ ) as well as the low-frequency shifts of  $\nu_{as}(\text{C}\equiv\text{N})$  ( $2141$  vs.  $2149\text{ cm}^{-1}$ ) and  $\nu_{as}(\text{C–N}) + \delta(\text{NH}_2)$  ( $1653$  vs.  $1663\text{ cm}^{-1}$ ) may tentatively be associated with the hydrogen bonding network and local geometric differences. The most evident shift associated with the band at  $3450\text{ cm}^{-1}$  might be traced back to the less dense hydrogen network in the  $\beta$ -form compared to the  $\alpha$ -form: Whereas in the latter, all H atoms participate in hydrogen bonding and three H are involved in a bifurcated hydrogen bond, in the former one hydrogen (H11) does not possess a nearest neighbor acceptor within a sphere of 283 pm and only two bifurcated hydrogen bonds are present. However, comparing the strengths of the existing hydrogen bridges in the two modifications, there is evidence for slightly stronger bonding in the  $\beta$ -form, which might be substantiated by the red-shift of the  $\nu_{as}(\text{C}\equiv\text{N})$  and the slight-blue shift of  $\delta(\text{NH}_2)$ .

### 5.2.4 Thermal Behavior

#### 5.2.4.1 *In situ* X-ray powder diffraction

Variable temperature X-ray powder diffraction measurements have been conducted between 293 and 410 K. When starting from  $\beta\text{-}[\text{C}(\text{NH}_2)_3][\text{N}(\text{CN})_2]$ , the transformation into  $\alpha\text{-}[\text{C}(\text{NH}_2)_3][\text{N}(\text{CN})_2]$  can clearly be distinguished at temperatures between 315 and 323 K. Subsequently, melting occurs at 329 K, being followed by a re-solidification around 387 K (Fig. 5.10, top). The solidification is accompanied by the emergence of a new phase which was identified as melamine by X-ray powder diffractometry. When heating  $\alpha\text{-}[\text{C}(\text{NH}_2)_3][\text{N}(\text{CN})_2]$  from room temperature, no phase transition is observed prior to the melting of the sample (Fig. 5.10, bottom). Comparing the melting points in both temperature runs, minor deviations in the melting onsets become apparent, while the principal temperature characteristics

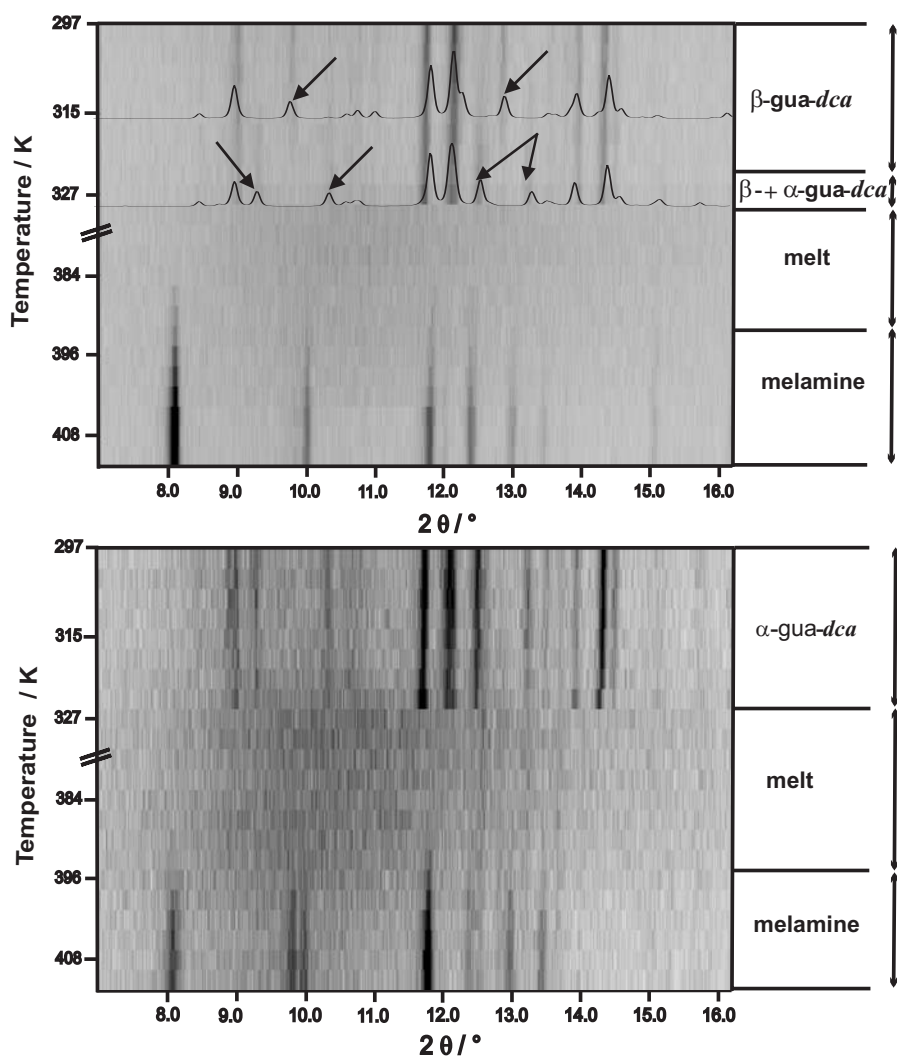


**Figure 5.10:** Variable temperature X-ray powder diffraction patterns of  $\beta$ -[C(NH<sub>2</sub>)<sub>3</sub>][N(CN)<sub>2</sub>] (top) and  $\alpha$ -[C(NH<sub>2</sub>)<sub>3</sub>][N(CN)<sub>2</sub>] (bottom) conducted in a temperature range between 297 and 410 K at intervals of 3 K. The measuring time for each diffractogram ( $2\theta = 7 - 16 {}^\circ$ ) was 20 minutes and the heating rate for each step 5 K min<sup>-1</sup>. The  $\beta \rightarrow \alpha$  phase transition is indicated by arrows.

and transformation products are identical for both measurements. Whereas in the case of  $\alpha$ -[C(NH<sub>2</sub>)<sub>3</sub>][N(CN)<sub>2</sub>], melting already occurs between 325 and 326 K,  $\beta$ -[C(NH<sub>2</sub>)<sub>3</sub>][N(CN)<sub>2</sub>] does not melt until the transformation into  $\alpha$ -[C(NH<sub>2</sub>)<sub>3</sub>][N(CN)<sub>2</sub>] is complete (328 – 329 K), which effectively delays the melting process slightly.

#### 5.2.4.2 Differential scanning calorimetry

As a supplement to the temperature-dependent X-ray powder experiments, DSC measurements with samples of both modifications were carried out. The resulting curves (Fig. 5.11) exhibit two well distinguishable features between RT and 473 K and several weak thermal

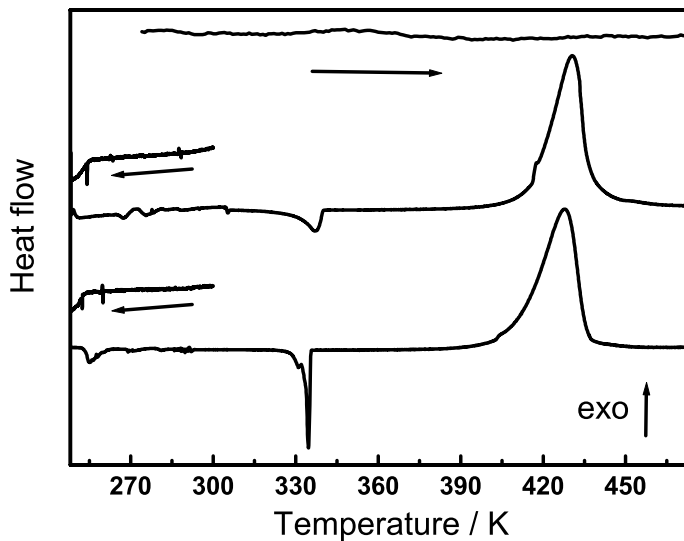


**Figure 5.11:** DSC heating curves and cooling curves of  $\beta$ -[C(NH<sub>2</sub>)<sub>3</sub>][N(CN)<sub>2</sub>] (bottom) and  $\alpha$ -[C(NH<sub>2</sub>)<sub>3</sub>][N(CN)<sub>2</sub>] (top) between 247 and 473 K, as well as a TG heating curve of the  $\alpha$ -phase, each recorded with a heating (cooling) rate of 0.5 K min<sup>-1</sup> (the DSC heating curves are normalized and the cooling curves are plotted enlarged). Due to the facile conversion of the  $\beta$ - into the  $\alpha$ -polymorph upon gentle heating, the cooling curves for the  $\beta$ -form were only recorded from 300 K downwards. The endothermic signal of the phase transition  $\beta \rightarrow \alpha$  prior to the melting onset is clearly distinguishable in the lower curve.

events in the range 247 K – 293 K. Using a heating ramp of 0.5 K min<sup>-1</sup>, a sharp endothermic melting signal peaking at 335 K (onset: 325 K) is observed for  $\beta$ -[C(NH<sub>2</sub>)<sub>3</sub>][N(CN)<sub>2</sub>], which exhibits a shoulder peak at 332 K prior to the melting signal. This feature, which is not observed when heating the  $\alpha$ -form, can be attributed to the phase transformation of  $\beta$ - into  $\alpha$ -[C(NH<sub>2</sub>)<sub>3</sub>][N(CN)<sub>2</sub>]. A strongly exothermic signal with a maximum at 427 K (onset: 388 K) can be attributed to the formation of melamine from the melt.

Similarly,  $\alpha$ -[C(NH<sub>2</sub>)<sub>3</sub>][N(CN)<sub>2</sub>] is melting at 338 K (onset: 318 K) and exhibits an exothermic signal at 431 K (onset: 395 K). Two more heat anomalies may be distinguishable at 255 K (endo,  $\alpha$ ) / 254 K (endo,  $\beta$ ) and at 293 K (exo,  $\beta$  / endo,  $\alpha$ ), where for the latter event the sign of energy flow is not clearly distinguishable due to the uneven baseline. The appearance of the cooling curves is strongly dependent on the thermal history of the sample, typically lacking reproducibility of the onset temperatures and appearance of the signals due to the extreme weakness of the thermal events (< 0.2 mW). Whereas for  $\beta$ -[C(NH<sub>2</sub>)<sub>3</sub>][N(CN)<sub>2</sub>], weak anomalies are observed at 260 K and 252 K (– 0.5 K min<sup>-1</sup>), for  $\alpha$ -[C(NH<sub>2</sub>)<sub>3</sub>][N(CN)<sub>2</sub>] three signals (288 – 285, 262 and 255 K; – 0.5 K min<sup>-1</sup>) are present, which in general are not classifiable unambiguously with respect to the sign of energy flow (Fig. 5.11). Correlation

with the signals obtained from the heating curves is complicated by the variable onsets and large hystereses and was therefore not attempted.

Complementing these measurements with low-temperature X-ray diffraction at various temperatures between 268 and 200 K reveals that the low-temperature events detected by thermal analyses do not correspond to major structural rearrangements (such as the transformation  $\alpha \rightarrow \beta$ ), since no significant changes in the powder patterns of both phases are observed. The heat anomalies below the melting signal may therefore be attributable to phase transitions induced by a change of the reorientational state of the guanidinium ions. A feature typical of guanidinium salts is the onset of two-dimensional jumps in a three-fold potential around the molecular  $C_3$  axis at sufficiently high temperatures, which may be followed by diffusive rotational motion at higher temperatures. The associated thermal events are observed in a wide temperature range (103 – 493 K) [82, 368–370] largely depending on the anionic sublattice, and are interpreted not only in terms of changes in the rotational state of the cations (order-disorder transitions) but also in the activation energies [369]. If these phase transitions were only associated with an entropy (and no enthalpy) change as observed for glass transitions, an increase of the heat capacity and, thus, a step in the DSC curve would result, which is not observed for the thermal anomalies at low-temperatures for both modifications. As suggested in the literature [368, 369], they may therefore be associated with a first-order phase transition whose heat tonality is composed of both enthalpic and entropic contributions, or with a continuous second-order phase-transition with only minor structural rearrangements. To shed light on this issue, spectroscopic approaches such as  $^2H$  solid-state NMR measurements will be necessary. The  $\alpha \rightarrow \beta$  conversion was not observed to proceed within the measuring interval of typically 2 – 14 h within the investigated temperature range.

Observations pertaining to the preparation procedures may provide additional information on the relative stability of the two modifications.  $\beta$ -[C(NH<sub>2</sub>)<sub>3</sub>][N(CN)<sub>2</sub>] was only obtained from aqueous solutions that were concentrated under vacuum. Upon storing this polymorph under humid air it deliquesced and subsequently recrystallized as  $\alpha$ -phase. Moreover, samples originally crystallized as  $\beta$ -[C(NH<sub>2</sub>)<sub>3</sub>][N(CN)<sub>2</sub>] that were stored under atmospheric conditions (regular air humidity) transformed into the  $\alpha$ -modification within weeks at room temperature.

The following conclusions may therefore be drawn:

$\beta$ -[C(NH<sub>2</sub>)<sub>3</sub>][N(CN)<sub>2</sub>] is transformed into  $\alpha$ -[C(NH<sub>2</sub>)<sub>3</sub>][N(CN)<sub>2</sub>] under atmospheric conditions within weeks and with increased rates upon heating above room temperature. The transformation proceeds endothermically, which may indicate the thermodynamic stability of the  $\beta$ -form at room temperature, while the reverse transformation  $\alpha \rightarrow \beta$  cannot be effected and, therefore, seems to be kinetically hindered in the temperature range accessible to diffraction

experiments. However, since the presence of moisture and / or pressure seems to play a vital role for the conversion of  $\beta$ - into  $\alpha$ -[C(NH<sub>2</sub>)<sub>3</sub>][N(CN)<sub>2</sub>] and seems to promote the transformation even at room temperature, the formation of  $\beta$ -[C(NH<sub>2</sub>)<sub>3</sub>][N(CN)<sub>2</sub>] may require special crystallization conditions.  $\alpha$ -[C(NH<sub>2</sub>)<sub>3</sub>][N(CN)<sub>2</sub>] is stable at temperatures at  $\geq 303$  K and, while being metastable, may be super-cooled down to temperatures as low as  $\leq 200$  K.

### 5.2.4.3 Mechanistic considerations

Regarding the transformation of guanidinium dicyanamide into melamine from the melt reveals an interesting analogy to the thermal behavior of ammonium dicyanamide. The latter dicyanamide transforms into dicyandiamide according to a solid-state transformation which was discussed in detail above (cf. section 4.1). In case this mechanism is transferable to other solid-state systems, its application to guanidinium dicyanamide results exactly in the observed reactivity (Fig. 5.12).

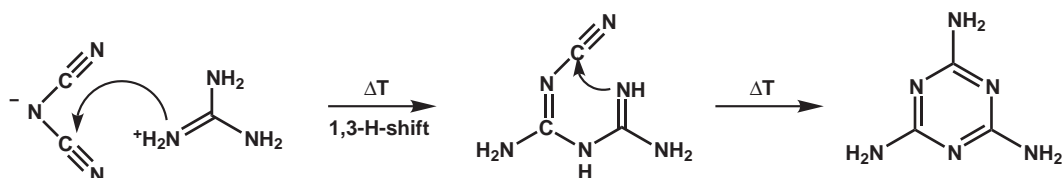


**Figure 5.12:** Mechanism of the transformation of guanidinium dicyanamide into melamine drawn by analogy with the solid-phase reaction of ammonium dicyanamide. *N*-guanyl-cyanoguanidine (cyano-biguanide) may be formed as an intermediate.

According to the sketched mechanism, the reaction may be initiated by a proton transfer from the cation to one of the basic centers (terminal N) of the anion, followed by the nucleophilic attack of a guanidinium nitrogen atom at an electrophilic nitrile carbon. As a result, the intermediate formation of *N*-guanyl-cyanoguanidine (cyano-biguanide) may occur. Different to ammonium dicyanamide, the possibility for an intramolecular nucleophilic addition at the remaining nitrile carbon is given, resulting in a ring closure with subsequent formation of melamine.

The observed thermal behavior of guanidinium dicyanamide may be further strong evidence for the validity of the mechanism proposed for the thermal reactivity of ammonium dicyanamide. It should however be noted that since the melamine formation proceeds *via* the melt, no identical “solid-state approach” to the reaction pathway is possible and the comparability of the two systems is thus limited. Nevertheless, one may assume the reaction mechanism to operate in an analogous manner as observed for ammonium dicyanamide, yet “solution-like” due to the significantly increased mobility of the molecular ions in the melt.

## 5.3 Melaminium Dicyanamide

### 5.3.1 Introduction

As seen in section 5.2, the intramolecular reaction of the components of guanidinium dicyanamide essentially yield melamine, a prototypic  $CN_x$  precursor. In order to provide an additional reactive “linkage” for further condensation to occur, melaminium dicyanamide monohydrate was synthesized, by means of which the feasibility of connecting melamine residues with the dicyanamide ions *via* guanyl-type linkers should be tested (Fig. 5.13). The unsaturated imine-type endgroups may then be prone to additional condensation reactions upon thermal treatment, leading to 1D or even highly cross-linked carbon(IV) nitride aggregates. Melaminium dicyanamide hydrate  $[C_3N_3H(NH_2)_3][N(CN)_2] \cdot H_2O$  was prepared by metathesis reaction in aqueous or methanolic solution (cf. section 10.1 on page 355). The compound crystallizes in the form of very thin, long needles, rendering the crystal quality insufficient, irrespective of the solvents used for recrystallization (MeOH, EtOH, DMSO). Therefore, only crystals with very poor  $I/\sigma$  and accordingly moderate R-values could be grown (cf. Table 5.4), the crystal structure solution of which is presented in brief in the following section.

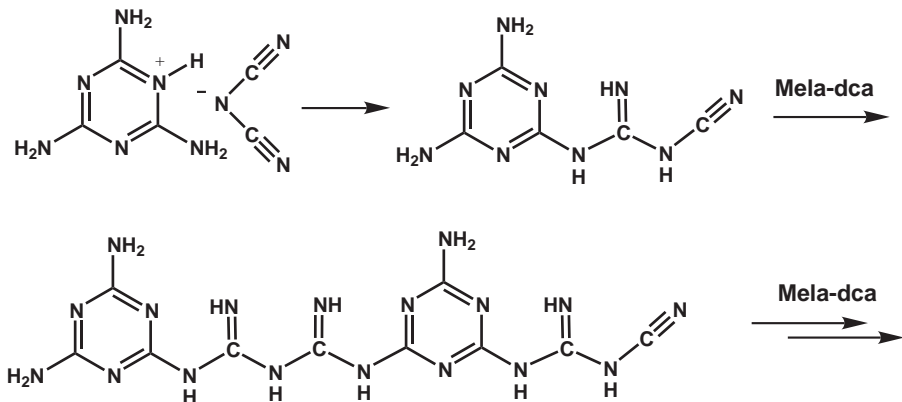


**Figure 5.13:** Cross-linking of the ions in melaminium dicyanamide hydrate to form covalently bonded, extended arrays. Only a possible linear 1D polymer is shown; other variants may also be formed.

### 5.3.2 Crystal Structure

Selected data of the crystal structure solution and refinement are summarized in Table 5.4. Although the data quality is only moderate owing to the weak scattering power of the single crystal, all hydrogen positions have been located from difference Fourier syntheses and refined isotropically without using restraints.

Melaminium dicyanamide crystallizes in the form of a mono-hydrate ( $P2_1/c$ ), which is made up by a mono-protonated melaminium cation and a dicyanamide anion. The protonated site

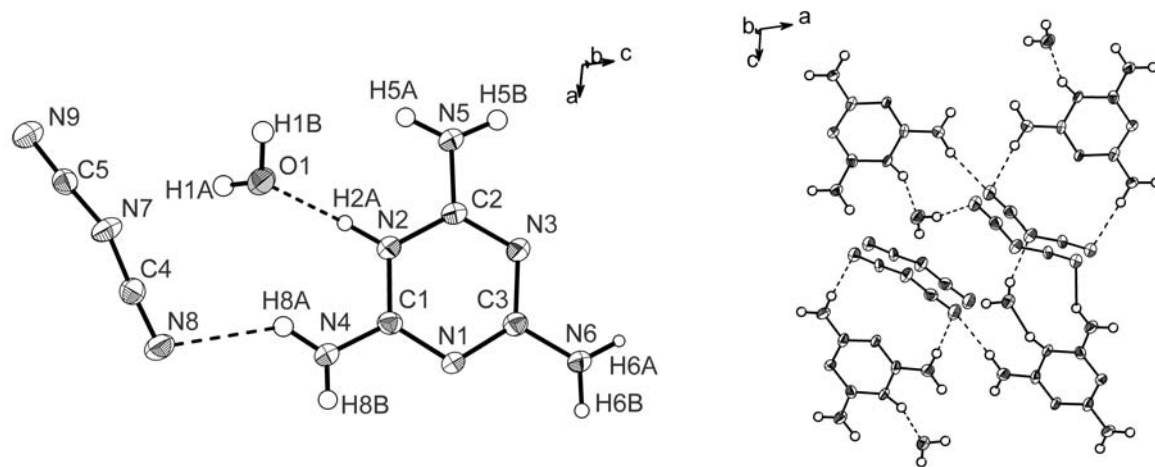


**Figure 5.14:** Asymmetric unit of melaminium dicyanamide hydrate (left) and hydrogen bonding network linking neighbored ions (right). Thermal displacement ellipsoids are drawn at the 50 % probability level.

at the planar melaminium core (N2) can be easily identified, as the crystal water (O1) is directly hydrogen-bonded *via* H2A (Fig. 5.14, left) to the donor nitrogen atom N2 with a short donor-acceptor distance of 267 pm. In addition, C–N bond lengths within the triazine ring are significantly alternating, being by more than 2 pm longer adjacent (C1–N2 / C2–N2: 136 – 137 pm) and opposite (C3–N1 / C3–N3: 135 – 136 pm) to the protonated nitrogen atom as compared to those in between (C1–N1 / C2–N3: 132 – 133 pm). This trend is

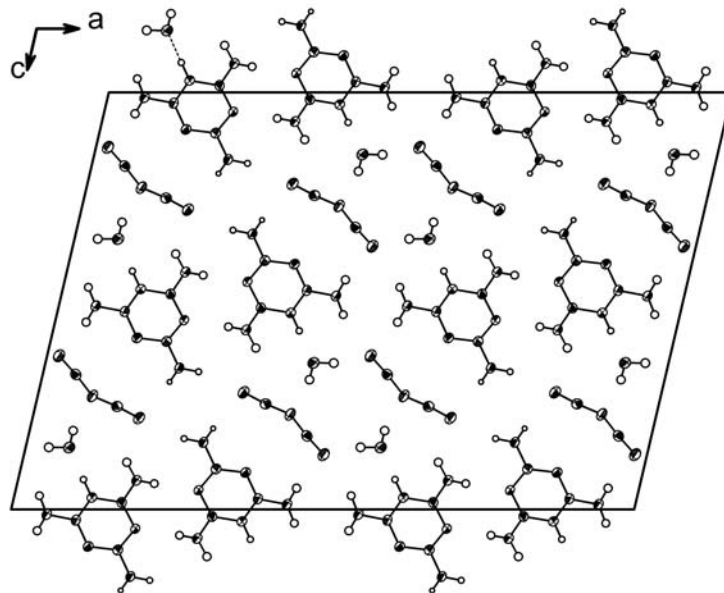


**Figure 5.15:** Unit cell of melaminium dicyanamide monohydrate, view along [010]. Thermal displacement ellipsoids (except for H) are drawn at the 50 % probability level.

observable also for other melaminium cations as well as protonated tricyanomelamine anions (cf. 5.6 on page 170) [127, 371–392]. Interestingly, the exogenous C–N bond lengths ( $C_{1/2/3}^- N_{4/5/6}$ ) exhibit pronounced double-bond character (131 – 133 pm), forcing the amide groups to planarize within the triazine ring plane.

**Table 5.4:** Crystallographic data for melaminium dicyanamide hydrate.

Formula	$[C_3N_6H_7][N(CN)_2] \cdot H_2O$
$M_w$ / g · mol <sup>−1</sup>	211.21
crystal system	monolinic
space group	$C2/c$ (no. 15)
$T$ / K	150
diffractometer	Nonius Kappa CCD
radiation ( $\lambda$ / pm)	Mo–K $\alpha$ (71.073)
monochromator	graphite
$a$ / pm	2735.5(6)
$b$ / pm	364.43(7)
$c$ / pm	1884.1(4)
$\beta$ / °	103.17(3)
$V$ / $10^6 \cdot pm^3$	1828.9(6)
$Z$	8
$\rho_{calcd}$ / g · cm <sup>−3</sup>	1.534
$F(000)$	880
$\mu$ / mm <sup>−1</sup>	0.119
crystal size / mm <sup>3</sup>	0.48 x 0.08 x 0.05
$I$ / $\sigma$	3.18
diffraction range	$4.17 \leq \theta \leq 24.98$
index range	$-32 \leq h \leq 32, -4 \leq k \leq 4,$ $-22 \leq l \leq 22$
total no. reflections	11736
independent reflections	1617 ( $R_{int} = 0.1449$ )
observed reflections	1037
refined parameters / restraints	with $F_o^2 \geq 2\sigma(F_o^2)$
extinction coefficient $\chi$	173 / 0
GooF on $F^2$	0.0034(6)
$R$ indices (all data)	1.038
	$R_1 = 0.0504$ (0.1004)
	$wR_2 = 0.0977$ (0.1165)
	with $w = [\sigma^2(F_o^2)$
	$+(0.0340P)^2 + 2.7576P]^{-1}$
	where $P = (F_o^2 + 2F_c^2)/3$
min./max. residual	
electron density /	– 0.226 / 0.234
$e \cdot 10^{-6} pm^{-3}$	

The C–N bond lengths of the dicyanamide anion clearly support the carbodiimide-type notation of the bent planar species with significant delocalization of electron density from the central nitrogen atom into the nitrile moieties (N7–C4/5: 131 pm; C4–N8 / C5–N9: 116 pm). The dicyanamide ion is hydrogen-bonded by medium strong hydrogen contacts to four surrounding melaminium cations (not all shown in Fig. 5.14, right) *via* the terminal nitrogen atoms N8 / N9 (N … N: 304 – 311 pm), and to two water molecules *via* the central and terminal nitrogen atoms N7 and N9 (N … O: 286 pm). The melaminium cations are arranged in chains along [100], exhibiting identical tilting angles with respect to [010], with pairs of adjacent cations being hydrogen-bonded (N1 … N4: 295 pm) and embedded in a “matrix” of anions and water molecules as outlined in Figure 5.15. The molecular planes of the triazine rings are stacked along [010] with distances corresponding to the lengths of the *b*-axis (360 pm).

### 5.3.3 Thermal Behavior

#### 5.3.3.1 Thermal analysis and *In situ* X-ray powder diffraction

The thermal behavior of melaminium dicyanamide hydrate was investigated by means of differential scanning calorimetry, thermogravimetry and temperature programmed XRD (TPXRD) in a temperature range between  $\approx$  300 and 750 K. From Figure 5.16 a very complex thermal behavior can be derived, which is characterized by a rapid succession of phase transitions associated with different degrees of mass loss. A similar scenario is disclosed by TPXRD, which, however, is not as sensitive with respect to thermal events with small heat of reaction (Fig. 5.17). It should be noted that on performing the DSC scans with different samples, varying curves are obtained, which though exhibiting the same approximate pattern show differences in the peak positions and exo- or endothermicity of the respective events. Thus, a strong dependence on the heating conditions (heating rate, pressure) may be inferred.

In the low-temperature range (300 – 450 K) a succession of two major and one minor endothermic event is observed in the DSC curve, which is approximately reproduced by the TPXRD measurement.

The phase transition commencing at 350 K, which is accompanied by a mass loss of about 7.0 % is most probably due to the loss of crystal water (theor. 8.5 %), upon which unsolvated melaminium dicyanamide is retained as evidenced by IR measurements at 423 K (“phase X”). The second and third endothermic signal may be associated with structural changes in the dehydrated phase, as minimal mass loss is observed by TG and the majority of reflections in the TPXRD measurements remains unaffected. The intense exothermic signal at 475 K is related to the formation of melamine, which is clearly visible by TPXRD. A very similar

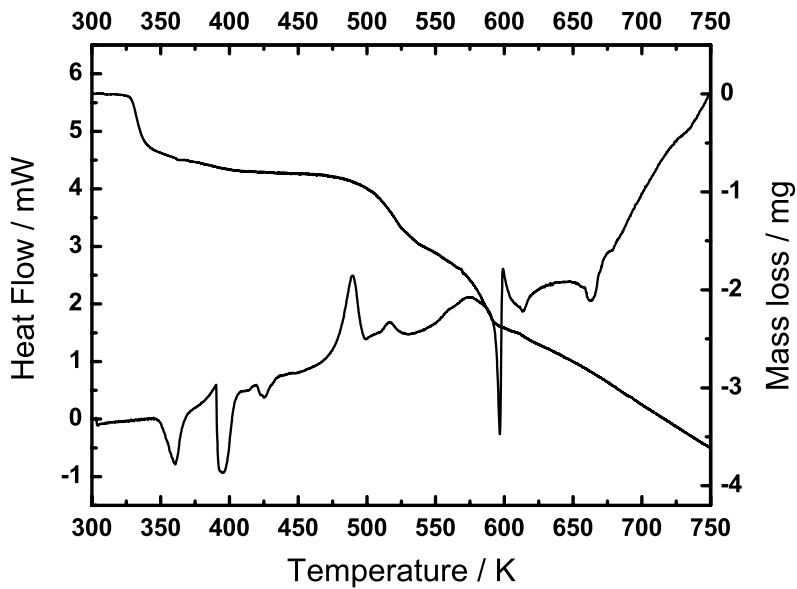


**Figure 5.16:** DSC and TG curves recorded for melaminium dicyanamide hydrate in a temperature range between RT and 750 K with a heating rate of  $1\text{ K min}^{-1}$ .

curve progression is observed for guanylurea dicyanamide, which transforms into melamine at even lower temperatures (cf. section 5.4.4.1 on page 160). The significant mass loss proceeding in two steps (5.7 % and 8.7 %, respectively) between 500 and 600 K may result from the sublimation of melamine as well as from the beginning decomposition of the latter upon polymerization, during which ammonia is evolved. In particular, the endothermic signal at 595 K may be associated with both sublimation of melamine and the onset of the formation of melem as well as adduct phases, which will be discussed in Chapter 6 on page 196. Owing to the poor signal-to-noise ratio of the powder patterns, the latter events are not visible by TPXRD. However, a broad signal around  $12^\circ 2\theta$  can be observed from temperatures around 570 K onwards, which is typical of graphite-like  $CN_x$  phases of varying composition. In contrast to the decomposition of pure melamine, however, the corresponding onset temperatures for melaminium dicyanamide are significantly lower, presumably indicating an increased reactivity of this  $CN_x$  precursor.

In general, the expected cross-linking by intramolecular condensation reactions is not observed by thermal analysis nor by X-ray diffraction, yet melamine is formed as the only crystalline phase by a simple acid-base reaction. However, the formation of  $CN_x$  networks may not be completely excluded, as they may form to a small extent as amorphous side-phases, which are not detectable by X-ray powder diffraction.

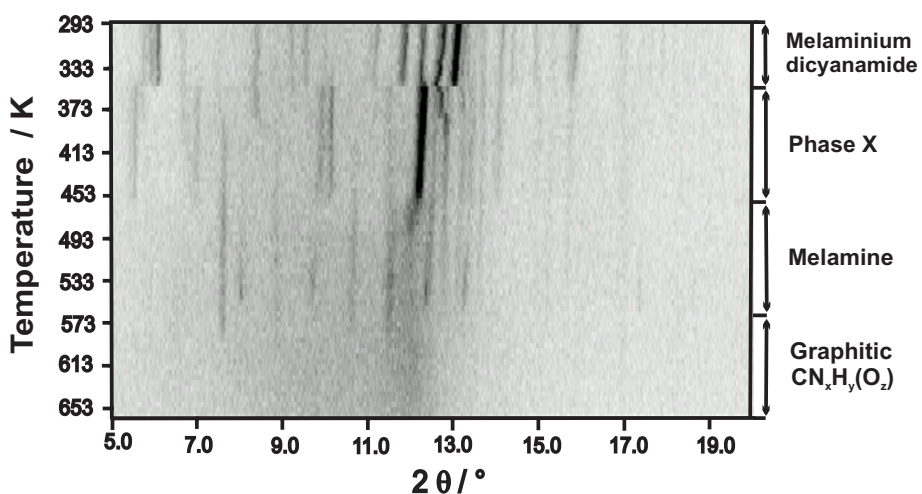


**Figure 5.17:** Variable temperature X-ray powder diffraction patterns of melaminium dicyanamide hydrate conducted in a temperature range between 293 and 663 K at intervals of 5 K. The measuring time for each diffractogram (5–20°  $2\theta$ ) was 26 minutes and the heating rate between the steps 50 K  $min^{-1}$ .

#### 5.3.4 Temperature-Dependent FTIR Spectroscopy

In order to independently identify the products of the thermal transformations of melaminium dicyanamide hydrate, *ex situ* IR measurements were carried out on samples heated in closed aluminium crucibles as used for the DSC measurements, which were placed in glass tubes under pressure equalization. Owing to the different temperature characteristics and heat transfer of the different heating procedures, direct comparison of the absolute temperature values is critical.

The room temperature spectrum of melaminium dicyanamide hydrate is characterized by a ring-sextant out-of-plane bending vibration at  $780\text{ cm}^{-1}$ , which is characteristically red-shifted for protonated triazine (and heptazine) rings as compared to the non-protonated rings [293, 383, 384, 393, 394]. Furthermore, the typical dicyanamide vibrations (cf. section 5.2 on page 135) and those of the melaminium core [240, 383–385] are evident. The medium intense and strong bands at  $1708$  and  $1660\text{ cm}^{-1}$ , which are assigned to the  $\text{NH}_2$  bending and ring  $\text{C}=\text{N}$  stretching vibrations [383, 384], gradually shift towards lower wavenumbers upon heating, whereas the band at  $1500\text{ cm}^{-1}$  vanishes, giving rise to two new bands at higher (centered at  $1553\text{ cm}^{-1}$ ) and lower (centered at  $1450\text{ cm}^{-1}$ ) wavenumbers, respectively. At the same time, the sextant-bend is blue-shifted by  $\approx 30\text{ cm}^{-1}$ , indicating the deprotonation of the triazine ring. The intensity of the characteristic dicyanamide triplet between  $2166$  and  $2286\text{ cm}^{-1}$  continuously decreases, as does the intense band at  $3391\text{ cm}^{-1}$ . The latter is additionally red-shifted on heating by about  $30\text{ cm}^{-1}$ .

Taken these findings together, the following picture of the thermal behavior of the dicyanamide

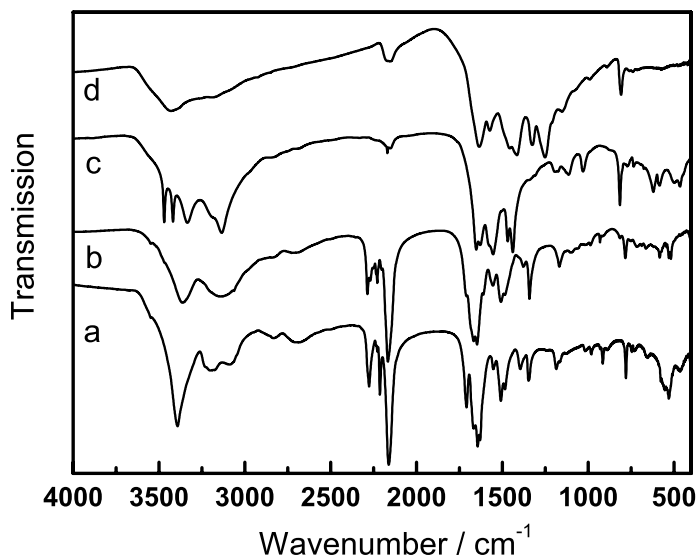


**Figure 5.18:** IR spectra of melaminium dicyanamide (a) recorded after temperature treatment at increasing temperatures: (b) 423 K, (c) 533 K, (d) 773 K.

salt can be outlined: At 423 K, the principal arrangement still seems largely unaffected apart from the loss of crystal water ((b) in Fig. 5.18). The IR spectrum of (c) is essentially identical with that of melamine, visible in particular by the characteristic  $\nu(NH_2)$  doublet at 3470 / 3419  $cm^{-1}$ ; this is in agreement with the DSC and TPXRD measurements. The IR spectrum (d) for the sample decomposed at 773 K shows well-resolved bands in the C=N and also C–N stretching region between 1650 and 1250  $cm^{-1}$ . As will be discussed in Chapter 7 on page 280, this pattern is reminiscent of that of graphitic carbon nitride, apart from the low-intensity band at 2200  $cm^{-1}$ , which is presumably due to non-consumed melaminium dicyanamide. Therefore, the reflection at  $2\theta = 12^\circ$  seen in the TPXRD patterns above 570 K can be correlated with the formation of a graphitic  $CN_xH_y$  material made up from triazine or heptazine rings as indicated by the sharp band at 810  $cm^{-1}$  (for a more detailed discussion see Chapter 7 on page 280).

The thermal decomposition of melaminium dicyanamide hydrate was also probed by temperature-dependent gas phase vibrational spectroscopy by heating up the powdered sample in an evacuated IR cell to 743 K ( $1\text{ K min}^{-1}$ ) while scanning the range between 450 and 4000  $cm^{-1}$  at intervals of 5 – 10 K. Figure 5.19 clearly shows the evolution of HNCO at temperatures as low as 390 K, ceasing around 513 K. The subsequently observed traces of  $CO_2$  are presumably a consequence of the decomposition of HNCO in the presence of water according to  $HNCO(g) + H_2O(g) \longrightarrow CO_2(g) + NH_3(g)$ , the latter of which being the dominant gas

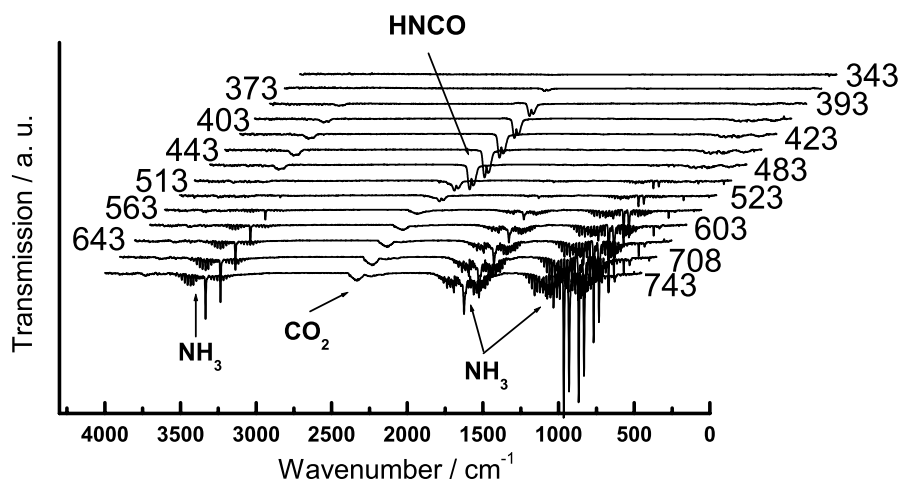


**Figure 5.19:** Temperature dependent FTIR gas spectra of melaminium dicyanamide collected between 343 and 743 K (back to front). The peak assignments are indicated by arrows; rotational side bands are visible for  $NH_3$ .

phase species at  $T \geq 560$  K.

The origin of HNCO remains critical in so far as it cannot be ruled out completely that HNCO is formed by reaction of water with traces of cyanamide, which may be formed as a reactive intermediate from depolymerization of melamine or decomposition of the free acid dicyanamide. The latter presumably forms together with melamine as an unstable product of the intramolecular proton transfer between the melaminium cation and the anion. Dicyanamide may then rapidly decompose by the action of crystal water present either in the gas phase or within the solid, forming HNCO and cyanamide.  $H_2NCN$  then trimerizes to melamine, thereby providing an alternative source for melamine in addition to the proton-transfer reaction (Fig. 5.20).

Melamine subsequently decomposes to melem, finally yielding condensed  $CN_xH_y$  polymers accompanied by the evolution of ammonia as can be seen at temperatures between 500 and 743 K. The latter transformations proceed in close agreement with the processes observed for pure melamine, which together with its condensation products presumably is the only solid product of the decomposition of melaminium dicyanamide hydrate.

### 5.3.5 Discussion

The comparability of the DSC, TPXRD and *ex situ* IR measurements with the TIR experiment may be limited in so far as the gas phase in the IR measurement represents a closed system, from which water vapor may not escape, but react with the solid phase in an equilibrium reaction. Thus, whereas the reaction pathway in an open system may be initiated by the evaporation of crystal water, followed by the formation of melamine and polymerization of the

free acid dicyanamide,  $HNCO$  may be formed by the reaction of water with the (protonated) anion. This hypothesis is supported by the fact that the existence of a dehydrated phase of melaminium dicyanamide can be inferred from systematic IR measurements of the sample after treatment at different temperatures below  $\approx 773$  K in an open system. This observation could not be explained if the first phase transition around 350 K was associated with the reaction of crystal water with the dicyanamide anion, yielding isocyanic acid and melamine *via* cyanamide. The two alternative reaction pathways are sketched in Figure 5.20.

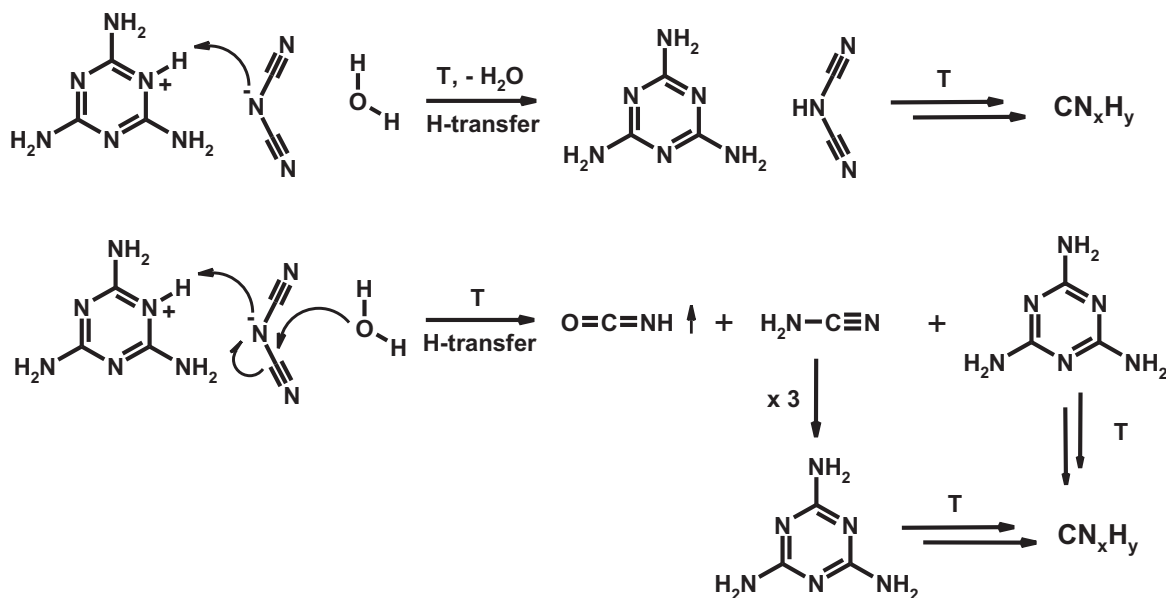


**Figure 5.20:** Two alternative reaction pathways for the thermal decomposition of melaminium dicyanamide hydrate in open (top) and closed systems (bottom). Whereas crystal water plays an important role for the latter, it is evaporated in open systems, leaving behind a pure  $CN_xH_y$  precursor.

The above results demonstrate that the initially proposed condensation pathway (Fig. 5.13) does not adequately represent the thermal behavior of melaminium dicyanamide hydrate. As observed for the previously investigated dicyanamides, an intramolecular proton transfer seems to initiate the thermal decomposition, yet no evidence is found for condensation of the as-formed neutral species melamine and dicyanamide to build up oligo- or polymeric  $CN_xH_y$  networks as put forward above. Instead, melamine is the only identifiable reaction product, whose thermal behavior accordingly dominates the decomposition of melaminium dicyanamide hydrate. Although the reactivity of the latter seems to be somewhat increased as compared to that of melamine, this dicyanamide represents yet another potential  $CN_x$  precursor whose functionality can be reduced to that of melamine.

## 5.4 Guanylurea Dicyanamide

### 5.4.1 Introduction

In order to extend the study of reactive molecular systems with potential thermal solid-state reactivity, another dicyanamide salt, guanylurea dicyanamide, was synthesized by ion-exchange reaction (cf. section 10.1 on page 355). Its solid-phase transformation was compared with previously observed reaction schemes of related systems as outlined in the previous sections 4.1 on page 71, 5.2 on page 135, and 5.3 on page 148. Though not being a pure  $\text{CN}_x\text{H}_y$  compound, the suitability of guanylurea dicyanamide as a precursor will be probed owing to the possibility of unexpected condensation pathways stimulated by the presence of oxygen in the starting material. The following study, which is based on ref. [124], is thus intended to investigate the temperature response of this model system and to place it in the broader context of the observed thermal solid-state reactivity of molecular – especially dicyanamide- and tricyanomelamine-based –  $\text{CN}_x$  precursors.

### 5.4.2 Crystal Structure

Guanylurea dicyanamide  $[(\text{H}_2\text{N})\text{C}(=\text{O})\text{NHC}(\text{NH}_2)_2][\text{N}(\text{CN})_2]$  crystallizes in the space group  $C2/c$  with eight formula units in the unit cell. Both anions and cations are loosely embedded in a hydrogen bonding network consisting of medium strong and weak hydrogen bonds with  $\text{H} \cdots \text{N}/\text{O}$  contacts between 207 and 250 pm. The first “coordination sphere” of the cations consists of three guanylurea and four dicyanamide ions, while the anions are surrounded solely by cations (Fig. 5.21, left).

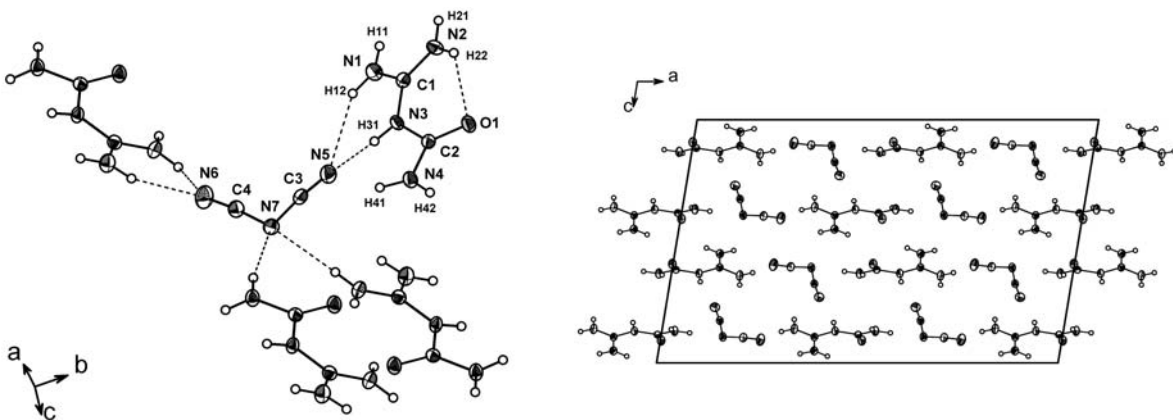


**Figure 5.21:** Left: Coordination sphere of the dicyanamide ion and hydrogen bonding to neighboring guanylurea cations (dotted lines). Right: Unit cell of guanylurea dicyanamide, view along [010] onto the chains composed of alternating ions running along [100]. The displacement ellipsoids are drawn at the 50 % probability level.

In the latter case, both bridging and terminal nitrogen atoms of the anion are involved in one medium strong and one weaker hydrogen bridge each. Details of the crystal structure determination and refinement for guanylurea dicyanamide are listed in Table 5.5.

*Table 5.5: Crystallographic data for guanylurea dicyanamide.*

Formula	$[H_2NC(=O)NHC(NH_2)NH_2][N(CN)_2]$
$M_w$ / g · mol <sup>-1</sup>	169.17
crystal system	monoclinic
space group	$C2/c$ (no. 15)
$T$ / K	130
diffractometer	STOE IPDS
radiation ( $\lambda$ / pm)	Mo–K $\alpha$ (71.073)
monochromator	graphite
$a$ / pm	2249.0(5)
$b$ / pm	483.9(1)
$c$ / pm	1382.4(3)
$\beta$ / °	99.49(3)
$V$ / $10^6$ · pm <sup>3</sup>	1483.8(5)
$Z$	8
$\rho_{calcd}$ / g · cm <sup>-3</sup>	1.514
$F(000)$	704
$\mu$ / mm <sup>-1</sup>	0.119
crystal size / mm <sup>3</sup>	0.20 x 0.16 x 0.10
diffraction range	$2.99 \leq \theta \leq 30.50$
index range	$-32 \leq h \leq 32, -6 \leq k \leq 6,$ $-19 \leq l \leq 19$
total no. reflections	8419
independent reflections	2170 ( $R_{int} = 0.0581$ )
observed reflections	1496
refined parameters	with $F_o^2 \geq 2\sigma(F_o^2)$
GooF on $F^2$	137
$R$ indices (all data)	0.910
	$R_1 = 0.0352$ (0.0617)
	$wR_2 = 0.0758$ (0.0826)
	with $w = [\sigma^2(F_o^2)$
	$+(0.0453P)^2 + 0.0000P]^{-1}$
	where $P = (F_o^2 + 2F_c^2)/3$
min./max. residual	– 0.201 / 0.202
electron density / $e \cdot 10^{-6}$ pm <sup>-3</sup>	

The deviation of the molecular geometry of the protonated guanylurea species from planarity is more pronounced than in the other structurally characterized guanylurea salts [395–397]. The guanyl-fragment is twisted about 11° relative to the plane of the urea portion, which

may be due to packing effects in the solid state. Despite the non-planar arrangement, an intramolecular chelate-like hydrogen bond  $O1 \cdots H22-N2$  is formed. The C–N distances of the guanidinium fragment are similar ( $N2-C1$ : 131.4 and  $N1-C1$ : 132.4 pm), indicating significant delocalization of the double bond over the involved guanyl-backbone. The distances found for the urea fragment ( $O1-C2$ : 122.7 pm,  $N4-C2$ : 133.4 pm) also suggest at least partial resonance within the N–C–O portion. The bond distances of the inner  $C1-N3-C2$  fragment are close to those observed for C–N single bonds (136.3 and 140.4 pm). The molecular ions are stacked alternately in chains along [100], forming hydrogen bonds both within a chain and to adjacent chains running parallel (Fig. 5.21, right), thus building up a loosely packed quasi two-dimensional network.

#### 5.4.3 Spectroscopic Characterization

Guanylurea dicyanamide can easily be identified by its  $^{13}C$  NMR spectrum, which in  $DMSO-d_6$  solution exhibits characteristic signals of  $sp^2$ -hybridized carbon at 155.2 and 156.1 ppm, as well as a weaker signal at 119.2 ppm, indicating the presence of a nitrile group. The  $^1H$  spectrum is less meaningful, since the three signals found at 7.1 (amide- $NH_2$ ), 8.1 (2  $NH_2$ , guanidine moiety) and 10.0 ppm (NH) are broadened owing to rapid exchange of the protons at room temperature. Mass spectra acquired in the FAB+ mode also give strong evidence for the salt like character of the title compound by indicating the presence of guanylurea cations

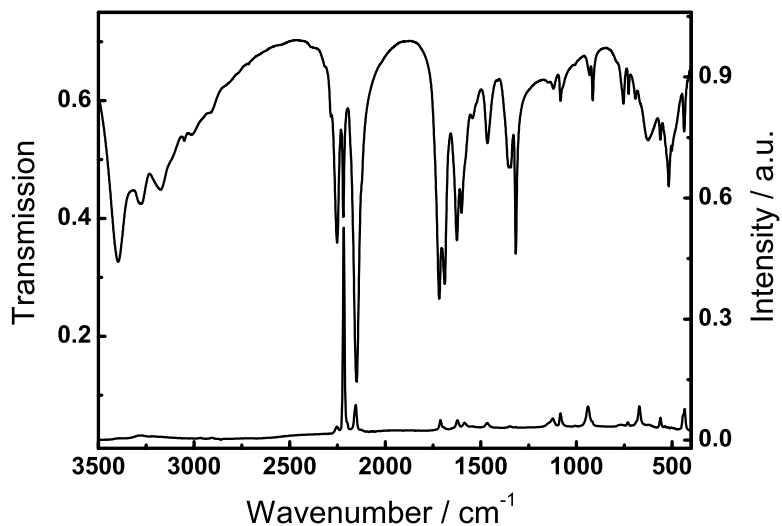


**Figure 5.22:** FTIR (top, left axis) and Raman spectrum (bottom, right axis) of guanylurea dicyanamide, recorded between 3500 and 400  $cm^{-1}$  at room temperature.

with  $m/z = 103$  (100 %).

The vibrational spectra of guanylurea dicyanamide are characterized by the typical dicyanamide triplet in the  $\nu_{s/as}(C\equiv N)$  region at 2252 (*m*), 2219 (*m*) and 2150  $\text{cm}^{-1}$  (*s*), which can rudimentarily be observed with reversed intensity distribution in the Raman spectrum at 2252 (*w*), 2217 (*s*) and 2154  $\text{cm}^{-1}$  (*m*) (Fig. 5.22). Strong absorption due to the cation is found in the C=N stretching and N–H bending region between 1450 and 1700  $\text{cm}^{-1}$ , as well as for the C=O oxygen giving rise to a sharp band at 1717  $\text{cm}^{-1}$ . Typical dicyanamide bands are located at 1317 ( $\nu_{as}(C-N)$ ), 914 ( $\nu_s(C-N)$ ), 518 ( $\gamma_{as}(N-C\equiv N)$ ) and 501  $\text{cm}^{-1}$  ( $\delta_{as}(N-C\equiv N)$ ) [332, 333].

#### 5.4.4 Thermal Behavior

##### 5.4.4.1 Thermal analysis

DSC measurements recorded with a heating rate of 1 K  $\text{min}^{-1}$  reveal a pronounced exothermic event around 390 K, which is preceded by an endothermic “spike” in the baseline (Fig. 5.23). At 430 K a broad, though less exothermic signal is observed, which is followed by an endothermic process around 610 K and another broad endothermic event with an onset around 635 K. A first hint at the nature of the processes observed is the resemblance of the high-temperature part of this DSC curve with that of melamine, which decomposes at 620 K and transforms

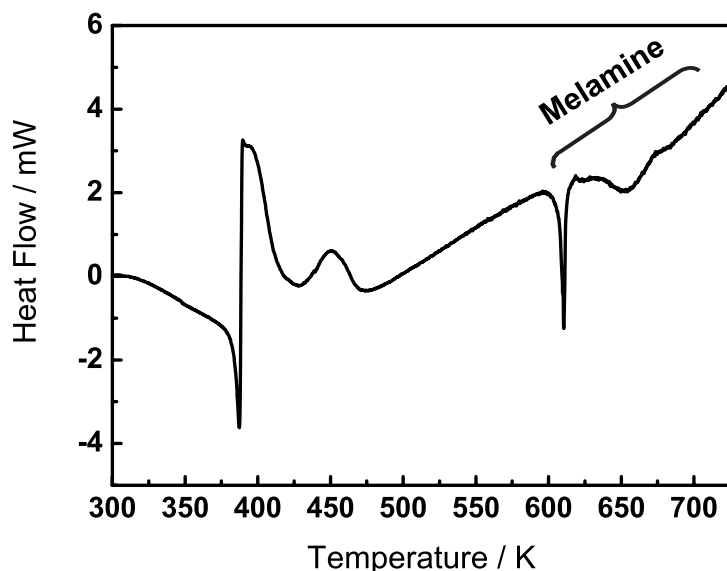


**Figure 5.23:** DSC heating curve of guanylurea dicyanamide recorded between 300 and 740 K with a heating rate of 1 K  $\text{min}^{-1}$ .

into melem around 660 K [82, 240]. Thus, the formation of melamine, presumably following a two-step process, may be considered further as working hypothesis.

#### 5.4.4.2 *In situ* X-ray powder diffraction

Temperature programmed X-ray powder patterns collected at intervals of 5 K show a clear break at 378 K, after which the sample temporarily passes through an essentially X-ray amorphous state (Fig. 5.24). Regarding however the single powder patterns collected between 378 and 405 K, a weak reflection at  $2\theta = 12.4^\circ$  can be observed, suggesting a small degree of long range order to be retained in this temperature range. Around 405 K, a crystalline phase emerges, which can easily be identified as melamine [240]. At 585 K, the reflections largely disappear, leaving a single broad peak around  $2\theta \approx 12^\circ$ , corresponding to  $d \approx 340$  pm; this may be assigned to an intermediate phase being discussed as a yet unidentified pre-stage of melem (cf. Chapter 6 on page 196). At 650 K, low intensity reflections of melem can be observed, which disappear around 760 K, yielding a graphitic  $CN_x$  material with an approximate d-spacing of 340 pm [42, 73, 83, 84, 300].

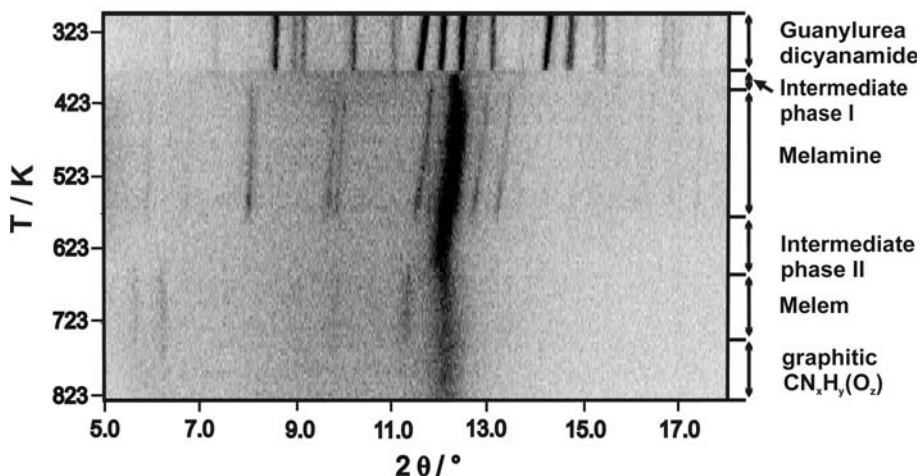


**Figure 5.24:** Variable temperature X-ray powder diffraction patterns of guanylurea dicyanamide recorded in a  $2\theta$  range from 5 to  $18^\circ$  between 303 and 823 K. Starting material, intermediate phases and products are indicated at the right margin.

The above observations clearly indicate that melamine is formed without passing through crystalline intermediates detectable by X-ray powder diffraction. Slight discrepancies of the respective onset temperatures found for the complementary analytical methods are a trivial consequence of the different heating and pressure conditions. The stepwise character of the transformation as observed in the DSC measurements is however not detectable by X-ray powder diffraction. Since the collection time for a single scan amounts to 20 minutes, events

that appear on a shorter time scale such as the formation of short lived intermediates may not be accessible by this technique. Furthermore, low crystallinity of the intermediate phases may further deteriorate their observability and differentiation.

#### 5.4.4.3 Temperature dependent mass spectrometry

In order to detect volatile species being potentially evolved during the observed transformation of the title compound, mass spectra were acquired while heating an evacuated sample of guanylurea dicyanamide in a furnace up to 493 K. Since no significant thermal event was expected up to about 353 K, a heating rate of  $2\text{ K min}^{-1}$  was applied until 348 K. Subsequently, the sample was heated with  $1\text{ K min}^{-1}$ . Until 365 K, a peak of relatively low intensity with  $m/z = 18$  is dominating the spectra, which can be attributed to water adsorbed on the sample and adhering to the inside wall of the spectrometer and glass tube. At 333 K, a peak at  $m/z = 43$  is appearing, which is rapidly growing and by 369 K dominates the spectra (Fig. 5.25).

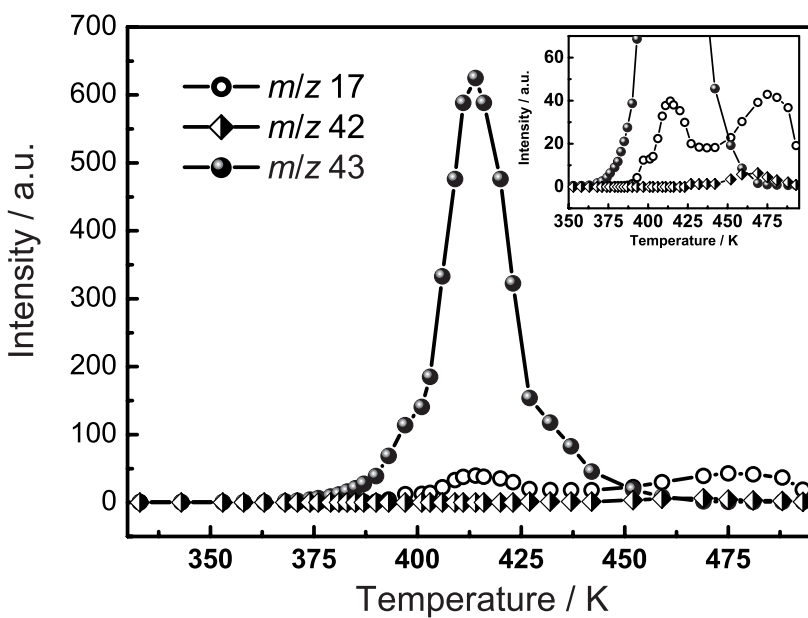


**Figure 5.25:**  $M/z$  curves for the most significant mass peaks obtained by thermal decomposition of guanylurea dicyanamide while conducting temperature-dependent DEI mass spectrometry between 313 and 493 K. Heating rates for  $T \leq 348\text{ K}$  and  $T > 348\text{ K}$  were  $2\text{ K min}^{-1}$  and  $1\text{ K min}^{-1}$ , respectively. The temperature range between 350 and 493 K is displayed enlarged in the inset.

In view of the potential decomposition pathways of the title compound as will be discussed in the following sections, this peak can be attributed to isocyanic acid HNCO. Ammonia ( $m/z = 17$ ) simultaneously appears, the associated intensity, however, being orders of magnitude smaller as compared to that of HNCO. The maximum intensity of the latter is reached around 411 K, and commences to drop continuously until 440 K. Here again, the peak at  $m/z = 17$ ,

together with a low intensity peak at  $m/z = 42$ , is steadily increasing as shown in the inset of Figure 5.25. The maximum of the peak at  $m/z = 42$ , which may indicate the presence of small amounts of cyanamide  $H_2N-C\equiv N$ , is shifted to lower temperatures with respect to the maximum intensity of  $m/z = 17$ , indicating two different underlying processes at least partly decoupled from each other. Beyond 450 K ammonia is the prevailing species in the system, while the peak at  $m/z = 43$  is hardly detectable up to 470 K. From a local maximum of the total intensity at 578 K on, the latter is continuously diminishing and no additional volatile compounds are observed.

#### 5.4.4.4 Temperature-dependent FTIR spectroscopy

The identity of the species evolved during the mass spectrometric experiments can best be probed by temperature-dependent gas-phase vibrational spectroscopy. To this end, an evacuated IR cell containing the powdered sample was heated to 740 K ( $1\text{ K min}^{-1}$ ) while scanning the range between 450 and  $4000\text{ cm}^{-1}$  at intervals of 5 – 10 K. For clarity, the spectra obtained are shown in Figure 5.26 in the reverse order (back to front).

Around 363 K, an asymmetric doublet in the nitrile region ( $2260\text{ cm}^{-1}$ ) is rapidly gaining intensity, which – together with the absorption at  $3550\text{ cm}^{-1}$  and between 680 and  $820\text{ cm}^{-1}$  – can be assigned to isocyanic acid HNCO [398]. After reaching its maximum intensity around 413 K, the bands have essentially disappeared by 453 K. As observed by mass spectrometry, strong absorption due to ammonia is emerging around 470 K and growing continuously up to

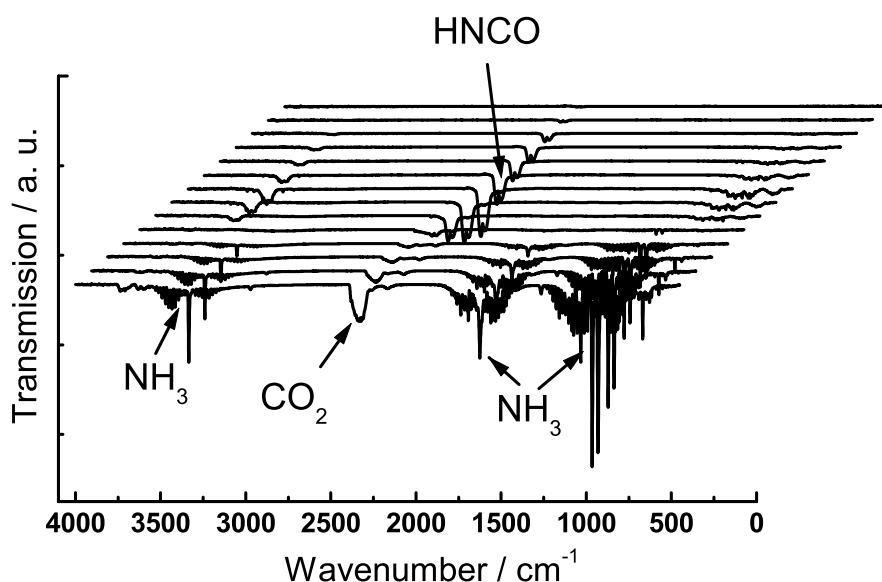


**Figure 5.26:** Temperature dependent FTIR gas spectra of guanylurea dicyanamide collected between 368 and 693 K (back to front). The peak assignments are indicated by arrows; rotational side bands are visible for  $NH_3$ .

the end of the measurements at 740 K. Strong  $NH_3$  bands together with their well resolved rotational side bands are found at 929, 964, 1625 and  $3333\text{ cm}^{-1}$ . At the same time a broad band located around  $2330\text{ cm}^{-1}$ , together with a weak band around  $2970\text{ cm}^{-1}$ , both being presumably due to  $CO_2$ , is increasing. The simultaneous presence of the latter may result from the ongoing decomposition of HNCO at elevated temperatures by trace amounts of water, yielding  $NH_3$  and  $CO_2$  [398]. However, at the end of the experiment a sublimation zone is visible, which has formed just outside the furnace. Besides melamine, a glassy substance together with small white crystals were recovered, which by IR spectroscopy and powder X-ray diffractometry were identified as urea containing small amounts of X-ray amorphous material. Absorption around  $2145\text{ cm}^{-1}$  in the IR spectrum can best be explained by traces of  $NH_4NCO$ , yet – owing to weak additional absorption at  $2255\text{ cm}^{-1}$  – the presence of small amounts of sublimed starting material or cyanamide cannot be excluded. Thus, according to the expectations the simultaneous presence of HNCO and  $NH_3$  in a closed glass tube leads to the formation of urea *via*  $NH_4NCO$ . There is no evidence for the formation of other decomposition products of HNCO such as biuret or cyanuric acid.

The differences in the relative intensity of the main species isocyanic acid and ammonia found for IR and mass spectrometry may be due to the intrinsic, non-quantitative sensitivity of IR spectroscopy for particular vibrations depending on symmetry considerations. In addition, the ongoing chemical decomposition of guanylurea dicyanamide is largely dependent on the pressure and temperature conditions, which are necessarily different for both analytical techniques. Thus, as will be discussed in the following, the condensation of melamine and, as a result, the amount of ammonia evaporated will be affected particularly strong by the respective reaction conditions.

#### 5.4.4.5 Discussion

As evidenced by the entirety of the temperature-programmed spectroscopy and diffraction experiments, the following conclusions concerning the thermal behavior of guanylurea dicyanamide may be drawn:

At temperatures around 373 K an exothermic transformation leads to the formation of melamine, the latter being detectable around 405 K by X-ray powder diffraction. Whether or not melting occurs prior to the decomposition reaction cannot be unambiguously resolved, yet visual inspection during sample decomposition in a sealed glass tube, as well as during the temperature-dependent spectroscopic experiments, strongly supports the solid-state character of the observed transformation process. However, the powder appears to be sintering while being heated, adopting a sort of porous outer appearance.

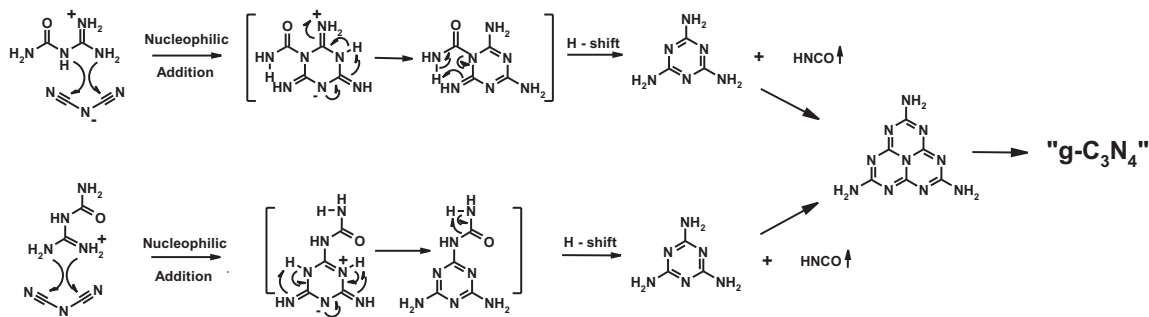


**Figure 5.27:** Tentative reaction pathways for the formation of melem from guanylurea dicyanamide. In the top mechanism a non-aromatic intermediate is passed through, whereas the bottom pathway yields the stable ureido-melamine as intermediate. After 1,3-H-shift and subsequent HNCO elimination melamine is formed as an intermediate product in both cases. Condensation yields graphitic  $CN_xH_y$  material via melem.

Whereas the DSC measurements indicate two essentially exothermic events to accompany the formation of melamine, this two-step character is neither visible by X-ray powder diffraction nor by the spectroscopic measurements.

In accordance with the results from temperature-dependent IR and mass spectrometry, the major thermal event around 390 K is most likely associated with the onset of HNCO formation, whereas the second exothermic signal may rather be due to the evaporation of ammonia or caused by structural changes owing to molecular reorientations or “recrystallization” of the sample from an intermediate amorphous stage. Possibly, the decomposition or polymerization of the evolved HNCO may also give rise to the observed broad signal.

Based on the above experimental evidence, the microscopic mechanism of the melamine formation may be sketched as follows:

Given the presence of nucleophilic and electrophilic sites carried by the molecular ions which are situated in close proximity within the crystalline structure, a cyclization reaction may proceed as depicted in Figure 5.27. Two alternative ring closure reactions are possible, which owing to the guanidinium-like delocalized system of the cation are assumed to be very similar in terms of activation energy; both finally yield melamine and HNCO in accordance with the above results. However, as may be seen from the proposed transition states, the top reaction pathway necessitates the passage of a non-aromatic intermediate, which is subsequently stabilized by facile elimination of HNCO via a 6-membered cyclic transition state similar to a [1,5]-sigmatropic rearrangement. The alternative pathway results in the formation of ureido-melamine ((4,6-diamino-1,3,5-triazine-2-yl)-urea), which is known to be stable up to temperatures above 500 K [399–402]. Given the transformation into melamine proceeds at  $T < 450$  K, the top pathway seems to be clearly more realistic.

In general, the cyclization reaction follows a pattern analogous to that observed for the thermal conversion of both ammonium dicyanamide into dicyandiamide and guanidinium dicyanamide into melamine. Both transformations proceed *via* addition of the nucleophilic component (cation) after an initial proton transfer to the electrophile (anion), followed by a 1,3-H-shift and – in the case of guanidinium dicyanamide and presumably in the present case as well – a second nucleophilic addition leading to a ring closure reaction and subsequent proton rearrangement. Cyclization taking place at the urea moiety of the cation would analogously yield ammeline (4,6-diamino-1,3,5-triazin-2(1H)-one,  $C_3N_5H_5O$ ) and cyanamide  $NCNH_2$ , the latter of which is known to undergo trimerization giving melamine at temperatures around 443 K [82, 240]. This pathway may occur to a small extent in a side reaction as indicated by the  $m/z = 42$  peak observed in the mass spectrometry experiments.

The evolution of ammonia at temperatures above 450 K can be correlated with the onset of melamine condensation, resulting directly or *via* the crystalline intermediate melem in the formation of amorphous  $CN_xH_y$  condensation products. In addition, hydrolysis of HNCO also contributes to the evolution of ammonia, the amount of which is dependent on the reaction conditions and the presence of traces of water. It is assumed that by conducting the reaction under vacuum, the equilibrium between melamine and its condensation products will be pushed to the latter side by enhancing the formation of volatile ammonia. Accordingly, the early onset of ammonia formation as detected by mass and IR spectroscopy and the production of relatively large amounts of amorphous  $CN_xH_y$  phases can be explained. The yellowish residue of the decomposition carried out in closed glass ampoules at 743 K mainly consists of melem together with an unidentified crystalline side phase as well as graphitic  $CN_xH_y$  material. Taking into account the elemental composition of melamine, which is isolated as a sublimate at the cold zone of the ampoule, and the oxygen content of the residue, which amounts to 5.6 wt.%, indicates the initial oxygen content of the starting material (theor. 9.5 wt.%) to be significantly reduced in the final product though working in a closed system.

Presumably, the generated HNCO partly decomposes irreversibly into  $CO_2$  and  $NH_3$  as described above. Thus, an “inert gas atmosphere” is produced which does not further affect or inhibit the formation of condensed  $CN_xH_y$  phases. According to the above results, the formation of melem is favored in closed systems under  $NH_3$  back pressure. In contrast, the evaporation of HNCO is supported when conducting the reaction under vacuum, which, however, stimulates the uncontrolled condensation of melamine to amorphous hydrogen containing carbon nitride materials. Thus, optimal conditions are given when working in “semi-closed” systems where pressure equalization is possible, as for instance in tightly filled glass capillaries used for XRD.

## 5.5 Tricyanomelamines

The chemistry of molecular carbon-nitrogen compounds is largely shaped by the reactivity of the functional groups and the types of reactions induced accordingly. Molecules containing unsaturated moieties are prone to oligo- and polymerization reactions, thereby providing the elementary building blocks for the design of heterocycles and polymeric materials. Carbon nitride chemistry offers a plentitude of thermal addition reactions, versatile representatives of which being oligomerization reactions of cyanogen derivatives and organic nitriles [403].

By analogy to the trimerization of acetylene to benzene, of formaldehyde to 1,3,5-trioxane, or the synthesis of 1,5,9-cyclododecatriene from 1,3-butadiene [403–405], simple cyanide derivatives of the general composition  $R-CN-R'$  ( $R, R' = H, \text{alkyl, aryl, halogen, O...}$ ) undergo heat induced or catalytic trimerization reactions according to Figure 5.28.

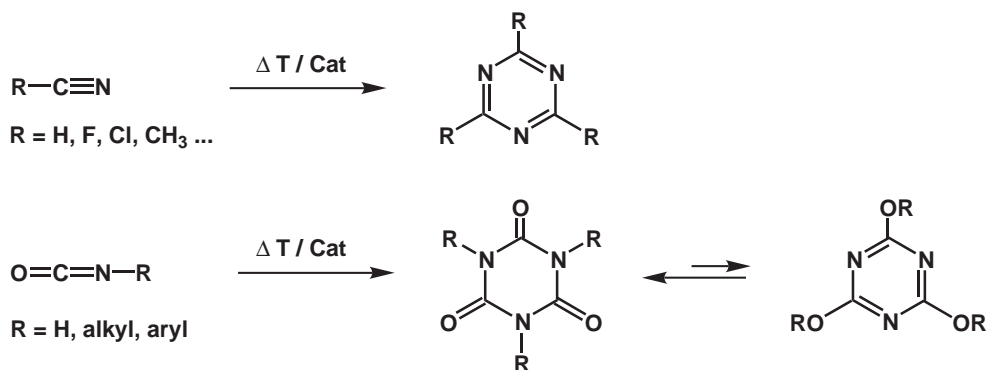


**Figure 5.28:** Top: Trimerization of cyanide derivatives forming symmetrical triazines; bottom: Trimerization of isocyanates, leading to cyanuric acid derivatives. Cyanuric acid adopts the keto-form (left) in the solid-state.

Dimerization or trimerization of nitriles, the latter leading to aromatic *s*-triazines, is effected under a variety of conditions [406, 407]. Hydrogen cyanide derivatives tend to polymerize to form dimers, trimers or polymers [406, 408]. In the presence of acid catalysts, cyanogen chloride trimerizes very easily to cyanuric chloride [409, 410]. While mixed trimerization of trichloroacetonitrile and acetonitriles in the presence of anhydrous hydrogen chloride results in the formation of 2,4-bistrichloromethyl-6-methyl-1,3,5-triazines, the reaction of hydrogen cyanide and cyanogen chloride yield 2,4-dichloro-1,3,5-triazine [411]. Traditionally, triazines as well as higher nitrile-oligomers are obtained by trimerization of the appropriate nitrile under pressure at elevated temperatures (570 – 620 K) [412–415]. However, Schaefer has demonstrated that trimerization and cotrimerization reactions of amidines  $RC(=NH)NH_2$  as well as imidates  $RC(=NH)OR'$  under acid catalysis and less vigorous conditions give comparable yields of *s*-triazines [416–419]. Recently, trimerization reactions of nitriles and alkynes have been optimized by use of transition-metal catalysts [420] or microwave techniques [421].

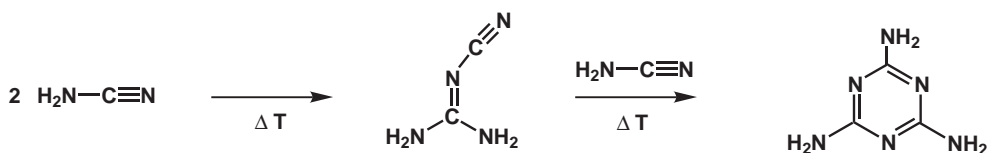


**Figure 5.29:** Formal trimerization of cyanamide into melamine. The oligomerization proceeds in a stepwise manner via dicyandiamide.

The important trimerization of cyanic acid  $HO CN$  and isocyanic acid  $HNCO$  to cyanuric acid is shown at the bottom part of Scheme 5.28. Besides the main product, varying amounts of N-oligomers of  $HNCO$ , such as cyamelide, are formed during the reaction [240].

Cyanamide is dimerized under alkaline conditions to dicyandiamide, formally yielding 1,3,5-triamino-*s*-triazine (melamine) in an overall trimerization reaction according to Scheme 5.29 [406, 422]:

Although 1,3,5-triamino-*s*-triazine can be formally considered a trimer of cyanamide, the transformation must be considered a two-step reaction *via* the stable dimer dicyandiamide, rather than a concerted one-step trimerization of cyanamide to melamine [240, 408, 423, 424]. Along these lines, similar oligomerization reactions of dicyanamides may be conjectured owing to their close relationship to other unsaturated *ammonocarbonic acids*. In fact, *Madelung* and *Kern* first observed the formation of a substance of formula “ $Na_3C_6N_9$ ” by heating sodium dicyanamide to dark redness, as well as by pyrolyzing a sodium salt of dicyandiamide (Scheme 5.30, Eq. 5.6) [425].

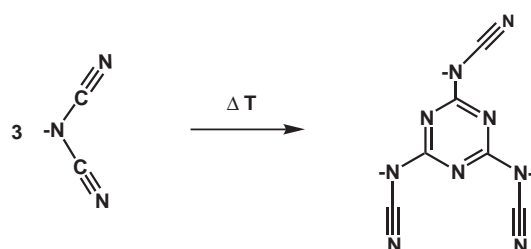


**Figure 5.30:** Trimerization of dicyanamide anions to the tricyanomelamine trianion.

*Franklin* prepared sodium tricyanomelamine by the action of fused sodium amide on melon ( $H_3C_2N_3$ )<sub>x</sub>, but interestingly also obtained the acids  $NaH_2C_6N_9$  and  $NaH_2C_6N_9 \cdot 2 H_2O$  in solution by adding glacial acetic acid or hydrochloric acid to a solution of  $Na[N(CN)_2]$  [80]. *Burdick* described a synthesis of sodium tricyanomelamine starting from dicyandiamide and sodium cyanamide (Eq. 5.7) [304].





No clear statements were available from the original work as to whether sodium dicyanamide passed the melt before transforming into sodium tricyanomelamine. Recently, this issue was resolved by *Jürgens*, who was able to classify this trimerization reaction as a non-topochemical solid-state reaction [125, 240].

In section 5.1 on page 130 the importance of the counter ions for the thermal reactivity of dicyanamides was delineated. The same line of argument is applicable for tricyanomelamines, which owing to their cyanamide moieties are potentially susceptible to a versatile thermal solid-state reactivity. In previous works, the alkali salts of the free acid tricyanomelamine  $M_3[C_6N_9]$  with  $M = Na - Rb$  have been prepared utilizing the trimerization reaction of the respective dicyanamide salts  $M[N(CN)_2]$  ( $M = Na - Rb$ ) [125, 126, 240]. In addition, the hydrated forms  $M_3[C_6N_9] \cdot H_2O$  ( $M = Na, K, Rb$ ) as well as the hydrogentricyanomelamines  $M[HC_6N_9] \cdot 3 H_2O$  ( $M = Co, Ni, Cu, Cd$ ),  $Co[H_2C_6N_9]_2(H_2O)_4 \cdot 6 H_2O$  and  $Rb[H_2C_6N_9] \cdot 0.5 H_2O$  were obtained by recrystallization of the parent tricyanomelamines from acidic aqueous solutions [302, 426–429]. Though being stable up to temperatures around 773 K (K, Rb) or 873 K (Na), no information on the identity as well as the metal content of the amorphous thermolysis products is available. Attempts to synthesize the free acid tricyanomelamine in crystalline form invariably failed owing to its inherent tendency towards polymerization [80, 240, 304, 425]. By introducing non-metal  $CN_xH_y$ -based counter ions, tricyanomelamines may represent triazine-based, thermally reactive model systems possessing potential relevance as carbon nitride precursors. In particular, the presence of moderately “acidic” complex cations provides a means of *in situ* formation of the free acid tricyanomelamine, which may further undergo condensation processes toward triazine-based extended polymers, possibly involving the reactive cyanamide moieties.

The following section is dedicated to the characterization of the first non-metal tricyanomelamines with respect to both structure and thermal behavior, placed in the context of  $CN_x$ -precursor chemistry.

## 5.6 Non-Metal Tricyanomelamines

### 5.6.1 Crystal Structures and Spectroscopic Characterization

Below the structural characteristics of five non-metal tricyanomelamines will be outlined so as to work out principal analogies and differences of the non-isotypic molecular salts, according to ref. [127]. Solid-state NMR investigations have been carried out for the ammonium and melaminium salts, whereas in case of the guanidinium salt the poor signal-to-noise ratio of the  $^{15}N$  rendered further investigations futile.

#### 5.6.1.1 Ammonium Tricyanomelamines

Three forms of ammonium tricyanomelamine were obtained starting from similar synthesis conditions (cf. section 10.1 on page 355). The metastable hydrated form **1a** with the preliminary formula “[NH<sub>4</sub>]<sub>2</sub>[C<sub>6</sub>N<sub>9</sub>H] · 2 H<sub>2</sub>O” loses crystal water when exposed to air under ambient conditions, transforming into the stable, non-hydrated species [NH<sub>4</sub>]<sub>2</sub>[C<sub>6</sub>N<sub>9</sub>H] (**1**) within days. This process is retarded by storing the dry sample in a refrigerator, or alternatively in a wet state under ambient conditions. Another NH<sub>4</sub>-TCM phase can be assigned the approximate formula [NH<sub>4</sub>]<sub>2</sub>[C<sub>6</sub>N<sub>9</sub>H] · 0.5 H<sub>2</sub>O according to elemental analysis, if a mono-protonated TCM ring is inferred. This phase, which could not be characterized by single-crystal X-ray diffraction, behaves analogously to **1a** and will not be discussed further.

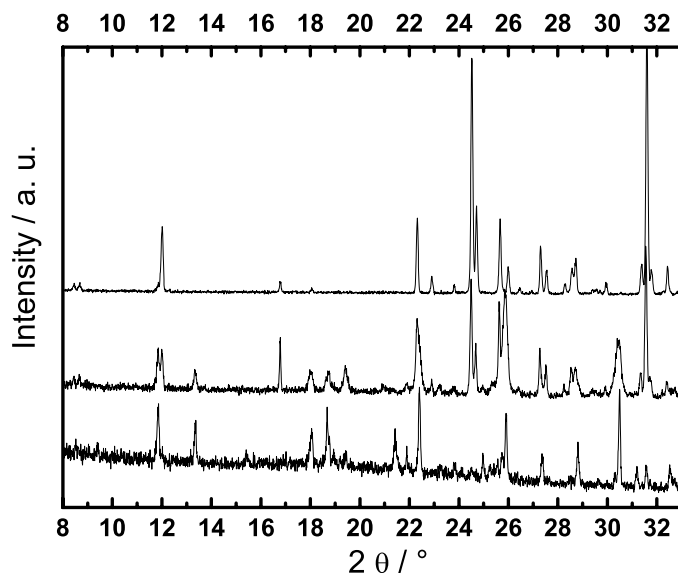


**Figure 5.31:** Powder X-ray diffractograms of **1** (bottom), a sample of **1a** stored between acetate foils in air for 7 days (middle), and of **1a** (top).

Remarkably, isolatable intermediate stages of the transformation process are revealed by powder X-ray diffraction as demonstrated in Figure 5.31, however no evidence is found for extensive amorphization during the transformation from **1a** into **1**. These observations suggest a *topochemical* transformation of the two chemically different phases to occur, associated with a minimum disruption of the molecular arrangements. Nevertheless, a *topotactic* transformation seems rather unlikely on inspection of the crystal structures of both species, which are not transferable into each other by means of a group-subgroup relationship (see discussion of the crystal structures below).

The crystal structure solution of **1a** reveals disorder phenomena associated with one of the two ammonium and crystal water sites. Electron density roughly corresponding to four hydrogen positions is distributed around each of *three* central atom sites, whereas according to electroneutrality arguments only *two* charge compensating ammonium groups are required: From the difference Fourier synthesis one H atom can be located at the TCM ring, yielding a monoprotonated TCM dianion, which is also supported by the intramolecular C–N distances of the triazine residue (see below). Furthermore, the electron density distribution around two of the above sites is such that two protons of adjacent “ammonium groups” would come as close as 85 pm. However, this is far smaller than the sum of the van-der-Waals radii of two hydrogen atoms (120 pm per H) and far below the theoretically determined limit of H ··· H contacts reported so far for “dihydrogen bonds” [430]. These hydrogen positions should therefore be treated as split positions according to a double-well potential (dynamic disorder), or be fully attributed to either one of the neighbored atoms at a time if static disorder applies. The separation between the “nitrogen” sites amounts to 274 pm, which is at the lower end of the spectrum of known N ··· N distances, resulting in a tightly hydrogen bonded pair of nitrogen atoms [363, 431–433]. The third nitrogen position in question, which is located separately at the site denoted N10 in Fig. 5.33, can be attributed to an ammonium ion, as the overall geometry of the associated electron density distribution (N–H distances and angles) in combination with charge balance requirements render this assignment most probable. These facts can only be harmonized by three interpretations delineated in the following:

Firstly, the pair of closely spaced atoms may be attributed to an ammonium-ammine complex as reported previously by *Berthold* [434–436] and *Korber* [437–440]. Complexes of type  $[(\text{NH}_4)_x(\text{NH}_3)_y]^+$  with  $x = 1, 4$  and  $y = 1 - 4$  were shown to exhibit N ··· N distances expanding from 281 to 292 pm on increasing the number of ammonia ligands around the central ammonium ion [437, 438]. According to *Berthold et al.* the N ··· N distance of the  $\text{N}_2\text{H}_7^+$  cation in  $\text{NH}_4\text{I} \cdot \text{NH}_3$  amounts to 269(5) pm, which is slightly smaller than the theoretically calculated distance of 273.1 pm [434–436, 441]. Apart from the latter compound, which

**Table 5.6:** Details for the structure refinement of **1a** assuming an ammonium-ammine complex as structural motif. Left: Refinement with fixed hydrogen positions, right: free refinement. Further details of the structure solution and refinement are given in Table 5.7

	N(11)H <sub>4</sub> ··· N(12)H <sub>3</sub>	vs.	N(11)H <sub>3</sub> ··· N(12)H <sub>4</sub>
refined parameters / restraints	201 / 0		225 / 0
GooF on $F^2$	1.047		1.044
$R$ indices (all data)	$R_1 = 0.0439$ (0.0569) $wR_2 = 0.1192$ (0.1290)		$R_1 = 0.0356$ (0.0483) $wR_2 = 0.0888$ (0.0967)
fraction N(11)H <sub>4</sub> / N(12)H <sub>4</sub>	0.42(4) / 0.58(4)		0.46(4) / 0.54(4)

is stable also at room temperature, all molecular ammoniates are thermally unstable under ambient conditions.

As the interatomic distance found in **1a** appears to be short, yet chemically sensible, a data refinement was attempted inferring an ammonium-ammine complex with interchangeable ammonium and ammonia positions to account for the assumed split position for the hydrogen bonded proton [363, 432]. Therefore, the occupation factors of the two hydrogen positions located between the nitrogen atoms were constrained to sum up to 1. Selected results of the refinements with and without fixed hydrogen positions after localizing them from difference Fourier syntheses are shown in Table 5.6. Refinement yields hydrogen positions which do not correspond to physically reasonable values (N–H = 50 – 95 pm). The occupancy factors for both hydrogen sites participating in the hydrogen-bond roughly correspond to an equal (i.e. random) distribution of the ammonium and ammonia species. Whereas the refinement rather supports the presence of an ammine-ammonium cation, three strong arguments against this interpretation may be adduced: The thermal stability of **1a**, which can be stored at RT for several days, is rather exceptional for molecular ammoniates. In addition, **1a** can be obtained from **1** upon recrystallization from aqueous solution without supply of additional ammonia or ammonium ions.

The strongest argument for an alternative interpretation is given by elemental analysis, by which the formula  $[NH_4]_2[C_6N_9H] \cdot 2H_2O$  can be attributed to **1a**, calling for a substitution of ammonia by crystal water (wt% exp. (theor.): C, 26.65 (26.54); N, 57.00 (56.77); H, 4.81 (4.79)). Thus, a re-interpretation of the data is advisable:

The electron density corresponding to hydrogen atom sites around one member of the cationic atom pair may be an artefact or due to a disordered, hydrogen containing species and thus, one of the nitrogen atoms may in fact be identified as oxygen in form of crystal water. The observed N ··· O distance corresponds to a very strong hydrogen bond with a donor-acceptor

distance less than the average value tabulated in the literature for NH<sub>3</sub><sup>+</sup>–H ··· O arrangements (291(1) pm) [363,433,442,443]. The final assignment of the two sites to an ammonium ion and

**Table 5.7:** Crystallographic data for ammonium tricyanomelamine (**1**) (left) and ammonium tricyanomelamine hydrate (**1a**) (right). The latter data refer to the disordered scenario (“free refinement”).

Formula	[NH <sub>4</sub> ] <sub>2</sub> [C <sub>6</sub> N <sub>9</sub> H] ( <b>1</b> )	[NH <sub>4</sub> ] <sub>2</sub> [C <sub>6</sub> N <sub>9</sub> H] · 2 H <sub>2</sub> O ( <b>1a</b> )
<i>M<sub>w</sub></i> / g · mol <sup>-1</sup>	235.24	271.27
crystal system	monoclinic	monoclinic
space group	<i>P</i> 2 <sub>1</sub> /c (no. 14)	<i>C</i> 2/c (no. 15)
<i>T</i> / K	200	130
diffractometer	STOE IPDS	Nonius Kappa CCD
radiation ( $\lambda$ / pm)	Mo–K $\alpha$ (71.073)	Mo–K $\alpha$ (71.073)
monochromator	graphite	graphite
<i>a</i> / pm	1060.8(2)	3181.8(6)
<i>b</i> / pm	1146.2(2)	360.01(7)
<i>c</i> / pm	913.32(18)	2190.4(4)
$\beta$ / °	112.36(3)	112.39(3)
<i>V</i> / 10 <sup>6</sup> · pm <sup>3</sup>	1027.0(4)	2319.9(8)
<i>Z</i>	4	8
$\rho_{calcd}$ / g · cm <sup>-3</sup>	1.521	1.165
F(000)	488	1136
$\mu$ / mm <sup>-1</sup>	0.113	0.093
crystal size / mm <sup>3</sup>	0.29 x 0.19 x 0.17	0.45 x 0.15 x 0.07
diffraction range	2.73 ≤ $\theta$ ≤ 27.49	3.72 ≤ $\theta$ ≤ 25.98
index range	–13 ≤ <i>h</i> ≤ 13, –14 ≤ <i>k</i> ≤ 14, –11 ≤ <i>l</i> ≤ 11	–38 ≤ <i>h</i> ≤ 38, –4 ≤ <i>k</i> ≤ 4, –26 ≤ <i>l</i> ≤ 26
total no. reflections	8307	17246
independent reflections	2257 ( <i>R</i> <sub>int</sub> = 0.0475)	2289 ( <i>R</i> <sub>int</sub> = 0.0419)
observed reflections	1640	1891
refined parameters / restraints	with $F_o^2 \geq 2\sigma(F_o^2)$ 190 / 0	with $F_o^2 \geq 2\sigma(F_o^2)$ 207 / 0
GooF on <i>F</i> <sup>2</sup>	0.914	1.042
<i>R</i> indices (all data)	$R_1 = 0.0295$ (0.0471) $wR_2 = 0.0680$ (0.0721) with w = $[\sigma^2(F_o^2) + (0.0435P)^2 + 0.0000P]^{-1}$ where <i>P</i> = ( $F_o^2 + 2F_c^2$ )/3	$R_1 = 0.0368$ (0.0496) $wR_2 = 0.0923$ (0.1007) with w = $[\sigma^2(F_o^2) + (0.0507P)^2 + 2.6082P]^{-1}$ where <i>P</i> = ( $F_o^2 + 2F_c^2$ )/3
min./max. residual electron density / <i>e</i> · 10 <sup>-6</sup> pm <sup>-3</sup>	– 0.153 / 0.166	– 0.276 / 0.192
fraction		0.53(2) / 0.47(2)
N11/O2 vs. O3/N12		

a water molecule, respectively, is feasible based on the  $R$  values for the respective refinements (complete ordering case). The resulting borderline cases are in the following referred to as N11/O2 and O3/N12, indicating the alternative assignments of nitrogen and oxygen within the hydrogen-bonded N/O pair. Note that the same atomic site is occupied by a nitrogen atom in one case and by an oxygen atom in the other case such that N11 has the same positional parameters as O3, the same applying to O2 and N12.

Alternatively, a disorder scenario may be applicable, in which an ammonium ion and a water molecule are statically disorderd such that  $NH_4^+$  and  $H_2O$  are *statistically* distributed over the two sites in question, resulting in approximately equal proton density around both central atoms. In case of preferential location of the two species on a particular site, the borderline case desribed above (complete ordering) is approached.

In order to distinguish between the different scenarios, refinements were carried out for both ordered distributions and the disorder case, the results of which are listed together with the refinement data for **1** in Tables 5.7 and 5.8. A critical feature common to all scenarios is the relatively poor data / parameter ratio, rendering the free refinement of all hydrogen positions rather unstable. Therefore, restraints were included into the refinements by fixing the hydrogen positions once they are found from difference Fourier syntheses. In all cases, N–H distances ( $\approx 80$  – 111 pm) and angles of the ammonium ions N11 or N12 ( $\approx 80$  – 123°) showed significant deviations from the physically required bond lengths and tetrahedral symmetry. Therefore, restraints equalizing the H ··· H distances in the ammonium groups and restraining the N–H distances to 86(6) pm were introduced for the ordered scenarios. For reasons of consistency, the same procedure was applied for *both* ammonium groups as well as for crystal water. For the disordered scenario a “free” refinement including the chemically reasonable coupling of the proton occupation factors to those of the central atom (ammonium

**Table 5.8:** Details for the structure refinement of ammonium tricyanomelamine hydrate **1a** based on the two ordered scenarios: N11/O2 (left) and O3/N12 (right). Refinements with restraints are given in columns 1 and 3, those without restraints in 2 and 4.

Order variant	N11 / O2		O3 / N12	
refined parameters /	218 /	208 /	218 /	208 /
restraints	42	0	42	0
Goof on $F^2$	1.048	1.052	1.052	1.075
Restrained Goof	1.053		1.059	
	$R_1 = 0.0401$ (0.0529)	$R_1 = 0.0392$ (0.0519)	$R_1 = 0.0414$ (0.0543)	$R_1 = 0.0402$ (0.0533)
$R$ indices (all data)	$wR_2 = 0.1038$ (0.1125)	$wR_2 = 0.0985$ (0.1069)	$wR_2 = 0.1096$ (0.1192)	$wR_2 = 0.105$ (0.1142)

ion or crystal water) was attempted without restraints concerning the tetrahedral symmetry or bond lengths. This procedure was chosen in order to determine the relative distribution of  $NH_4^+$  and  $H_2O$  over the two possible sites by introducing an additional free variable into the refinement. The distribution was only constrained by the requirement to yield *one* ammonium ion and *one* crystal water in total occupying the two sites.

The “free” refinement yields a fraction of 0.53(2) *vs.* 0.47(2) for the combinations N11/O2 and O3/N12, respectively, suggesting an approximately equal distribution of the nitrogen and oxygen atoms on the two neighbored sites in question<sup>2</sup>. The resulting *R* values are given in Table 5.7. Refinements based on the ordered scenarios invariably yield *R* values which are slightly higher than those from the “free” refinement, irrespective of the use of restraints for the bond lengths and angles (Table 5.8). Furthermore, the quality criteria for the O3/N12 case are slightly worse as compared to the N11/O2 scenario. Considering these findings, the ordered variants appear somewhat less likely than the disorder case, although it has to be noted that the data quality may not be sufficient to unambiguously discriminate between the order and disorder scenarios.

To add another piece of evidence to the above line of argument, solid-state NMR investigations have been carried out for **1** and **1a**. One might expect to find only *two* different ammonium species in both cases if one of the ordered variants applies for **1a**, whereas *three* ammonium sites with approximate intensity ratios of 1 : 0.5 : 0.5 would be expected for **1a** if the disordered scenario was valid. Assuming an ammonium-ammine complex, three nitrogen signals of about equal intensity would be expected. Differentiating the  $^{15}N$  signals of an ammonium-ammine complex on the basis of their chemical shifts, however, is critical owing to the lack of literature data for the solid-state. Nevertheless, one would expect a high-field shift (more negative ppm-values) for ammonia as compared to ammonium ions due to shielding effects in the free base [444, 445].

Whereas the  $^{15}N$  CP-MAS spectra for **1** could be recorded under ambient conditions, cooling had to be applied for **1a**, as rapid transformation into **1** occurred due to the heat of friction when spinning under MAS conditions. Spectra of the hydrate were recorded in a temperature range between 230 and 270 K. The  $^{15}N$  CP-MAS spectra for **1** and **1a** are shown in Figure 5.32. All principal assignments could be made in coincidence with the crystal structure data, the similar signal patterns for both compounds being evident. Notably, the ammonium region ( $\approx$  – 330 to – 360 ppm) exhibits two clearly separated signals of equal intensity in the spectrum of **1**, whereas a poorly separated signal group is visible for **1a**. Enlargement

<sup>2</sup>If the hydrogen atoms are not included into the refinement, the combination N11/O2 is exclusively obtained.

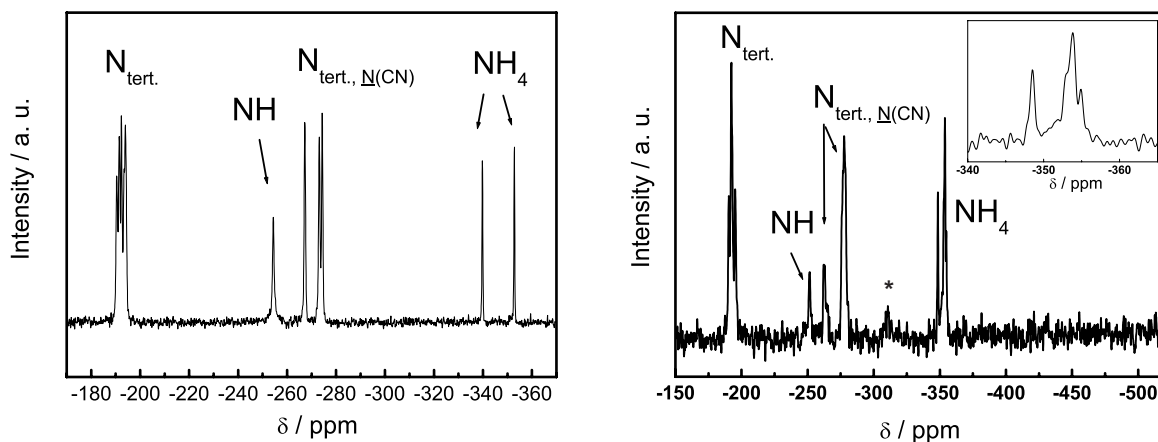


**Figure 5.32:**  $^{15}N$  MAS solid-state NMR spectra of **1** taken at RT (left) and of **1a**, recorded at 230 K (right). Contact times of 20 ms (**1**) and 8 ms (**1a**) were used, the recycle delays were 1 s (**1** and **1a**). The ammonium region is shown enlarged in the inset (right). Spinning side bands are marked by asterisks.

of the latter shows the presence of three separable signals, with the central signal exhibiting a shoulder on the low-field side. This observation supports the presence of a disordered N ... O pair, since clearly more than two  $NH_4^+$  signals are visible. The intensities cannot be evaluated quantitatively due to the limitations associated with a CP experiment (see below). Nevertheless, the relative intensities suggest an assignment of the central signal to N10 with a normalized intensity of 1, whereas the two “satellite” signals are assigned to the ammonium nitrogen atoms of the N11/O2 and O3/N12 scenarios; the latter appear to be roughly equally probable in agreement with the X-ray data. The fact that a broadening of the N10 signal is observed may be rationalized with a slight change of the electronic environment of N10 when interchanging the sites of nitrogen and oxygen in the respective N11/O2 and O3/N12 configurations. The similar chemical shift values for all nitrogen signals, as well as the observed intensity distribution, further renders an ammonium-ammine complex improbable.

Based on both X-ray structure analysis and NMR data the compound **1a** will henceforth be referred to as ammonium TCM hydrate characterized by a random distribution of one ammonium ion and one crystal water over two hydrogen-bonded sites. In the following one of the ordered cases (N11/O2) will be used representatively in order to facilitate the crystal structure visualization.

The non-crystallographic point symmetry of all TCM residues is  $C_s$  (Fig. 5.33). In **1** the molecular planes of the TCM anions form 2D sheets, which are separated by an array of ammonium ions (Fig. 5.34, left), thereby giving rise to a layered structure with an interlayer spacing of approximately 350 pm. The layers are stabilized by weak hydrogen bonding contacts between the TCM N–H groups and adjacent nitrile nitrogen atoms (N3–H3A ... N8: 223 pm);

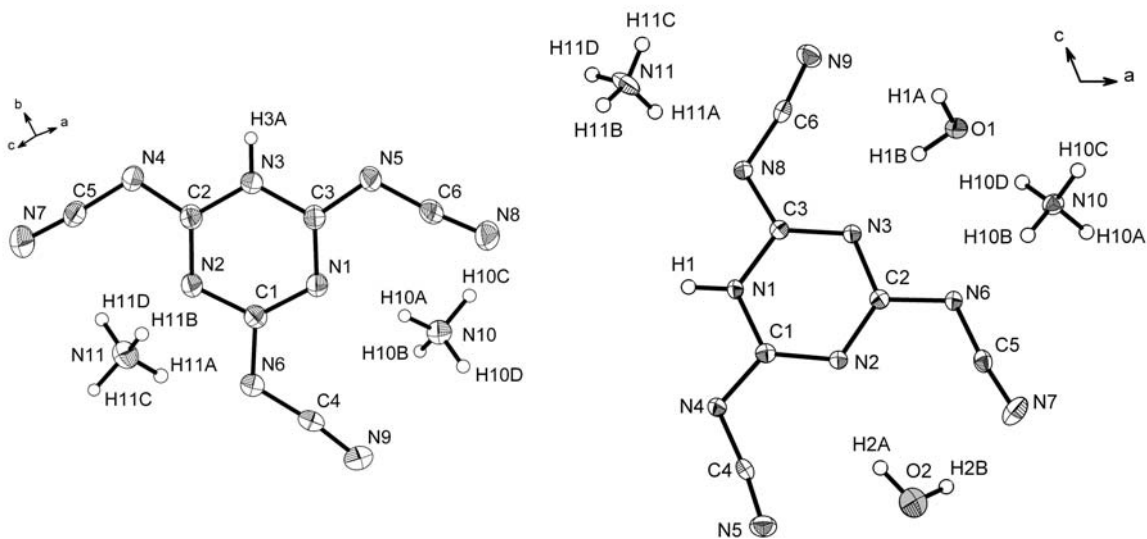


**Figure 5.33:** Asymmetric units of ammonium tricyanomelamine **1** (left) and ammonium tricyanomelamine hydrate **1a** (right). Thermal displacement ellipsoids (except for H) are drawn at the 50 % probability level.

the ammonium ions are hydrogen-bonded to the layers with donor acceptor distances between 292 and 317 pm. However, adjacent layers are shifted with respect to each other such that the planes of the triazine rings do not overlap along the stacking direction [407]. Therefore,  $\pi - \sigma$  rather than  $\pi - \pi$  interactions seem to be the dominant dispersion forces between the layers.

In contrast, **1a** forms a “columnar” structure where pairs of TCM strands are stacked along

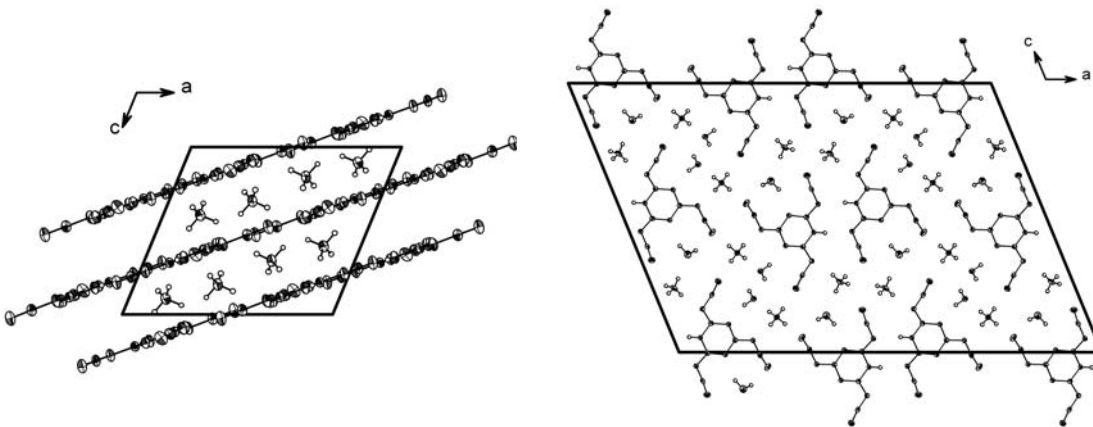


**Figure 5.34:** Unit cells of ammonium tricyanomelamine **1** (left, view along *[010]*) and ammonium tricyanomelamine hydrate **1a** (right, view along *[010]*). For **1a** the ordered variant with N11 and O2 is shown (for nomenclature see text). Thermal displacement ellipsoids (except for H) are drawn at the 50 % probability level.

[010] with a separation of the triazine rings of  $\approx 360$  pm and the  $\pi$ -stacking vector (normal to the molecular planes) being inclined with respect to  $b$ . The water and ammonium molecules are inserted between the strands, thereby lying below and on top of the “extended” molecular planes spanned by the triazine rings and cyanamide moieties. Cations and water molecules are connected *via* medium strong and weak hydrogen contacts with the cyanamide functions ( $O/N \cdots N/O$ : 274 – 333 pm) and, to a lesser extent, with the triazine cores ( $O \cdots N$ : 282 – 311 pm). The intramolecular C–N distances are in close agreement with those observed for the melaminium tricyanomelaminates and will be discussed in more detail below.

### 5.6.1.2 Guanidinium Tricyanomelamine

While in the ammonium and melaminium salts the tricyanomelamine anions are singly protonated, the guanidinium salt  $[C(NH_2)_3]_3[C_6N_9] \cdot 2 H_2O$  ( $P2_12_12_1$ ) contains a non-protonated anionic core, which is charge-balanced by three guanidinium cations. This tendency may be due to the basicity of the parent bases melamine, ammonia and guanidine, which is increasing in this order. In contrast to all protonated TCM moieties in **2** the non-crystallographic point symmetry of the tricyanomelamine anion in **2** is approximately represented by  $C_{3h}$  as found for  $Na_3[C_6N_9] \cdot 3 H_2O$  [302, 361, 446]. Remarkably, **2** is composed of cations, anions and crystal water mutually linked by hydrogen-bridges ( $N/O \cdots H = 194$  – 262 pm) into a quasi three-dimensional array such that no pronounced  $\pi$ -stacking of the triazine rings is feasible and no layered structure is formed (Fig. 5.35, right).

The intramolecular C–N distances within the triazine ring are largely similar ( $\approx 135$  pm) and do not show significant variations as observed for the protonated TCM species. The distance pattern encoded in the cyanamide moieties again reflects the carbodiimide character with a

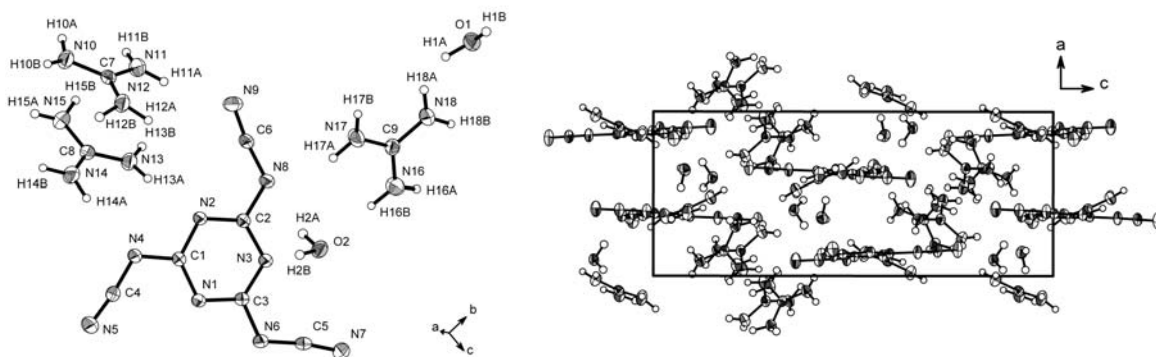


**Figure 5.35:** Formula unit (left) and unit cell of guanidinium TCM (2), the latter demonstrating the spatially extended, non-layered structure resulting from mutual tilting of the guanidinium and TCM residues in 2. Thermal displacement ellipsoids (except for H) are drawn at the 50 % probability level.

**Table 5.9:** Crystallographic data for guanidinium tricyanomelamine (2).

Formula	$[C(NH_2)_3]_3[C_6N_9] \cdot 2 H_2O$
$M_w$ / g · mol <sup>-1</sup>	414.45
crystal system	orthorhombic
space group	$P2_12_12_1$ (no. 19)
$T$ / K	200
diffractometer	Nonius Kappa CCD
radiation ( $\lambda$ / pm)	Mo-K $\alpha$ (71.073)
monochromator	graphite
$a$ / pm	762.12(15)
$b$ / pm	1333.6(3)
$c$ / pm	1856.6(4)
$V$ / $10^6 \cdot pm^3$	1887.0(7)
$Z$	4
$\rho_{calcd}$ / g · cm <sup>-3</sup>	1.459
F(000)	872
$\mu$ / mm <sup>-1</sup>	0.113
crystal size / mm <sup>3</sup>	0.49 x 0.35 x 0.30
diffraction range	$3.25 \leq \theta \leq 27.44$
index range	$-9 \leq h \leq 9, -17 \leq k \leq 17,$ $-24 \leq l \leq 24$
total no. reflections	24736
independent reflections	4274 ( $R_{int} = 0.0371$ )
observed reflections	4077
refined parameters / restraints	with $F_o^2 \geq 2\sigma(F_o^2)$
GooF on $F^2$	351 / 0
$R$ indices (all data)	1.087
	$R_1 = 0.0253$ (0.0277)
	$wR_2 = 0.0652$ (0.0666)
	with w = $[\sigma^2(F_o^2)$
	$+(0.0372P)^2 + 0.1866P]^{-1}$
	where $P = (F_o^2 + 2F_c^2)/3$
min./max. residual	
electron density /	- 0.181 / 0.113
$e \cdot 10^{-6} pm^{-3}$	

single (130 – 132 pm) and a triple bond each (116 – 117 pm). Whereas the single bonds are slightly shorter and the triple bonds longer as compared to the protonated TCM species, the external distances  $C_{1/3/2}-N_{4/6/8}$  are slightly extended (135 – 136 pm, cf. below), suggesting a smaller extent of delocalization of electron density from the carbodiimide moieties into the less electron deficient triazine ring (Fig. 5.35, left).

### 5.6.1.3 Melaminium Tricyanomelamines

As outlined in section 10.1 on page 355, two different melamine tricyanomelamines were obtained from solutions with different concentrations of the starting materials sodium tri-cyanomelamine and melaminium sulfate, as well as different solvent ratios ( $H_2O / MeOH$ ).

By their compositions, melaminium tricyanomelamine hydrate  $[(C_3N_6H_7)_2][C_6N_9H] \cdot 2.4H_2O$  (**3**, space group  $P\bar{1}$ ) and melaminium melamine tricyanomelamine hydrate  $[C_3N_6H_7]_2[C_6N_6H_6][C_6N_9H] \cdot 2H_2O$  (**3a**, space group  $P2_1/c$ ) can be identified as ionic tricyanomelamines containing crystal water and, in the latter case, an additional neutral melamine molecule as co-crystallizing species (Fig. 5.36). Apart from charge balance considerations, evaluation of the intramolecular distances found for the different melamine residues in **3a** strongly suggests the presence of two cationic melaminium species and one neutral melamine as “solvent” molecule apart from crystal water. A number of examples is known to date where melamine is incorporated into a hydrogen bonded array of neutral or ionic “framework species” in a similar fashion, thus interlinking and stabilizing the supramolecular framework [447–452]. One reason for the facile incorporation of melamine as “co-crystallisate” may be its optimal shape in combination with beneficial  $\pi$ -stacking interactions, which are particular favored in terms of a charge-transfer-type interaction between protonated (i.e. electron deficient, acceptor) and non-protonated melamine functioning as donor species. Accordingly, melamine and melaminium cations are stacked alternately with their molecular planes parallel, as are mono-protonated TCM anions and melaminium cations. The ability of melamine to form hydrogen-bonded co-crystallisates will be revisited in another context in Chapter 6 on page 196.

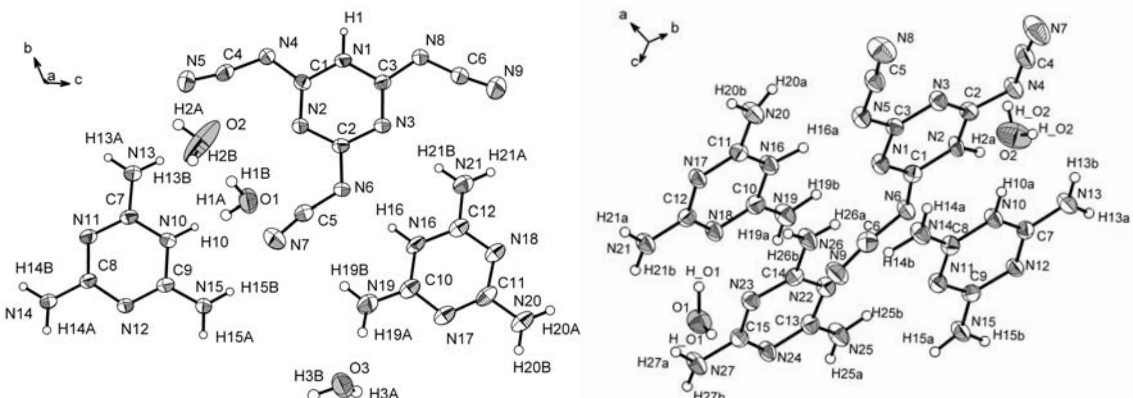


**Figure 5.36:** Representation of one formula unit of **3** (left), and **3a** (right). Thermal displacement ellipsoids (except for H) are drawn at the 50 % probability level.

The non-crystallographic point group of the TCM anions in **3** and **3a** is  $C_s$ , which may be attributable to the steric requirements of the proton attached to the triazine rings with respect to the adjacent cyanamide moieties (Fig. 5.36). Although non-protonated tricyanomelamine salts with anions possessing  $C_s$  symmetry are also known [125, 126, 240], the latter point symmetry may be enforced by the cyanamide moieties on avoiding the proton attached to the triazine core between them. Both melaminium salts crystallize with two or more molecules of crystal water, which is largely disordered (O2) with site occupation factors  $\leq 1$  (O3) in **3**, whereas it does not show pronounced signs of disorder in **3a**. This difference may predominantly be rationalized by the pronounced layered structure of **3**, where the water molecules are loosely embedded between the layers, linking them by hydrogen bridges. The layers are made up by both cations and anions which – due to their “complementary” shape – smoothly pack into an extended two-dimensional array. The latter arrangement is fixed by medium strong to weak intralayer hydrogen bonding contacts (N / O  $\cdots$  H: 184 – 259 pm) with donor-acceptor distances ranging between 274 and 347 pm. The water molecules are either inserted between the layers (O1), or serve as cross linkers within the sheets (O2/O3). In **3a** the layer-like character is much less pronounced, instead 1D strands of  $\pi$ -stacked molecules are formed along [100], where two pairs of adjacent strands exhibit the same stacking vector, and the pairs are tilted by about 20 – 25° with respect to each other. The two water molecules are fixed between adjacent strands, linking them up by medium strong to weak hydrogen bridges with the closest donor-acceptor distances amounting to 275 (O2  $\cdots$  N10) and 281 pm (O1  $\cdots$  N18). The N  $\cdots$  N hydrogen-bonding donor-acceptor distances between adjacent strands are in the range 280 pm (N16  $\cdots$  N5) to 339 pm (N26  $\cdots$  N7) (Fig. 5.37).

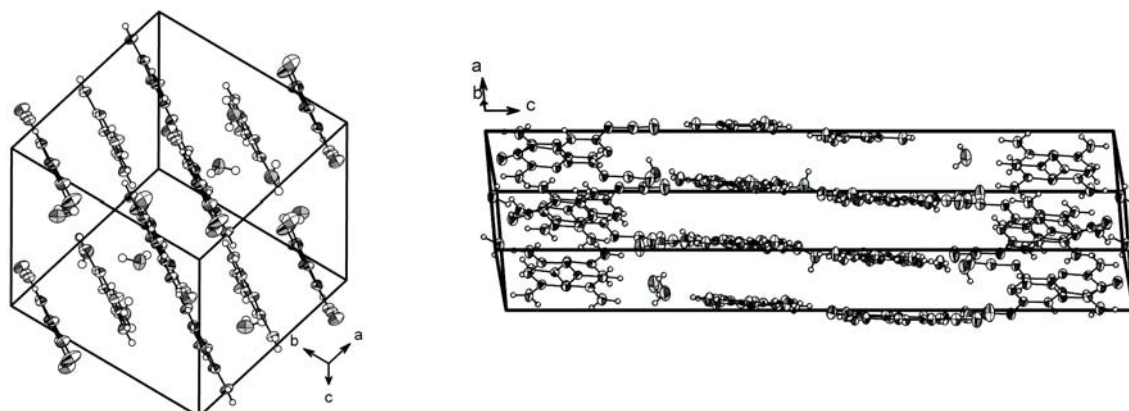


**Figure 5.37:** Unit cells of **3** (left), **3a** (right), clarifying the pronounced layered structure of **3** in contrast to 1D strands of  $\pi$ -stacked triazine molecules in **3a**. Thermal displacement ellipsoids (except for H) are drawn at the 50 % probability level.

**Table 5.10:** Crystallographic data for melaminium (**3**) (left) and melaminium melamine tricyanomelamine (**3a**) (right).

Formula	$[(C_3N_6H_7)_2][C_6N_9H]$ · 2.4 H <sub>2</sub> O ( <b>3</b> )	$[C_3N_6H_7]_2[C_6N_6H_6][C_6N_9H]$ · 2 H <sub>2</sub> O ( <b>3a</b> )
$M_w$ / g · mol <sup>-1</sup>	496.69	615.62
crystal system	triclinic	monoclinic
space group	$P\bar{1}$ (no. 2)	$P2_1/c$ (no. 14)
$T$ / K	200	200
diffractometer	Nonius Kappa CCD	Nonius Kappa CCD
radiation ( $\lambda$ / pm)	Mo-K $\alpha$ (71.073)	Mo-K $\alpha$ (71.073)
monochromator	graphite	graphite
$a$ / pm	1029.5(2)	674.7(5)
$b$ / pm	1120.3(2)	1123.6(5)
$c$ / pm	1120.7(2)	3400.2(5)
$\alpha$ / °	104.22(3)	
$\beta$ / °	112.74(3)	95.398(5)
$\gamma$ / °	104.62(3)	
$V$ / $10^6$ · pm <sup>3</sup>	1064.8(4)	2566(2)
$Z$	2	4
$\rho_{calcd}$ / g · cm <sup>-3</sup>	1.555	1.593
F(000)	516	1280
$\mu$ / mm <sup>-1</sup>	0.120	0.122
crystal size / mm <sup>3</sup>	0.30 x 0.14 x 0.04	0.25 x 0.04 x 0.03
diffraction range	$3.44 \leq \theta \leq 26.00$	$3.16 \leq \theta \leq 24.14$
index range	$-12 \leq h \leq 12, -13 \leq k \leq 13,$ $-13 \leq l \leq 13$	$-7 \leq h \leq 7, -12 \leq k \leq 12,$ $-39 \leq l \leq 38$
total no. reflections	12076	7652
independent reflections	4111 ( $R_{int} = 0.0443$ )	4050 ( $R_{int} = 0.0638$ )
observed reflections	2671	2325
refined parameters / restraints	with $F_o^2 \geq 2\sigma(F_o^2)$	with $F_o^2 \geq 2\sigma(F_o^2)$
GooF on $F^2$	345 / 9	497 / 0
$R$ indices (all data)	$R_1 = 0.0570$ (0.1015) $wR_2 = 0.1230$ (0.1458) with w = $[\sigma^2(F_o^2) + (0.0496P)^2 + 0.9337P]^{-1}$ where $P = (F_o^2 + 2F_c^2)/3$	$R_1 = 0.0470$ (0.1091) $wR_2 = 0.0983$ (0.1183) with w = $[\sigma^2(F_o^2) + (0.0567P)^2 + 0.0000P]^{-1}$ where $P = (F_o^2 + 2F_c^2)/3$
min./max. residual electron density / $e \cdot 10^{-6}$ pm <sup>-3</sup>	- 0.537 / 0.481	- 0.209 / 0.199

The interlayer distance (**3**) and stacking distance (**3a**) amount to approximately 350 pm and 337 pm ( $\equiv a/2$ ), respectively (327 pm in melem [82, 240]), which is similar to the typical

values expected for extended graphitic  $CN_x$  structures (310 – 350 pm) [54].

As in **1/1a** and **2**, the local structural parameters for both cations and anions in **3** and **3a** largely coincide with literature data [125, 126, 240, 302, 426–428]. Interestingly, the intramolecular distances for the melaminium, melamine and TCM residues in **3** and **3a** follow similar patterns in terms of the succession of longer and shorter bonds within the rings. Mono-protonated species (melaminium cations and TCM dianions) show a greater variety in their bond lengths than does neutral melamine. In **3** the melaminium ions exhibit C–N distances within the rings of 133 – 137 or 132 – 136 pm, respectively; in **3a** we find distances in the range 132 – 136 and 133 – 136 pm. For the TCM anions in **3** C–N distances between 133 and 136 pm are observed, in **3a** between 134 and 137 pm. These values closely correspond to those obtained for the ammonium salts (133 – 136 pm (**1**); 133 – 137 pm (**1a**)). In particular, for all mono-protonated species the C–N bonds adjacent to the N–H group as well as the two opposite ones are longer by 3 pm on average as compared to those in between, the latter of which consistently range between 132 and 134 pm. In contrast, neutral melamine in **3a** does not exhibit significantly alternating C–N bond lengths as similarly found for the non-protonated TCM anion in **2**; all C–N distances amount to 134 – 135 pm. Another noticeable feature is the short C–N bond lengths external to the ring in protonated melamine residues (130 – 133 pm), which are shorter by more than 2 pm on average as compared to the longest C–N distances within the rings. This effect is less pronounced, yet nevertheless significant, for the TCM anions of **3** and **3a**, **1** and **1a**, and also for melamine, where C–N<sub>exo</sub> of  $\approx$  133 – 135 pm, 134 – 135 pm, and 133 pm, respectively, are found.

The C–N bond distances of the cyanamide moieties of the TCM anions in **3** are slightly shorter than those in **3a**, but they are all consistent with a carbodiimide-type structure with C–N single bonds of 131 – 133 pm (**3**) and 133 – 134 pm (**3a**), C≡N triple bonds of 115 pm (**3**) and 115 – 116 pm (**3a**), and angles of 170 – 173° (**3**) and 171 – 177° (**3a**), respectively (Fig. 5.36).

In addition to the X-ray structure analysis, the local structure of **3** was probed by <sup>15</sup>N solid-state NMR spectroscopy (Fig. 5.38). While applying fast MAS conditions allows for the acquisition of high-resolution chemical shift spectra, “spectral editing” utilizing the CPPI impulse sequence permits the identification of <sup>15</sup>N sites according to their proton environments (cf. section 3.3.3) [82, 194]. All nitrogen resonances of **3** could be assigned on account of their isotropic chemical shift spectrum (bottom), as well as by their polarization behavior, as expressed by the relative intensities in the CPPI experiment (top).

For the particular inversion time chosen in this experiment (100  $\mu$ s), the normalized intensity

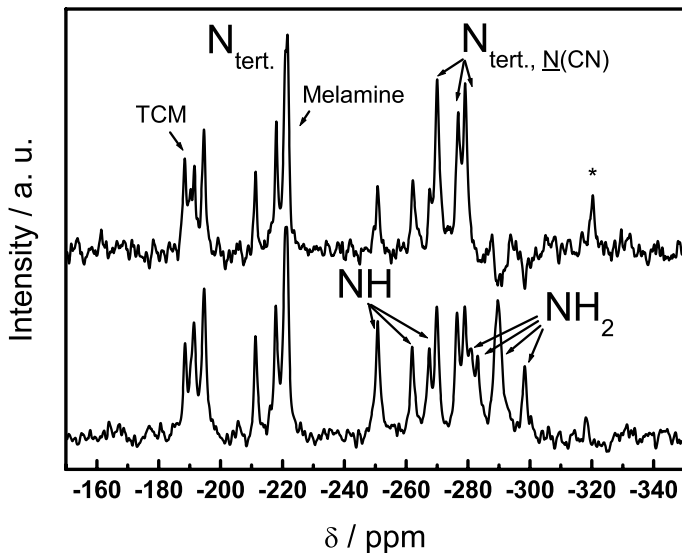


**Figure 5.38:**  $^{15}N$  MAS solid-state NMR spectra of **3**. Top: CPPI experiment (inversion time  $100\ \mu s$ , contact time  $2\ ms$ , recycle delay  $5\ s$ ); bottom: CP experiment (contact time  $10\ ms$ , recycle delay  $5\ s$ ). Spinning side bands are marked by asterisks.

of the NH groups (crossover at 0) is expected to be slightly positive, whereas that of  $NH_2$  groups (crossover at  $-1/3$ ) is expected to be negative, and that of tertiary N atoms should be decreased only slightly according to previous studies [82, 194].

Thus, the CPPI experimental data allow for the accurate correlation of the observed resonances with the according  $NH_n$  moieties: As demonstrated in Figure 5.38 (top), the experimental intensities of the tertiary nitrogen sites are in fact essentially unaffected, while the magnetization of the NH moieties has dropped significantly, though still being positive. According to theory, the signals arising from the  $NH_2$  groups are close to the zero-crossing, yet with inverted signs, all of which being in coincidence with the crystallographic data. The quantification of the intensities extracted from CP experiments, however, must be inherently inaccurate due to the different cross polarization dynamics of chemically inequivalent  $^{15}N$  sites. Nevertheless, comparison of the experimental spectrum with the chemical shift and the number of signals theoretically expected for the crystallographic asymmetric unit provides independent support for the adequacy of the molecular structure and local symmetry of **3** as derived from X-ray analysis.

### 5.6.2 Thermal Behavior

In view of the identity of the model compounds established above, an interesting aspect of their thermal behavior relates to the possible conservation of the triazine ring systems upon heating. In order to pursue this issue more concisely, the three compounds **1**, **2**, and **3** were chosen representatively for further study. The analogous behavior of **1a** and **3a** can be inferred due to the fact that **1a** rapidly transforms into **1** upon slight heating, and **3a** contains molecular building blocks identical to **3**. Owing to the largely amorphous character of the as-formed polymeric  $CN_xH_y$  materials and the spectroscopic similarities of triazine and heptazine systems, unequivocally resolving this issue by a combination of diffraction techniques and vibrational spectroscopy is still out of reach. However, by shifting the focus to the intermediates formed during the pyrolyses, basic conclusions concerning the structures of the polymeric materials may nevertheless be possible. In principle, similar condensation pathways of ammonium-, guanidinium as well as melaminium-TCM can be envisaged due to the – albeit gradually differing – acidity of the respective cations. As previously observed for related systems (see sections 4.1 on page 71, 5.2 on page 135, 5.3 on page 148 and 5.4 on page 157), a proton transfer from the cation to the tricyanomelamine anion may initiate thermal condensation, thereby releasing the thus formed neutral species either as gas ( $NH_3$ ) or

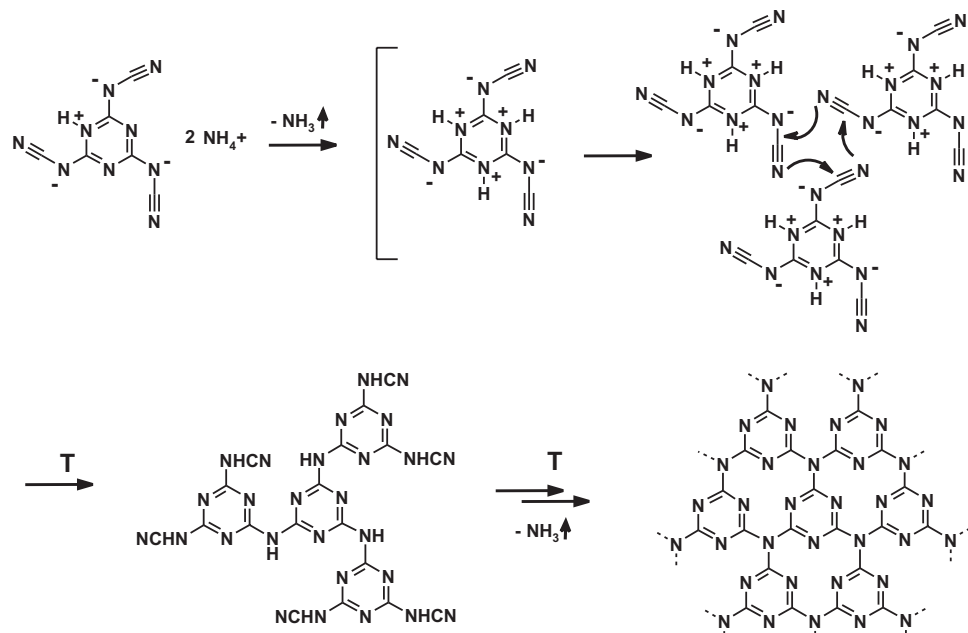


**Figure 5.39:** Possible reaction pathway drawn exemplarily for the thermal decomposition of ammonium tricyanomelamine **1**. According to this simplified scheme, the tricyanomelamine free acid undergoes polymerization yielding an extended triazine-based network.

as potentially nucleophilic agents ( $(H_2N)_2C=NH$  and  $C_3N_6H_6$ ) in further thermally induced reaction steps [122–124, 303]. The *in situ* generated free acid tricyanomelamine, being liable to oligomerization or polymerization [230, 240], may then form highly condensed triazine-based species as exemplarily sketched for the ammonium salt (**1**) (Fig. 5.39). Analogously, in **3** the release of free melamine possessing nucleophilic sites in the presence of electrophilic cyanamide groups of TCM may contribute to the formation of triazine-based networks.

### 5.6.3 DSC and *In Situ* X-Ray Diffraction

The principal succession of thermal events in the pyrolysis processes of **1** – **3** was followed by DSC measurements (Fig. 5.40). Both **2** and **3** exhibit pronounced endothermic signals between 380 and 425 K, which may be attributed to the loss of crystal water. The splitting of the signals may be due to the stepwise release of  $\approx 2.4$  (**3**) or 2 (**2**) molecules  $H_2O$  per formula unit, respectively. Accordingly, temperature programmed X-ray diffractometry (TPXRD) clearly shows the respective conversions to occur between 380 and 400 K (Fig. 5.41).

In coincidence with the absence of crystal water in **1**, a thermal event is observed neither by DSC nor by X-ray diffraction in this temperature range. While the thermal behavior of **1** and **2** shows obvious similarities in the temperature range above 420 K, the temperature response of **3** differs significantly. Between 440 and 460 K an accurately defined exothermic decomposition reaction is observed for salts **1** and **2**, which is associated with an amorphization of the samples. At temperatures above 580 K, a succession of exothermic and endothermic signals

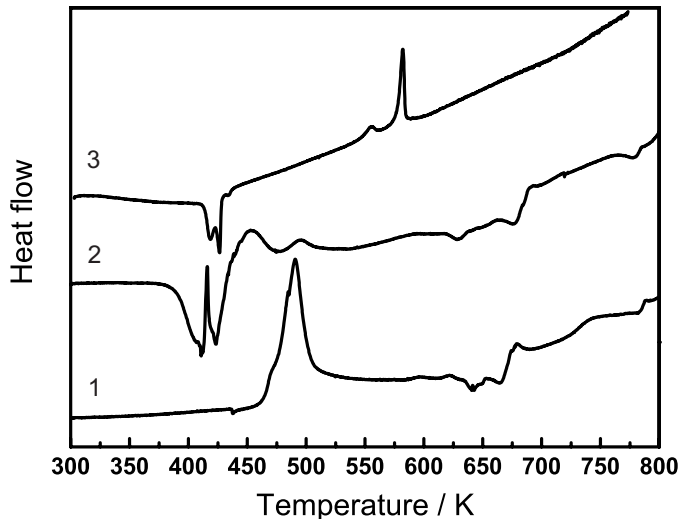


**Figure 5.40:** DSC curves recorded between room temperature and 800 K for **1** (bottom), **2** (middle), and **3** (top).

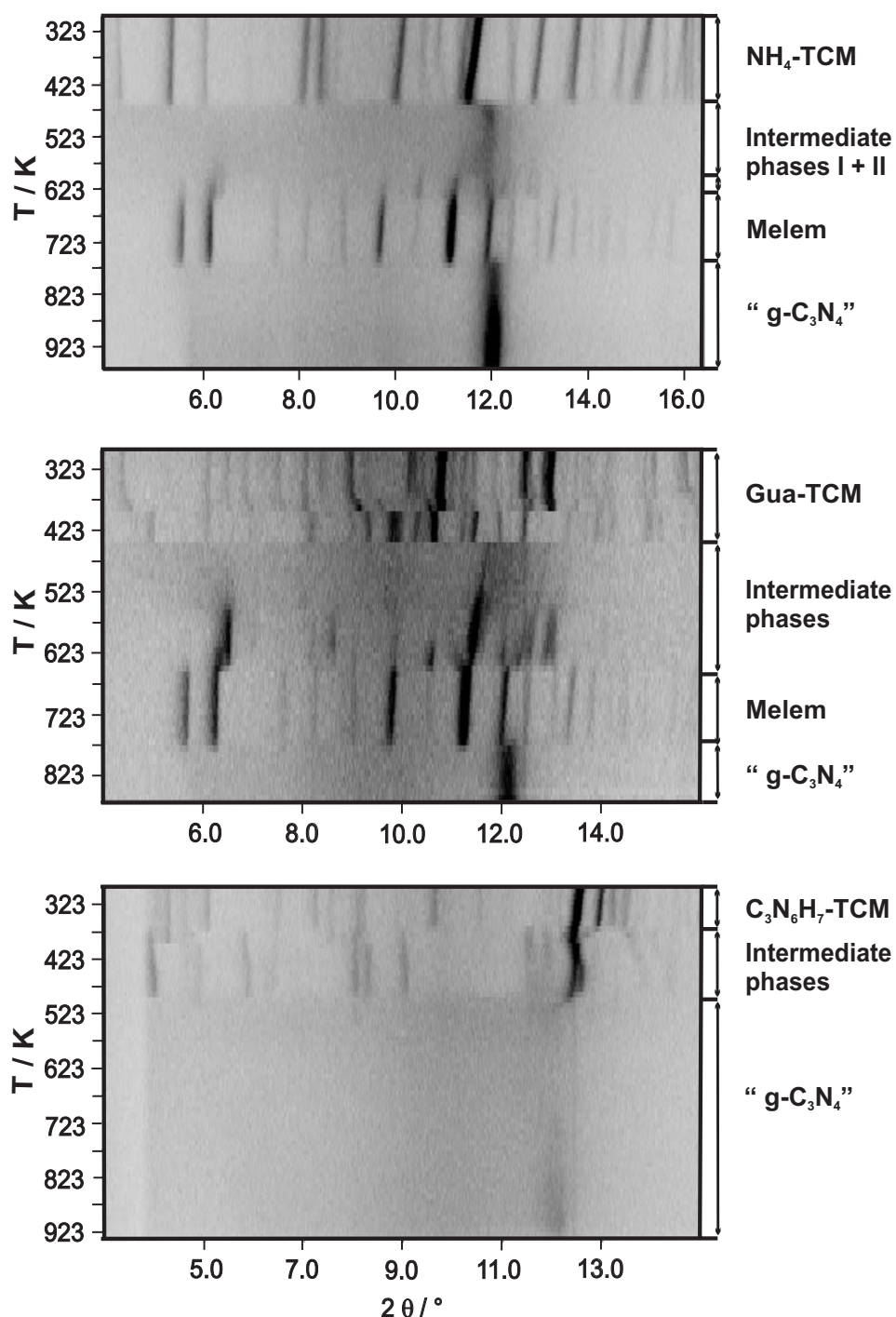


**Figure 5.41:** *In situ* temperature-dependent X-ray diffraction measurements (Mo- $K_{\alpha 1}$  radiation) of the non-metal tricyanomelamines **1**, **2**, and **3** recorded between room temperature and  $T > 850$  K. Whereas the decomposition pathways of **1** and **2** show evident similarities, that of **3** differs significantly in the medium temperature regime. All patterns are dominated at high temperatures by a broad reflection at  $\vartheta \approx 12.1^\circ$  ( $d \approx 336$  pm).

is visible in the DSC curves, which based on the X-ray data are likely to originate from the same underlying decomposition processes.

Thus, at 620 K a crystalline phase commences to form, which is easily identified as melem, a prototypic heptazine-based  $CN_x$ -precursor [82]. Prior to the formation of melem, the reflections of another phase emerge around 550 K, the latter being familiar from decomposition studies of melamine [82, 240]. The identity of the latter phase, which is assumed to be composed of both melamine and melem will be discussed in more detail in Chapter 6 on page 196. However, no evidence by TPXRD was found for the formation of single-phase melamine to a significant extent throughout the pyrolyses of both **1** and **2**. At 770 K, **1** and **2** transform into a semi-crystalline phase with a relatively broad reflection at  $2\theta \approx 12.1^\circ$  ( $\equiv 336$  pm, Mo-K $_{\alpha 1}$  radiation) characteristic of graphitic carbon nitride materials [84, 240, 300, 453]. Melaminium-TCM (**3**) exhibits a succession of solid-solid transitions between crystalline phases commencing at 380 K, while beyond 580 K the sample becomes essentially X-ray amorphous. At temperatures around 700 K, a broad reflection at  $2\theta \approx 12.1^\circ$  indicates the formation of a disordered layered  $CN_xH_y$  structure. As opposed to the thermolyses of **1** and **2**, neither melamine nor melem are observed as crystalline intermediates, which is supported by the lack of thermal events characteristic of melamine above 600 K in the DSC curve of **3**.

#### 5.6.4 IR Spectroscopy

Vibrational spectroscopy was utilized as a probe for structural aspects of the quasi amorphous intermediates of the thermal decomposition reactions. As evidenced by the pyrolysis behavior outlined in Figures 5.40 and 5.41, the crystalline transformation products passed through by **1** and **2** at temperatures  $\geq 500$  K, which are associated with a break-down of the cyanamide moieties as well as a deprotonation of the triazine rings in **1**, are essentially identical. Since a marked difference in the high-temperature thermal behavior is only observed for **3** as compared to **1** and **2** in the TPXRD measurements, the following discussion will exemplarily be focused on the thermal decomposition of **2** and **3**.

The measurements were performed on samples heated to the respective temperatures in sealed glass or quartz ampoules. The composition of the resulting graphitic materials according to elemental analysis was C, 34.49; N, 61.38; H, 1.86 for **2** and C, 35.45; N, 62.42; H, 1.72 for **3**, with the difference from a total of 100 wt% being presumably due to the presence of small amounts of oxygen. Contrasting the sequence of spectra obtained for **2** (Fig. 5.42, left) and **3** (Fig. 5.42, right), the following noticeable aspects may be pointed out:

As **2** is heated, the bands characteristic of both the tricyanomelamine core and the cyanamide moiety decrease continuously. However, the sharp band around  $800\text{ cm}^{-1}$  fea-

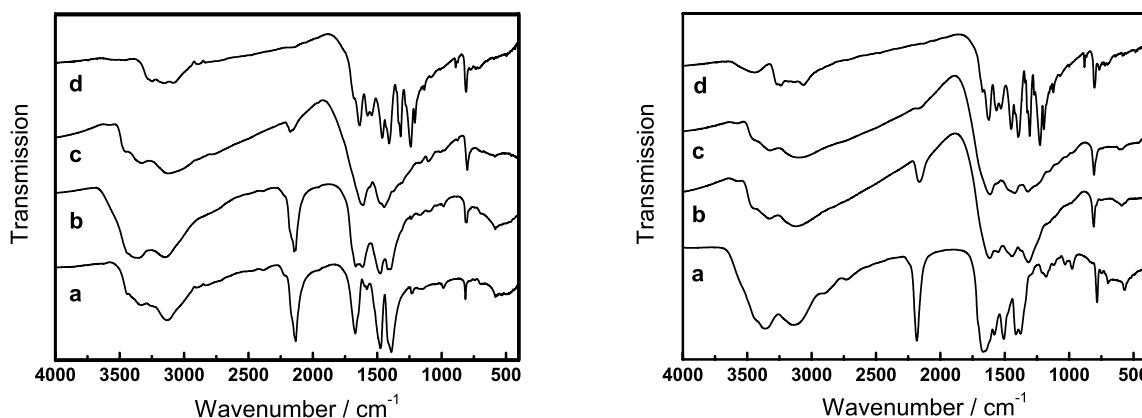


**Figure 5.42:** IR spectra of **2** (left) and **3** (right) before (a) and after ((b) – (d)) thermal treatment in sealed glass ampoules. Spectra are shown exemplarily for the decomposition products at 470 (b), 550 (c), and 740 K (d) for **2** and at 500 (b), 570 (c), and 890 K (d) for **3**.

turing the ring breath vibration typical of both triazine and heptazine cores persists, though slightly broadened, throughout the decomposition process. Interestingly, the formation of melem is indicated already around 500 K by the appearance of a strong absorption around  $1610\text{ cm}^{-1}$ , a minor absorption at  $1107\text{ cm}^{-1}$ , and the disappearance of the TCM and guanidinium bands at  $1669$  and  $1390\text{ cm}^{-1}$ . The band at  $1475\text{ cm}^{-1}$  splits up into a broad doublet originating from the triamino-heptazine (melem) vibrations.

At 550 K, the spectrum is almost entirely dominated by the heptazine vibrations, with the low energy flank being slightly broadened ( $1350$  –  $1200\text{ cm}^{-1}$ ), thus mapping the envelope of the high-temperature absorption pattern. The well-resolved spectrum at 740 K shows strong absorption between  $1636$  and  $1240\text{ cm}^{-1}$  as well as the ring breath at  $809\text{ cm}^{-1}$ , suggesting the polymeric material to be fairly well-ordered on the molecular level.

While the thermal behavior of melaminium tricyanomelamine (**3**) appears to be largely equivalent, amorphization commences earlier, leading to the rapid disappearance of the  $\nu(C\equiv N)$  vibrations and, notably, to a significant broadening in the  $\nu(C-N)$  region around  $1320\text{ cm}^{-1}$  at temperatures as low as 500 K. This feature is accompanied by pronounced absorption around  $1620$ ,  $1550$  and  $1440\text{ cm}^{-1}$ , the pattern being reminiscent of the triazine absorption as found in melamine. Simultaneously, the characteristic ring breath, which is located at  $782\text{ cm}^{-1}$  in the starting material, is shifted to  $807\text{ cm}^{-1}$ , thus substantiating the deprotonation of the initially mono-protonated triazine rings.

The essence of the above observations may be interpreted in line with the formation of an intermediate low-temperature phase, exhibiting a significant degree of cross-linking between intact triazine cores as indicated by the pronounced absorption below  $1400\text{ cm}^{-1}$ . Low ther-

mal stability of this intermediate phase is inferred by its facile conversion into melem above 580 K when extending the heat treatment in sealed glass ampoules to several hours.

Thus, the thermal decomposition behavior of **3** may be rationalized by assuming significantly differing decomposition pathways under kinetic or thermodynamic control; the gradual shift between these leads to the superposition of features characteristic of both the assumed polymeric low-temperature phase and melem. Therefore, although neither melamine nor melem were detected by thermoanalytical and *in situ* X-ray investigations of **3**, the successive formation of both precursors could unambiguously be established when conducting the reaction in ampoules under pressure of ammonia.

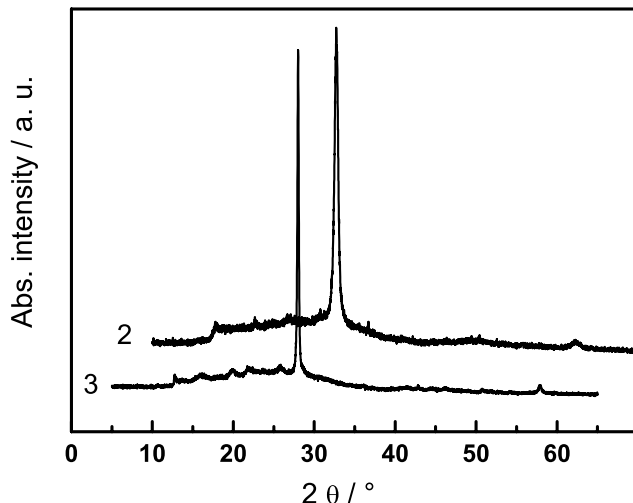


**Figure 5.43:** X-ray powder patterns ( $Cu - K_{\alpha 1}$  radiation) of the final decomposition products of **2** (top) and **3** (bottom). The top curve is drawn with an offset of  $2\theta = 5^\circ$  with respect to the bottom curve. Both materials exhibit a similar pattern of broad low-intensity peaks between  $2\theta = 10^\circ - 27^\circ$  and a single sharp reflection at  $2\theta \approx 27.8^\circ$ , corresponding to an average interlayer distance of approximately 320 pm.

This is in accord with previous studies [124], where thermodynamically controlled reactions effecting the formation of melem are predominantly encountered when working in closed systems under  $NH_3$  back pressure. In spite of the differing low temperature decomposition behavior of **2** and **3**, the final decomposition products of **2** and **3** are essentially identical as demonstrated by their IR spectra (Fig. 5.42, top spectra). As further evidenced by the respective XRD patterns (Fig. 5.43), the high-temperature decomposition products exhibit a pronounced graphitic character, the single reflection at  $2\theta = 27.7 - 27.9^\circ$  corresponding to an interlayer distance of  $\approx 320$  pm.<sup>3</sup>

<sup>3</sup>The discrepancy with the d-value stated above ( $12.1^\circ \equiv 336$  pm) was found not to be an intrinsic effect but rather to result from a temperature shift of the lattice parameters.

### 5.6.5 Solid-State NMR

$^{15}N$  CP-MAS solid-state NMR experiments were carried out with the high-temperature decomposition products of **2** and **3**. The latter are shown in Figure 5.44, together with the decomposition product of  $^{15}N$  melamine (top), all of which were obtained in sealed quartz ampoules at 740 K (**2**) and 890 K (melamine and **3**). In spite of the semi-amorphous character of all products, which are characterized by their X-ray powder patterns exhibiting only one single sharp reflection around  $2\theta = 27.8^\circ$  (Fig. 5.43), the appearance of their NMR spectra is strikingly well-resolved and, at the same time, largely identical. A similar reaction product of melamine and **2** may be ascribed to the favored formation of melem as a high-temperature crystalline intermediate observed during the pyrolyses of both melamine and **2** under various conditions (Figs. 5.40 and 5.41). Thus, the spectral features in both cases simply represent the decomposition product of melem, though obtained at different temperatures. Notably, as indicated previously when discussing the vibrational spectra (Fig. 5.42), comparison with the middle spectrum reveals the decomposition of **3** to yield the same product, which could not be anticipated solely on the basis of the DSC and TPXRD measurements.

This adds to the interpretation of the thermal conversion of **3** to proceed *via* melem, if thermodynamic conditions (NH<sub>3</sub> back pressure, high temperature, long reaction time) can be premised. A qualitative interpretation of the isotropic chemical shifts observed can be

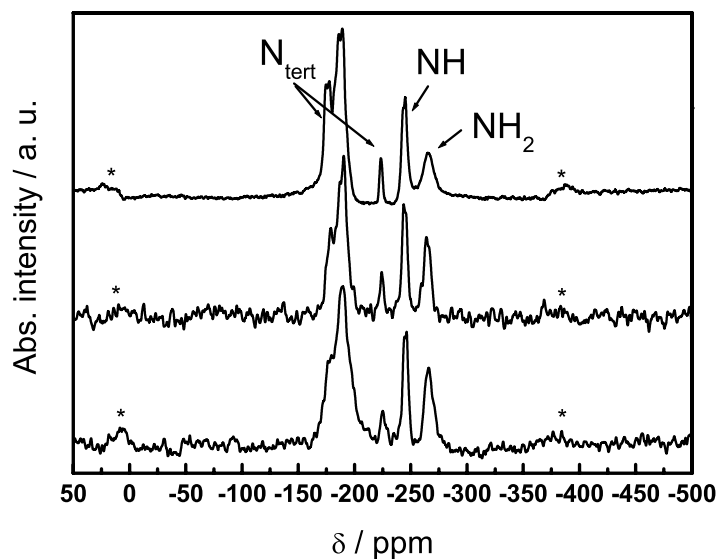


**Figure 5.44:**  $^{15}N$  CP-MAS solid-state NMR spectra of the final decomposition products of **2** (740 K, bottom) and **3** (890 K, middle). In the top spectrum the pyrolysis product of  $^{15}N$  enriched melamine at 890 K is shown. Spinning sidebands are denoted with an asterisk, the rotation frequency was 10 kHz.

put forward by analogy with the  $^{15}N$  CP-MAS NMR spectra of the model systems melem and melamine, respectively, as discussed previously by *Jürgens et al.* and will be outlined in Chapter 7 on page 280 [82, 240]. Firstly, comparison of the basic signal patterns allows for the differentiation into tertiary ( $-195$  and  $-225$  ppm), secondary ( $NH$ ,  $-246$  ppm) as well as amino ( $NH_2$ ,  $-266$  ppm) nitrogen atoms, which is clearly supported by CPPI measurements using the decomposition product (Fig. 5.44, top) of a  $^{15}N$  enriched sample of melamine. Secondly, a noteworthy similarity between the chemical shift spectrum of melem and that of the decomposition products of **1** – **3** is evident, on the basis of which the assignment of the signals in Figure 5.44 is feasible. In particular, the unique  $N_{tert}$  resonance at  $-225$  ppm, which is located at  $-234$  ppm in melem but is absent in the spectrum of melamine, is likely to represent the central nitrogen atom of condensed heptazine cores.

According to these findings, the heptazine-based structure of melem is likely to be preserved in the final products, yet further evidence supporting this hypothesis will be presented in Chapter 7 on page 280.

### 5.6.6 Discussion

The results of the previous discussion will shortly be summarized in view of the issues set out in section 5.6.2 on page 185. First, the thermal decomposition of the tricyanomelamine salts presented above appears to be markedly different from that of metal-containing TCMs [240]. While the latter have been found to become completely X-ray amorphous at elevated temperatures, leading to unidentified products [126, 240, 428], a common well-defined reaction product was obtained for compounds **1** – **3**. Combined diffraction, thermoanalytical as well as spectroscopic investigations indicate layered  $CN_xH_y$  materials to be formed as high-temperature decomposition products, corresponding to those commonly denoted as “graphitic carbon nitride” in the literature.

As to the correlation of the local structure of the pyrolysis products with that of the starting materials, evidence is put forward for the transformation of the triazine building blocks into heptazine rings as a result of thermal condensation processes. This fact can unambiguously be derived from the TPXRD patterns recorded for **1** and **2**, where melem is observed as high-temperature crystalline phase between 650 and 770 K. For **3**, however, reflections pertaining to melem are absent in the TPXRD measurements, and the intermediate formation of a hypothetical metastable, triazine-based networked phase at low temperatures may tentatively be inferred on the basis of IR spectroscopic investigations. Principally, though differing markedly in the low temperature region, the decomposition pathway of **3** appears to gradually conform to that observed for **1** and **2** at elevated temperatures and  $NH_3$  back pressure. Thus, decom-

posing **3** in closed systems clearly promotes the formation of melamine and melem, ultimately leading to a reaction product identical with those obtained from **1** and **2**. The conservation of the triazine units at temperatures beyond  $\approx 600$  K can therefore be discarded under the reaction conditions applied here, even if a preformed, purely triazine-based structure is used as molecular precursor. This is particularly noteworthy in the case of **3**, which is composed of potentially nucleophilic melamine units as well as tricyanomelamine rings containing electrophilic cyanamide moieties, both of which may be capable of mutually interlinking upon heating.

The thermodynamically favored formation of melem therefore seems to be the driving force dominating the thermal reactivity of  $\text{CN}_x$ -based precursors in the high-temperature regime, suggesting purely triazine-based structures to become unstable and to essentially yield layered compounds made up from heptazine building blocks. If, however, the resulting polymer is identical with melon  $[\text{C}_6\text{N}_7(\text{NH}_2)(\text{NH})]_n$  ( $\equiv [\text{C}_2\text{N}_3\text{H}]_n$ ), or if the graphitic carbon nitride material is based on a larger 2-D polymer of only partly condensed heptazine cores and frequent  $\text{NH} / \text{NH}_2$  terminations within the layers, or if extended sheets of fully condensed heptazines are formed, which are terminated by  $\text{NH}$  and  $\text{NH}_2$  groups at the layer-edges, will be the subject of further studies presented in Chapter 7 on page 280.

## 5.7 Preliminary Conclusion

In the previous chapter several dicyanamides and tricyanomelamines have been introduced, which all have the capability of transforming into  $\text{CN}_x\text{H}_y$  polymers upon thermal treatment. For all potential precursors, the reaction pathways were studied in the context of their molecular composition and inherent reactivity, and a qualitative picture of the intermediate stages and final products could be drawn.

Comparing all model systems presented above, their common behavior is highly visible: Starting from the different precursors, any one of them transforms into melamine during thermal treatment, irrespective of their principal chemical identity and stoichiometry. In fact, as particularly observable for oxygen containing precursors, the composition plays only a minor role with respect to the reaction products, as volatile species during the transformation must not be ignored.

In general, the tendency towards formation of melamine is striking, the latter representing a thermodynamic drain with a particularly beneficial energy balance at elevated temperatures (Fig. 5.45). The triazine ring system is highly stable until the formation of the heptazin ring is favored at even higher temperatures. Since all thermal treatments invariably yield melamine as a common intermediate or the final product, depending on the temperature range, the

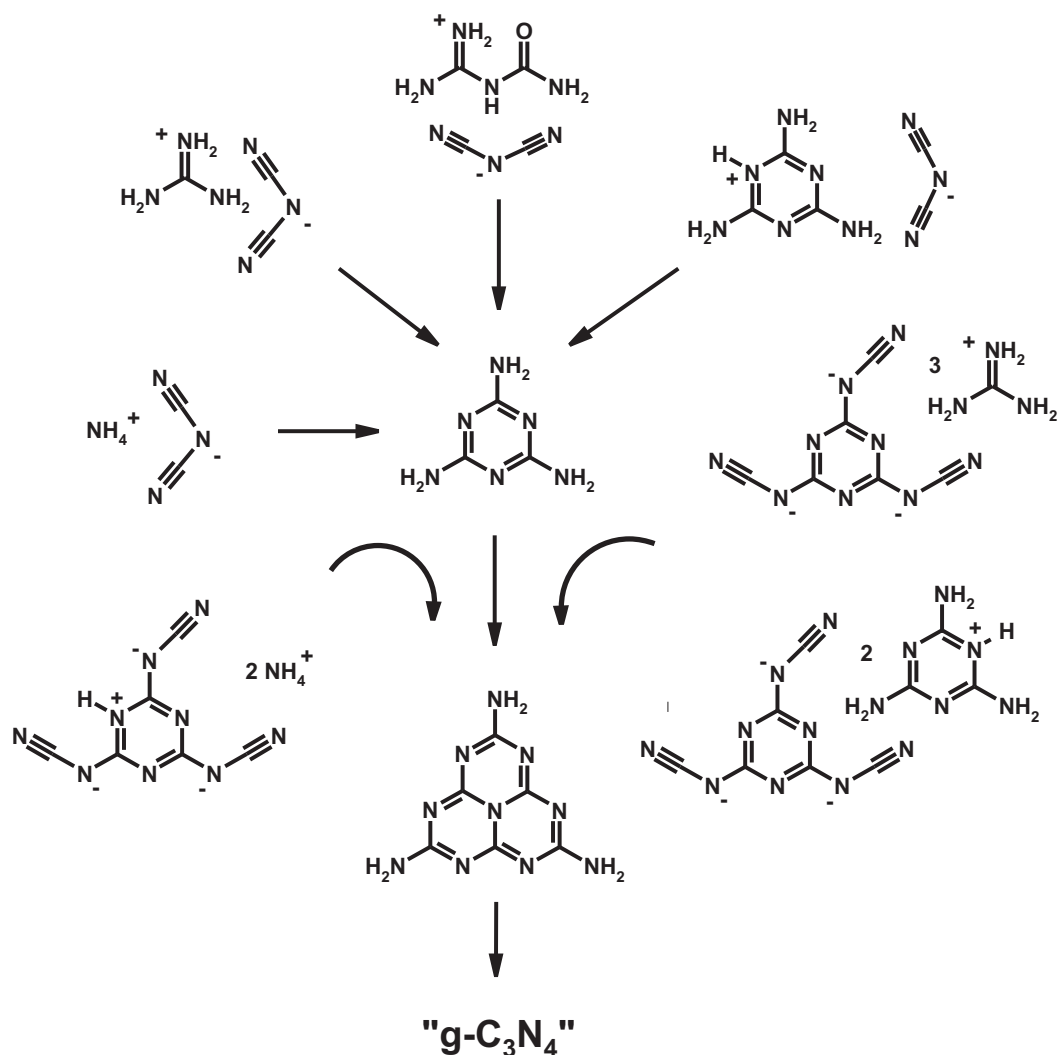


**Figure 5.45:** Thermal transformation of various  $CN_x$  precursors into the thermodynamic “drain” melamine, irrespective of their exact chemical composition. Melamine then further transforms into the heptazine-based compound melem, which finally decomposes into “graphitic carbon nitride”.

suitability of the above precursors must be critically re-evaluated:

Although the reactivity may be higher and, hence, the respective transformation temperatures of the model systems into graphitic  $CN_x\text{H}_y$  polymers may be lower as compared to those of melamine, the simple composition and easy availability of the latter by far outperform the advantages of the dicyanamide- and TCM-based precursors. In addition, unwanted side products, especially prominent if hydrated species are thermolysed in closed systems, can be excluded if melamine is used as starting material.

It should, however, be noted that melamine can only be formed if hydrogen is present in the sample, requiring a hydrogenated cationic species, as has been used in the above cases.

It may be argued that hydrogen-free  $\text{CN}_x$  networks may be accessible by making use of hydrogen-free precursors, yet most examples reported so far suffer from complete amorphization of the resulting polymers, from inappropriate C:N ratios usually higher than the desired value of 0.75 for g-C<sub>3</sub>N<sub>4</sub>, or from inclusion of heteroatoms other than hydrogen into the sample [42, 63, 65, 454, 455].

Therefore, the route towards carbon nitride polymers presented in the previous chapter constitutes one out of several possible pathways, with the focus being on the analysis and description of the intermediate stages passed during *controlled* thermal treatment of *stable* and *easily accessible* starting materials.

The above line of argument may be concluded by stating the necessity of understanding in great detail the thermal reactivity of melamine, as this prototypic  $\text{CN}_x$  precursor was found to represent the least common denominator of all model systems under study. Therefore, the next chapter will build upon the previous one in focussing the discussion on this important “intermediate”, trying to bridge the gap between the model systems studied in Chapter 5 and the carbon nitride material presented in Chapter 7.

## Chapter 6

# Carbon(IV)Nitride Precursors III. On the Existence and Formation of Melam

In Chapter 5 the thermal behavior of various dicyanamide and tricyanomelamine precursors has been studied and evaluated in terms of their suitability for the synthesis of extended carbon nitride networks. It was pointed out that the thermal transformations are inevitably governed by the thermodynamically favored formation of melamine as a common intermediate, thus reducing the complexity of the different precursor systems to one single “prototype” precursor. As a next step, the thermal behavior of this key intermediate as discussed in the literature will be surveyed, and attempts to critically evaluate and possibly unify the diverging opinions will be made.

In this context, a central question pertains to the existence and role of melam in the pyrolysis process of melamine, which has not yet satisfactorily been settled. Though formally representing a simple condensation product of melamine and thus being of fundamental importance for the understanding of the ternary system C/N/H, its ways of formation and molecular as well as crystal structure are not yet agreed upon or available.

A major task of this work has therefore been the re-investigation of the processes constituting the pyrolysis of melamine, and the characterization of the encountered intermediates. As much progress has been made recently with respect to the formation and solid-state structure of melem [82, 240], the focus of this work will be on the “missing members” of the pyrolysis process of melamine, namely melam and polymers of melem. The possible formation and identity of melam will be subject of the following chapter, whereas that of melon will be treated separately in Chapter 7.

## 6.1 Introduction

Melam was first prepared in 1834 by *Liebig* on heating an intimate mixture of potassium thiocyanate and an excess of ammonium chloride at temperatures around 580 – 640 K until all volatile products were given off. From the grayish-white fusion product a compound was isolated after treatment with moderately concentrated potassium hydroxide solution, which was arbitrarily given the name “melam” by *Liebig*. On boiling melam in “caustic potash” solution for several hours, two unknown hydrolysis products were obtained, which were named “melamine” and “ammeline” [456]. Investigations of the thermal behavior of the above weak bases led *Liebig* to the discovery of two further insoluble compounds of the empirical formulas  $C_6N_{10}H_6$  and  $C_6N_9H_3$ , which were given the similarly unintuitive names “melem” and “melon”, respectively. They were conceived as condensation products of melamine, which form on successive elimination of ammonia from the starting material.

In the following years, much effort was devoted to the elucidation of the composition and structure of melamine and its pyrolysis products, which however was hampered by conflicting statements with respect to their elemental composition, ways of formation, and, above all, molecular structures [76,80,304,457]: Although general agreement had been achieved on their principal nature in that they may be considered as derivatives of cyanamide according to the general formula  $(CNH_2)_n \cdot m NH_3$ , suggestions for their structures were put forward at a much later date [76,80]. Likewise, whereas the identity of melamine was resolved by the elucidation of its crystal structure in 1941 [458], chemical inertness and low solubility of its condensation products has impeded the characterization apart from elemental analysis ever since their early discovery and despite the comparatively easy availability. Only recently the crystal structure of melem was solved from X-ray powder data [82], thereby putting an end to the long-standing debate about its heptazine-type structure [76, 77, 80, 459–461], and at the same time giving valuable incentives to the ongoing quest for graphitic carbon nitride (cf. Chapter 7 on page 280) [42,82,85,124,127].

Melam has been considered as the low-temperature de-ammoniation product of melamine, which is formed upon linking two molecules of melamine with concomitant release of one mole ammonia. The resulting “ditriazinylamine”-type structure model was set out as early as 1886 by *Klason* and accepted by later investigators [76,80,462], born out predominantly by its hydrolysis with 30 % aqueous ammonia to form ammeline and melamine [409,424]. Doubts on the correctness of this structure proposition were cast by several unsuccessful attempts to obtain melam by pyrolyzing melamine, the products of which were identified as melem by IR and UV spectroscopy based on the absorptions characteristic of cyameluric nuclei (“ $C_6N_7$ ”) [77,460,461,463,464]. In detail, *Finkel'shtein* noted the sharp spectral differences for

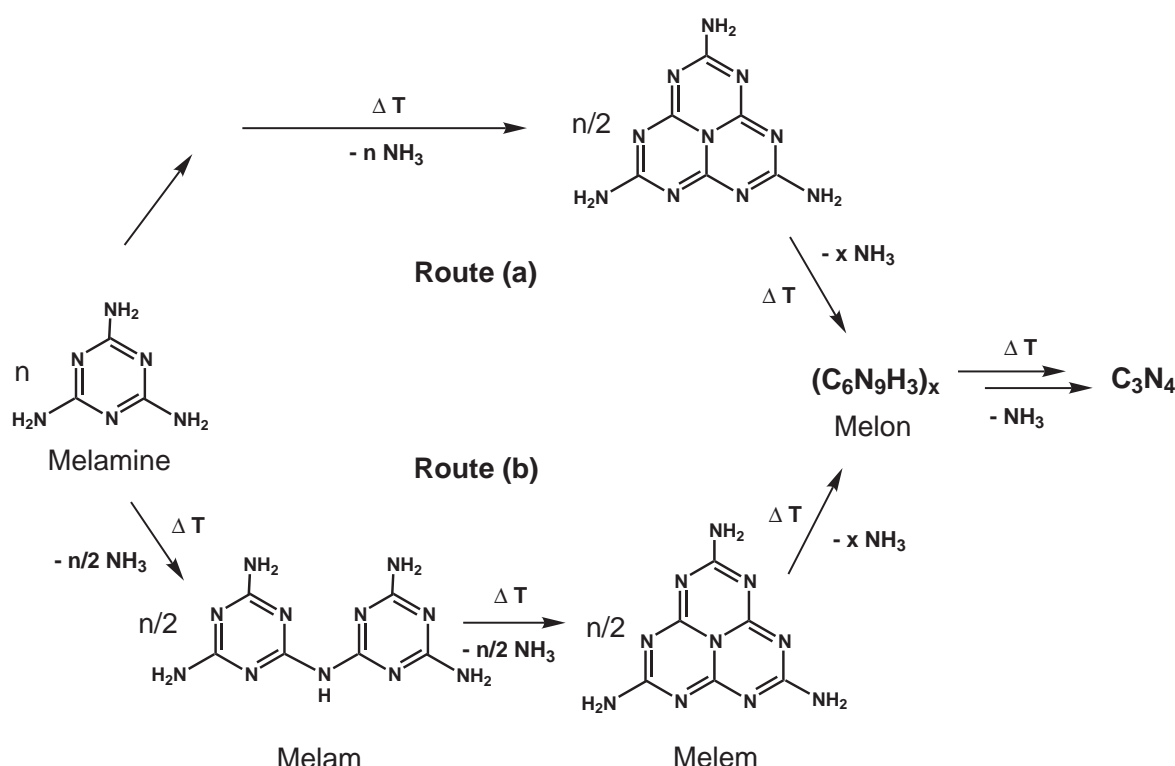


**Figure 6.1:** Schematic representation of the two pathways proposed for the thermal decomposition of melamine. Route (a) assumes direct formation of melem from the first condensation step, whereas according to route (b) melam is obtained prior to melem formation. Further loss of ammonia may yield polymers of melem (“melon”) and, ultimately, graphitic carbon nitride.

the de-ammoniation product from the spectrum of melamine, as well as the absence of a band at  $1560 \text{ cm}^{-1}$  in the IR spectrum typical of *s*-triazine derivatives [460,463]. These findings were corroborated by the hydrolysis of the de-ammoniation product in alkaline solution, yielding potassium cyamelurate rather than ammeline or ammelide derivatives [460]. In contrast, based on elemental analysis *May* reported on the isolation of melam, melem, and melon as the pyrolysis products of melamine obtained at 633, 673, and 773 K, respectively [459]. Thus, two alternative schemes have been proposed in the literature for the condensation process of melamine:

Route (a) is based on the formation of melem as the first condensation product, giving rise to a ratio of melamine to liberated ammonia of 1:1. Melem then affords the polymeric condensate melon, the identity of which has not been resolved as yet. [460,461,463]. Melon may further lose ammonia to form graphitic carbon nitride  $\text{g-C}_3\text{N}_4$ . In route (b) melamine progressively condenses to give melam (melamine : ammonia = 2:1), which then further fuses to melem and, *via* melon, to  $\text{g-C}_3\text{N}_4$  (Fig. 6.1) [459,465–467].

While the originally proposed formula for melam as sketched in Figure 6.1 has long been ac-

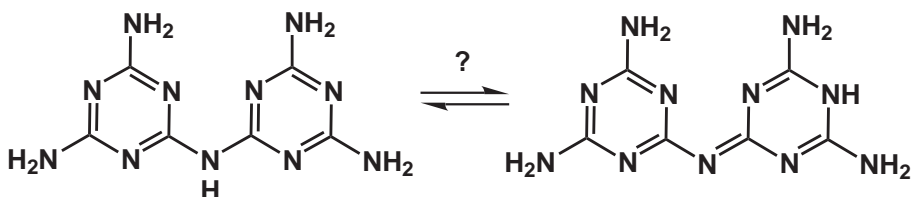


**Figure 6.2:** Two alternative tautomeric forms discussed for melam. The conjugated form (right) exhibits a chinoid triazine ring system.

knowledged, an alternative tautomeric form was introduced, accounting for resonance within the two triazine rings (Fig. 6.2) [79, 460, 465].

Despite the above controversy, reports have been published on the synthesis of melam based on combinations of melamine with electrophilic triazine-derivatives such as chloro-diamino-triazine [79], or from melamine in the presence of acids [77, 468].<sup>1</sup> By these authors the synthesis of several acid salts of melam, among which being melam hydrochloride hydrate, melam sulphate, melam nitrate, melam perchlorate and melam phosphate hydrate [77], as well as a zinc salt of assumed formula  $Zn^{2+}[C_6N_{11}H_8]^-$  [468], was claimed, however without giving any analytical data apart from elemental analysis in the latter case. *Jürgens* reported on two adduct compounds with notional formulas  $[C_6N_{11}H_{10}]Cl \cdot 0.5 NH_4Cl$  and  $[C_6N_{11}H_{10}]Br \cdot 0.5 NH_4Br$ , which were thoroughly characterized by IR, NMR and mass spectroscopic investigations [240]. *Costa et al.* had previously investigated the thermal behavior of melamine salts, thereby coming across an assumed melam hydrobromide of empirical composition  $C_6N_{11}H_9 \cdot HBr$ . However, no further studies on the postulated melam salt were carried out [469].

*Schnabel* already opened access to substituted melams by fusion of alkyl-substituted amino-triazines with chloro-triazines, which afforded hepta-, octa-, or nona-substituted melams, depending on the substituents. Utilizing this method, melam derivatives composed of three *s*-triazine nuclei have been prepared [467]. Chloro-derivatives of melam containing the amines  $HN(C_3N_3Cl_2)_2$  and  $N(C_3N_3Cl_2)_3$  were recently obtained by the reaction of melamine with cyanuric chloride [470]. Whereas the former crystallizes as an adduct with cyanuric chloride in  $HN(C_3N_3Cl_2)_2 \cdot C_3N_3Cl_3$ , the latter has first been synthesized by *Vodak et al.* and is being discussed as a potential intermediate in the formation of polymeric  $C_3N_4$  compounds [66, 470]. Presently melam and its derivatives are under consideration for flame-retardant formulations owing to their exceptional thermal stability and decomposition properties [471–473].

<sup>1</sup> *Finkel'shtein* and co-workers stated that “the synthesis of melam from melamine [...] is realized more successfully in the presence of zinc chloride if the melamine is submitted to reaction with acids or with substances which release acids under conditions of heating in the solid phase (the ammonium salts of mineral acids) before heating or during heating [...]” [77].

According to the literature data assembled above, the knowledge on the formation of melam from melamine, as well as its molecular structure, is scarce and subject to much controversy. In the following section we will re-evaluate the thermal behavior of melamine and present an alternative view on the formation and existence of melam.

## 6.2 Thermal Behavior of Melamine

A crucial factor when investigating the thermal behavior of melamine is the choice of the reaction conditions. Typically, such studies have been conducted in closed systems, as melamine exhibits a strong tendency toward sublimation above 570 K, which is peaking at 618 K. A lack of clarity, however, remains with regard to the processes taking place in this temperature range if melamine is kept in sealed tubes, as it has not yet been specified as to whether or what extent it undergoes sublimation [461], melting [460,464] or decomposition along the lines sketched above.

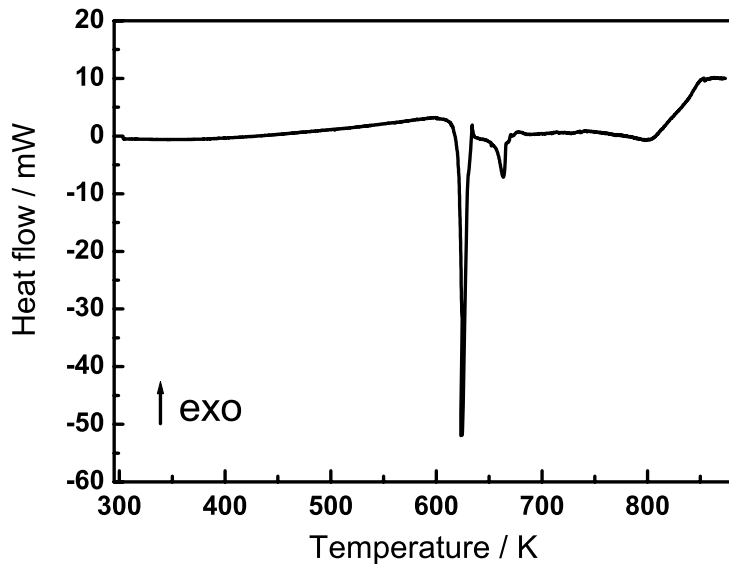


**Figure 6.3:** Differential scanning calorimetry conducted with melamine between RT and 873 K. The sample was contained in a cold-welded aluminium crucible, which was heated under an atmosphere of nitrogen.

Calorimetric measurements of melamine have been extensively discussed in ref. [240] and will therefore be treated only briefly. DSC measurements were conducted in cold-welded, only moderately pressure-resistant aluminium crucibles with a heating rate of  $1 \text{ K min}^{-1}$ . The DSC curve shows two major thermal events at 620 and 660 K, and a weak and broad signal around 800 K, all of which having an endothermic heat of reaction. The slight slope in the baseline

prior to the first exothermic signal can be rationalized by assuming continuous sublimation of the sample, which reaches its maximum at 620 K. Presumably, sublimation of the sample and the onset of thermal decomposition are interdependent, reinforcing each other *via* the gas phase (Fig. 6.3). The signal at 660 K may either be due to the formation of melem or pre-stages thereof which will be subject of the following section 6.3 on page 203. The broad signal with a minor heat turnover and an onset around 750 K may be due to cross-linking or decomposition of melem.

In addition, we have performed TPXRD measurements with heating rates of  $1 \text{ K min}^{-1}$  in a temperature range between 295 and 933 K (Fig. 6.4). It should be noted that heating a sample in an open quartz capillary affords conditions similar to those in closed systems as has been observed previously [124]. Therefore, the term “semi-closed system” will be used for this experimental set-up.

Contrary to previous TPXRD experiments [240], at least four phase transformations are observed. The reflections of melamine disappear at 590 K without passing through an amorphous state, with the new phase being stable until  $\approx 630$  K. At this temperature, new reflections gradually appear, however the phase change is defined rather poorly. Melem is formed around 653 K being stable until  $\approx 780$  K, where a single broad reflection characteristic of graphitic carbon nitride materials emerges, again without passing through the melt.

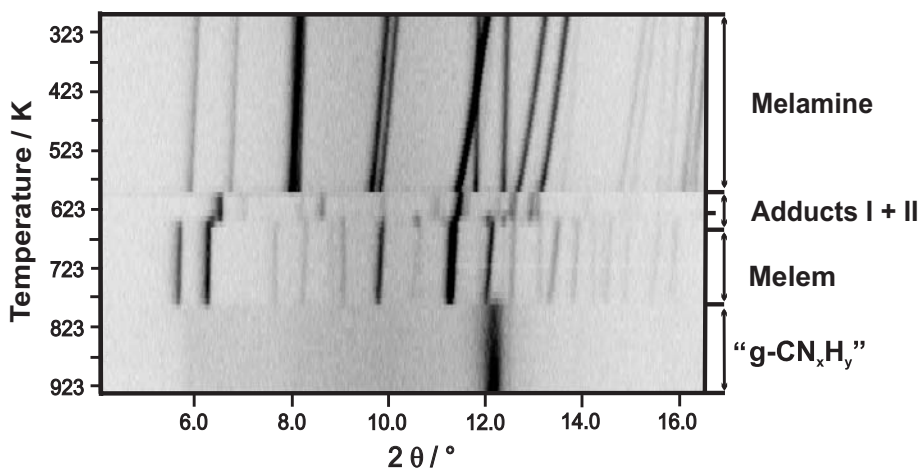


**Figure 6.4:** *In situ* temperature programmed X-ray powder diffraction measurements (Mo- $K_{\alpha 1}$  radiation) of melamine, recorded between RT and 923 K. Four phase transitions are observed prior to the formation of a graphitic carbon nitride material visible by a broad reflection at  $2\theta \approx 12.1^\circ$  ( $d \approx 336 \text{ pm}$ ).

When comparing with the above literature survey (cf. Fig. 6.1 on page 198), route (b) conforms quite well to these observations, whereas the direct formation of melem from melamine without the formation of detectable intermediates (route (a)) can be discarded under these conditions. The observed low-temperature (LT) phase transition may tentatively be associ-

ated with the proposed formation of melam, which however does not account for the second phase change (HT phase transition) observed at 630 K prior to the formation of melem.

*Jürgens* also reported the emergence of two intermediate phases, which were characterized by X-ray powder diffraction and mass spectrometry, but could not be isolated as pure phases [240]. According to these studies, no evidence of the formation of melam was found, but only the mass peaks of melamine ( $m/z = 126$ ) and melem ( $m/z = 218$ ) were found in the DEI+ mass experiments.<sup>2</sup> At this stage it should be noted that in ref. [240] the succession of the phases is reversed as compared to the present study, i.e. the phase named “phase 1” by *Jürgens* is observed as the high-temperature phase, whereas “phase 2” is formed directly from melamine.

A possible explanation could be the strong dependence of the phase formation on both temperature *and* time, as the second phase is formed by *isothermal* treatment from the low-temperature phase, the same applying to the formation of melem from the high-temperature phase. These observations were made by heating 200 mg of melamine in sealed glass tubes of

<sup>2</sup>It will be shown in sections 6.4 on page 213 and 6.5 on page 226 that the mass peak of melam ( $m/z = 235$ ) can in fact be observed in the DEI+ experiments if melam or melam derivatives are present in the sample.

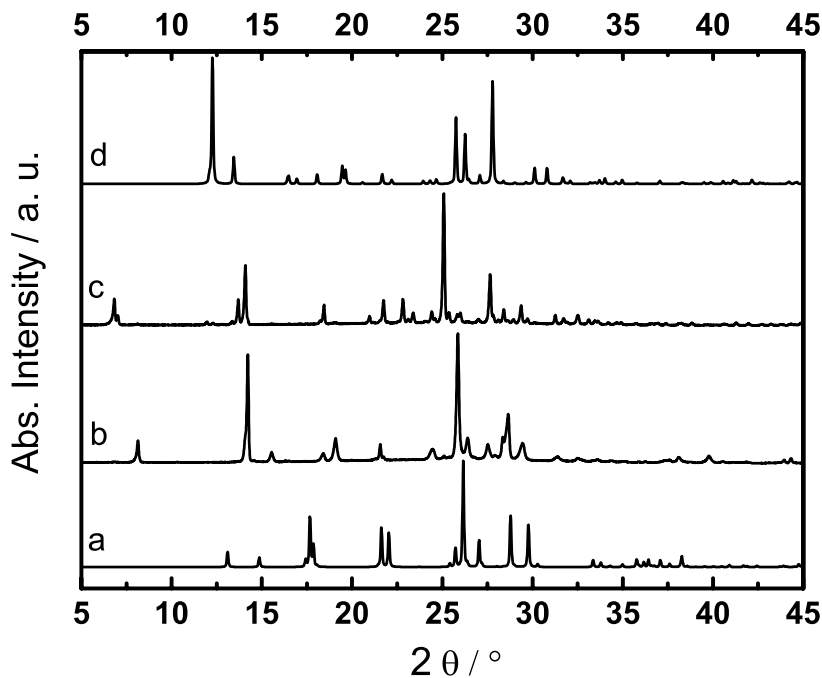


**Figure 6.5:** X-ray powder patterns, displayed for a  $2\theta$  range of  $5 - 45^\circ$  ( $\text{Cu}-\text{K}_{\alpha 1}$  radiation), of melamine (a), phase I (b), phase II (c), and melem (d) recorded at RT. All compounds exhibit well distinguishable powder patterns indicative of distinct crystallographic phases.

12 cm length placed in a vertical tube furnace to different temperatures between 630 and 660 K, and heating for different periods of time (LT-phase:  $\approx$  2.5 h; HT-phase  $\approx$  14 h).

Preparing the HT-phase without impurities by the LT-phase is particularly demanding and requires careful adjustment of the heating time. As only the low-temperature phase (“phase 2”) was observed in the TPXRD measurements carried out by *Jürgens*, no reference for the sequence of phase formations was available. Thus, if the time dependence of these transformations is neglected and only the absolute temperature is varied in an interval of less than 20 K [240], the “wrong” phase may easily be obtained when heating melamine on a preparative scale. After optimizing the heating conditions, both phases could be isolated in a pure state without admixtures of melamine, melem, or the LT / HT phase (Fig. 6.5). All efforts to index the powder patterns or grow single crystals were unsuccessful, by which reason the characterization of the two phases had to be primarily based on spectroscopic methods.

## 6.3 Adduct Phases

In order to not confuse the nomenclature introduced by *Jürgens* with that applicable here, we will refer to the LT-phase as phase I and to the HT-phase as phase II.

### 6.3.1 Mass Spectrometry

As a first step, mass spectrometry was carried out; the results are shown in Table 6.1. Although no quantitative information on the composition of the two compounds can be extracted, details on possible constituents may be furnished.

**Table 6.1:** Mass spectrometry data for phases I and II and those expected for melamine, melem, and melam.

Compound	<i>m/z</i> (rel. intensity, %)
phase I	126.1 (100) <sup>a</sup> , 218.1 (100) <sup>a</sup>
phase II	126.1 (62), 218.1 (100)
melamine	126.1 (100)
melam	235.1 (100)
melem	218.1 (100)

<sup>a</sup> successive scans

According to these results, which conform to the observations made by *Jürgens* [240], strong evidence is put forward for melamine and melem instead of melam to actually constitute the phases under consideration. Nevertheless, melam could be “silent” to DEI+ experiments due to facile rupture of the inferred bridging  $-\text{NH}-$  bond by rapid heating, giving rise to

$m/z = 126$  (melamine) instead if proton transfer reactions are possible in the ion source. This has been observed for instance in the case of the  $\text{ZnCl}_2$ -melam complex discussed in section 6.5.3.2 on page 249. However, melem cannot as easily be formed, since heat induced condensation to melem according to Figure 6.1 is by far less likely to occur than the cleavage of the amine bond. It can, however, not be totally excluded at this stage. The interpretation according to which the molecular mass peaks of melamine and melem are due to impurities of the latter being present in the sample is little convincing: no other potential molecular mass peaks are observed in the whole range scanned and the impurity portion cannot be larger than  $\approx 5\%$ , since no additional phase is observed in the X-ray powder patterns.

### 6.3.2 Elemental Analysis

The composition of both phases was determined by elemental analysis, yielding the results listed in Table 6.2. It gets immediately evident that the composition of phase I indeed closely corresponds to that of melam as stated by *May* and others [459]. The composition of phase II, however, does neither match that of melamine, nor that of melam or melem in first approximation.

Anticipating the results discussed below, the following noticeable item may be pointed out: In view of the fact that the elemental composition of melam is in between those of melamine and melem, it may be possible to obtain an identical composition by assembling melamine and melem in different ratios into a co-crystal. This has formally been done for two compositions corresponding to an 2:1 adduct as well as an 1:2 adduct of melamine and melem; the theoretically expected wt% of both are given in Table 6.2. Interestingly, the 2:1 adduct has

**Table 6.2:** Elemental analysis data for phases I and II, contrasted with those expected for melamine, melem, melam and co-crystals made up from melamine and melem in two different ratios.

Compound	N / wt%	C / wt%	H / wt%
phase I	65.93 (obs.)	30.56 (obs.)	3.63 (obs.)
2:1 adduct <sup>a</sup>	65.53 (theor.)	30.64 (theor.)	3.83 (theor.)
phase II	64.73 (obs.)	32.14 (obs.)	3.21 (obs.)
1:2 adduct <sup>b</sup>	64.77 (theor.)	32.02 (theor.)	3.18 (theor.)
melamine	66.67 (theor.)	28.57 (theor.)	4.76 (theor.)
melam	65.53 (theor.)	30.64 (theor.)	3.83 (theor.)
melem	64.22 (theor.)	33.03 (theor.)	2.75 (theor.)

<sup>a</sup> melamine : melem = 2 : 1

<sup>b</sup> melamine : melem = 1 : 2

exactly the same composition as melam, and is thus in agreement with the experimental data obtained for phase I. With the same accuracy the elemental compositions of phase II and the hypothetical 1 : 2 adduct coincide. In fact, these observations can nicely explain the results from mass spectrometry, in which only the molecular mass peaks of melamine and melem were found.

It should therefore be emphasized that an ultimate proof of melam formation solely based on elemental analysis data is intrinsically critical and demands for corroboration by complementary methods. This may entail the somewhat awkward case that correct experimental data result in the assignment of a wrong molecular formula, which may easily have occurred in conjunction with melam.

As will be shown below, the analytical data clearly suggest the adduct compounds to actually represent phases I and II rather than melam. However, it will be necessary to shed light on the exact chemical nature of these presumed adduct compounds and possible formation pathways, as will be done in the following.

### 6.3.3 IR Spectroscopy

The IR spectra of phases I and II are shown in Figure 6.6 (right), together with the spectra of melamine and melem (left) for comparison.

The principal absorption “envelopes” of phases I and II in the characteristic ring-stretching and NH<sub>2</sub>-bending region of strongest absorption between 1350 and 1700 cm<sup>-1</sup> are largely identical, apart from pronounced differences of the relative band intensities and splittings. Whereas for phase II (top) a split band is seen at 1600 – 1630 cm<sup>-1</sup>, this band is broadened and

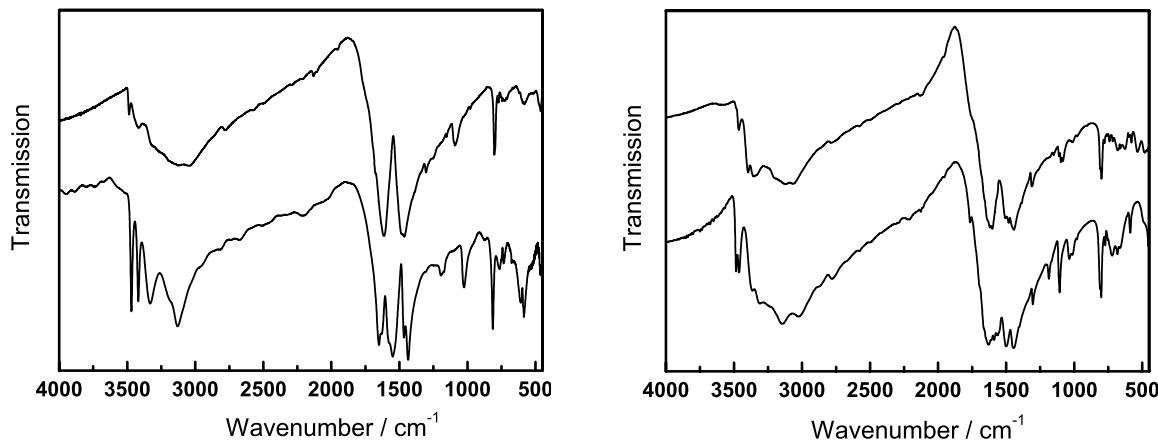


**Figure 6.6:** FTIR spectra of melamine (bottom, left) and melem (top, left) and of the LT phase I (bottom, right) and the HT phase II (top, right), measured in reflection geometry (neat solids).

slightly weaker in the spectrum of phase I (bottom). However, bands at  $1585$  and  $1561\text{ cm}^{-1}$  observed for the latter, which are typical of triazine-based compounds, are absent in phase II. Remarkably, whereas for melamine a band assigned to  $\delta(\text{NH}_2)$  is visible at  $1650\text{ cm}^{-1}$ , no absorption is found for both I and II higher than  $\approx 1630\text{ cm}^{-1}$ , which may be indicative of a significantly altered hydrogen-bonding network. This is supported by the fact that the sharp  $\nu(\text{NH})$  stretching vibrations for melamine at  $3468$  and  $3419\text{ cm}^{-1}$  are replaced by a weak, though sharp band centered at  $\approx 3464\text{ cm}^{-1}$  for I and II. In addition, the broad  $\nu(\text{NH})$  band found in melamine at  $3129$  and  $3329\text{ cm}^{-1}$  is red-shifted in I and II, similar to the situation encountered for melem. Phases I and II exhibit a strong *split* band around  $800\text{ cm}^{-1}$  attributable to the sextant bend of both triazine and heptazine rings, which is located intermediate between those found in melamine and melem.

In principle, similarities between the spectra of I and II and those of melamine and melem are evident, which is particularly true for phase II, where the resemblance with spectra obtained for heptazine-derivatives is significant [82, 240]. In addition, phase I contains spectral features characteristic of both triazine and heptazine nuclei in the ring-stretching region. Although no ultimate conclusions can be drawn from vibrational spectroscopy, the following aspects may be pointed out:

For melam one would expect more pronounced absorption in the  $\nu(\text{C}-\text{N})/\delta(\text{N}-\text{H})$  region between  $1200$  and  $1350\text{ cm}^{-1}$  [240], which is not observed for I and II.

A simple superposition of the spectra of melamine and melem can also be discarded (see also Fig. 6.5), as too many band shifts are observed for both phases relative to the former. Nevertheless, a particularly significant similarity between the spectrum of phase II and that of melem is evident. In addition, the over-all resemblance of the spectra for I and II suggests that the two phases are related with respect to their constituents.

### 6.3.4 NMR Spectroscopy

#### 6.3.4.1 Solid-State NMR Spectroscopy

NMR investigations have been carried out both in the solid state and in solution. The  $^{15}\text{N}$  solid-state NMR experiments severely suffer from the long relaxation times of the samples, rendering the signal/noise ratio rather low. Nevertheless, some important conclusions can be drawn from the experiments.

The  $^{13}\text{C}$  CP-MAS solid-state NMR spectrum of phase I shows two signal groups, one of which is located at  $155.3\text{ ppm}$ , and a split signal has maxima at  $166$  and  $168\text{ ppm}$  (Fig. 6.7, left). A similar spectrum, yet with a slight high-field shift of the signal group now centered around  $166\text{ ppm}$ , is obtained for phase II (Fig. 6.9, left). While the resonance at  $155.3\text{ ppm}$  is

unchanged, the intensity at 165.0 ppm is increased, and the signal portion around 167.4 ppm is reduced with respect to phase I. Both “patterns” contain features reminiscent of melem (middle curve) [82, 240], whose peaks are located at 155.1/156.0 ppm and 164.3 – 166.4 ppm, and melamine, which has two close-by signals at 167.5 and 169.2 ppm (bottom curve). Hence, from the  $^{13}\text{C}$  spectra of the two intermediates an increasing similarity with melem gets evident on going from phase I to phase II.

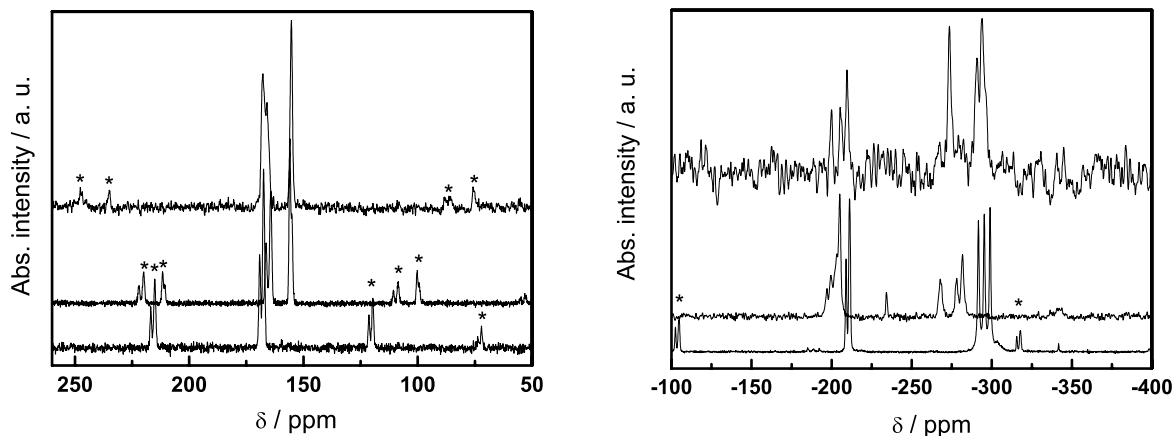


**Figure 6.7:**  $^{13}\text{C}$  (left) and  $^{15}\text{N}$  (right) CP-MAS solid-state NMR spectra of the LT phase I (top; recycle delay: 300 s;  $\tau_c$ : 4 ms for both measurements; spinning frequency 10 kHz) in comparison with melem (middle; recycle delay: 160 ( $^{13}\text{C}$ ) and 30s ( $^{15}\text{N}$ );  $\tau_c$ : 4 ms for both measurements; spinning frequency: 7 kHz) and melamine (bottom; recycle delay: 20 s;  $\tau_c$ : 8 ms ( $^{13}\text{C}$ ) and 4 ms ( $^{15}\text{N}$ ); spinning frequencies: 6 kHz ( $^{13}\text{C}$ ) and 5.5 kHz ( $^{15}\text{N}$ )). Spinning side bands are marked by asterisks.

The  $^{15}\text{N}$  spectrum of phase I shows peaks between –198 and –210 ppm and two signals in the high-field region (–274 ppm, doublet at –291/–294 ppm, Fig. 6.7, right). In order to assess their proton environment, a CPPI experiment has been carried out, which is shown in Figure 6.8. In agreement with their chemical shifts, the signal group around –200 ppm shows a much slower decrease in magnetization than do the signals below –270 ppm. The latter invert signs, passing through zero intensity at an inversion time of 60  $\mu\text{s}$ , which equals the polarization inversion behavior of previously investigated systems with  $\text{NH}_2$  groups (cf. section 5.6.1.3 on page 180) [82, 127, 194, 240]. Owing to their similar behavior, both high-field signals can thus be associated with  $\text{NH}_2$  groups, whereas the down-field signal group can be assigned to tertiary nitrogen atoms due to the slow polarization transfer. Furthermore, the signal characteristic of the central nitrogen atom of the heptazine ring is absent. It is considered likely that this may be simply due to the insufficient signal-to-noise ratio, rendering the observation of a single tertiary nitrogen signal futile.

Figure 6.7 (right) shows a synopsis of the  $^{15}\text{N}$  spectra of melamine, melem and phase I. The  $^{15}\text{N}$  spectrum of phase II exhibits both slightly different signal positions and numbers, with

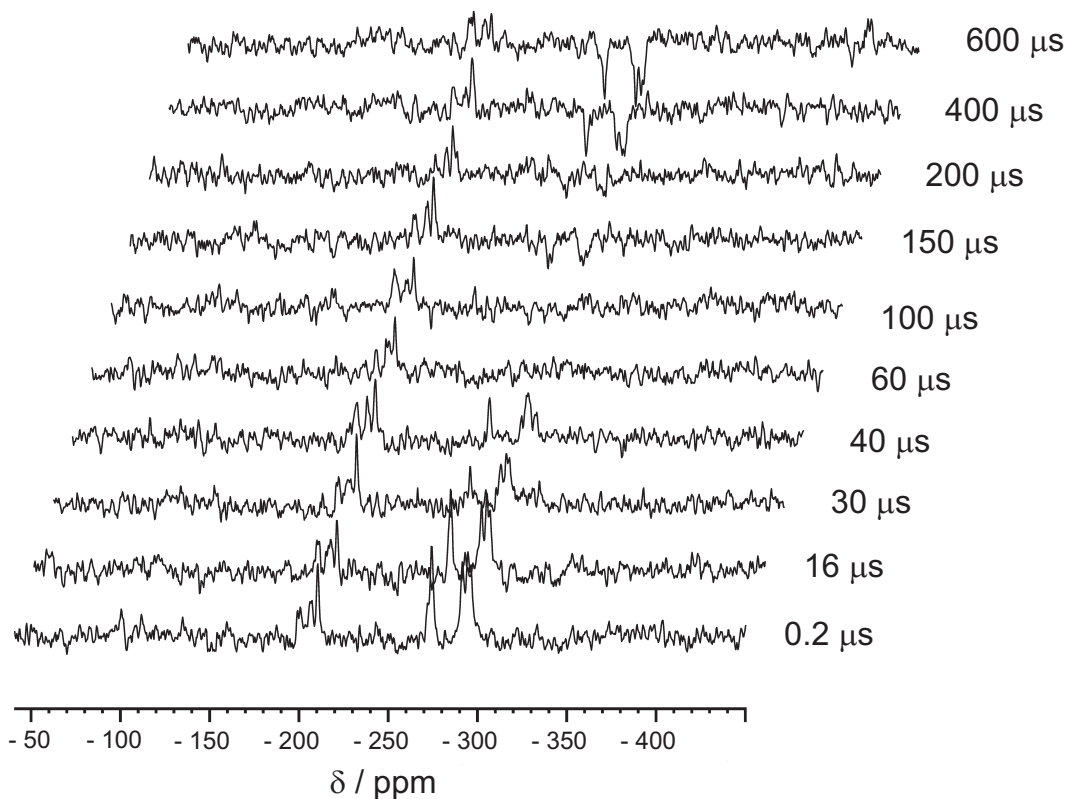


**Figure 6.8:**  $^{15}\text{N}$  2D CPPI solid-state NMR spectrum of the LT phase I (recycle delay: 300 s;  $\tau_c$ : 2 ms, spinning frequency 5 kHz). The respective inversion times  $\tau_i$  are indicated at the right margin.

an increase of signal multiplicity in the chemical shift region characteristic of the melem-type  $\text{N}_{\text{tert}}$  and  $\text{NH}_2$  groups (– 198.5 to – 204.4 ppm and – 269.2 to – 295.9 ppm). Remarkably, the two up-field  $\text{NH}_2$  signals in phase I, which may be attributable to the triazine part of the compound, are collapsed to one single resonance at – 295.9 ppm in phase II. The signals of the presumed triazine nitrogen atoms typically observed around – 210 ppm in melamine and phase I is obviously shifted down-field in phase II (Fig. 6.7, right). A resonance attributable to the central nitrogen of the cyameluric nucleus can be weakly distinguished at – 233 ppm. The following aspects need to be emphasized:

Although the spectra of phases I and II largely parallel those of melamine and melem with respect to the signal positions, obvious differences are observed regarding the number of signals. This is especially obvious when the  $\text{NH}_2$  regions for phases I and II are compared to those of melem and melamine, respectively. Whereas melem exhibits three well separated  $\text{NH}_2$  signals, only one signal with a high-field shoulder is seen in this chemical shift range for phase I, whereas a similar situation is encountered on comparing the spectra of phase II and melamine. This observation may reflect the varying ratios of melamine and melem in the two adduct compounds, as well as pronounced differences in terms of the molecular arrangements

in the solid state.

Notably, the lack of signals pertaining to NH groups is a strong indication that none of the nitrogen atoms of the constituents of phases I and II is protonated (or deprotonated), and that no larger molecular aggregates condensed *via* NH bridges are present. This, however, further substantiates the view that both phases are built up from a co-crystallise of melamine and melem, forming an array glued together by hydrogen-bonding forces rather than by an acid-base or cross-linking reaction. The noticeable differences between the spectrum of phases I and II on the one hand, and that of a simple superposition of the spectra of melamine and melem on the other hand suggest that no simple heterogeneous mixture of melamine and melem crystals is present, and that the molecular arrangement and intermolecular forces in the adduct phases are significantly different from those dominant in the crystal structures of the pure compounds.

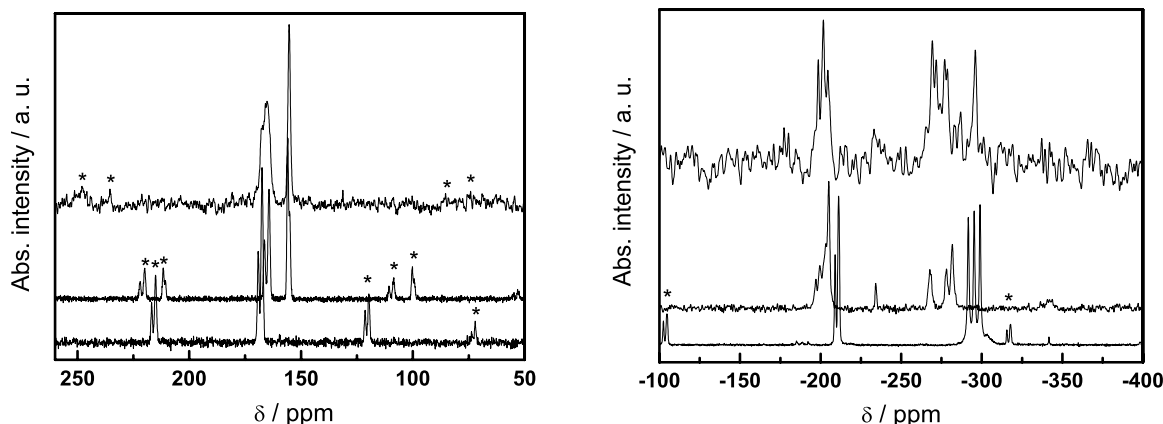


**Figure 6.9:**  $^{13}\text{C}$  (left) and  $^{15}\text{N}$  (right) CP-MAS solid-state NMR spectra of the HT phase II (top; recycle delay: 360 s;  $\tau_c$ : 4 ms for both measurements; spinning frequency 10 kHz) in comparison with melem (middle) and melamine (bottom; for parameters cf. Fig. 6.7). Spinning side bands are marked by asterisks.

### 6.3.4.2 Solution-State NMR Spectroscopy

The solution NMR spectra would be expected to be similar to the solid-state NMR spectra in case the principal molecular arrangement is retained in solution. Owing to the low solubility of the solids even in DMSO, only the  $^1\text{H}$  and  $^{13}\text{C}$  spectra are available.

Figure 6.10 outlines the NMR spectra for phases I and II, as well as for melamine and melem for comparison.

The chemical shifts of both  $^1\text{H}$  and  $^{13}\text{C}$  signals being similar, it gets immediately evident that the spectra of I and II appear to be identical to a superposition of the spectra of melamine

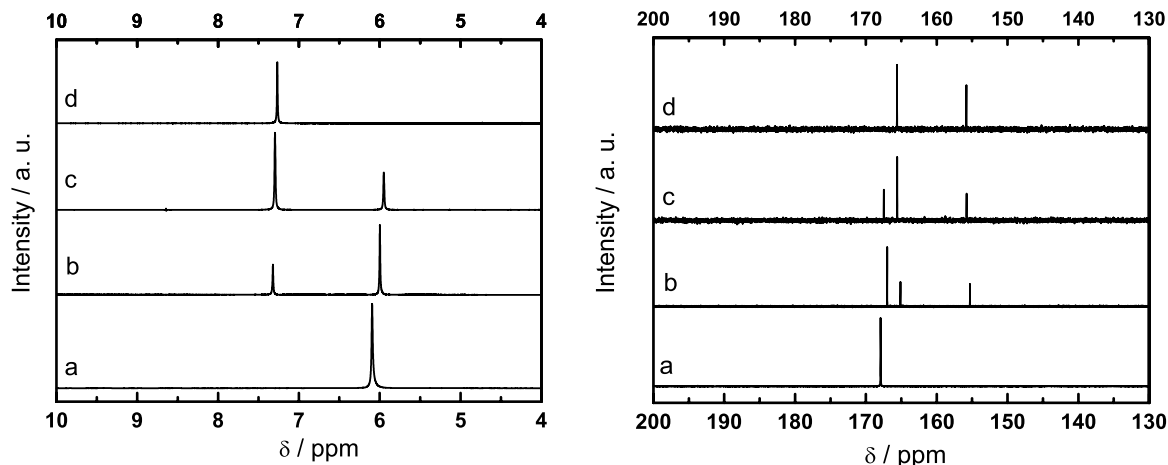


**Figure 6.10:**  $^1H$  (left) and  $^{13}C$  (right) NMR spectra of the adducts I (b) and II (c) measured in DMSO- $d_6$  solution. The respective spectra of melamine (a) and melem (d) are shown for comparison.

and melem (Table 6.3).<sup>3</sup> Whereas no quantitative information can be extracted from the  $^{13}C$  spectra owing to the polarization transfer from the protons utilized in the experiment, the ratio of the  $^1H$  signals is more reliable.

**Table 6.3:** Synopsis of the experimental  $^1H$  and  $^{13}C$  chemical shift data obtained for adducts I and II as well as melamine and melem for comparison.

Compound	$\delta$ / ppm $^1H$ (multiplicity, intensity)	$\delta$ / ppm $^{13}C$
phase I	7.3 (s, 6 H), 6.0 (s, 12 H)	167.0, 165.1, 153.3
phase II	7.3 (s, 12 H), 6.0 (s, 6 H)	167.5, 165.6, 155.8
melamine	6.1 (s, 6 H)	167.9
melem	7.3 (s, 6 H)	165.6, 155.8

Whereas for phase I, the intensity of the proton signals belonging to melamine outweigh that of the melem protons (ratio  $\approx 2.3 : 1.0$ ), the situation is opposed for phase II (ratio  $\approx 1.4 : 2.0$ ). These findings must, however, be treated with some caution as in both cases the sample was not completely dissolved in DMSO, so that a preferential uptake of a single component may not be excluded. Nevertheless, the significant variation in the intensities between phase I and II suggest that the latter effect may not be particularly strong.

On evaporating the DMSO solution, the residue was found to be largely amorphous, yet a small amount of crystalline material could be isolated, which was identified as melamine. The amorphous residue together with a poorly crystalline phase can presumably be attributed to

<sup>3</sup>The slight low-field shift observed for the melamine signals ( $^1H$  and  $^{13}C$ ) is predominantly due to differences in the instrument calibration or concentration effects, since a 2:1 mixture of melamine and melem yields a spectrum essentially identical to that of phase I.

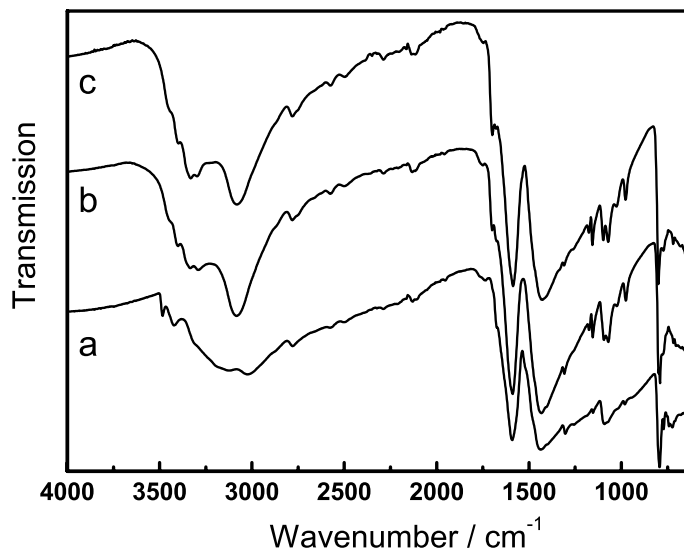


**Figure 6.11:** FTIR spectra (reflection geometry, neat solids) of the residues obtained from refluxing the adduct phases I (b) and II (c) in aqueous solution. For comparison the spectrum of melem is shown (a). Differences in the spectra result from hydration of the samples (b) and (c), which give off water under heating, thereby yielding pure melem. Evaporating the filtrate solution affords melamine in both cases.

a melem-DMSO adduct, which is known to form when dissolving melem in DMSO [474]. Further proof to the validity of this interpretation was sought by boiling a suspension of the adduct phases in water so as to “extract” melamine which is soluble in hot aqueous solution. In fact, melamine was isolated from the filtrates, whereas the white residues of adduct I and II exhibit identical IR spectra, which were identified as melem-hydrate phases (Fig. 6.11) by comparing the X-ray powder patterns of the residues before and after heat treatment with that of melem. These results corroborate the above line of argument that phases I and II in fact consist of co-crystals formed by melamine and melem in two different, yet well-defined ratios. Hence, the solid-state architecture is destroyed when dissolving the material in DMSO or other solvents, presumably by interference of the solvate molecules with the hydrogen-bonding array essential for the formation of I and II.

The UV/vis spectra of the adduct phases will be discussed in section 6.4.7 on page 222.

### 6.3.5 Thermal Analysis

DSC measurements have been carried out with phases I and II under the same conditions as described for melamine (Fig. 6.12). Interestingly, only one sharp endothermic signal is visible for phase I at 660 K, whereas about three thermal events appear for phase II at 660 (endothermic), 688 (endothermic/exothermic) and 788 K (endothermic).

It may be conjectured that the events at 660 and 688 K observed for phase II are correlated, indicating melamine sublimation and melem formation in a similar temperature range, or possibly the intermediate formation of melam as will be discussed below. Presumably, the differences between the spectra for both phases in this temperature range are due to different pressure conditions or sample amounts.

The endothermic signal at 660 K (688 K) may be associated with the second thermal event observed for melamine at the same temperature (cf. Fig. 6.3 on page 200). As will be seen below, this signal is most probably due to melem formation. The weak endothermic event around 790 K presumably indicates the thermal disintegration of melem by polymerization.

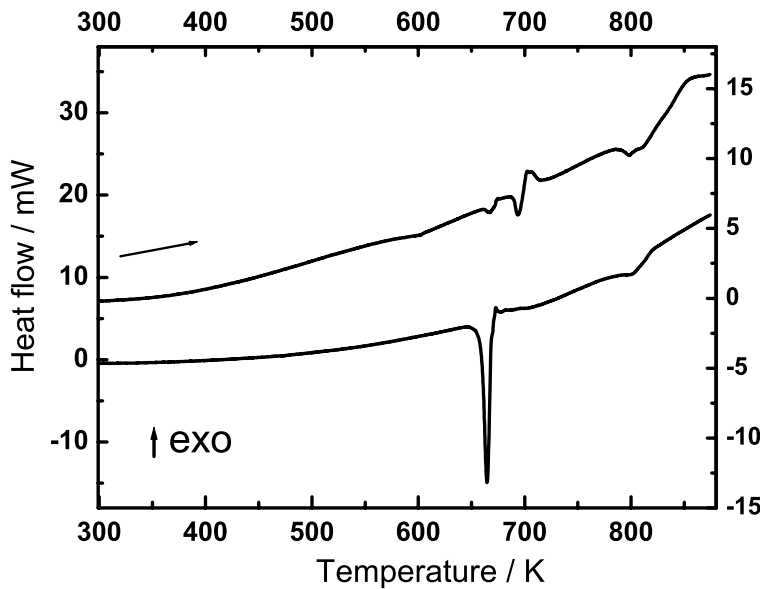


**Figure 6.12:** DSC heating curves recorded between RT and 880 K for the LT phase (bottom) and the HT phase (top).

The temperature response of I and II was also followed by TPXRD measurements, which are shown in Figure 6.13. As expected, the thermal behavior of the two compounds is largely identical and is characterized by the decomposition into melem, which is then further transformed into graphitic carbon nitride materials at 780 K. The onset of melem formation

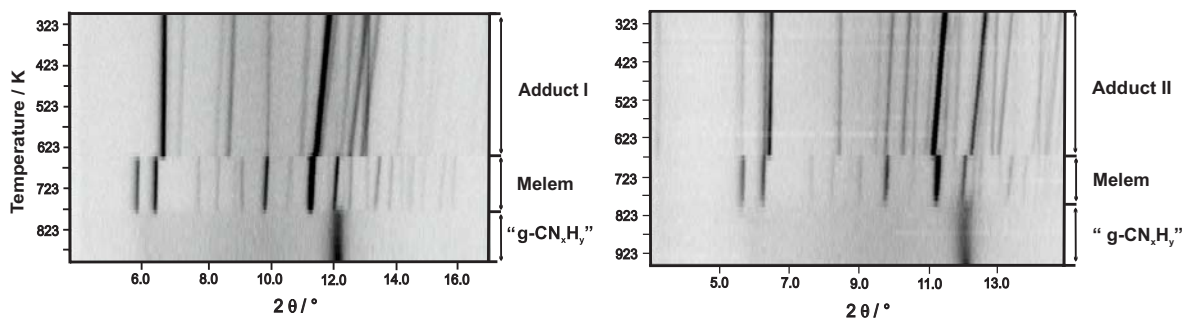


**Figure 6.13:** *In situ* temperature programmed X-ray powder diffraction measurements (Mo- $K\alpha_1$  radiation) of adduct I (left) and adduct II (right), showing the transformation of both phases into melem at  $\approx 650$  K, which then yields a graphitic carbon nitride material above 780 K.

is slightly earlier (640 K) as compared to that of phase II (660 K), which may, however, also result from minor deviations in the temperature calibration. Also, no evidence is found for the transformation of phase I into phase II prior to melem formation, which may be due to slightly different heating conditions as compared to the TPXRD measurements for melamine sketched in Figure 6.4 on page 201.

Although no evidence for melam was found by thermal decomposition of melamine under the above conditions, the existence of melam cannot be disputed based on these findings alone. It may not even be legitimate to reject the possibility that melam is indeed formed as a condensation product of melamine if different reaction conditions apply. Alternatively, melam may occur as a reactive intermediate not detectable by the analytical techniques used here, which exhibit response times on the time scale of minutes. In order to pursue this thread, the decomposition of melamine under atmospheric pressure was studied.

## 6.4 Melam

A porcelain crucible of about 2 cm height and 1 cm diameter was loaded with 2 – 10 g melamine, loosely covered with a lid and placed in a muffle furnace. After heating at 613 – 633 K for approx. 2 days, tiny colorless crystals had formed on the surface of the greyish bulk material. Single-crystal X-ray diffraction revealed that the crystals were not melamine as had been expected.

Instead, pure melam had been isolated. The bulk material was shown by X-ray powder diffraction to be different from melam; the patterns, however, resembled that of a mixture of the adduct phases I and II, with admixtures of melem and an unknown phase (see below), though of poor crystallinity (Fig. 6.14). Melam was only present to a very small extent, such

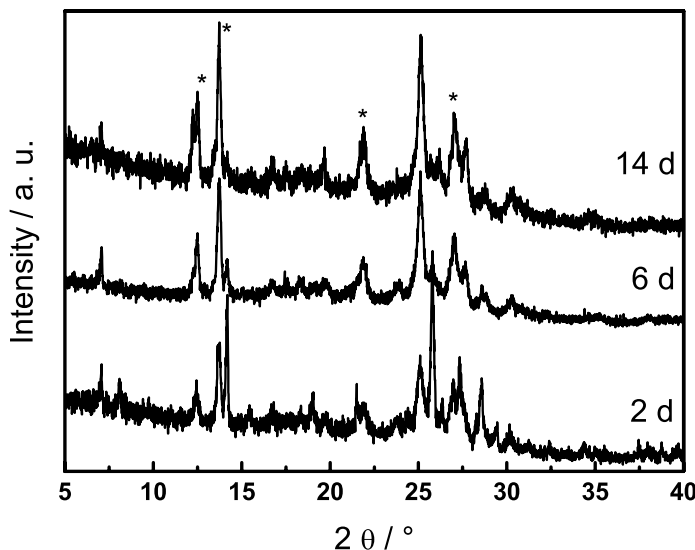


**Figure 6.14:** X-ray powder patterns ( $\text{Cu}-\text{K}\alpha_1$  radiation) showing the phase compositions of the bulk material after prolonged heating at 623 K. After two days (bottom), phase I is still visible, whereas the portion of phase II continuously increases (middle, top). After 14 days, reflections of melem and a presumed melem-dimer or -oligomer (reflections of the latter are indicated by asterisks) are visible in the powder pattern (top).

that it is essentially invisible in the X-ray powder pattern, even if the sample is taken from the surface region. On prolonged heating at the same temperature, all crystals completely vanished.

Another noticeable detail should be pointed out: After passing through the intermediate phases I and II, apart from melem the reflections of an unknown phase appear (marked by asterisks in Fig. 6.14), which can, however, not be unambiguously assigned owing to the heavy overlap and low crystallinity of the multi-phase mixture. The IR spectrum is largely identical to that of melem, except for an increase in absorption in the  $\nu(\text{C}-\text{N})$  /  $\delta(\text{N}-\text{H})$  stretching region. It is therefore conjectured that a “melem-dimer” (or “-oligomer”) similar to the “melamine-dimer” melam is formed, but cannot add further proof to this hypothesis at this stage. For further details see Chapter 7.

Although based on this observation the existence of melam has been unambiguously proven, it should be noted that it is detectable only if the heating and tempering conditions are very carefully chosen. It appears that only a certain time-window, as well as the condition of atmospheric pressure, allow for the observation of melam.

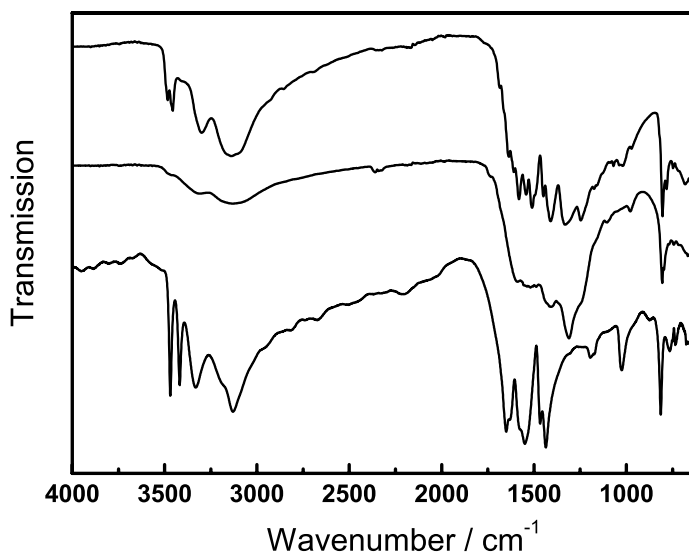


**Figure 6.15:** FTIR spectra of melamine (bottom), of an amorphous intermediate phase (middle), and of melam (top), recorded with the neat solids in reflection geometry.

#### 6.4.1 IR Spectroscopy I: Formation

When heating melamine for one day at 603 K, an amorphous material of extremely soft and velvety consistency was isolated. At the same time, the surface was covered with a grayish-beige surface, which could be identified as melam. The IR spectra of the starting material (melamine), the amorphous bulk and melam are contrasted in Figure 6.15. Note the strong absorption for both the intermediate phase and melam in the  $\nu(\text{C}-\text{N})$  region between 1200 and 1370  $\text{cm}^{-1}$ , as well as the absence of the  $\delta(\text{NH}_2)$  band found at 1650  $\text{cm}^{-1}$  for melamine. The intensity maximum at 1312  $\text{cm}^{-1}$  (C–N stretching region) for the intermediate may be indicative of a more extensively cross-linked phase as compared to melam, which subsequently breaks up into NH-bridged triazine pairs as found in melam. Generally, the absorption patterns of the intermediate and product are quite similar, especially with respect to the band intensities between 1400 and 1600  $\text{cm}^{-1}$ , which are markedly different for melamine. Obviously, the hydrogen-bonding network differs in all three stages, which can be inferred from the varying band intensities in the  $\nu(\text{N}-\text{H})$  region and the sharp absorptions at different positions found for melamine and melam, but not for the intermediate phase.

### 6.4.2 Analytical Data

The ESI+ mass spectrum of melam clearly shows the  $[M + H]^+$  peak at  $m/z = 236.11$ .

**Table 6.4:** Elemental analysis data for melam. The analyzed material was obtained from thermal dehydration of melam hydrate. The experimental values are obtained from a sample which was heated in *vacuo* prior to the analysis, the latter being performed under a flow of nitrogen in order to avoid re-uptake of water.

Compound	N / wt%	C / wt%	H / wt%
melam	64.25	30.67	3.60
melam	65.53	30.64	3.83

Elemental analysis has been carried out using a dehydrated sample of melam hydrate (see below), as only small amounts of pure melam are accessible by decomposition of melamine (see above), which in addition are difficult to separate from the bulk. Despite prolonged heating of the hydrate at different temperatures between 423 and 623 K, the nitrogen content shows rather large variations and is systematically lower as would be expected theoretically. Table 6.4 displays the data obtained for the elemental analysis that matches best the theoretical values. The observed discrepancy may be attributable to impurities already contained in melam hydrate; a more likely explanation, however, is the hygroscopic nature of melam, which “adsorbs” water on its surface to some extent when exposed to air.<sup>4</sup>

### 6.4.3 Crystal Structure

Melam crystallizes in the space group  $C2/c$  with 1.5 formula units in the monoclinic unit cell, such that two independent melam molecules are present. Relevant crystallographic data are given in Table 6.5. The molecular structure is characterized by two triazine units condensed *via* a bridging NH group (Fig. 6.16). Both rings are essentially equivalent and *non-protonated*, which is in agreement with the special position occupied by N15 and the generation of the second triazine unit by a screw axis. Although the second melam molecule is fully contained in the asymmetric unit, both triazine rings exhibit similar geometric features and are grouped around N4 in a “staggered” arrangement. It should be noted at this stage that the hydrogen positions at the bridging nitrogen atoms can be found explicitly from difference Fourier syntheses, therefore supporting the tautomeric form without conjugation between the triazine systems (ditriazinylamine, cf. Fig. 6.2, left).

Notably, the melam molecules are not planar but are twisted about the central nitrogen, having dihedral angles about the bridging NH-groups of  $\approx 11^\circ$  (N15) and  $14^\circ$  (N4), respec-

<sup>4</sup>Melam hydrate used for elemental analysis was either obtained from a melam–ammonium chloride adduct (see section 6.5 on page 226) or from *Agrolinz Melamine International GmbH* (AMI) as a gift.

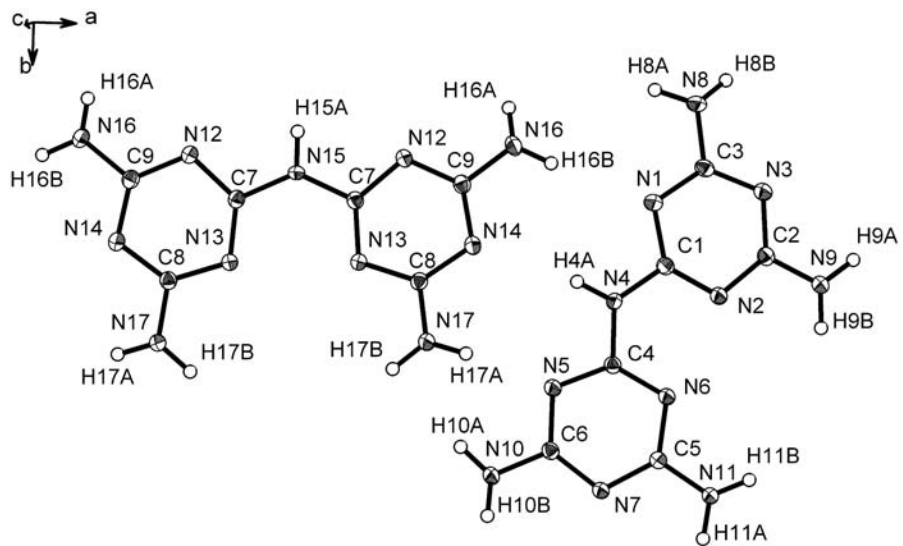


**Figure 6.16:** Representation of the molecular structure of melam. The two crystallographically independent melam molecules are shown. Thermal displacement ellipsoids (except for H) are drawn at the 50 % probability level.

tively. Thus, the molecules exhibit a non-crystallographic point symmetry which is close to  $C_2$ . Accordingly, the amino groups attached to the triazine rings do not interfere, which together with a more efficient hydrogen bonding network may be the reason for the observed non-planarity. The angle C–N–C at the NH group is significantly widened ( $129^\circ$  (N4),  $132^\circ$  (N15)) and strongly deviates from tetrahedral symmetry, giving rise to a rather trigonal planar arrangement. The C–NH–C bond lengths are by up to 4 pm longer as compared to those in the triazine rings (see below). The amino groups also depart from planarity in that they slightly bend out of the triazine ring plane. This may be indicative of only moderate participation of the free electron pair at the amino nitrogen atoms in the ring  $\pi$ -system, which is also supported by the fact that the C–N<sub>exo</sub> bonds (133 – 135 pm) are slightly elongated by analogy with melamine (cf. section 5.6.1.3 on page 180) [458]. Thus, besides steric reasons electronic factors may also be responsible for the observed non-planarity of the melam ring system.

Another noticeable feature is the distortion of the triazine rings, which are neither completely flat, nor regular hexagons, the latter being characteristic of both triazine and heptazine rings [82, 240, 458, 475]. While the N–C–N angles are close to  $126^\circ$ , the C–N–C angles vary between  $113^\circ$  and  $114^\circ$ . The C–N bond lengths within the rings do not vary to a large extent, amounting to 134 – 135 pm on average, whereas the bonds C4–N6, C1–N2, and C7–N13 adjacent to the bridging NH group are systematically shorter (133 pm).

The molecules are connected *via* medium strong and weak hydrogen bonds with donor-

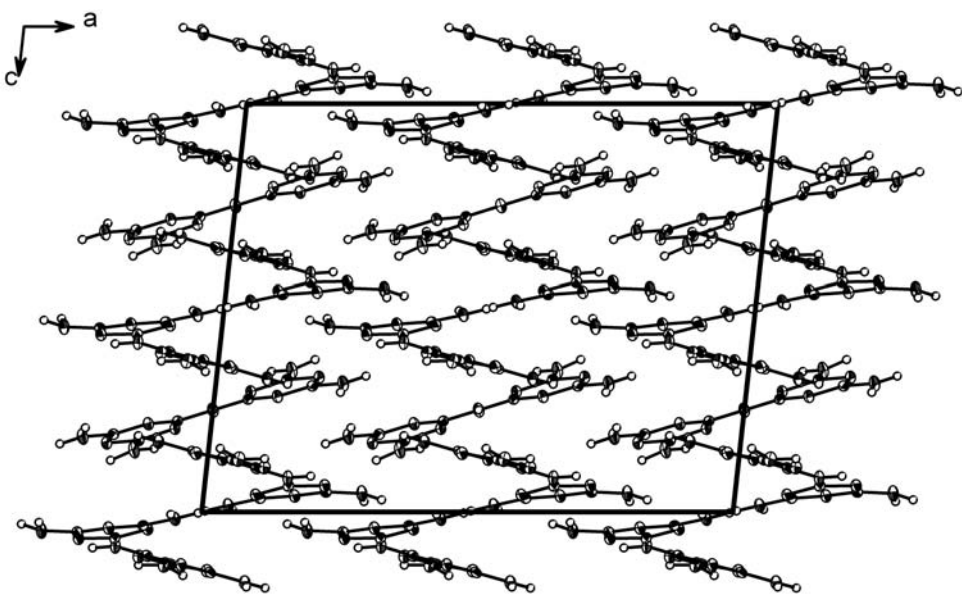


**Figure 6.17:** Unit cell of melam (view along [010]), showing the spatially extended, helix-like arrangement of the molecules. Thermal displacement ellipsoids (except for H) are drawn at the 50 % probability level.

acceptor distances ranging from 297 to 333 pm. No pronounced  $\pi$ -stacking is observed, which coincides with a screw-like arrangement of the molecules, giving rise to a 3D network of mutually tilted melam molecules (Fig. 6.17).

#### 6.4.4 IR Spectroscopy II: Structure

The IR spectrum of melam is displayed in Fig. 6.15 (top spectrum). The similarities to the spectrum of melamine (bottom spectrum) is evident, which is particularly pronounced in the  $\nu(\text{NH})$  region above  $3100\text{ cm}^{-1}$  as well as for the  $\nu(\text{NH}_2)$  and  $\nu(\text{C}=\text{N})$  absorption between 1640 and  $1414\text{ cm}^{-1}$ . Though having similar intensities, the latter bands are well resolved and sharp in contrast to those of melamine, and an additional band at  $1583\text{ cm}^{-1}$  is found for melam which is absent in both melamine and melem. Similar to melamine, the characteristic sextant ring bend is located at  $807\text{ cm}^{-1}$ , accompanied by an additional weak band at  $782\text{ cm}^{-1}$ . Whereas for melamine and melem no pronounced absorption is found below  $1400\text{ cm}^{-1}$ , two strong bands attributable to the C–N stretching or N–H deformation vibrations (imino group, see ref. [240]) are found for melam at  $1338$  and  $1250\text{ cm}^{-1}$ .

#### 6.4.5 Solid-State NMR Spectroscopy

$^{13}\text{C}$  CP-MAS NMR spectra have been obtained for melam and its hydrate (recrystallized from NaOH solution, see below), which is a valuable starting material for the synthesis of

**Table 6.5:** Crystallographic data for melam.

Formula	C <sub>6</sub> N <sub>11</sub> H <sub>9</sub>
$M_w$ / g · mol <sup>-1</sup>	235.24
crystal system	monoclinic
space group	$C2/c$ (no. 15)
$T$ / K	130
diffractometer	Nonius Kappa CCD
radiation ( $\lambda$ / pm)	Mo-K <sub>α</sub> (71.073)
monochromator	graphite
$a$ / pm	1811.0(4)
$b$ / pm	1086.7(2)
$c$ / pm	1398.4(3)
$\beta$ / °	96.31(3)
$V$ / 10 <sup>6</sup> · pm <sup>3</sup>	2735.3(9)
$Z$	12
$\rho_{calcd}$ / g · cm <sup>-3</sup>	1.714
F(000)	1464
$\mu$ / mm <sup>-1</sup>	0.127
crystal size / mm <sup>3</sup>	0.20 x 0.12 x 0.04
diffraction range	3.56 ≤ $\theta$ ≤ 27.48
index range	-23 ≤ $h$ ≤ 23, -13 ≤ $k$ ≤ 14, -18 ≤ $l$ ≤ 18
total no. reflections	5976
independent reflections	3125 ( $R_{int} = 0.0162$ )
observed reflections	2706
refined parameters / restraints	with $F_o^2 \geq 2\sigma(F_o^2)$
GooF on $F^2$	285 / 0
$R$ indices (all data)	1.048
	$R_1 = 0.0350$ (0.0414)
	$wR_2 = 0.0926$ (0.0970)
	with w = $[\sigma^2(F_o^2)$
	$+(0.0535P)^2 + 1.9821P]^{-1}$
	where $P = (F_o^2 + 2F_c^2)/3$
min./max. residual	
electron density /	- 0.244 / 0.205
$e \cdot 10^{-6}$ pm <sup>-3</sup>	

several melam salts (cf. section 6.5 on page 226). Figure 6.18 (left) reveals two close-by signals at 164.0 and 167.2 ppm for melam, the latter having a shoulder on the high-field side. Presumably, these hardly separable resonances correspond to the three distinguishable carbon sites within a single triazine nucleus. The theoretically possible number of nine carbon sites can clearly not be resolved. The chemical shift values are almost identical with those observed

for melam hydrate (top spectrum) and very similar to the signal positions in the  $\text{ZnCl}_2$ -melam complex (cf. Fig. 6.40 on page 253).

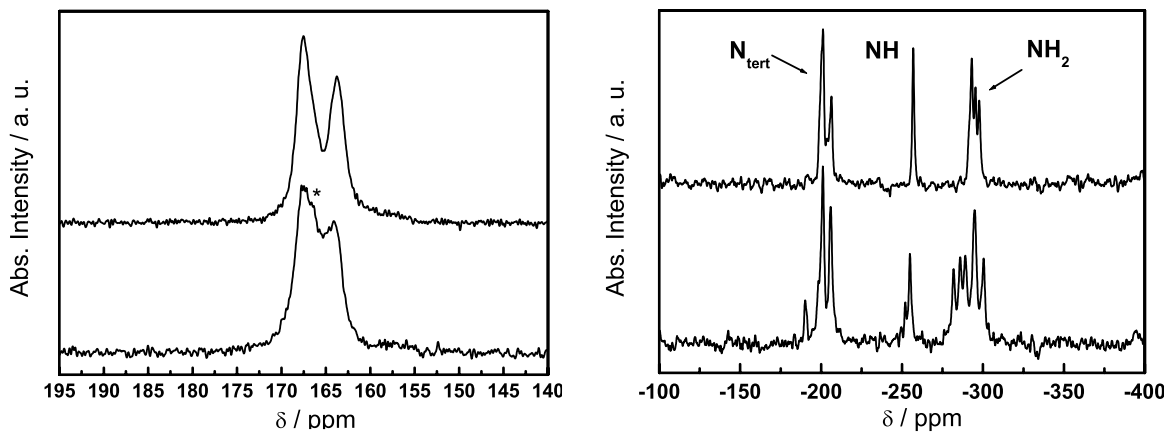


**Figure 6.18:**  $^{13}\text{C}$  (left) and  $^{15}\text{N}$  (right) CP-MAS solid-state NMR spectra of melam (bottom spectra) and melam hydrate (recrystallized from 1M NaOH, top spectra). The shoulder in the  $^{13}\text{C}$  spectrum of melam is denoted by an asterisk. The recycle delay was 16 s for melam and 4 s for melam hydrate, the contact time  $\tau_c$  was 4 ms for all measurements, the spinning frequency 10 kHz.

The  $^{15}\text{N}$  CP-MAS NMR spectrum of melam (bottom) is again contrasted with that of melam hydrate (top) in Figure 6.18 (right). Both spectra reveal three signal groups, which are located in the regions typical of  $\text{N}_{\text{tert}}$ ,  $\text{NH}$ , and  $\text{NH}_2$  groups.

Three separable tertiary nitrogen signals are observed for melam between  $-190.0$  and  $-205.9$  ppm, whereas two  $\text{NH}$  signals are distinguishable at  $-252.0$  and  $-254.8$  ppm, the former one being less than half as intense as the latter. Five different  $\text{NH}_2$  signals are visible at  $-282.8$ ,  $-286.0$ ,  $-288.9$ ,  $-295.0$ , and  $-300.4$  ppm. These findings correspond well to the crystal structure analysis, according to which one would expect two  $\text{NH}$  groups with an intensity ratio of 2:1 (one bridging nitrogen on a special position with site occupation factor 0.5). This is almost exactly reproduced in the experimental spectrum. In addition, a maximum of six different  $\text{NH}_2$  groups and up to nine tertiary nitrogen atoms, all of which belonging to 1.5 melam molecules in the asymmetric unit, would be expected. However, from the different intensities of the signals in the  $\text{N}_{\text{tert}}$  and  $\text{NH}_2$  regions signal overlap due to similar electronic and geometric environments is clearly evident, which reduces the maximum number of independent  $^{15}\text{N}$  signals in both cases.

Melam hydrate shows  $\text{N}_{\text{tert}}$  signals at  $-200.9$ ,  $-203.9$  and  $-205.6$  ppm, one  $\text{NH}$  signal at  $-257.0$  ppm, and a group of poorly separable  $\text{NH}_2$  resonances at  $-293.1$ ,  $-295.4$ , and  $-297.8$  ppm (Fig. 6.18, right, top spectrum).

The two spectra show major similarities with respect to the observed chemical shifts, suggesting a similar constitution of melam in both compounds. However, the chemical shift range

for the tertiary and  $\text{NH}_2$  nitrogen atoms is significantly larger than that for melam hydrate, which may indicate that the latter contains one or even only half a melam molecule within the asymmetric unit. As the crystal structure for melam hydrate is not available, no further statements on the geometry of the triazine rings can be made, although it may be inferred that owing to the less pronounced chemical shift range for the  $^{15}\text{N}$  nuclei in melam hydrate, the geometry of the triazine rings is likely to be more regular as compared to those in pure melam.

#### 6.4.6 Thermal Behavior

The thermal behavior of melam was studied by differential scanning calorimetry as well as indirectly by TPXRD measurements in that the latter were conducted starting from melam hydrate. As shown in Figure 6.19, only one sharp endothermic event appears during heating between 300 and 880 K. The signal with an onset around 650 K can be correlated with the formation of melem. Further thermal events cannot be distinguished, however TXRD measurements clearly reveal the conversion of melem in a polymeric  $\text{CN}_x\text{H}_y$  material to take place above 723 K (see below).

Starting from melam hydrate, a first phase transition is observed in the TPXRD measurements at  $\approx 385$  K, which by comparison of the respective 1D X-ray patterns can be correlated with

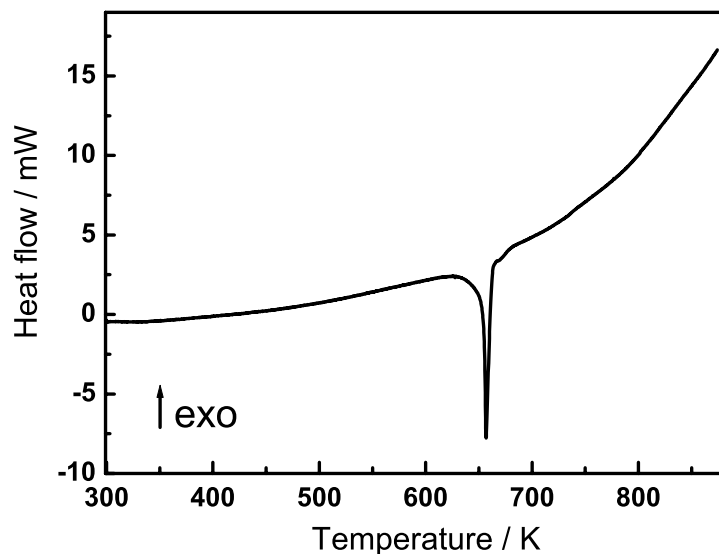


**Figure 6.19:** DSC measurement of melam between RT and 873 K. Only one thermal event is observed, which can be attributed to the formation of melem at 660 K.

the dehydration reaction yielding melam (Fig. 6.20). In principal agreement with the DSC measurements, melam is stable up to 640 K, above which temperature it transforms into melem as can be seen from the appearance of weak reflections pertaining to the latter. Beyond 723 K the reflections of melem disappear, leaving behind a graphitic material with a broad reflection at  $2\theta \approx 12^\circ$ .

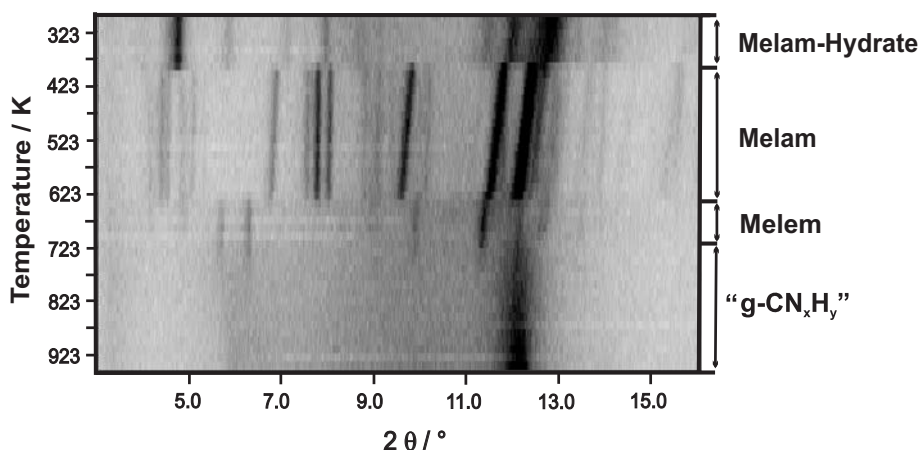


**Figure 6.20:** *In situ* temperature dependent X-ray diffraction measurements (Mo- $K\alpha_1$  radiation) of melam hydrate recorded between RT and 953 K. At 385 K melam hydrate loses its crystal water and transforms into melam without significant amorphization.

#### 6.4.7 UV/Vis Spectroscopy

Although the distinct identities and compositions of melam on the one hand and the adduct phases I and II on the other hand have in detail been outlined above, an additional, somewhat indirect proof of the different chromophores present in the three compounds can be adduced by their UV/vis reflectance spectra. Figure 6.21 gives a synopsis of the spectra of adducts I, II and melam (left), as well as of melamine and melem (right) for comparison. The curve pertaining to melam can be identified by three local maxima at  $\approx 226$ ,  $265$  and  $320$  nm, whereas the absorption pattern of phases I and II is similar, being highest around  $268$  and  $338$  nm.

According to *Finkel'shtein* the experimental absorption spectrum of melam has maxima at  $210$  and  $240$  nm [78], which is in accordance with the calculated spectra for the chinoid form B sketched in Figure 6.29 on page 235 with absorption maxima at  $207$  and  $238$  nm. The spectrum obtained in this work, however, differs significantly from the literature data and can rather be associated with the spectrum calculated for the non-conjugated form A with peak absorptions at  $296$  and  $336$  nm [78] (see also section 6.5.1.3 on page 233). As this tautomer is in fact the one found experimentally, we conjecture that the melam species investigated

by *Finkel'shtein* rather corresponds to a hydrated melam species as will be discussed below. Interestingly, although melam is present in the non-conjugated form, its absorption maximum is red-shifted as compared to the triazine ring absorption in melamine, which may be indicative of some degree of resonance between the two triazine rings.

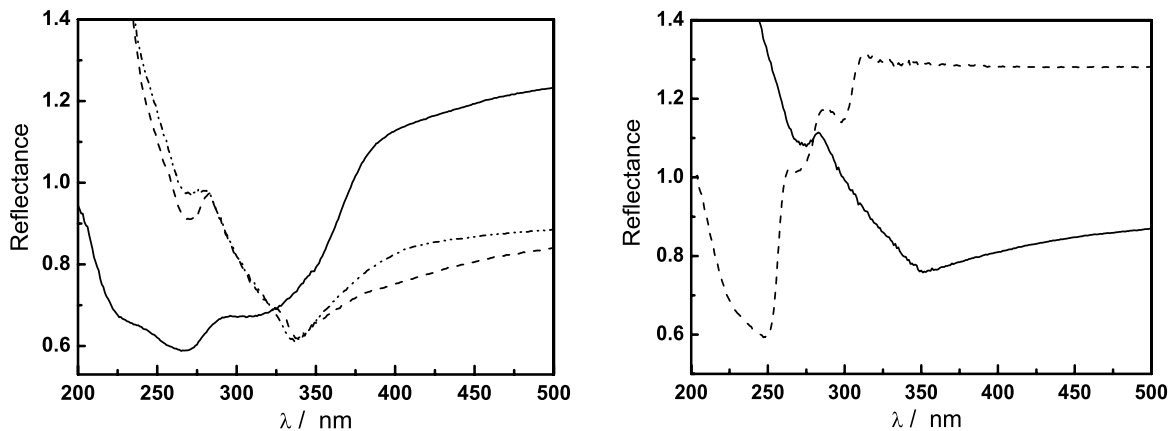


**Figure 6.21:** Left: UV/vis spectra of melam (solid line) and the adduct phases I (dash dotted line) and II (dashed line). Right: UV/vis spectra of melamine (dashed line) and melem (solid line).

The spectra found for adducts I and II exhibit only slightly different intensities for the two absorption maxima. When however comparing with the reflectance spectra of melamine and melem, a striking similarity of both adduct spectra with that of melem is evident, whereas the absorption maximum of the triazine ring at  $\approx 250$  nm is essentially absent. Two conclusions may be drawn from these results:

Firstly, another piece of evidence can be added that the adduct phases are distinctly different from melamine and melem with respect to the arrangement of the molecules in the solid state. Secondly, the electronic states of the heterocycles in the adduct phases are greatly affected by the altered solid-state interactions, which may correlate with major variations in the  $\pi$ -stacking and/or hydrogen-bonding interactions. In particular, the energy levels of the triazine ring must be significantly different as compared to pure melamine, since the typical triazine  $\pi \rightarrow \pi^*$  or  $n \rightarrow \pi^*$  transition [476, 477] is not only diminished, but essentially absent or hyperchromically shifted such that overlap with the heptazine transition occurs.

In summary, the UV/vis measurements again highlight the similarity of the adduct phases I and II in terms of composition and at the same time are indicative of the markedly different nature of melam and the profound changes in the electronic states of melamine and melem occurring upon formation of the adduct phases.

### 6.4.8 Discussion

The results presented above are suitable to provide a new basis for the controversial view on melam formation from melamine.

On pyrolyzing melamine in closed or semi-closed systems as outlined in section 6.3, melam cannot be isolated as the first condensation product of the starting material (see below). This may, however, result from its high reactivity in the respective temperature range. Similarly, the direct formation of melem from melamine without the formation of *detectable* intermediates lacks experimental evidence. Therefore, an alternative picture of melamine pyrolysis must be drawn:

*Van der Plaats* suggested that between 593 and 673 K melamine forms mixed crystals with its decomposition product [464], however without further substantiating this hypothesis. We are now in a position to confirm this view, as two intermediate phases could be isolated which are stoichiometrically built up by melamine and melem. According to NMR investigations and dissolution/extraction studies, the homogeneous phases are made up by hydrogen-bonded arrays of neutral melamine and melem molecules rather than salts originating from chemical reactions of the components (i. e. acid-base or condensation reactions). This line of argument is in agreement with the fact that the relative acidities and basicities of neutral melamine and melem do not support a proton transfer from the more acidic melem to melamine, which in contrast to melem is known to form salts also with medium strong acids [372, 372, 375–378, 386, 474, 478, 479].

Presumably, melem is gradually formed at elevated temperatures and reintegrated into the starting material melamine, upon which a crystallographically distinct phase is formed. It may be argued that the onset of melamine sublimation greatly facilitates the condensation reaction to melem, as melamine in the gas phase may be far more reactive than the melamine residue. However, note that under the reaction conditions chosen a huge part of melamine eludes the condensation reaction and resublimes at the cold end of the ampoule. In fact, whereas for phase I the yield amounts to 60 – 70 %, it is only 30 – 35 % for phase II. This strongly suggests that the transformation from phase I into II is simply a consequence of melamine sublimation, which is thus removed from the solid. The formation of two adducts with distinct stoichiometries may therefore be driven by the particularly beneficial arrangements of the components in the solid at the particular melamine : melem ratios, together with the possibility for melamine to be removed from the solid phase by sublimation. By this equilibrium between the solid and the gas phase, the transformation of phase I into phase II is feasible without major molecular rearrangements, and possibly even without further condensation of melamine into melem.

From the above statements it gets immediately evident that the adduct phases can only be metastable, which is evidenced by the strong time dependence of their synthesis. Once the temperature sufficient for melem formation is reached, the latter is continuously produced until all melamine present in the solid is consumed. Thus, the adduct phases I and II are only intermediate stages, stable for a limited time, on the way from melamine to the thermodynamically stable product melem. Therefore, thermal recrystallization of the adducts, which are only available as polycrystalline powders, is not feasible, as this would lead to the “extraction” of melamine from the solid. Likewise, recrystallization in solution results in the disruption of the hydrogen-bonding network and, ultimately, phase separation into the components melamine and melem.

Despite the dominant formation of the adduct phases I and II during melamine pyrolysis, the existence of melam and its formation from melamine under special reaction conditions has now been proven unambiguously. According to our findings and as noted previously by *Finkel'shtein* [460], melam is detectable to only a small extent and only under specifically tuned reaction conditions. This observation may be rationalized by invoking the formation of melam as a minor by-product instead of a true intermediate of the condensation cascade of melamine. Along these lines, a scenario may be envisaged involving the comparatively slow, reversible formation of melam from melamine. In a parallel reaction, the latter may transform into melem *via* volatile species such as cyanamide or dicyandiamide, which are generated rapidly by depolymerization of melamine under increased pressure of ammonia. Melam may be transformed back into melamine at elevated temperatures, which then reacts to melem in an alternative reaction pathway with a significantly increased reaction rate as compared to that of melam formation. Lowering the pressure of ammonia may enhance melam formation (by slowing down the re-transformation into melamine), while depolymerization of melamine and, thus, generation of melem, is concomitantly slowed down.

A more straightforward rationale is the rapid consumption and further transformation of melam into melem as the condensation reaction proceeds, which is in accord with *in situ* X-ray studies of the thermal behavior of melam (cf. Fig. 6.20 on page 222). Accordingly, melam may be viewed as a highly reactive intermediate of the thermolysis of melamine, which owing to its rapid transformation into melem is short-lived and – contrary to the adduct phases – essentially undetectable on the time scale of TPXRD. The fact that melam is only observed when working in open systems may be indicative of a deceleration of its transformation kinetics with decreasing pressure as outlined above. This slow-down may again correlate with the reduced availability of ammonia in the gas phase, a species which is known to enhance melem formation.

## 6.5 Melam Derivatives

As we have stated above, melam can be isolated to only a very small extent and only under special conditions. Thus, an alternative way for melam formation on a preparative scale was sought in order to explore the largely unknown chemistry of this important  $\text{CN}_x$  precursor compound.

To this end, different pathways have been pursued, which are summarized in Figure 6.22.

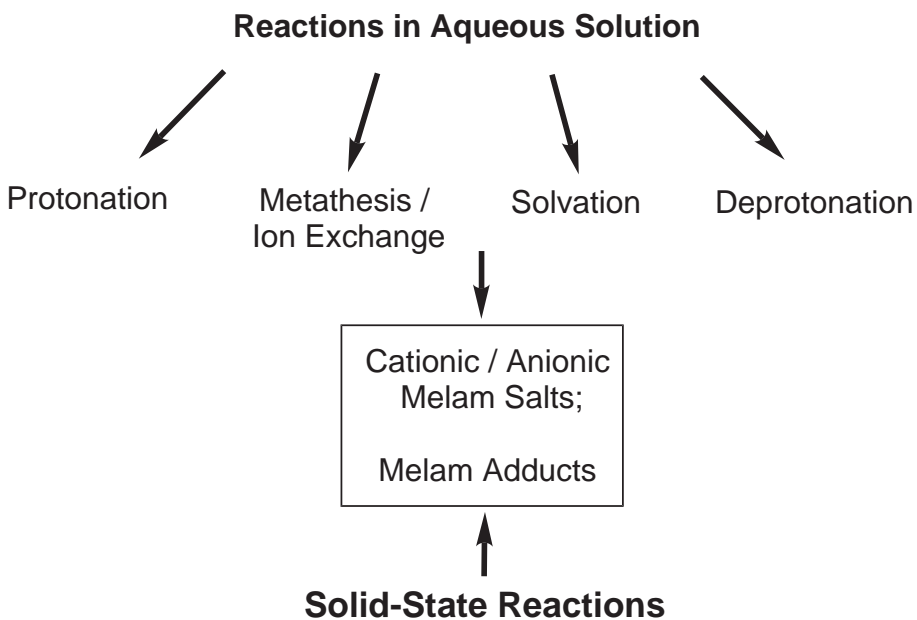


Figure 6.22: Schematic diagram of the different synthetic approaches to obtain derivatives of melam.

One feasible approach is based on the melam–ammonium chloride adduct  $[\text{C}_6\text{N}_{11}\text{H}_{10}]\text{Cl} \cdot 0.5 \text{NH}_4\text{Cl}$  mentioned in the introduction 6.1 on page 197, which has been synthesized according to the procedure given by Jürgens [240]. Typically, 365 mg ( $2.9 \cdot 10^{-3}$  mol) melamine was reacted with 83 mg ( $1.6 \cdot 10^{-3}$  mol) ammonium chloride in a closed Duran ampoule with ground neck at 723 K over night (heating rate  $1 \text{ K min}^{-1}$ ). The product, which was isolated from the cap of the ampoule (yield  $\approx 50\%$ ) was partially contaminated with ammonium chloride. The melam – ammonium chloride adduct was then suspended in aq.  $\text{NH}_3$  (25 %; 550 mg in 60 mL) for about 1 hour in order to remove the ammonium chloride and at the same time liberate the weak base melam from its hydrochloride. Although no complete solution of the adduct in ammonia was achieved, the absence of chloride in the product was established by elemental analysis. The white, poorly crystalline residue was isolated and dried by suction. The product, melam hydrate, was then used for further conversions.

### 6.5.1 Melam Solvates

To learn about melam and its compounds, a knowledge about neutral melam adducts or solvates seemed to be beneficial. Therefore, various solvents were tested with respect to their ability to dissolve melam hydrate and to form crystalline solvates by exchanging the crystal water by the respective solvent molecules. The list of solvents is given in Table 6.6.

*Table 6.6: List of solvents and their dissolving power for melam hydrate.*

Solvent	Solubility
DMSO	soluble
water	moderately soluble
methanol	insoluble
ethanol	insoluble
THF	insoluble
acetonitrile	insoluble
DMF	moderately soluble
acetone	insoluble
diethylether	insoluble
chloroform	insoluble
methylenechloride	insoluble

Dissolving melam was found to be particularly difficult, and only DMSO was suitable to dissolve large amounts of melam. Therefore, no solvates apart from hydrates and a DMSO–adduct have been obtained, which will be subject of the following section. It is assumed that melam forms a dense intra- and intermolecular hydrogen-bonding network, which together with beneficial  $\pi$ -stacking interactions between the molecules hampers the penetration of the solvent into the bulk material. Hence, solution chemistry of neutral melam seems to be impeded by its low solubility, so that alternative approaches to the synthesis of melam compounds have to be considered (cf. section 6.5.2 on page 234 and 6.5.3 on page 246).

#### 6.5.1.1 Melam Hydrates

Melam hydrates can be isolated from aqueous solutions in a large pH range, apart from strongly acidic or alkaline solutions in which cases melam salts are formed or hydrolysis occurs, respectively. The latter reactions typically involve complete dissolution of the melam precursor, whereas the formation of hydrates usually proceeds without complete dissolution, or with rapid precipitation of the dissolved hydrate from solution.

Precipitation of melam from aqueous solution affords compounds with idealized formula  $\text{C}_6\text{N}_{11}\text{H}_9 \cdot 2\text{H}_2\text{O}$ ; however, elemental analysis indicates a rather non-stoichiometric composition with respect to the amount of crystal water contained in melam hydrate, depending on

**Table 6.7:** Elemental analysis data for melam hydrates of varying compositions as obtained under different synthesis conditions.

Compound number	N / wt%	C / wt%	H / wt%	Synthesis conditions
1	59.18	28.22	4.22	AMI, Linz
2	52.59	25.49	4.62	1 M NaOH solution
3	54.93	26.29	4.78	5 % KOH solution
4	55.44	26.36	4.85	5 % KOH solution
5	54.98	26.67	4.36	$(\text{NH}_4)_2\text{CO}_3$ solution
6	55.41	26.11	4.69	melam- $\text{NH}_4\text{Cl}$ , $\text{NH}_3$ aq.
7	56.19	26.13	3.87	melam- $\text{NH}_4\text{Cl}$ , $\text{NH}_3$ aq.
Calcd.	56.83	26.57	4.80	

the synthesis conditions. The different compositions found by elemental analysis are listed in Table 6.7.

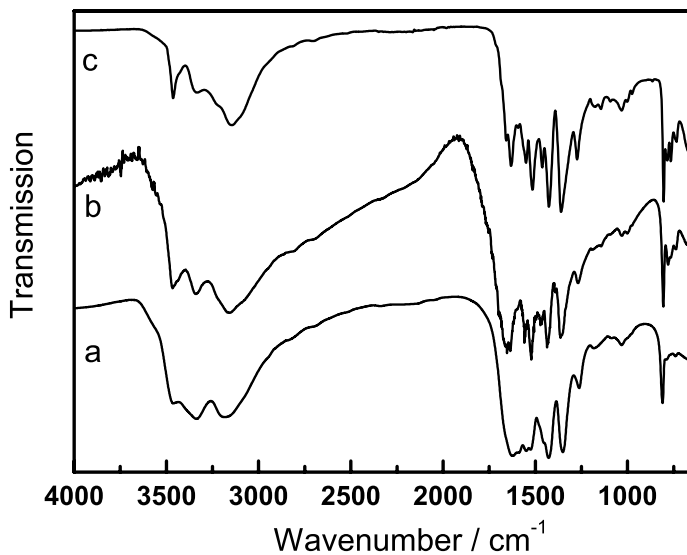


**Figure 6.23:** FTIR spectra of different melam hydrates. Bottom (a): melam hydrate obtained from Agrolinz Melamine International; middle (b): melam hydrate synthesized from an ammonium chloride-melam adduct by treatment with  $\text{NH}_3$  aq.; top (c): melam hydrate obtained by recrystallization of (b) in aqueous NaOH.

If melam hydrate (200 mg) is suspended in 1M NaOH solution (50 mL) and recovered without dissolution after heating at 343 K for approximately 30 minutes, melam hydrate of increased crystallinity is obtained, which, however, is accompanied by a significant change in the elemental composition (cf. Table 6.7). A similar effect is observed when suspending melam hydrate (15 mg) in 40 mL 5 – 40 % KOH solution.

The IR spectra of two different samples of melam hydrate (**a**<sup>5</sup> and **b**), as well as melam hydrate recrystallized from NaOH solution (**c**) are shown in Figure 6.23. Although the spectra exhibit similar absorption patterns, the position and intensity of some bands vary. Notably, the spectrum of **b** somewhat differs from those of **a** and **c** with respect to the bands at 1650 and 1390  $\text{cm}^{-1}$ , as well as in the N–H stretching region, showing very pronounced absorption in **b**. However, the band observed around 1580  $\text{cm}^{-1}$  in **a** and also in melam (cf. Fig. 6.15 on page 215) is absent in both **b** and **c**. In addition, the triazine ring bend around 800  $\text{cm}^{-1}$  is split in **b** and **c** such that an intense band is found at 805  $\text{cm}^{-1}$  and a minor sharp band at 781 (**b**) and 786  $\text{cm}^{-1}$  (**c**), respectively. The position of the latter is reminiscent of a red-shifted ring sextant bend found for protonated triazine rings (cf. section 5.3 on page 148). It may therefore be argued that the two tautomeric forms discussed above (Fig. 6.2) both appear to a significant extent in the hydrated species **b** and **c**, whereas this disorder phenomenon is less pronounced or absent in melam and the hydrate **a**.

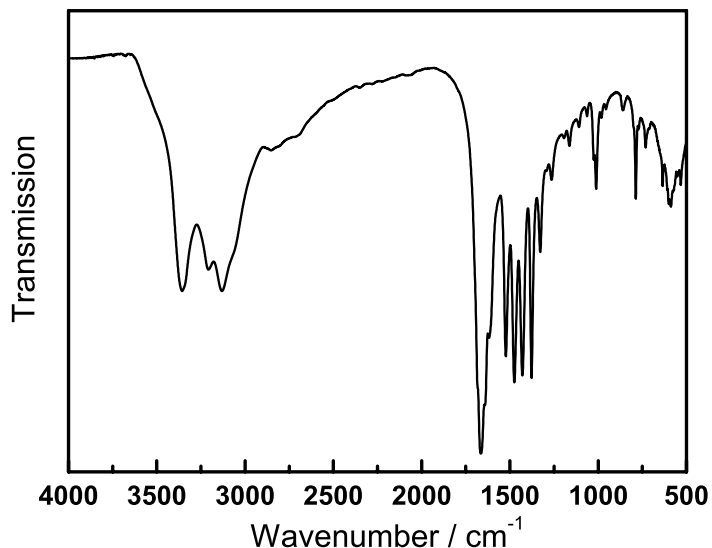


**Figure 6.24:** FTIR spectrum (4000 – 500  $\text{cm}^{-1}$ , KBr pellet) of melam hydrate after treatment with formic acid.

On dissolving a melam hydrate suspension (50 mg in 40 mL  $\text{H}_2\text{O}$ ) in weak acids such as formic acid (12 mL, 100 %) and acetic acid (3 mL, 100 %) under reflux, the same poly-crystalline phase is obtained, whose X-ray powder pattern is different from that of melam hydrate. The fact that identical phases result from treatment with different weak acids strongly indicates that no salts are formed with the respective acids. Apparently, recrystallization has taken

<sup>5</sup>used as obtained from *Agrolinz Melamine International* (AMI), Linz

place or another hydrated phase has been formed. This behavior typically only occurs in association with diluted or weak acids; reaction of melam hydrate with strong acids will be discussed in section 6.5.2 on page 234. The IR spectrum of melam hydrate after treatment with formic acid is displayed in Figure 6.24. Notably, the absorption pattern, though being typical of melam compounds with respect to the  $\nu(\text{C}-\text{N})$  region, is markedly different from that of the melam hydrates shown in Figure 6.23. In particular, no absorption is found between 1530 and 1600  $\text{cm}^{-1}$  and the characteristic ring sextant bend is shifted toward lower wavenumbers (787  $\text{cm}^{-1}$ ). This observation is in line with the spectra **b** and **c** in Figure 6.23, where the same correlation holds. Thus, the tautomeric equilibrium may be quantitatively shifted towards the ring-protonated form upon treatment of the sample with formic acid. For better comparison, some spectroscopic properties of melam hydrate have already been contrasted with those of pure melam in section 6.4 on page 213; further details will be discussed in the next section.

### 6.5.1.2 Melam – DMSO Solvate

A melam–DMSO adduct was obtained by heating a suspension of 150 mg melam hydrate in 50 mL DMSO at 393 K for 1 h until a clear solution if formed. Evaporating the solution at 313 K yielded transparent block-like crystals.

The obtained crystals turned out to be highly defective (twinning, reflections smeared out in conjunction with superstructure reflections), so that no satisfactory crystal structure solution and refinement was possible. Selected data of the crystal structure solution and refinement are given in Table 6.8. Despite the consequently low data quality, the principal arrangement of the molecules in the cell and, thus, the identity of the obtained melam–DMSO adduct can be substantiated.

Although no definite statements on the hydrogen positions can be made, Figure 6.25 demonstrates that the compound of formula  $\text{C}_6\text{N}_{11}\text{H}_9 \cdot 2 \text{O=S(CH}_3\text{)}_2$  is in fact a neutral adduct made up from layers of melam molecules separated by DMSO solvent molecules. The molecular structure of melam in the adduct resembles quite closely that of pure melam (Fig. 6.16 on page 217) in that the molecules are again twisted about the bridging nitrogen atom and therefore depart significantly from planarity, the triazine rings, however, being essentially planar. The layers made up from melam molecules are shown for clarity without solvent molecules in Figure 6.25 (right). Within these layers, the molecules are hydrogen-bonded to adjacent melam molecules *via* the amino groups and ring nitrogen atoms, respectively, whereas the melam and DMSO layers are hydrogen-bonded between the oxygen atoms and amino nitrogen atoms.

**Table 6.8:** Crystallographic data for the melam–DMSO adduct.

Formula	C <sub>6</sub> N <sub>11</sub> H <sub>9</sub> · 2 O=S(CH <sub>3</sub> ) <sub>2</sub>
<i>M<sub>w</sub></i> / g · mol <sup>-1</sup>	391.2
crystal system	monoclinic
space group	<i>P</i> 2 <sub>1</sub> /c (no. 14)
<i>T</i> / K	293
diffractometer	Stoe IPDS
radiation ( $\lambda$ / pm)	Mo-K <sub>α</sub> (71.073)
monochromator	graphite
<i>a</i> / pm	3068.3(6)
<i>b</i> / pm	1042.0(2)
<i>c</i> / pm	1199.5(2)
$\beta$ / °	92.26(3)
<i>V</i> / 10 <sup>6</sup> · pm <sup>3</sup>	3832.0(13)
<i>Z</i>	16
$\rho_{calcd}$ / g · cm <sup>-3</sup>	1.284
$\mu$ / mm <sup>-1</sup>	0.305
crystal size / mm <sup>3</sup>	
total no. reflections	24025
independent reflections	6744 ( $R_{int}$ = 0.1138)
observed reflections	4710
refined parameters / restraints	with $F_o^2 \geq 2\sigma(F_o^2)$ 447 / 0
GooF on $F^2$	
<i>R</i> indices (all data)	$R_1 = 0.2269$ (0.2525) $wR_2 = 0.5116$ (0.5167) with w = $[\sigma^2(F_o^2) + (0.1000P)^2 + 0.0000P]^{-1}$ where $P = (F_o^2 + 2F_c^2)/3$

The IR spectrum of the adduct is displayed in Figure 6.26. The similarity to the spectrum of melam hydrate **a** (Fig. 6.23 on page 228) is evident, although most bands are slightly ( $\approx 6\text{ cm}^{-1}$ ) blue-shifted and well resolved in the DMSO adduct, and the absorption at 1591 cm<sup>-1</sup> is less pronounced than the corresponding band in melam hydrate. However, the ring sextant bend is located at 814 cm<sup>-1</sup>, which is indicative of non-protonated triazine rings and, thus, the symmetric tautomeric form of melam (cf. Fig. 6.2 on page 199).

The <sup>15</sup>N CP-MAS solid-state NMR spectrum of the DMSO–adduct (**c**) is shown in Figure 6.27 together with those of melam hydrate **a** and the recrystallized hydrate **b** (cf. Fig. 6.18 on page 220, right). The spectra of **a** and **b** are largely identical apart from the better signal resolution in the recrystallized form **b**, and the DMSO–adduct differs only slightly in that one of the *N*<sub>tert</sub> signals is shifted downfield ( $-188.1$  ppm) with respect to the others

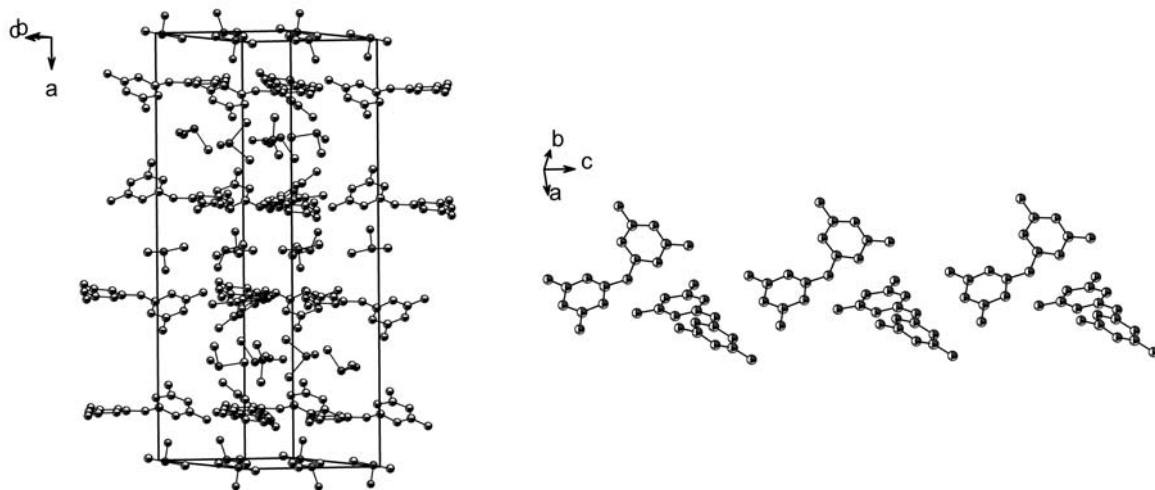


**Figure 6.25:** Left: Unit cell of the solvate  $C_6N_{11}H_9 \cdot 2 O=S(CH_3)_2$ . Layers of melam molecules separated by solvent molecules are extending in the  $b-c$  plane. Right: Twisted conformation of the neutral melam molecules (DMSO molecules are omitted for clarity).

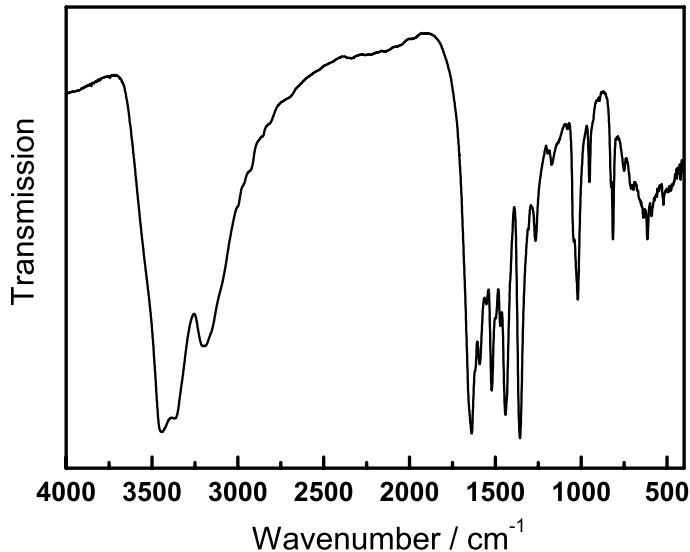


**Figure 6.26:** FTIR spectrum of the melam-DMSO solvate, recorded between 4000 and 400  $cm^{-1}$  as KBr pellet.

(-198.2 to -207.5 ppm), which is also observed for pure melam (see above). In addition, the  $NH_2$  signals are found between - 285.8 and - 293.1 ppm for the adduct, whereas they are shifted upfield between - 293.0 and - 297.9 ppm for the hydrates. All  $^{15}N$  spectra are in agreement with non-protonated, neutral melam molecules, as two different NH signals would be expected if melam acted as a base. However, spectrum (b) also shows no evidence for the

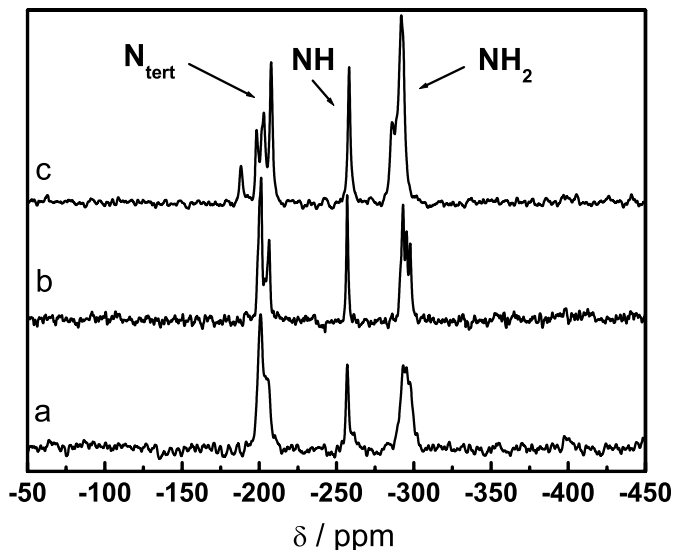


**Figure 6.27:**  $^{15}\text{N}$  CP-MAS solid-state NMR spectra of the melam hydrate (a) (bottom, Agrolinz Melamine International GmbH) and (b) (middle, recrystallized from  $\text{NaOH}$  solution), as well as the melam–DMSO solvate (c) (top). The recycle delay was 4 s for (a), 5 s for (b), and 2 s for (c); the contact time  $\tau_c$  was 4 ms and the spinning frequency 10 kHz for all measurements.

conjugated tautomeric form suggested to be present to some extent from IR spectroscopy, as the spectra would presumably become more complex in this case owing to the reduced non-crystallographic point symmetry of the melam molecules. In addition, the bridging nitrogen in the conjugated tautomer would be expected in a chemical shift range intermediate between the  $\text{N}_{\text{tert}}$  and  $\text{NH}$  signals ( $\approx -220$  ppm), where no resonance is found. It may be conjectured that the conjugated tautomer is formed only to such a small extent that it is invisible to NMR, which intrinsically is a non-quantitative method, yet no ultimate conclusion as for the prevailing tautomer in the solid-state can be made.

### 6.5.1.3 UV/Vis Spectroscopy

The UV/vis spectra of melam, melam hydrate and melam–DMSO solvate are displayed in Figure 6.28. Whereas the spectra of melam hydrate (dash dotted line) and melam–DMSO solvate are quite similar, exhibiting absorption maxima around 230 / 265 nm (shoulder at 335 nm) and 225 / 265 nm (shoulder at 295 nm), respectively, melam shows an additional broad band centered around 320 nm (cf. section 6.21 on page 223). One rationale for the observed absence of this low energy band in the solvates may be the modification of energy levels by the presence of the solvate molecules. A more likely explanation however is a change

in the tautomeric state of the melam molecules, which could be present in a chinoid form in the solvates. According to the literature, a change in the prototropic form entails a shift in the UV/vis absorption maxima as outlined in Figure 6.29 [78].

Whereas for melam the tautomer A matches best the calculated wavelengths, the solvates rather seem to adopt the tautomeric form B according to this hypothesis. In all cases, however, tautomer C seems to be the least likely resonance structure. These observations support the results from IR spectroscopy (Fig. 6.23 on page 228), according to which the tautomeric state of melam and its hydrates seems to be different, or at least “interchangeable” to some extent.

### 6.5.2 Melamium Salts

As outlined above, the melam–ammonium chloride adduct can be thought of as a “melam hydrochloride · ammonium chloride” co-crystallisate, in which the melam core is protonated [240]. In addition, *Finkel'shtein* already reported on the syntheses of simple melam salts obtained from reactions with various inorganic acids in aqueous solution [77]. Therefore, attention will be paid in the following section to the acid-base behavior of melam and to the synthesis and characterization of novel melam salts.

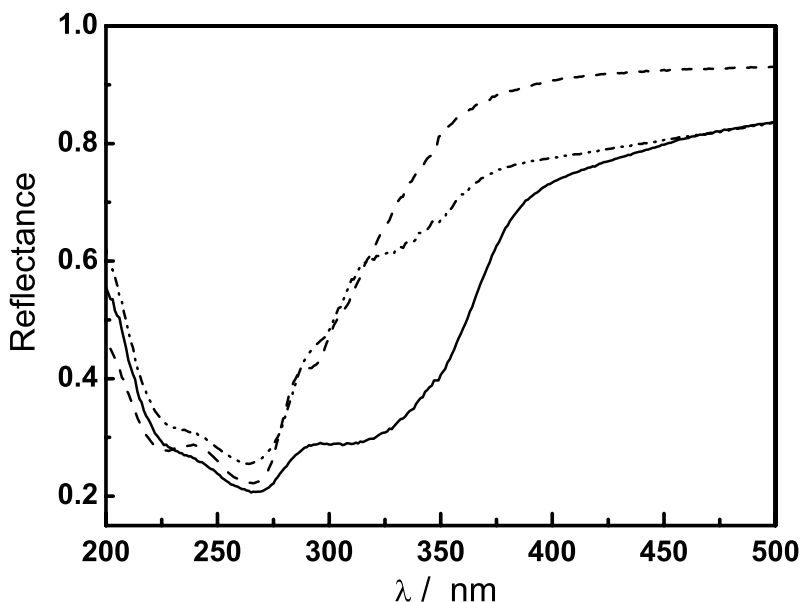


**Figure 6.28:** UV/vis spectra of melam (solid line), melam hydrate (dash dotted line) and melam–DMSO solvate (dashed line).

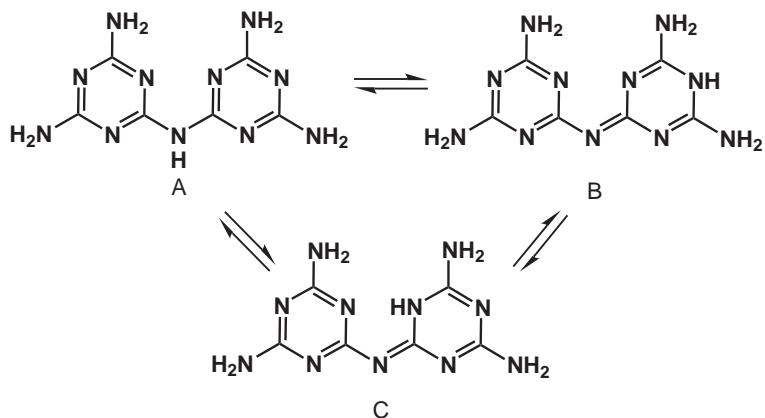


**Figure 6.29:** Three prototropic forms of melam with calculated absorption maxima at 296 / 336 nm (A), 207 / 238 nm (B), and 188 / 270 nm (C) [78].

#### 6.5.2.1 General Procedure

As outlined in Figure 6.22 on page 226 the synthesis of melam salts may be conducted in solution or in the solid state. In principle, whereas melam hydrate and melam perchlorate (see below) were used predominantly as the starting materials in solution reactions, melamine was the substance of choice when conducting the conversions in the solid state.

Reactions based on melam hydrate were typically conducted using 15 mg ( $5.53 \cdot 10^{-5}$  mol) of melam hydrate, which were suspended in 40 mL H<sub>2</sub>O. The suspension was heated under reflux and acid / base was added until a clear solution was formed. After heating for another 5 – 15 minutes, the solution was cooled down slowly and either evaporated at room temperature or transferred into the refrigerator. Alternatively, melam hydrate was added to a diluted ( $\approx 20\%$ ) solution of acid / base and the suspension was heated under reflux until all starting material had dissolved, then cooled down and left standing for crystallization.

A major problem when using melam hydrate is its low solubility in essentially all solvents tested (cf. Table 6.6 on page 227). However, most melam salts exhibit better solubilities so that the target salt could nevertheless be isolated quantitatively. In cases where no suitable acid was available or it was too weak to completely dissolve melam hydrate, melam perchlorate was used instead as the starting material, since its solubility in aqueous solution is significantly better as compared to the hydrate. The latter approach is based on the metathesis reaction between melam perchlorate and the respective salt added to the solution, so that different anions may be exchanged for the perchlorate ion. In order to shift the equilibrium of the reaction toward the product side, the potassium salts were chosen as the component added, so that the comparatively low solubility of the formed potassium perchlorate could be utilized. However, this method turned out to be only little effective as melam perchlorate

**Table 6.9:** List of solution reactions carried out for the synthesis of melam compounds. Starting materials and reaction conditions are given.

Starting material	Component added	Conc. / Conditions	Observation / Products
melam hydrate (80 mg)	$\text{H}_3\text{PO}_4$ (20 mL)	20 %, 338 K	no crystallization
melam hydrate (20 mg / 40 mL HOAc)	$\text{H}_3\text{PO}_4$ (6 mL)	85 %, 373 K	no crystallization
melam hydrate (80 mg)	$\text{H}_2\text{SO}_4$ (32 mL)	20 %, 363 K	no crystallization
melam hydrate (20 mg / 40 mL HOAc)	$\text{H}_2\text{SO}_4$ (8 mL)	96 %, 373 K	no crystallization
melam hydrate (40 mg)	HCl (90 mL)	20 %, 363 K	melam hydrochloride
melam hydrate (20 mg / 40 mL $\text{H}_2\text{O}$ )	HBr (2 mL)	47 %, 373 K	melam hydrobromide
melam hydrate (20 mg / 40 mL $\text{H}_2\text{O}$ )	HI (2 mL)	98 %, 273 K	amorphous precipitate
melam hydrate (50 mg)	$\text{HNO}_3$ (20 mL)	20 %, 363 K	ammelinium nitrate
melam hydrate (120 mg / 40 mL $\text{H}_2\text{O}$ )	$\text{HClO}_4$ (1.6 mL)	60 %, 373 K	melamium perchlorate
melam hydrate (20 mg / 40 mL $\text{H}_2\text{O}$ )	TFA <sup>a</sup> (1.5 mL)	98 %, 350 K	amorphous precipitate
melam hydrate (20 mg / 40 mL $\text{H}_2\text{O}$ )	TFMS <sup>b</sup> (0.4 mL)	> 98 %, 373 K	amorphous precipitate
melam hydrate (85 mg / 40 mL $\text{H}_2\text{O}$ )	$\text{CH}_2\text{O}_2$ (12 mL)	100 %, 368 K	melam hydrate
melam hydrate (50 mg / 40 mL $\text{H}_2\text{O}$ )	$\text{CH}_3\text{CO}_2\text{H}$ (3 mL)	100 %, 373 K	melam hydrate
melam perchlorate (30 mg / 40 mL $\text{H}_2\text{O}$ )	$\text{K}_2\text{SO}_4$ (11 mg)	360 K	amorphous precipitate
melam perchlorate (30 mg / 40 mL $\text{H}_2\text{O}$ )	$\text{KNO}_3$ (13 mg)	353 K	amorphous precipitate
melam perchlorate (30 mg / 30 mL $\text{H}_2\text{O}$ )	$\text{KH}_2\text{PO}_4$ (18 mg)	333 K	amorphous precipitate
melam perchlorate (30 mg / 40 mL $\text{H}_2\text{O}$ )	KSCN (13 mg/10 mL $\text{H}_2\text{O}$ )	373 K	amorphous precipitate
melam perchlorate (30 mg / 40 mL $\text{H}_2\text{O}$ )	KOCN (10 mg/5 mL $\text{H}_2\text{O}$ )	373 K	amorphous precipitate
melam perchlorate (30 mg / 40 mL $\text{H}_2\text{O}$ )	$\text{KIO}_4$ (29 mg/7 mL $\text{H}_2\text{O}$ )	363 K	amorphous precipitate

<sup>a</sup> trifluoracetic acid

<sup>b</sup> trifluormethylsulfonic acid

tends to form amorphous precipitates when dissolved in aqueous solution after an “induction time” of several hours or even days. Presumably, melam perchlorate is only stable in acidic solution, as in neutral solution the melamium cation acts as an acid and loses its protons, thereby transforming into melam hydrate or a similar species. We also tried to adapt this procedure to classical metathesis reactions using ion exchange resins, however, melam perchlorate turned out to be unstable in contact with the – slightly basic – anion exchange resin so that an amorphous precipitate was already formed before exchange could occur.

Reactions of melam hydrate with concentrated and diluted bases did not lead to deprotonation of melam; instead recrystallization from aqueous solution occurred (cf. section 6.5.1.1 on page 227). Since deprotonated melam is most certainly a stronger base than water, deprotonation should only be observable in non-aqueous and preferably aprotic solvents, the use of which was not systematically pursued in the present work.

**Table 6.10:** Representative examples for solid-state reactions aiming at the synthesis of melam compounds starting from melamine and acid salts. A summary of the reaction conditions and products is given.

Starting material	Component added <sup>a</sup>	Conditions	Observation / Products
melamine (140 mg)	NH <sub>4</sub> OAc (56 mg)	ampoule, 623 K	unidentified
melamine (140 mg)	NH <sub>4</sub> OAc (56 mg)	ampoule, 723 K	melem
melamine (140 mg)	NH <sub>4</sub> Br (71 mg)	ampoule, 573 K	starting materials + unidentified phase
melamine (140 mg)	NH <sub>4</sub> Br (71 mg)	ampoule, 723 K	melam salt
melamine (160 mg)	NH <sub>4</sub> Br (98 mg)	ampoule, 743 K	melam salt
melamine (140 mg)	NH <sub>4</sub> H <sub>2</sub> PO <sub>4</sub> (83 mg)	ampoule, 623 K	unidentified phosphate
melamine (140 mg)	NH <sub>4</sub> H <sub>2</sub> PO <sub>4</sub> (83 mg)	ampoule, 723 K	amorphous
melamine (140 mg)	(NH <sub>4</sub> ) <sub>2</sub> HPO <sub>4</sub> (95 mg)	ampoule, 723 K	melamine
melamine (140 mg)	(NH <sub>4</sub> ) <sub>2</sub> HPO <sub>4</sub> (95 mg)	ampoule, 703 K	melem + unidentified phase
melamine (160 mg)	(NH <sub>4</sub> ) <sub>2</sub> HPO <sub>4</sub> (84 mg)	ampoule, 673 K	NH <sub>4</sub> PO <sub>3</sub>
melamine (140 mg)	(NH <sub>4</sub> ) <sub>2</sub> SO <sub>4</sub> (95 mg)	ampoule, 773 K	unidentified
melamine (160 mg)	(NH <sub>4</sub> ) <sub>2</sub> SO <sub>4</sub> (56 mg)	ampoule, 623 K	unidentified heptazine deriv.
melamine (60 mg)	melamine sulphate <sup>b</sup> (77 mg)	ampoule, 623 K	unidentified

<sup>a</sup> declarations of weight (in mg) are rounded off

<sup>b</sup> [C<sub>3</sub>N<sub>6</sub>H<sub>7</sub>]<sub>2</sub> SO<sub>4</sub> · 2 H<sub>2</sub>O

An overview of the reactions designed to obtain melam salts is given in Tables 6.9 and 6.10, listing selected reactions in solution and solid-state reactions, respectively. The latter were carried out in ampoules (length 120 mm, outer diameter 16 mm, wall thickness 1.5 mm) at

temperatures between 573 and 773 K, using a heating rate of 1 K min<sup>-1</sup> and heating times of approx. 12 h.

As can be seen from Tables 6.9 and 6.10, the majority of the reactions carried out in solution failed owing to the precipitation of a gelatinous white solid, which could not be identified by means of X-ray powder diffraction, but may be an amorphous melam hydrate species.

Reactions carried out with aqueous phosphoric and sulfuric acid were not successful, as no precipitation from solution occurred. Attempts to facilitate precipitation by conducting the reaction in acetic acid did not yield products either. Therefore, solid-state reactions were carried out using the respective salts, however, in the case of phosphate salts the desired product was not obtained since no suitable combination of temperature and stoichiometry of the reactants was found. In several cases, the formation of melem species could be inferred based on the IR data.

Only the addition of hydrochloric, hydrobromic and perchloric acid afforded crystalline melam salts which were characterized by single-crystal X-ray diffraction and will be discussed in the next section. The product recovered from treatment with nitric acid was found to be the hydrolysis product of melamium nitrate, namely ammelinium nitrate (cf. section 6.6 on page 263). The same observation was made when evaporating melam halogenide solutions at 313 K; presumably melam nitrate is more sensitive to hydrolysis but can be stabilized on careful evaporation of the solvent or by crystallization below room temperature.

### 6.5.2.2 Melamium Halides

As described above, a melam–ammonium chloride adduct of the notional formula  $[C_6N_{11}H_{10}]Cl \cdot 0.5 NH_4Cl$  has been synthesized by reaction of melamine with ammonium chloride (see above) and thoroughly characterized by *Jürgens* [240]. In order to explore alternative pathways to the formation of melam hydrohalides and to test as to whether the co-crystallization of ammonium chloride can be circumvented, melam hydrate was reacted with diluted hydrochloric acid according to Table 6.9 on page 236.

In addition both reaction pathways (solid state and solution) have been adapted to the use of ammonium bromide or hydrobromic acid instead. The IR spectrum of the product obtained from the reaction of melamine with  $NH_4Br$  is shown in Figure 6.30 (bottom spectrum, (a)). For comparison the IR spectrum of the crystalline compound obtained by addition of conc. HBr to an aqueous suspension of melam hydrate according to Table 6.9 on page 236 is displayed (top spectrum, (b)). The spectra are very similar, yet small differences especially between 3100 and 3400 cm<sup>-1</sup> and between 1520 and 1324 cm<sup>-1</sup> are evident. Notably, the triazine ring bend observed at 801 cm<sup>-1</sup> in the bottom spectrum (broad band) is shifted to

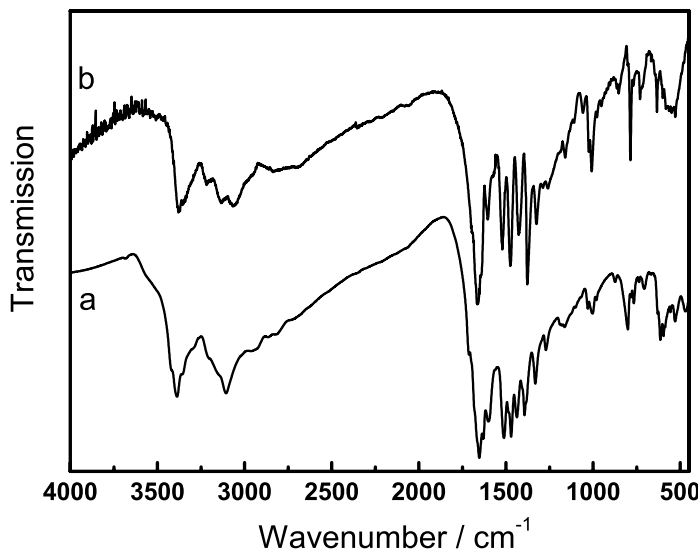


**Figure 6.30:** FTIR spectra (KBr pellets) of the products obtained from the solid-state reaction between melamine and ammonium bromide (a) and from the reaction of melam hydrate with hydrobromide acid in aqueous solution (b).

786  $\text{cm}^{-1}$  in the top spectrum (sharp band). The observed bands, though being very similar, do not conform in every detail to those reported by Jürgens for a compound with tentative formula  $[\text{C}_6\text{N}_{11}\text{H}_{10}]\text{Br} \cdot 0.5 \text{NH}_4\text{Br}$ , which may in part be due to impurities or different measuring conditions.<sup>6</sup> Both spectra can clearly be attributed to compounds containing the melam core owing to the characteristic  $\nu(\text{C}-\text{N})$  stretching vibrations between 1260 and 1400  $\text{cm}^{-1}$ . The spectra, however, lack evidence for the presence of ammonium bromide in a homogeneous phase together with melam.

Whereas the products of the solid-state reactions were only obtained as polycrystalline powders and could not be recrystallized due to their extremely low solubility in all solvents except for DMSO, the solution reactions afforded products in single-crystalline form. The compounds were identified by single-crystal X-ray diffraction as melam hydrochloride hydrate and melam hydrobromide hydrate, respectively. However, in all cases the crystals were partial pseudo-merohedral twins or consisted of more than one individual, yielding data sets that could not be separated without loosing the majority of data, owing to heavy overlap of the reflections pertaining to different individuals. The best results were obtained by using the *complete* set

<sup>6</sup>Elemental analysis of the two compounds (a) and (b) (cf. Fig. 6.30) yields similar results, which do not allow for an unambiguous assignment of their compositions.

of reflections as input files for the structure solution. Selected crystallographic data are listed in Table 6.11.

**Table 6.11:** Selected crystallographic data for melam hydrochloride hydrate and melam hydrobromide hydrate.

Formula	$[\text{C}_6\text{N}_{11}\text{H}_{10}]\text{Cl} \cdot \text{H}_2\text{O}$	$[\text{C}_6\text{N}_{11}\text{H}_{10}]\text{Br} \cdot \text{H}_2\text{O}$
$M_w / \text{g} \cdot \text{mol}^{-1}$	289.72	334.18
crystal system	monoclinic	monoclinic
space group	$P2_1/c$ (no. 14)	$P2_1/c$ (no. 14)
$T / \text{K}$	298	298
diffractometer	Nonius Kappa CCD	Xcalibur S (Oxford Diffraction)
radiation ( $\lambda / \text{pm}$ )	Mo- $\text{K}_\alpha$ (71.073)	Mo- $\text{K}_\alpha$ (71.073)
monochromator	graphite	graphite
$a / \text{pm}$	6.1064(12)	6.1114(5)
$b / \text{pm}$	7.8157(16)	7.9362(6)
$c / \text{pm}$	24.518(5)	25.231(2)
$\beta / {}^\circ$	93.67(3)	93.89(1)
$V / 10^6 \cdot \text{pm}^3$	1167.8(4)	1220.9(6)
$Z$	4	4
$\rho_{\text{calcd}} / \text{g} \cdot \text{cm}^{-3}$	1.236	1.818
$\mu / \text{mm}^{-1}$	0.258	3.383
total no. reflections	15876	10845
independent reflections	2647 ( $R_{\text{int}} = 0.1247$ )	2137 ( $R_{\text{int}} = 0.0867$ )
observed reflections	2169	2011
refined parameters / restraints	with $F_o^2 \geq 2\sigma(F_o^2)$ 189 / 0	with $F_o^2 \geq 2\sigma(F_o^2)$ 172 / 0
GooF on $F^2$	1.196	1.143
$R$ indices (all data)	$R_1 = 0.0972$ (0.1087) $wR_2 = 0.2744$ (0.2788) with $w = [\sigma^2(F_o^2) + (0.0171P)^2 + 10.5419P]^{-1}$ where $P = (F_o^2 + 2F_c^2)/3$	$R_1 = 0.1382$ (0.1428) $wR_2 = 0.3169$ (0.3193) with $w = [\sigma^2(F_o^2) + (0.0000P)^2 + 100.4706P]^{-1}$ where $P = (F_o^2 + 2F_c^2)/3$
min./max. residual electron density / $e \cdot 10^{-6} \text{ pm}^{-3}$	- 0.476 / 1.207	- 2.422 / 2.505

The molecular and crystal structure of both melam hydrohalide hydrates are displayed in Figures 6.31 and 6.32. Considering the almost identical metrics as well as the arrangement of the ions in the unit cell, the two melam salts are isotypic. Whereas the hydrogen positions are shown for the hydrochloride salt, they could not be determined for melam hydrobromide. Owing to the low data quality in both cases, only the most significant observations that can be extracted from the data will shortly be summarized.

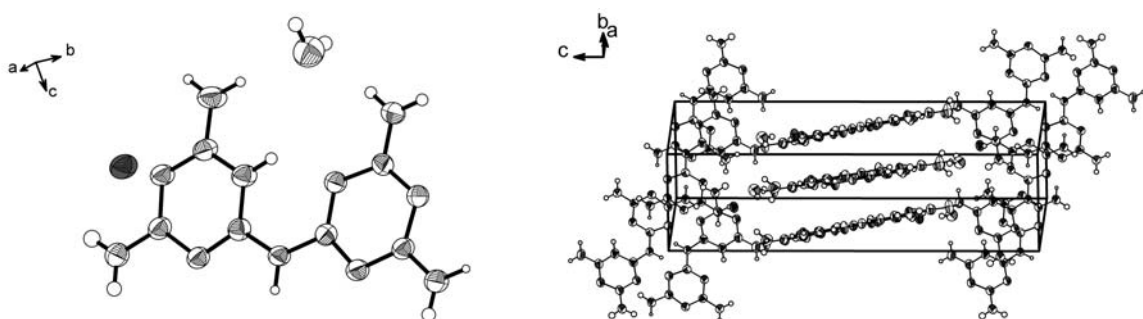


**Figure 6.31:** Asymmetric unit (left) and unit cell (right) of melam hydrochloride hydrate. The thermal ellipsoids are drawn at the 50 % probability level.

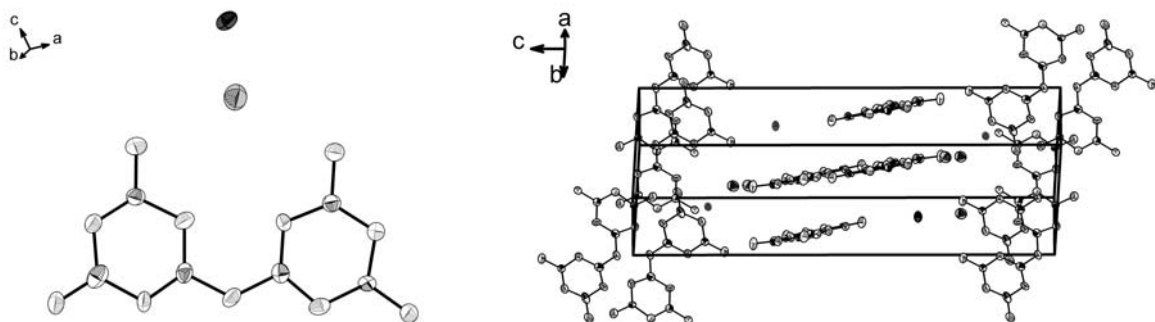


**Figure 6.32:** Asymmetric unit (left) and unit cell (right) of melam hydrobromide hydrate. The thermal ellipsoids are drawn at the 50 % probability level.

In both salts melam is mono-protonated according to the presence of one counter anion, and all melam cations are planar within experimental error. The melam core in the hydrochloride is protonated at a ring nitrogen atom such that a hydrogen-bond is formed between the two ring nitrogen atoms of adjacent rings facing each other.

The cations form strands of pairwise  $\pi$ -stacked molecules, with the halides and water molecules being inserted between the strands. Adjacent strands exhibit a different stacking sense such that the molecular planes of the melam cations enclose an angle of about  $60^\circ$ .

### 6.5.2.3 Melamium Diperchlorate Dihydrate

Melamium perchlorate was obtained from reaction of melam hydrate with perchloric acid in aqueous solution according to Table 6.9 on page 236. Relevant crystallographic data are summarized in Table 6.12. The unit cell (space group  $C2/c$ ) is built up from four formula units, each consisting of a doubly protonated melam molecule, two perchlorate anions, and two molecules of crystal water. Only one triazine ring and one perchlorate anion are contained in the asymmetric unit, therefore the cation is made up from two identical triazine units and

all perchlorate anions are identical.

**Table 6.12:** Crystallographic data for melamium diperchlorate dihydrate.

Formula	“[C <sub>6</sub> N <sub>11</sub> H <sub>11</sub> ] · 2 ClO <sub>4</sub> · 2 H <sub>2</sub> O” <sup>a</sup>
<i>M<sub>w</sub></i> / g · mol <sup>-1</sup>	472.84
crystal system	monoclinic
space group	<i>C</i> 2/c (no. 15)
<i>T</i> / K	130
diffractometer	STOE IPDS, graphite
radiation ( $\lambda$ / pm)	Mo-K $\alpha$ (71.073)
monochromator	graphite
<i>a</i> / pm	1747.8(4)
<i>b</i> / pm	1148.2(2)
<i>c</i> / pm	993.6(2)
$\beta$ / °	118.79(3)
<i>V</i> / 10 <sup>6</sup> · pm <sup>3</sup>	1747.4(6)
<i>Z</i>	4
$\rho_{calcd}$ / g · cm <sup>-3</sup>	1.797
F(000)	967
$\mu$ / mm <sup>-1</sup>	0.453
crystal size / mm <sup>3</sup>	0.23 x 0.14 x 0.12
diffraction range	3.66 $\leq \theta \leq$ 27.49
index range	-22 $\leq h \leq$ 22, -14 $\leq k \leq$ 13, -11 $\leq l \leq$ 12
total no. reflections	7067
independent reflections	1907 ( $R_{int} = 0.0359$ )
observed reflections	1620
refined parameters / restraints	with $F_o^2 \geq 2\sigma(F_o^2)$ 170 / 0
GooF on $F^2$	1.058
<i>R</i> indices (all data)	$R_1 = 0.0400$ (0.0493) $wR_2 = 0.1009$ (0.1048) with w = $[\sigma^2(F_o^2)$ $+(0.0535P)^2 + 1.9821P]^{-1}$ where $P = (F_o^2 + 2F_c^2)/3$
min./max. residual	
electron density /	- 0.437 / 0.465
$e \cdot 10^{-6}$ pm <sup>-3</sup>	

<sup>a</sup> idealized formula

Several noticeable features have to be pointed out: In contrast to structures containing neutral melam molecules the cationic melam unit is planar within experimental error. Also, the distortion of the triazine rings is obvious, yet less pronounced, with the average angles C–

N–C and N–C–N within the rings amounting to  $117^\circ$  and  $124^\circ$ , respectively. The internal C–N distances vary between 132 and 136 pm, whereas the external C–N<sub>exo</sub> bond lengths are shorter by about 2–3 pm (131/132 pm).

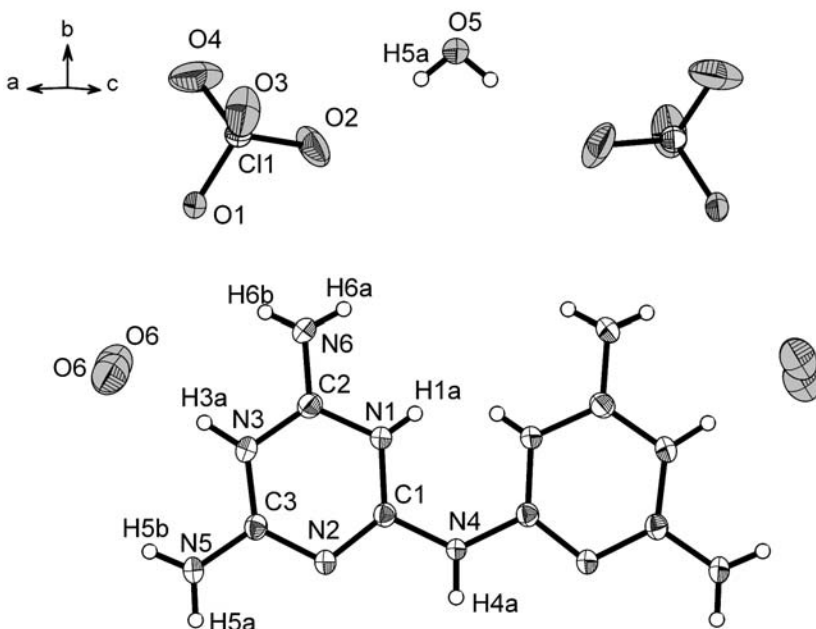


**Figure 6.33:** Representation of the molecular structure of melamium perchlorate hydrate, of which one half is contained in the asymmetric unit. The oxygen positions O6 are only half occupied, and the proton positions H1a and H3a are disordered over the melam backbone with SOFs being close to 0.5. Thermal displacement ellipsoids (except for H) are drawn at the 50 % probability level.

Notably, the two triazine rings do not possess a chinoid structure with a bridging C1–N4=C1 unit, but a C1–N4H–C1 bridge with the bond lengths elongated (138 pm) and the angle widened up ( $128^\circ$ ) in analogy to the situation in melam. The presence of two perchlorate ions per melam molecule suggests melam to be present as a doubly protonated cation. However, four proton sites attached to the ring nitrogen atoms are found from difference Fourier synthesis, which have site occupation factors on free refinement between 0.5(1) (H3a) and 0.7(1) (H1a).<sup>7</sup> Thus, static disorder has to be inferred, entailing an almost equal protonation of N1 and N3 so that in total two protons are attached to the rings (Fig. 6.33).

Another sign of static disorder is found at the crystal water site O6. Instead of a single oxygen, a split position is found in the refinement with the centers of mass lying 119 pm apart, which is clearly too short for two adjacent water molecules.<sup>8</sup> The refined site occupation factor for

<sup>7</sup>Note that the refinement of the site occupation factors for hydrogen positions is intrinsically critical; the results should therefore not be overestimated.

<sup>8</sup>The O–O distance in a dioxygen molecule is 128 pm [8]; for chemical reasons and the O6 site occupation factors of  $\approx 0.5$  the co-crystallization of an oxygen molecule is considered highly unlikely.

O6 is 0.562(9), thereby indicating an about equal occupation of both split positions with the sum being 1.

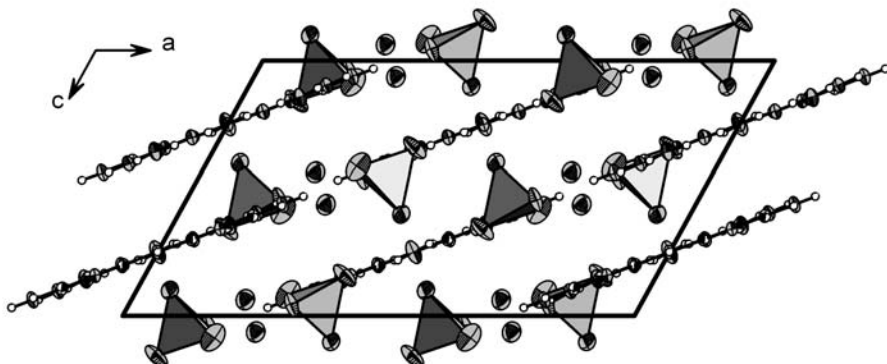


**Figure 6.34:** Unit cell of melamium perchlorate hydrate, view along [010]. Thermal displacement ellipsoids (except for H) are drawn at the 50 % probability level.

It has to be noted, however, that – in contrast to the situation for O5 – no hydrogen positions were found around the presumed crystal water O6. Both split positions of the latter are hydrogen-bonded to N3 with relatively short donor-acceptor distances of 274 and 282 pm, respectively. The distances between the split positions of O6 and O1 (314 and 335 pm) are close to the sum of the van-der-Waals radii.<sup>9</sup> It may be conjectured that the existence of the split position at O6 is a consequence of the short interatomic distance of O1 and O6, which forces the “mobile” crystal water in two more beneficial positions with slightly longer O1 – O6 distances. However, the distance O5 – O2 (298 pm) is even shorter as compared to O1 – O6, which may be rationalized by the influence of the hydrogen bonding contact O5–H5a … O2. The Cl–O distances within the perchlorate anion lie in the usual range from 142 to 144 pm.

The melam molecules form planar layers extending along *b*, the long molecular axes being parallel to the [10 $\bar{1}$ ] direction (Fig. 6.34). The perchlorate ions are inserted between the melam molecules, linking the latter by hydrogen contacts with donor-acceptor distances between 288 pm (N6 … O1) and 301 pm (N6 … O3).

The molecular planes of the cations are not stacked in an eclipsed manner, but molecules of adjacent sheets are displaced by about one triazine unit. Remarkably, the stacking distance between adjacent planes is as small as 325 pm.

The IR spectrum of melamium perchlorate is displayed in Figure 6.35. Strong absorption is visible in the  $\nu(\text{C}=\text{N})$  and  $\delta(\text{NH}_2)$  region between 1687 and 1445  $\text{cm}^{-1}$ , as well as between 1089 and 1018  $\text{cm}^{-1}$  attributable to the  $\nu(\text{Cl–O})$  vibrations [480]. The triazine sextant bend is

<sup>9</sup>Van-der-Waals radius of oxygen: 152 pm

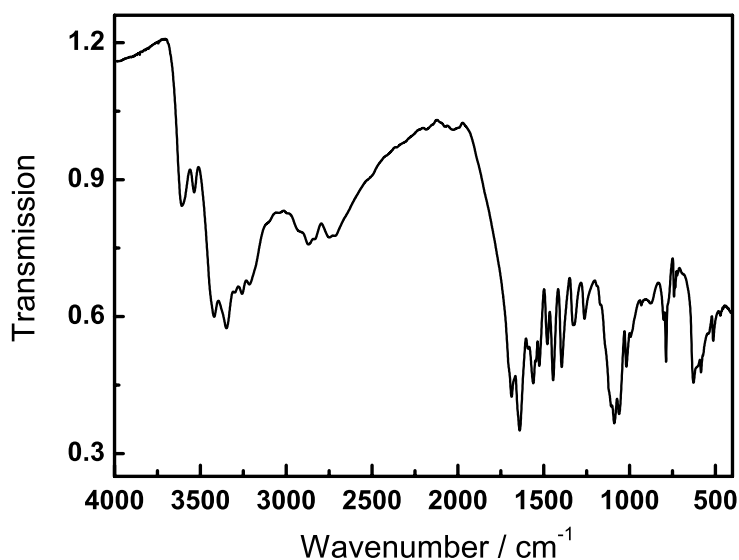


**Figure 6.35:** FTIR spectrum of melamium perchlorate dihydrate measured between  $4000$  and  $400\text{ cm}^{-1}$  at RT as  $\text{KBr}$  pellet.

located at  $787\text{ cm}^{-1}$ , which is in agreement with two singly protonated triazine rings. Notably, the  $\nu(\text{C}-\text{N})$  vibrations characteristic of melam are located at  $1395$ ,  $1329$ , and  $1262\text{ cm}^{-1}$ . The  $\text{O}-\text{H}$  and  $\text{N}-\text{H}$  stretching vibrations cover a comparatively large range between  $3608$  and  $2749\text{ cm}^{-1}$ , which is indicative of significantly varying hydrogen-bonding strengths.

### 6.5.3 Metal-Melam Complexes

#### 6.5.3.1 General Methodology

As we have seen above, melam exhibits weakly basic properties, thus forming salts with Brønstedt acids or the respective acid salts. The question arises as to whether Lewis acids are also suitable agents to form complexes with melam. To this end, the solid-state reactions of melamine with metal chlorides were studied, using a general protocol of which representative examples are listed in Table 6.14.

**Table 6.13:** List of solvents and their dissolving power for three representative melam complexes.

Solvent	Solubility Zn-melam complex	Solubility Fe-melam complex	Solubility Al-melam complex
DMSO	soluble	soluble	soluble
water	moderately soluble <sup>a</sup>	moderately soluble <sup>a</sup>	moderately soluble <sup>a</sup>
methanol	insoluble	insoluble	insoluble
water / methanol	moderately soluble	insoluble	insoluble
ethanol	insoluble	insoluble	insoluble
THF	insoluble	insoluble	insoluble
acetonitrile	insoluble	insoluble	insoluble
acetone	insoluble	insoluble	insoluble
diethylether	insoluble	insoluble	insoluble
chloroform	insoluble	insoluble	insoluble
methylenechloride	insoluble	insoluble	insoluble

<sup>a</sup> partial or complete decomposition

The results demonstrate that indeed the synthesis of complex melam salts or melam complexes is feasible,<sup>10</sup> with the tendency of formation being observed within a considerably large temperature range. In almost all cases except for the Zn-melam complex, identification of the products was exclusively based on elemental analysis, mass spectrometry and vibrational spectroscopy. In selected cases, solid-state NMR spectroscopy was also used as an analytical tool. Crystallization at high-temperatures was exceptional and only observed for the Zn compound under special reaction conditions. In all other cases, poorly crystalline products were obtained, and attempts to recrystallize from solution inevitably failed owing to the very poor solubility or instability of the products in almost all solvents tested. A list of the solvents together with their dissolving power for three representative salts is given in Table 6.13.

Dissolving the complexes in water presumably leads to their disintegration, and, ultimately,

<sup>10</sup>The term “complex” will be used in the following irrespective of the nature of the melam compound; in this context it simply signifies the *potential* coordination of melam to the metal center and to distinguish these compounds from simple ionic melam salts (cf. section 6.5.2 on page 234).

**Table 6.14:** Representative examples for solid-state reactions between different starting materials and metal chlorides, aiming at the synthesis of complex melam salts. A summary of the reaction conditions and products is given.

Starting material	Component added <sup>a</sup>	Conditions	Observation / Products
melamine (200 mg)	ZnCl <sub>2</sub> (54 – 108 mg)	ampoule, 593 – 703 K	Zn-melam complex <sup>b</sup>
melamine (160 mg)	FeCl <sub>3</sub> · 6 H <sub>2</sub> O (86 mg)	ampoule, 593 K	Fe-melam complex <sup>b</sup>
melamine (160 mg)	AlCl <sub>3</sub> · 6 H <sub>2</sub> O (77 mg)	ampoule, 593 K	Al-melam complex <sup>b</sup>
melamine (200 mg)	CuCl <sub>2</sub> (71 – 107 mg)	ampoule, 643 K	Cu-melam complex <sup>b</sup>
melamine (100 mg)	MgCl <sub>2</sub> · 6 H <sub>2</sub> O (323 mg)	ampoule, 673 K	Mg <sub>2</sub> (OH) <sub>3</sub> Cl
melamine (100 mg)	CaCl <sub>2</sub> (176 mg)	ampoule, 673 K	CaCl <sub>2</sub> hydrate + unknown phase
melam hydrate (100 mg)	ZnCl <sub>2</sub> (50 mg)	ampoule, 673 K	Zn-melam complex <sup>a</sup>
melam hydrate (100 mg)	AlCl <sub>3</sub> · 6 H <sub>2</sub> O (89 mg)	ampoule, 673 K	amorphous Al-melam complex
melam hydrate (100 mg)	CuCl <sub>2</sub> (50 mg)	ampoule, 643 K	Cu-melam complex
melem (90 mg)	ZnCl <sub>2</sub> (31 – 61 mg)	ampoule, 673 K	Zn-melam complex <sup>a</sup>
melem (87 mg)	AlCl <sub>3</sub> · 6 H <sub>2</sub> O (98 mg)	ampoule, 673 K	Al-melam complex
melem (100 mg)	FeCl <sub>3</sub> (74 – 223 mg)	ampoule, 623 K	amorphous
“melon” (200 mg)	ZnCl <sub>2</sub> (94 mg)	ampoule, 743 K	unidentified, layered compound
“melon” <sup>c</sup> (200 mg)	ZnCl <sub>2</sub> (47 mg)	ampoule, 673 K	unidentified, no reaction
“melon” (200 mg)	AlCl <sub>3</sub> · 6 H <sub>2</sub> O (160 mg)	ampoule, 673 K	melem
“melon” (200 mg)	AlCl <sub>3</sub> · 6 H <sub>2</sub> O (160 mg)	ampoule, 623 K	Al-melam complex <sup>b</sup>
“melon” <sup>c</sup> (60 mg)	AlCl <sub>3</sub> · 6 H <sub>2</sub> O (51 mg)	ampoule, 673 K	no reaction
“melon” (100 mg)	FeCl <sub>3</sub> · 6 H <sub>2</sub> O (54 mg)	ampoule, 573 K	amorphous

<sup>a</sup> Declarations of weight (in mg) are rounded off.

<sup>b</sup> The term “complex” as used here does not differentiate between salt-like and coordinative “complex” compounds.

<sup>c</sup> Crystalline form, well-defined interlayer distance, dark color (brown).

to melam hydrate formation. Recrystallization from DMSO only resulted in the precipitation of less crystalline powdered products.

Notably, metal chlorides without particularly pronounced Lewis acidity such as magnesium or calcium chloride do not afford the respective melam complexes. This finding highlights the necessity of a Lewis acid site for condensation of two triazine rings, which is probably facilitated by the coordination of the Lewis acid to the ring nitrogen atoms, thus bringing the

ring systems into close contact with each other and stimulating the separation of ammonia by draining electron density from the triazine cores.

Reactions between melam hydrate and metal salts were used as an additional piece of evidence for the formation of melam complexes, which worked for the Zn-, Cu- and Al-melam complexes.

An unexpected synthetic access to the Zn-melam and Al-melam complexes was observed by reacting *melem* with  $ZnCl_2$  and  $AlCl_3$  at 673 K, respectively (cf. Table 6.14). This observation is particularly instructive as it furnishes insight into the role of the Lewis acid metal salts in the reactions with carbon nitride systems. Obviously, the condensation of melam to melem is in part “reversible” in the presence of Lewis acids, which is in so far unexpected as the closed reaction system lacks ammonia. The latter, however, is necessary to increase the nitrogen content of the system and break up the more heavily condensed heptazine ring by nucleophilic attack. Presumably, the heptazine core is partly destroyed, at the same time giving off ammonia, while the remains are converted into the metal-melam complex by action of the Lewis acid.

This remarkable reaction thus indicates the following facts:

- The condensation of triazine to heptazine ring systems is reversible and presumably stimulated by the presence of Lewis acid sites together with ammonia.
- The stability of the heptazine ring is therefore limited, even at temperatures below 700 K. The thermal stability of the heptazine core is in fact greater than its chemical stability.
- The heptazine core may partly be broken-off at elevated temperatures and an equilibrium between the intact ring and its elementary constituents such as dicyandiamide, cyanamide and ammonia may be sustained, which allows for the dis- and reassembly of the heptazine and ditriazinyl-systems, respectively.

A similar observation has been made when reacting aluminium chloride hydrate with a poorly crystalline, low-temperature form of “melon”. If the reaction is conducted at 673 K, the only crystalline product that could be isolated was melem. If the temperature is lowered to 623 K, the X-ray powder pattern indicated the formation of the Al-melam complex. These observations again furnish information exceeding the issue of melam formation:

- Lewis acids are suitable to disintegrate the otherwise thermally stable “melon” at temperatures as low as 623 K. Nevertheless it has to be noted that this is true only for the non-crystalline (yellow) form of “melon”, which is more reactive than its crystalline (brown) counterpart. The latter does not disassemble under these reaction conditions.

- However, no general statement can be made with respect to the elementary building blocks of melon on the basis of these data. The fact that melem is afforded at higher temperatures, whereas at lower temperatures melam is obtained, presumably indicates that – as outlined above – an equilibrium between intact and disassembled building blocks is present, yielding those ring systems which are thermodynamically stable at the respective reaction temperatures.
- The tendency of Lewis acids to form complexes with melam is greater as compared to complex formation with melem.

The formation of metal-melam complexes briefly outlined above in a rather general context will be discussed in more detail with respect to the identification and characterization of the products in the following section.

### 6.5.3.2 Zn-Melam Complex $\text{Zn}[\text{C}_6\text{N}_{11}\text{H}_9]\text{Cl}_2$

The  $\text{ZnCl}_2$ -melam complex was synthesized from melamine and  $\text{ZnCl}_2$  according to the procedure described above (cf. Table 6.14). The neutral adduct crystallizes in the monoclinic space group  $P2_1/c$  with four formula units in the unit cell. Crystallographic data for  $\text{Zn}[\text{C}_6\text{N}_{11}\text{H}_9]\text{Cl}_2$  are summarized in Table 6.15, for elemental analysis data, cf. Table 6.16 on page 254. In the molecular complex melam functions as a neutral “ligand” coordinated to a  $\text{ZnCl}_2$  molecule *via* the ring nitrogen atoms N2 and N5, so that the Zn1 atom is located in a distorted tetrahedral environment made up from two N and two Cl atoms (Fig. 6.36). The Zn  $\cdots$  N contacts are roughly 200 pm, the Zn–Cl bonds amount to 223 and 225 pm, respectively. The steric requirements in the Lewis acid-base complex forces the melam ligand to slightly

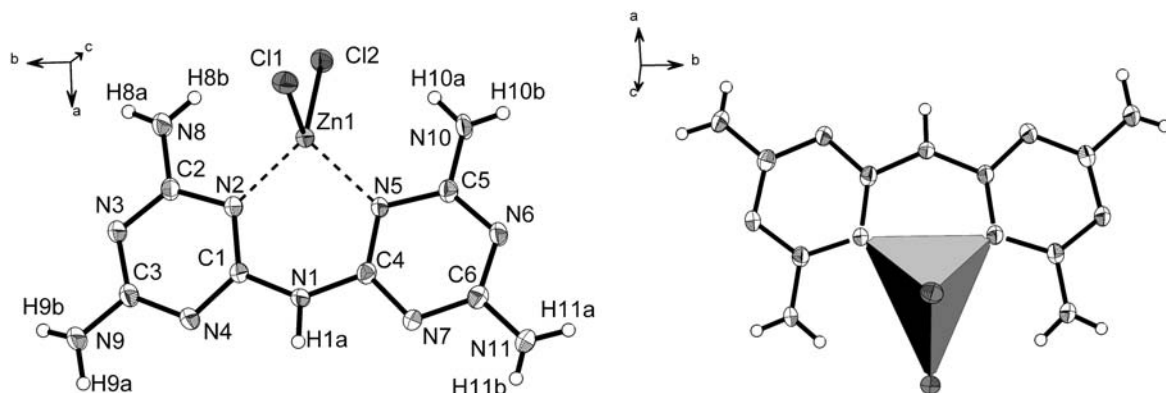


**Figure 6.36:** Asymmetric unit of the neutral zinc chloride - melam complex, in which melam functions as a bidentate ligand. Thermal displacement ellipsoids (except for H) are drawn at the 50 % probability level.

bend out of the molecular plane, thereby introducing a symmetrical distortion about the bridging nitrogen atom with a torsion angle  $\angle \text{N}5\text{--C}4\text{--N}1\text{--C}1$  of about  $14^\circ$ . The distortion is different from that found in pure melam, which again highlights the flexibility of the N-bridged triazine core.

The triazine rings slightly deviate from planarity, with the angles C–N–C and N–C–N

**Table 6.15:** Crystallographic data for  $\text{ZnCl}_2\text{--melam}$ .

Formula	$[\text{C}_6\text{N}_{11}\text{H}_9]\text{ZnCl}_2$
$M_w$ / g · mol <sup>-1</sup>	371.51
crystal system	monoclinic
space group	$P2_1/c$ (no. 14)
$T$ / K	200
diffractometer	Nonius Kappa CCD
radiation ( $\lambda$ / pm)	Mo–K $\alpha$ (71.073)
monochromator	graphite
$a$ / pm	743.0(2)
$b$ / pm	2233.2(5)
$c$ / pm	762.5(2)
$\beta$ / °	99.86(3)
$V$ / $10^6 \cdot \text{pm}^3$	1246.5(4)
$Z$	4
$\rho_{calcd}$ / g · cm <sup>-3</sup>	1.980
$F(000)$	744
$\mu$ / mm <sup>-1</sup>	2.409
crystal size / mm <sup>3</sup>	0.16 x 0.12 x 0.03
diffraction range	$3.27 \leq \theta \leq 27.50$
index range	$-9 \leq h \leq 9, -28 \leq k \leq 29,$ $-9 \leq l \leq 9$
total no. reflections	5595
independent reflections	2857 ( $R_{int} = 0.0378$ )
observed reflections	2186
refined parameters / restraints	with $F_o^2 \geq 2\sigma(F_o^2)$
GooF on $F^2$	217 / 0
$R$ indices (all data)	1.057
	$R_1 = 0.0306$ (0.0505)
	$wR_2 = 0.0697$ (0.0754)
	with $w = [\sigma^2(F_o^2)$
	$+(0.0323P)^2 + 0.1549P]^{-1}$
	where $P = (F_o^2 + 2F_c^2)/3$
min./max. residual	
electron density /	– 0.491 / 0.345
$e \cdot 10^{-6} \text{ pm}^{-3}$	

systematically alternating between  $114^\circ/115^\circ$  and  $124 - 126^\circ$ , respectively. Differences in the C–N bond lengths within the rings (132 – 138 pm) are more pronounced than in melam and melamium perchlorate, the variations in both rings appearing to be systematic. In particular, the distances C2–N2 (138 pm) and C5–N5 (137 pm) are significantly longer than the adjacent bonds C2–N3 / C1–N4 (133/132 pm) and C5–N6 / C4–N7 (132 pm). This effect can most probably be ascribed to a drain of electron density from the ring to the Lewis acid Zn site, which is compensated by a rearrangement of the charge distribution according to a chinoid-type structure as schematically shown in Figure 6.37. The C–N<sub>exo</sub> distances are shorter on average by  $\approx 2$  pm (133 pm) as compared to the ring C–N bonds. The triazine rings are again bridged by a C1–N1H–C4 unit with equally elongated bond lengths (138 pm) and an angle at the imino nitrogen of  $134^\circ$ .

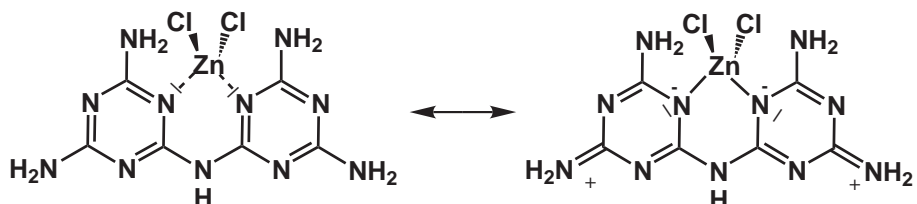


**Figure 6.37:** Resonance structures proposed for the  $\text{ZnCl}_2$ -melam complex. Based on a combination of the displayed mesomeric forms, the bond length variations in the melam backbone found from crystal-structure analysis may be rationalized.

The complexes form undulated strands extending along  $[0\ 1\ 0]$ , with neighbored melam molecules being hydrogen-bonded to each other by weak N · · · N contacts of 306 and 309 pm. The “layers” are spaced by approximately 362 pm and stacked irregularly such that the triazine ring planes of adjacent sheets exhibit varying offsets (Fig. 6.38).

The IR spectrum of the complex is shown in Figure 6.39. The  $\nu(\text{N–H})$  region with a sharp absorption centered at  $3430\ \text{cm}^{-1}$  is reminiscent of pure melam, which has a similar “duplett”

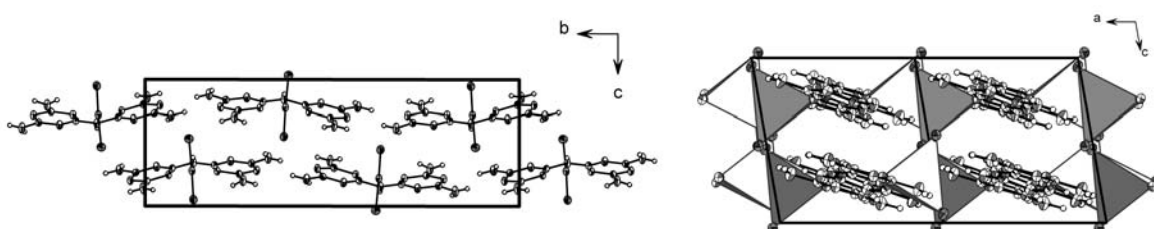


**Figure 6.38:** Unit cell of melam– $\text{ZnCl}_2$ , displaying the undulated strands composed of hydrogen-bonded complex molecules extending along  $[0\ 1\ 0]$ . Thermal displacement ellipsoids (except for H) are drawn at the 50 % probability level.

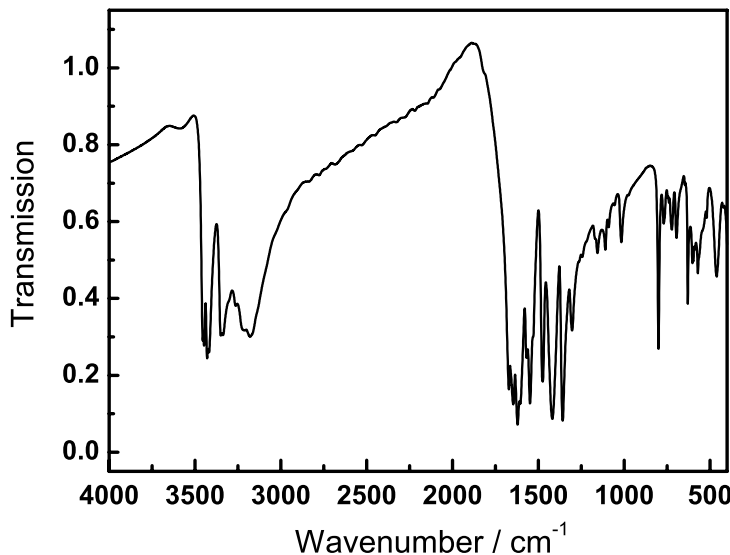


**Figure 6.39:** FTIR spectrum of  $\text{ZnCl}_2$ -melam recorded between  $4000$  and  $400\text{ cm}^{-1}$  as  $\text{KBr}$  pellet.

at  $3456 - 3483\text{ cm}^{-1}$ . The  $\nu(\text{C}=\text{N})$  and  $\delta(\text{NH}_2)$  bands are slightly blue-shifted with respect to those of melam, whereas the ring sextant bend is located at  $797\text{ cm}^{-1}$ . This is somewhat intermediate between non-protonated and singly protonated triazine cores as would be expected for electron deficient, neutral triazine rings. Characteristic bands pertaining to single bond C–N stretching vibrations are found between  $1411$  and  $1256\text{ cm}^{-1}$ .

The  $^{13}\text{C}$  solid-state CP-MAS NMR spectrum reveals three resonances, the small chemical shift differences of which indicating comparatively similar electronic environments of all  $^{13}\text{C}$  nuclei. Nevertheless, the number of signals nicely correlates with the three different carbon positions in each ring and the symmetry of the complex, which is close to  $C_m$ .

Conducting the CP-MAS measurements with different contact times as shown in Figure 6.40 (left) enables a differentiation between those  $(2 + 2)$  carbon atoms adjacent to amino groups ( $163.4 / 165.7\text{ ppm}$ ), which exhibit faster magnetization transfers from the proton bath, and those two which are neighbored to the bridging amino group ( $161.4\text{ ppm}$ ) and exhibit higher intensities at longer contact times (spectrum (a)).

In the  $^{15}\text{N}$  CP-MAS NMR spectrum (Fig. 6.40, right, top spectrum) six signal groups are found, of which the signals at  $-193.8$  and  $-207\text{ ppm}$  are located in the chemical shift range characteristic of tertiary nitrogen atoms of triazine rings. The signal at  $-254.0\text{ ppm}$  exhibits a chemical shift typical of NH groups, whereas the signals at  $-280.7$  and  $-291.6\text{ ppm}$  lie in

the  $\text{NH}_2$  region. The signal at  $-238.1$  ppm is located intermediate between the  $\text{N}_{\text{tert}}$  and  $\text{NH}$  region and can – apart from chemical considerations based on the crystal structure – not be assigned unambiguously without further data. Thus, a CPPI experiment has been

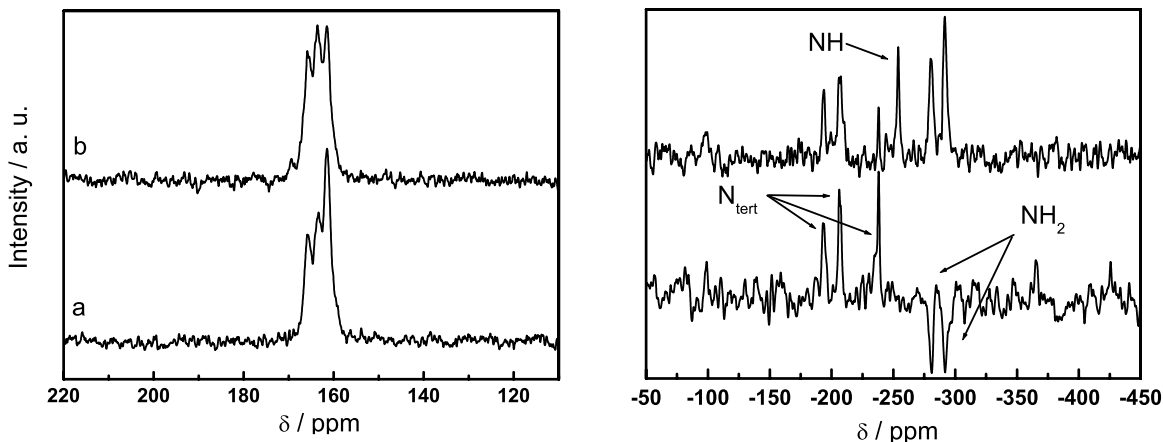


**Figure 6.40:** CP-MAS solid-state NMR spectra of the melam- $\text{ZnCl}_2$  complex. Left:  $^{13}\text{C}$  spectra recorded with two different contact times to identify the proton environment of the different carbon sites (top: 2 ms, bottom: 10 ms; recycle delay: 60 s). Right:  $^{15}\text{N}$  CP (top, spinning frequency 10 kHz) and CPPI spectra (bottom, spinning frequency 5.5 kHz); the signal assignments are indicated (recycle delay: 60 s;  $\tau_c$ : 4 ms; inversion time  $\tau_i$ : 160  $\mu\text{s}$ ).

carried out with an inversion time typical of  $\text{NH}$  signals to pass zero intensity (160  $\mu\text{s}$ ). As shown in Figure 6.40 (right, bottom spectrum), the magnetization of the  $\text{NH}$  signal at  $-254$  ppm is zero, whereas according to the expectations that of the  $\text{NH}_2$  groups is negative (cf. section 3.3.3 on page 63). The signal at  $-238$  ppm clearly has hardly lost intensity and can therefore be assigned to a tertiary nitrogen resonance.

The above results suggest that the coordination of melam at two ring nitrogen sites to the  $\text{Zn}$  cation lead to a high-field shift for the  $^{15}\text{N}$  nuclei (shielding) according to the right resonance structure in Figure 6.37. The remaining two signals can then be attributed to ring nitrogen sites not involved in the  $\text{Zn}$  coordination. Two of the four amino groups exhibit almost identical chemical shifts each, so that the observation of two  $\text{NH}_2$  signals can be rationalized.

Note that the above characterization of the  $\text{Zn}$ -melam complex does not conform to the results of *Galperin et al.* according to which an anionic  $\text{Zn}$ -melam salt with postulated formula “ $\text{Zn}^{2+}[\text{C}_6\text{N}_{11}\text{H}_8]^-$ ” was obtained by reaction of melamine with  $\text{ZnCl}_2$  under similar reaction conditions [468]. In this work, no analytical data apart from elemental analysis was presented such that the identity of the obtained compound could not be unambiguously clarified. We believe that the authors in fact had obtained the  $\text{ZnCl}_2$ -melam complex described above.

### 6.5.3.3 Other Metal-Melam Complexes

The products obtained from reacting melamine with the respective metal chlorides at temperatures between 593 and 673 K (Table 6.14) were primarily identified by vibrational spectroscopy owing to the poor solubility and the polycrystalline character of these materials. Elemental analysis data indicate the presence of both chloride and the respective metal ions, however, no conclusive sum formula can be given in all cases owing to the significant variations in the elemental compositions found for the different samples. In addition, the presence of crystal water or hydroxy-groups must be assumed for the Al- and Fe-compounds, which cannot be quantified unless all impurities are excluded. The removal of impurities such as metal chloride species, however, is limited by the fact that some of the products are sensitive to hydrolysis or oxidation; the compositions derived from elemental analysis must therefore be evaluated with caution. Note that the data obtained for the copper complex strongly indicate that reduction of the copper(II) ion has taken place and a copper(I)Cl-melam complex is formed. This is also supported by the beige color of this compound and by the solid-state NMR investigations (see below).

Most notably, on comparing the spectra of the copper, iron and aluminium compounds with

**Table 6.16:** Average values of the elemental compositions obtained for the melam-metal complexes from different samples and theoretical values according to the formulas given below.<sup>a</sup>

Compound	N / wt% obs. (theor.)	C / wt% obs. (theor.)	H / wt% obs. (theor.)	Cl / wt% obs. (theor.)	M / wt% obs. (theor.)
“Zn-melam”	40.5 (41.5)	18.8 (19.4)	2.5 (2.4)	18.4 (19.1)	17.7 (17.6)
“Zn[C <sub>6</sub> N <sub>11</sub> H <sub>9</sub> ]Cl <sub>2</sub> ”					
“Cu-melam”	46.1 (46.1)	21.6 (21.6)	2.6 (2.7)	10.7 (10.6)	19.5 (19.0)
“Cu[C <sub>6</sub> N <sub>11</sub> H <sub>9</sub> ]Cl”					
“Fe-melam”	38.8 (40.7)	17.7 (19.0)	3.0 (2.6)	19.8 (18.7)	14.8 (14.7)
“Fe[C <sub>6</sub> N <sub>11</sub> H <sub>9</sub> ]Cl <sub>2</sub> (OH)”					
“Al-melam”	44.8 (44.1)	21.7 (20.6)	4.0 (4.0)	14.9 (10.2)	7.7 (7.7)
“Al[C <sub>6</sub> N <sub>11</sub> H <sub>10</sub> ]Cl(OH) <sub>3</sub> ”					

<sup>a</sup> The idealized formulas have been calculated so as to reproduce the experimentally found compositions, and to conform to the spectroscopic data. They are thus by no means to be understood as the binding sum formulas. At most they indicate likely compositions.

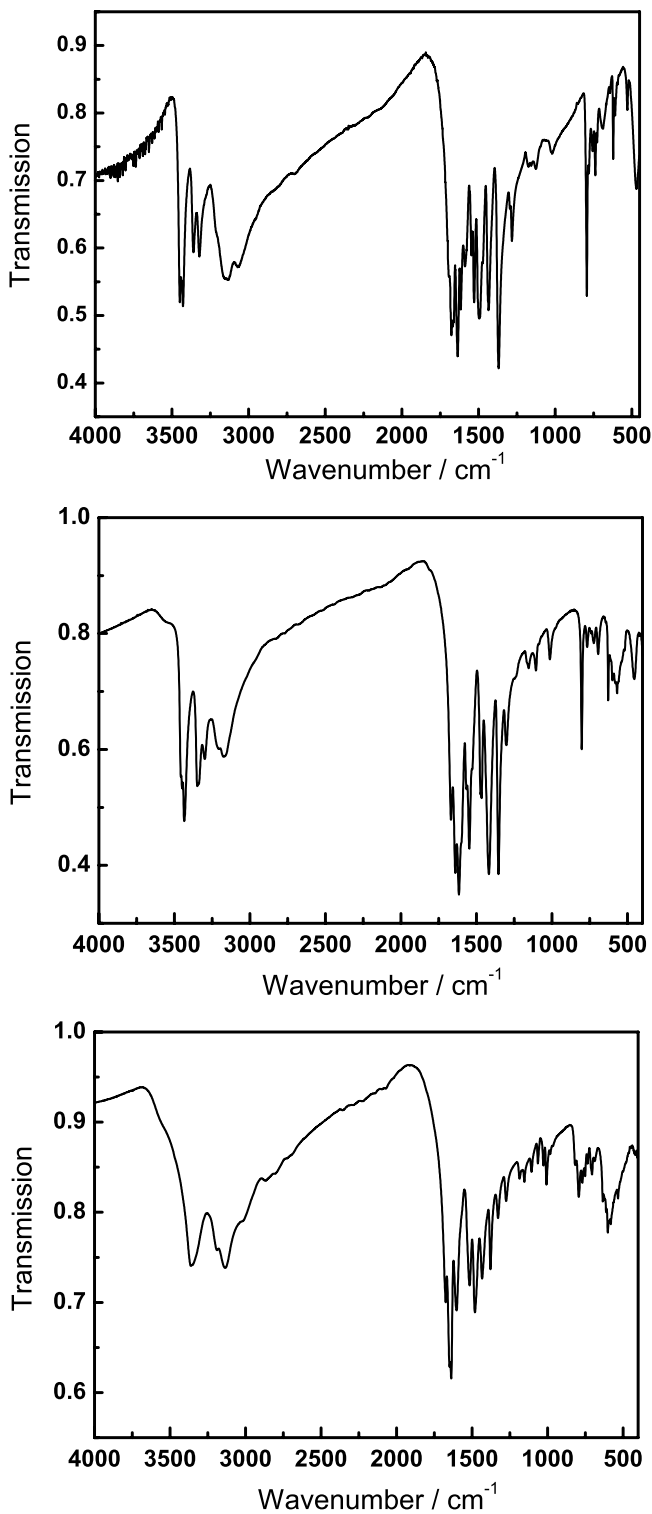


**Figure 6.41:** FTIR spectra of the Cu-melam complex (top), the Fe-melam complex (middle), and the Al-melam complex (bottom), recorded between 4000 and 400  $\text{cm}^{-1}$  at RT as KBr pellet.

**Table 6.17:** IR band positions (in  $\text{cm}^{-1}$ ) of the different metal-melam species. The principal assignments indicated in the rightmost column are adapted from the assignments based on the  $[\text{C}_3\text{N}_3\text{H}(\text{NH}_2)_3]^+$  cation.

“Zn-melam”	“Cu-melam”	“Fe-melam”	“Al-melam”	Assignment [240, 481]
3455				
3447	3448	3449		
3429	3427	3435		$\nu_s(\text{NH}_2)$
3350	3359	3348	3362	
	3320	3299		
3179	3132	3174	3134	$\nu_{as}(\text{NH}_2)$
1672	1677	1668	1675	
1646	1636	1639	1649	$\nu_1(\text{C}=\text{N})$
1621	1616	1616	1638	
			1602	
1568	1589	1566		$\nu_3(\text{C}=\text{N})$
1548	1546	1547		
	1529		1516	
1474	1492	1466	1481	$\nu_4(\text{C}=\text{N})$
1418	1434	1417	1433	
1358	1369	1354	1378	$\nu_2(\text{C}=\text{N})$
1303		1301	1328	$\delta(\text{N}-\text{H})/$
	1282		1274	$\nu(\text{C}-\text{N})$
1155	1125	1154	1185	
			1153	$\rho(\text{NH}_2)$
1109		1106	1106	
1089			1064	
1016	1017	1013	1027	$\nu(\text{ring})$ breath
			1007	
800	794	803	793	ring sextant bend
769	781	766	770	
	756		751	$\omega(\text{NH})$
739	739	740	735	$\gamma(\text{ring})$
722	727	722	705	
695	690	694	687	
629	622	627	634	$\omega(\text{NH}_2)$
602	609	599	612	
571	529	568	581	$\delta(\text{CN})$
			533	(backbone)
461	470	454		

that obtained for the Zn-melam complex a striking similarity is apparent and the bands characteristic of melam species in the  $\nu(\text{C}-\text{N})$  and  $\delta(\text{N}-\text{H})$  region are clearly visible in all cases. Furthermore, the Zn-complex as well as the Cu- (top) and Fe-compounds (middle) exhibit a high degree of coincidence with respect to the band positions and intensities, which are slightly different for the aluminium species (bottom, Fig. 6.41). A synopsis of the observed band shifts is given in Table 6.17.

For the Al- and Cu-compounds sharp, medium intense bands are found at  $1481 / 1516 \text{ cm}^{-1}$  and  $1492 / 1529 \text{ cm}^{-1}$ , respectively, whereas these bands are absent in the two other complexes. In addition, the triazine sextant bend is red-shifted in the former ( $\approx 793 \text{ cm}^{-1}$ ) as compared to the spectra of the Zn- ( $800 \text{ cm}^{-1}$ ) and Fe-complexes ( $803 \text{ cm}^{-1}$ ); this may be rationalized by the protonation of a triazine ring system in the Al- and Cu-complexes. On the other hand, the band patterns in the  $\nu(\text{NH})$  stretching region observed for the Zn-, Fe- and Cu-species exhibit similar features, whereas the Al-complex shows rather broad bands indicating that essentially all hydrogen atoms are involved in hydrogen-bonding. Owing to the conspicuous overall resemblance of the spectra of the Zn- and Fe-complexes we may conjecture that at least these two compounds contain neutral melam molecules in the same “bonding state” with similar crystal-packing features (cf. 6.5.3.2 on page 249).

Further information about the protonation state of the Al- and Cu-melam species was furnished by solid-state NMR spectroscopy. To this end,  $^{13}\text{C}$  CP and/or  $^{15}\text{N}$  CP- and CPPI-MAS solid-state NMR spectra have been recorded and are displayed in Figures 6.42 and 6.43.

In contrast to the chemical shift distribution in the Zn-spectrum, two well-separated  $^{13}\text{C}$  signals are visible at 167.6 and 163.8 ppm for the Al-species, which is reminiscent of the

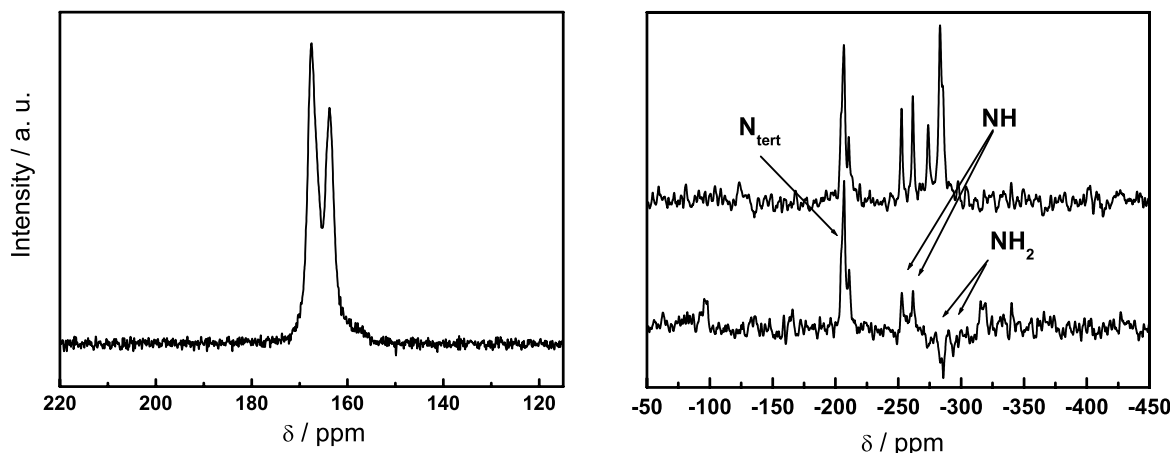


**Figure 6.42:** CP-MAS solid-state NMR spectra of the Al-melam complex. Left:  $^{13}\text{C}$  spectrum ( $\tau_c: 4 \text{ ms}$ ; recycle delay: 10 s). Right:  $^{15}\text{N}$  CP (top, spinning frequency 10 kHz) and CPPI spectra (bottom, spinning frequency 5 kHz); the signal assignments are indicated (recycle delay: 10 s;  $\tau_c: 4 \text{ ms}$ ; inversion time  $\tau_i: 120 \mu\text{s}$ ).

melam-hydrate and melam spectra as displayed in Figure 6.18 on page 220. However, comparing the  $^{15}\text{N}$  spectra with those of  $\text{ZnCl}_2$ -melam and melam-hydrate, the NH regions differ with respect to the number of signals, since for the Al-compound two NH groups at  $-252.5$  and  $-261.5$  ppm are found as identified by their polarization inversion behavior (Fig. 6.42, bottom): Whereas the  $\text{NH}_2$  groups ( $-273.8$ ,  $-283.2$  and  $-285.6$  ppm) exhibit slightly negative polarization and the intensity of the  $\text{N}_{\text{tert}}$  signals is only little affected, the intensity of the NH-signals has dropped significantly in the CPPI experiment at the particular inversion time chosen. Owing to the relatively large separation of the NH chemical shifts as well as the relatively small signal multiplicity observed in the  $\text{NH}_2$  and  $\text{N}_{\text{tert}}$  region, we may infer that these signals can be assigned to a bridging NH group and the NH signal of a protonated triazine ring rather than two bridging NH groups of crystallographically different melam molecules as found in melam (see Fig. 6.18 on page 220, right).

The  $^{15}\text{N}$  CP (top) and CPPI (bottom) spectra are displayed in Figure 6.43. In the  $\text{N}_{\text{tert}}$  region four resonances at  $-200.8$ ,  $-204.3$ ,  $-208.1$ , and  $-209.9$  ppm are distinguishable, whereas only one NH signal ( $-258.3$  ppm) and three  $\text{NH}_2$  signals ( $-278.8$ ,  $-284.5$ ,  $-287.0$  ppm) with approximate intensity ratios of  $1:1:2$  are observed. In addition, a comparatively weak multiplett is visible between  $-220$  and  $-229$  ppm. Owing to the location of this signal group

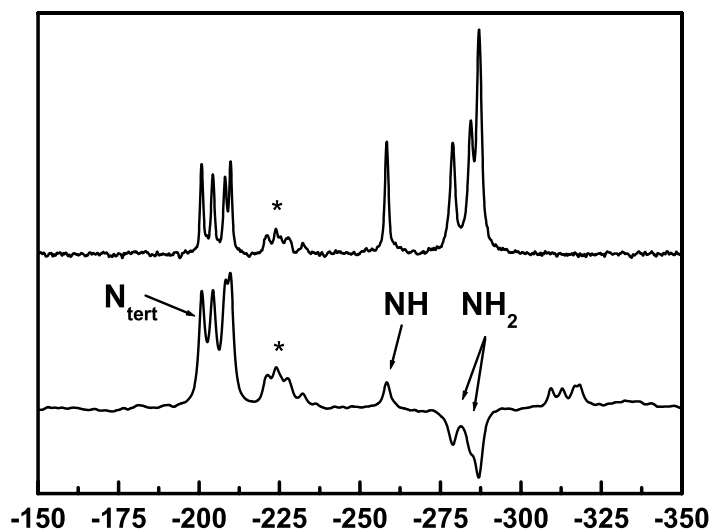


**Figure 6.43:**  $^{15}\text{N}$  CP (top, spinning frequency  $10\text{ kHz}$ ) and CPPI (bottom, spinning frequency  $5.5\text{ kHz}$ ) MAS solid-state NMR spectra of the copper melam complex; the signal assignments are indicated. Asterisks denote the multiplett assigned to the metal-nitrogen spin coupling. Recycle delay:  $2\text{ s}$ ;  $\tau_c$ :  $8\text{ ms}$ ; inversion time  $\tau_i$ :  $160\text{ }\mu\text{s}$ .

as well as the observed multiplett structure, the following effect is proposed to operate: On the one hand, both copper isotopes  $^{63}\text{Cu}$  and  $^{65}\text{Cu}$  are spin  $\frac{3}{2}$  nuclei with large quadrupole moments, and on the other hand, the structural information obtained in section 6.5.3.2 on page 249 reveals the Zn ion to be coordinated to two ring nitrogen sites.

As outlined above, a very similar structure can be inferred for the copper compound, which accordingly is assumed to exhibit a similar “ligand-type” coordination of a neutral melam molecule to the copper site. Therefore, the signal of the two ring nitrogen atoms directly bonded to the copper ion are split into multiplets owing to dipolar and scalar interactions with the copper isotopes. This effect is due to the presence of strong nuclear electric quadrupole interactions experienced by the copper isotopes [482]. Note that if copper was present in the oxidation state +II, a significant broadening and paramagnetic shift of all nitrogen resonances would be expected owing to the  $d^9$  electron configuration of copper(II).

The suggested bonding situation is clearly supported by the up-field shift of this particular signal group (signal at  $-238$  ppm in the Zn-complex, cf. Fig. 6.40 on page 253) that in turn independently confirms the assignment of this resonance to the coordinating  $\text{N}_{\text{tert}}$  signals as outlined above. Thus, one can also rationalize why only four tertiary nitrogen signals are observed between  $-200.8$  and  $-209.9$  ppm; in total, six  $\text{N}_{\text{tert}}$  resonances are found. This finding either suggests that the  $^{15}\text{N}$  signals of the two melam ligands according to Figure 6.44 have very similar chemical shifts, or that only one half of the dimer is contained in the asymmetric unit.

It may, however, also indicate that in fact a monomeric structure similar to that of the zinc compound has to be assumed for the melam-copper complex. We can therefore state that the copper-melam species is most probably closely related to the Zn-complex in terms of the structural arrangement and the protonation state of the melam molecule (neutral melam ligand). A possible structure model for this complex is outlined in Figure 6.44. If Cu-melam indeed adopts a dimeric form, very similar (or symmetry-related) crystallographic environments have to be inferred for the melam ligands; otherwise the NMR spectrum would be more complex than observed.

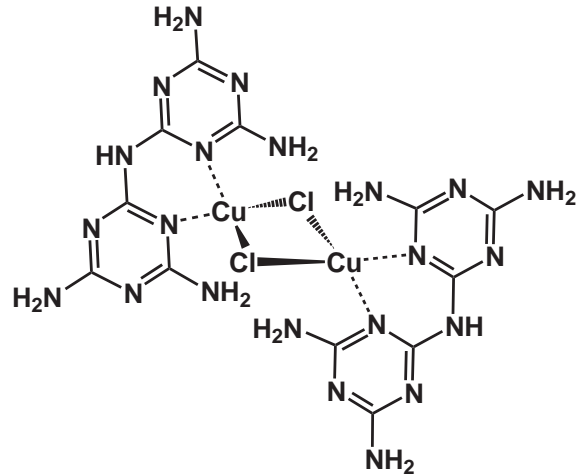


**Figure 6.44:** Schematic drawing of a structure proposition for the copper-melam species based on a dimeric form with bridging Cl-ligands.

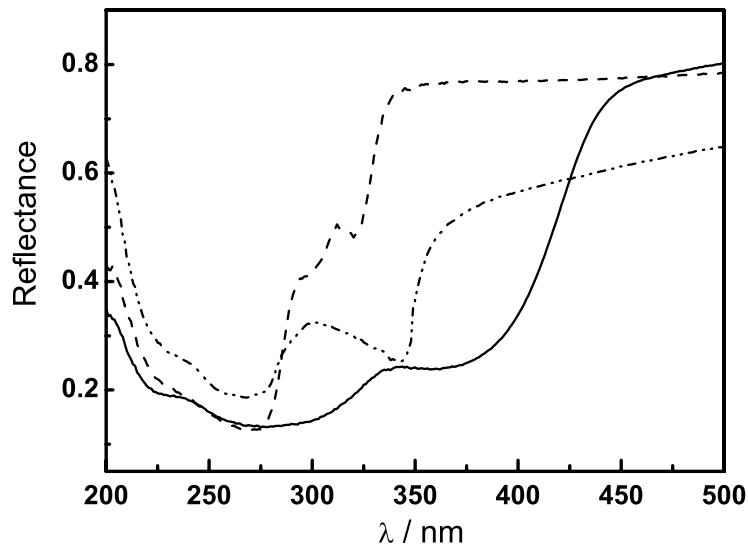


**Figure 6.45:** UV/vis spectra of the copper-melam (solid line), zinc-melam (dash dotted line) and aluminium-melam complexes (dashed line).

In contrast, the Al-species differs in that melam is mono-protonated, which presumably correlates with the water content and presence of hydroxy-species in the latter. It is therefore likely that the Al-melam species contains a protonated melam core as opposed to the situation in the Zn-melam complex. This reasoning is also supported by the fact that the high-field shift observed for one  $N_{tert}$  signal in the zinc-melam compound is absent in the Al-melam complex, and by the red-shift of the ring sextant bend in the IR spectrum of the aluminium compound.

The UV/vis spectra of the copper-, zinc- and aluminium-melam species are displayed in Figure 6.45. The largest red-shift of the absorption maxima is observed for the copper-melam complex, which exhibits maxima at 280 (shoulder at 230 nm) and 380 nm. Whereas the high-energy bands are located in a similar region for the Zn- (230, 270 nm) and Al-species (230, 267 nm), the absorptions of highest wavelengths are found at 340 nm for the Zn- and at 320 nm (weak) for the Al-complex. Whereas according to the previously discussed UV/vis spectra (cf. Figs. 6.21 on page 223 and 6.28 on page 234) the high-energy absorption may be associated with ligand-based electronic transitions, the low-energy bands are most probably due to transitions between the electronic states of the metal ions.

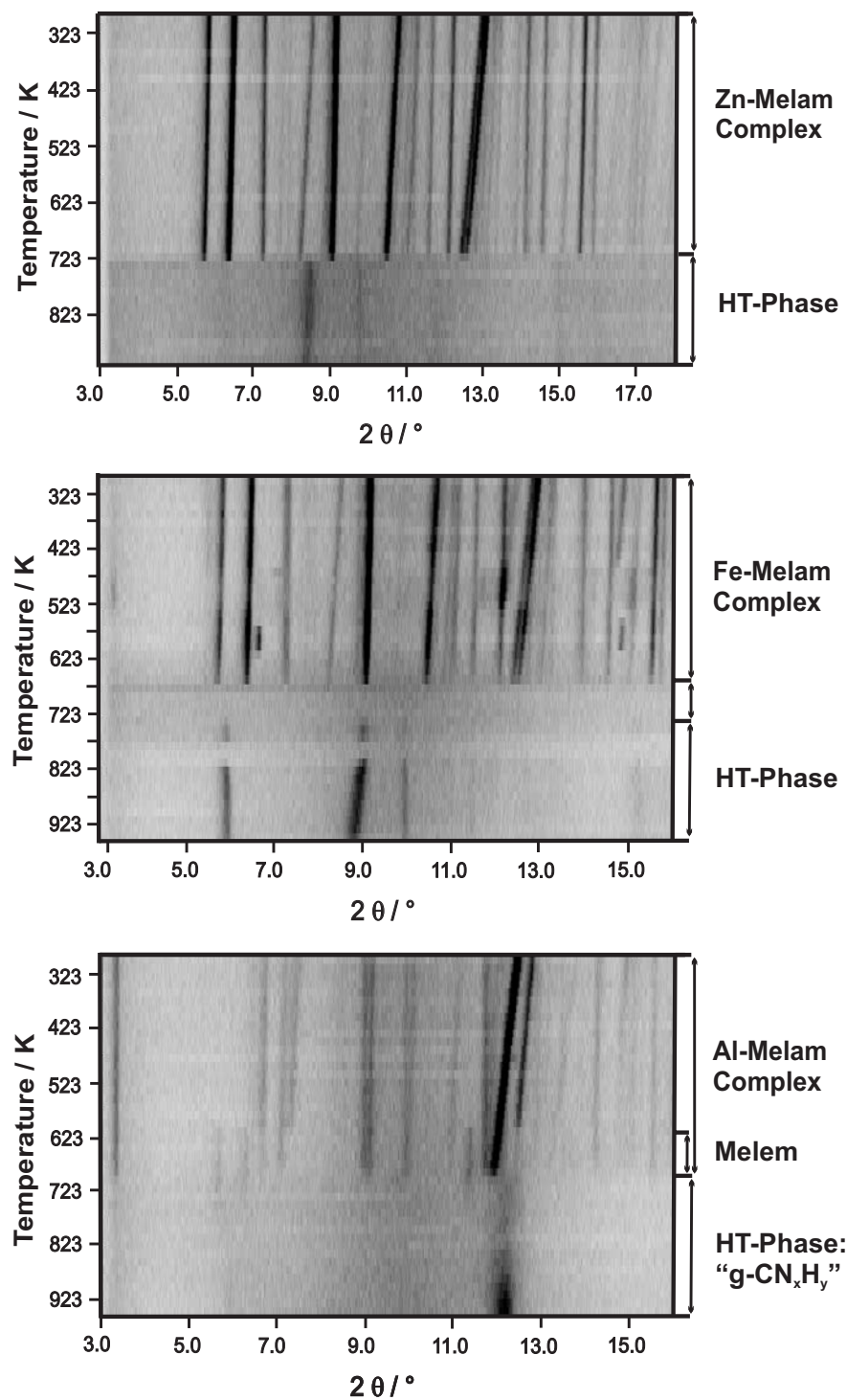


**Figure 6.46:** *In situ* temperature programmed X-ray powder diffraction measurements (Mo- $K_{\alpha 1}$  radiation) of the  $ZnCl_2$ -melam complex (top), the Fe- (middle) and Al-melam species (bottom) recorded between RT and 950 K. The temporary intensity drop above 773 and 823 K in the middle series of powder patterns is probably due to an experimental artefact.

The thermal behavior of the Zn-, Fe- and Al-melam species was monitored by TPXRD measurements between RT and 950 K (Fig. 6.46). It has to be noted that the phase purity of these compounds cannot be assured; the powder patterns may exhibit side-phases and must therefore not be over-interpreted.

The RT phase of the Zn-melam complex (top pattern) is stable up to temperatures of 723 K and then decomposes to a poorly crystalline phase that could not be identified, but may be associated with a poorly crystalline zinc containing carbon nitride material. The Fe-melam species (middle pattern) is retained up to 670 K, however, transient intermediate phases are visible in the powder patterns whose identity could not be resolved. The same applies for the HT-phase, which starts to form at  $T \geq 738$  K and is stable beyond 950 K; this suggests that no pure carbon nitride material is formed. However, the identification of the HT-phase as iron oxide, iron chloride or iron oxide chloride species failed.

In contrast, the Al-melam compound (bottom pattern) seems to partly decompose into melem, the reflections of which are weakly visible between 613 and 700 K. However, the reflections of the starting material completely disappear no earlier than at  $\approx 693$  K, from which fact an only incomplete transformation of the Al-melam complex into melem can be inferred. Above  $\approx 830$  K a single broad reflection indicative of a graphitic carbon nitride material emerges.

In summary, all complexes exhibit a similar temperature stability, but lack of knowledge on the HT-phases limits the statements that can be made on the suitability of these materials as carbon nitride precursors.

## 6.6 Ammeline Salts

### 6.6.1 Introduction

The sensitivity of melam to hydrolysis in aqueous solution required the optimization of the reaction conditions when preparing melamium salts such as melam hydrochloride or hydrobromide. During this optimization process, a number of hydrolysis products of melam and its salts were obtained, especially if the syntheses of the latter were attempted at temperatures higher than 310 K, or after prolonged standing of the aqueous solutions of the products. While extensive boiling of basic melam solutions yielded melam hydrates and, ultimately, carbonate and ammonia, acid melam solutions were easily hydrolyzed at the bridging nitrogen atom to form the respective melaminium or ammelinium salt (cf. section 10.1). Whereas in that effect three ammelinium salts could be isolated in the form of single-crystalline material, only one crystalline melaminium salt was detected, the structure of which will be discussed below.

Ammeline [ $C_3H_5N_5O$ ], synonymous for 2,4-diamino-1,3,5-triazin-6-one or 2,4-diamino-6-hydroxy-1,3,5-triazine, has been known since the 1830s as an important starting material as well as ubiquitous decomposition product in carbon nitride chemistry. *Liebig* and *Wöhler* were among the first to glean its close relationship to melamine (2,4,6-triamino-1,3,5-triazine), classifying the latter together with ammeline and ammelide (2-amino-1,3,5-triazin-4,6-dione) as simple organic bases which can uniformly be derived from the related compound cyanuric acid (1,3,5-triazin-2,4,6-trione) by successive replacement of the oxygen functions by amide moieties.

Conversely, successive hydrolysis of melamine (cyanuric triamide) yields cyanuric acid as the final stage *via* ammeline (cyanuric diamide) and ammelide (cyanuric monoamide) as partial hydrolysis products [409, 483–485]. Owing to the triazine core as a common motif, the amides of cyanuric acid appear to be structurally related to melamine and its condensation products melam, melem and melon (cf. section 7 on page 280) [42–44].

Apart from its fundamental relevance for carbon nitride chemistry, ammeline has turned out to be a beneficial additive in melamine-formaldehyde resins [486, 487], flame-retardant mate-

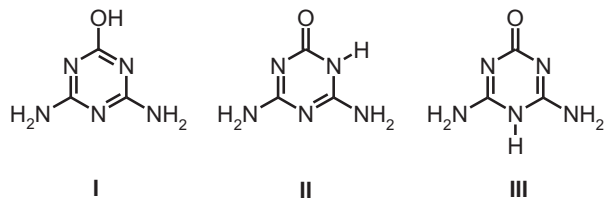


**Figure 6.47:** Different tautomers of ammeline. Left: Enol (hydroxy) tautomer (**I**), middle: keto (carbonyl) tautomer (**II**), right: quinoid carbonyl tautomer (**III**).

rials [488, 489], and lubricating greases [490], as well as component of photoresists [491, 492]. However, though being an important target molecule, intermediate and by-product in various industrially important processes such as melamine production, ammeline still lacks detailed investigations concerning its solid-state structure and spectroscopic properties. Thus, the question relating to the energetic preference of the hydroxy or carbonyl tautomer of ammeline is still a matter of dispute owing to the unavailability of crystallographic data for both ammeline and simple derivatives thereof [409, 493], see Figure 6.47.

Although a progression from the conjugated ring structure of melamine to the completely “iso” (i.e. keto) structure of cyanuric acid was evident from studies of the IR absorption spectra of various triazine derivatives, it was not possible to resolve the actual equilibrium position of the tautomeric forms for solid ammeline [493]. According to *ab initio* calculations carried out by *Wang et al.* for the gas phase structures, the enol (hydroxy) form is expected to be by 4.82 kcal mol<sup>-1</sup> more stable than the keto (carbonyl) tautomer, and by 23.8 kcal mol<sup>-1</sup> more stable than the quinoid carbonyl tautomer [494]. Protonation of ammeline was also studied, assuming, however, the hydroxy-tautomer as neutral substrate (Figure 6.49). As a result, the energies of all three ring-protonated species were predicted to be lower than those of the species protonated at the amino-groups. Furthermore, the ring N positions adjacent to the hydroxy group were found to be the most basic ones [494]. First studies on the protonation of ammeline date back to the beginning of the last century. *Hantzsch* described the synthesis of ammeline salts by addition of strong acids and AgNO<sub>3</sub> to ammeline, and *Kaiser* reported on the preparation of ammeline hydrohalide salts by the reaction of potassium dicyanodiamide with HCl and HBr, respectively [495, 496].

In the following, the first characterization of ammeline derivatives will be outlined according to ref. [497].

### 6.6.2 Crystal Structures

The ammeline salts described in the present work uniformly crystallize in the centrosymmetric space group *P*2<sub>1</sub>/c with four formula units in the monoclinic unit cell. Though being similar in terms of their molecular structures, with the cells of the hydrochloride **1** and hydrobromide **2** having almost identical lattice parameters and cell volumes (Tables 6.18 and 6.19), none of the structures are isotropic.

Notably, a common feature of these three crystal structures is the presence of the keto tautomer rather than the hydroxy tautomer, as can clearly be seen from the proton distribution as well as from the relevant bond lengths constituting the ammeline rings (Figs. 6.50 and 6.51, Table 6.19): The C2–O1 bond lengths in **1** – **3** (122 pm) are almost identical and corre-

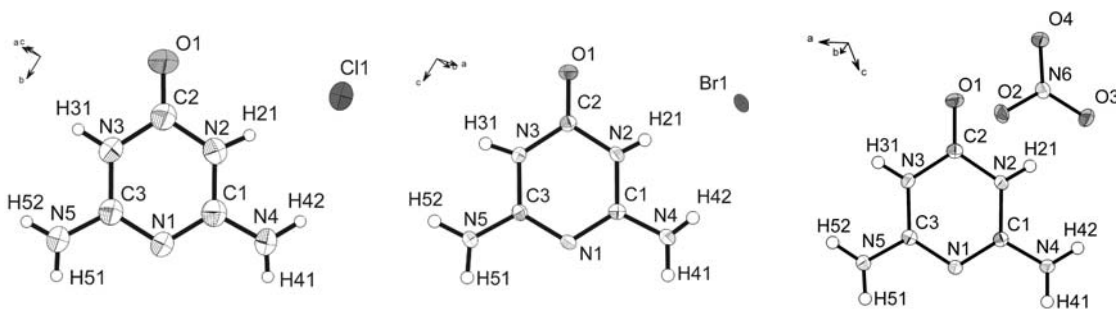


**Figure 6.48:** Asymmetric unit of ammelinium chloride (**1**), ammelinium bromide (**2**), and ammelinium nitrate (**3**). Thermal ellipsoids (apart from those for H) are drawn at the 50 % probability level.

spond to C=O bond lengths commonly found for carbonyl groups, featuring a C=O double bond [124,278]. For comparison, the length of the C–O bond calculated by Wang *et al.* for the hydroxyammeline tautomer was given as 131.6 pm [494] and is therefore significantly larger than those experimentally found in this study.

The C2–N2 / C2–N3 bond lengths adjacent to the carbonyl groups (**1**: 136 – 137 pm, **2**: 136 – 138 pm, **3**: 138 pm) are slightly extended compared to N2–C1 / N3–C3 (**1**: 136 pm, **2**: 136 pm, **3**: 137 pm), and significantly elongated compared to C1–N1 and C3–N1 (**1**: 134 pm, **2**: 134 – 135 pm, **3**: 134 pm).

Interestingly, the C–N<sub>amide</sub> bonds C1–N4 and C3–N5 (131 – 132 pm) are shorter than all C–N<sub>ring</sub> bonds. Thus, protonation of the ammeline moiety results in an equal distribution of the positive charge over N2 and N3, with the double bond character decreasing along the line C1/C3–N1 > C1/C3–N2/3 > C2–N2/N3, the latter ones possessing a significant degree

of single bond character. The short C1–N4 / C3–N5 bonds indicate a pronounced donation of electron density from the amino nitrogen atoms into the ring, thereby providing for extensive delocalization of the positive charge over the whole ring system. The participation of the nitrogen lone pairs situated on the amino groups in the  $\pi$ -delocalization within the electron-deficient triazine ring is also supported by the planarity of all amino groups in compounds **1** – **3**. The absolute values of the above bond lengths, together with the observed bond length distribution over the ammeline backbone corresponding to  $C_{2v}$  symmetry therefore suggest the tautomer **IIa** to represent the actual proton distribution rather than formula **Ia** with approximated  $C_s$  symmetry (Fig. 6.49).

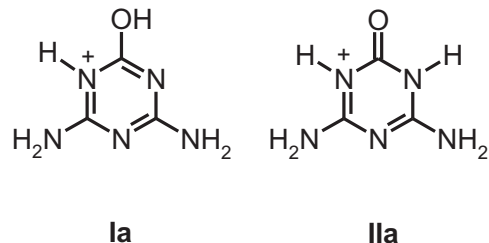


**Figure 6.49:** Possible structures of a mono-protonated ammelinium cation. Left: Protonated hydroxy tautomer (**Ia**), right: protonated keto tautomer (**IIa**). In both cases, protonation is assumed to take place on a nitrogen atom adjacent to the hydroxy or keto group, respectively.

**Table 6.18:** Crystallographic data for ammelinium chloride **1** (left) and ammelinium bromide **2** (right).

Formula	[C <sub>3</sub> H <sub>6</sub> N <sub>5</sub> O]Cl	[C <sub>3</sub> H <sub>6</sub> N <sub>5</sub> O]Br
<i>M<sub>w</sub></i> / g · mol <sup>-1</sup>	163.58	208.04
crystal system	monoclinic	monoclinic
space group	<i>P</i> 2 <sub>1</sub> /c (no. 14)	<i>P</i> 2 <sub>1</sub> /c (no. 14)
<i>T</i> / K	293	130
diffractometer	STOE IPDS	STOE IPDS
radiation ( $\lambda$ / pm)	Mo-K $\alpha$ (71.073)	Mo-K $\alpha$ (71.073)
monochromator	graphite	graphite
<i>a</i> / pm	535.4(2)	521.2(1)
<i>b</i> / pm	1467.3(3)	883.1(2)
<i>c</i> / pm	815.2(2)	1457.7(3)
$\alpha$ , $\beta$ , $\gamma$ / °	90.00(3)	98.97(3)
<i>V</i> / 10 <sup>6</sup> · pm <sup>3</sup>	640.4(2)	662.7(2)
<i>Z</i>	4	4
$\rho_{calcd}$ / g · cm <sup>-3</sup>	1.697	2.085
F(000)	336	408
$\mu$ / mm <sup>-1</sup>	0.529	6.138
crystal size / mm <sup>3</sup>	0.37 x 0.16 x 0.11	0.16 x 0.10 x 0.09
diffraction range	2.78 ≤ $\theta$ ≤ 27.48	2.71 ≤ $\theta$ ≤ 27.50
index range	-6 ≤ <i>h</i> ≤ 6, -19 ≤ <i>k</i> ≤ 19, -10 ≤ <i>l</i> ≤ 10	-6 ≤ <i>h</i> ≤ 6, -10 ≤ <i>k</i> ≤ 11, -18 ≤ <i>l</i> ≤ 18
twin fraction	0.845(2) / 0.155(2)	
total no. reflections	5388	5350
independent reflections	1410 ( $R_{int}$ = 0.0470)	1499 ( $R_{int}$ = 0.0886)
observed reflections	922	1282
refined parameters / restraints	with $F_o^2 \geq 2\sigma(F_o^2)$	with $F_o^2 \geq 2\sigma(F_o^2)$
extinction coefficient $\chi$	116 / 0	116 / 0
GooF on $F^2$	0.867	0.016(3)
<i>R</i> indices (all data)	$R_1 = 0.0325$ (0.0608) $wR_2 = 0.0690$ (0.0758) with w = $[\sigma^2(F_o^2) + (0.0422P)^2 + 0.0000P]^{-1}$ where $P = (F_o^2 + 2F_c^2)/3$	$R_1 = 0.0349$ (0.0426) $wR_2 = 0.0780$ (0.0835) with w = $[\sigma^2(F_o^2) + (0.0437P)^2 + 0.0000P]^{-1}$ where $P = (F_o^2 + 2F_c^2)/3$
min./max. residual electron density / $e \cdot 10^{-6}$ pm <sup>-3</sup>	- 0.151 / 0.226	- 0.735 / 1.004

Thus, a loss of aromaticity of the triazine ring system seems to be overcompensated by a gain in energy resulting presumably from more beneficial van-der-Waals / hydrogen-bonding interactions, or steric factors. In all compounds, mono-protonated ammeline cations form

**Table 6.19:** Crystallographic data for ammeline nitrate 3.

Formula	$[\text{C}_3\text{H}_6\text{N}_5\text{O}]\text{NO}_3$
$M_w$ / g · mol <sup>-1</sup>	190.14
crystal system	monoclinic
space group	$P2_1/c$ (no. 14)
$T$ / K	130
diffractometer	STOE IPDS
radiation ( $\lambda$ / pm)	Mo-K $\alpha$ (71.073)
monochromator	graphite
$a$ / pm	933.2(2)
$b$ / pm	625.6(2)
$c$ / pm	1351.1(3)
$\beta$ / °	108.05(3)
$V$ / $10^6 \cdot \text{pm}^3$	750.0(3)
$Z$	4
$\rho_{\text{calcd}}$ / g · cm <sup>-3</sup>	1.684
$F(000)$	392
$\mu$ / mm <sup>-1</sup>	0.152
crystal size / mm <sup>3</sup>	0.30 x 0.14 x 0.04
diffraction range	$2.30 \leq \theta \leq 27.95$
index range	$-12 \leq h \leq 12, -8 \leq k \leq 7,$ $-15 \leq l \leq 15$
total no. reflections	6897
independent reflections	1666 ( $R_{\text{int}} = 0.0321$ )
observed reflections	1254
refined parameters / restraints	with $F_o^2 \geq 2\sigma(F_o^2)$
GooF on $F^2$	142 / 0
$R$ indices (all data)	0.945
	$R_1 = 0.0301$ (0.0425)
	$wR_2 = 0.0789$ (0.0817)
	with $w = [\sigma^2(F_o^2)$
	$+(0.0569P)^2 + 0.0000P]^{-1}$
	where $P = (F_o^2 + 2F_c^2)/3$
min./max. residual	
electron density /	- 0.272 / 0.189
$e \cdot 10^{-6} \text{ pm}^{-3}$	

layers or strands, which are stacked perpendicular to their molecular planes in one or two directions. In ammeline hydrochloride, Cl<sup>-</sup> ions are inserted “pairwise” into layers composed of hydrogen-bonded arrays of cations extending in the (102) plane. Within the essentially planar layers, neighboring ammeline cations slightly move upwards or downwards such that cations from adjacent layers somewhat approach each other (Fig. 6.50). This minor distor-

tion results in short interlayer N … O contacts of 314 pm, which approach the lower level of interlayer distances commonly found in layered triazine or heptazine derivatives [82, 127, 458]. Within the layers, all cations and anions are involved in medium strong hydrogen-bonding, the donor-acceptor distances ranging from 298.0(3) pm (N4 … O1) to 361.2(3) pm (N5 … Cl1). Interestingly, the strongest hydrogen-bonds (217(3) pm) found in the structure result from Cl1 … H21(–N2) interactions, whereas the shortest O1 … H41(–N4) contacts due to oxygen-amide interactions amount to 219(3) pm (Table 6.21).

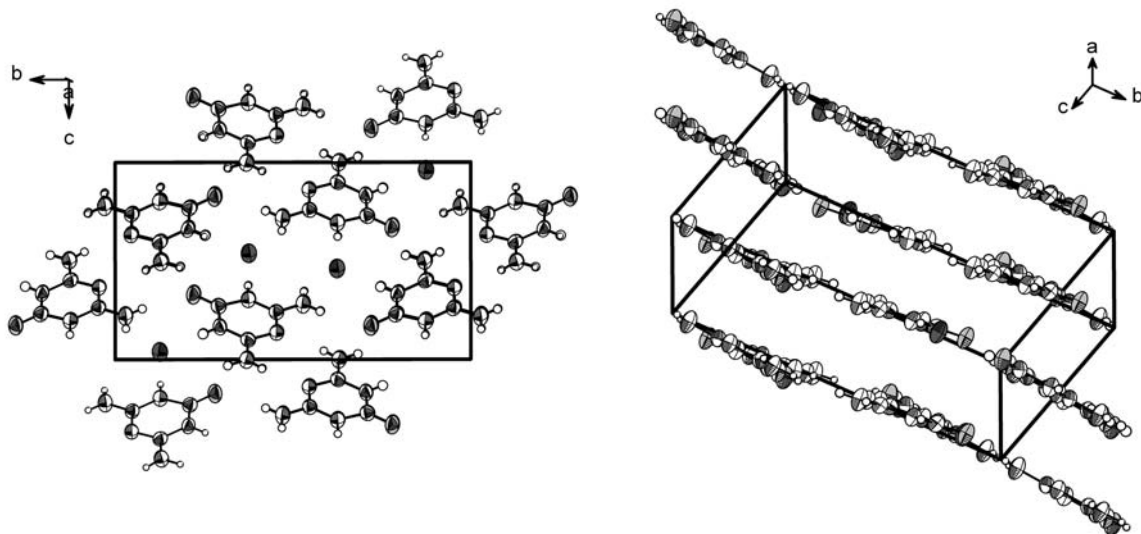


**Figure 6.50:** Different perspectives of the unit cell of ammelinium chloride (**1**). Left: View along [100] towards the layers composed of cations and anions; right: View along [211] parallel to the layers. Thermal ellipsoids (apart from those for H) are drawn at the 50 % probability level.

Although the dimensions of the unit cell are almost identical, the arrangement of the ions is significantly different in ammeline hydrobromide (**2**) as compared to the ammelinium hydrochloride salt (Fig. 6.51). In **2**, two types of strands are distinguishable, which are composed of two parallel stacks of ammelinium ions along their molecular planes. The normals of the cationic rings in neighboring strands are approximately perpendicular to each other. The bromide atoms are inserted between adjacent strands, such that one bromide ion is hydrogen-bonded to 2 + 1 cations from “orthogonal” strands. In addition, all ammelinium ions are linked up by extensive N–H … N or N–H … O hydrogen-bonding within the strands and with adjacent strands. The overall hydrogen-bonding network is composed of medium strong hydrogen-bonds (209(6) – 293(5) pm) with donor-acceptor distances ranging between 298.3(5) pm (N4–H41 … N1) and 368.4(5) pm (N5–H52 … Br1) (Table 6.21).

In ammelinium nitrate (**3**) the cations are stacked with an offset along [010], such that every molecule is in an eclipsed arrangement with its second nearest neighbor along the *b*-axis

**Table 6.20:** Selected bond lengths (in pm) and angles (in  $^{\circ}$ ) for the ammeliinium salts **1**, **2**, and **3**.

	<b>1</b>	<b>2</b>	<b>3</b>
	Distances / pm		
C1–N4	130.9(3)	132.0(5)	132.08(16)
C1–N1	133.8(3)	134.5(4)	133.49(15)
C1–N2	135.5(3)	135.7(5)	136.99(16)
C2–O1	121.7(3)	121.9(4)	121.93(15)
C2–N2	136.9(3)	136.4(4)	137.47(16)
C2–N3	136.1(3)	137.8(4)	137.86(15)
C3–N5	130.8(3)	131.9(5)	132.08(15)
C3–N1	133.6(3)	134.0(4)	133.66(16)
C3–N3	135.9(3)	135.5(5)	136.73(16)
O2–N6			126.14(12)
O3–N6			125.55(13)
O4–N6			125.53(14)
	Angles / $^{\circ}$		
C1–N2–C2	122.8(2)	123.3(3)	122.2(1)
C3–N3–C2	122.9(2)	122.7(3)	121.9(2)
C3–N1–C1	116.4(2)	116.3(3)	116.7(2)
N1–C1–N2	122.1(2)	121.9(3)	122.3(2)
N4–C1–N2	117.7(2)	117.4(3)	117.7(2)
N4–C1–N1	120.2(2)	120.7(3)	120.0(2)
N3–C2–N2	113.7(2)	113.2(3)	114.3(2)
O1–C2–N2	122.4(2)	122.9(3)	122.7(1)
O1–C2–N3	123.9(2)	123.9(3)	123.0(2)
N1–C3–N3	122.1(2)	122.2(3)	122.6(1)
N5–C3–N3	118.4(2)	118.0(3)	118.2(1)
N5–C3–N1	119.5(2)	119.8(3)	119.2(1)
O3–N6–O2			119.2(1)
O4–N6–O2			120.0(1)
O4–N6–O3			120.8(1)

(Fig. 6.52). The normals of the molecular planes of adjacent cations in the (010) plane are tilted with respect to each other, thus forming two different strands with angles of about  $+ 25^{\circ}$  and  $- 25^{\circ}$  with the *b*-axis, respectively. Notably, the formation of buckled layers by tilting the molecular planes of the cations causes the keto function of the ammeliinium ions to move closer to H31 in an adjacent layer. Thus, interlayer hydrogen contacts of 298 pm are formed, while the average distance between two layers is approximately half the *b* parameter (313 pm). Weak interlayer hydrogen-bonding also occurs between nitrate ions and ammeliinium cations of neighbored layers (H  $\cdots$  O: 307 – 325 pm) (Table 6.21).

**Table 6.21:** Hydrogen-bonding geometries (pm, °) found in the ammeliinium salts **1** – **3**.

D–H … A1/A2/A3	d(D–H)			d(H … A)		
N2–H21…Cl1/Br1/O3	86(3)	74(5)	85(2)	217(3)	243(5)	199(2)
N3–H31…Cl1/Br1/O2	83(3)	83(5)	85(2)	220(3)	244(5)	204(2)
N4–H41…O1/N1/O1	81(3)	90(6)	86(2)	219(3)	209(6)	201(2)
N4–H42…Cl1/Br1/O4	79(3)	75(6)	87(2)	250(3)	292(6)	206(2)
N5–H51…N1/O1/O2	78(3)	90(6)	87(2)	229(3)	212(6)	225(2)
N5–H51…O3						259(2)
N5–H52…O1/Br1/O4	88(3)	93(5)	90(2)	241(3)	263(5)	210(2)
N5–H52…Cl1/Br1	88(3)	93(5)		290(3)	293(5)	
D–H … A1/A2/A3	d(D–H)			d(D … A)		
N2–H21…Cl1/Br1/O3	176(3)	169(4)	175(1)	302.7(3)	316.4(5)	284.5(2)
N3–H31…Cl1/Br1/O2	179(3)	176(4)	177(1)	303.3(3)	327.1(5)	289.6(2)
N4–H41…O1/N1/O1	165(3)	173(4)	167(1)	298.0(3)	298.3(5)	285.2(2)
N4–H42…Cl1/Br1/O4	146(3)	150(4)	171(1)	318.5(3)	359.0(5)	292.5(2)
N5–H51…N1/O1/O2	171(3)	163(4)	165(1)	305.3(3)	299.3(5)	309.4(2)
N5–H51…O3			141(1)			331.1(2)
N5–H52…O1/Br1/O4	130(3)	135(4)	168(1)	305.8(3)	335.9(5)	298.9(2)
N5–H52…Cl1/Br1	139(3)	138(4)		361.2(3)	368.4(5)	

Each cation is hydrogen-bonded to three nitrate ions located in the same plane (H … A: 199 – 225 pm), with the tilting sense of the two anions in the same strand being opposite with respect to that of the cation (Fig. 6.52). The ammeliinium ions are additionally linked among each other by O1 … H41 contacts (201(2) pm) within the planes.

### 6.6.3 IR Spectroscopy

The IR absorption spectra of the ammeliinium salts **1** – **3**, while revealing some common features typical of triazine derivatives, differ markedly when comparing the halide salts (**1** and **2**) on the one hand with the nitrate salt (**3**) on the other hand (Fig. 6.53): In contrast to the situation in **3**, the  $\nu(\text{N–H})$  stretching region in **1** and **2** shows significant absorption below 3000  $\text{cm}^{-1}$ . In fact, medium strong, rather broad bands are observed at wavenumbers as low as 2692 (**1**) and 2748  $\text{cm}^{-1}$  (**2**), respectively, which closely corresponds to the absorption found in solid ammeline [493].

A rationalization of these findings is somewhat awkward, since they suggest rather strong hydrogen-bonding to be present in **1** and **2**, causing a red-shift of the N–H stretching vibrations, which cannot be corroborated by the single-crystal X-ray data. Particularly linear

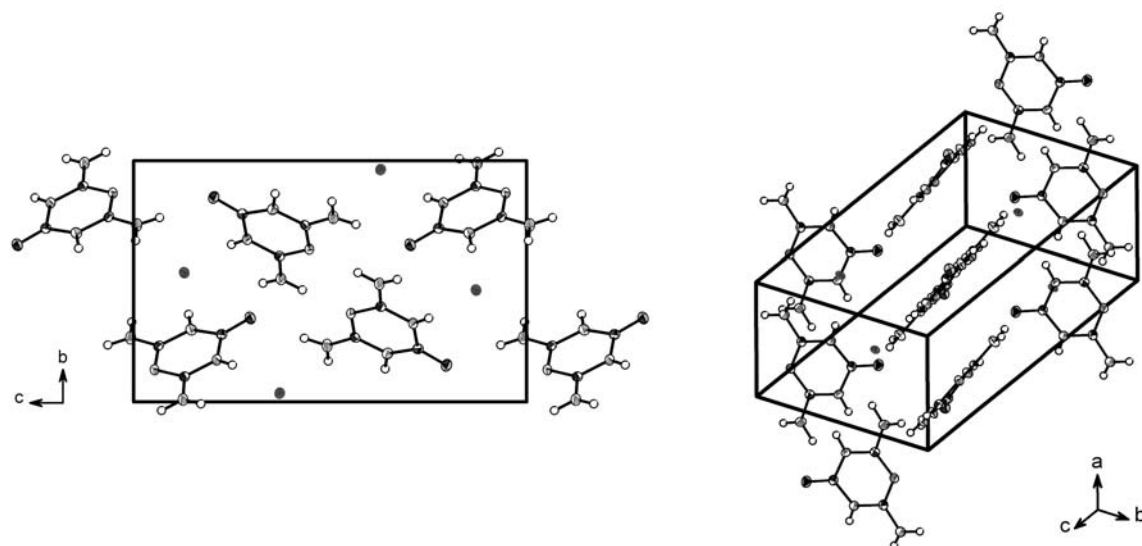


**Figure 6.51:** Different representations of the unit cell of ammeliinium bromide (2). Left: View along [100]; right: View along [211], showing the two different types of stacking directions. Thermal ellipsoids (apart from those for H) are drawn at the 50 % probability level.

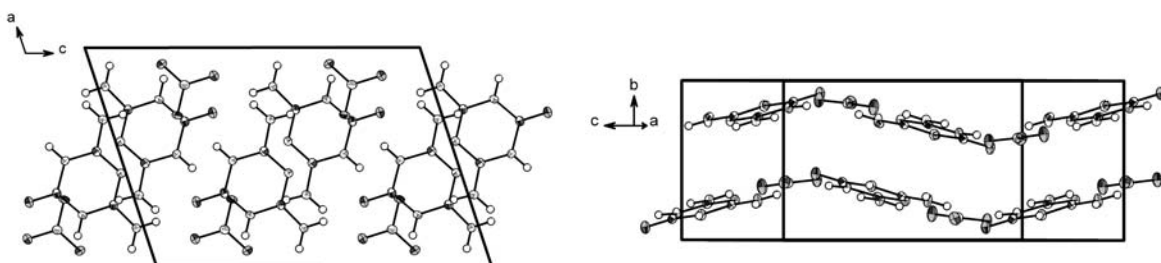


**Figure 6.52:** Different drawings of the unit cell of ammeliinium nitrate (3). Left: View along [010], demonstrating the displacement of the cations stacked along the b-axis with respect to each other; right: View along [401] parallel to the corrugated layers formed by cations and anions. Thermal ellipsoids (apart from those for H) are drawn at the 50 % probability level.

hydrogen-bonds with  $\text{N}-\text{H} \cdots \text{X}$  angles  $> 170^\circ$  are present equally frequently in all compounds, and can therefore not account for the pronounced absorption below  $3000 \text{ cm}^{-1}$  only observed in **1** and **2**. Overtones or combination bands seem to be unlikely owing to the relatively broad bands and their comparatively high intensity.

The carbonyl stretch is represented by a sharp band of medium intensity at  $1736$  (**1**) –  $1757 \text{ cm}^{-1}$  (**3**). Characteristic triazine bands involve ring and side chain C–N stretching as well as  $\delta(\text{N}-\text{H})$  vibrations, which are located uniformly in the range  $1660$  –  $1400 \text{ cm}^{-1}$ .

As compared to the vibrational spectra of ammeline, ammelide, and cyanuric acid [493, 498], the latter of which being known to adopt exclusively the “keto” form in the solid phase, the bands attributed to the C=O stretch in **1** – **3** are of comparatively low intensity with

respect to that in ammeline [498], which is particularly evident for the HCl and HNO<sub>3</sub> salts.

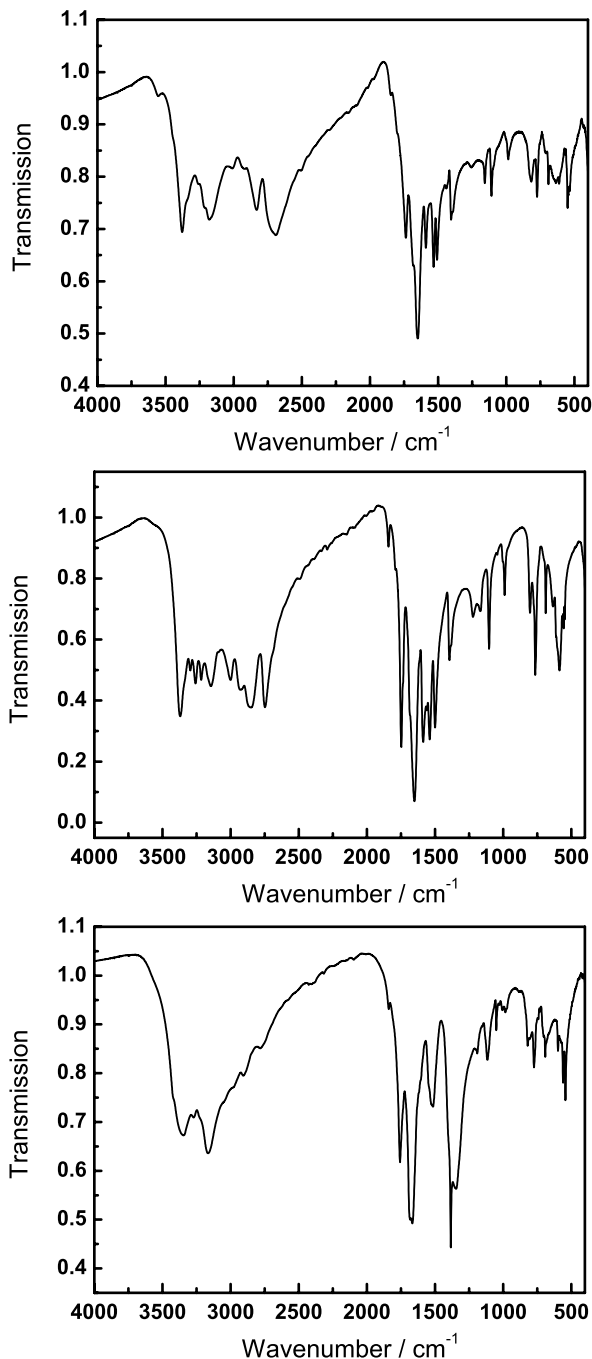


**Figure 6.53:** IR spectra of the ammeliinium salts **1** – **3**. Top: ammeliinium chloride (**1**); middle: ammeliinium bromide (**2**); bottom: ammeliinium nitrate (**3**).

Whereas symmetry reasons may hold responsible for this observation, another rationalization for the observed phenomenon could be a change of the tautomeric equilibrium induced by the KBr matrix, which, though being questionable, has nevertheless to be taken into account.

To probe the effect of the KBr matrix both on the hydrogen-bonding portion and on the keto-enol tautomerism, IR spectra were recorded in reflection geometry by using the pure substances without matrix support. The obtained IR spectra show distinct changes in the band positions (systematic red-shift in the reflection spectra of up to 20 cm<sup>-1</sup>) as well as in the band intensities. However, the basic features of the spectra, including the bands below 3000 cm<sup>-1</sup> for **1** and **2**, and the weak absorption of the C=O stretch are identical, in the latter case even more pronounced. Thus, the KBr matrix obviously does not interfere fundamentally with the hydrogen-bonding geometries and tautomerism, and therefore a conclusive rationalization of the above findings cannot be given at this stage (cf. section 6.6.4 on the facing page).

The position of all  $\nu(\text{C}=\text{O})$  bands of the ammeline salts are shifted to higher frequencies (1737 – 1757 cm<sup>-1</sup>) as compared to that of ammeline (1718 cm<sup>-1</sup>),

which also applies for the triazine ring stretch in **1** – **3** ranging from 1651 to 1682  $\text{cm}^{-1}$  (ammeline: 1615/1638  $\text{cm}^{-1}$ ).

The characteristic triazine bands at 774 (**1**), 765 (**2**) and 773 (**3**)  $\text{cm}^{-1}$ , which are attributed to the ring-sextant out-of-plane bend [383,384], are red-shifted with respect to the band of ammeline ( $795 \text{ cm}^{-1}$ ) [498]. This is in coincidence with protonated melamine derivatives, where the degree of protonation of the triazine core is directly associated with a lowering of the sextant bend of about  $15 - 25 \text{ cm}^{-1}$  per proton. Assuming ammeline to adopt the keto form and, thus, to possess a mono-protonated ring system, the positions of the sextant bend of the doubly protonated triazine rings in the ammelinium salts conform quite well to the expectations.

#### 6.6.4 Discussion

In the previous section first structural characterization of ammeline-derivatives based on single-crystal data has been presented. Owing to difficulties in the band assignment and lack of supporting single-crystal X-ray data, former investigations of the vibrational spectra of ammeline as well as ammelide could not be interpreted unambiguously in favor of either keto or hydroxy tautomer. Theoretical calculations on the stability of the different possible tautomers of ammeline, however, were indicative of the hydroxy tautomer to be slightly favored with respect to the keto tautomer [494]. The calculations were carried out for the gas phase species, thus naturally neglecting intermolecular interactions such as packing effects, hydrogen bonding etc. which may dominate the energetic “ranking” of the tautomers in the solid phase. In contrast to these studies, our findings demonstrate the keto form to represent the most stable solid-state tautomer in the case of the ammelinium cations presented here. The C–O distances found in **1** – **3** are consistent with C=O double bonds, and all protons could be localized such that a diamide-type structure results.

It may be instructive to compare the unexpectedly weak absorption of the C=O stretch in the IR spectra of **1** – **3** with the situation encountered for the related heptazine compounds cyameluric acid [ $\text{H}_3\text{C}_6\text{N}_7\text{O}_3$ ], as well as its mono- and diamide. The crystal structures of the latter two, partly amorphous compounds are still unknown to date, whereas that of the former has been elucidated recently [499,500]. *Finkel'shtein et al.* claimed the hydroxy form to dominate for cyameluric acid and some of its salts, and the oxo form to prevail in the amides [479,501]. These conclusions were made on the basis of the IR spectra owing to the absence or presence of absorption in the carbonyl stretching region [479]. Solid-state NMR spectroscopic investigations, however, led *Horath-Bordon et al.* [502] to the conclusion that although only a weak shoulder at  $1720 \text{ cm}^{-1}$  is visible in the IR spectrum, cyameluric acid

in fact adopts the keto rather than the hydroxy form. This hypothesis was substantiated quite recently by the crystal structure report on sodium dihydrogenycamelurate tetrahydrate,  $\text{Na}[\text{H}_2(\text{C}_6\text{N}_7)\text{O}_3] \cdot 4 \text{ H}_2\text{O}$ , where exclusively the all-keto tautomer is found [503]. The reported  $\text{C}=\text{O}$  bond lengths of 122 pm correspond very closely to those found in **1** – **3** (cf. section 6.6.2). The keto-form of cyameluric acid was finally verified by *Sattler et al.* and *Wagler et al.* by the crystal structure elucidation of cyameluric acid hydrate and a DMSO solvate thereof [499, 500].

The obvious discrepancy between the tautomers suggested by *Finkel'shtein et al.* from the IR spectra and those based on the single-crystal data could be indicative of a general trend according to which the carbonyl stretch in the IR spectra is either very weak or shifted towards lower wavenumbers, thereby overlapping with the heptazine/triazine core vibrations and thus being difficult to distinguish.

The question as to whether protonation of ammeline is accompanied by a change in the tautomeric state on going from the neutral to the mono-protonated form, or the energetic minima are actually represented in both cases by the carbonyl tautomers, cannot be resolved exclusively on the basis of our findings. The former case may be supported by assuming ring protonation to increase the  $\pi$ -delocalization of the oxygen lone pair into the triazine ring, accompanied by a change from the enol to the keto form. However, as also pointed out by *Wang et al.* [494], crystal packing and hydrogen bonding may exert a serious influence on both conformation and tautomerism, and must therefore be taken into account in the calculations, if reliable information on the solid-state molecular structures is an issue. It is evident that these factors may easily change the energetic succession of the keto and enol forms on going from the gas phase or solution to the condensed phase. Therefore, while the hydroxy tautomers could be the dominant ones for both ammeline and its salts in the gas phase, the respective keto tautomers may prevail in the solid state. However, it is most likely that a tautomeric equilibrium also exists in the solid state, where the prevailing tautomer is determined by various factors such as the counter ion, crystal packing or van-der-Waals interactions [479].

## 6.7 Melaminium Dinitrate

Melaminium dinitrate has been obtained as a by-product when heating a suspension of 20 mg melam perchlorate in 30 ml  $\text{H}_2\text{O}$  at 333 K and adding 5 ml of conc. nitric acid until a clear solution was obtained. If the solution was then further heated at temperatures  $\geq 314$  K, hydrolysis of the melam species occurred, yielding both ammelinium nitrate and melaminium nitrate. Most probably, the mono-nitrate salt was also formed but could not be isolated in crystalline form.

Melaminium salts have recently attracted attention as potential NLO (non-linear optical) materials if they crystallize in non-centrosymmetric space groups. Therefore, a plethora of melaminium salts has been synthesized and surveyed in recent years, both with respect to their NLO properties and as building blocks for hydrogen-bonded supramolecular aggregates [371–392]. According to theoretical investigations, melamine salts containing the melamine residue in doubly protonated form should exhibit the most beneficial hyperpolarizability values and are therefore expected to be most promising for NLO studies [504]. Until now, doubly protonated melamine rings have only been observed in a few salts [505], among which are the pyromellitic acid salt [392], melamine-cyanuric acid hydrochloride [506], 4-hydroxybenzenesulfonate [380], perchlorate hydrate [390], tetrachlorocuprate [389], and bis(trifluoroacetate) trihydrate as well as bis(trichloroacetate) dihydrate [379].

Melaminium mononitrate was synthesized by *Tanbug et al.* and classified as a novel energetic material with a high density ( $1.71 \text{ g} \cdot \text{cm}^{-3}$ ), however, no further experimental evidence was added to substantiate this claim. In this salt, the distinct monoprotonated melaminium cations and nitrate anions form hydrogen-bonded two-dimensional zig-zag ribbons, resulting in an efficient solid-state packing arrangement [507].

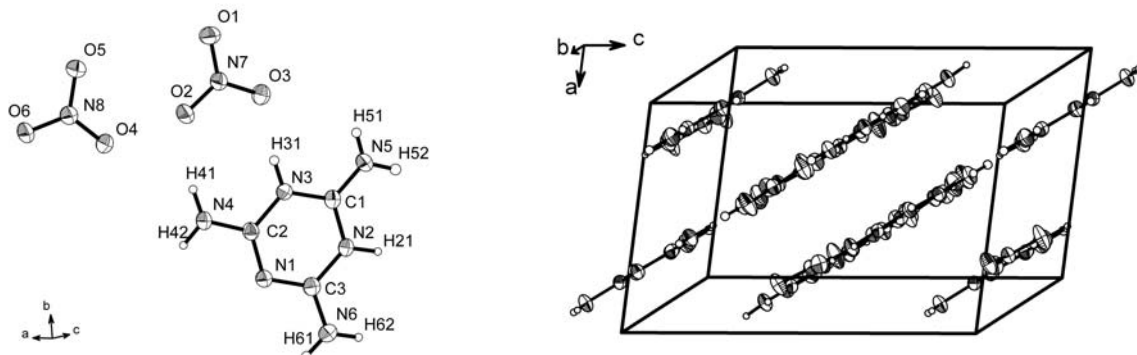


**Figure 6.54:** Asymmetric unit (left) and unit cell (right) of melaminium dinitrate. The layered structure is clearly evident. Thermal ellipsoids are drawn at the 50 % probability level.

In contrast, the doubly protonated analogue exhibits a classical layered structure. The layers are made up from hydrogen-bonded arrays of melaminium cations and nitrate anions (Fig. 6.54), and the calculated density is even larger as compared to the monoprotonated counterpart ( $1.80 \text{ g} \cdot \text{cm}^{-3}$ ). Details of the structure solution and refinement are summarized in Table 6.22.

In contrast to the mononitrate, the melaminium cations are essentially planar and show only neglectable deviations of the amino groups from the mean aromatic plane. This feature is probably due to the chemical environment in the solid state (packing effects, hydrogen bonding) [507]. According to the expectations, protonation of the melamine core results in a

Table 6.22: Crystallographic data for melaminium dinitrate.

Formula	$[\text{C}_3\text{N}_3\text{H}_7](\text{NO}_3)_2$
$M_w$ / g · mol <sup>-1</sup>	252.17
crystal system	monoclinic
space group	$P2_1/c$ (no. 14)
$T$ / K	200
diffractometer	Nonius Kappa CCD
radiation ( $\lambda$ / pm)	Mo-K $\alpha$ (71.073)
monochromator	graphite
$a$ / pm	783.63(16)
$b$ / pm	988.9(2)
$c$ / pm	1351.1(3)
$\beta$ / °	100.43(3)
$V$ / $10^6$ · pm <sup>3</sup>	931.8(3)
$Z$	4
$\rho_{\text{calcd}}$ / g · cm <sup>-3</sup>	1.798
F(000)	520
$\mu$ / mm <sup>-1</sup>	0.168
crystal size / mm <sup>3</sup>	0.12 x 0.10 x 0.08
diffraction range	$3.35 \leq \theta \leq 27.52$
index range	$-10 \leq h \leq 10, -12 \leq k \leq 12,$ $-15 \leq l \leq 15$
total no. reflections	16913
independent reflections	2138 ( $R_{\text{int}} = 0.0895$ )
observed reflections	1646
refined parameters / restraints	with $F_o^2 \geq 2\sigma(F_o^2)$
GooF on $F^2$	187 / 0
$R$ indices (all data)	1.047
	$R_1 = 0.0398$ (0.0567)
	$wR_2 = 0.0971$ ( 0.1073)
	with w = $[\sigma^2(F_o^2)$
	$+(0.0549P)^2 + 0.2275P]^{-1}$
	where $P = (F_o^2 + 2F_c^2)/3$
min./max. residual	
electron density /	- 0.256 / 0.291
$e \cdot 10^{-6}$ pm <sup>-3</sup>	

redistribution of the  $\pi$ -electrons, thereby increasing the bond order of the exocyclic C–NH<sub>2</sub> bonds (129 – 132 pm), which are by about 4 pm shorter on average as compared to the parent neutral base (134 – 136 pm) [508]. The resulting resonance forms involving a NH<sub>2</sub><sup>+</sup>=C bond clearly manifest themselves in a differentiation of the C–N bonds within the triazine ring. The C–N bonds *between* the two imino groups are intermediate in length (C1–N2 / C1–N3

135 pm), whereas the bonds N2–C3 and N3–C2 are the longest (138/137 pm), and the bonds located furthest away from the imino groups (C3–N1 and N1–C2) are significantly shortened (133/132 pm).

Apart from introducing a deviation from the ideal  $D_{3h}$  symmetry in the bond lengths, protonation also causes the bond angles within the six-membered ring to become highly asymmetric. The angles C–NH–C associated with the imino-groups are significantly widened (121°), the angle C2–N1–C3 showing the same tendency, yet less pronounced (117°). The corresponding angles in melamine range from 114 to 115°. In contrast, the angles at the carbon atoms N–C–N (117 – 123°) are notably smaller than the analogous angles observed in melamine (125 – 126°) [507, 508].

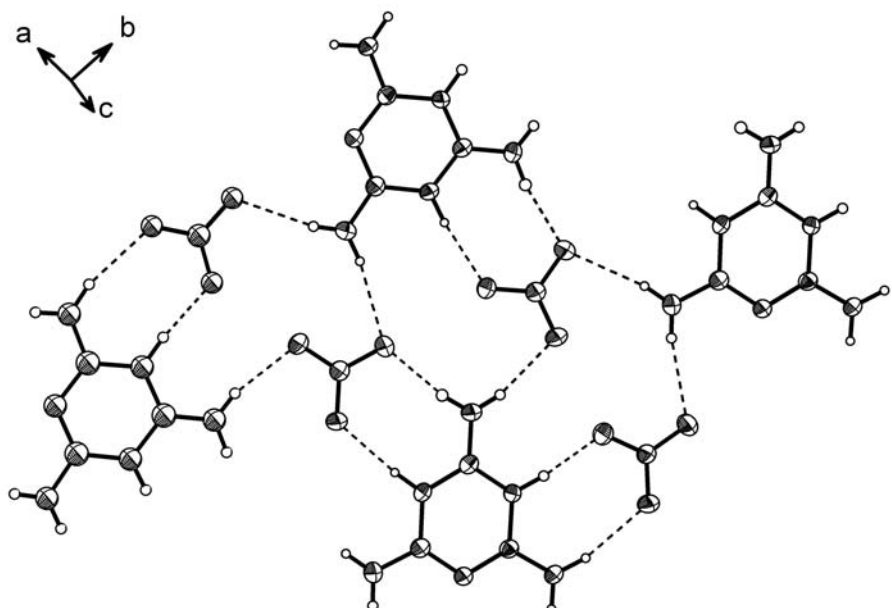


**Figure 6.55:** Hydrogen-bonding arrangement within the two-dimensional planar layers in melaminium dinitrate, made up from doubly protonated melaminium cations and two nitrate anions each. Thermal ellipsoids are drawn at the 50 % probability level.

The cations and anions in adjacent layers are stacked such that the cations are followed by anions and *vice versa*, rendering  $\pi$ -stacking interactions difficult (Fig. 6.54, right). Nevertheless, the spacing between adjacent layers is as small as 334 pm. Within the planar 2D layers a tight hydrogen-bonding network is formed, with donor-acceptor distances ranging from 269 to 305 pm. The corresponding H · · · A contacts cover the range from 180 to 222 pm, thus demonstrating the remarkably efficient packing of the ions within the planar sheets (Fig. 6.55).

## 6.8 Preliminary Conclusion

In the previous chapter an important stage in the condensation process of melamine has been outlined and the identity and special formation conditions of the controversially discussed species melam has been resolved (for a general discussion see section 6.4.8 on page 224). In fact, melam can be isolated only in small amounts and is therefore difficult to obtain on a preparative scale. An amenable route to melam, however, is based on its salts, which are accessible by reacting the commercially available melamine with acid salts, preferably ammonium salts, in closed ampoules at temperatures between 593 and 723 K.

We emphasize that the tendency of melam formation – or “stabilization” – from melamine is greatly enhanced in the presence of acid salts, which presumably facilitate the condensation of the triazine rings. If melamine is heated with ammonium halides, polycrystalline melam hydrohalide–ammonium halide adducts are formed, from which melam hydrate can easily be isolated on treatment with bases. Melam can then be obtained from the hydrated phase upon dehydration at elevated temperatures. We note that not only Brønstedt acids can induce the formation of melam salts, but also Lewis acids are suitable reactants, which may electronically modify the triazine ring system in a way similar to that observed for Brønstedt acids. In addition, Lewis acids may bring the reactive triazine sites into close contact by coordinating to two ring systems, thereby functioning as connectors and facilitating the separation of ammonia.

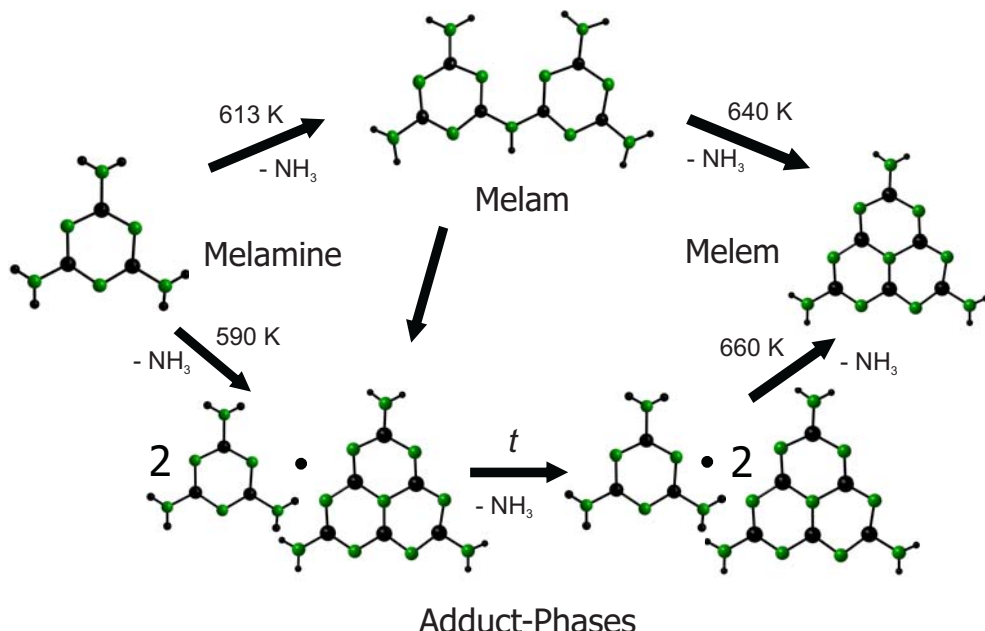


**Figure 6.56:** Condensation cascade of melamine sketched for the “low-temperature” regime. “t” denotes isothermal heating.

The fact that melam can be “stabilized” in the presence of salts may rationalize the early discovery of melam by *Liebig* who unwittingly prepared melam *via* its thiocyanate salt or hydrochloride–ammonium chloride adduct, liberating the neutral molecule by “purification” with potassium hydroxide [456, 462]. This fact indeed can be considered the seed of the historic controversy according to which the formation of melam from melamine has repeatedly been disputed, although the mere existence of this simple molecule was not actually challenged. Furthermore, the persistence of this argument may have been stimulated by the accidental coincidence of the elemental compositions of melam and the 2:1 melamine-melem co-crystallisate, which we hypothesize has in several cases been mistaken for melam.

The low-temperature pyrolysis reactions of melamine have now been clarified, and together with the knowledge of all intermediate stages and their tendency of formation including melam, the adduct phases and melem, a comprehensive picture of the thermal condensation of this important  $\text{CN}_x$  precursor can be drawn.

In addition, approaches to a better access and understanding of the chemistry of melam, its derivatives as well as its hydrolysis products have been pointed out, the latter of which still awaiting comprehensive structural characterization.

The next and final step of our investigation will focus on the high-temperature pyrolysis reactions in the condensation cascade of melamine, starting either from melamine itself or, which in this case is in fact equivalent, directly from the HT-intermediate melem. Ultimately, the identities of melon and graphitic carbon nitride are to be resolved, which will be the underlying objective dealt with in Chapter 7.

## Chapter 7

# Carbon(IV)Nitride Precursors IV. Melon

The following chapter will conclude the attempts made to provide a comprehensive understanding of the reactivity of melamine and, consequentially, of a vast number of related carbon nitride precursor compounds. The condensation processes occurring beyond melem formation still lack sufficient insight to reliably characterize the polymeric, inert carbon nitride species with respect to their molecular and solid-state structures. Hence, the identity of both “melon”, a hydrogen-containing carbon nitride polymer with idealized formula “ $C_2N_3H$ ”, and the ultimate condensation product of melamine, the binary carbon nitride with presumed formula  $C_3N_4$ , has not been resolved as yet.

Stimulated by the present revival of carbon nitride in the context of ultra-hard and novel chemically inert graphite-like materials, a reconciliation of the historic approach with the actual – somewhat biased and defective – view on the controversial compound  $C_3N_4$  will be attempted. Thus, by delineating the “high-temperature” regime of the condensation cascade of melamine, the nature of the highly disputed intermediate “melon” will be studied and linked with the current issue of the identity and structure of graphitic carbon nitride.

## 7.1 Introduction

The quest for binary carbon nitride  $C_3N_4$ , whose postulated material properties are believed to push the borders of ultra-hard materials, has provided a tight link between *Liebig*'s historic work and modern materials chemistry [41, 46–52].

While being re-invented in a thoroughly new context in the 1980s, carbon nitride had been discussed as the ultimate de-ammonation product of a series of ammonocarbonic acid derivatives such as cyanamide or melamine as early as 1834 [80, 456, 509]. All attempts to synthesize pure carbon nitride were invariably spoiled by the presence of small amounts of hydrogen, yielding a yellow, amorphous, infusible material, which was first obtained by *Berzelius* and given the name “melon” by *Liebig* [80, 509]. As reviewed by *Franklin* (see [80] and references therein), the latter was obtained by heating to redness the yellow precipitate formed by the action of chlorine on a solution of potassium or sodium thiocyanate, by heating ammonium or mercury thiocyanate, and as the final de-ammonation product on heating mixed aquo-ammonocarbonic acids such as ammeline or urea [76, 424].

Despite the lack of sharply defined composition, melon was assigned the empirical formula  $C_6N_9H_3$ , which led *Redemann* and *Lucas* to draw two alternative planar structure models based on the cyameluric (heptazine) core  $C_6N_7$  (Fig. 7.1, **1a** + **1b**), whose structure had been established by *Pauling* and *Sturdivant* [75, 76]. Alternatively, a symmetric triangular form was proposed, whose empirical formula approaches asymptotically the limit  $C_3N_4$  if condensations extend indefinitely (**1c**). Other structure models, including triazine-based ones [459, 469], have been put forward for melon owing to the lack of detailed knowledge on the structure of its presumed monomer, melem. *Franklin* found that the empirical composition of melon varied with the method of preparation, as he obtained samples of hydrogen content varying from 1.1 to 2.0 wt%. Products with a hydrogen content of only 0.6 wt% were rationalized by assuming a mixture of several “compact” condensation products of triangular shape as for example **1c** in Figure 7.1 [76, 80]. On this background, it was conjectured that “*it is probably incorrect to assign any one structure to melon, for it is more than likely a mixture of molecules of different sizes and shapes. This gives rise to its amorphous character*” [76].

The gap between historic and modern carbon nitride chemistry can be bridged by the hypothetical graphitic modification of  $C_3N_4$  (g- $C_3N_4$ ), which has been calculated to be the most stable form of carbon nitride, and, owing to its analogy with graphite, was attributed the triazine core  $C_3N_3$  as elementary building block (Fig. 7.2, **2a**, and Chapter 1) [51, 73, 90, 91, 128, 301, 453, 510–512]. Only recently, an alternative structure model based on the heptazine core emerged (Fig. 7.2, **2b**), strongly reminiscent of the work on melon fallen into oblivion in the second half of the last century [42, 82, 85, 124, 127, 513, 514]. Since then,

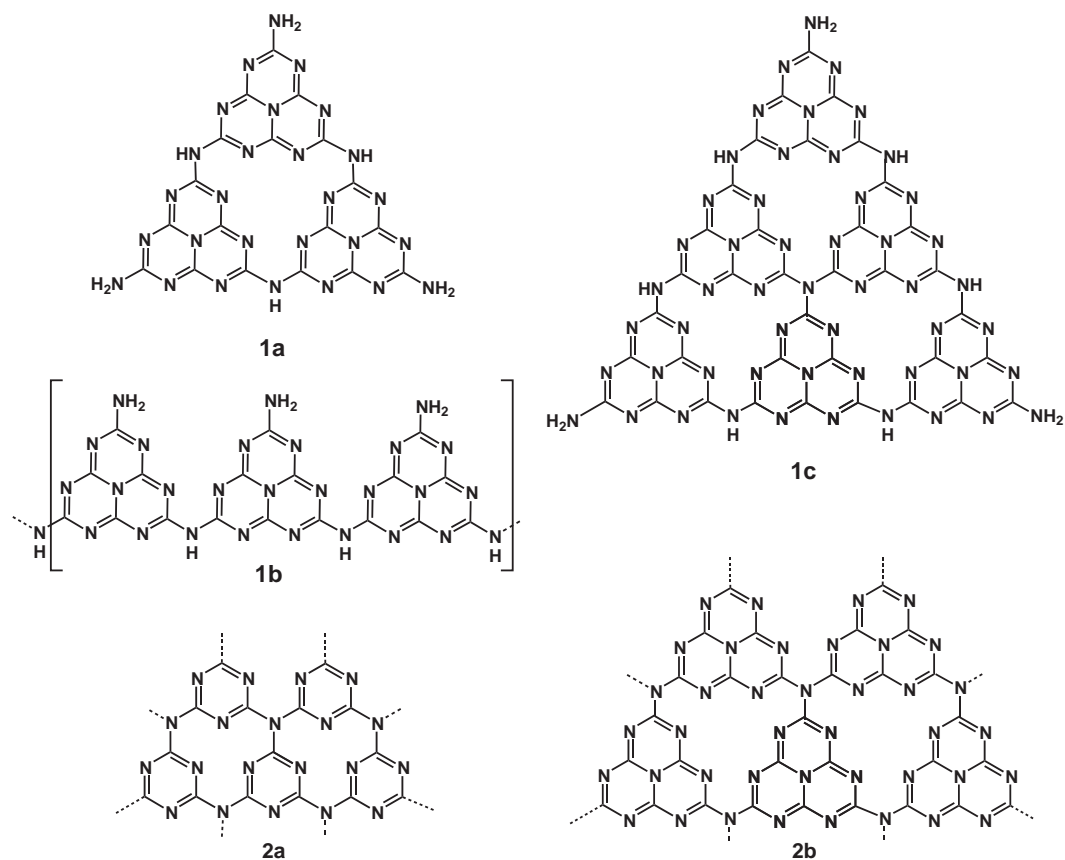


**Figure 7.1:** Structure models proposed for melon (**1a**, **1b**) and cutouts of hypothetical structure models of graphitic carbon nitride based on triazine (**2a**) and heptazine building blocks (**2b**). The melon-derived, compact triangular structure of composition  $C_{36}N_{52}H_{12}$  (**1c**) has an empirical formula intermediate between melon and  $g\text{-}C_3N_4$ .

a plethora of experimental and theoretical efforts have been made to elucidate the structure of  $g\text{-}C_3N_4$ , which inevitably failed due to the ill-defined nature of the obtained polymeric, often hydrogen-containing materials [42]. Whereas a vast number of possible triazine-based structures has been devised and their topologies as well as their relative stabilities computed [42, 44, 51, 515, 516], only very few heptazine-based models have been put forward until now [42, 65, 85, 513, 514].

*Komatsu* proposed polymers of melem to form upon polycondensation / pyrolysis of various tri-functional tri-*s*-triazine derivatives, such as potassium melonate, starting from melamine or ammonium thiocyanate [84, 517]. The as-obtained graphite-like “pseudo carbon nitrides” were classified according to their N/C ratio and hydrogen content ( $CN_xH_y$  with  $x = 0.63 - 1.0$  and  $y = 0.1 - 0.3$ ) as “symmetric triangular forms” (cf. model **1c**) or partially condensed, irregular forms of heptazine-based carbon nitride polymers with molecular weights ranging between 1937 and 4941 g mol<sup>-1</sup> and hexagonal symmetry of the X-ray powder pat-

terns ( $a = 2.4 \text{ \AA}$ ,  $c = 6.7 \text{ \AA}$ ) [84]. In contrast, solid polymerization of potassium melonate and cyameluric trichloride in an autoclave was reported to yield a triangular heptazine-based polymer with presumed composition  $\text{C}_{91}\text{N}_{124}\text{H}_{14}$ , whose X-ray powder pattern was indexed on an orthorhombic cell with  $a = 7.1 \text{ \AA}$ ,  $b = 16.2 \text{ \AA}$ ,  $c = 12.9 \text{ \AA}$  [83].

A hardly recognized work by *Komatsu* describes the synthesis of a “cyameluric high polymer” by thermal de-ammonation of melon *via* a “melem-dimer”. In this context, melon was assigned the empirical formula  $\text{C}_{60}\text{N}_{91}\text{H}_{33}$  and associated with a poorly crystalline, linear decamer of melem. For the “cyameluric high polymer”, a degree of condensation corresponding to a linear polymer based on 42 monomers was suggested, and an orthorhombic unit cell was established by means of X-ray powder diffraction with  $a = 7.2 \text{ \AA}$ ,  $b = 21.5 \text{ \AA}$ ,  $c = 13.6 \text{ \AA}$  [517].

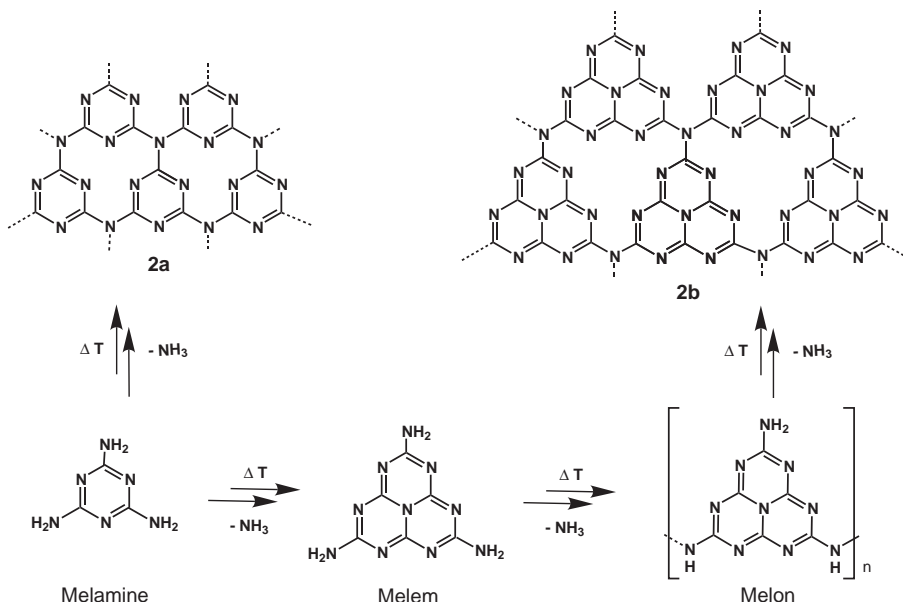


**Figure 7.2:** Simplified representation of the condensation cascade of melamine, leading to extended carbon nitride solids of unknown composition and structure. Both fully condensed triazine- (**2a**) and heptazine-based models (**2b**) are consistent with the structural motifs appearing before or during condensation.

Alongside the above reports on partially condensed, predominantly melon-type products, the quest for graphitic carbon nitride typically emanates from derivatives or precursors of triazine, whose structural integrity is most commonly believed to be preserved upon thermal treatment of the starting materials. One important synthetic technique among the most ambitiously pursued approaches toward the synthesis of g-C<sub>3</sub>N<sub>4</sub> has been the pyrolysis of numerous molecular compounds such as cyanamide, dicyandiamide, melamine [300, 509], 2,4,6-tricyano-melaminic acid, hydromelonic acid [83, 84], tri-azido-*s*-triazine and tri-azido-heptazine [128, 518], or of functionalized single-source precursors such as C<sub>3</sub>N<sub>3</sub>(NHCl)<sub>3</sub> [519], C<sub>3</sub>N<sub>3</sub>(NH<sub>2</sub>)Cl<sub>2</sub> [91, 520] or C<sub>3</sub>N<sub>3</sub>X<sub>2</sub>N(Y(CH<sub>3</sub>)<sub>3</sub>)<sub>2</sub> (X = F, Cl; Y = Si, Sn) [301, 512]. For example, the attempt to

prepare triazine-based carbon nitrides by polycondensation of melamine with the Lewis acid  $\text{ZnCl}_2$  afforded a polymeric material with an orthorhombic unit cell ( $a = 7.3 \text{ \AA}$ ,  $b = 8.5 \text{ \AA}$ ,  $c = 6.5 \text{ \AA}$ ). It was assigned a vacancy-network structure consisting of triazine nuclei, owing to the residual hydrogen content of 1.84 wt% [300].

A rather classical approach utilizes sulphur-containing species such as thiosemicarbazides or ammonium thiocyanate, all of which decompose upon moderate heating, while giving off low-weight, volatile sulphur species such as carbon disulfide [509, 521, 522]. However, in the majority of cases the resulting products were at most poorly crystalline and partially contaminated with significant degrees of impurities according to multinary mixtures of composition  $\text{CN}_x\text{H}_y\text{X/Y}_z$  and N/C ratios typically far below the theoretical value of 1.33.

Alternatively, two-component reactions as for instance in the systems cyanuric chloride / melamine [510, 520], or cyanuric chloride / metal nitride, azide, amide [66, 90, 453, 511, 523], were carried out, as well as conversions under high-temperature and -pressure conditions [44, 73, 74, 91, 524, 525]. Thus, *Kawaguchi et al.* synthesized a material with presumed formula  $[(\text{C}_3\text{N}_3)_2(\text{NH})_3]_n$  by polycondensation of cyanuric chloride and melamine, whose electron diffraction pattern was indexed on a hexagonal cell with  $a = 8.2 \text{ \AA}$  and  $d_{100} = 7.1 \text{ \AA}$  [510]. *Demazeau et al.* reported on the solvothermal synthesis of  $\text{g-C}_3\text{N}_4$  by reacting melamine with hydrazine as nitriding agent under supercritical conditions, using a Belt-apparatus at 1073 K and 3 GPa [73, 74, 91, 524, 525].

The synthetic strategy which appears to be most promising to obtain reasonably well-defined, moderately crystalline carbon nitride materials includes the controlled pyrolysis of  $\text{CN}_x\text{H}_y$  precursor compounds, as has been shown in the previous chapters [124, 127]. Nevertheless, the advantage of comparatively high crystallinity usually comes along with the presence of hydrogen in the products, which at the same time seems to stabilize the structure and to function as defect site, thereby breaking up the otherwise more highly condensed carbon nitride building blocks.

The literature, however, offers little or no alternatives. High energy techniques (ion beam sputtering, CVD, laser- or shock-wave techniques), yielding amorphous materials with sub-stoichiometric nitrogen content, or pyrolyses of molecular precursors typically affording layered carbon nitrides containing 1 – 2 wt% hydrogen, seem to be the only viable approaches.

The synthesis of layered carbon nitride materials based on melamine or related precursors offers the advantage of convenient accessibility of melamine next to the “pre-formed” carbon nitride core ( $\text{C}_3\text{N}_3$ ), which is being discussed as the major building block of graphitic carbon nitride (Fig. 7.2).

## 7.2 “Melem Oligomer”

On heating melamine for about 2 days in a porcelain dish loosely covered with a lid at temperatures of  $\approx 763$  K, a new phase emerges besides melem, which is not identical with either melamine, or adduct phases I and II (Fig. 7.3; cf. Chapter 6 on page 196). Melem is almost completely converted into the unknown phase after about 8 days, whereas after another 6 days the X-ray powder pattern has become almost amorphous with a broad reflection around  $2\theta \approx 27^\circ$ . The same phase has been obtained in traces at 623 K after  $\approx 14$  days, which together with the above observation indicates the metastable character of this compound owing to the pronounced dependence on both temperature *and* time (cf. section 6.4 on page 213).

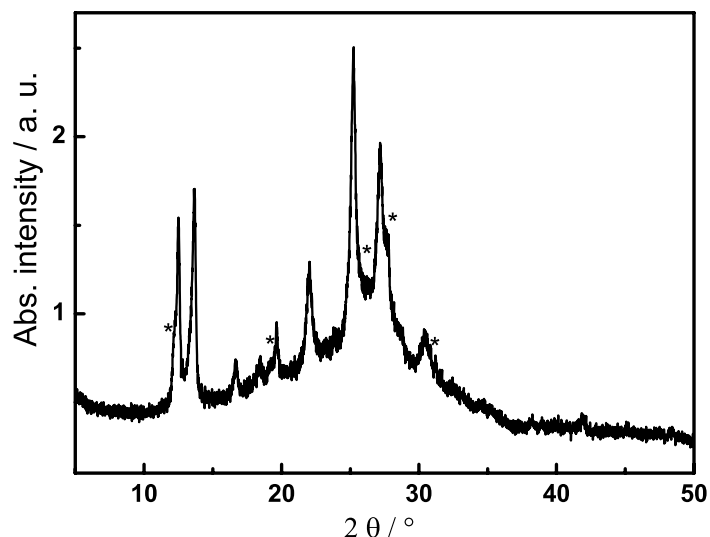


**Figure 7.3:** X-ray powder pattern (Cu- $K_{\alpha 1}$  radiation) of a new phase emerging from melem after heating of melamine at 763 K for 8 days. Small amounts of melem still present as impurities (mainly visible as shoulders to the reflections of the major phase) are indicated by asterisks.

The IR spectrum of the yellowish phase is displayed in Figure 7.4, together with that of melem as reference. The similarity to the spectrum of melem is clearly evidenced by the two strong bands at  $1612$  and  $1464$   $\text{cm}^{-1}$ , as well as the sharp semicircle ring stretch at  $804$   $\text{cm}^{-1}$ , diagnostic of a non-protonated heptazine core. Marked differences are only visible in the  $\nu(\text{C}-\text{N}) / \delta(\text{N}-\text{H})$  region, where two bands are observed at  $1330$  and  $1252$   $\text{cm}^{-1}$ , that are absent in melem. Since these bands are indicative of  $\text{C}-\text{NH}-\text{C}$  moieties as observed for melam at  $1338$  and  $1250$   $\text{cm}^{-1}$  (cf. Fig. 6.15 on page 215), an analogous or similarly condensed structure based on heptazine rings may be inferred.

It is therefore conjectured that melem dimers or oligomers are formed on prolonged heating

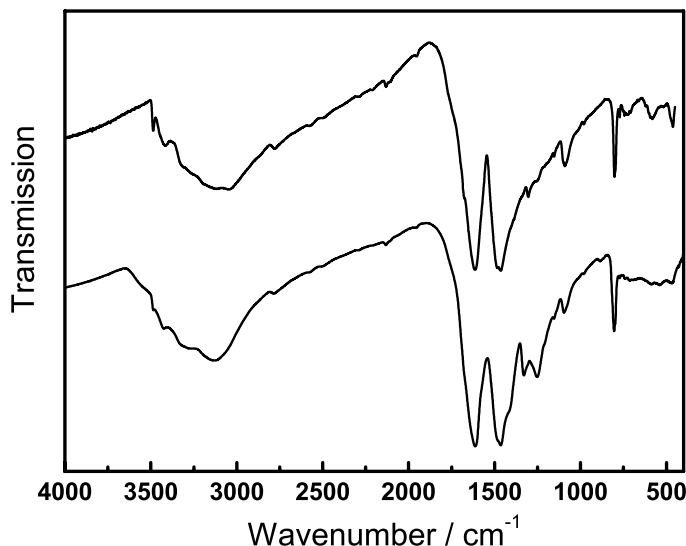


**Figure 7.4:** FTIR spectra of the presumed melem oligomer (bottom) and melem (top), recorded as KBr pellets at RT.

of melem, which upon further condensation gradually become amorphous. The similarity of the XRD patterns of melem and its presumed oligomer (cf. Fig. 6.5 on page 202) suggests that the initial state of the oligomerization process may proceed without significant structural changes, whereas amorphization associated with a broad reflection at  $2\theta \approx 27^\circ$  may indicate the formation of a layered structure with poorly defined interlayer spacing. It should be pointed out that – depending on the heating conditions ( $T \geq 673$  K, hours to days, open system) – polymeric materials with different colors are obtained, ranging from light yellow to dark beige. Whereas in open systems only yellow, largely amorphous compounds are accessible, the crystallinity can be significantly enhanced by pyrolyzing melamine in sealed silica glass ampoules at  $T \geq 893$  K as detailed below. The colors of the as-obtained products are typically brownish, indicating that higher crystallinity comes along with the onset of carbonization of the sample under the high-pressure and high-temperature conditions applied. The above findings forbode the possibility of melem-polymerization, which in turn is a strong indication for the existence of highly condensed networks made up from heptazine or, less likely, triazine building blocks. This thread will be pursued in the following sections.

### 7.3 Synthesis and Composition

As an extension of the experiments carried out in an open system at moderate temperatures as outlined above, pyrolyses of melamine were carried out in sealed silica glass ampoules under vacuum at temperatures between 833 and 873 K, or predominantly under dry argon at temperatures between 893 and 913 K.

Typically, 230 mg ( $1.83 \cdot 10^{-3}$  mol) melamine were transferred into a thick-walled silica glass tube ( $\varnothing_{ext.}$  15 mm,  $\varnothing_{int.}$  11 mm), from which water had been removed by thorough heating and evacuation. The tube was sealed using a oxyhydrogen burner at a length of  $\approx 120$  mm. Increasing the amount of melamine to 250 mg results in facile rupture of the ampoule due to the pressure arising from the gases being evolved during the reaction. The ampoule was then placed in a vertical<sup>1</sup> tube furnace and heated ( $1 \text{ K min}^{-1}$ ) to 903 K, at which temperature the sample was held for 12 to 36 h. The cooling rates did not notably affect the crystallinity of the products, so that the furnace was typically switched off with the sample cooling down to RT within several hours. The sample was then isolated by carefully breaking the ampoule, upon which a significant amount of HCN and ammonia was released. The yield of brownish residue typically amounted to 38 – 57 %; approx. 8 – 10 % were recovered from the top of the ampoule in the form of a brown sublimate mixed together with long, needle-shaped melamine crystals.

The latter presumably result from depolymerization of the product, which is induced by ammonolysis at elevated pressures of ammonia. The occurrence of ring opening reactions of heptazine derivatives in the presence of Lewis acids has been discussed in section 6.5.3 on page 246. Furthermore, this tendency is implicitly evident from the synthesis of uniformly  $^{15}\text{N}$ -enriched melamine from sodium tricyanomelaminate and  $^{15}\text{NH}_4\text{Cl}$  [82, 240], as well as from the detection of dicyandiamide as a sublimation product when pyrolyzing melamine in a vertical tube with pressure equalization. In addition, the ammonolysis of triazine derivatives at elevated temperatures has been subject to detailed studies in the literature [526]. Although possible depolymerization products other than melamine, such as dicyandiamide, were not observed as crystalline side phases by XRD, very small amounts of amorphous by-products such as (poly)imides below the detection level of solid-state NMR spectroscopy ( $\leq 3 \%$  for CP measurements) may not entirely be excluded. Also, as has been pointed out above (cf. section 7.2 on page 285) and in the literature, the comparatively harsh synthetic conditions applied in the present context likely induce heterogeneous crystallization, yielding a broad spectrum of differently ordered domains, ranging from amorphous to nanocrystalline. Presumably, a mixture of polymers with different chain lengths is obtained, which can be considered a feature

---

<sup>1</sup>A horizontal setup is also possible and may even lead to increased yields.

intrinsic to thermally induced polymerization processes. In this sense only, the as-synthesized material, which will be referred to as C/N/H-graphite for the time being, cannot be considered to represent an overall homogenous phase. Though being considered unlikely, the simultaneous formation of structural isomers discussed in section 7.1 on page 281 cannot be completely discarded (for a more comprehensive discussion, cf. section 7.8 on page 295).

**Table 7.1:** Elemental analysis data for the pyrolysis product obtained from the condensation of melamine at 893 – 913 K, given as average over several analyses. Theoretical values of  $g\text{-C}_3\text{N}_4$  are given for comparison.

Temperature / K	N / wt%	C / wt%	H / wt%
893	61.7	36.0	1.9
903	61.2	36.0	1.8
913	57.3	38.1	2.3
$\text{C}_3\text{N}_4$ (theor.)	60.87	39.13	–

In order to purify the residue and eliminate melamine and – present to only a small extent – melem crystals, the product ( $\approx 80$  – 100 mg) was transferred into a Duran ampoule (pre-dried *in vacuo* under heating), which was sealed off under argon and heated to temperatures around 873 K ( $1 \text{ K min}^{-1}$ ) for at least 12 h. Alternatively, admixtures of the starting material melamine were removed by sublimation using a cold finger integrated into a glass tube (cf. section 2.1.4.2 on page 23). Upon purification, the brownish material lightened up, thereby changing its color into reddish-brown.

According to elemental analysis, the sublimate contained a larger amount of hydrogen (typically  $\geq 2$  wt%), its X-ray powder pattern being slightly less crystalline, yet overall similar to that of the residue. Therefore, the sublimate may represent a polymeric carbon nitride material with a degree of condensation slightly less than that found for the residue, hence having a higher volatility.

According to Table 7.1, the product compositions at 893 and 903 K are similar, whereas rapidly increasing carbonization is observed at  $T \geq 913$  K. In addition, the hydrogen content is minimal at 903 K and notably increases at higher temperatures. Therefore, under the relevant pressure conditions, the thermal stability of the C/N/H-graphite is limited to temperatures of about 903 – 907 K. At higher temperatures, nitrogen is increasingly lost from the material in the form of HCN,  $(\text{CN})_2$  and  $\text{N}_2$ , and a hydrogenated, graphitic material of black color remains. This points to the re-integration of hydrogen into the bulk material at elevated temperatures under the pressure of gaseous ammonia.<sup>2</sup> Furthermore, small “heteroatom” contents (up to 2 wt%; typically  $\approx 0.5$  – 0.7 wt%), presumably oxygen, are

<sup>2</sup>This tendency has further been corroborated by elemental analysis of a material heated at 943 K (N, 49.29; C, 46.04; H, 3.15).

detected in the bulk as impurities. As has been pointed out in the literature, polymeric carbon nitrides may be prone to water absorption on exposure to air, yielding compositions with up to 8 wt% oxygen [527].

Lowering the reaction temperature to 893 K led to a slight increase of the residual melamine impurities, whereas temperatures below 893 K did not furnish full conversion of the starting material and, as a consequence, melem was found in the products.

Clearly, the average molar C/N ratio of  $\approx 0.68$  is lower than the one expected for  $\text{C}_3\text{N}_4$  (0.75), thus indicating a surplus of nitrogen in the samples. In addition, the non-negligible hydrogen content of approximately 1.8 wt% suggests that a hydrogen-containing  $\text{CN}_x\text{H}_y$  polymer was obtained, whose composition of  $\approx \text{C}_3\text{N}_{4.4}\text{H}_{1.8}$  is somewhat close, yet not identical to that of graphitic carbon nitride.

Mass spectrometry was attempted using different techniques (MALDI-TOF, DEI, FAB, ESI), but did not furnish conclusive results, since typically no mass peaks were observed that could be interpreted in terms of characteristic fragments of the  $\text{CN}_x\text{H}_y$  material. Therefore, it is assumed that a highly condensed, polymeric material was formed that cannot be easily broken up into volatile species detectable by the experimental techniques applied.

## 7.4 Reactivity

The chemical reactivity of the condensation product was exemplarily tested by a number of reactions with acids, bases, and potentially nucleophilic agents. The latter were chosen so as to either break up the polymeric material and, thus, to chemically identify its elementary building blocks, or to change the solubility of the otherwise insoluble compound by (de)protonation. The reactions and their results, together with the principal reaction conditions, are summarized in Table 7.2.

None of the above reactions turned out to be suited to conclusively identify the elementary building blocks of the polymeric  $\text{CN}_x\text{H}_y$  material. Instead, most of the products could not be identified owing to their amorphous character or to the insolubility and chemical inertness of the polymeric material, therefore rendering the structure elucidation by means of physical methods indispensable. However, heating the yellow oligomer (polymer) described in section 7.2 on page 285 in 1 – 4 M NaOH or KOH affords the respective cyamelurate salts and varying amounts of cyanurates. The extent of hydrolysis is strongly dependent on the temperature and concentration of the solution, as it is well known that the cyameluric nucleus further hydrolyzes in alkaline solution to give cyanuric acid salts [76, 83, 84, 424, 499, 503, 517]. Furthermore, potassium melonate is obtained by adding the yellow material to potassium

**Table 7.2:** Reactions of the high-temperature condensation product of melamine.

Reaction partner	Temperature	Reaction products
$\text{NH}_4\text{Cl}$	743 K	no reaction
$\text{NH}_3$ (aq.)	RT	no reaction
$\text{LiOH}$ (0.01 M)	373 K	partially insoluble, amorphous filtrate
$\text{NaOH}$ (0.7 M) / $\text{MeOH}$	373 K	partially insoluble, unidentified filtrate
K	423 – 723 K	$\text{K}_2\text{CO}_3$ , $\text{KCN}$
KI	773 K	no reaction
$\text{HBr}$ (conc.)	373 K	largely insoluble
$\text{HNO}_3$ (conc.)	353 K	largely insoluble
$\text{H}_2\text{SO}_4$ (conc.)	373 K	partially insoluble, amorphous filtrate
$\text{HClO}_4$ (conc.)	373 K	partially insoluble, amorphous filtrate
$\text{ZnCl}_2$	743 K	XRD: semi-amorphous, unidentified
$\text{AlCl}_3$	673 K	melem
$\text{AlCl}_3$	623 K	Al-melam complex

thiocyanate and heating [76, 83, 424]. These observations can be assessed as indirect evidence for the heptazine-based nature of the C/N/H material, which is assumed to be a more highly condensed condensation product of the yellowish oligomer (polymer).

The thermal behavior of the polymer was probed by *in situ* TPXRD measurements (Fig. 7.5). As a result, the material is stable up to  $\approx 1043$  K without passing through phase transitions prior to its decomposition. The observed considerable thermal stability of this light-weight material is therefore comparable to or somewhat higher than that of aromatic polyamides and -imides [517].

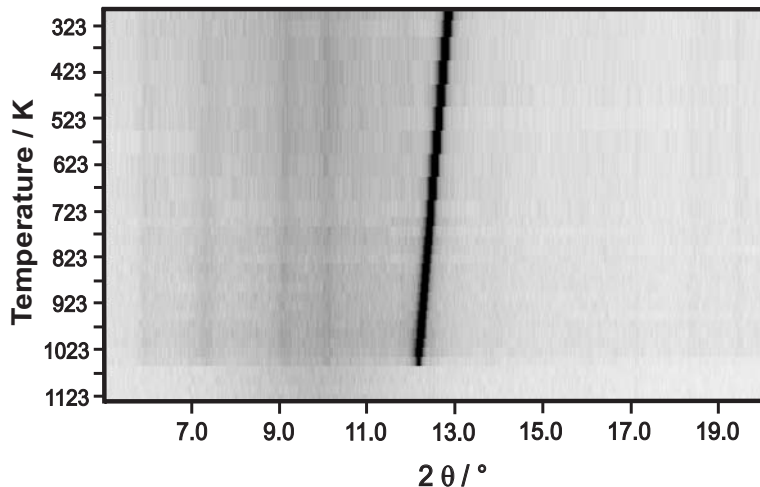


**Figure 7.5:** *In situ* temperature-dependent X-ray diffraction measurements (Mo- $\text{K}_{\alpha 1}$  radiation) of the C/N/H-graphite recorded between room temperature (top) and  $T \approx 1123$  K (bottom).

## 7.5 Morphology

Scanning electron microscopy images demonstrate the micro- and submicrocrystalline character of the  $\text{CN}_x\text{H}_y$  material as shown in Figure 7.6. The morphology of the material resembles

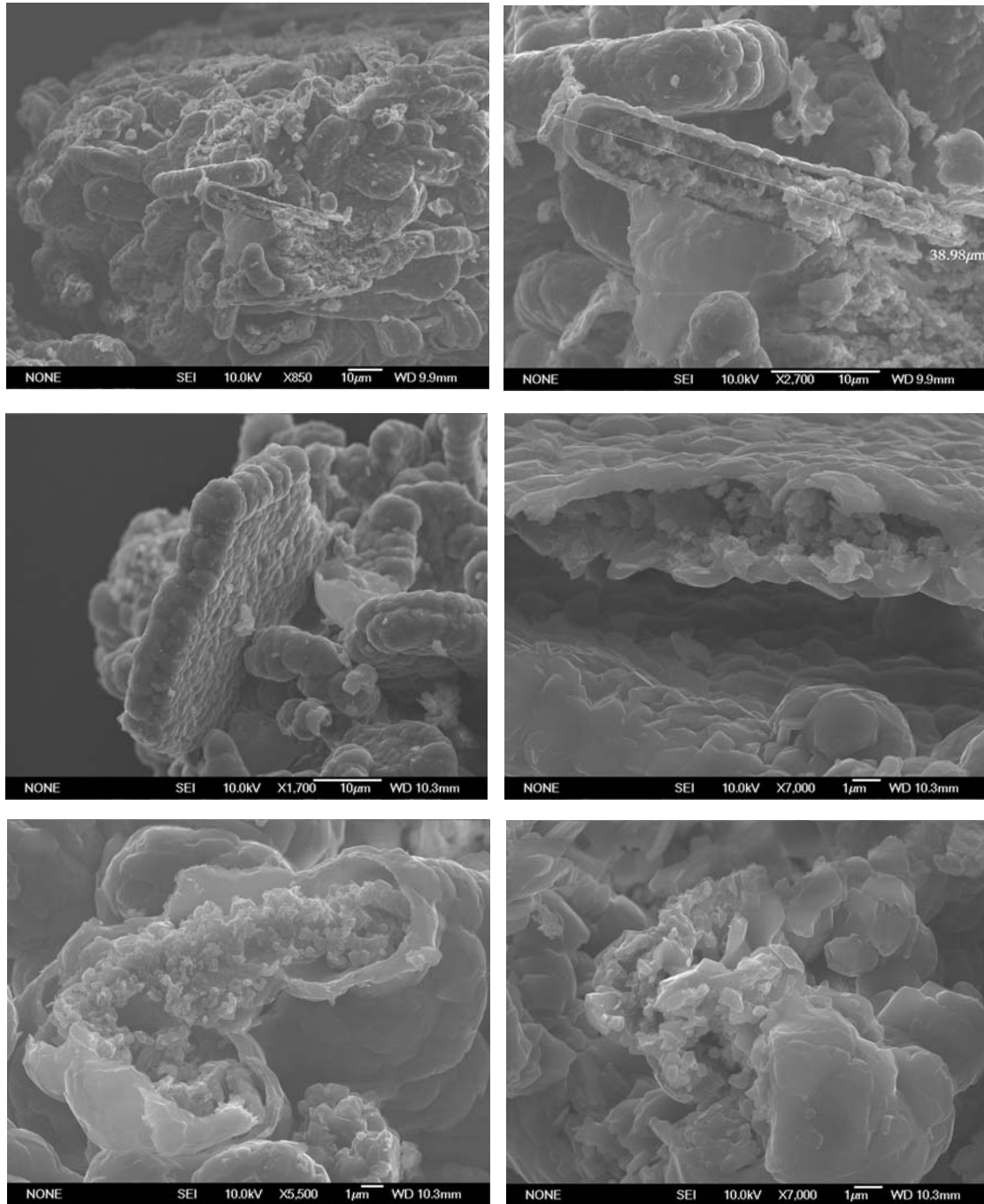


**Figure 7.6:** Representative scanning electron microscopy images of the  $\text{C}/\text{N}/\text{H}$  graphite, taken from various sample regions. The images reveal crystallite sizes on the nanometer and micrometer length scales, as well as the porous morphology of the sample.

that of microcapsules, the hollow tubes and spheres with a diameter of several micrometers containing crystallites on the nanometer length scale. While the crystalline particles appear to be plate-like, the spheres presumably result from the particular reaction conditions (see above): The evolution of ammonia, together with the rising of the inner pressure within the tube during condensation most likely stimulates the bulging of the particles. As will be shown in the following, it is considered unlikely that this type of morphology directly reflects the structure of the material on a molecular level, as would be expected for onion-type layered materials exhibiting a pronounced curvature of the layers.

Owing to the small size of the crystallites, together with the pronounced disorder dominating the layered structure of the material (cf. sections 7.7 on page 294 and 7.9 on page 303), structure elucidation by X-ray methods does not seem to be particularly promising in the present case.

EDX was used to qualitatively ensure that the composition of the observed particles corresponds to that of a carbon nitride material. As a result, in essentially all sample regions the carbon and nitrogen distribution was observed to be uniform and to correspond to the expected C/N ratio within experimental error.

## 7.6 Vibrational Spectroscopy

Vibrational spectroscopy is a valuable tool to identify the elementary molecular moieties constituting a material, irrespective of its semi-crystalline or amorphous character. The FTIR spectrum of the condensation product of melamine is displayed in Figure 7.7; the observed wavenumbers, together with a tentative band assignment, are given in Table 7.3.

The following instructive features of the spectrum need to be emphasized:

- The IR spectrum is clearly indicative of an at least partially ordered material owing to its well-resolved band structure and the absence of high absorptive background at lower wavenumbers typical of amorphous materials.
- The medium intense, sharp band at  $\approx 810 \text{ cm}^{-1}$  suggests the material to consist of triazine or heptazine building-blocks, while a clear assignment to either of the two is not possible.
- The prominent absorption bands at  $1203$  and  $1234 \text{ cm}^{-1}$ , and possibly  $1313 \text{ cm}^{-1}$ , indicate the presence of C–N stretching and / or N–H bending vibrations, which have been shown to be characteristic of the C–NH–C unit in melam. Therefore, a similar structural motif, corresponding to either trigonal C–N(–C)–C (full condensation) or bridging C–NH–C units (partial condensation), can be inferred for the polymeric material.

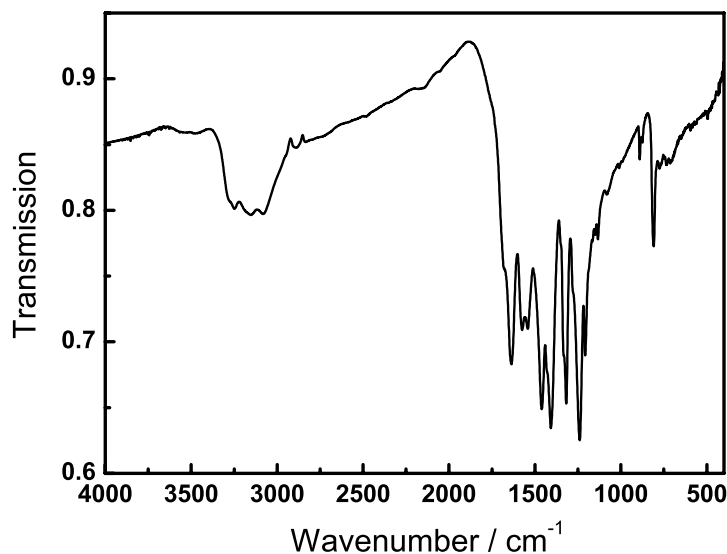


**Figure 7.7:** FTIR spectrum of the  $CN_xH_y$  polymer, recorded between  $4000$  and  $400\text{ cm}^{-1}$  as  $KBr$  pellet.

**Table 7.3:** Vibrational frequencies (in  $\text{cm}^{-1}$ ) of the high-temperature condensation product of melamine as observed by FTIR spectroscopy at RT ( $KBr$  pellet). Tentative assignments are given in the right column ( $\nu$  = stretching,  $\delta$  = in-plane deformation,  $\gamma$  = out-of-plane deformation,  $\rho$  = rocking,  $\omega$  = wagging; *vs*: very strong, *s*: strong, *ms*: medium strong, *w*: weak, *vw*: very weak, *b*: broad).

IR <sub>obs</sub>	Assignment [240]
3245, 3147, 3076 (ms, <i>b</i> )	$\nu_{s/as}(\text{NH}_2)$ , $\nu(\text{NH})$
1633 ( <i>s</i> )	$\delta(\text{NH}_2)$
1572, 1534 (ms)	$\nu(\text{N}=\text{C})$
1457, 1401 ( <i>s</i> )	$\nu(\text{N}=\text{C})$
1313 ( <i>s</i> )	$\delta(\text{NH})$ , $\nu(\text{C}-\text{N})$
1234 ( <i>vs</i> ), 1203 ( <i>s</i> )	$\nu(\text{C}-\text{N})$
1129, 1076 ( <i>w</i> )	$\rho(\text{NH}_2)$
1005 ( <i>vw</i> )	$\nu_{ring}$
887 ( <i>w</i> )	
810 ( <i>m</i> )	ring sextant bend
775 ( <i>w</i> )	$\omega(\text{NH})$
731, 712 ( <i>vw</i> )	$\gamma(\text{ring})$
646, 592, 493 ( <i>vw</i> )	$\omega(\text{NH}_2)$ , $\delta(\text{CN}_{ring})$

- Medium strong bands are found at  $1572$  and  $1534\text{ cm}^{-1}$ , which are not usually observed in heptazine-based materials, but are characteristic of many triazine-based ones [463, 501]. This feature has been observed in several carbon nitride materials with an assumed heptazine-based structure [81, 84, 127, 517]. However, as no unambiguous assignment of the bands can be made unless theoretical calculations have been carried out, far-reaching conclusions based on this fact cannot be drawn.
- Absorption found in the N–H stretching region between  $3250$  and  $3070\text{ cm}^{-1}$  strongly suggests the presence of NH and / or  $\text{NH}_2$  groups. O–H vibrations due to water adsorbed on the surface of the material would be expected at higher wavenumbers. As the presumed  $\nu(\text{N–H})$  bands are of medium intensity, the N–H moieties are most likely integral parts of the structure.

## 7.7 X-ray Powder Diffraction

In accordance with literature data [42, 73, 124, 127, 128, 240, 453, 510, 513, 514, 523], the X-ray diffraction pattern is indicative of a layered substance with an interlayer spacing of  $3.19\text{ \AA}$ . The powder pattern resembles that of graphite, which has an interlayer spacing slightly larger than that of the carbon nitride material ( $3.33\text{ \AA}$ ) as shown in Figure 7.8.

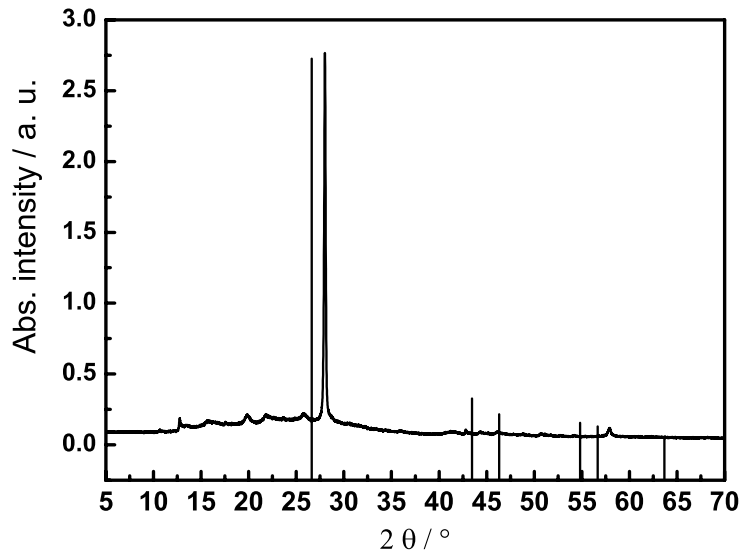


**Figure 7.8:** Experimental X-ray powder pattern ( $\text{Cu}-\text{K}_{\alpha 1}$  radiation) of the  $\text{CN}_x\text{H}_y$  polymer (continuous line) and simulation for graphite (bars). The broad and low intensity  $h\bar{k}0$  reflections indicate 2D planar defects; the interlayer distance (sharp 001 reflection) amounts to  $3.19\text{ \AA}$ .

Remarkably, the 001 reflection (for assignment see section 7.9 on page 303), which is commonly indexed as 002 by analogy with graphite, is very pronounced and sharp, whereas all  $hk0$  and  $h0l$  reflections – if present at all – are extremely weak and significantly broadened. In addition, asymmetric shapes of the reflections (“tailing” towards higher  $2\theta$  values, as seen for the low-angle reflection at  $2\theta \approx 12.6^\circ$ ), are visible. These features may be indicative of diffuse scattering with a modulated continuous intensity distribution along  $\mathbf{c}^*$  (cf. “streaking”, section 7.9 on page 303). Therefore, a pronounced 2D planar disorder has to be inferred, yielding X-ray powder patterns with relatively sharp base peaks and broad, asymmetric “bands” resulting from two-dimensional scattering by single layers. Three-dimensional peaks ( $h, k, l \neq 0$ ) are missing, their positions being located on the “tail” of the  $hk$ -bands [528], whereas the interlayer distance is well-defined. In addition, the absence of splitting of the 001 (002) reflection suggests *planar* layers, as corrugation of the layers would lead to the observation of additional  $hkl$  reflections in the region around  $2\theta = 27 - 30^\circ$ .<sup>3</sup>

## 7.8 Solid-State NMR Spectroscopy

*The experiments presented in the following section have been carried out in cooperation with Lena Seyfarth and Prof. J. Senker (both University of Bayreuth) and will also be published as part of the PhD thesis by L. Seyfarth.*

### 7.8.1 CP- and CPPI-MAS Experiments

Solid-state NMR spectroscopy is a valuable tool for probing the structure of semi-crystalline or amorphous materials on local and intermediate length scales, as it is not dependent on the long-range order in contrast to diffraction techniques.

The low sensitivity of the  $^{15}N$  nucleus as well as the expected broad line shapes due to the partial disorder would lead to insufficient signal intensity, thereby impeding experiments other than those based on standard CP-MAS techniques. Thus, a  $^{15}N$ -enriched material was synthesized according to a procedure described in section 10.1 on page 355 as established by Jürgens [82, 240]. Mass spectrometry of the  $^{15}N$ -labelled melamine allows for the estimation of the degree of  $^{15}N$  enrichment to be  $\approx 20 - 30 \%$ , corresponding to an average of 1 – 2  $^{15}N$  nuclei per molecule of melamine.<sup>4</sup> According to the CP spectra of  $^{15}N$ -melamine, a

<sup>3</sup>The appearance of a multitude of additional  $hkl$  reflections in case of corrugation of the layers has been verified by simulation and indexing of the powder patterns of non-planar variants of melon (see section 7.9 on page 303). Note however, that a uniform, periodic undulation of the layers with a unique interlayer spacing would presumably not lead to a splitting of the 001 reflection.

<sup>4</sup>Note that the difference of the signal intensities for the CP spectra of  $^{15}N$ -melamine and “natural” melamine suggests a degree of enrichment far higher than that obtained from mass spectrometry ( $\approx 78 - 79 \%$ );

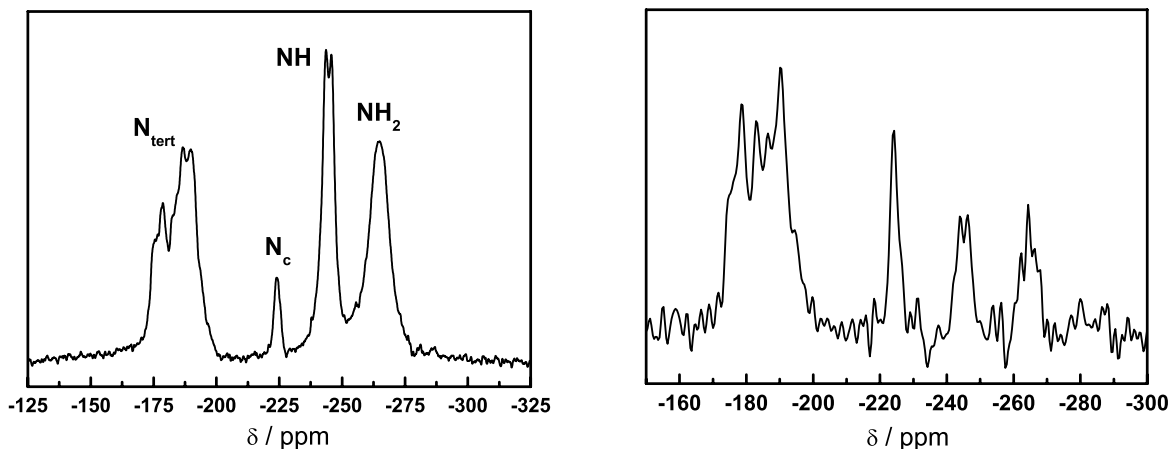


**Figure 7.9:** Left:  $^{15}\text{N}$  CP-MAS spectrum of the C/N/H-graphite; the signal assignments are based on the CPPI experiment and typical chemical shift data; “N<sub>c</sub>” relates to the central nitrogen atom of the heptazine ring, which this tertiary nitrogen signal is tentatively associated with (recycle delay: 20 s;  $\tau_c$ : 10 ms; spinning frequency: 7 kHz). Right:  $^{15}\text{N}$  direct excitation spectrum using a recycle delay of 28800 s (= 8 h) as estimated from a  $^{15}\text{N}$  T1 measurement to ensure a total recovery of the magnetization. Number of scans: 16; spinning frequency: 9 kHz.

largely uniform enrichment can be assumed, i. e. no significant intensity variations for the tertiary and amino nitrogen signals are visible when comparing the spectra of  $^{15}\text{N}$ -enriched and “natural” melamine.

The  $^{15}\text{N}$  CP-MAS spectrum of the C/N/H-graphite is displayed in Figure 7.9 (left). The comparatively good resolution is diagnostic of a semi-crystalline rather than an amorphous material.

For a reliable signal assignment as indicated in Figure 7.9, a CPPI (cross-polarization with polarization inversion) experiment was carried out. By quantitatively evaluating the characteristic time dependence of the polarization inversion dynamics of the different  $^{15}\text{N}$  nuclei, the number of protons covalently bonded to the latter can be ascertained. As outlined in Figure 7.10, three types of signals can be distinguished: The signals between – 177 and – 195 ppm, as well as the resonance at – 225 ppm exhibit a moderate intensity loss, the continuous, slow decrease of the polarization being characteristic of tertiary nitrogen atoms. In contrast, the polarization of the signals at – 245 and – 265 ppm follows a two-step process induced by the covalently bonded protons. The intensity at the cross-over between the dipolar and spin-diffusion regime is given by  $[2 / (n + 1)] - 1$  ( $n = 0, 1, 2$ ), thereby allowing for the differentiation between NH (crossover at 0) and NH<sub>2</sub> (crossover at – 1/3) nitrogen nuclei (cf. section 3.3.3 on page 63) [82, 194].

a possible explanation for this overestimation may be the shorter relaxation times for the  $^{15}\text{N}$ -enriched material. In addition, the *signal heights* were used directly instead of their *integrated areas*; thus, smaller lineshapes of the  $^{15}\text{N}$ -labelled material may significantly enhance the observed intensities.

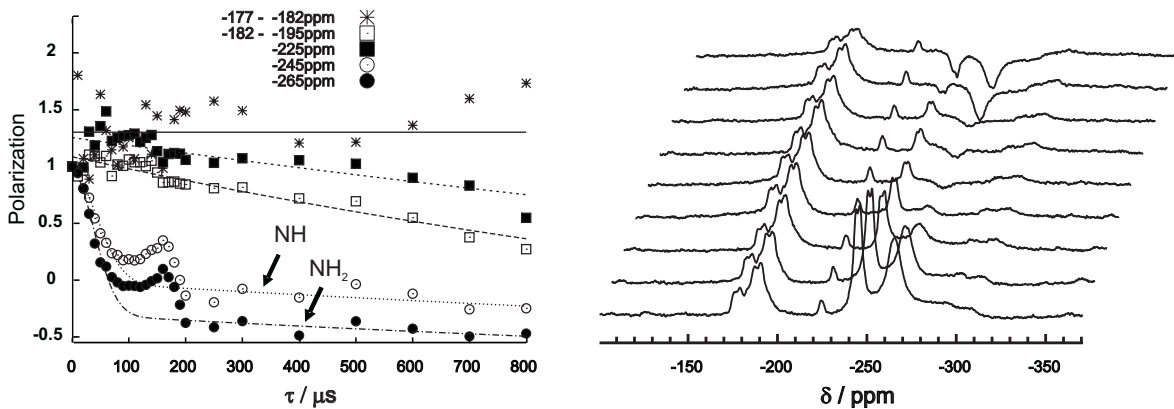


**Figure 7.10:** Left: Curve fits of the  $^{15}\text{N}$  CPPI experiment. The polarization of the  $^{15}\text{N}$  nuclei is given as a function of inversion time  $\tau_i$ . Right: CPPI spectrum of the C/N/H-graphite. The polarization inversion behavior was monitored by varying the inversion time from 0.2 to 800  $\mu\text{s}$  (front to back). Contact time  $\tau_c$ : 2 ms, spinning frequency  $\nu_{\text{rot}}$ : 6 kHz.

Therefore, an unambiguous assignment of all signals according to the proton environment of the  $^{15}\text{N}$  nuclei is feasible as outlined in Figure 7.9. Notably, apart from tertiary nitrogen nuclei expected for a fully condensed graphitic carbon nitride network, NH and NH<sub>2</sub> groups are also present, which clearly suggests the formation of a hydrogen-containing and, hence, only partially condensed C/N/H-network. Furthermore, the isolated tertiary nitrogen resonance located at  $-225$  ppm is reminiscent of the central nitrogen of the heptazine core, as it exhibits an up-field shift as compared to the “outer” nitrogen nuclei of the ring in essentially all heptazine-based compounds studied so far [474, 529]. For example, this nitrogen resonance is observed at  $-234.2$  ppm for melem [82, 240]. Thus, the above findings furnish the first significant indication of the heptazine-based nature of the graphitic C/N/H material and simultaneously suggest that a significant portion of structurally integrated hydrogen is present. In order to quantitatively evaluate the relative  $^{15}\text{N}$  signal intensities and, hence, to draw conclusions on the degree of condensation of the presumed heptazine cores, a  $^{15}\text{N}$  experiment using direct excitation of the  $^{15}\text{N}$  nuclei was carried out.<sup>5</sup>

Owing to the very long relaxation time of the  $^{15}\text{N}$  nuclei, a recycle delay between successive scans of 8 h had to be applied in order to ensure total magnetization recovery before each scan. Comparatively long relaxation times are diagnostic of well-ordered materials and are typically not observed for amorphous polymeric compounds. Due to the isotopic enrichment of melon, 16 scans were sufficient to acquire a spectrum with a reasonable signal-to-noise ratio. As depicted in Figure 7.9 (right), the signal intensities show significant variations as compared to

<sup>5</sup> By circumventing the magnetization transfer from the abundant protons to the  $^{15}\text{N}$  nuclei, the signal intensity of the latter is no more dependent on the number of protons in spatial proximity. Therefore, the signal intensity is directly proportional to the number of the respective types of  $^{15}\text{N}$  nuclei.

the CP-MAS spectrum (left). According to the expectations, the tertiary nitrogen resonances have gained intensity at the expense of the protonated nitrogen signals. A quantitative fit of the relative intensities indicates a ratio of the four signal groups  $N_{tert} : N_c : NH : NH_2$  of about 7:1:1:1. In particular, the equal intensities of  $N_c$ ,  $NH$ , and  $NH_2$  suggest a degree of condensation corresponding to that expected for melon (6:1:1:1, cf. **1a** + **1b**, Fig. 7.1 on page 282).

A “screening” for partially condensed, solely heptazine- or triazine-based structures, which would exactly reproduce the experimentally observed signal ratio and account for the somewhat higher intensity of the  $N_{tert}$  signal, did not yield satisfactory results. Non-fully condensed, mixed heptazine / triazine variants furnished structure models which in part were somewhat closer to the experimental ratio. An important argument against such structures is, however, the small number of nitrogen resonances observed in the CP-MAS spectrum. Since atom connectivities and, hence, local structural motifs are dominating the chemical shift of the nuclei, this missing spread in chemical shift values renders a structure composed of only one single ring system by far more likely.

In addition, DFT calculations of the chemical shift parameters of fully condensed triazine- and heptazine-based  $C_3N_4$  systems<sup>6</sup> suggest that the chemical shift range expected for triazine-based structures would spread out way downfield as compared to the observed data, for both planar and corrugated geometries. This adds to the above evidence that the C/N/H-graphite is composed of heptazine rather than triazine building blocks. Accordingly, the somewhat higher intensity observed for  $N_{tert}$  may likely result from the admixture of minor, heptazine-based side-phases exhibiting a slightly higher degree of condensation (cf. for instance structure **1c**, Fig. 7.1 on page 282).

Figure 7.11 displays the  $^1H$  MAS (left) and  $^{13}C$  CP-MAS spectra (right) of the product. The proton spectrum exhibits one signal peaking at  $\approx 9$  ppm, which spreads out over roughly 10 ppm; in addition, a shoulder (indicated by an arrow) is distinguishable at lower field ( $\approx 11$  ppm). This low-field resonance may be assigned to the  $NH_2$  groups owing to their broadness, whereas the relatively sharp resonance at 9 ppm may be appendant to the  $NH$  moieties. However, an ultimate assignment can only be given based on correlation spectroscopy, such as a HETCOR experiment.

As demonstrated in Figure 7.11 (right), the  $^{13}C$  CP-MAS spectrum of the product shows remarkable similarity with that of melem. In detail, two signal groups are found with peak maxima at  $\approx 164$  ppm and 157 ppm. In melem, two groups of carbon resonances are observed at 164.3 / 166.4 ppm and 155.1 / 156.0 ppm, respectively [82, 240]. The spectra have

<sup>6</sup> A more detailed discussion of these results will be subject of the PhD thesis by J. Sehnert, University of Bayreuth.

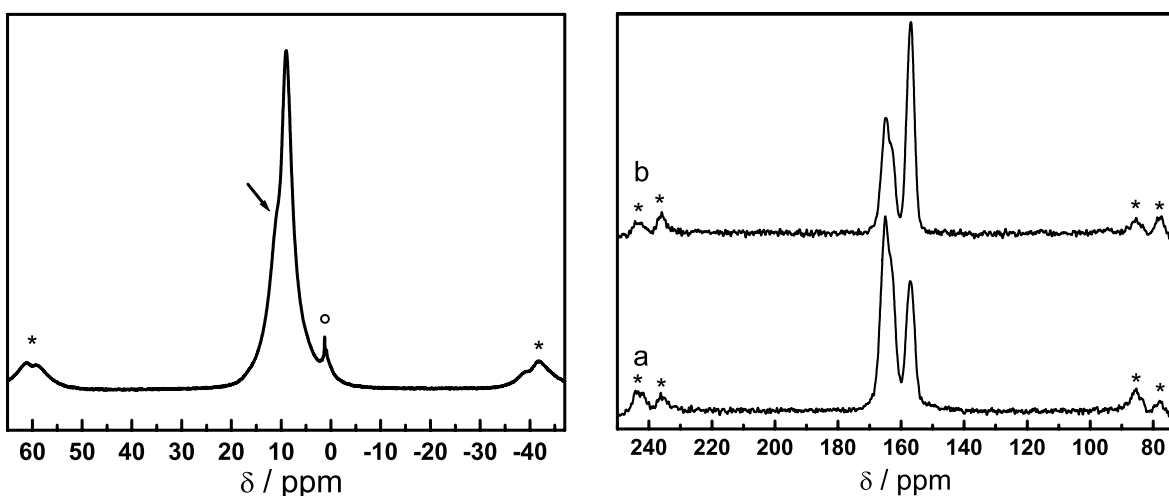


**Figure 7.11:** Left:  $^1\text{H}$  MAS spectrum of the C/N/H-graphite (2.5 mm rotor; recycle delay: 10 s, spinning frequency: 25 kHz). The observed low-field shoulder is indicated by an arrow;  $\circ$  denotes an impurity. Right:  $^{13}\text{C}$  CP-MAS spectra recorded with different contact times  $\tau_c$ : (a): 2 ms; (b): 15 ms (recycle delay: 10 s; spinning frequency: 10 kHz.) Spinning side-bands are marked by asterisks.

been recorded using two different contact times  $\tau_c$  in order to differentiate between carbon nuclei situated adjacent to or more distant from protonated nitrogen atoms. According to the distance dependence of the dipolar magnetization transfer under CP conditions, a more rapid magnetization build-up would be expected for carbon nuclei in spatial proximity of hydrogen atoms. For shorter contact times (spectrum (a)) the signals at 163 – 165 ppm exhibit higher intensity as compared to (b), the reverse situation holding for the resonance at 157 ppm. Thus, the  $^{13}\text{C}$  nuclei associated with the low-field resonance are located closer to hydrogen atoms ( $\text{CN}_2(\text{NH}_x)$  moieties) than are those attributable to the signal at 157 ppm ( $\text{CN}_3$  moieties).

This observation is in agreement with the results obtained for melem, where the low-field resonances (164 – 166 ppm) were assigned to the carbon positions adjacent to the amino groups. The signal assignments for the  $^{15}\text{N}$  and/or  $^{13}\text{C}$  spectra will further be discussed in the following section as well as in section 7.10 on page 314.

The line width observed in the NMR spectra is slightly increased (120 – 170 Hz in the  $^{15}\text{N}$  spectra) as compared to typical line widths observed for crystalline molecular compounds ( $\approx 60$  Hz), which is likely to be diagnostic of slightly varying chemical environments of the heptazine nuclei, depending on the orientation of the adjacent layers as determined by the local stacking sequence. Similar effects may be induced by different polymer lengths, giving rise to slightly altered local magnetic fields at the sites of nuclei in the vicinity of chain or layer terminations. In contrast, line widths in the range of 500 – 1000 Hz would be expected for amorphous compounds.

### 7.8.1.1 *fp*-RFDR Experiment

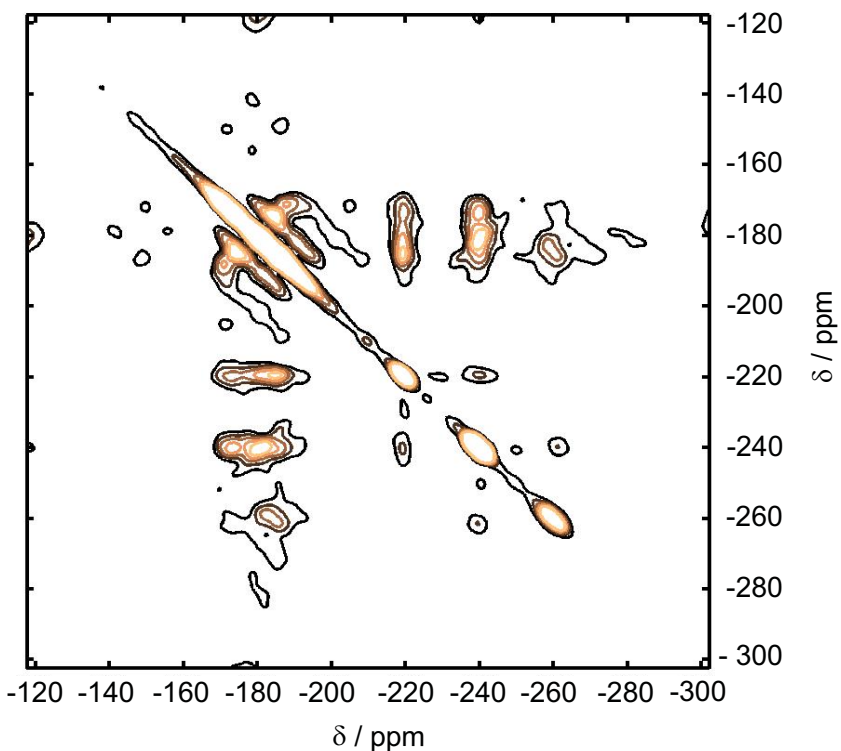


**Figure 7.12:**  $^{15}\text{N}$  2D-*fp*-RFDR experiment to probe the homonuclear dipolar coupling. The mixing time was 50 ms. Recycle delay: 5 s, contact time  $\tau_c$ : 20 ms, spinning frequency: 15 kHz.

A *finite pulse radio frequency driven dipolar recoupling* experiment (*fp*-RFDR) probes the homonuclear, through-space magnetization transfer between the  $^{15}\text{N}$  nuclei and can therefore be considered as a sensor for spatial proximities of these nuclei. The experiment is based on spin-diffusion (“flip-flop”) processes and can be classified as a zero-quantum experiment.

Two versions of the RFDR experiment have been carried out. A 2D spectrum was recorded with a mixing time of 50 ms as outlined in Figure 7.12. During the mixing period, magnetization transfer proceeds between all  $^{15}\text{N}$  nuclei which are sufficiently close to each other to allow for the dipolar coupling to operate. Exchange of magnetization and, thus, spatial proximity is indicated by off-diagonal signals, whereas the diagonal simply contains the information encoded in a 1D-CP spectrum. In Figure 7.12 cross-peaks are observed between the outer nitrogen resonances of the assumed heptazine ring ( $-176$  and  $-195$  ppm) and *all* other nitrogen nuclei. This is a strong indication for a homogeneous phase, in which all nitrogen nuclei exhibit close proximity on the length scale of a few nanometers. However, couplings between  $\text{N}_c$  and  $\text{NH}$ , as well as  $\text{NH}$  and  $\text{NH}_2$  are observed, whereas no off-diagonal peak due to the coupling between  $\text{N}_c$  and the amino nitrogen atoms is visible. As will be detailed below,

this absence is presumably due to low signal intensity; the spatial proximity of the central and amino nitrogen atoms could be established by means of a 1D-RFDR experiment with selective excitation of the amino nitrogen nuclei (see below).

In principle, a change of the mixing period  $\tau_m$  may allow for a qualitative evaluation of the relative distances between the  $^{15}\text{N}$  nuclei. However, this requires the realization of several time-consuming 2D experiments in order to reliably assess the relative time-dependence of the spin-diffusion processes. In order to avoid this inconvenience, a modified variant of the *fp*-RFDR experiment was carried out. To continuously monitor the magnetization build-up, a single  $^{15}\text{N}$  signal was excited selectively and the mixing time varied successively in small intervals. In the following, only the selective excitation of the  $\text{NH}_2$  nuclei will be discussed.<sup>7</sup>

Figure 7.14 outlines the 1D-RFDR spectra obtained for three mixing times ( $\tau_m = 1, 25$ , and 205 ms) corresponding to short, intermediate and long periods of magnetization transfer. Whereas for  $\tau_m = 1$  ms no magnetization transfer to the other nitrogen nuclei is visible, exchange commences at  $\tau_m = 25$  ms for the high-field part of the tertiary nitrogen signals, which is visible by the growing intensity of the latter.

Very weak signals can also be distinguished for the  $\text{N}_c$  and  $\text{NH}$  resonances. For long mixing times, all initial resonances are observable, which is again indicative of a dipolar exchange of magnetization among the  $\text{NH}_2$  nitrogen and *all* other  $^{15}\text{N}$  nuclei in the sample. This observation is confirmed by the build-up curves shown in Figures 7.15 and 7.13, which represent the increase of magnetization at the tertiary and  $\text{NH}$  nitrogen nuclei and the concomitant loss of signal intensity (magnetization “drain”) at the  $\text{NH}_2$  nitrogen atoms (left).

Build-up is fastest for the tertiary  $^{15}\text{N}$  nuclei from  $-195$  ppm to  $-187$  ppm. Thus, these represent the closest neighbors of the  $\text{NH}_2$  group. This finding is in agreement with the *ab initio*  $^{15}\text{N}$  chemical shift parameters calculated for the DFT optimized cell based on the structure solution from electron diffraction, as will be discussed in section 7.10 on page 314.

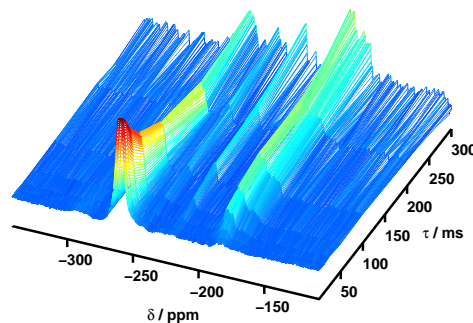


**Figure 7.13:** Contour plot of the 1D *fp*-RFDR experiments using selective excitation of the  $\text{NH}_2$  nitrogen nuclei. The 3D representation displays the succession of spectra recorded with increasing mixing times  $\tau_m$  (front to back).

<sup>7</sup>An analogous procedure was chosen for the  $\text{NH}$  nuclei, whereas a slightly different “filter” had to be applied in case of the central nitrogen resonance.

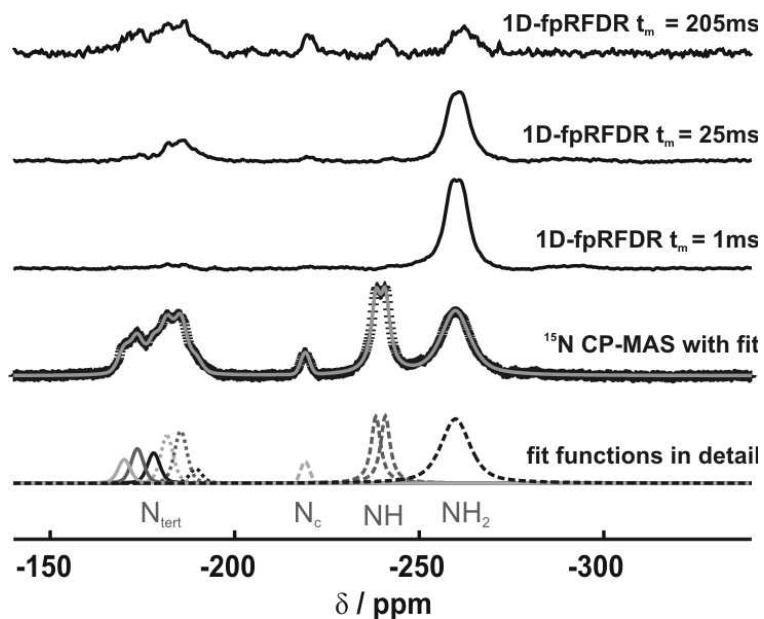


**Figure 7.14:**  $^{15}\text{N}$  spectrum of the C/N/H-graphite and the corresponding overall fit (gray line; 2<sup>nd</sup> spectrum from bottom). Fits of the individual resonances (bottom) and 1D-fp-RFDR for mixing times  $\tau_m = 1, 25, 205$  ms.

This exchange behavior strongly suggests homogeneity of the sample in a regime of at least 50 Å. Note that the co-existence of different domains with an extension of several nanometers cannot be excluded, but their constitution may essentially be limited to different stacking variants and possibly heptazine-based structural isomers, which do not give rise to additional signals in the 1D CP-MAS spectrum as outlined above. Thus, this experiment indicates that *all*  $^{15}\text{N}$  nuclei are in spatial neighborhood and no isolated, structurally distinct phases

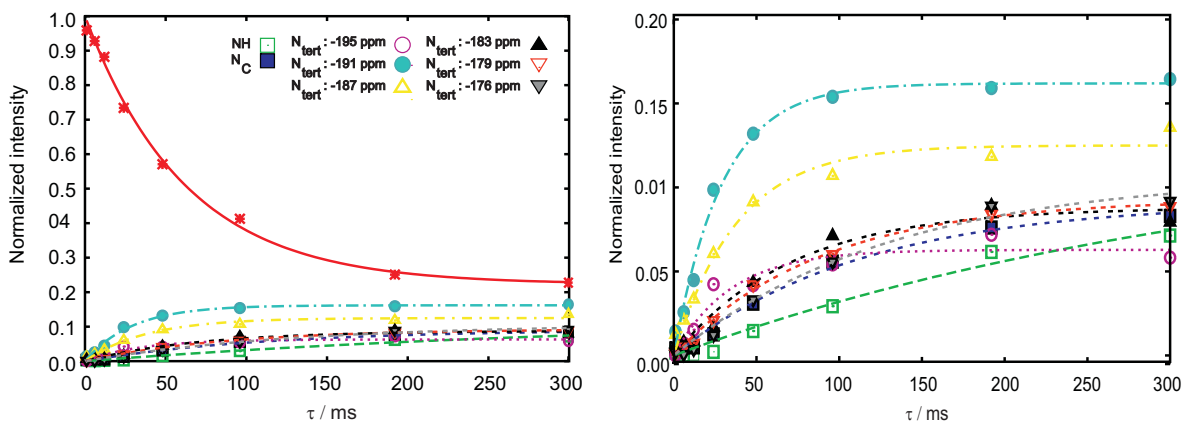


**Figure 7.15:**  $^{15}\text{N}$  fp-RFDR curves after selective excitation of the  $\text{NH}_2$  nuclei. Left: Plot of all magnetization transfer curves, including the magnetization loss of the  $\text{NH}_2$  nuclei. Right: Enlarged plot of the magnetization build-up at the tertiary and NH nitrogen atoms.

(in terms of the principal atom connectivity) are detectable by  $^{15}\text{N}$  NMR. Thus, in spite of different degrees of crystallinity observed by electron diffraction, the RFDR experiment, together with the 1D spectra, strongly suggests at least a *structural homogeneity* in terms of the local molecular motifs present in the sample.

## 7.9 Electron Diffraction

*Electron diffraction and TEM measurements, including data evaluation, have been carried out by Dr. M. Döblinger, University of Munich.*

### 7.9.1 Phenomenological Descripton

As compared to X-ray diffraction, electron diffraction (ED) provides structural insights into nanometer-sized materials. The dimensions of the C/N/H graphite can be estimated by the size of the crystallites viewed on a carbon coated copper grid in the microscopy (TEM) mode (Fig. 7.16).

In the diffraction mode, the presence of domains (Fig. 7.17) exhibiting various levels of crystallinity is evident, which typically show a “corona-shaped” diffuse background.<sup>8</sup> A noticeable feature common to most diffraction patterns is the pseudo-hexagonal intensity distribution, which is reminiscent of the diffraction pattern of graphite (cf. Fig. 7.19 on page 305, right).

<sup>8</sup>The background may also be due to amorphous cover layers and amorphous domains in general.

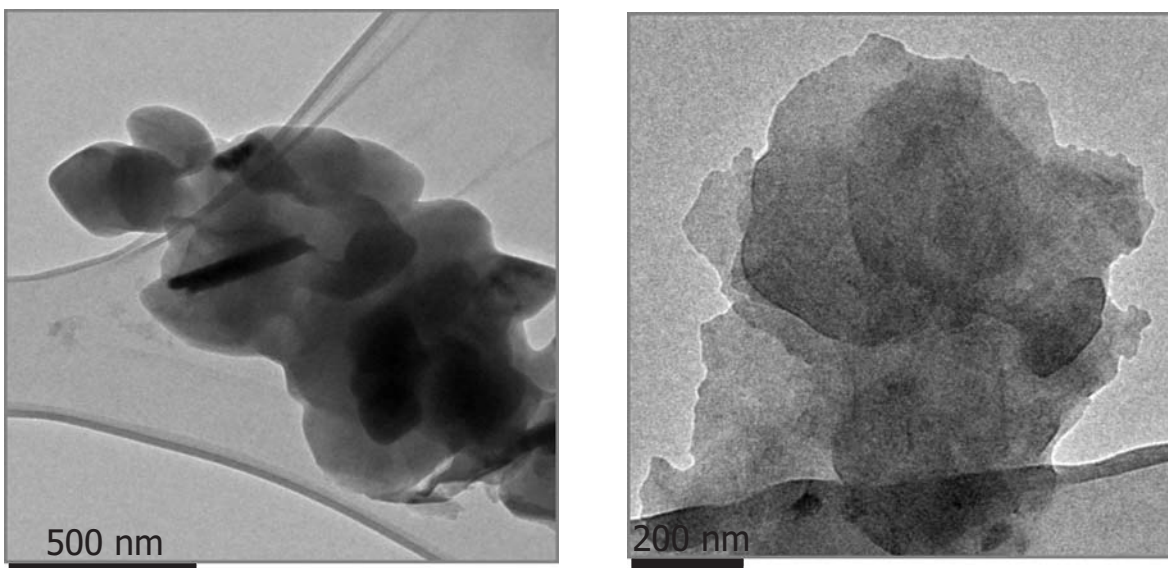


**Figure 7.16:** TEM images of C/N/H graphite after sample preparation for electron diffraction (copper grid), showing the plate-like nano- and microcrystals.

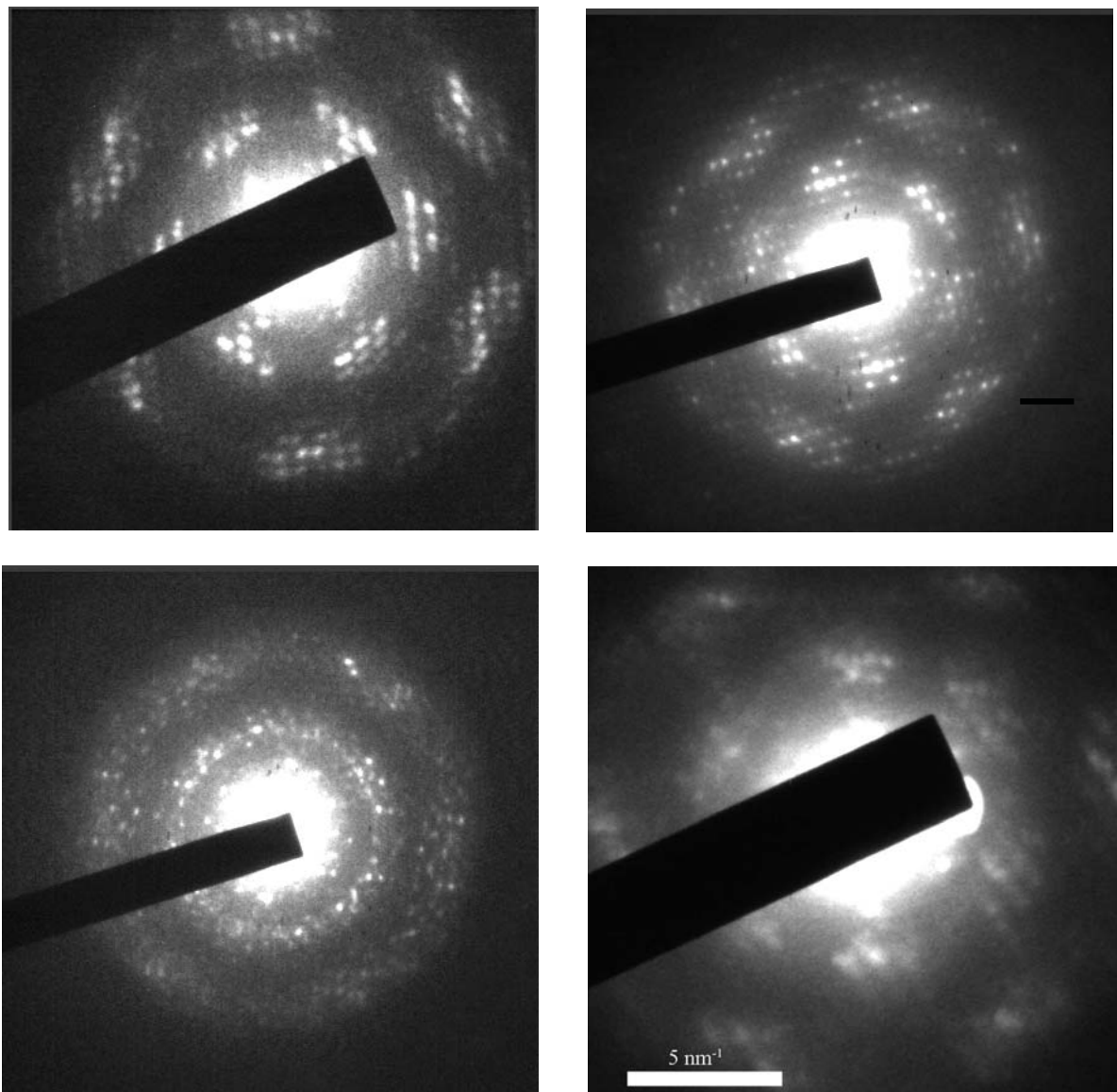


**Figure 7.17:** Selected area electron diffraction patterns along zone axis [001] of C/N/H graphite. All patterns exhibit different degrees of diffuse scattering and are indicative of partial disorder and/or thick sample sizes.

In agreement with the plate-like shape of the crystallites (Fig. 7.16), the preferred orientation is such that almost all diffraction patterns are taken along the [001] zone axis. Owing to the limitations imposed by the single tilt holder ( $\pm 30^\circ$ ) and the preferred orientation of the crystallites, other zone axes are hardly accessible and, thus, essentially restrict the description of reciprocal space to the  $hk0$  plane. Nevertheless, two examples of diffraction patterns obtained from zone axes perpendicular to  $\mathbf{c}^*$  are displayed in Figure 7.18.

In agreement with the X-ray powder patterns, varying degrees of “streaking” along  $\mathbf{c}^*$  are observable, resulting from planar defects or even turbostratic stacking disorder. Note that the

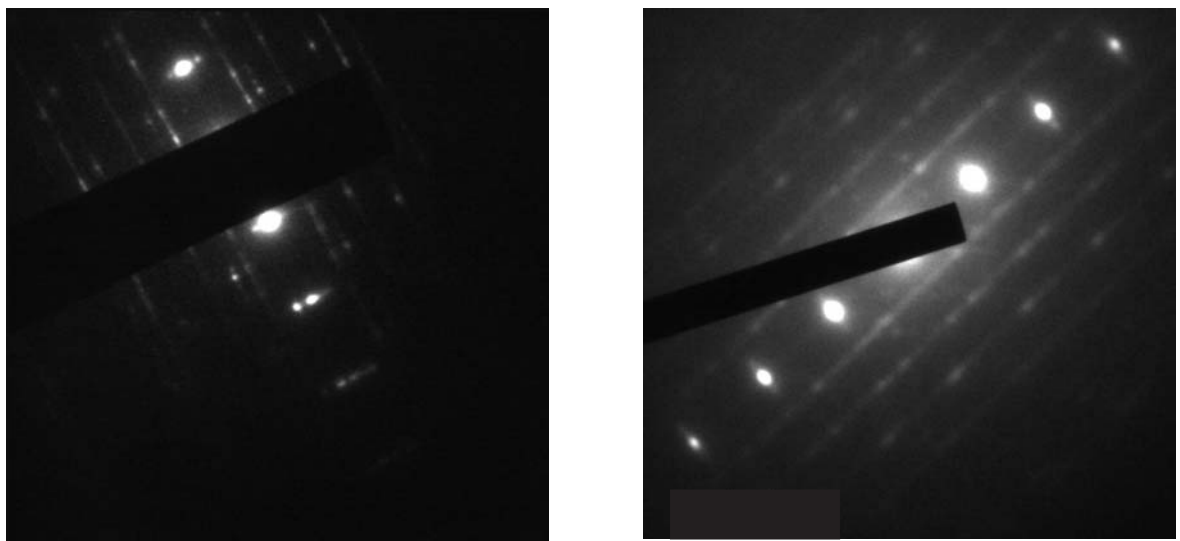


**Figure 7.18:** Electron diffraction patterns viewed perpendicular  $c^*$ . Whereas the  $00l$  reflections are clearly visible, “diffuse bars” are observed parallel to  $c^*$  with a non-discrete intensity distribution (“streaking”).

diffraction patterns recorded along [001] typically do not exhibit reflections which are smeared out in a cone-like manner so that at its extreme isotropic “diffraction rings” would be formed. Therefore, rotational planar defects are less likely than translational defects due to a lateral displacement of the layers with respect to each other.

Although many disordered domains are found in the sample (Fig. 7.17), SAED patterns of

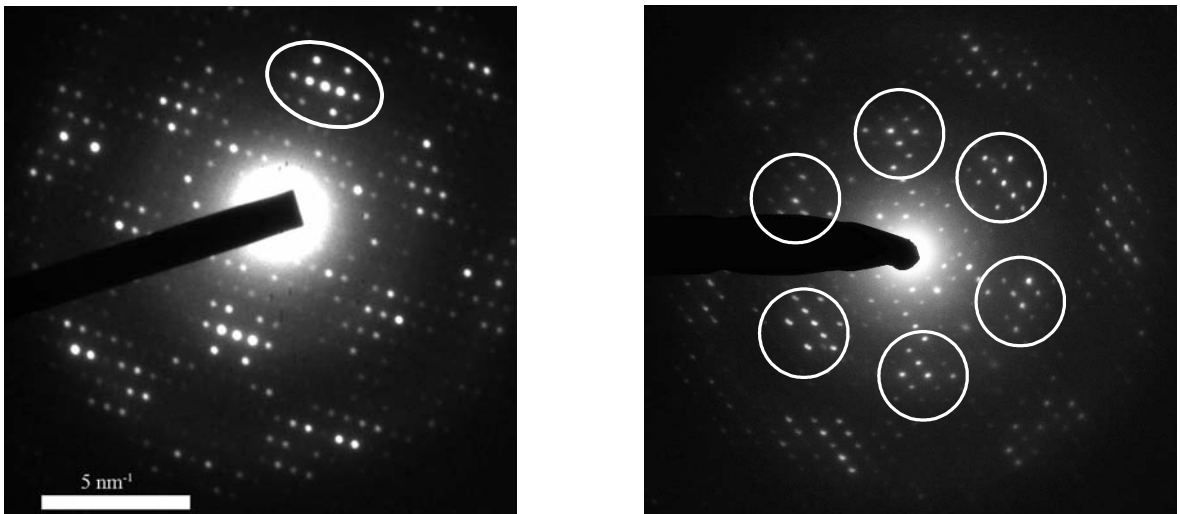


**Figure 7.19:** Electron diffraction patterns along zone axis [001]. Left: Recorded under “static” conditions. The “double cross” reflection motif, also found – in a distorted form – in the reflection patterns of a presumed side phase (see below), is highlighted by a white ellipsoid. Right: Recorded using the precession technique. The pseudo-hexagonal intensity distribution is indicated by white circles. Merging the reflection groups contained in the circles (shown exemplarily; the same applies for all reflection groups) into one single spot would generate a diffraction image similar to that of graphite.

almost perfectly crystalline domains (at least in two dimensions) were obtained. As can be seen from Figure 7.19, the “pseudo-hexagonal” intensity distribution is visible, which not only with respect to its symmetry, but also regarding the encoded distance information resembles that of graphite.

Therefore, the graphite-like character of this compound, which has led to the generally accepted assumption that these materials are related to graphitic carbon nitride, can in principle be confirmed. However, despite this resemblance, the  $hk0$  patterns can be indexed on a *rectangular* mesh with cell parameters  $a = 16.7 \text{ \AA}$ ,  $b = 12.4 \text{ \AA}$ . Note that these values, when taking into account a layer distance of  $3.2 \text{ \AA}$ , are similar to those found by *Komatsu* with a halved  $a$  lattice parameter (in the direction of the layer stacking) as outlined above (cf. section 7.1) [83].

### 7.9.2 Structure Elucidation

Taking advantage of the small sample thickness, the light atom structure and large unit cell, all of which result in small structure factors or a minimum of dynamical effects, a structure solution in projection was attempted. To this end, the kinematical approximation  $I_{hkl} \propto |F_{hkl}|^2$  was used. To quantify all strong  $hk0$  reflections, intensities of two  $hk0$  diffraction patterns were merged and extracted using the ELD program package [143, 144], yielding a dataset of 208 independent reflections. Symmetry averaging and merging of the patterns resulted in an overall redundancy-independent merging  $R$ -factor of  $R_{\text{rim}} = 40.2\%$  [530].

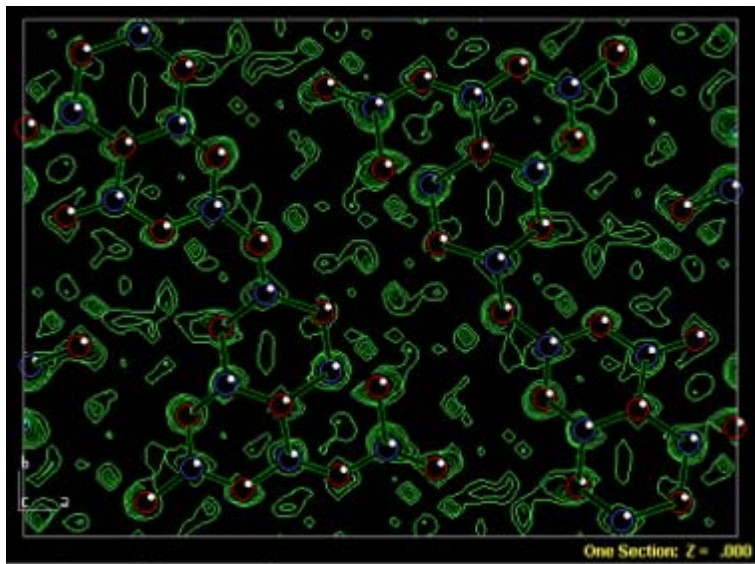


**Figure 7.20:** Projection of the electrostatic potential (green) obtained from  $hk0$  reflections (plane group  $p2gg$ ) as determined using the programm SIR-97. Carbon (blue) and nitrogen (red) atoms are differentiated by color, although for the structure solution only carbon atoms were used.

Table 7.4: Crystallographic data of melon.

Formula	C <sub>6</sub> N <sub>9</sub> H <sub>3</sub>
$M_w$ / g · mol <sup>-1</sup>	201
plane group	<i>p2gg</i>
instrument type	JEOL 2011
instrument details	single tilt holder, TVIPS CCD camera (F114)
incident radiation energy / kV	200
$d_{min}$ / Å	0.65
$a$ / Å	16.7 <sup>a</sup>
$b$ / Å	12.4 <sup>a</sup>
$Z$	4
symmetry-independent reflections	208
number of parameters	46
observations per parameter	4.5
$R1$	26.44 %
$wR(F^2)$	27.72 %
$R_{rim}$ <sup>b</sup>	40.2 %

<sup>a</sup> The error for determination of the lattice parameters from ED is estimated to be  $\approx 5\%$ .

<sup>b</sup> Defined as

$$\frac{\sum_{hkl} \sqrt{(N/(N-1))} \sum_i |I_i(hkl) - I_{av}(hkl)|}{\sum_{hkl} \sum_i I_i(hkl)},$$

where N is the redundancy of the reflection [530].

Evaluation of the observed absences in the base plane ( $h0$ :  $h = 2n+1$ ;  $0k$ :  $k = 2n+1$ ) strongly suggests glide lines to be present along  $a$  and  $b$ , yielding the plane group *p2gg*.

The structure was solved using space group *P2<sub>1</sub>2<sub>1</sub>2*, which corresponds to the plane group *p2gg* in (001)-projection. The most probable solution as found by SIR-97 [148] had a residual value of 20.06 %.<sup>9</sup> All carbon and nitrogen atoms were found with reasonable bond lengths and angles. The arrangement of the atoms reveals the structure to consist of *heptazine* units interlinked *via* N(-H) bridges, which are arranged in two strands in the planar cell as can be seen from the projected potential distribution displayed in Figure 7.20.

Although the heptazine core is evident, note that the potential map shows a number of residual peaks, whose intensity is comparable to or only lightly less than that associated with carbon and nitrogen atoms. These peaks are predominantly located halfway between the two adjacent strands. Therefore, one has to consider the possibility that these peaks partly reflect a non-eclipsed ABA... type layer stacking by which the electrostatic potential from adjacent layers is projected onto the 2D potential map. However, low data quality or a slight

<sup>9</sup> Atomic scattering factors for electrons were used as implemented in SIR-97 according to Jiang and Li [531].

**Table 7.5:** Fractional atomic coordinates for melon obtained upon structure solution in projection. The potential density at N8, which was tentatively attributed to the imino hydrogen atom, is not included in the list. The z-coordinates and site occupation factors are only included for clarity.

Atom	x	y	z	Occ.
C1	0.338	0.470	0	1
C2	0.216	0.795	0	1
C3	0.265	0.632	0	1
C4	0.128	0.649	0	1
C5	0.993	0.669	0	1
C6	0.069	0.820	0	1
N1	0.139	0.755	0	1
N2	0.081	0.933	0	1
N3	0.224	0.903	0	1
N4	0.269	0.733	0	1
N5	0.193	0.592	0	1
N6	0.058	0.619	0	1
N7	0.003	0.790	0	1
N8	0.328	0.566	0	1
N9	0.923	0.631	0	1

misalignment of the zone axis may also result in “artificial” residual peaks in the potential map. Nevertheless, it should be pointed out that although this lateral shift of the layers may easily result from the weak interlayer forces, the observed projection does not allow for a layer sequence other than AAA... A more comprehensive discussion of the third dimension, which cannot be provided based on ED data, is postponed to sections 7.10 on page 314 and 7.11 on page 320.

Upon structure refinement (208 reflections, 46 parameters),  $R1$  was 26.44 % ( $wR2$  27.72 %). The reflection intensities are probably too strongly affected by dynamical diffraction and planar defects to obtain better residuals. Note however, that least-squares refinement is unusual in the context of electron crystallography because of the sparsity of the measured intensity data set and the problems of systematic errors due to multiple dynamical scattering [532]. The residuals obtained in the present study are nevertheless found in the usual range reported for structure solutions and refinements by ED [532–536]. In principle, it is still possible to solve a structure if the strong reflections remain sufficiently strong to find phase relationships using *direct methods* [534].

The reflection intensities of  $hk0$  diffraction patterns exhibit considerable variations. Apart from dynamical contributions and sample misalignment, different portions of planar defects are most likely the main cause for this behavior.

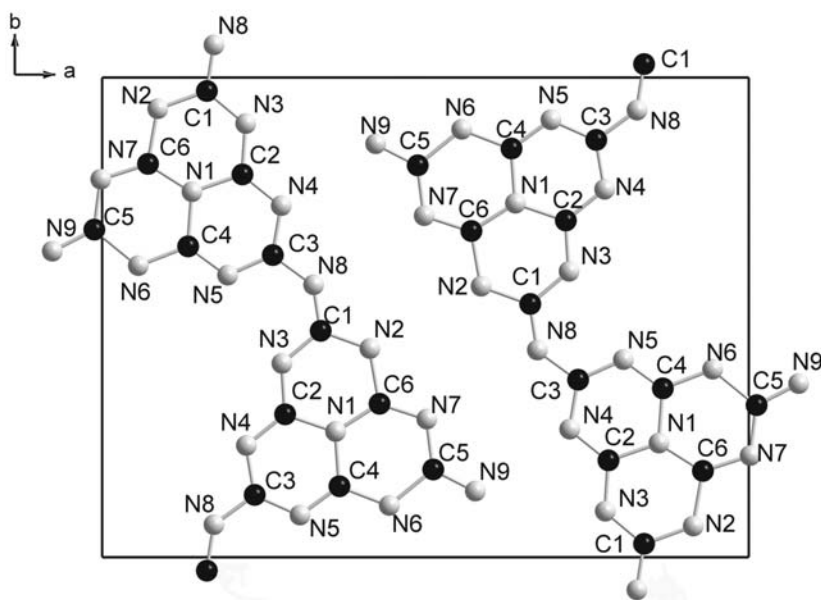


**Figure 7.21:** Labelling scheme of the atoms located in the unit cell of melon based on the structure refinement (gray: nitrogen; black: carbon; the single hydrogen atom found by ED is omitted for clarity).

**Table 7.6:** Fractional atomic coordinates and isotropic thermal displacement parameters for melon as obtained after structure refinement using SIR-97. Standard deviations in brackets<sup>a</sup>

Atom	x	y	z	$U_{iso}$
C1	0.338(2)	0.472(3)	0	0.001
C2	0.217(2)	0.798(3)	0	0.001
C3	0.264(2)	0.630(3)	0	0.002
C4	0.133(2)	0.648(3)	0	0.001
C5	0.988(2)	0.683(3)	0	0.001
C6	0.071(2)	0.820(3)	0	0.001
N1	0.139(2)	0.762(3)	0	0.011
N2	0.086(2)	0.935(2)	0	0.001
N3	0.222(2)	0.904(3)	0	0.022
N4	0.277(2)	0.733(2)	0	0.001
N5	0.194(2)	0.588(2)	0	0.001
N6	0.056(2)	0.608(2)	0	0.001
N7	0.998(2)	0.788(2)	0	0.001
N8	0.327(2)	0.568(2)	0	0.001
N9	0.923(2)	0.638(3)	0	0.017

<sup>a</sup> Note that the atomic parameters cannot be considered to be more reliable than those obtained after initial structure solution. The large variations in the  $U_{iso}$  values indicate that the data are not good enough to allow for proper refinement of these parameters.

X-ray powder diffraction, theoretical calculations (see section 7.10 on page 314) and chemical considerations (planar heptazine cores and amide / imide moieties) [42, 66, 73, 128, 510, 513, 514] indicate planarity of the layers. The maximum symmetry of the structure in the hypothetical 3D case of eclipsed layers is given by space group *Pbam*. However, by comparing the results with familiar principles associated with  $\pi$ -stacking interactions [537, 538] and theoretical calculations, a lateral displacement of adjacent layers seems to be more likely. Some details of the structure solution are given in Table 7.4, atomic coordinates, bond lengths and angles as obtained from the structure refinement are listed in Tables 7.6 and 7.7. For comparison, the atomic coordinates obtained from the initial structure solution are summarized in Table 7.5. The atomic numbering scheme can be taken from Figure 7.21.

To countercheck the consistency of the obtained structure solution, electron diffraction patterns based on the above structural parameters were simulated using the program package VEC [146]. The simulation of the  $hk0$  plane is shown in Figure 7.22, together with the experimental patterns used for structure solution after merging equivalent reflection intensities.

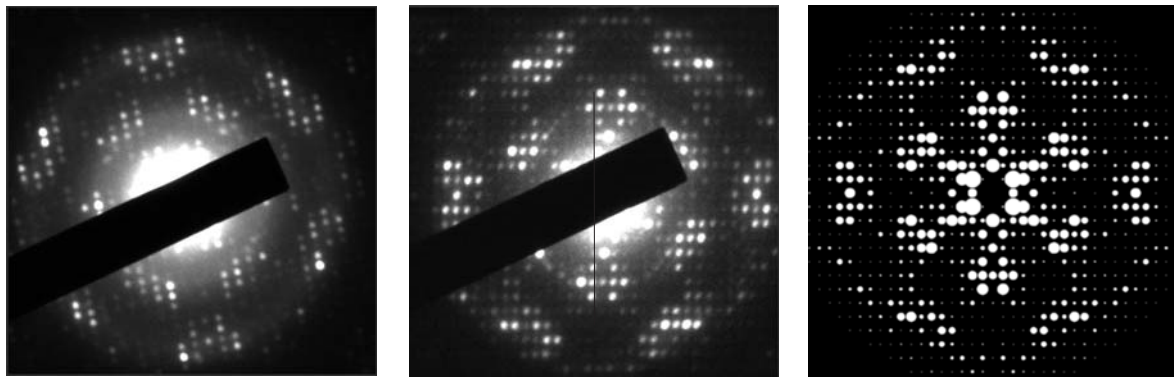


**Figure 7.22:** Experimental (left, middle)  $hk0$  diffraction patterns, from which the structure solution in projection was accomplished after merging the respective intensities; right: simulation of the electron diffraction pattern of the  $0^{\text{th}}$  layer based on the proposed structural model, assuming ideal kinematical scattering of electrons.

The principal agreement of the patterns is evident, although the intensity distribution of the experimental patterns does not entirely fulfill the requirements imposed by the symmetry of the plane group. Note however, that the *mm2* symmetry of the diffraction patterns recorded using the precession technique is significantly less violated as compared to those obtained under conventional “static” conditions. Therefore, the projected *p2gg* symmetry is likely to be valid at least in special cases, and will further be used as working hypothesis when discussing implications for the 3D arrangement of the layers (cf. section 7.11 on page 320). To verify the reproducibility of the structure solution, intensities were extracted from a  $hk0$  precession pattern. Owing to its robustness with respect to sample misalignment and the

minimization of dynamical effects, the data quality is likely to be superior to that achieved by the conventional experimental set-up. Accordingly,  $R_{\text{rim}}$  (cf. Table 7.4 on page 307) was determined to be 20 %.

As a result, the structure could again successfully be solved, the final residual value of the most probable solution being 19.5 %.<sup>10</sup> The solution was accomplished in space group  $Pbam$  and was then “generalized” by using the subgroup  $P2_1/a$ , which essentially yielded the same results and  $R$  values. According to the chosen cell setting,  $\beta$  angles  $\neq 90$  ( $\approx 92 - 115^\circ$ ) were introduced, corresponding to a lateral shift of the layers along the  $a$ -axis. Note that a moderate layer offset along the  $b$ -axis – after appropriately adjusting the cell-setting – will have the same (negligible) effect on the structure solution. This flexibility in the choice of the layer offset should be borne in mind when discussing the 3D structure of melon.

The structure refinement was rather inaccurate in that it afforded residuals  $R1$  and  $wR2$  on the order of 34 – 35 %. These high values are most probably associated with the comparatively large sample thickness as indicated by strong diffuse scattering, which gives rise to stronger dynamical effects. Figure 7.23 presents the diffraction pattern based on which the structure solution was accomplished, together with the corresponding simulation for a layer offset of  $\beta = 115^\circ$ .

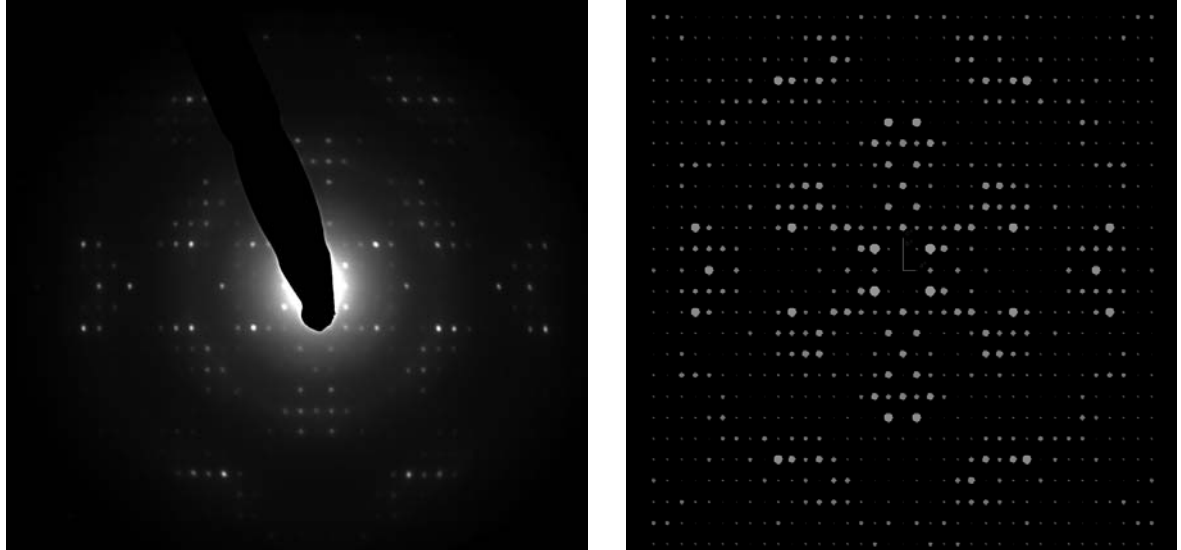


**Figure 7.23:** Experimental (left)  $hk0$  precession diffraction pattern, from which the structure solution in projection was accomplished in space group  $P2_1/a$  with an angle  $\beta$  of  $115^\circ$  (arbitrarily chosen). Right: Kinematical simulation of the  $0^{\text{th}}$  layer using the program *JSV108.lite* [145].

<sup>10</sup>184 independent reflections, no. of reflections / param.  $\approx 6$ ,  $d_{\text{min.}}: 0.78 \text{ \AA}$

### 7.9.3 Structure Description

The above data are one example of *ab initio* structure solution from electron diffraction data [532, 534–536, 539]. Melon represents a light atom structure which is well suited for ED investigations, as critical dynamical effects may reduce to a minimum. However, the structure solution might not be representative of the whole sample and cannot account for the 3D structural arrangement of the molecular building-blocks.

The 2D projection of the crystal structure is displayed in Figure 7.24. The layers are made up from infinite chains of “melem-monomers” condensed *via* N(H)-bridges, thereby forming a closely packed two-dimensional array. The heptazine strands are arranged in a zig-zag-type fashion, allowing for close N ··· N contacts of 3.1 – 3.4 Å between adjacent strands, which are bridged by medium strong hydrogen bonds between the ring-nitrogen atoms and the NH- and NH<sub>2</sub>-groups, respectively. Although the array of heptazine strands may be additionally

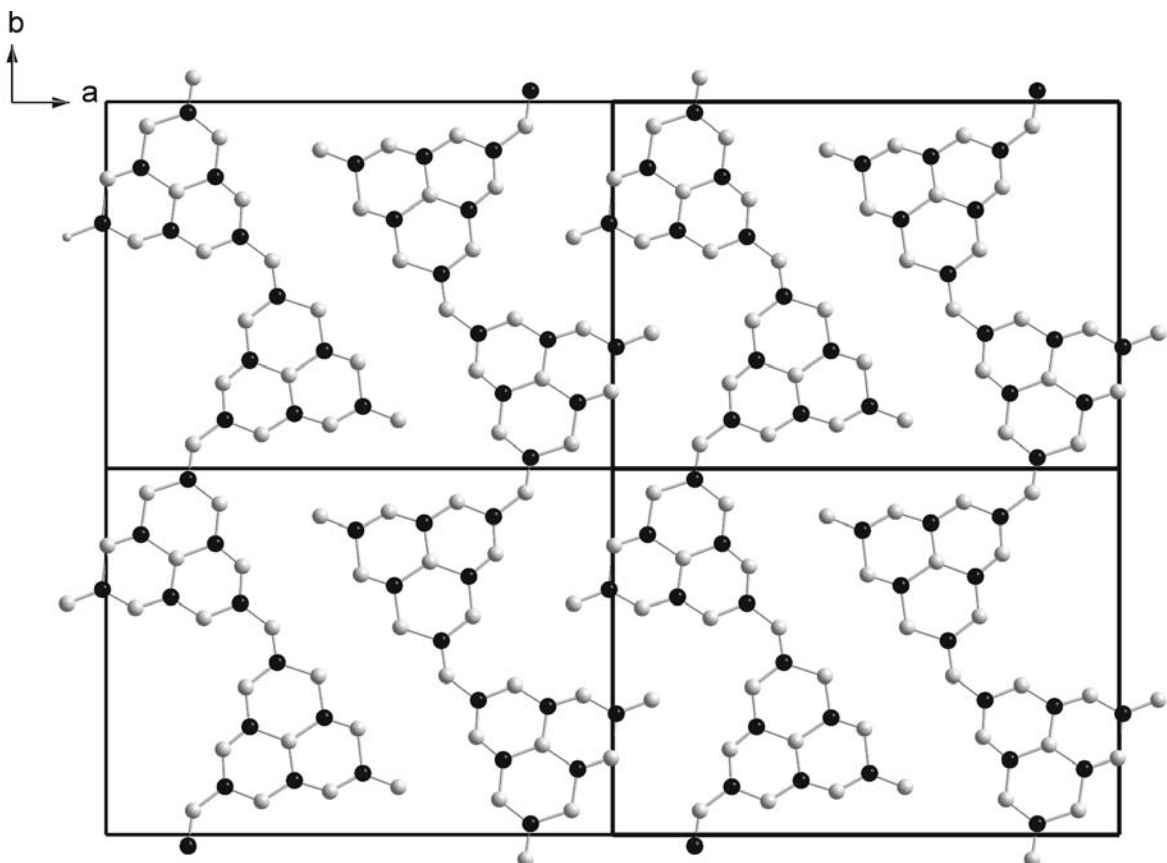


**Figure 7.24:** 2D structure projection of melon based on the initial structure solution (gray: nitrogen; black: carbon); the single hydrogen atom “found” by ED is omitted for clarity; thermal displacement ellipsoids exhibit unit size. To emphasize the polymeric character of the compound, four planar unit cells with projected symmetry  $p2gg$ ) are displayed.

**Table 7.7:** Bond lengths (in Å) and angles (in °) for melon obtained from the refined ED data. Note that the estimated standard deviations are large, such that a detailed discussion of the geometric parameters is not advisable.

N(1)–C(2)	1.38(5)	N(7)–C(6)	1.28(5)
N(4)–C(2)	1.28(4)	N(6)–C(5)	1.47(4)
N(3)–C(2)	1.31(5)	N(6)–C(4)	1.37(5)
N(3)–C(1)	1.31(5)	N(1)–C(4)	1.42(5)
N(9)–C(5)	1.22(5)	N(4)–C(3)	1.30(4)
N(1)–C(6)	1.35(5)	N(5)–C(4)	1.25(4)
N(2)–C(1)	1.35(4)	N(8)–C(3)	1.30(4)
N(2)–C(6)	1.45(4)	N(5)–C(3)	1.29(4)
N(7)–C(5)	1.31(5)		
<hr/>			
N(4)–C(2)–N(1)	121(3)	C(6)–N(1)–C(2)	128(3)
N(3)–C(2)–N(1)	112(3)	C(4)–N(1)–C(2)	113(3)
N(3)–C(2)–N(4)	125(3)	C(4)–N(1)–C(6)	117(3)
C(6)–N(2)–C(1)	119(2)	C(3)–N(4)–C(2)	119(3)
C(6)–N(7)–C(5)	115(3)	N(1)–C(4)–N(6)	115(3)
C(4)–N(6)–C(5)	119(2)	N(5)–C(4)–N(6)	123(3)
N(3)–C(1)–N(2)	120(3)	N(5)–C(4)–N(1)	121(3)
N(6)–C(5)–N(7)	121(2)	C(3)–N(5)–C(4)	120(3)
N(9)–C(5)–N(7)	124(3)	C(1)–N(3)–C(2)	126(3)
N(9)–C(5)–N(6)	114(3)	N(8)–C(3)–N(4)	116(3)
N(7)–C(6)–N(2)	118(2)	N(5)–C(3)–N(4)	122(3)
N(1)–C(6)–N(2)	112(2)	N(5)–C(3)–N(8)	120(3)
N(1)–C(6)–N(7)	129(3)		

stabilized and the planarity retained by the efficient 2D arrangement driven by hydrogen-bonding interactions, semiempirical cluster calculations suggest the planarity of the chains to be a characteristic feature even if single zig-zag strands are optimized in the gas phase (see section 7.10 on the next page). Therefore, it appears that covalent interactions within the heptazine backbone (formation of an extended  $\pi$ -system) play a pivotal role in fixing the planar geometry of the strands.

Van-der-Waals-type interactions between the layers appear to be in large part unselective toward a particular kind of stacking sequence. This results in planar defects caused by translations of adjacent sheets with respect to each other, as discussed in section 7.7 on page 294. Nevertheless, crystallites with an ordered stacking sequence – which may vary between different crystallites – are an integral part of the sample, yielding the structure projection presented above.

From these statements one can conclude the following:

The structure is built up from infinite 1D chains instead of 2D atomic arrays and does therefore not represent the structure postulated for the prototype g-C<sub>3</sub>N<sub>4</sub>. In contrast, it corresponds to the “polymer” structure model proposed for melon [75, 76, 80], whose existence has therefore been substantiated. Statements as to the geometry of the melon strands are now possible, as for instance the zig-zag-type arrangement of the heptazine motifs as well as the close packing of the chains leading to a tightly hydrogen-bonded 2D array.

Furthermore, no evidence was found for the alternative structure model postulated for melon, which is based on a trimer of melem with triangular shape (Fig. 7.1, **1a**). Moreover, according to calculations presented in section 7.10, melem-trimers tend to corrugate, thus rendering the formation of planar graphite-like layers rather implausible. It should, however, be emphasized that this does not in principle disavow the existence of this structural isomer of melon.

## 7.10 Melon: Theoretical Calculations

*Theoretical calculations, including the calculations of NMR parameters (cf. section 7.10.2 on page 319 and structure models for g-C<sub>3</sub>N<sub>4</sub> (cf. section 7.13 on page 329) were carried out by Jan Sehnert (advisor: Prof. J. Senker, University of Bayreuth) and will also be published as part of the PhD thesis by J. Sehnert.*

### 7.10.1 Structural Models

To countercheck the consistency of the structure solution obtained by electron diffraction, theoretical calculations were carried out using three different computational methods. As a starting basis, semiempirical structure optimizations of different molecular clusters taken from the structure proposal were carried out: Both a single chain comprising nine heptazine molecules, as well as an array of six chains containing six heptazine monomers each were optimized using the PM3 method [540, 541]. Hydrogen atoms were located at the assumed

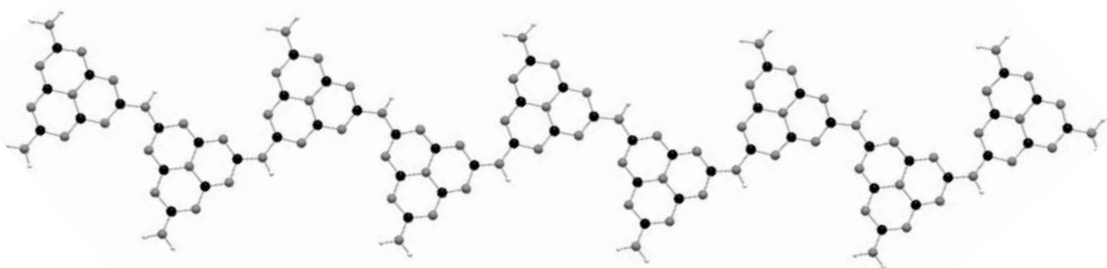


**Figure 7.25:** Zig-zag chain of melon after geometry optimization based on the semiempirical PM3 method. Gray: nitrogen; black: carbon; gray: hydrogen; the positions of the latter are empirically fitted.

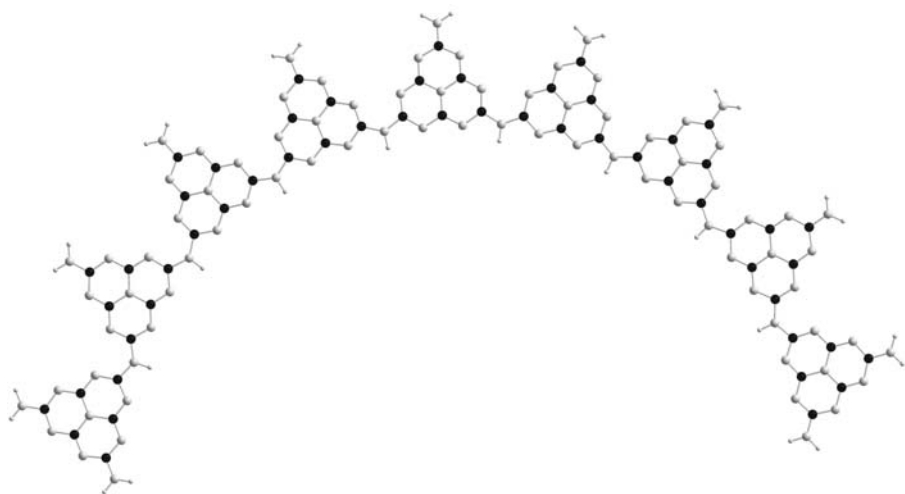


**Figure 7.26:** “Classical” model of an initially linear melon chain after geometry optimization based on the semiempirical PM3 method. Gray: nitrogen; black: carbon; gray: hydrogen; the positions of the latter are empirically fitted. The linear chain bends upon energy minimization.

$\text{NH}$  and  $\text{NH}_2$  positions according to standard geometric considerations, and the structure was then subjected to an overall structure optimization. Energy minimization reveals that the single zig-zag chain as found by ED already poses a stable molecular arrangement in the gas phase. The geometry of the zig-zag chain after optimization is outlined in Figure 7.25.

As an alternative, the classically proposed straight melon chain (see Fig. 7.1 on page 282, **1b**) was optimized using the same approach. As expected, this molecular arrangement bends upon energy minimization as demonstrated in Figure 7.26. The tendency of a pair of  $\text{NH}$ -bridged heptazine rings to bend apart is also visible in the zig-zag arrangement, whereby the alternating curvatures about every  $\text{NH}$ -bridge compensate, yielding an overall straight chain. However, if the geometry about the  $\text{NH}$ -bridge is further propagated as is the case for the initially linear geometry, the melon chain is forced into the observed bent arrangement.

Thus, on further increasing the number of monomers, a helix-like 3D arrangement is obtained after optimization, which most probably hampers the formation of a regular two-dimensional array (Fig. 7.27).

When assembling six zig-zag chains into a 2D arrangement according to the ED structure proposition, a planar oligomer is obtained upon optimization, which is highly stabilized by a tight hydrogen-bonding network.

In order to calculate the NMR chemical shift parameters for a single layer of melon, the latter was further optimized under periodic boundary conditions using DFT with plane waves and pseudopotentials [542]. The periodicity of the PM3-optimized core region of the above planar oligomer allowed for the extraction of the  $a / b$  cell parameters to establish a rectangular unit

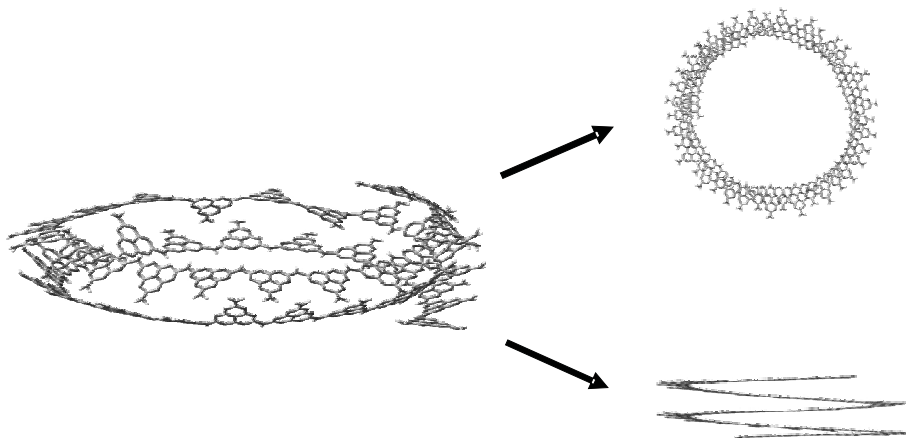


**Figure 7.27:** Screw-like distortion of an initially linear melon chain upon geometry optimization using PM3 after increasing the number of heptazine monomers as compared to the arrangement in Figure 7.26. The helix-like arrangement is shown for three different perspectives.

mesh. To ensure that the interaction between neighboring layers does not influence the NMR parameters, the interlayer distance was fixed to 4.43 Å, where dispersion interactions between the layers should be essentially negligible. Note that although the symmetry restrictions were lifted during structure optimization by using space group *P*1 for the calculations, the rectangular metrics of the planar structure was retained. Whereas the resulting *b*-axis matches the value found with PM3, the *a*-axis is slightly elongated (Table 7.8). As the length of the latter is highly dependent on the hydrogen-bonding network, an overestimation of the *a*-axis can be rationalized by the naturally poor description of dispersion forces using DFT and plane waves. Note that attempts to optimize the structure based on an orthorhombic unit cell with an interlayer distance of 3.2 Å failed, as the layers systematically moved apart for eclipsed layer arrangements.

**Table 7.8:** Experimental and calculated lattice parameters (in Å) for the structure of melon obtained from ED and different theoretical approaches.

Method	<i>a</i>	<i>b</i>	<i>c</i>
PM3 <sup>1</sup>	16.6	12.7	
CASTEP <sup>2</sup>	17.1	12.8	(4.43) <sup>2</sup>
DREIDING	16.8	12.8	3.4
TEM / XRD	16.7 <sup>3</sup>	12.4 <sup>3</sup>	3.2 <sup>4</sup>

<sup>1</sup> Cluster of 36 heptazine units arranged in 6 planar zig-zag chains.

<sup>2</sup> Constrained during geometry optimization.

<sup>3</sup> Estimated error  $\approx$  5 %.

<sup>4</sup> X-ray powder diffraction.

An overall description including dispersion interactions between individual layers is possible based on force field methods [543]. Using the Dreiding force field and partial charges fitted to the ESP, a full optimization of the input cell (Table 7.8) [544, 545] could be performed. Whereas the *a*- and *b*-axes match well the values found using PM3 and CASTEP, the *c*-axis is larger as compared to the experiment.

This finding most probably results from the eclipsed arrangement of the layers, which is considered to be energetically unfavorable in terms of interlayer van-der-Waals interactions and does not represent a local minimum on the energy hypersurface. Note that  $\pi$ -stacking interactions in general require a slight displacement of adjacent layers to ensure an optimal interaction of the  $\pi$ -orbitals. Therefore, an eclipsed layer stacking is expected to maximize the repulsive inter-plane forces. The correctness of this line of argument is evidenced by the fact that for slightly shifted layer arrangements – in which case the orthorhombic cell symmetry is broken – the energy of the system is reduced and cells with interlayer distances of 3.2 Å were found by force field calculations.

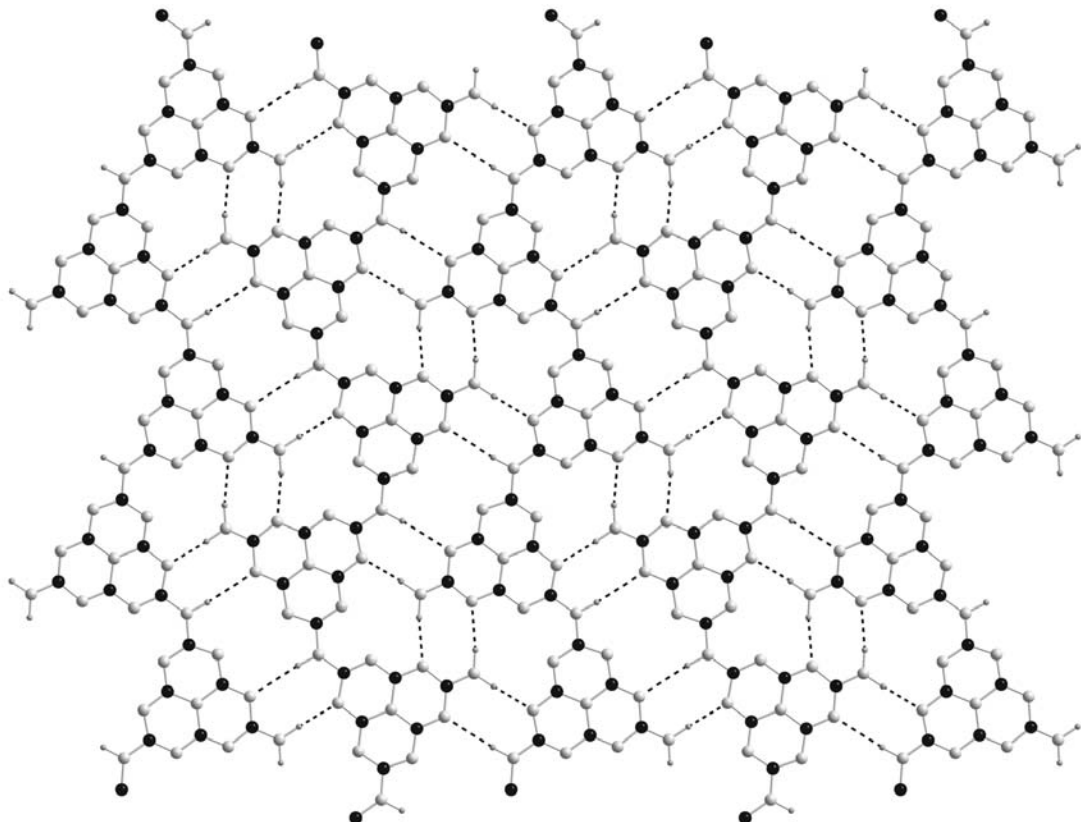


**Figure 7.28:** Planar cluster of melon after geometry optimization under periodic boundary conditions using CASTEP. The hydrogen positions are empirically fitted and the hydrogen-bonding network is indicated by black dots. Gray: nitrogen; black: carbon; gray: hydrogen.

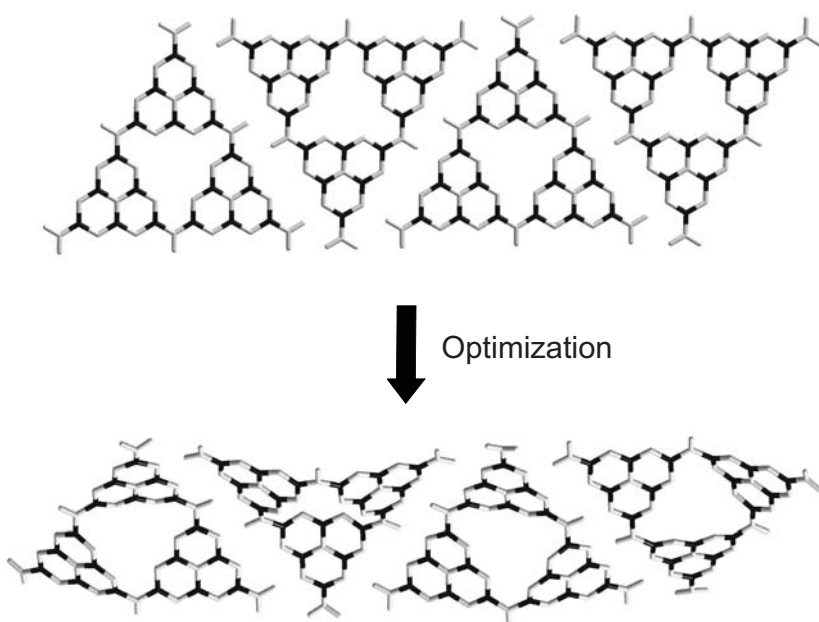


**Figure 7.29:** Possible arrangement of four melem-trimers before (top) and after (bottom) semiempirical geometry optimization at the PM3 level of theory.

Although according to the above discussion the structure of melon has been established to conform to the polymeric structure model, the question addressing the existence and 3D structure of the alternative trimeric structure proposition remains (Fig. 7.1 on page 282, **1b** and **1a**, respectively). To this end, a possible arrangement of four “melem-trimers” assembled in a close-packed, planar strand (Fig. 7.29) or layered structure (18 trimers) was optimized using the PM3 method. Notably, in contrast to the polymeric structure, geometry optimization of different clusters yields both planar as well as corrugated arrangements. For an array of only two trimers, no twisting of the individual melem-trimers is observed, whereas for larger cluster sizes a significant tendency towards undulation of the strands or layers is evident. Obviously, strain built up within the trimeric units is released upon corrugation about the bridging NH-groups. The hydrogen contacts between the trimers are retained upon optimization, thereby keeping the overall 2D arrangement largely intact. The observed exception of a planar arrangement in the case of two trimers has to be substantiated by additional calculations, and only 3D calculations using force field methods can afford a more reliable estimate of the geometry of extended layered systems. In principle, if the trimeric model of melon can in fact be obtained, it presumably will – according to the above results – not bear significant resemblance with a *graphitic* (i. e. planar) structure as found in the case of the melon-polymer.

### 7.10.2 *Ab Initio* NMR Calculations

An additional confirmation of the structural model was furnished by the calculation of the *ab initio* NMR chemical shift parameters for the DFT-optimized unit mesh. As demonstrated in Figure 7.30, the calculated  $^{13}\text{C}$  and  $^{15}\text{N}$  chemical shifts are in good agreement with the experimental spectra and confirm the overall signal assignments extracted from the CPPI experiment. The chemical shift range covered in the experimental  $^{13}\text{C}$  spectrum is essentially reproduced by the calculations, the match being optimized further by adding a Gaussian broadening to the calculated curves. In the theoretical  $^{15}\text{N}$  spectrum, the resonance of the central nitrogen is shifted towards higher field, the same tendency applying for the NH and  $\text{NH}_2$  groups.

As indicated in Figure 7.31 the calculated chemical shifts also allow to distinguish between tertiary nitrogen atoms bonded to different  $\text{NH}_x$  groups, since they are directly affected by

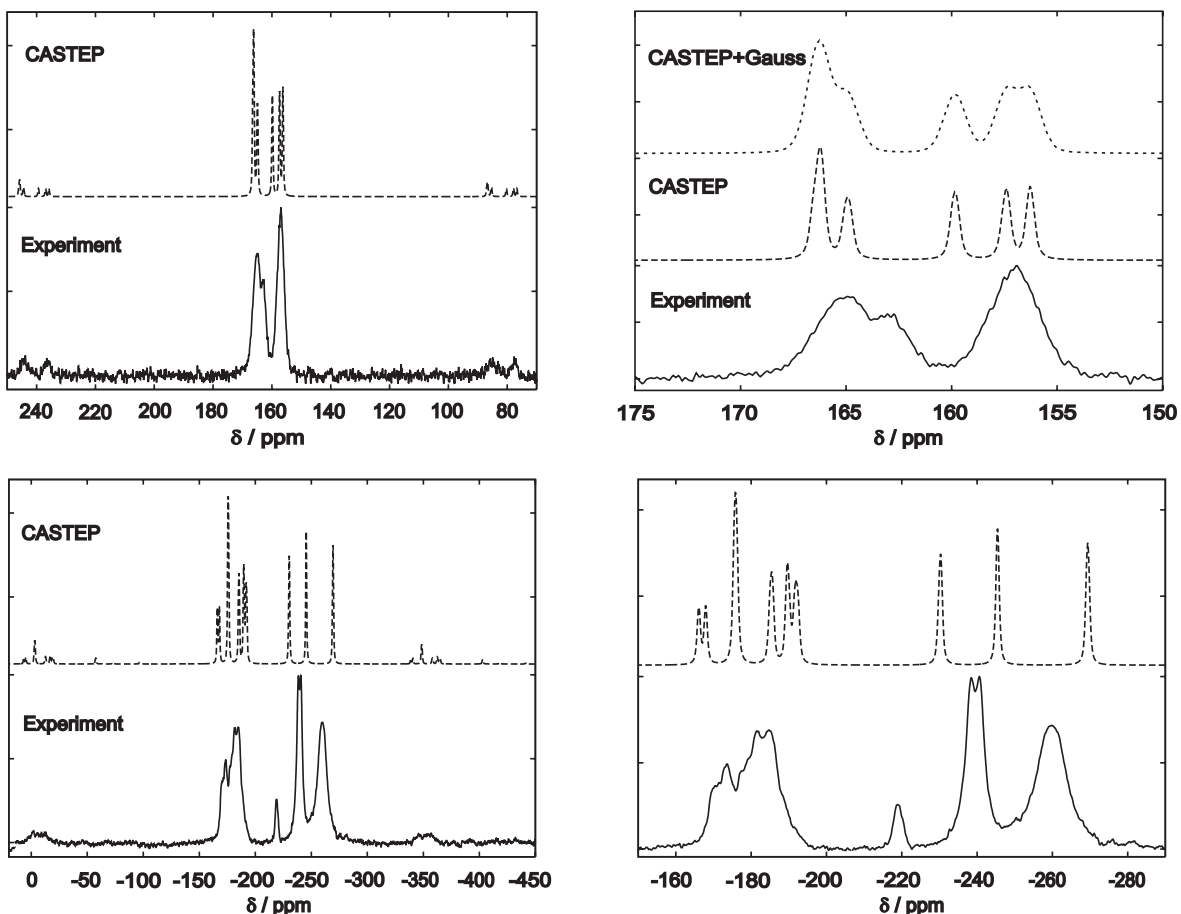


**Figure 7.30:** Top left: Calculated (CASTEP) and measured  $^{13}\text{C}$  CP-MAS spectrum of melon. Top right: Enlarged cutout including the result from adding Gauss broadening to the calculated spectrum (top). Bottom left: Calculated (CASTEP) and measured  $^{15}\text{N}$  CP-MAS spectrum of melon. Bottom right: Enlarged cutout.

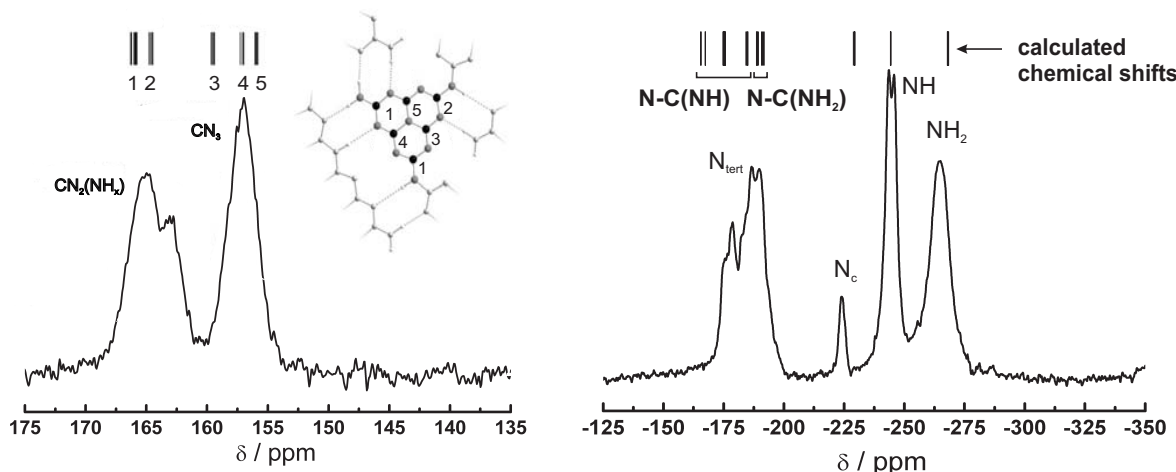


**Figure 7.31:** Experimental  $^{13}\text{C}$  (left) and  $^{15}\text{N}$  CP-MAS spectrum (right) and signal assignments (bars, top) obtained by *ab initio* calculations of the chemical shift values for the DFT optimized cell of melon. The respective carbon sites in the structure are indicated by numbers.

the surrounding NH (low-field shift) and NH<sub>2</sub> moieties (high-field shift), respectively. As stated in section 7.14 on page 302, these observations match well with the results from the 1D *fp*-RFDR NMR experiment, which lead to identical conclusions. Similarly, the assignment of the two  $^{13}\text{C}$  signal groups based on the variation of  $\tau_c$  (cf. Fig. 7.11 on page 299, right) is in agreement with the *ab initio* calculations.

## 7.11 3D Approaches

Until now, only an account of the projected structure of melon has been given. Nevertheless, as evidence was found for the planarity of the layers, the missing information with respect to the spatial arrangement can be reduced to the stacking sequence of the layers. As a starting basis, it can be assumed that the 2D projection delineated above, which may hold for a sizeable number of crystallites, is only compatible with some sort of AAA... type stacking. However, other more or less likely 3D stacking arrangements, which are compatible with the above results, will briefly be reviewed in the following.

The projected symmetry  $p2gg$  is compatible with several orthorhombic space groups, such as those acting as a makeshift for structure solution ( $P2_12_12$  and  $Pbam$ ). Although an eclipsed layer stacking is evidently compatible with the structure projection, alternative layer stackings (such as ABA...) may also give rise to the observed symmetry. On the other hand, a possible violation of the orthorhombic symmetry, either by the layer stacking or by an in-plane distortion of the layer content, cannot be excluded.

In general, all “bulk” 3D models appear to be intrinsically affected by the inherent planar

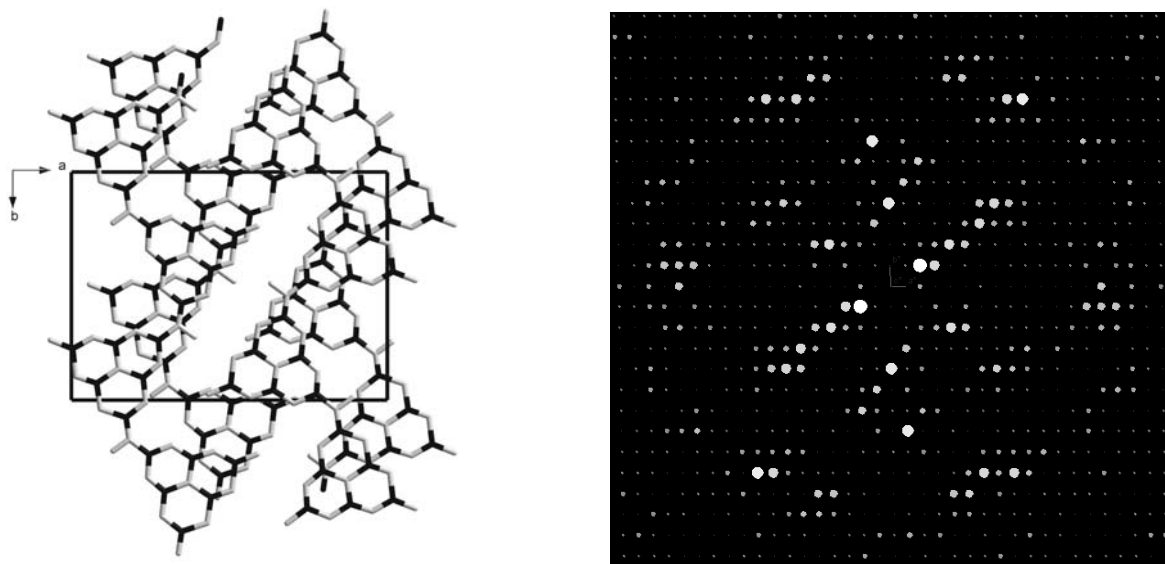


**Figure 7.32:** 3D structure model with pseudo-orthorhombic metrics (left) and the corresponding simulated kinematical  $hk$  diffraction pattern (right). Adjacent layers are offset with a translation vector (in fractional coordinates) of  $(x/a, y/b) = (0.124, -0.244)$ ; the in-plane structure is based on the structure model obtained from ED.

defects, resulting in “streaking” along  $c^*$ . *Lowther* examined three types of graphitic  $\text{C}_3\text{N}_4$  structure models with different stacking sequences of triazine-based layers using the local-density approximation plane-wave pseudopotential approach [546]. His findings confirm that there are only little energy differences for the three models, all of them representing stable structures which are easily interconvertable by applying hydrostatic or uniaxial compression. The forces between adjacent layers were reported to be very small, suggesting the graphitic carbon nitride to be extremely “soft” along the  $c$ -axis. Accordingly, the overall stability of the graphitic phases was assumed to relate to the *intralayer* rather than the *interlayer* structure, which again corroborates the experimentally found stacking disorder phenomena.<sup>11</sup>

In fact, only local approximations in terms of different, energetically similar stacking modes seem to be feasible, or the extraction of an average model leading to an idealized description in terms of a superposition structure. Using the former, one may approach a correct description of the 3D structure in the borderline case of ultra-thin crystals with a *locally* ordered layer sequence, giving rise to “quasi” 2D scattering. Thus, the idealized case of an ordered layer stacking may result from an energetically preferential piling – either leading to a doubled  $c$ -axis (ABA... stacking) or to ordered polytypes – or simply from the limited extension of the crystal over only a few unit cells. According to the calculations presented in section 7.10 on

<sup>11</sup>Note that the LDA approach used by *Lowther* is questionable in that it cannot satisfactorily account for dispersion interactions. Therefore, only relative stabilities of different layer stackings should be considered.

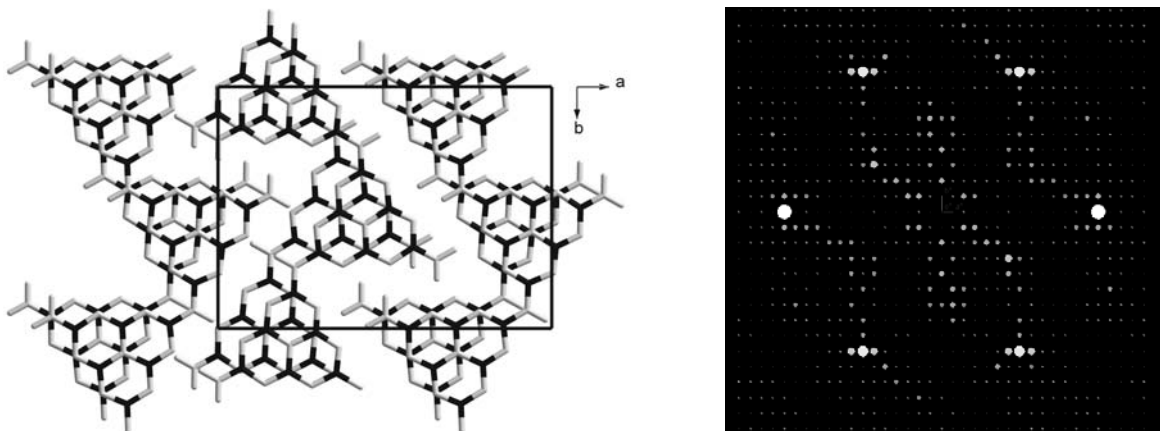


**Figure 7.33:** 3D structure model with pseudo-orthorhombic metrics (left) and the corresponding kinematical  $h\bar{k}$  diffraction pattern (right). The layer stacking is such that the centers of the C<sub>3</sub>N<sub>3</sub> units are essentially covered by adjacent layers (offset vector  $(x/a, y/b) = (0.072, 0.054)$ ); the in-plane structure is based on the structure model obtained from ED (the cell origin exhibits a slight offset).

page 314, a face-to-face alignment of the heptazine rings corresponding to an AAA... stacking sequence and orthorhombic symmetry, is disfavored as compared to the offset arrangements. It has been pointed out in the literature that a face-to-face alignment of aromatic rings (the more so for electron-rich heterocycles) is extremely rare. Usual  $\pi$ -stacking interactions imply an offset or slipped geometry, that is, the rings are parallel displaced up to distances (between the ring centers) of 3.8 Å, with a typical ring-plane overlap below 30 % [537].

Therefore, alternative layer sequences may be thought of, which – though being in agreement with orthorhombic symmetry – allow for a parallel displacement of the layers with respect to each other. To probe the impact of the layer offset on the diffraction patterns, different models with varying layer offsets were set up and their diffraction images calculated.

An example for an ABA... stacking sequence associated with a doubled *c*-axis and orthorhombic metrics ( $\gamma = 90^\circ$ ) is displayed in Figure 7.32 (left). The offset of adjacent layers is chosen at random so that all symmetry along the *a*- and *b*-axes is lost. Accordingly, the (centrosymmetric) intensity distribution of the calculated diffraction pattern (right) does not conform to the experimental patterns despite its “pseudo-orthorhombic” metrics.

Searching further for an orthorhombic structure with an ABA... stacking sequence, kinematical diffraction patterns of different stacking variants were simulated. The results are depicted in Figures 7.33 and 7.34. In the former, the heptazine polymers are offset along the cell diagonal, resulting in a stacking mode corresponding to that in graphite. This arrangement is also in agreement with the residual density found within the C<sub>3</sub>N<sub>3</sub> units in the potential map (cf. Fig. 7.20 on page 306). However, the orthorhombic (*mm2*) symmetry is lost in the theoretical diffraction pattern.

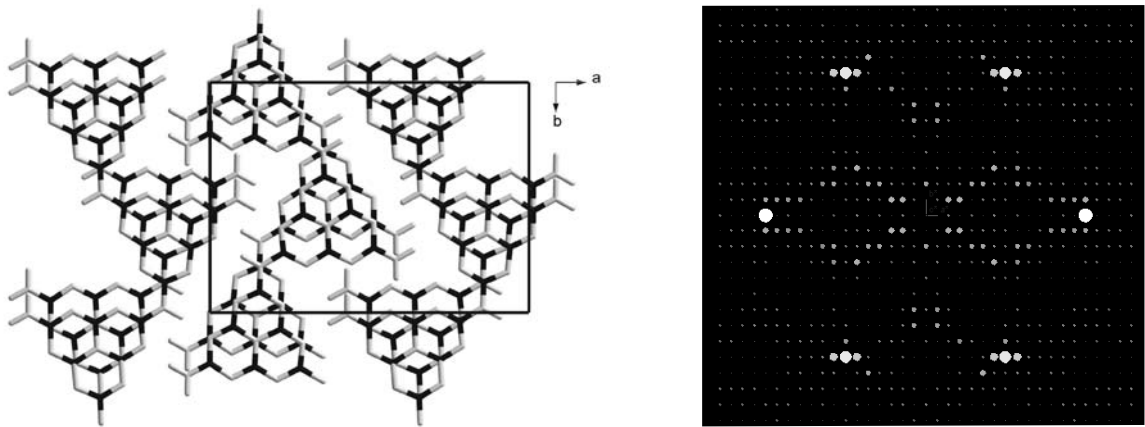


**Figure 7.34:** 3D structure model with pseudo-orthorhombic metrics and an ABA... stacking sequence (left), and the corresponding kinematical  $hk$  diffraction pattern (right). Offset vector  $(x/a, y/b) = (0.000, 0.109)$ . The in-plane structure is based on the structure model obtained from ED (the cell origin exhibits a slight offset).

A different situation is encountered for the second example, in which the layers are only offset along the  $b$ -axis, resulting in a projected  $pg$  symmetry, as only one glide plane is retained and the calculated diffraction patterns still exhibit  $mm2$  symmetry (Fig. 7.34, right). With respect to the intensity distribution, the overall resemblance of the theoretical with the experimental pattern is inferior to that observed for the pattern calculated from the ED structure model (cf. Fig. 7.22 on page 310).

A more systematic approach to the elucidation of preferred stacking sequences is given by

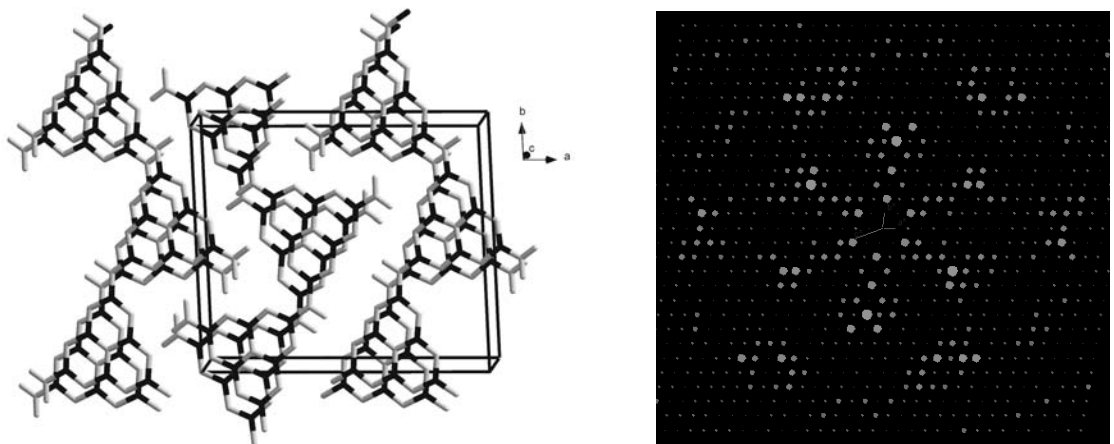


**Figure 7.35:** Triclinic 3D structure model obtained from force field calculations (left) and calculated kinematical  $hk$  diffraction pattern (right). Adjacent layers exhibit an offset with respect to each other; the in-plane structure is based on the structure model obtained from ED.

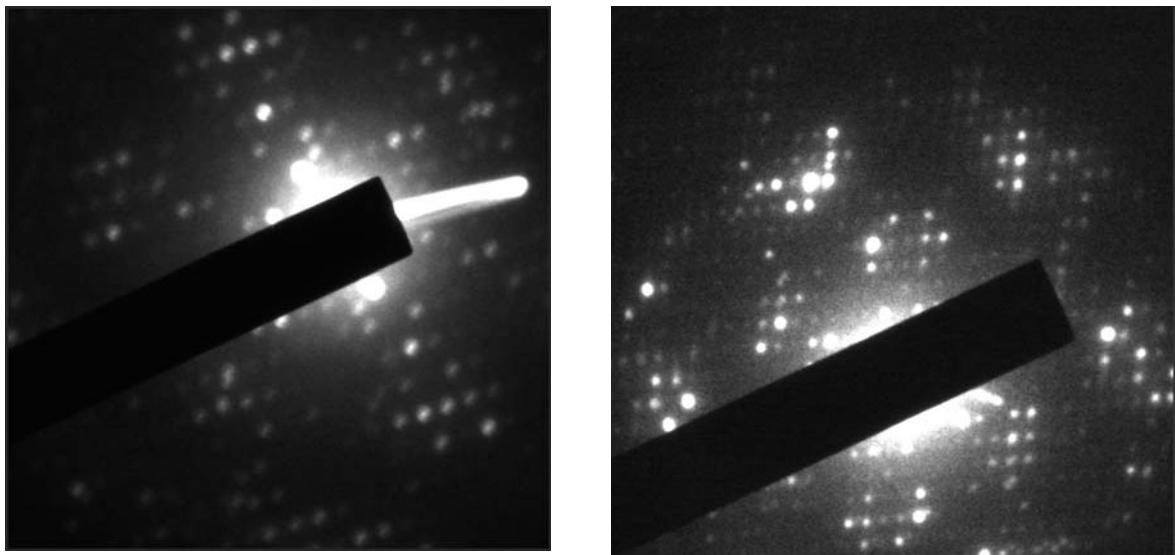


**Figure 7.36:** Experimental  $hk0$  diffraction patterns which show a significant deviation of  $\gamma$  (in-plane angle) from  $90^\circ$ .

the use of force field calculations. Figure 7.35 (left) displays a 3D arrangement based on the planar model extracted from ED and structure optimization using Mulliken point charges. Adjacent layers are preferentially displaced with respect to each other, resulting in a triclinic unit cell ( $a = 16.389 \text{ \AA}$ ,  $b = 12.635 \text{ \AA}$ ,  $c = 4.065 \text{ \AA}$ ,  $\alpha = 74.704^\circ$ ,  $\beta = 57.067^\circ$ ,  $\gamma = 89.991^\circ$ ). The corresponding calculated diffraction image is shown in Figure 7.35 (right). The projected rectangular metrics as well as the  $mm2$  symmetry is obviously violated. Though deviating from the experimental patterns in terms of the above aspects, the “intensity symmetry” is largely matched by the simulation. Although the majority of the experimental diffraction patterns clearly have an angle  $\gamma = 90^\circ$ , “distorted” variants with  $\gamma \neq 90^\circ$  are sporadically encountered as shown in Figure 7.36. These patterns may well be diagnostic of parallel displaced layers in a way similar to that outlined in the example above (Fig. 7.35). Therefore, the triclinic scenario with layer offsets along both the  $a$ - and  $b$ -axes is worthwhile considering as a – though minor – stacking variant.

We therefore conclude that in the first instance those layer-offsets have to be considered, in which the Laue symmetry of the projection is  $mm2$ . In other words, the 3D symmetry has to be monoclinic, which implies that the layers are laterally shifted only along a unique axis ( $a$  or  $b$ , if the stacking direction is along  $c$ ).

As already pointed out above, shifting the layers with respect to each other along either  $a$  or  $b$  affords a unit cell with a monoclinic angle  $\neq 90^\circ$  and an AAA... type of stacking. Interestingly, when viewed along the  $[001]$  zone axis, the associated diffraction patterns are indistinguishable from those obtained for an orthorhombic setting. Figure 7.37 demonstrates

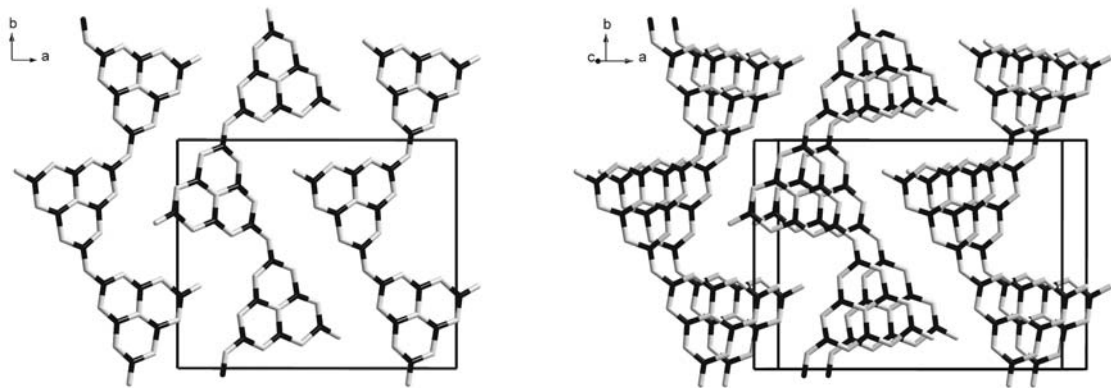


**Figure 7.37:** Triclinic 3D structure model obtained from force field calculations (left) and the corresponding theoretical  $hkl$  diffraction pattern (right). Adjacent layers exhibit an offset with respect to each other; the in-plane structure is based on the structure model obtained from ED.

two alternative views of the unit cell obtained when introducing an angle  $\beta$  of  $115^\circ$ , which is equivalent to a lateral shift of the layers along the  $a$ -axis. Note that a particularly large angle was chosen in order to clarify its effect on the structure projection in real space. The corresponding theoretical diffraction image is shown in Figure 7.38.

Note the (expected) resemblance with the simulations for the alternative scenarios: layer offset along the *short* axis (Fig. 7.23 on page 311, right), and eclipsed layer stacking assuming orthorhombic symmetry (Fig. 7.22 on page 310, right). From the above it is evident that the monoclinic model is best suited to unify the results from ED, theoretical calculations and chemical considerations. While all other models exhibit serious incompatibilities, the monoclinic AAA... stacking can accommodate both the observed structure projection and beneficial  $\pi$ -stacking interactions. Still no *quantitative* interpretation of the 3D structure of melon can be given for two reasons: The disorder phenomenon is dominating the layer piling, so that at most a *preferred* stacking sequence may be inferred. In addition, if the monoclinic AAA... variant in fact holds, no statements can be made as to the extent of the layer offset and, hence, the value of the monoclinic angle and the size of the  $c$ -axis. Nevertheless, the monoclinic model appears to be superior to any other of those presented above and should

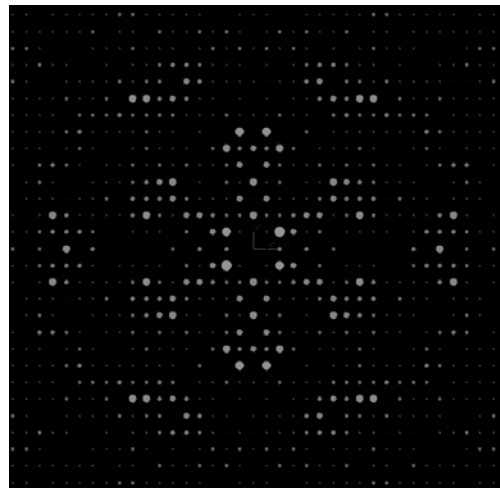


**Figure 7.38:** Kinematical diffraction pattern of the  $0^{\text{th}}$  layer, corresponding to the monoclinic “offset-model” ( $\beta = 115^\circ$ ) presented in Fig. 7.37.

be considered the most plausible working hypothesis for further attempts to elucidate the 3D structure of melon.

## 7.12 Side Phases

Apart from diffraction images of the dominant melon phase (“phase I”, Fig. 7.19), SAED patterns were observed which exhibit some similarities with the “prototypic” ones, but can most probably be assigned to domains with a different – though potentially related – arrangement of atoms (named “phase II” for simplicity).

Besides similar intensity distributions of the strong reflections, the relationship between the diffraction patterns becomes manifest in the “distortion” of particular reflection motifs, such as the “double cross” indicated in Figure 7.39, which is present in an undistorted form in the patterns displayed by Figure 7.19.

If in analogy to phase I the  $c$ -axis can be assumed perpendicular to  $a$  and  $b$ , a *monoclinic* unit cell with the following lattice parameters can be extracted:

$a = 11.9 \text{ \AA}$  (instead of  $12.4 \text{ \AA}$  for phase I;  $\Rightarrow$  similar within experimental error),

$b = 12.9 \text{ \AA}$  (instead of  $16.7 \text{ \AA}$  for phase I),  $\gamma = 109^\circ$ .

Rather speculative interpretations may be put forward for the assumed distortion. In principle, the structure of melon – though being tightly fixed by hydrogen bonds – is flexible and allows for a lateral displacement or buckling of the 1D chains with respect to each other.

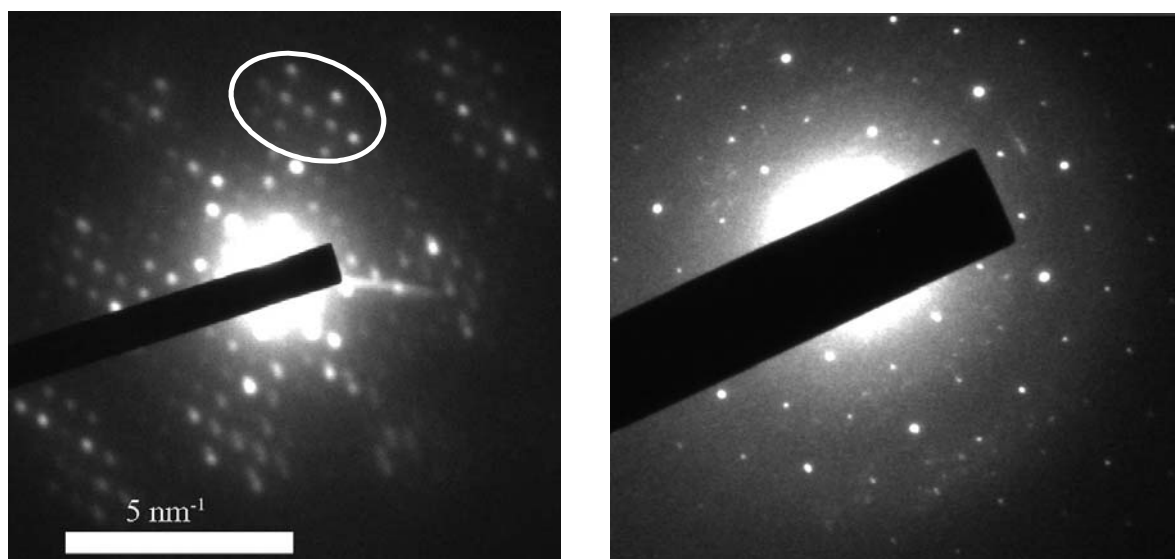


**Figure 7.39:** Left: Electron diffraction pattern of “phase II”; the reflection motif indicated by a white ellipsoid is similar to that observed for the melon structure. Right: Diffraction pattern with simple hexagonal symmetry and a lattice parameter of  $a = 5.6 \text{ \AA}$ .

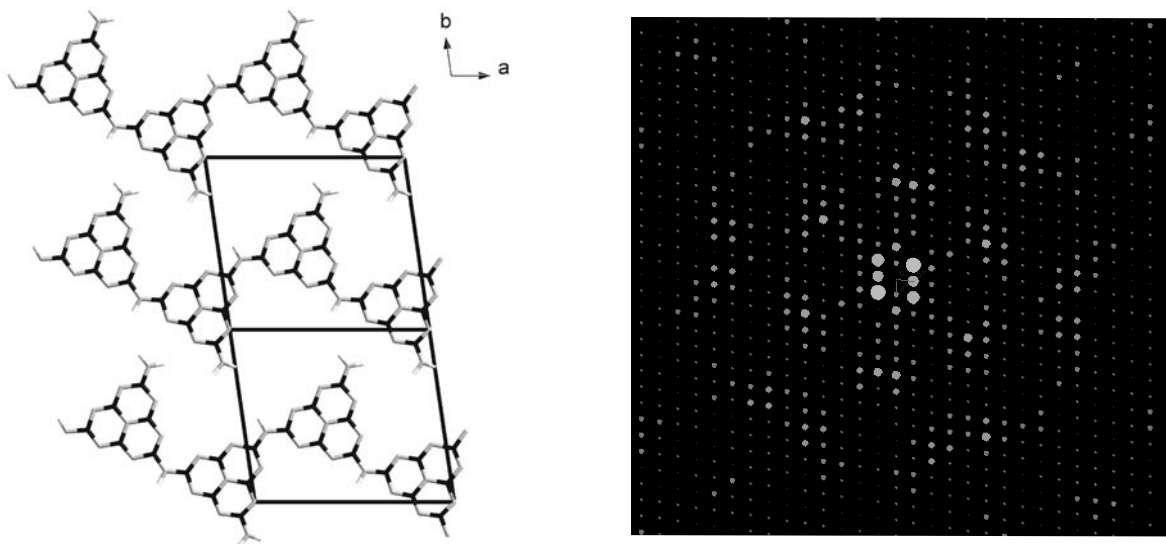


**Figure 7.40:** Left: Model structure of a less dense melon modification, view along [001]. The lattice parameters after geometry optimization ( $a = 13.33 \text{ \AA}$ ,  $b = 11.67 \text{ \AA}$ ,  $c = 3.23 \text{ \AA}$ ,  $\gamma = 98.22^\circ$ ;  $\alpha$  and  $\beta$  were assumed to be  $90.00^\circ$ .) are similar to those observed for “phase II” (left). Calculated kinematical diffraction pattern of the  $hk0$  plane for the case of eclipsed layers (right).

Owing to the small unit cell dimensions of the “distorted phase” as compared to those of melon, only one single chain could be accommodated if again a *planar* arrangement was assumed. A possible model based on two melem-strands of six molecules each has been set up and optimized using PM3, the refined cell parameters being  $a = 13.33 \text{ \AA}$ ,  $b = 11.67 \text{ \AA}$ ,  $c = 3.23 \text{ \AA}$ ,  $\gamma = 98.22^\circ$ . The angles  $\alpha$  and  $\beta$  were fixed at  $90.00^\circ$  for simplicity and the structure was optimized only with respect to the  $a / b$  plane. Though having cell parameters similar to the observed ones, the resulting structure is not as “compact” as that of melon and presumably less favorable in terms of hydrogen-bonding interactions (Fig. 7.40, left). Nevertheless, the theoretical diffraction pattern has been calculated and is shown in Figure 7.40 (right). Comparing the calculated pattern with the experimental one (Fig. 7.39, left), similarities are clearly evident; however, owing to the significant distortions of the reflections in the latter, the degree of agreement cannot be quantified.

Since other SAED patterns similar to that of “phase II”, yet with slightly different metrics, have been observed, we conjecture that several distorted variants of the prototypic melon structure exist, the structure solution of which may be tackled by a concerted approach based on electron diffraction and theoretical calculations.

The right picture of Figure 7.39 displays another SAED pattern, which represents a minority phase. The pattern exhibits hexagonal symmetry, the lattice parameter corresponding to  $5.6 \text{ \AA}$ . Possibly, this pattern results from a more highly condensed carbon nitride material

close to the hypothetical models commonly put forward for  $g\text{-C}_3\text{N}_4$  (cf. Fig. 7.2, **2a** and **2b**). In order to visualize the diffraction patterns expected for fully condensed, *planar* triazine- and heptazine-based structures (for a more detailed discussion of these idealized structure models see section 7.13 on the next page), the atomic positions for both models were calculated based on the known structural parameters of the two heterocycles. Diffraction images were then computed for two stacking variants (AAA... and ABA...) with trigonal symmetry in all cases. As can clearly be seen from Figures 7.41 and 7.42, which are shown exemplarily, simple diffraction patterns with hexagonal symmetry result in both cases.

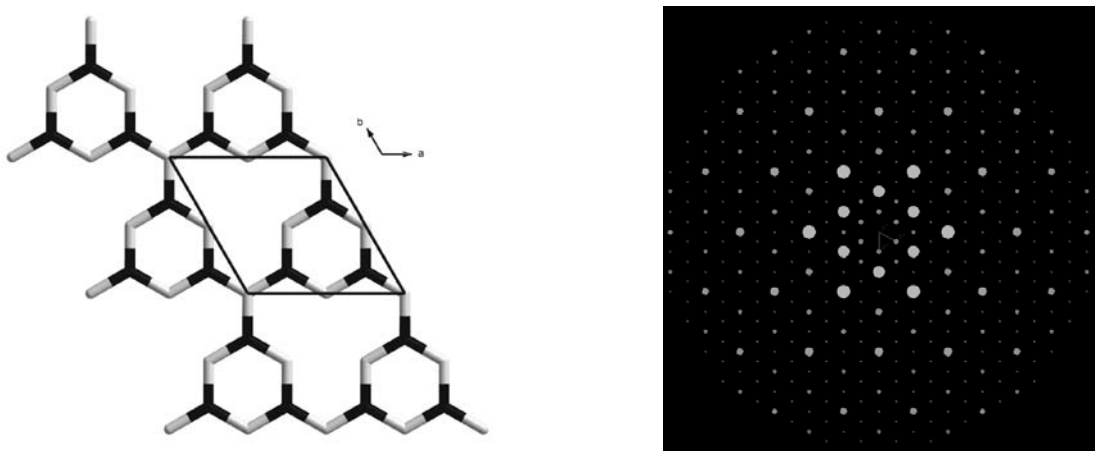


**Figure 7.41:** Triazine-based model for  $g\text{-C}_3\text{N}_4$  ( $a = 4.45 \text{ \AA}$ ,  $b = 4.45 \text{ \AA}$ ,  $c = 3.19 \text{ \AA}$ ,  $\alpha = 90^\circ$ ,  $\beta = 90^\circ$ ,  $\gamma = 120^\circ$ ) with an AAA... stacking sequence in space group  $P3m1$  (left) and the corresponding kinematical diffraction pattern of the  $hk0$  plane (right).

However, the lattice parameters theoretically expected for the triazine models with trigonal symmetry are significantly smaller ( $4.5 \text{ \AA}$ ) than those found experimentally. In contrast, considering heptazine-based structures requires unit cell dimensions which can accommodate at least one heptazine molecule together with a minimum of two bridging nitrogen atoms. The resulting width of the smallest entity, corresponding to the  $a$ -axis in the above model (Fig. 7.42, left), amounts to  $\approx 6.7 \text{ \AA}$ , which is significantly too large for the experimentally observed lattice parameters.<sup>12</sup> Nevertheless, the diffraction patterns displayed in Figures 7.39 on page 326 (right) and 7.42 exhibit principal analogies, which may be indicative of a relationship between the respective underlying structures.

Interestingly, the  $001$  reflection ( $5.544 \text{ \AA}$ ) of the hypothetical hexagonal phase  $\beta\text{-C}_3\text{N}_4$  with a  $\beta\text{-Si}_3\text{N}_4$ -type structure exactly corresponds to the observed  $d$ -value ( $5.6 \text{ \AA}$ ) [42, 43, 45, 51], as does the lattice parameter calculated for the willemite-II-type structure of  $\text{C}_3\text{N}_4$  (space group

<sup>12</sup>The same line of argument applies to possible triazine-based defect phases as for instance the hexagonal phase “[ $(\text{C}_3\text{N}_3)_2(\text{NH})_3$ ] <sub>$n$</sub> ” proposed by Kawaguchi *et al.* with  $a = 8.23 \text{ \AA}$  [510].

$I\bar{4}3d$ ,  $a = 5.3973 \text{ \AA}$ ) [51, 547]. Furthermore, a suspected cubic phase of  $\text{C}_3\text{N}_4$  recovered at ambient pressure after treatment of “g- $\text{C}_3\text{N}_4$ ” at 21 GPa in a diamond anvil cell was indexed with  $a = 5.484 \text{ \AA}$  (body centered setting) or  $3.877 \text{ \AA}$  (primitive setting). The latter phase, however, would not exhibit a diffraction pattern of hexagonal symmetry [547]. Nevertheless, at this stage no conclusive interpretation of the observed metrics can be given, but a more detailed investigation of possible structure models matching the diffraction patterns of the side-phases is certainly one of the most promising future tasks.

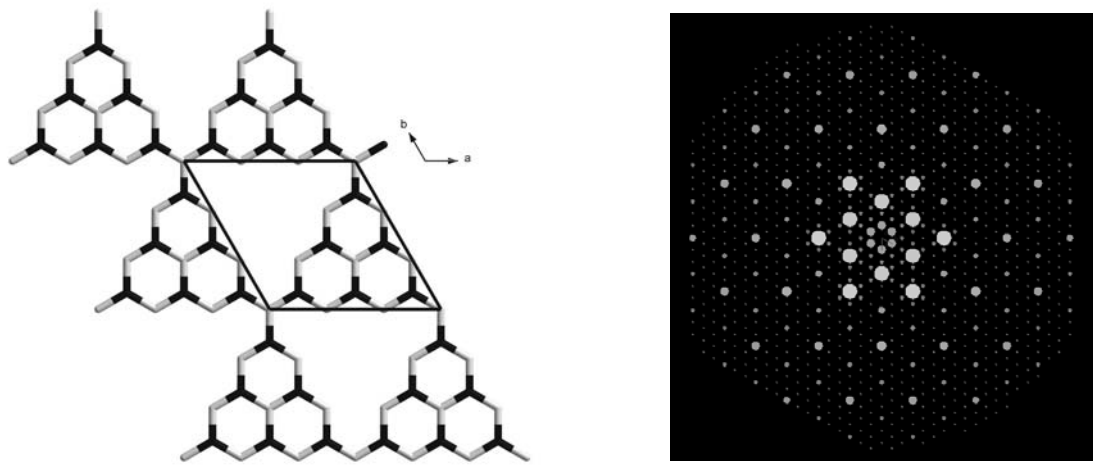


**Figure 7.42:** Heptazine-based model for g- $\text{C}_3\text{N}_4$  ( $a = 6.72 \text{ \AA}$ ,  $b = 6.72 \text{ \AA}$ ,  $c = 3.19 \text{ \AA}$ ,  $\alpha = 90^\circ$ ,  $\beta = 90^\circ$ ,  $\gamma = 120^\circ$ ) with an AAA... stacking sequence in space group  $P3m1$  (left) and the corresponding kinematical diffraction pattern of the  $hk0$  plane (right).

## 7.13 General Trends: Models for Graphitic Carbon Nitride

### 7.13.1 Fully Condensed Structure Models

The relevance of graphitic carbon nitride has launched a plethora of theoretical investigations on possible structure models for g- $\text{C}_3\text{N}_4$  by various methods. Surprisingly, almost all models discussed in the literature are “biased” both with respect to their molecular building blocks and to the 3D conformation these motifs adopt. In detail, most models are based on a *planar* arrangement of *triazine* building blocks [42, 51, 53, 299, 515, 546]; it is, however, increasingly recognized that a nitrogen concentration in graphite-like sheets above 15 % leads to a considerable buckling of the latter as observed for the borderline case of  $\text{CN}_x$  nanotubes [42, 61, 515, 516, 548]. *Kroke et al.* performed total energy calculations of various structures using DFT with a plane wave basis set [85]. According to these calculations, the fully condensed heptazine-based structure model for g- $\text{C}_3\text{N}_4$  was found to be by  $\approx 30 \text{ kJ}$

$\text{mol}^{-1}$  more stable than the triazine-based analogues. At least three different, non-eclipsed stacking variants for the heptazine-based system were computed, which were separated by an energy difference of less than  $10 \text{ kJ mol}^{-1}$ . An extensive account of the literature data will not be given in this work; instead, a brief summary of the results from semiempirical structure optimizations at the PM3 level using a large number of different “input” structure models is presented [42, 515, 516]. For all models, both imino and amino hydrogen positions were included and fitted empirically.

As a first step, *fully condensed* structures based on either triazine or heptazine building blocks were calculated as outlined in Figure 7.43. The energy optimizations were carried out in either case using a systematic screening by varying the cluster sizes; a maximum of 91 and 61 monomers were used in the triazine and in the heptazine case, respectively.

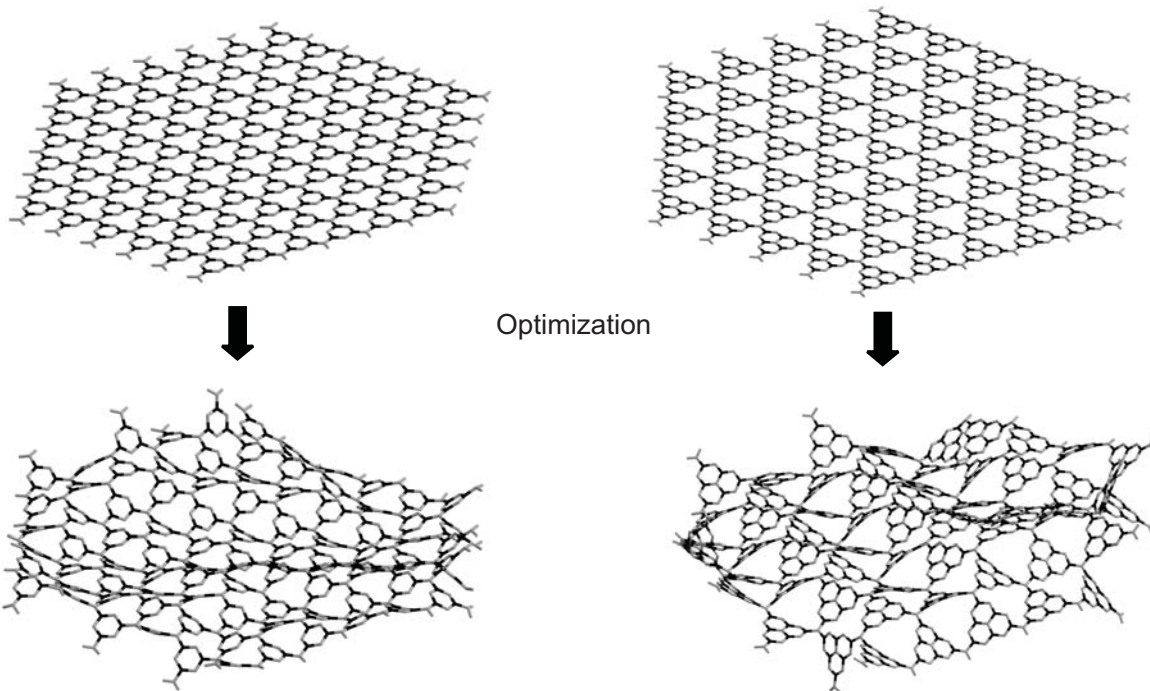


**Figure 7.43:** Starting geometries (top) and optimized structures (bottom) of fully condensed triazine- (left) and heptazine-based networks (right), using the PM3 method.

Most notably and in contrast to previous statements [51, 73, 301, 520] both arrangements are highly strained in the planar case, releasing strain upon optimization by forming undulated arrangements without obvious periodicity. Therefore, a *quasi-amorphous* layered structure with a non-periodic intra- as well as a poorly defined interlayer spacing is to be expected in both cases. Notably, the heptazine and triazine rings are slightly distorted from the ideal planar geometry and twisted about the bridging trigonal nitrogen atoms. The structure as-

sociated with minimum energy may thus result from the minimization of both the repulsion imposed by the nonbonded  $\text{N} \cdots \text{N}$  interactions and the ring strain enforced by the overall planar arrangement. It should, however, be noted that unless a 3D array made up from several layers or an infinite structure using periodic boundary conditions is optimized, the observed buckling of the layers can only be considered as a preliminary result.

Evidence for a possible buckling of the  $\text{g-C}_3\text{N}_4$  layers was reported by *Vodak et al.* who carried out computations of possible triazine-based  $\text{C}_3\text{N}_4$  networks using the semiempirical AM1 method as well as DFT calculations [66]. By analogy to the results of geometry optimizations for the molecular precursor tris(2,4-dichloro-1,3,5-triazine)amine (TDT), *planar*  $\text{g-C}_3\text{N}_4$  extended solids were calculated to be significantly destabilized relative to the corrugated (out-of-plane) deformations owing to the presence of highly repulsive  $\text{N} \cdots \text{N}$  nonbonded distances in the range of  $2.380 - 2.436 \text{ \AA}$ . This trend was obvious irrespective of the calculated stacking variants, thereby demonstrating that planar geometries are highest in energy. In addition, possible 3D analogues based on the Si networks of  $\text{SrSi}_2$ - and  $\text{ThSi}_2$ -type structures were shown to be similar ( $\text{SrSi}_2$ ) or significantly lower ( $\text{ThSi}_2$ ) in energy as compared to the structures with a corrugated graphite-type topology [66].

The above findings suggest that the classical planar structure models for  $\text{g-C}_3\text{N}_4$  are highly unfavorable and alternatives have to be sought, which, however, will most probably differ significantly from the idealized graphite-like topology.

### 7.13.2 “Defect” Structure Models

Apart from the fully condensed networks described above, the difficulties in synthesizing hydrogen-free graphitic carbon nitride demonstrates the necessity of devising alternative “defect” structure models, of which melon represents the first structurally characterized example. An intriguing feature of such defect  $\text{g-C}_3\text{N}_4$  structures may be a less strained geometry owing to a lower degree of condensation, thereby leading to the formation of essentially planar layers. To check this possibility, different hypothetical structure models have been set up and optimized using the semiempirical PM3 method.

First, an extension of the polymeric melon structure was tested, which is made up from a double strand of melem monomers condensed *via* trigonal nitrogen atoms (Fig. 7.44). The ratio of tertiary nitrogen atoms to  $\text{NH}$  and  $\text{NH}_2$  groups is higher as compared to that in melon; in addition, a structural motif representative of a high degree of condensation is introduced by the tri-coordinated tertiary nitrogen atoms. Upon energy minimization of an isolated cutout of the 1D infinite band, the planarity of the arrangement is essentially retained. However, a notable “planar deflection” is introduced into the strand, which presumably entails a release

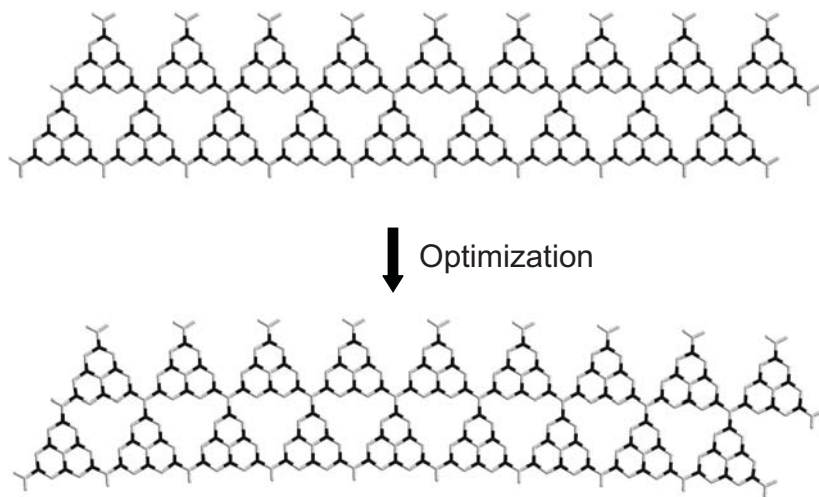


**Figure 7.44:** Double strand made up of melem monomers before (top) and after (bottom) geometry optimization at the PM3 level of theory.

of strain at the trigonal planar nitrogen atoms.

A larger assembly of heptazine rings is displayed in Figure 7.45. In this structural model, large “cavities” are present leading to an open network with frequent layer terminations by  $\text{NH}_2$  and  $\text{NH}$  groups. In contrast to the situation encountered for fully condensed networks (cf. Fig. 7.43), the vacancies allow for a “planar” release of strain, which is accompanied by an in-plane distortion of the overall arrangement. This observation may be generalized with respect to the favored formation of *planar* systems in case of *partial* network condensation,

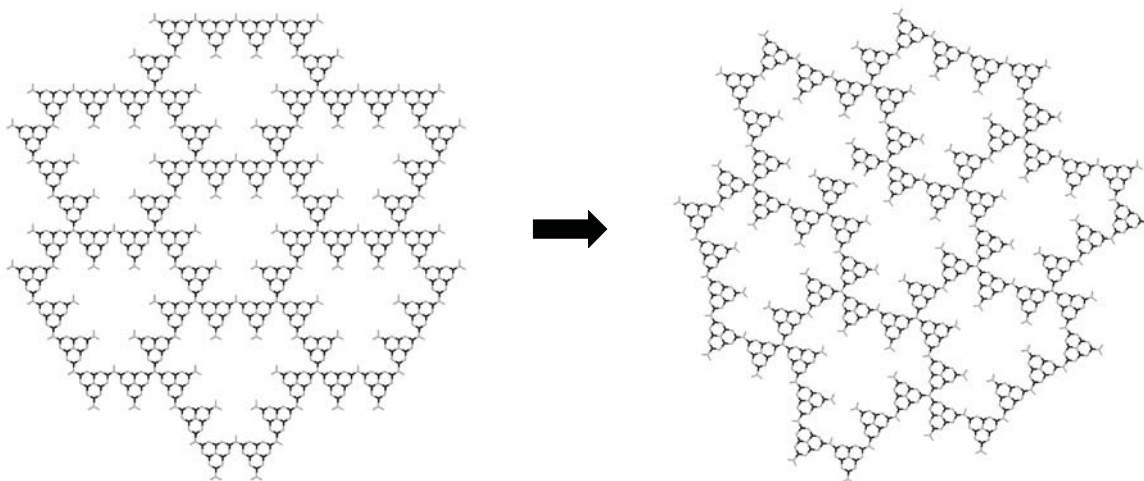


**Figure 7.45:** Finite trigonal assembly of only partially condensed heptazine monomers before (left) and after (right) optimization using PM3. The large vacancies within the layer allow for the release of strain without buckling of the planar arrangement.

whereas *undulation* of the layers is observed in *highly condensed* structures.

However, it should be noted that large vacancies as encountered in the above model may not be favorable in terms of the overall energetic stabilization of the network. Thus, a compromise of strain reduction and close packing of the molecular building blocks may be energetically most beneficial and will have to be the guiding theme in the search for the most realistic defect structure models.

### 7.13.3 “Mixed” Structure Models

Owing to the observation of melamine crystals in the bulk material recovered after heat treatment at 903 K, an extraordinary thermal stability of the starting material under the pressure of ammonia may be conjectured. In addition, various synthetic routes have been devised based on triazine derivatives, in which under certain reaction conditions (for instance two-component reactions between appropriately functionalized precursors) the triazine ring system might in fact be preserved. Therefore, the integration of melamine into the resulting products, leading either to purely triazine or to mixed triazine-heptazine-based materials, may not in principle be excluded.

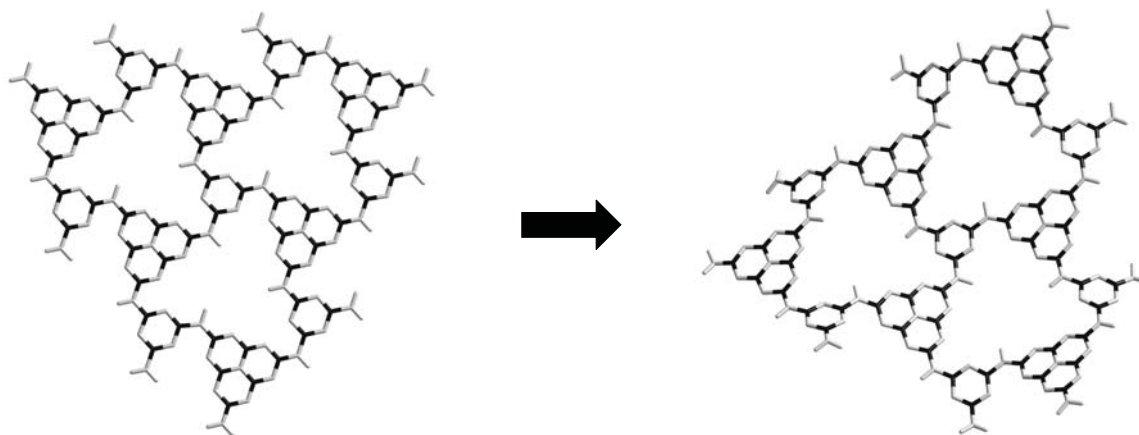


**Figure 7.46:** Mixed cluster containing both triazine and heptazine ring systems, which are loosely condensed via NH bridges. Geometry optimization (PM3) leads to corrugation (right) of the initially planar arrangement (left).

Hence, several clusters of predominantly trigonal starting geometry have been devised and optimized using the semiempirical PM3 method. Both examples presented in the following do not contain trigonal planar nitrogen atoms, indicating the low degree of condensation of the molecular building blocks. As a major result, the geometry optimization is largely dependent on the cluster size and the special arrangement of the heterocycles. As outlined in Figures 7.46 and 7.47, energy minimization may furnish heavily corrugated structures as well as essentially

planar topologies, in which strain is released by displacement of the rings with respect to each other.

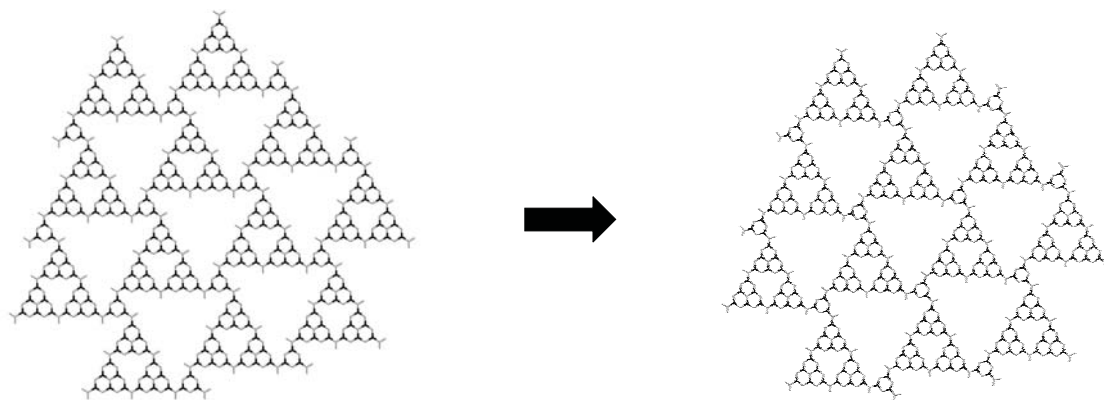


**Figure 7.47:** Starting geometry of a larger cluster containing both triazine and heptazine rings, the latter representing the main species (left). Upon geometry optimization (PM3), strain is released within the layer, thereby avoiding a buckling of the planar sheet (right).

The above discussion again demonstrates the versatility of arrangements based on both triazine and heptazine building blocks, as well as the various possibilities of interlinking the latter. A large number of structural motifs may be synthetically accessible under suitably tuned reaction conditions. However, the interplay of theoretical predictions, preparative presuppositions and analytical findings may greatly facilitate the systematic identification of the energetically most favorable and realistic structure models.

## 7.14 Preliminary Conclusion

To conclude, in the previous sections the first example of the structural characterization of a polymeric carbon nitride material was presented based on a concerted approach using a broad spectrum of analytical techniques. The above study represents a further example of an *ab initio* structure solution by means of electron diffraction.

The above results shed light on the long-standing debate on the identity of Liebig's inert compound "melon", whose existence has now been proven for the first time. The polymer model of melon, put forward by *Redemann* and *Lucas* as early as 1940 [76], was confirmed and extended with respect to the overall geometric arrangement of the polymer chains.

Considering the fact that melon is composed of planar layers built up by a "carbon(IV) nitride core" (heptazine units), this compound may on the one hand be conceived of as a "defective

g-C<sub>3</sub>N<sub>4</sub>” material, whose graphite-like topology may in fact result from the presence of “network terminations” in the form of NH and NH<sub>2</sub> groups. These function as triggers for strain release in a way that a buckling of the sheets is prevented.

The similarity to graphite is complemented by the exceptional thermal and chemical stability of melon. As has recently been noted [514], melon (in this work called g-C<sub>3</sub>N<sub>4</sub>) may therefore be considered a promising functional material in catalysis or surface science, and at the same time represent the ultimate pre-stage of graphitic carbon nitride.

On the other hand, however, the existence of melon highlights characteristic differences between graphite and “graphitic” carbon nitride materials, and in doing so, point out that the analogy between the two systems (C and C / N) – both with respect to chemical and structural aspects – is clearly limited.

Given the fact that essentially all attempts to prepare g-C<sub>3</sub>N<sub>4</sub> from hydrogen containing precursors yield materials with similar structural features and hydrogen contents, one may hypothesize that the products of the frequently claimed syntheses of graphitic carbon nitride have in fact rather been the carbon nitride polymer melon or related compounds [42, 73, 83, 84, 90, 91, 300, 301, 453, 510, 512–514, 518, 519, 523, 525].

We can thus add the first direct evidence to the ongoing debate on the structure of the hypothetical g-C<sub>3</sub>N<sub>4</sub>, that triazine-based models, which are still being predominantly discussed in the literature, should henceforward be assessed very critical.

As a next step, a comprehensive description of the stacking disorder governing large parts of the sample is essential, with the long-term objective being the elucidation of the “real structure” of melon.

A glimpse of other, perhaps more highly condensed carbon nitride phases, has already been caught; the combination of electron diffraction with solid-state NMR spectroscopy and theoretical screening of possible structure models will have the potential to fully enter the realm of structure elucidation of graphitic carbon nitride materials.



## Chapter 8

# Discussion and Outlook

The scope of this thesis was defined by three major issues, which have been arising from the requirement to further extend and to deepen research on carbon nitride chemistry.

As the progress of the precursor approach to carbon nitrides has gradually been meeting “saturation” during the past years, the main objectives at the outset of this study were centered on the following leitmotifs:

- To gain a deeper understanding of the reactivity of precursors and the mechanisms governing solid-state reactions, the latter being the key to the directed synthesis of novel precursor systems as well as to extended carbon nitride solids with tailored properties.
- To develop novel  $\text{CN}_x$  precursors based on the evaluation of reactivity principles and solid-phase reaction trajectories thus established.
- To provide an *experimental* basis for the predominantly *speculative* discussion centered on the structure of graphitic carbon nitride-type systems, with the major focus on the nature of the structural building-blocks of polymeric  $\text{CN}_x\text{H}_y$  solids:  
Triazine or heptazine?

The interplay between structural requirements of suitable  $\text{CN}_x$  precursors and their thermal reactivity was demonstrated in Chapter 4. Although ammonium cyanourea  $\text{NH}_4[\text{H}_2\text{NC}(=\text{O})\text{NCN}]$  can be considered a “hydrate” of ammonium dicyanamide  $\text{NH}_4[\text{N}(\text{CN})_2]$ , the conversion of the latter affords the prototypic  $\text{CN}_x$  precursor dicyandiamide, whereas the former transforms into urea and cyanoguanylurea along significantly different reaction trajectories. The conversion of urea and its derivatives into melamine is principally feasible; however, they can at best be considered “indirect”  $\text{CN}_x$  precursors. While both reactions – if carefully adjusting the reaction conditions – proceed in the solid state,

the decomposition of ammonium cyanoureate is highly complex, giving rise to several side-products. These could be identified by taking the different functionalities of the precursor into account. Only subtle changes in the constitution of the precursor species thus lead to a profound modification of the observed solid-state reactivity and the overall performance and suitability as  $\text{CN}_x$  precursor.

As outlined for the model system ammonium dicyanamide, the kinetics and mechanism of the transformation into dicyandiamide by fractionalizing the latter into elementary reaction steps could be assessed on a molecular level, thus highlighting the potential of combining a variety of complementary analytical techniques. Extending the system under study to the gas phase by monitoring the volatile species evolved and their interplay with the solid may allow for an optimization of the reaction conditions (pressure, temperature), as was demonstrated in the case of ammonium dicyanamide.

A consequent methodological extension will be the *quantitative* study of more complex systems exhibiting competing modes of reaction, as well as of those where none or only a few of the species involved are crystalline. An appropriate handling of increased levels of complexity will certainly demand for elaborate spectroscopic techniques, which are being developed for instance in the field of multi-dimensional zero- and double-quantum solid-state NMR spectroscopy. The scope of the latter is not restricted to crystalline compounds, and by exploiting and correlating different types of interactions, a vast amount of structural information is accessible. By specifically tuning the type of probe nucleus, as has been done in the present work by switching from  $^{13}\text{C}$  /  $^{15}\text{N}$  CP-MAS NMR [163] to static  $^2\text{H}$  NMR, the regime of dynamics and reaction kinetics may also be entered, opening up another fundamental dimension governing solid-phase reactions. In particular, nucleation, growth and interface dynamics, as well as structural inhomogeneities or amorphous intermediates may be identified by taking advantage of the versatility of solid-state NMR spectroscopy. In addition, *in situ* vibrational spectroscopy – both of the gas and the solid phase – may serve as a useful probe of substructural subtleties, as for instance of proton transfer reactions, volatile condensation products or structural building blocks in amorphous materials.

Chapter 5 was conceived as an attempt to apply the principles worked out in Chapter 4 and to accordingly screen various precursors for potential *thermal solid-phase reactivity*. As outlined previously, dicyanamides and tricyanomelamines represent particularly promising systems owing to their composition (hydrogen-free, nitrogen-rich carbon(IV) nitrides) and well-established thermal reactivity. Since the structural chemistry and reactivity of metal dicyanamides and tricyanomelamines was comprehensively delineated by *Jürgens* [240], the focus of this theses was directed to an extension of dicyanamide and tricyanomelamine

chemistry toward the non-metal salts. As indicated by the significantly different reactivity of ammonium dicyanamide as compared to the metal dicyanamides, tuning the reaction modes by deliberately choosing the cation seemed to be feasible. Therefore, a number of different dicyanamides and tricyanomelamines, among which being the ammonium, guanylurea, guanidinium and melaminium salts, were synthesized by means of metathesis reactions and were structurally characterized. Although the structural features of the non-metal species are largely identical to that of the metal-analogues, the thermally induced reactivity appears to be significantly influenced by the choice of the cation, thereby no longer being governed solely by the cyanamide functional groups of the anions.

Since the cation may function as “covered” nucleophile, being released upon proton transfer to the anion, the nucleophilic addition of the cation to the electrophilic nitrile carbon sites of the anion is feasible. For the dicyanamides, this reaction pathway is indeed realized *twice* for the guanidinium and guanylurea salts owing to the N–C–N backbone of the cation and the symmetric C–N–C moiety of the anion. Thus, ring closure reactions, giving rise to the triazine core ( $C_3N_3$ ), are observed for these molecular salts, which is in close analogy to the “monofunctional” ammonium dicyanamide and therefore nicely supports the validity of the structure-reactivity principle.

Guanidinium dicyanamide is exceptional both in terms of the high heat of formation accompanying the cyclization into the isomeric compound melamine, and regarding the fact that melting occurs prior to the transformation. Since molecular motion is therefore governed by solution-like conditions, typical solid-state approaches to probing the reaction mechanism were doomed to fail in this case and therefore not pursued any further.

In contrast, an extension of the scope of precursor systems to less common compounds was advised by studying the thermal reactivity of guanylurea dicyanamide. It could be demonstrated that an in fact unfavorable heteroatom content – in this case oxygen – does not necessarily deteriorate the performance of the precursor. In this particular case, the thermally induced evolution of the volatile species HNCO gives rise to the elimination of unwanted constituents and the intermediate formation of the purely C/N/H-based precursor melamine. This *in situ* generation of the actual  $CN_x$  precursor species may therefore be considered as an alternative guiding theme for the selection of suitable precursors.

Melaminium dicyanamide contrasts the above thermal behavior in that the anion is not integrated into the reaction product but solely functions as a base in the initial proton transfer reaction. As the as-formed free acid dicyanamide is particularly prone to polymerization, the only crystalline species detected is melamine. A reaction mechanism according to the principles established above does not seem to be applicable in this case.

Interestingly, similar findings – in terms of the absence of nucleophilic addition to the anion – can be adduced for the class of non-metal tricyanomelamines. The thermal behavior of tricyanomelamines in general had until now been a largely unknown variable, except for a TG-MS study of a mixture of  $\text{Na}[\text{C}_6\text{N}_9]$  and  $\text{Na}[\text{C}_6\text{N}_9] \cdot 3 \text{H}_2\text{O}$ , where total decomposition was observed beyond 910 K. At first sight, the non-metal tricyanomelamines may seem less thermally stable, yet – unlike the metal analogues – the potentially reactive nitrile sites may give rise to cross-linking reactions leading to a 2D triazine-based array. However, none of these potentialities is in fact observed, but a rather simple and unified mode of reaction occurs instead. It was conjectured that melaminium TCM may form a hypothetical network phase composed of triazine units, but ultimate evidence was only found for the formation of melamine and melem, irrespective of the type of cation. Although the exact mechanism of the respective solid-phase transformations is still subject to speculation, all tricyanomelamines lose their structural integrity at relatively low temperatures, with the triazine core however staying intact and giving rise to a significant gain in thermal stability by the subsequent formation of melem.

Considering the findings outlined above, a remarkable tendency is disclosed:

The formation of melamine is observed in *all* precursor systems studied and may therefore be considered a major thermodynamic driving force. Although this tendency may already be imparted in some of the starting materials, the inevitable formation of this prototypic carbon nitride precursor is nevertheless striking as well as instructive. Thus, the concept of creating suitably functionalized precursors must be re-considered, as it can obviously be reduced to the common intermediate melamine. As this  $\text{CN}_x$  species is commercially available and easy to handle, the lesson that can be learned from the precursor screening is to simply reduce the pool of precursors to their functional prototype melamine.

Although consequentially the search for suitable precursors may be greatly simplified, the thermal reactivity of melamine is somewhat “biased” by its triazine ring system as well as the presence of hydrogen atoms, which taken together may impede the formation of  $\text{g-C}_3\text{N}_4$ .

Alternative precursors may therefore be sought, which are either acyclic or hydrogen-free. Some of the most promising candidates for further research are displayed in Figure 8.1. For example, by preparing salts from the triazidocarbenium cation (**a**) [549–554] and the tricyanoguanidinate dianion (**b**) [555], both requirements – high nitrogen content and absence of hydrogen or elements other than C and N – would be met. Only the latter criterion is fulfilled for the isonitrile derivatives of melamine (**c**) and melem (**d**), whereas tricyanoamine (**e**) as well as the hexacyano-derivatives of melamine (**f**) and melem (**g**) exhibit the idealized formula  $\text{C}_3\text{N}_4$ , thus representing the molecular “monomeric” forms of the binary carbon

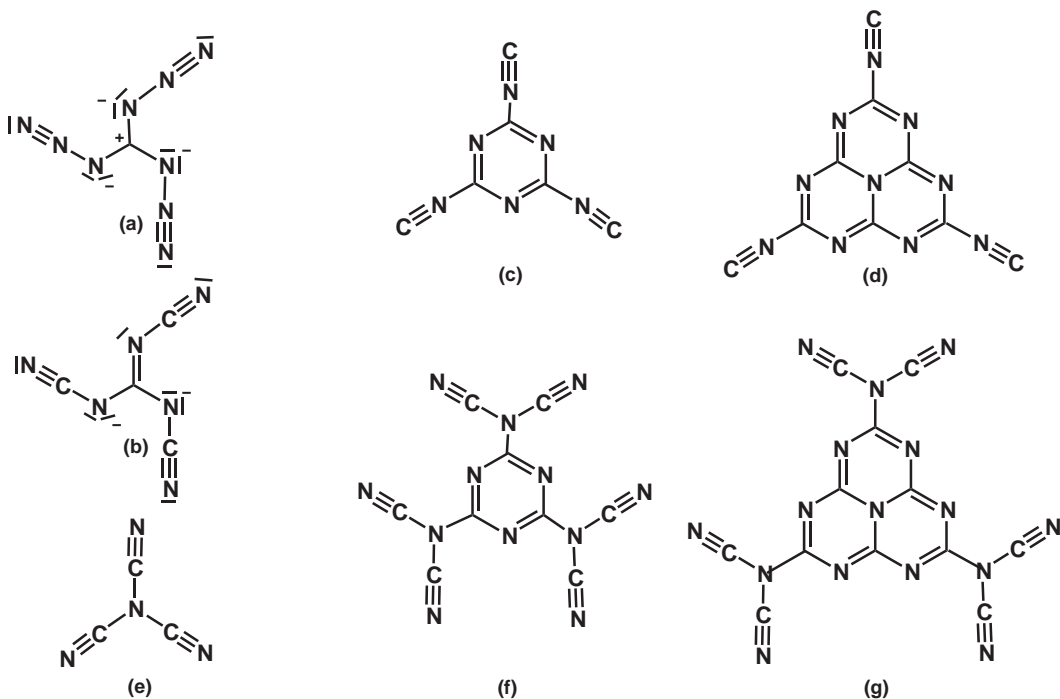


**Figure 8.1:** Hydrogen-free  $\text{CN}_x$  precursors: Triazidocarbonium cation (**a**) and tricyanoguanidinate dianion (**b**), isonitrile derivatives of melamine (**c**) and melem (**d**), tricyanoamine (**e**), hexacyano-derivatives of melamine (**f**) and melem (**g**).

nitride. The above species demonstrate that various types of precursors may be envisaged, which under thermal treatment or high-pressure conditions may give rise to the formation of hydrogen-free  $\text{C}_3\text{N}_4$ . However, it remains doubtful whether well-defined, crystalline materials will be obtained. Also, the challenge of safe and convenient handling of these compounds might be too high to pursue the commercial application of these systems.

Following the above thread, a natural consequence of simplifying the precursor screening to one single prototype, is the study of the thermal behavior of this very precursor – melamine – as was done in Chapter 6.

The pyrolysis of melamine and the identities of the intermediates has been a highly controversial issue during the past decades. Whereas the identity of the condensation product melem has been resolved recently [82, 240], the existence and, above all, molecular structures of the other conjectured intermediates, melam  $[(\text{H}_2\text{N})_2(\text{C}_3\text{N}_3)]_2\text{NH}$  and melon “[ $\text{C}_6\text{N}_7(\text{NH})(\text{NH}_2)]_n$ ”, have not been resolved as yet. However, owing to their prototypic carbon(IV) nitride backbones, clarifying the identities of these fundamental  $\text{CN}_x$  precursors may entail far-reaching implications for the structure and formation of  $\text{g-C}_3\text{N}_4$ .

The present work provides the missing links located in the intermediate temperature regime between the stability ranges of melamine and melem, respectively. The existence of melam

was proven and its crystal structure elucidated, while it was demonstrated that it is accessible only in small amounts and under ambient pressure conditions during melamine pyrolysis, presumably owing to its rapid successive transformation into melem.

Apart from clarifying the role of melam in the condensation cascade, the identities of two *true* intermediate phases were resolved, which are observed prior to the formation of melem between 590 and 650 K. The crystallographically distinct, metastable phases were identified as 2:1 and 1:2 adducts of melamine and melem, which consecutively form on depletion of melamine in the solid phase. Comparing the elemental composition of the 2:1 adduct with that of melam, one finds that the two are exactly identical. Therefore, it is strongly indicated that for decades the 2:1 co-crystallise of melamine and melem has been mistaken for melam owing to the misinterpretation of elemental analysis data.

Along these lines, the need for a detailed insight into reaction mechanisms on a molecular level, together with an understanding of the processes governing the interface between solid and gas phase, was demonstrated in the context of melam and adduct formation. Adjusting the reaction conditions is a vital issue and successfully led to the discovery of melam, which is not accessible when working in closed systems under the counter-pressure of ammonia.

Nevertheless, we could show that melam can alternatively be produced on a preparative scale by reacting melamine with acid salts and treating the resulting melamium salts with aqueous bases. As a result, melam hydrates with non-stoichiometric water content are formed, which can subsequently be dehydrated by thermal treatment. Though being largely unexplored as yet, some glimpses on the multi-faceted chemistry of melam could be given in the present work. Besides several crystalline melamium salts, melam-complexes such as the species  $Zn[C_6N_{11}H_9]Cl_2$  were synthesized, in which melam functions as a neutral bidentate ligand. It may be envisaged that melam could serve as a complex ligand in much the same way as its phosphorus analogue, which is presently being studied as a complex ligand for catalysis applications.

As the crystal structure of the adduct phases are not yet established, it is a major point of interest to resolve their structures, possibly by a combination of X-ray powder diffraction and real-space methods for structure solution. The latter have been successfully applied by elucidating the crystal structure of polycrystalline cyameluric acid and are particularly suited for compounds whose molecular building-blocks are well-established as in the present case.

As the intermediates occurring in the “low-temperature” regime of melamine thermolysis have been identified and characterized, Chapter 7 closes the last gap present in the otherwise complete account of the condensation cascade of melamine. Simultaneously, a link is provided between the historic roots of carbon nitride chemistry in the 19<sup>th</sup> century and the present

quest for graphitic carbon nitride.

The identity of the  $\text{CN}_x\text{H}_y$  polymer obtained by pyrolysis of melamine at 893 – 913 K was resolved by a concerted approach based on electron diffraction, solid-state NMR spectroscopy, and theoretical investigations. It was demonstrated that the material commonly associated with a hydrogen-contaminated graphitic carbon nitride material is in fact melon, a 1D polymer composed of NH-bridged heptazine rings first described by Liebig in 1834. Thus, melon represents a so far unique example of a structurally characterized polymeric carbon nitride material, and at the same time sheds new light on the present discussion regarding the identity and structure of graphitic carbon nitride. The nanocrystalline character of the material as well as the preponderance of 2D planar defects render structure elucidation particularly challenging and at the same time highlight the potential of electron diffraction as a tool for non-conventional structure analysis of disordered materials. However, a full, i. e. 3D account of the structure of melon seems only feasible by combining ED with spectroscopic methods and theoretical calculations. In particular, using force field calculations together with solid-state NMR experiments probing the through-space homo- or heteronuclear dipolar couplings may allow for the elucidation of the – either average or local – stacking sequence of the graphite-like layers. In addition, an extension of ED to electron microscopy may be advisable, taking however into account the sensitivity of carbon nitrides to damage caused by the electron beam. Thus, low-dose methods may be employed, and EELS experiments and simulations are a promising technique for probing the validity of the proposed structure model.

Although melon is obtained as the dominant species when adhering to the established synthetic procedure, side phases are observed by ED. These could be associated with different distorted variants and structural isomers of melon, oligomers with varying molecular masses, or even more highly condensed heptazine- or triazine-based species. It should be worthwhile focussing on the structure elucidation of such minority phases to gain a more complete picture of the bulk composition of “melon”.

Apart from further structural insights, the chemical potential of melon needs to be elaborated. On the one hand, the synthesis of intercalation compounds of melon may be thought of by analogy to the well-known graphite intercalates. In this respect, the reaction of melon with potassium or other alkali metals in liquid ammonia as solvent may show promise. On the other hand, melon or heptazine oligomers may have potential as complex ligands, which, however, could be limited by the obvious difficulties in finding an appropriate solvent. Thus, functionalizing the polymer, either by derivatization or by using protonated or deprotonated forms thereof, may be indispensable.

Besides its evident use as flame-retardant material, melon may show interesting properties as functional material in various fields, such as catalysis and surface science, and may even be tested as dye or chemically inert, conducting polymer after suitable doping or electrochemical treatment [556].

A major implication of the structure of melon is the extraordinary stability of the heptazine core at temperatures beyond 900 K, which seems to be an important criterion for challenging the commonly employed triazine-model of g-C<sub>3</sub>N<sub>4</sub>. Obviously, when starting from melamine, the stability range of the triazine core is limited by temperatures favoring the formation of melem. Models relying on extended triazine-based layers therefore have to be critically evaluated, if not entirely abandoned.

Although melon was found to be made up from planar layers, which owing to the sp<sup>2</sup>-hybridized carbon(IV) nitride backbone is somewhat akin to graphite, it is questionable whether sheets of fully condensed triazine or heptazine building-blocks will retain their planar topology. As has been shown by semiempirical structure optimizations of medium large cutouts of model structures, only partially condensed clusters with frequent NH and NH<sub>2</sub> layer terminations form planar sheets, whereas fully condensed layers tend to release strain by significantly corrugating. These findings may be relevant to the observed difficulties in preparing fully condensed, i. e. hydrogen-free carbon nitrides, and at the same time explain, why the formation of melon may be favored if hydrogen is present in the system. As a consequence, the use of hydrogenated precursors should be re-evaluated, as hydrogen may impede complete condensation of the monomers. Directing the focus on hydrogen-free precursors is again advisable, as are attempts to convert melon as well as hydrogen-free carbon nitride polymers into 3D modifications of C<sub>3</sub>N<sub>4</sub> under high-pressure conditions.

# Chapter 9

## Summary

This thesis provides a detailed account of the reactivity, structures and thermal behavior of a variety of different molecular carbon nitride precursor species. A brief summary of the different aspects touched on in this work is given below.

### 1. Dynamics and reactivity of ammonium dicyanamide $\text{NH}_4[\text{N}(\text{CN})_2]$ as probed by $^2\text{H}$ NMR and QNS / INS (Chapter 4, section 4.1 on page 71)

The model system ammonium dicyanamide  $\text{NH}_4[\text{N}(\text{CN})_2]$  and its deuterated analogue were synthesized by ion exchange reaction using  $\text{Na}[\text{N}(\text{CN})_2]$  and  $\text{NH}_4\text{Cl}$  in aqueous solution, and by repeated crystallization from  $\text{D}_2\text{O}$ , respectively. The temperature-dependent reorientational dynamics of the ammonium ion in  $\text{ND}_4[\text{N}(\text{CN})_2]$ , as well as the solid-state transformation of  $\text{ND}_4dca$  into  $dda$  was investigated *in situ* by means of  $^2\text{H}$  wide-line solid-state NMR spectroscopy and quasielastic neutron scattering between 5 and 390 K. The reorientational dynamics of the ammonium group was classified as an isotropic jump motion in a distorted tetrahedral potential with  $E_a$  in the order of 23.7 (QNS) – 25.8  $\text{kJ mol}^{-1}$  ( $^2\text{H}$  NMR) and an attempt frequency  $\tau_0^{-1}$  in the range 38 (QNS) – 435 THz ( $^2\text{H}$  NMR). INS measurements evaluated in the framework of the SPM support the energy characteristics of the jump process ( $23 \text{ kJ mol}^{-1}$ ), as well as the librational behavior of the protons ( $\phi_{Lib/2} = 14^\circ$ ) and furnish qualitative information on the phonon modes in the regime of lattice vibrations.

Line shape analysis of the deuteron spectra as well as  $^{14}\text{N}$  NMR suggest an increasing *asymmetric* distortion of the  $\text{ND}_4^+$  tetrahedron with increasing temperature, which roughly amounts to  $\Delta\gamma = 6^\circ$  and  $\Delta\epsilon = 0.5^\circ$  at RT. The static powder spectra exhibit three distinct QCCs of 161, 175 and 193 kHz with intensity ratios 1:2:1 and  $\eta = 0.02(1)$ , which was verified by a specially designed program capable of accounting for more than one input QCC.

Librational amplitudes of the deuterons observed between 10 and 380 K show a – likely model-dependent – larger spread according to NMR (5 – 26°) as compared to QNS and neutron diffraction (7 – 13°). Correlation times  $\tau$  between  $10^{-3}$  and  $10^{-11}$ , obeying an Arrhenius-like temperature dependence characteristic of thermally activated single particle jump processes, were established by  $T_1$  relaxation measurements. The time scale of the jump frequencies indicates the possible coupling of the reorientational motion with the lattice modes. Thus, it provides a potential reaction trajectory for the instantaneous detachment of the deuteron and transfer to the anion as required by the transformation of  $\text{ND}_4\text{dca}$  into  $\text{dda}$ . The high-temperature regime was probed by both  $^2\text{H}$  NMR and QNS, both of which suggest the evolution of ammonia at  $T \geq 372$  K during the course of the transformation onset. The heterogeneous  $^2\text{H}$  spectra were deconvoluted and the temperature-dependent liberation of ammonia was monitored at 372, 375, 378, and 380 K. The transformation proceeds in a two-step fashion involving the fast liberation of  $\text{ND}_3$  and the slow “re-integration” of ammonia into the sample. The extent of completion of the latter step, dependent on both temperature and pressure, is vital to the quantitative conversion of  $\text{ND}_4\text{dca}$  into  $\text{dda}$ .

## 2. Crystal structure and thermal reactivity of ammonium cyanoureate $\text{NH}_4[\text{H}_2\text{NC}(=\text{O})\text{NCN}]$ (Chapter 4, section 4.2 on page 105)

The ammonium salt of cyanourea ( $P2_1/c$ ,  $a = 388.95(8)$  pm,  $b = 1121.0(2)$  pm,  $c = 1096.4(2)$  pm,  $\beta = 92.57(3)$ °,  $V = 477.5(2) \times 10^6$  pm $^3$ ,  $T = 140$  K,  $R1 = 0.0297$ ,  $wR2 = 0.0769$ ) was synthesized *via* an acid-base route from the parent acid. It undergoes a non-topochemical transformation at  $T \geq 355$  K, which despite its complexity proceeds in the solid phase. Competing reaction pathways have been identified by thermal analysis, vibrational spectroscopy, solution NMR and mass spectrometry. Typically, a microcrystalline product mixture is afforded with the main products being urea  $\text{H}_2\text{NC}(=\text{O})\text{NH}_2$  and cyanoguanylurea  $\text{H}_2\text{NC}(=\text{O})\text{NHC}(\text{NH}_2)\text{NCN}$ , or the isomeric compound ammeline ( $\text{C}_3\text{N}_3$ ) $(\text{NH}_2)_2(\text{OH})$ , depending on the reaction conditions. Small amounts of guanidinium cyanoureate  $[\text{C}(\text{NH}_2)_3][\text{H}_2\text{NC}(=\text{O})\text{NCN}]$  and (1-cyanoguanyl-3-guanyl)urea  $(\text{H}_2\text{N})_2\text{NC}(=\text{O})\text{NHC}(\text{NH}_2)\text{NCN}$  have been identified as side products, resulting from consecutive reactions of the intermediate cyanamide with either ammonia or cyanoguanylurea. The thermal reactivity of ammonium cyanoureate fundamentally differs from that of its formal “dehydration product” ammonium dicyanamide. This observation was tentatively correlated with the differing hydrogen bonding network, resulting in a more facile release of ammonia, and with the altered reactivity of the anion due to the presence of an electrophilic amide carbon.

**3. Catalytic formation and crystal structure of cyanoguanylurea  $\text{H}_2\text{NC}(=\text{O})\text{NHC}(\text{NH}_2)\text{NCN}$  from ammonium cyanoureat  $\text{NH}_4[\text{H}_2\text{NC}(=\text{O})\text{NCN}]$  (Chapter 4, section 4.2.4 on page 121)**

The ion exchange reaction between ammonium cyanoureat  $\text{NH}_4[\text{H}_2\text{NC}(=\text{O})\text{NCN}]$  and zinc chloride yields single crystals of the urea derivative cyanoguanylurea  $\text{H}_2\text{NC}(=\text{O})\text{NHC}(\text{NH}_2)\text{NCN}$ . It is obtained as a by-product alongside zinc cyanoureat and traces of ammonium chloride, which may act as a mineralizing agent. It is assumed that owing to its Lewis and Brønsted acidity, the hydrated  $\text{Zn}^{2+}$  ions act as catalyst, promoting the degradation of the cyanoureat anion with subsequent formation of cyanoguanylurea. The crystal structure ( $P2_1/n$ ,  $a = 476.7(1)$  pm,  $b = 965.3(2)$  pm,  $c = 1165.6(2)$  pm,  $\beta = 97.75(3)^\circ$ ,  $V = 531.4(2) \cdot 10^6$  pm $^3$ ,  $T = 200$  K,  $R1 = 0.0357$ ,  $wR2 = 0.0964$ ) is made up from non-planar cyanoguanylurea molecules with a dicyandiamide-type C–N system. This can only be adequately described by invoking the contribution of several charge separated structures in addition to the neutral prototype structure with a conjugated  $\pi$ -system. The molecular structure is fully consistent with that proposed for the main product of the decomposition of ammonium cyanoureat on the basis of IR and NMR spectroscopic data.

**4. Crystal structures of two polymorphs of guanidinium dicyanamide  $\text{C}(\text{NH}_2)_3[\text{N}(\text{CN})_2]$  and their thermal conversion into melamine (Chapter 5, section 5.2 on page 135)**

Two modifications of guanidinium dicyanamide were synthesized by means of ion-exchange reaction in aqueous or methanolic solution. The hygroscopic compounds were characterized by solution-state NMR, mass spectrometry and vibrational spectroscopy. The crystal structures of the polymorphs ( $\beta$ -form:  $Pna2_1$ ,  $a = 1373.1(3)$  pm,  $b = 495.5(1)$  pm,  $c = 1802.9(4)$  pm,  $V = 1226.7(4) \cdot 10^6$  pm $^3$ ,  $R1 = 0.0423$ ,  $wR2 = 0.0967$ ;  $\alpha$ -form:  $P2_1/c$ ,  $a = 1924.9(4)$  pm,  $b = 496.0(1)$  pm,  $c = 1372.4(3)$  pm,  $\beta = 110.46(3)^\circ$ ,  $V = 1227.5(4) \cdot 10^6$  pm $^3$ ,  $R1 = 0.0474$ ,  $wR2 = 0.1118$ ) were found to be largely equivalent in terms of the overall assembly of the molecular ions. While both modifications are obtained at room temperature, the  $\beta$ -form slowly transforms into the  $\alpha$ -polymorph at temperatures between 303 – 325 K, however, detection of the reverse transformation failed. Both polymorphs melt around 430 K and recrystallize in the form of the isomeric compound melamine  $\text{C}_3\text{N}_3(\text{NH}_2)_3$  at  $\approx 400$  K, which serves as yet another acknowledgement of the thermal reactivity of dicyanamides inferred by previous model studies of ammonium dicyanamide.

**5. Crystal structure and thermal behavior of melaminium dicyanamide hydrate  $\text{C}_3\text{N}_3(\text{NH}_2)_3[\text{N}(\text{CN})_2]\cdot\text{H}_2\text{O}$  (Chapter 5, section 5.3 on page 148)**

Melaminium dicyanamide ( $C2/c$ ,  $a = 2735.5(6)$  pm,  $b = 364.43(7)$  pm,  $c = 1884.1(4)$  pm,  $\beta = 103.17(3)^\circ$ ,  $V = 1828.9(6) \cdot 10^6$  pm $^3$ ,  $T = 150$  K,  $R1 = 0.0504$ ,  $wR2 = 0.0977$ ) was prepared by metathesis reaction in aqueous or methanolic solution. Two competing thermal transformation pathways were discovered, which can be distinguished by the role of crystal water when working in closed systems, the latter leading to the formation of HNCO as a by-product. The major transformation reaction is initiated by a proton transfer from the melaminium cation to the anion with subsequent polymerization of the latter and thermal transformation of the as-formed melamine to melem and polymeric CN $_x$  species.

**6. Crystal structure and thermal conversion of guanylurea dicyanamide  $[(\text{H}_2\text{N})\text{C}(=\text{O})\text{NHC}(\text{NH}_2)_2][\text{N}(\text{CN})_2]$  into prototype CN $_x$  precursors (Chapter 5, section 5.4 on page 157)**

Guanylurea dicyanamide ( $C2/c$ ,  $a = 2249.0(5)$  pm,  $b = 483.9(1)$  pm,  $c = 1382.4(3)$  pm,  $\beta = 99.49(3)^\circ$ ,  $V = 1483.8(5) \cdot 10^6$  pm $^3$ ,  $T = 130$  K,  $R1 = 0.0352$ ,  $wR2 = 0.0758$ ) was synthesized by ion exchange reaction in aqueous solution starting from Nadca and guanylurea sulfate. Upon heating, a sequence of thermally induced addition, cyclization and elimination reactions is observed at temperatures  $T \geq 390$  K. Melamine is formed with concomitant loss of HNCO by a cyclization reaction following a pattern analogous to that observed for the thermal conversion of both ammonium dicyanamide and guanidinium dicyanamide into melamine. The transformation proceeds *via* addition of the nucleophilic component guanylurea after an initial proton transfer to the electrophile dicyanamide, followed by a 1,3-H-shift and a second nucleophilic addition leading to a ring closure reaction and subsequent proton rearrangement. Further condensation of melamine yields the prototypic CN $_x$  precursor melem, which alongside varying amounts of directly formed CN $_x$ H $_y$  material transforms into layered CN $_x$ H $_y$  phases without significant integration of oxygen into the core framework. The observed mode of reaction may be generalized with respect to the formation of volatile compounds such as HNCO during thermal decomposition, thereby rendering a large variety of previously not considered molecular compounds possible CN $_x$  precursors.

## 7. Crystal structures and thermal behavior of non-metal tricyanomelamines (Chapter 5, section 5.6 on page 170)

The first non-metal tricyanomelamines were synthesized *via* ion exchange reactions in aqueous solution and characterized by means of single-crystal X-ray diffraction, vibrational and solid-state NMR spectroscopy. Three forms of ammonium tricyanomelamine were obtained starting from similar synthesis conditions, of which two species were structurally characterized. Single-crystal X-ray diffraction of the metastable hydrated form  $[\text{NH}_4]_2[\text{C}_6\text{N}_9\text{H}] \cdot 2\text{H}_2\text{O}$  (**1a**) ( $C2/c$ ,  $a = 3181.8(6)$  pm,  $b = 360.01(7)$  pm,  $c = 2190.4(4)$  pm,  $\beta = 112.39(3)^\circ$ ,  $V = 2319.9(8) \cdot 10^6$  pm $^3$ ,  $T = 130$  K,  $R1 = 0.0368$ ,  $wR2 = 0.0923$ ) reveals cation / solvent disorder involving one ammonium ion and water molecule each, which are statistically (fraction 0.53(2) / 0.47(2)) distributed on two inequivalent sites. The disorder scenario was substantiated by means of  $^{15}\text{N}$  solid-state NMR. The ammonium-TCM hydrate loses crystal water when exposed to air under ambient conditions, transforming within days into the thermodynamically stable, non-hydrated species  $[\text{NH}_4]_2[\text{C}_6\text{N}_9\text{H}]$  (**1**) ( $P2_1/c$ ,  $a = 1060.8(2)$  pm,  $b = 1146.2(2)$  pm,  $c = 913.3(2)$  pm,  $\beta = 112.36(3)^\circ$ ,  $V = 1027.0(4) \cdot 10^6$  pm $^3$ ,  $T = 200$  K,  $R1 = 0.0295$ ,  $wR2 = 0.0680$ ).

Whereas all other tricyanomelamines exhibit monoprotonated anions, guanidinium-TCM  $[\text{C}(\text{NH}_2)_3]_3[\text{C}_6\text{N}_9] \cdot 2\text{H}_2\text{O}$  (**2**) ( $P2_12_12_1$ ,  $a = 762.1(2)$  pm,  $b = 1333.6(3)$  pm,  $c = 1856.6(4)$  pm,  $V = 1887.0(7) \cdot 10^6$  pm $^3$ ,  $T = 200$  K,  $R1 = 0.0253$ ,  $wR2 = 0.0652$ ) possesses a non-protonated anionic core. Two different melamine tricyanomelamines were obtained from solutions with different concentration of the starting materials sodium tricyanomelamine and melaminium sulfate. Whereas  $[\text{C}_3\text{N}_6\text{H}_7]_2[\text{C}_6\text{N}_9\text{H}] \cdot 2.4\text{H}_2\text{O}$  (**3**) ( $\text{P}\bar{1}$ ,  $a = 1029.5(2)$  pm,  $b = 1120.3(2)$  pm,  $c = 1120.7(2)$  pm,  $\alpha = 104.22(3)^\circ$ ,  $\beta = 112.74(3)^\circ$ ,  $\gamma = 104.62(3)^\circ$ ,  $V = 1064.8(4) \cdot 10^6$  pm $^3$ ,  $T = 200$  K,  $R1 = 0.0570$ ,  $wR2 = 0.1230$ ) exhibits a layered structure with the solvent water loosely embedded and disordered,  $[\text{C}_3\text{N}_6\text{H}_7]_2[\text{C}_6\text{N}_6\text{H}_6][\text{C}_6\text{N}_9\text{H}] \cdot 2\text{H}_2\text{O}$  (**3a**) ( $P2_1/c$ ,  $a = 674.7(5)$  pm,  $b = 1123.6(5)$  pm,  $c = 3400.2(5)$  pm,  $\beta = 95.398(5)^\circ$ ,  $V = 2566(2) \cdot 10^6$  pm $^3$ ,  $T = 200$  K,  $R1 = 0.0470$ ,  $wR2 = 0.0983$ ) is characterized by a 3D array of 1D strands made up from TCM anions as well as monoprotonated melaminium cations and neutral melamine molecules.

Particular emphasis has been placed on the elucidation of the thermal reactivity of **1**, **2**, and **3** by means of thermal analysis, vibrational and NMR spectroscopy, as well as temperature dependent X-ray powder diffraction. Upon heating, ammonium and guanidinium tricyanomelamine uniformly pass the crystalline, heptazine-based intermediate melem, which ultimately decomposes forming melon at 770 K. Though being entirely triazine-based with potentially reactive electrophilic *and* nucleophilic sites, identical pyrolysis products are

obtained for the melaminium salt after passing an intermediate, possibly cross-linked phase at low temperatures. The thermodynamically favored formation of melem therefore seems to be the driving force dominating the thermal reactivity of the TCM precursors in the high-temperature regime, suggesting that in general purely triazine-based structures become unstable and essentially yield layered compounds made up from heptazine building blocks.

#### **8. Melamine–Melem adducts (Chapter 6, section 6.3 on page 203)**

Contrary to previous reports, the formation of melam or melem as the first condensation products of the starting material melamine could not be verified by pyrolyzing melamine in closed or semi-closed systems. Instead, the major decomposition pathway yields two crystallographically distinct adduct phases made up from neutral melamine and melem molecules with distinct compositions  $[C_3N_3(NH_2)_3]_2[C_6N_7(NH_2)_3]$  (I) and  $[C_3N_3(NH_2)_3][C_6N_7(NH_2)_3]_2$  (II). The co-crystallisates were identified by means of elemental analysis, solution-state NMR, vibrational spectroscopy and mass spectrometry and were found to be stable between 590 and 650 K, after which temperature adduct II transforms into melem. According to solid-state NMR investigations and dissolution / extraction studies, the homogeneous phases are made up by hydrogen-bonded arrays of neutral melamine and melem molecules rather than salts originating from chemical reactions of the components (acid-base reactions). Accordingly, the DMSO solutions of the adduct phases are identical to the solutions of 2 : 1 and 1 : 2 mixtures of melamine and melem, respectively. The significant decrease in yield of adduct II (30 – 35 %) as compared to I (60 – 70 %) strongly suggests that the transformation from phase I into II is simply a consequence of melamine sublimation, which is continuously removed from the solid, leaving behind metastable adducts in equilibrium with gas phase melamine. Elemental analysis data of adduct I (obs. (theor.) N, 65.93 (65.53); C, 30.56 (30.64); H, 3.63 (3.83)) not only corroborate the inferred composition, but also demonstrate that the latter is identical to that expected for melam.

#### **9. Melam [ $C_6N_{11}H_9$ ] (Chapter 6, section 6.4 on page 213)**

The existence and formation of the carbon nitride precursor melam ( $H_2N_2(C_3N_3)NH(C_3N_3)(NH_2)_2$ ) has been disclosed by studying the complex thermal condensation of melamine under varying reaction conditions. At ambient pressure small amounts of melam single crystals can be isolated, which may either be considered as a *side product* of melamine condensation, or are rapidly consumed by successive transformation into melem. Melam was characterized by single-crystal X-ray diffraction, *in situ* X-ray powder diffraction, vibrational spectroscopy, mass spectrometry and solid-state NMR spectroscopy.

$^{13}C$  chemical shifts are observed at 164.0 and 167.2 ppm; the  $^{15}N$  CP-MAS spectrum exhibits  $N_{tert}$  signals between – 190.0 and – 205.9 ppm, two NH signals at – 252.0 and – 254.8 ppm, and five NH<sub>2</sub> signals at – 282.8, – 286.0, – 288.9, – 295.0, and – 300.4 ppm. The CN<sub>x</sub> precursor melam ( $C2/c$ ,  $a = 1811.0(4)$  pm,  $b = 1086.7(2)$  pm,  $c = 1398.4(3)$  pm,  $\beta = 96.31(3)^\circ$ ,  $V = 2735.3(9) \cdot 10^6$  pm<sup>3</sup>,  $T = 130$  K,  $R1 = 0.0350$ ,  $wR2 = 0.0926$ ) adopts a ditriazinylamine-type structure with a twisted conformation about the bridging NH moiety. Therefore, the non-conjugated tautomeric form, made up from two non-protonated triazine rings, was shown to be the prevailing species in the solid state. The molecules are connected *via* medium strong hydrogen bonds (D · · · A: 297 – 333 pm). No pronounced  $\pi$ -stacking is observed, reflected by a screw-like arrangement of the molecules, giving rise to a 3D network of mutually tilted melam molecules. Melam transforms into melem at 640 K without passing through the melt. Though being accessible from melamine only with difficulties, melam can be produced on a preparative scale by reacting melamine with acid salts and treating the resulting melamium salts with aqueous bases, upon which melam hydrates are formed.

#### 10. Melam derivatives (Chapter 6, section 6.5 on page 226)

Several melam derivatives were synthesized *via* solution and solid-state reactions and characterized by means of vibrational spectroscopy, mass spectrometry and solid-state NMR spectroscopy. The melam solvates “[C<sub>6</sub>N<sub>11</sub>H<sub>9</sub>] · 2 H<sub>2</sub>O” and [C<sub>6</sub>N<sub>11</sub>H<sub>9</sub>] · 2 O=S(CH<sub>3</sub>)<sub>2</sub> were obtained by treatment of [C<sub>6</sub>N<sub>11</sub>H<sub>10</sub>]Cl · 0.5 NH<sub>4</sub>Cl with aq. NH<sub>3</sub> and by recrystallization of melam hydrate in DMSO, respectively. Crystalline melam salts were obtained as monohydrates by reacting melam hydrate with diluted hydrochloric and hydrobromic acid. The crystal structures of both compounds are isotypic ( $P2_1/c$ ) with lattice parameters  $a = 6.1064(12)$  pm,  $b = 7.8157(16)$  pm,  $c = 24.518(5)$  pm,  $\beta = 93.67(3)^\circ$ ,  $V = 1167.8(4) \cdot 10^6$  pm<sup>3</sup> ([C<sub>6</sub>N<sub>11</sub>H<sub>10</sub>]Cl · H<sub>2</sub>O) and  $a = 6.1114(5)$  pm,  $b = 7.9362(6)$  pm,  $c = 25.231(2)$  pm,  $\beta = 93.89(1)^\circ$ ,  $V = 1220.9(6) \cdot 10^6$  pm<sup>3</sup> ([C<sub>6</sub>N<sub>11</sub>H<sub>10</sub>]Br · H<sub>2</sub>O), both crystallizing as pseudo-merohedral twins with significant reflection overlap. Unlike pure melam, the monoprotonated melam cations are planar within experimental error.

The salt melamium diperchlorate C<sub>6</sub>N<sub>11</sub>H<sub>11</sub>(ClO<sub>4</sub>)<sub>2</sub> · 2 H<sub>2</sub>O ( $C2/c$ ,  $a = 1747.8(4)$  pm,  $b = 1148.2(2)$  pm,  $c = 993.6(2)$  pm,  $\beta = 118.79(3)^\circ$ ,  $V = 1747.4(6) \cdot 10^6$  pm<sup>3</sup>,  $T = 130$  K,  $R1 = 0.0400$ ,  $wR2 = 0.1009$ ) was obtained from reaction of melam hydrate with perchloric acid in aqueous solution. It crystallizes as a dihydrate with the oxygen atom of a crystal water on a split position and only one triazine ring in the asymmetric unit. The protons are approximately equally distributed about four ring nitrogen atoms, such that in total two protons are attached to the rings, yielding a planar melam core.

A  $\text{ZnCl}_2$ -melam complex was synthesized from melamine and  $\text{ZnCl}_2$  in closed Duran-ampoules between 593 and 703 K. In the neutral complex  $\text{Zn}[\text{C}_6\text{N}_{11}\text{H}_9]\text{Cl}_2$  ( $P2_1/c$ ,  $a = 743.00(15)$  pm,  $b = 2233.2(5)$  pm,  $c = 762.5(2)$  pm,  $\beta = 99.86(3)^\circ$ ,  $V = 1246.5(4) \cdot 10^6$  pm $^3$ ,  $T = 200$  K,  $R1 = 0.0306$ ,  $wR2 = 0.0697$ ), melam acts as a symmetrically bent bidentate ligand, which is coordinated to the Lewis acid Zn-site *via* two ring nitrogen atoms.

In analogous solid-state reactions, Fe-, Al-, and Cu-melam species were obtained, which were characterized by vibrational and solid-state NMR spectroscopy. Although no crystal structures were available, the Fe- and Cu-melam species are most likely based on neutral melam ligands, whereas the Al-species contains a monoprotonated melamium cation.

### 11. Ammeline salts (Chapter 6, section 6.6 on page 263)

The salts ammelinium chloride  $[\text{C}_3\text{H}_6\text{N}_5\text{O}]\text{Cl}$ , ammelinium bromide  $[\text{C}_3\text{H}_6\text{N}_5\text{O}]\text{Br}$ , and ammelinium nitrate  $[\text{C}_3\text{H}_6\text{N}_5\text{O}]\text{NO}_3$  were obtained by hydrolysis of melam hydrate with the respective concentrated mineral acids. The structures of the molecular salts were elucidated by single-crystal X-ray diffraction and vibrational spectroscopy, thereby representing the first examples of structurally characterized ammeline derivatives. All ammeline salts crystallize in the monoclinic space group  $P2_1/c$  with 4 formula units in the unit cell. The hydrochloride ( $a = 535.4(2)$  pm,  $b = 1467.3(3)$  pm,  $c = 815.2(2)$  pm,  $\beta = 90.00(3)^\circ$ ,  $V = 640.4(2) \cdot 10^6$  pm $^3$ ,  $T = 293$  K,  $R1 = 0.0325$ ,  $wR2 = 0.0690$ , twin fraction 0.845(2) / 0.155(2)), hydrobromide ( $a = 521.2(1)$  pm,  $b = 883.1(2)$  pm,  $c = 1457.7(3)$  pm,  $\beta = 98.97(3)^\circ$ ,  $V = 662.7(2) \cdot 10^6$  pm $^3$ ,  $T = 130$  K,  $R1 = 0.0349$ ,  $wR2 = 0.0780$ ), and nitrate salt ( $a = 933.2(2)$  pm,  $b = 625.6(2)$  pm,  $c = 1351.1(3)$  pm,  $\beta = 108.05(3)^\circ$ ,  $V = 750.0(3) \cdot 10^6$  pm $^3$ ,  $T = 130$  K,  $R1 = 0.0301$ ,  $wR2 = 0.0789$ ) all contain planar, mono-protonated ammelinium cations which are hydrogen-bonded to the respective halide or nitrate anions. The non-isotypic structures are composed of anion–cation arrays forming either planar (chloride) or corrugated (nitrate) layers, or strands with differing stacking sense (bromide). The keto tautomer with  $C_{2v}$  symmetry is representing the actual proton distribution rather than the hydroxy tautomer.

### 12. Melaminium dinitrate (Chapter 6, section 6.7 on page 274)

The potential high-energy-density material melaminium dinitrate ( $P2_1/c$ ,  $a = 783.63(16)$  pm,  $b = 988.9(2)$  pm,  $c = 1351.1(3)$  pm,  $\beta = 100.43(3)^\circ$ ,  $V = 931.8(3) \cdot 10^6$  pm $^3$ ,  $\rho = 1.798$  g cm $^{-3}$ ,  $T = 200$  K,  $R1 = 0.0398$ ,  $wR2 = 0.0971$ ) was obtained as a by-product when heating an aqueous suspension of melam perchlorate at 333 K and adding conc. nitric acid. The compound is made up from planar, doubly protonated melaminium cations and nitrate ions, which form a layered arrangement with a short interlayer spacing of 334 pm.

**13. Melon (Chapter 7 on page 280)**

Chapter 7 presents the first structure elucidation of a polymeric carbon nitride material by ED, solid-state NMR and *ab initio* DFT calculations.

When heating melamine under pressure equalization, a yellowish, poorly crystalline material is obtained, which is tentatively associated with a heptazine-based oligomer, likely a dimer of melem. By heating melamine in sealed quartz ampoules at 903 K for 12 – 24 h, a brownish material is obtained with an average composition “C<sub>3</sub>N<sub>4.4</sub>H<sub>1.8</sub>”. The X-ray powder pattern is dominated by a sharp reflection corresponding to  $d = 319$  pm, and several broad peaks of asymmetric shape indicative of 2D planar defects. The <sup>1</sup>H solid-state NMR spectrum shows a broad resonance peaking at  $\approx 9$  ppm; in the <sup>13</sup>C CP-MAS NMR spectrum two signals centered at 164 and 157 ppm are observed. <sup>15</sup>N signals of the <sup>15</sup>N-labelled compound are located between –177 and –195 ppm (N<sub>tert</sub>), –225 ppm (N<sub>c</sub>), –245 ppm (NH) and –265 ppm (NH<sub>2</sub>), where the assignment was carried out based on a CPPI experiment. <sup>15</sup>N direct excitation yields signal intensities N<sub>tert</sub>:N<sub>c</sub>:NH:NH<sub>2</sub> of roughly 7.4:1.1:1.0:1.0. According to a *fp*-RFDR experiment using selective excitation of the NH<sub>2</sub> signal, the sample appears to be single-phase, as exchange is observed between *all* <sup>15</sup>N nuclei in the sample.

Nanometer-sized crystals with domains exhibiting different degrees of crystallinity were observed by TEM and ED. Diffraction patterns of the *hk0* plane show a pseudo-hexagonal intensity distribution and were indexed on an orthorhombic cell with  $a = 1670$  pm,  $b = 1240$  pm,  $c = 320$  pm. Structure solution in projection was successfully carried out based on ED data (plane group *p2gg*,  $R1 = 26.44\%$ ,  $wR2 = 27.72\%$  after refinement;  $R_{rim} = 40.1\%$ ), revealing *planar* heptazine strands connected *via* NH-bridges and arranged in a zig-zag-type fashion. The structure model (metrics, planarity) was independently verified and extended with respect to the most likely hydrogen positions by semiempirical, DFT / plane wave calculations under periodic boundary conditions, and by force field calculations. The dominant stacking sequence of the layers cannot be determined from ED; however, force field calculations suggest the energetically most favorable layer stacking to occur with an offset of adjacent layers. An additional confirmation of the structural model was furnished by calculation of the *ab initio* <sup>15</sup>N and <sup>13</sup>C NMR parameters for the DFT optimized cell, which support the signal assignments based on the CPPI experiment.

Different crystalline side-phases detected by ED besides melon suggest the formation of more highly condensed phases as well as distortion variants of the melon structure, or domains with different stacking variants. The latter were partially addressed by simulation of the kinematical diffraction patterns of 3D model structures; however, no convincing model was found as yet.

The structure elucidation of this  $\text{CN}_x\text{H}_y$  polymer, which represents the ultimate pre-stage of graphitic carbon nitride, resolves the long-standing debate on the identity of Liebig's inert compound "melon", whose existence has now been proven. The similarity to graphite expressed by its planar layered arrangement is complemented by an exceptional thermal and chemical stability, which may render melon a promising functional material in catalysis or surface science.

# Chapter 10

## Appendix

### 10.1 Syntheses

The synthesis procedures which have not been dealt with in detail in the respective chapters are listed in the following. In addition, some analytical data are given where appropriate.

#### 10.1.1 Ammonium Dicyanamide $\text{NH}_4[\text{N}(\text{CN})_2]$

$\text{NH}_4[\text{N}(\text{CN})_2]$  was prepared by ion exchange in aqueous solution. An aqueous solution (1 – 2.5 M) of  $\text{NH}_4\text{Cl}$ , corresponding to 3 – 7 times the theoretical exchange capacity, was given on a column containing an ion exchange resin in strongly acidic form (Ionenaustauscher I,  $\text{H}^+$ -Form). The  $\text{H}^+/\text{NH}_4^+$  exchange was considered to be complete when the pH of the eluate reached that of a saturated  $\text{NH}_4\text{Cl}$  solution (pH 4 – 5). Subsequently, the exchange resin was washed thoroughly with deionized water and the removal of excess chloride was substantiated by the  $\text{AgNO}_3$  method. To provide the counter ion, a solution containing  $\text{Na}[\text{N}(\text{CN})_2]$  (0.5 M) was passed through the column and the eluate, which was evaporated at room temperature, gave colorless, needle-shaped crystals (yield  $\geq 99\%$ ).

#### 10.1.2 $\text{ND}_4[\text{N}(\text{CN})_2]$

The deuteration of ammonium dicyanamide was effected by dissolving  $\text{NH}_4[\text{N}(\text{CN})_2]$  (3.0 g) in  $\text{D}_2\text{O}$  (20 mL) and stirring the colorless solution under argon at 313 K for 1 h. After drying the product in vacuo the procedure was repeated twice and the white powdered product stored under argon.

### 10.1.3 Ammonium Cyanoureate $\text{NH}_4[\text{H}_2\text{NC}(=\text{O})\text{NCN}]$

Ammonium cyanoureate was synthesized by neutralisation of the free acid cyanourea with aqueous ammonia. Typically, to 500 mg ( $5.9 \cdot 10^{-3}$  mol) cyanourea were added 1 – 3 mL ( $13.3 \cdot 10^{-3}$  mol) conc.  $\text{NH}_3$  solution (25 %) and the white suspension was dissolved in 12 mL water ( $\text{pH} = 9 – 10$ ) and stirred for one hour. Afterwards the solution was filtered and left for crystallisation by slow evaporation. Cyanourea was synthesized by loading 8.0 g ( $50.6 \cdot 10^{-3}$  mol) urea-phosphate on a strongly acidic ion exchange resin (Ionenaustauscher I,  $\text{H}^+$ -Form), washing the resin with water and passing a solution (0.5 M) of 1.0 g ( $11.2 \cdot 10^{-3}$  mol) sodium dicyanamide  $\text{Na}[\text{N}(\text{CN})_2]$  through the column. As a result, the dicyanamide was converted into cyanourea by acid hydrolysis without ion exchange taking place. A more convenient and direct synthesis for cyanourea, however, is the alkaline hydrolysis of dicyandiamide in boiling  $\text{NaOH}$  (3M) solution for 2 hours.

$^1\text{H}$  NMR (400.0 MHz,  $\text{DMSO-d}_6$ ):  $\delta = 5.3$  ppm (s, 2H,  $\text{NH}_2$ ), 7.2 ppm (s, 4H,  $\text{NH}_4$ );  $^{13}\text{C}\{^1\text{H}\}$  NMR (100.5 MHz,  $\text{DMSO-d}_6$ ):  $\delta = 123.5$  ppm ( $\text{C}\equiv\text{N}$ ), 167.0 ppm ( $\text{C}=\text{O}$ ); MS (FAB $^-$ , 6 kV):  $m/z$  (%) = 84 (11)  $[\text{H}_2\text{NC}(=\text{O})\text{NCN}]^-$ .

### 10.1.4 Cyanoguanylurea $\text{H}_2\text{NC}(=\text{O})\text{NHC}(\text{NH}_2)\text{NCN}$

Cyanoguanylurea was synthesized quantitatively by constantly stirring 706 mg ( $6.9 \cdot 10^{-3}$  mol) of ammonium cyanoureate with 196 mg ( $2.3 \cdot 10^{-3}$  mol) of cyanourea in 15 mL water at 308 K. After 3 – 4 days, the white product commenced to precipitate, yet the reaction was sustained for another 4 – 5 days and the insoluble product isolated by filtration. In order to increase the yield, 100 mg cyanourea was added to the filtrate and the mixture again subjected the above reaction conditions.

Cyanoguanylurea was also obtained as a side product in the synthesis of the zinc salt of cyanourea from ammonium cyanoureate (for synthesis of the latter, see above) by ion metathesis in aqueous solution. A column filled with 3 mL of a strongly acidic ion exchange resin (Ionenaustauscher I,  $\text{H}^+$ -Form) was loaded with 20 mL of an aqueous solution containing 4.2 g of  $\text{ZnCl}_2$ . After washing with 200 mL of water, 12 mL of an aqueous solution of 0.2 g ammonium cyanoureate was poured onto the column. The eluate was evaporated at room temperature. Besides the polycrystalline main product, cyanoguanylurea was obtained as a minor phase along with traces of ammonium chloride.

### 10.1.5 Guanidinium Dicyanamide $[\text{C}(\text{NH}_2)_3][\text{N}(\text{CN})_2]$

Guanidinium dicyanamide was prepared by ion exchange reaction in aqueous or methanolic solution. Several guanidinium salts, among which were guanidine hydrochloride  $[\text{C}(\text{NH}_2)_3]\text{Cl}$ ,

guanidine acetate  $[C(NH_2)_3]C_2H_3O_2$  and guanidine nitrate  $[C(NH_2)_3]NO_3$ , have been tested as starting materials, yielding similar results. Typically, an aqueous solution of the guanidine salt (1 M), corresponding to 1.5 times the theoretical ion exchange capacity, was poured onto a column containing 20 mL of a strongly acidic ion exchange resin (Ionenaustauscher I,  $H^+$ -Form). After washing the resin with water (2 – 3 l), a solution of sodium dicyanamide  $Na[N(CN)_2]$  (0.5 M, 0.5 times the theoretical exchange capacity) was given onto the column. The eluate yielded a strongly hygroscopic white product after evaporation of the water. After re-loading the column with HCl solution (1 M) and cation substitution by means of the respective guanidine salt, the product was purified from residual sodium dicyanamide by dissolving it in little water and repeating the ion exchange reaction. The aqueous product solution was concentrated at room temperature and the deliquescent product either dried under vacuum or slowly crystallized using KOH platelets as water extracting agent. To this end, a bent glass tube filled with KOH and the product in one part each, was slightly evacuated, yielding a glassy dry product within days which was stored under argon. It was observed, however, that evaporating the aqueous solution in a beaker open to the atmosphere yielded crystals whose moisture presumably depend on atmospheric conditions such as temperature and relative humidity. Crystals of  $\beta$ - $[C(NH_2)_3][N(CN)_2]$  suitable for single-crystal X-ray diffraction were obtained from fresh samples extensively dried under argon and stored at room temperature. Crystals of  $\alpha$ - $[C(NH_2)_3][N(CN)_2]$  were obtained from aged crystals contained in a watery bulk and stored open to the atmosphere.

Anal. Calcd (in wt%) for  $[C(NH_2)_3][N(CN)_2]$ : C, 28.57; H, 4.76; N, 66.67. Found: C, 28.37; H, 4.41; N, 64.45 ( $\beta$ ); C, 29.27; H, 5.12; N, 64.72 ( $\alpha$ ).  $^1H$  NMR (400.0 MHz, DMSO-d<sub>6</sub>):  $\delta$  = 6.9 ppm (s, NH<sub>2</sub>);  $^{13}C\{^1H\}$  NMR (100.5 MHz, DMSO-d<sub>6</sub>):  $\delta$  = 119.3 ppm (s, C≡N), 158.4 ppm (s, C=NH<sub>2</sub>); MS (FAB<sup>+</sup>):  $m/z$  (%) = 60 (100),  $[C(NH_2)_3]^+$ .

### 10.1.6 Melaminium Dicyanamide $[C_3N_3H(NH_2)_3][N(CN)_2] \cdot H_2O$

Melaminium dicyanamide was synthesized by metathesis reaction of melaminium sulfate (see section 10.1.8) and barium dicyanamide in aqueous solution, or in a MeOH / H<sub>2</sub>O mixture ( $\approx 3:1$ ).

Ba[N(CN)<sub>2</sub>]<sub>2</sub> was synthesized by ion exchange reaction in aqueous solution. An aqueous solution of barium chloride (4 – 7 times the theoretical exchange capacity) was poured onto the ion exchange resin (Ionenaustauscher I,  $H^+$ -Form). Full loading was indicated by a pH change from pH  $\approx 1$  to pH  $\approx 5$ . After washing the column with H<sub>2</sub>O, an aqueous solution (25 mL) of sodium dicyanamide Na[N(CN)<sub>2</sub>] (2.27 g,  $25.50 \cdot 10^{-3}$  mol) was given onto the resin, corresponding to less than half the theoretical exchange capacity. After evaporation of

the solvent, 1.84 g ( $9.02 \cdot 10^{-3}$  mol) colorless crystals of barium dicyanamide were obtained. If impurities of sodium dicyanamide were detected in the product, the ion exchange process was repeated using an aqueous solution of the product instead of sodium dicyanamide. Typically, melaminium sulfate  $[C_3N_6H_7]_2[SO_4] \cdot 2 H_2O$  (460 mg,  $1.16 \cdot 10^{-3}$  mol) was dissolved in 250 mL  $H_2O$  at 343 K. An aqueous solution (18 mL) of barium dicyanamide  $Ba[N(CN)_2]_2$  (320 mg,  $1.57 \cdot 10^{-3}$  mol) was added dropwise and the  $BaSO_4$  precipitate removed by suction of the hot solution. Upon slowly evaporating the filtrate at RT, 310 mg ( $1.88 \cdot 10^{-3}$  mol) colorless crystals of melaminium dicyanamide monohydrate were obtained.

### 10.1.7 Guanylurea Dicyanamide $[(H_2N)C(=O)NHC(NH_2)_2][N(CN)_2]$

Guanylurea dicyanamide was obtained by ion exchange reaction in aqueous solution. 225 mL of an aqueous solution of 4.42 g ( $14.6 \cdot 10^{-3}$  mol) guanylurea sulfate, which was slightly heated for complete dissolution of the salt, were poured onto a column containing 6 mL (ion exchange capacity:  $10.2 \cdot 10^{-3}$  mol) of a strongly acidic ion exchange resin (Ionenaustauscher I,  $H^+$ -Form). Full loading was indicated by the change from acidic ( $H_2SO_4$ ) to neutral pH of the eluate, corresponding to that of a solution of guanylurea sulfate. After thoroughly washing the column with 3 l of deionized water, 0.420 g ( $4.7 \cdot 10^{-3}$  mol) sodium dicyanamide in 10 mL  $H_2O$  was poured onto the column. The eluate was collected and crystallized by evaporation of the solvent. When traces of the starting material sodium dicyanamide were found in the product, the ion exchange procedure was repeated.

Evidence was found for the formation of a metastable phase of guanylurea dicyanamide, whose chemical identity was probed by its vibrational spectra. Since upon recrystallization from aqueous solution or storing the sample in air for a couple of days the metastable modification transformed into that reported in this study, no crystals suitable for single-crystal X-ray analysis could be obtained as yet.

$^1H$  NMR (400.0 MHz, DMSO-d<sub>6</sub>):  $\delta = 7.1$  ppm (s, 2H,  $C(=O)NH_2$ ), 8.1 ppm (s, 4H,  $C(=NH_2)^+NH_2$ ), 10.0 ppm (s, 1H, NH);  $^{13}C\{^1H\}$  NMR (100.5 MHz, in DMSO-d<sub>6</sub>):  $\delta = 155.2$  ppm, 156.1 ppm ( $C=O/C=NH_2^+$ ), 119.2 ppm ( $C\equiv N$ ); MS (FAB<sup>-</sup>, 6 kV):  $m/z$  (%): 103.1 (100)  $[H_2NC(=O)NHC(=NH_2)NH_2]^+$ .

### 10.1.8 Non-Metal Tricyanomelamines

Sodium-TCM was prepared according to a method described in ref. [240]. Ammonium-TCM (**1**) and guanidinium-TCM (**2**) were synthesized by ion-exchange reactions. In a typical procedure, an aqueous solution of the respective chloride ( $XCl$ ,  $X = NH_4$ ,  $C(NH_2)_3$ ; 3.0 – 3.5 M), was poured on a column containing an ion exchange resin in strongly acidic form

(20 mL, Ionenaustauscher I, H<sup>+</sup>-Form). After full loading, the exchange resin was washed thoroughly with deionized water and the removal of excess chloride was substantiated by the AgNO<sub>3</sub> method. Subsequently, a solution of sodium-TCM (610 mg / 30 mL H<sub>2</sub>O (**1**) or 940 mg / 30 mL H<sub>2</sub>O (**2**)) was poured on the column and the eluate evaporated at room temperature. The product of the ammonium-TCM synthesis was found to be strongly dependent on the concentration of the sodium-TCM solution. Reducing the concentration from 0.10 M to 0.06 M resulted in the formation of the metastable hydrated phase (**1a**), which gradually dehydrated when exposed to air at ambient temperature.

Guanidinium-TCM was always obtained as a two-phase mixture composed of colorless crystals of **2** and ball-shaped aggregates of a white polycrystalline powder. Judging from its vibrational and solid-state NMR spectra, the latter phase may be described as [C(NH<sub>2</sub>)<sub>3</sub>]<sub>2</sub>[C<sub>6</sub>N<sub>6</sub>H] · H<sub>2</sub>O.

Melaminium-TCM (**3**) was prepared by adding a solution of sodium-TCM (207 mg, 0.78 · 10<sup>-3</sup> mol) to a hot methanol / water solution (1:3, 400 mL) of melaminium sulfate [C<sub>3</sub>N<sub>6</sub>H<sub>7</sub>]<sub>2</sub>[SO<sub>4</sub>] · 2 H<sub>2</sub>O (500 mg, 1.30 · 10<sup>-3</sup> mol). The solution was kept at 353 K until crystallization commenced.

Melaminium-melamine-TCM was obtained according to the above procedure on repeatedly removing the precipitating melaminium-TCM (**3**). The hot solution was then cooled down and evaporated at RT within several days. A heterogeneous mixture of **3a**, **3**, and melamine was obtained.

Melaminium sulfate was prepared by adding 16 % H<sub>2</sub>SO<sub>4</sub> (30 mL) to 270 mL of a hot aqueous solution of melamine (3.0 g, 23.80 · 10<sup>-3</sup> mol). The solution was cooled slowly and the obtained crystals filtered off.

Data for **1**: IR (KBr):  $\tilde{\nu}$  = 3456.8, 3237.0, 3051.4, 2840.9 (s,  $\nu$ (O–H),  $\nu$ (N–H)), 2182.7 (vs,  $\nu$ (N–C≡N), 1576.3 (vs,  $\delta$ (N–H)), 1532.4 (vs,  $\mu$ (CN<sub>ring</sub>)), 1456.3, 1438.5, 1408.2, 1392.6, 1334.5 (vs,  $\delta$ (CN<sub>ring</sub>) +  $\nu$ (C–NCN)), 1215.5 (w,  $\nu$ (NCN) +  $\delta$ (CN<sub>ring</sub>)), 1027.5 (w,  $\delta$ (skeleton) +  $\delta$ (NCN)), 980.4 (w,  $\delta$ (C<sub>3</sub>N<sub>3</sub>)), 788.9 (w,  $\gamma_s$ (C<sub>3</sub>N<sub>3</sub>)), 760.6 (w,  $\omega$ (N–H)), 747.9 (w,  $\gamma_{as}$ (C<sub>3</sub>N<sub>3</sub>)), 698.9 (w,  $\delta$ (NCN) +  $\delta$ (C<sub>3</sub>N<sub>3</sub>)), 570.1, 549.9 cm<sup>-1</sup> (w,  $\gamma$ (NCN)). Anal. Calcd (in wt%) for [(NH<sub>4</sub>)<sub>2</sub>][C<sub>6</sub>N<sub>9</sub>H] (**1**): C, 30.63; N, 65.51; H, 3.86. Found: C, 30.57; N, 65.68; H, 4.01.

Data for **2**: IR (KBr):  $\tilde{\nu}$  = 3333.1, 3133.0 (s,  $\nu$ (O–H),  $\nu$ (N–H)), 2132.8 (vs,  $\nu$ (N–C≡N)), 1669.6 (vs,  $\nu$ (C=N),  $\delta$ (N–H),  $\delta$ (O–H)), 1580.4 (w,  $\delta$ (N–H)), 1474.5 (vs,  $\nu$ (CN<sub>ring</sub>)), 1389.6 (vs,  $\delta$ (CN<sub>ring</sub>) +  $\nu$ (C–NCN)), 1249.8, 1145.5 (w,  $\nu$ (NCN) +  $\delta$ (CN<sub>ring</sub>)), 1006.5 (vw,  $\delta$ (skeleton) +  $\delta$ (NCN)), 985.6 (vw,  $\delta$ (C<sub>3</sub>N<sub>3</sub>)), 814.5 (m,  $\gamma$ (C<sub>3</sub>N<sub>3</sub>)), 582.5 cm<sup>-1</sup> (w,  $\gamma$ (NCN)).

Anal. Calcd (in wt %) for  $[\text{C}(\text{NH}_2)_3]_3[\text{C}_6\text{N}_9] \cdot 2 \text{ H}_2\text{O}$  (**2**): C, 26.08; N, 60.84; H, 5.36. Found: C, 26.11; N, 61.05; H, 5.26.

Data for **3**: IR (KBr):  $\tilde{\nu} = 3358.5, 3138.5, 2908.0, 2728.3$  (s,  $\nu(\text{O}-\text{H})$ ,  $\nu(\text{N}-\text{H})$ ), 2182.7 (vs,  $\nu(\text{N}-\text{C}\equiv\text{N})$ ), 1667.6 (vs,  $\nu(\text{CN}_{\text{ring},\text{melamine}})$ ,  $\delta(\text{N}-\text{H})$ ,  $\delta(\text{O}-\text{H})$ ), 1580.7 (vs,  $\delta(\text{N}-\text{H})$ ), 1506.7 (vs,  $\nu(\text{CN}_{\text{ring},\text{TCM}})$ ), 1413.7, 1377.5 (vs,  $\delta(\text{CN}_{\text{ring},\text{TCM}} + \nu(\text{C}-\text{NCN}))$ ), 1178.2 (w,  $\nu(\text{NCN}) + \delta(\text{CN}_{\text{ring},\text{TCM}})$ ), 1031.7 (w,  $\delta(\text{skeleton}) + \delta(\text{NCN})$ ), 975.5 (w,  $\delta(\text{C}_3\text{N}_3)$ ), 782.4 (m,  $\gamma_s(\text{C}_3\text{N}_3)$ ), 746.1 (vw,  $\gamma_{as}(\text{C}_3\text{N}_3)$ ), 697.7 (vw,  $\delta(\text{NCN}) + \delta(\text{C}_3\text{N}_3)$ ), 568.0  $\text{cm}^{-1}$  (w,  $\gamma(\text{NCN})$ , ring-bend<sub>melamine</sub>). Anal. Calcd (in wt%) for  $[(\text{C}_3\text{N}_6\text{H}_7)_2][\text{C}_6\text{N}_9\text{H}] \cdot 2.4 \text{ H}_2\text{O}$  (**3**): C, 28.91; N, 59.02; H, 4.05. Found: C, 28.78; N, 58.99; H, 4.12. MS (ESI-):  $m/z$  (%) = 200.05 (100) [A + H]<sup>-</sup>, 222.04 (20) [A + Na]<sup>-</sup>, 423.09 (45) [2 A + 2 H + Na]<sup>-</sup>; (DEI+):  $m/z$  (%) = 126.10 (12)  $[\text{C}_3\text{N}_6\text{H}_6]^+$ .

### 10.1.9 $^{15}\text{N}$ -Melamine $\text{C}_3^{15}\text{N}_6\text{H}_6$

According to a procedure developed by *Jürgens* [240],  $^{15}\text{N}$ -enriched melamine was prepared by reacting sodium tricyanomelamine  $\text{Na}_3[\text{C}_6\text{N}_9]$  (742.5 mg,  $2.78 \cdot 10^{-3}$  mol) with  $^{15}\text{NH}_4\text{Cl}$  (183 mg,  $3.36 \cdot 10^{-3}$  mol) in a Duran tube (length: 160 mm,  $\varnothing_{\text{ext.}}$  26 mm,  $\varnothing_{\text{int.}}$  24 mm) at 743 K (heating rate of 1 K  $\text{min}^{-1}$ ) for 12 h. The raw material was further purified by sublimation (1 Pa, 493 K).

### 10.1.10 Ammeline Salts

All ammeline salts were obtained by acid hydrolysis of melam hydrate according to the following procedure: A melam –  $\text{NH}_4\text{Cl}$  adduct of assumed composition  $[\text{C}_6\text{N}_{11}\text{H}_{10}]\text{Cl} \cdot 0.5 \text{ NH}_4\text{Cl}$  was synthesized according to *Jürgens* by heating melamine and  $\text{NH}_4\text{Cl}$  in a molar ratio of 2:1 at 723 K for several hours in a glass ampoule with ground neck [240]. The obtained melam –  $\text{NH}_4\text{Cl}$  adduct was stirred in aqueous  $\text{NH}_3$  (25 %) for 1 hour to remove the ammonium chloride and subsequently air-dried. The as-obtained melam hydrate,  $\text{C}_6\text{N}_{11}\text{H}_9 \cdot 2 \text{ H}_2\text{O}$  (12 mg,  $4.4 \cdot 10^{-5}$  mol) were suspended in  $\text{H}_2\text{O}$  (50 mL) and heated under reflux. Concentrated acid (2 mL  $\text{HCl}$ , 1 mL  $\text{HBr}$ , or 4 mL  $\text{HNO}_3$ ) was added to the hot suspension until complete dissolution was observed. The solution was stirred for another 10 minutes, then slowly cooled down and the solvent evaporated at 313 K until formation of colorless crystals commenced.

## 10.2 Chemicals

The sources of supply as well as the purity of the commercially available chemicals used in this work are listed in Table 10.1.

*Table 10.1: Source of supply and purity of the chemicals used in this work.*

Chemical	Formula	Purity	Source of Supply
Acetonitrile	$\text{H}_3\text{CCN}$	99.9 %	Riedel-de-Haën
Aluminium chloride Hexahydrate	$\text{AlCl}_3 \cdot 6 \text{ H}_2\text{O}$	99 %	Acros
Ammonia (25 % aq.)	$\text{NH}_3$	p. a.	Fluka
Ammonium bromide	$\text{NH}_4\text{Br}$	$\geq 99.5 \%$	Fluka
Ammonium chloride	$\text{NH}_4\text{Cl}$	$\geq 99.5\%$	Fluka
$^{15}\text{N}$ -Ammonium chloride	$^{15}\text{NH}_4\text{Cl}$	98 % ( $^{15}\text{N}$ )	Promochem
Ammonium iodide	$\text{NH}_4\text{I}$	$\geq 99 \%$	Fluka
Argon	$\text{Ar}$	99.998 %	Messer
Ammonium dihydrogen phosphate	$(\text{NH}_4)\text{H}_2\text{PO}_4$	p. a.	Merck
Barium chloride Hexahydrate	$\text{BaCl}_2 \cdot 6 \text{ H}_2\text{O}$	99 %	Merck
Calcium chloride Hexahydrate	$\text{CaCl}_2 \cdot 6 \text{ H}_2\text{O}$	p. a.	Merck
Copper chloride Dihydrate	$\text{CuCl}_2 \cdot 2 \text{ H}_2\text{O}$	99 %	Merck
Deuterium oxide	$\text{D}_2\text{O}$	$\geq 99.9 \%$	Deutero GmbH
Diammonium hydrogen phosphate	$(\text{NH}_4)_2\text{HPO}_4$	p. a.	Merck
Dicyandiamide	$\text{H}_4\text{C}_2\text{N}_4$	99%	AVOCADO
Dimethylformamide	$\text{OHCN}(\text{CH}_3)_2$	$\geq 99.995 \%$	Acros Organics
Dimethylsulfoxide	$\text{OS}(\text{CH}_3)_2$	$\geq 99.5 \%$	Merck
Dimethylsulfoxide-d <sub>6</sub>	$\text{OS}(\text{CD}_3)_2$	$\geq 99.9 \%$	Deutero GmbH
Formic Acid (100 %)	$\text{CHOOH}$	p. a.	Merck
Guanidinium chloride	$[\text{C}(\text{NH}_2)_3]\text{Cl}$	$\geq 98 \%$	Fluka
Guanidinium nitrate	$[\text{C}(\text{NH}_2)_3]\text{NO}_3$	$\geq 98 \%$	Fluka
Guanidinium sulfate	$[\text{C}(\text{NH}_2)_3]\text{NO}_3$	$\geq 97 \%$	Merck
Guanylurea sulfate	$[\text{C}_2\text{N}_4\text{H}_7\text{O}]_2\text{SO}_4$	98 %	Acros Organics
Hydrobromic acid (47 %)	$\text{HBr}$	p. a.	Bisterfeld-Graen
Hydrochloric acid (36 %)	$\text{HCl}$	p. a.	Bisterfeld-Graen
Ion exchanger I, $\text{H}^+$ -form		p. a.	Merck
Iron chloride	$\text{FeCl}_3$	$\geq 97 \%$	Grüssing
Iron chloride Hexahydrate	$\text{FeCl}_3 \cdot 6 \text{ H}_2\text{O}$	–	Caelo
Magnesium chloride Hexahydrate	$\text{MgCl}_2 \cdot 6 \text{ H}_2\text{O}$	p. a.	Merck
Melamine	$\text{C}_3\text{N}_3(\text{NH}_2)_3$	$\geq 99 \%$	Fluka
Nitric acid 65 %	$\text{HNO}_3$	p. a.	Bisterfeld-Graen
Ortho-phosphoric acid (85 %)	$\text{H}_3\text{PO}_4$	p. a.	Bisterfeld-Graen
Perchloric acid (60 %)	$\text{HClO}_4$	p. a.	Merck
Potassium	$\text{K}$	purum	Kochlight
Sodium dicyanamide	$\text{Na}[\text{N}(\text{CN})_2]$	$\geq 96 \%$	Fluka
Sulfuric acid (95 – 98 %)	$\text{H}_2\text{SO}_4$	p. a.	Bisterfeld-Graen
Tetrahydrofuran (stabilized)	$\text{C}_4\text{H}_8\text{O}$	p. a.	Acros Organics

## 10.3 Crystal Structures

### 10.3.1 2,4-Diamino-1,3,5-Triazine

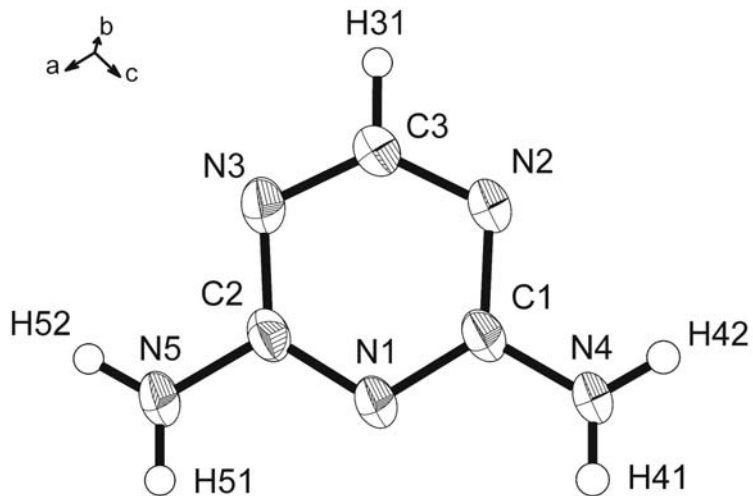


**Figure 10.1:** Asymmetric unit of 2,4-diamino-1,3,5-triazine. Displacement ellipsoids are drawn at the 50 % probability level.

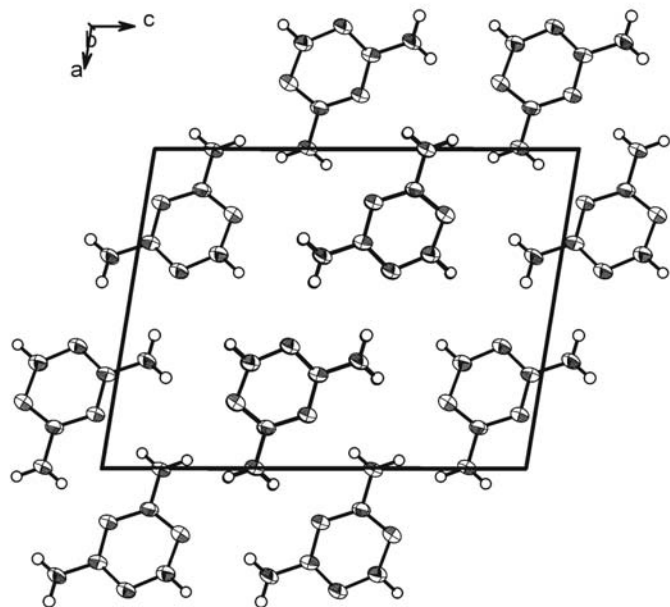


**Figure 10.2:** Unit cell of 2,4-diamino-1,3,5-triazine, view along [010]. Displacement ellipsoids are drawn at the 50 % probability level.

**Table 10.2:** Crystallographic data for 2,4-diamino-1,3,5-triazine.

Formula	C <sub>3</sub> N <sub>5</sub> H <sub>5</sub>
$M_w$ / g · mol <sup>-1</sup>	148.16
crystal system	monoclinic
space group	$P2_1/c$ (no. 14)
$T$ / K	200
diffractometer	Nonius Kappa CCD
radiation ( $\lambda$ / pm)	Mo-K $\alpha$ (71.073)
monochromator	graphite
$a$ / pm	987.5(2)
$b$ / pm	375.00(8)
$c$ / pm	1294.0(3)
$\beta$ / °	99.34(3)
$V$ / 10 <sup>6</sup> · pm <sup>3</sup>	472.85(17)
$Z$	4
$\rho_{calcd}$ / g · cm <sup>-3</sup>	1.561
F(000)	232
$\mu$ / mm <sup>-1</sup>	0.11
$\chi$	0.03(2)
crystal size / mm <sup>3</sup>	0.12 x 0.03 x 0.02
diffraction range	3.19 ≤ $\theta$ ≤ 25.00
index range	-11 ≤ $h$ ≤ 11, -4 ≤ $k$ ≤ 4, -15 ≤ $l$ ≤ 15
total no. reflections	5888
independent reflections	837 ( $R_{int} = 0.1452$ )
observed reflections	628
refined parameters / restraints	with $F_o^2 \geq 2\sigma(F_o^2)$
GooF on $F^2$	74 / 0
$R$ indices (all data)	1.070 $R_1 = 0.0631$ (0.0798) $wR_2 = 0.1836$ (0.1986) with w = $[\sigma^2(F_o^2)$ $+(0.1100P)^2 + 0.3045P]^{-1}$ where $P = (F_o^2 + 2F_c^2)/3$
min./max. residual	
electron density /	- 0.240 / 0.608
$e \cdot 10^{-6}$ pm <sup>-3</sup>	

## 10.3.2 Guanylurea Sulfate

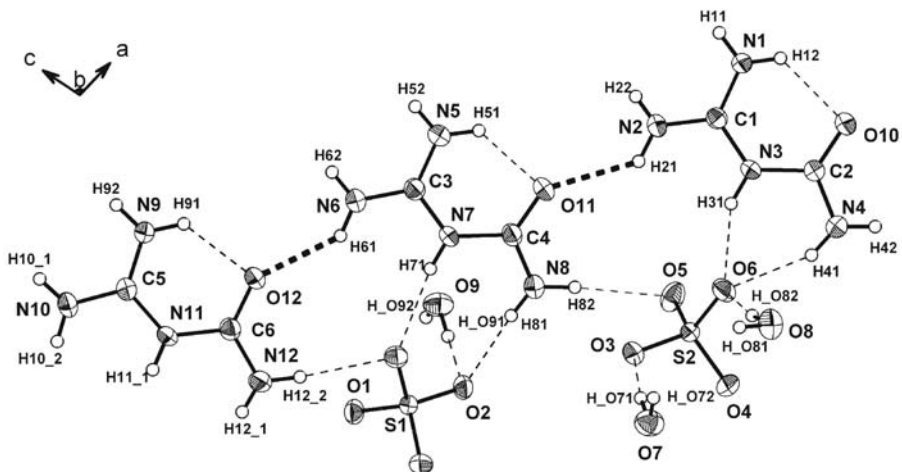


**Figure 10.3:** Hydrogen-bonded chains of guanylurea cations (dotted lines, bold) which are interconnected by sulphate ions and water molecules (dotted lines, thin). Displacement ellipsoids are drawn at the 50 % probability level.

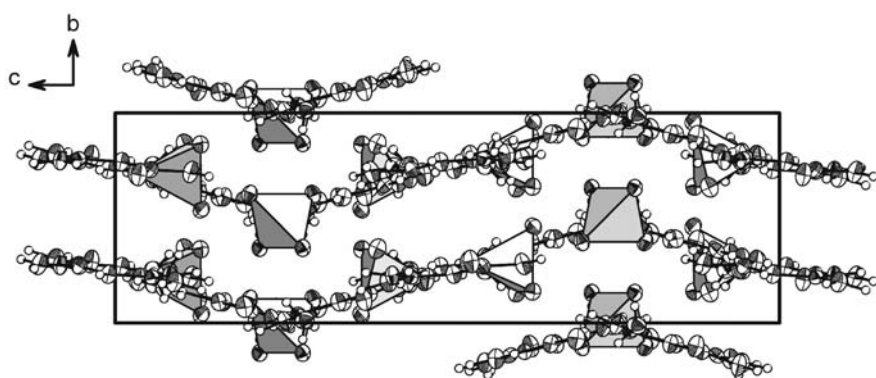


**Figure 10.4:** Unit cell of guanylurea sulphate hydrate, view along [100]. Displacement ellipsoids are drawn at the 50 % probability level.

**Table 10.3:** Crystallographic data for Guanylurea (carbamoylguanidinium) sulfate hydrate.

Formula	$[\text{C}_2\text{H}_7\text{N}_4\text{O}]_2\text{SO}_4 \cdot 2\text{H}_2\text{O}$
$M_w$ / g · mol <sup>-1</sup>	338.32
crystal system	monoclinic
space group	$C2/c$ (no. 15)
$T$ / K	200
diffractometer	Nonius Kappa CCD
radiation ( $\lambda$ / pm)	Mo-K $\alpha$ (71.073)
monochromator	graphite
$a$ / pm	3035.3(6)
$b$ / pm	661.62(13)
$c$ / pm	2120.4(4)
$\beta$ / °	99.37(3)
$V$ / $10^6 \cdot \text{pm}^3$	4201.4(14)
$Z$	4
$\rho_{\text{calcd}}$ / g · cm <sup>-3</sup>	1.605
$F(000)$	2136
$\mu$ / mm <sup>-1</sup>	0.287
absorption correction	semi-empirical, multiscan
$\chi$	0.00096(15)
crystal size / mm <sup>3</sup>	0.25 x 0.12 x 0.09
diffraction range	$3.15 \leq \theta \leq 27.49$
index range	$-38 \leq h \leq 38, -8 \leq k \leq 8,$ $-27 \leq l \leq 27$
total no. reflections	40605
independent reflections	4821 ( $R_{\text{int}} = 0.0475$ )
observed reflections	3959
refined parameters / restraints	with $F_o^2 \geq 2\sigma(F_o^2)$
GooF on $F^2$	394 / 0
$R$ indices (all data)	1.046
	$R_1 = 0.0475$ (0.0342)
	$wR_2 = 0.0823$ (0.0886)
	with $w = [\sigma^2(F_o^2)$
	$+(0.0411P)^2 + 3.7320P]^{-1}$
	where $P = (F_o^2 + 2F_c^2)/3$
min./max. residual	
electron density /	
$e \cdot 10^{-6} \text{ pm}^{-3}$	- 0.397 / 0.363

## 10.4 Melon: Electron Diffraction

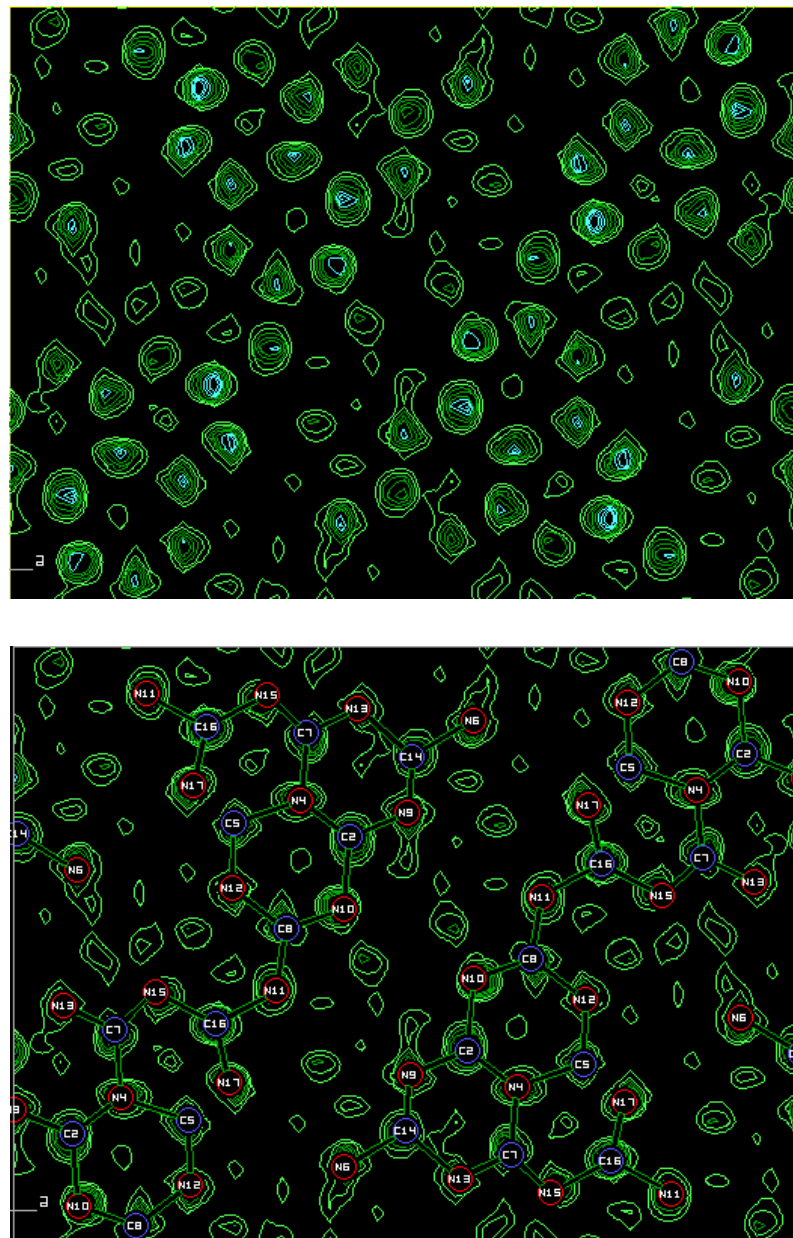


**Figure 10.5:** Potential map obtained after refinement of the precession electron diffraction data of the  $hk$  layer ( $wR2 \approx 35\%$ , weighting factor 1.0). Top: without atoms; bottom: C (blue) and N (red) atoms are indicated, showing a heptazine-based melon structure.

## 10.5 Solid-State NMR Spectroscopy

### 10.5.1 Line Shape Simulations

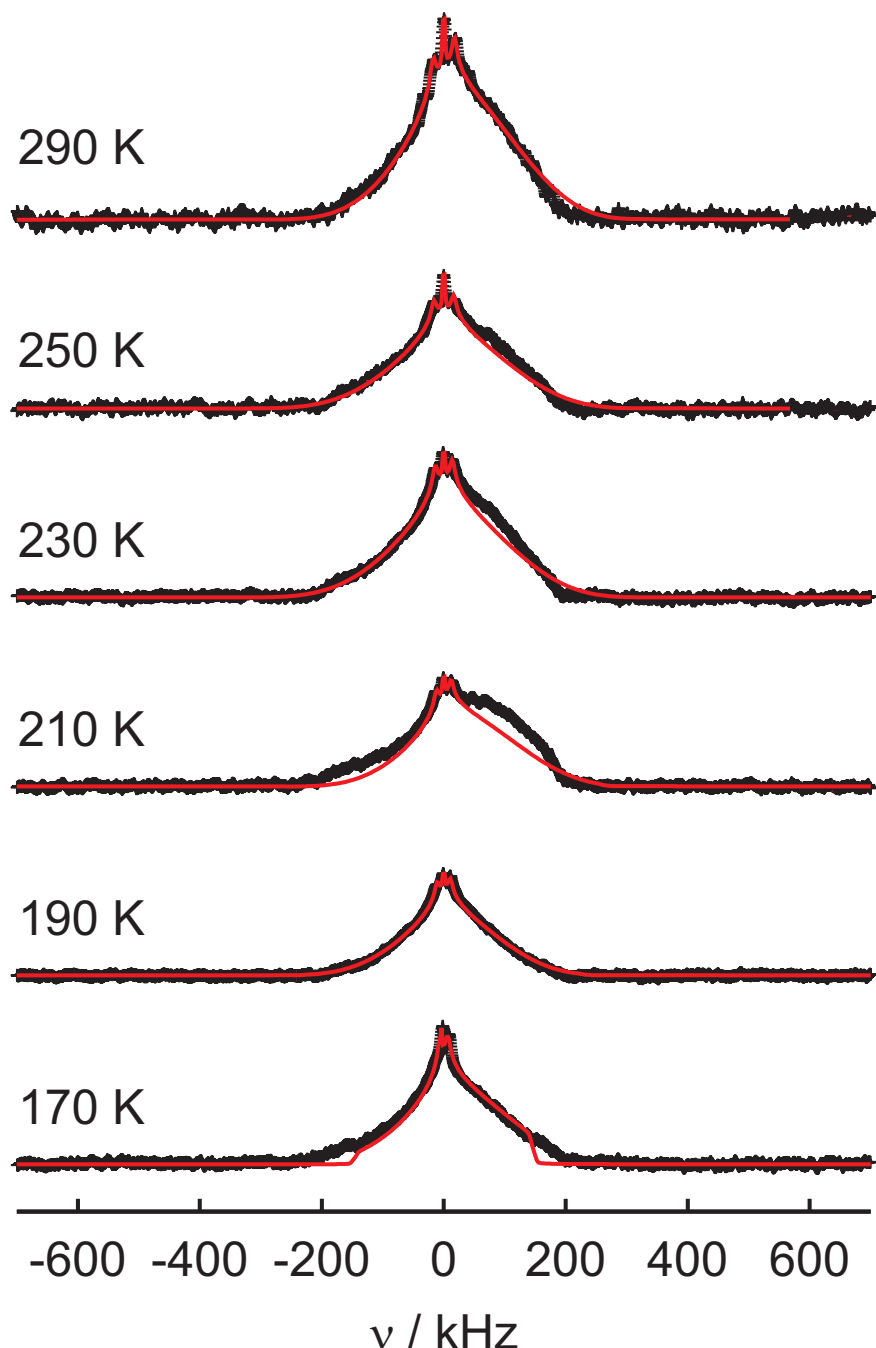


**Figure 10.6:**  $^{14}\text{N}$  wide-line solid-state NMR spectra measured between 170 K (bottom) and room temperature (top), together with the respective simulations employing  $\eta = 0.91$  and variable QCCs: 170 K: 200 kHz; 190 K: 320 kHz; 210 K: 360 kHz; 230 K: 420 kHz; 250 K: 480 kHz; 290 K: 520 kHz. The simulations were carried out using the program MXQET [181].

### 10.5.2 Program Code for the Analysis of $^2H$ Powder Spectra Using the NMR Library Gamma [186]

```

#include <gamma.h>
#include<iostream>
#include<string>
using namespace std;

complex null(0.0,0.0);
matrix cartesisch(space_T CS);
void Kristallite(int maxn, double theta[], double phi[], double wichte[]);

matrix cartesisch(space_T CS) {

    int i, j;
    matrix CSC(3,3);

    for (i=0;i<3;i++) {
        for (j=0;j<3;j++) {
            CSC(i,j)=CS.Ccomponent(i,j);
        }
    }
    return CSC;
}

void Kristallite(int maxn, double theta[], double phi[], double wichte[]){

//-----Einlesen der Repulsiondaten-----
    char file[15];
    int i;

    if (maxn<100000) {sprintf(file,"repulsion%5d",maxn);}
    if (maxn<10000) {sprintf(file,"repulsion%4d",maxn);}
    if (maxn<1000) {sprintf(file,"repulsion%3d",maxn);}
    if (maxn<100) {sprintf(file,"repulsion%2d",maxn);}
    if (maxn<10) {sprintf(file,"repulsion%1d",maxn);}
}

```

```

ifstream readrep(file, ios::in);
for(i=0;i<maxn;++i){
    readrep>>phi[i]>>theta[i]>>wichte[i];
}
}

main(int argc, char *argv[]) {

    int qn=1, Zspins, maxn;
    double QCC1, QCC2, QCC3, QCC4, etha, beta1, beta2, omega1, omega2, omega3, omega4;
    double sca1=0.5*sqrt(3./2.);
    double rate=1.e0, t1;

    coord pt1;
    pt1.xyz(0,0,1); //Orientierung des B0-Feldes entlang Z des Laborkoord.

    ask_set(argc, argv, qn++, "\n\tKopplungskonstante QCC1 [kHz]? ", QCC1);
    ask_set(argc, argv, qn++, "\n\tKopplungskonstante QCC2 [kHz]? ", QCC2);
    ask_set(argc, argv, qn++, "\n\tKopplungskonstante QCC3 [kHz]? ", QCC3);
    ask_set(argc, argv, qn++, "\n\tKopplungskonstante QCC4 [kHz]? ", QCC4);
    ask_set(argc, argv, qn++, "\n\tAsymmetrieparameter fuer 2H? ", etha);
    ask_set(argc, argv, qn++, "\n\tbeta1? ", beta1);
    ask_set(argc, argv, qn++, "\n\tbeta2? ", beta2);
    ask_set(argc, argv, qn++, "\n\tZahl der Pulverinkremente? ", maxn);
    ask_set(argc, argv, qn++, "\n\tRate? ", rate);
    ask_set(argc, argv, qn++, "\n\tt_1 in us? ", t1);
    t1=t1*1.e-6;

    double phi[maxn], theta[maxn], wichte[maxn];

    Kristallite(maxn, theta, phi, wichte);

    QCC1=QCC1*sca1*1000.*2*PI;
    QCC2=QCC2*sca1*1000.*2*PI;
    QCC3=QCC3*sca1*1000.*2*PI;
}

```

```
QCC4=QCC4*sca1*1000.*2*PI;

ofstream writeausgabe("Werte_TQCC.dat", ios::out);
spin_system sys;
sys.read("spindif1.sys");
writeausgabe<<"Spinsystem:\n"<<sys<<"\n\n";
Zspins=sys.spins();
writeausgabe<<"Zspins: "<<Zspins<<"\n";

space_T Q1,Q2,Q3,Q4, CS[4],CSr[4];

Q1=A2(0.,QCC1,etha);
Q2=A2(0.,QCC2,etha);
Q3=A2(0.,QCC3,etha);
Q4=A2(0.,QCC4,etha);

CS[0]=Q1.rotate(0.,beta1,0.);
CS[1]=Q2.rotate(0.,beta1,180.);
CS[2]=Q3.rotate(0.,beta2,90.);
CS[3]=Q4.rotate(0.,beta2,270.);

matrix pi(4,4);
pi.put(-3*rate,0,0);
pi.put(-3*rate,1,1);
pi.put(-3*rate,2,2);
pi.put(-3*rate,3,3);
pi.put(rate,0,1);
pi.put(rate,1,0);
pi.put(rate,0,2);
pi.put(rate,2,0);
pi.put(rate,0,3);
pi.put(rate,3,0);
pi.put(rate,1,2);
pi.put(rate,1,3);
pi.put(rate,2,1);
```

```

pi.put(rate,3,1);
pi.put(rate,2,3);
pi.put(rate,3,2);

int i,h,k,j;
matrix mR,mRdia,mX,momega(4,4,null),emRdia(4,4,null),R,Rdia,X;
matrix omega(4,4,null),eRdia(4,4, null),temp1(4,4,null);
complex z1(0,1),echo=null;
double t;
double dw=1.e-6;
col_vector G(4,0.25), temp2(4,null);
row_vector I(4,1),temp3(4,null) ;
col_vector echofin(2000,null),echosum(2000,null),
echocut(2048,null),fftecho(2048,null);

for(h=0; h<maxn; h++) {

    CSr[0]=CS[0].rotate(phi[h],theta[h],0.);
    CSr[1]=CS[1].rotate(phi[h],theta[h],0.);
    CSr[2]=CS[2].rotate(phi[h],theta[h],0.);
    CSr[3]=CS[3].rotate(phi[h],theta[h],0.);

    omega1=Re(CSr[0].component(2,0));
    omega2=Re(CSr[1].component(2,0));
    omega3=Re(CSr[2].component(2,0));
    omega4=Re(CSr[3].component(2,0));

//-----Def.: pi und (m)omega-----
    momega.put(-z1*omega1,0,0);
    momega.put(-z1*omega2,1,1);
    momega.put(-z1*omega3,2,2);
    momega.put(-z1*omega4,3,3);

    omega=-1.*momega;
}

```

```

mR=momega+pi;
diag(mR,mRdia,mX);

omega.put(z1*omega1,0,0);
omega.put(z1*omega2,1,1);
omega.put(z1*omega3,2,2);
omega.put(z1*omega4,3,3);

R=omega+pi;
diag(R,Rdia,X);

temp1=inv(mX)*X;
temp2=inv(X)*G;
temp3=I*mX;

//-----t-inkrementiertes e(m)Rdia, echo-----

for(k=0;k<2000;k++){
    t=k*dw;
    for(i=0;i<4;i++){
        emRdia.put(exp(mRdia(i,i)*(t-t1)),i,i);
        eRdia.put(exp(Rdia(i,i)*t1),i,i);
    }
    echo=temp3*emRdia*temp1*eRdia*temp2;
    echofin(k)=echo;
}
echosum+=echofin*wichte[h];
}

for(j=0;j<2000;j++){
    echosum.put(Re(echosum(j)),j);
}

//-----Multiplikation mit Gaußfunktion-----

```

```

row_vector gauss(2000);
gauss=Gaussian(2000,0,300.);

for(i=0;i<2000;i++){
    echosum(i)*=gauss(i);
}
//-----FFT-----

int Abschn=(int)(2.*(t1/dw));
cout<<"Abschneidepunkt: "<<Abschn<<"\n";

for(i=0;i<2000-Abschn;i++){
    echocut(i)=echosum(i+Abschn);
}

echocut(0)=echocut(0)*0.5;
fftecho=FFT(echocut);

//-----x-Achse, Spektrum-----

int l;

col_vector nue(2048), PLA(2048);
double SW=1/dw, tp=3.0e-6, omegat=5.24e5;
cout<<"SW: "<<SW<<"\n";
for(l=0;l<2048;l++){
    nue(l)=(SW/2047.*l-SW/2.)*2*PI;
}

//-----Pulslängenabschwächung-----

for(l=0;l<2048;l++){
    PLA(l)=omegat*(sin(tp*sqrt((omegat*omegat)+0.5*nue(l)*nue(l)))/
    (sqrt(omegat*omegat+0.25*nue(l)*nue(l)));
}

```

```
writeausgabe<<"fftecho_vorher: "<<fftecho<<"\n";  
  
for(l=0;l<2048;l++){  
    fftecho(l)*=PLA(l);  
}  
  
writeausgabe<<"fftecho_nachher: "<<fftecho<<"\n";  
ofstream spektrum("spc_TQCC.dat", ios::out);  
  
for(i=0;i<2048;i++){  
    spektrum<<Re(nue(i))<<"\t"<<Re(fftecho(i))<<"\t"<<Im(fftecho(i))<<"\n";}  
spektrum.close();  
ofstream fid("fid_TQCC.dat", ios::out);  
  
for(i=0;i<2000;i++){  
    fid<<i<<"\t"<<Re(echosum(i))<<"\t"<<Im(echosum(i))<<"\n";}  
fid.close();  
ofstream PLAB("PLAB.dat", ios::out);  
  
for(i=0;i<2048;i++){  
    PLAB<<Re(nue(i))<<"\t"<<Re(PLA(i))<<"\t"<<Im(PLA(i))<<"\n";}  
PLAB.close();  
}
```

## Abbreviations

---

acq	acquisition
BSS	backscattering spectrometer
CAS	crystal axis system
cf.	confer
conc.	concentrated
CP	cross-polarization
CPPI	cross-polarization with polarization inversion
CS	chemical shift
CSA	chemical shift anisotropy
d	day
<i>dca</i>	dicyanamide
<i>dda</i>	dicyandiamide
DCI	direct chemical ionization
DEI	direct electron impact
DFT	density functional theory
DSC	differential scanning calorimetry
DTA	differential thermal analysis
$\eta$	asymmetry parameter
ED	electron diffraction
EDX	energy dispersive X-ray analysis
EFG	electric field gradient
ESI	electrospray ionization
ESP	electrostatic potential
Eq.	equation
$F_c$	calculated structure factor
$F_o$	observed structure factor
FAB	fast atom bombardment
FID	free induction decay
Fig.	Figure

---

---

<i>fp</i> -RFDR	finite pulse radio frequency driven dipolar recoupling
FT	Fourier transformation
FWHM	full width at half maximum
Goof	goodness of fit
h	hour
HETCOR	heteronuclear correlation
HF	high frequency
INS	inelastic neutron scattering
IPDS	imaging plate diffraction system
IR	infrared
kHz	kilohertz
LAS	laboratory axis system
lb	line broadening
MAS	magic angle spinning
mg	milligram
MHz	megahertz
min	minute
mL	milliliter
MS	mass spectrometry
msec	milliseconds
NH <sub>4</sub> dca	ammonium dicyanamide
NMR	nuclear magnetic resonance
PAS	principal axis system
<i>pdf</i>	probability density function
pm	picometer
ppm	parts per million
Q	momentum transfer
QCC	quadrupole-coupling constant
QNS	quasielastic neutron scattering
R	residual
RFDR	radio-frequency driven dipolar recoupling
RT	room temperature
s	second
$\sigma_{iso}$	isotropic chemical shift

---

---

SAED	selected area electron diffraction
SEM	scanning electron microscopy
SOF	site occupation factor
SPM	single particle model
$t$	time
$T_1$	longitudinal (spin-lattice) relaxation time
$T_2$	transversal (spin-spin) relaxation time
$\tau_c$	contact time
$\tau_m$	mixing time
TCM	tricyanomelamine
TEM	transmission electron microscopy
TPXRD	temperature programmed X-ray powder diffraction
UV/vis	ultraviolet / visible

---

# Bibliography

- [1] Schnick, W. *Angew. Chem.* **1993**, *105*, 846; *Angew. Chem. Int. Ed. Engl.* **1993**, *32*, 806.
- [2] Schnick, W. *Angew. Chem.* **1993**, *105*, 1649; *Angew. Chem. Int. Ed. Engl.* **1993**, *32*, 1580.
- [3] Landskron, K.; Huppertz, H.; Senker, J.; Schnick, W. *Angew. Chem.* **2001**, *113*, 2713; *Angew. Chem. Int. Ed.* **2001**, *40*, 2643.
- [4] Kroll, P.; Schnick, W. *Chem. Eur. J.* **2002**, *8*, 3530.
- [5] Schnick, W. *Angew. Chem.* **1999**, *111*, 3511; *Angew. Chem. Int. Ed.* **1999**, *38*, 3309.
- [6] Schnick, W. *Comments Inorg. Chem.* **1995**, *17*, 189.
- [7] Janiak, C.; Klapötke, T. M.; Meyer, H.-J. *Moderne Anorganische Chemie*; Riedel, E. (Ed.), 2. Aufl.; Walter de Gruyter GmbH: Berlin, 2004.
- [8] Holleman, A. F.; Wiberg, E. *Lehrbuch der Anorganischen Chemie*; Wiberg, N. (Ed.); 101. Aufl.; Walter de Gruyter GmbH: Berlin, 1995.
- [9] Schnick, W.; Schlieper, T.; Huppertz, H.; Köllisch, K.; Orth, M.; Bettenhausen, R.; Schwarze, B.; Lauterbach, R. *Phosphorus Sulfur Silicon Relat. Elem.* **1997**, *124/125*, 163.
- [10] Schnick, W. *Int. J. Inorg. Mater.* **2001**, *3*, 1267.
- [11] Landskron, K.; Schnick, W. *J. Solid State Chem.* **2001**, *156*, 390.
- [12] Stock, N.; Irran, E.; Schnick, W. *Chem. Eur. J.* **1998**, *4*, 1822.
- [13] Horstmann, S.; Irran, E.; Schnick, W. *Angew. Chem.* **1997**, *109*, 2085; *Angew. Chem. Int. Ed. Engl.* **1997**, *36*, 1992.

[14] Horstmann, S. *Hochkondensierte Phosphor(V)-nitride aus Einkomponentenvorläufern - Von Tetraaminophosphoniumsalzen zu  $\alpha$ - $P_3N_5$* , PhD Thesis, Universität Bayreuth, **1997**.

[15] Horstmann, S.; Irran, E.; Schnick, W. *Z. Anorg. Allg. Chem.* **1998**, *624*, 620.

[16] Horstmann, S.; Irran, E.; Schnick, W. *Angew. Chem.* **1997**, *109*, 1938; *Angew. Chem. Int. Ed. Engl.* **1997**, *36*, 1873.

[17] Schnick, W.; Huppertz, H. *Chem. Eur. J.* **1997**, *3*, 679.

[18] Huppertz, H.; Schnick, W. *Angew. Chem.* **1996**, *108*, 2115; *Angew. Chem. Int. Ed. Engl.* **1996**, *35*, 1983.

[19] Schnick, W.; Huppertz, H.; Schlieper, T. *Nitridosilicates - High Temperature Materials with Interesting Properties*, in: *Organosilicon Chemistry III - From Molecules to Materials*; Auner, N.; Weis, J. (Eds.); WILEY-VCH Verlag GmbH: Weinheim, 1997, 691.

[20] Schnick, W. *Phosphorus Sulfur Silicon Relat. Elem.* **1993**, *76*, 443.

[21] Schnick, W.; Huppertz, H.; Lauterbach, R. *J. Mater. Chem.* **1999**, *9*, 289.

[22] *Europium-Activated Alkaline Earth Silicon Nitride Oxide Phosphors and Luminescent Screens and Light-Emitting Devices Employing the Phosphors*. Schmidt, P.; Juestel, T.; Mayr, W.; Bausen, H. D.; Schnick, W.; Hoepppe, H. A. International Patent, PTC Int. Appl. WO 2004036962 A1, **2004**, Philips Intellectual Property & Standards GmbH, Germany; Koninklijke Philips Electronics N.V.; Lumileds Lighting U.S. Llc.

[23] *Plasma Display Screen with Blue-emitting Phosphor*. Jüstel, T.; Mayr, W.; Schmidt, P. J.; Schnick, W. International Patent, PTC Int. Appl. WO 2004047138 A2, **2004**, Philips Intellectual Property & Standards GmbH, Germany; Koninklijke Philips Electronics N.V.; Lumileds Lighting U.S. Llc.

[24] *Illumination System Comprising a Radiation Source and a Fluorescent Lanthanide-doped Metal Oxide Nitride Silicate Phosphor*. Juestel, T.; Schmidt, P.; Hoepppe, H. A.; Schnick, W.; Mayr, W. International Patent, PTC Int. Appl. WO 2004055910 A1, **2004**, Philips Intellectual Property & Standards GmbH, Germany; Koninklijke Philips Electronics N.V.; Lumileds Lighting U.S. Llc.

[25] Mueller-Mach, R.; Mueller, G.; Krames, M. R.; Höppe, H. A.; Stadler, F.; Schnick, W.; Juestel, T.; Schmidt, P. *Phys. Status Solidi A* **2005**, *202*, 1727.

[26] *Illumination System Comprising a Radiation Source and a Fluorescent Material*. Juestel, T.; Schmidt, P.; Schnick, W.; Stadler, F. M. International Patent, PTC Int. Appl. WO 2006006099 A1, **2006**, Philips Intellectual Property & Standards GmbH, Germany; Koninklijke Philips Electronics N.V.; Lumileds Lighting U.S. Llc.

[27] Lauterbach, R.; Irran, E.; Henry, P. F.; Weller, M. T.; Schnick, W. *J. Mater. Chem.* **2000**, *10*, 1357.

[28] Irran, E.; Köllisch, K.; Leoni, S.; Nesper, R.; Henry, P. F.; Weller, M. T.; Schnick, W. *Chem. Eur. J.* **2000**, *6*, 2714.

[29] Koellisch, K.; Schnick, W. *Angew. Chem.* **1999**, *111*, 368; *Angew. Chem. Int. Ed.* **1999**, *38*, 357.

[30] Schwarz, M.; Zerr, A.; Kroke, E.; Miehe, G.; Chen, I.-W.; Heck, M.; Thybusch, B.; Poe, B. T.; Riedel, R. *Angew. Chem.* **2002**, *114*, 804; *Angew. Chem. Int. Ed.* **2002**, *41*, 789.

[31] Baldus, H.-P.; Jansen, M. *Angew. Chem.* **1997**, *109*, 338; *Angew. Chem. Int. Ed. Engl.* **1997**, *36*, 328.

[32] Baldus, H.-P.; Jansen, M.; Wagner, O. *Key Eng. Mater.* **1994**, *89-91*, 75.

[33] Baldus, H.-P.; Wagner, O.; Jansen, M. *Mater. Res. Soc. Symp. Proc.* **1992**, *271*, 821.

[34] Solozhenko, V. L.; Andrault, D.; Fiquet, G.; Mezouar, M.; Rubie, D. C. *Appl. Phys. Lett.* **2001**, *78*, 1385.

[35] Solozhenko, V. L. *High Press. Res.* **2002**, *22*, 519.

[36] Sun, H.; Jhi, S.-H.; Roundy, D.; Cohen, M. L.; Louie, S. G. *Phys. Rev. B* **2001**, *64*, 094108.

[37] Zerr, A.; Miehe, G.; Serghiou, G.; Schwarz, M.; Kroke, E.; Riedel, R.; Fueß, H.; Kroll, P.; Boehler, R. *Nature* **1999**, *400*, 340.

[38] Mo, S.-D.; Ouyang, L.; Ching, W. Y.; Tanaka, I.; Koyama, Y.; Riedel, R. *Phys. Rev. Lett.* **1999**, *83*, 5046.

[39] Sekine, T.; He, H.; Kobayashi, T.; Zhang, M.; Xu, F. *Appl. Phys. Lett.* **2000**, *76*, 3706.

[40] Kiefer, B.; Shieh, S. R.; Duffy, T. S.; Sekine, T. *Phys. Rev. B* **2005**, *72*, 014102.

[41] Liu, A. Y.; Cohen, M. L. *Phys. Rev. B* **1990**, *41*, 10727.

[42] Kroke, E.; Schwarz, M. *Coord. Chem. Rev.* **2004**, *248*, 493.

[43] Matsumoto, S.; Xie, E. Q.; Izumi, F. *Diamond Relat. Mater.* **1999**, *8*, 1175.

[44] Muhl, S.; Méndez, J. M. *Diamond Relat. Mater.* **1999**, *8*, 1809.

[45] Guo, Y.; Goddard III, W. A. *Chem. Phys. Lett.* **1995**, *237*, 72.

[46] Sung, C.-M.; Sung, M. *Mater. Chem. Phys.* **1996**, *43*, 1.

[47] Cohen, M. L. *Phys. Rev. B* **1985**, *32*, 7988.

[48] Cohen, M. L. *Science* **1993**, *261*, 307.

[49] Liu, A. Y.; Cohen, M. L. *Science* **1989**, *245*, 841.

[50] Niu, C.; Lu, Y. Z.; Lieber, C. M. *Science* **1993**, *261*, 334.

[51] Teter, D. M.; Hemley, R. J. *Science* **1996**, *271*, 53.

[52] Liu, A. Y.; Wentzcovich, R. M. *Phys. Rev. B* **1994**, *50*, 10362.

[53] Ortega, J.; Sankey, O. F. *Phys. Rev. B* **1995**, *51*, 2624.

[54] Mattesini, M.; Matar, S. F.; Snis, A.; Etourneau, J.; Mavromaras, A. *J. Mater. Chem.* **1999**, *9*, 3151.

[55] Mattesini, M.; Matar, S. F. *C. R. Acad. Sci., Ser. IIc: Chim.* **2001**, *4*, 255.

[56] Snis, A.; Matar, S. F. *Phys. Rev. B* **1999**, *60*, 10855.

[57] Weihrich, R.; Eyert, V.; Matar, S. F. *Chem. Phys. Lett.* **2003**, *373*, 636.

[58] Mattesini, M.; Matar, S. F. *Phys. Rev. B* **2002**, *65*, 075110.

[59] Kroll, P.; Hoffmann, R. *J. Am. Chem. Soc.* **1999**, *121*, 4696.

[60] Riedel, R.; Kroke, E.; Greiner, A.; Gabriel, A. O.; Ruwisch, L.; Nicolich, J.; Kroll, P. *Chem. Mater.* **1998**, *10*, 2964.

[61] Sjöström, H.; Stafström, S.; Boman, M.; Sundgren, J.-E. *Phys. Rev. Lett.* **1995**, *75*, 1336.

[62] Stafström, S. *Appl. Phys. Lett.* **2000**, *77*, 3941.

[63] Terrones, M.; Redlich, P.; Grobert, N.; Trasobares, S.; Hsu, W.-K.; Terrones, H.; Zhu, Y.-Q.; Hare, J. P.; Reeves, C. L.; Cheetham, A. K.; Rühle, M.; Kroto, H. W.; Walton, D. R. M. *Adv. Mater.* **1999**, *11*, 655.

[64] Schultz, D.; Droppa Jr., R.; Alvarez, F.; dos Santos, M. C. *Phys. Rev. Lett.* **2003**, *90*, 015501.

[65] Kroke, E.; Schwarz, M.; Buschmann, V.; Miehe, G.; Fuess, H.; Riedel, R. *Adv. Mater.* **1999**, *11*, 158.

[66] Vodak, D. T.; Kim, K.; Iordanidis, L.; Rasmussen, P. G.; Matzger, A. J.; Yaghi, O. M. *Chem. Eur. J.* **2003**, *9*, 4197.

[67] Zhang, Z. J.; Fan, S. S.; Lieber, C. M. *Appl. Phys. Lett.* **1995**, *66*, 3582.

[68] Zhou, Z. B.; Cui, R. Q.; Pang, Q. J.; Hadi, G. M.; Ding, Z. M.; Li, W. Y. *Sol. Energy Mater. Sol. Cells* **2002**, *70*, 487.

[69] Sugimura, H.; Sato, Y.; Tajima, N.; Takai, O. *Surf. Coat. Technol.* **2001**, *142*, 714.

[70] Kulisch, W.; Popov, C.; Zambov, L. *New Diamond Front. Carbon Technol.* **2001**, *11*, 53.

[71] *Ion-Sensitive Field Effect Transistor and a Method for Producing a Transistor of this Type*. Grueger, H.; Kunath, C. International Patent, PTC Int. Appl. WO 03069327 A1, 2003.

[72] Badding, J. V.; Nesting, D. C. *Chem. Mater.* **1996**, *8*, 535.

[73] Alves, I.; Demazeau, G.; Tanguy, B.; Weill, F. *Solid State Commun.* **1999**, *109*, 697.

[74] Montigaud, H.; Tanguy, B.; Demazeau, G.; Alves, I.; Birot, M.; Dunogues, J. *Diamond Rel. Mater.* **1999**, *8*, 1707.

[75] Pauling, L.; Sturdivant, J. H. *Proc. Natl. Acad. Sci. U. S. A.* **1937**, *23*, 615.

[76] Redemann, C. E.; Lucas, H. J. *J. Am. Chem. Soc.* **1940**, *62*, 842.

[77] Gavrilova, N. K.; Gal'perin, V. A.; Finkel'shtein, A. I.; Koryakin, A. G. *Zh. Org. Khim.* **1977**, *13*, 669.

[78] Moncharzh, E. M.; Gavrilova, N. K.; Gal'perin, V. A.; Finkel'shtein, A. I. *Zh. Strukt. Khim.* **1982**, *23*, 152.

[79] Spiridonova, N. V.; Finkel'shtein, A. I. *Khim. Geterotsikl. Soedin.* **1966**, *1*, 126.

[80] Franklin, E. C. *J. Am. Chem. Soc.* **1922**, *44*, 486.

[81] Khorosheva, V. V.; Finkel'shtein, A. I. *Zh. Fiz. Khim.* **1962**, *36*, 1055.

[82] Jürgens, B.; Irran, E.; Senker, J.; Kroll, P.; Müller, H.; Schnick, W. *J. Am. Chem. Soc.* **2003**, *125*, 10288.

[83] Komatsu, T. *J. Mater. Chem.* **2001**, *11*, 802.

[84] Komatsu, T.; Nakamura, T. *J. Mater. Chem.* **2001**, *11*, 474.

[85] Kroke, E.; Schwarz, M.; Horath-Bordon, E.; Kroll, P.; Noll, B.; Norman, A. D. *New J. Chem.* **2002**, *26*, 508.

[86] Kroke, E.; Schwarz, M. *GIT Labor-Fachzeitschrift* **2003**, *5*, 560.

[87] Wagner, O.; Jansen, M.; Baldus, H.-P. *Z. Anorg. Allg. Chem.* **1994**, *620*, 366.

[88] Jansen, M.; Löffelholz, J. *Adv. Mater.* **1992**, *4*, 746.

[89] Baldus, H.-P.; Schnick, W.; Lücke, J.; Wannagat, U.; Bogedain, G. *Chem. Mater.* **1993**, *5*, 845.

[90] Khabashesku, V. N.; Zimmerman, J. L.; Margrave, J. L. *Chem. Mater.* **2000**, *12*, 3264.

[91] Courjault, S.; Tanguy, B.; Demazeau, G. *C. R. Acad. Sci., Ser. IIc: Chim.* **1999**, *2*, 487.

[92] Rovnyak, D.; Baldus, M.; Itin, B. A.; Bennati, M.; Stevens, A.; Griffin, R. G. *J. Phys. Chem. B* **2000**, *104*, 9817.

[93] Li, D.; Chung, Y. W.; Yang, S.; Wong, M.-S.; Adibi, F.; Sproul, W. D. *J. Vac. Sci. Technol., A* **1994**, *12*, 1470.

[94] LaManna, J.; Braddock-Wilking, J.; Lin, S.-H.; Feldman, B. *Solid State Commun.* **1999**, *109*, 573.

[95] Toda, F., Ed. *Organic Solid State Reactions*; Kluwer Academic Publishers: Dordrecht, 2002.

[96] Toda, F. *Synlett* **1993**, *5*, 303.

[97] Kohlschütter, V. *Z. Anorg. Allg. Chem.* **1919**, *105*, 1.

[98] Hertel, Z. *Z. Elektrochem.* **1931**, *37*, 536.

[99] Schmidt, G. M. J. *J. Chem. Soc.* **1964**, 2014.

[100] Cohen, M. D.; Schmidt, G. M. J. *J. Chem. Soc.* **1964**, 1996.

[101] Cohen, M. D.; Schmidt, G. M. J.; Flavian, S. *J. Chem. Soc.* **1964**, 2041.

[102] Cohen, M. D.; Hirshberg, Y.; Schmidt, G. M. J. *J. Chem. Soc.* **1964**, 2051.

[103] Cohen, M. D.; Hirshberg, Y.; Schmidt, G. M. J. *J. Chem. Soc.* **1964**, 2060.

[104] Bregman, J.; Osaki, K.; Schmidt, G. M. J.; Sonntag, F. I. *J. Chem. Soc.* **1964**, 2021.

[105] Rabinovich, D.; Schmidt, G. M. J. *J. Chem. Soc.* **1964**, 2030.

[106] Bregman, J.; Leiserowitz, L.; Schmidt, G. M. J. *J. Chem. Soc.* **1964**, 2068.

[107] Bregman, J.; Leiserowitz, L.; Osaki, K. *J. Chem. Soc.* **1964**, 2086.

[108] Kaupp, G. *Int. J. Photoen.* **2001**, *3*, 55.

[109] Kaupp, G. *Angew. Chem.* **1992**, *104*, 606; *Angew. Chem. Int. Ed. Engl.* **1992**, *31*, 592.

[110] Kaupp, G. *Angew. Chem.* **1992**, *104*, 609; *Angew. Chem. Int. Ed. Engl.* **1992**, *31*, 595.

[111] Sekine, A.; Tatsuki, H.; Ohashi, Y. *Mol. Cryst. Liq. Cryst. Sect. A* **1994**, *242*, 377.

[112] Morawetz, H.; Jakabhaazy, S. Z.; Lando, J. B.; Shafer, J. *Proc. Natl. Acad. Sci. U. S. A.* **1963**, *49*, 789.

[113] Lotgering, F. K. *J. Inorg. Nuclear Chem.* **1959**, *9*, 113.

[114] Busse, G.; Tschentscher, T.; Plech, A.; Wulff, M.; Frederichs, B.; Techert, S. *Faraday Discuss.* **2002**, *122*, 105.

[115] Cohen, M. D.; Schmidt, G. M. J.; Sonntag, F. I. *J. Chem. Soc.* **1964**, 2000.

[116] Tanaka, Y.; Sasaki, S.; Kobayashi, A. *J. Inclusion Phenom. Macrocyclic Chem.* **1984**, *2*, 851.

[117] Tanaka, K.; Toda, F. *Chem. Rev.* **2000**, *100*, 1025.

[118] Enkelmann, V.; Leyrer, R. J.; Wegner, G. *Makromol. Chem.* **1979**, *180*, 1787.

[119] Egerton, P. L.; Hyde, E. M.; Trigg, J.; A. Payne, P. B.; Mijovic, M. V.; Reiser, A. *J. Am. Chem. Soc.* **1981**, *103*, 3859.

[120] Tanaka, K.; Toda, F. *J. Chem. Soc., Chem. Commun.* **1983**, 593.

[121] Jürgens, B.; Höppe, H. A.; Schnick, W. *Inorg. Chem.* **2002**, *41*, 4849.

[122] Lotsch, B. V.; Senker, J.; Kockelmann, W.; Schnick, W. *J. Solid State Chem.* **2003**, *176*, 180.

[123] Lotsch, B. V.; Senker, J.; Schnick, W. *Inorg. Chem.* **2004**, *43*, 895.

[124] Lotsch, B. V.; Schnick, W. *Chem. Mater.* **2005**, *17*, 3976.

[125] Jürgens, B.; Irran, E.; Schneider, J.; Schnick, W. *Inorg. Chem.* **2000**, *39*, 665.

[126] Irran, E.; Jürgens, B.; Schnick, W. *Chem. Eur. J.* **2001**, *7*, 5372.

[127] Lotsch, B. V.; Schnick, W. *Chem. Mater.* **2006**, *18*, 1891.

[128] Gillan, E. G. *Chem. Mater.* **2000**, *12*, 3906.

[129] Giacovazzo, C.; Monaco, H. L.; Artioli, G.; Viterbo, D.; Ferraris, G.; Gilli, G.; Zanotti, G.; Catti, M. *Fundamentals of Crystallography*, IUCr Texts on Crystallography; 2<sup>nd</sup> Ed.; Oxford University Press: New York, 2002.

[130] Vainstein, B. K. *Fundamentals of Crystals. Symmetry, and Methods of Structural Crystallography*, Modern Crystallography I; Springer Verlag: Berlin, 1996.

[131] Zou, X. *Electron Crystallography of Inorganic Structures - Theory and Practice*; Stockholm University: Stockholm, 1995.

[132] *BASREADER*; v2.13a; Raytest Isotopenmessgeräte GmbH: Straubenhardt, 1994.

[133] *TINA*; v2.10g; Raytest Isotopenmessgeräte GmbH: Straubenhardt, 1993.

[134] Sheldrick, G. M. *XPREP, Data Preparation & Reciprocal Space Exploration*; v6.12; Siemens Analytical X-ray Instruments, 1996.

[135] Sheldrick, G. M. *SHELXS-97, Program for the Solution of Crystal Structures*; University of Göttingen: Göttingen, 1997.

[136] Sheldrick, G. M. *SHELXL-97, Program for the Refinement of Crystal Structures*; University of Göttingen: Göttingen, 1997.

[137] Speck, A. L. *PLATON, A Multipurpose Crystallographic Tool*; Utrecht University: Utrecht, 2003.

[138] Speck, A. L. *Acta Crystallogr. A* **2003**, *46*, c34.

[139] Farrugia, L. J. *WinGX*; v1.61; University of Glasgow: Glasgow, 1998.

[140] Brandenburg, K. *DIAMOND, Program for X-ray Structure Analysis*; v3.1a; Crystal Impact GbR: Bonn, 2005.

[141] Rannabauer, S. *Vom Silazan zum Nanokomposit*, PhD Thesis, Universität München, **2004**.

[142] Williams, D. B.; Carter, C. B. *Diffraction II*, Transmission Electron Microscopy; Springer Science + Business Media Inc.: New York, 1996.

[143] Zou, X. D.; Sukharev, Y.; Hovmöller, S. *Ultramicroscopy* **1993**, *49*, 147.

[144] Zou, X. D.; Sukharev, Y.; Hovmöller, S. *Ultramicroscopy* **1993**, *52*, 436.

[145] Weber, S. *Java Structure Viewer*; v1.08, 1999.

[146] Wan, Z. H.; Liu, Y. D.; Fu, Z. Q.; Li, Y.; Cheng, T. Z.; Li, F. H.; Fan, H. F. *Z. Krist.* **2003**, *218*, 308.

[147] Stadelmann, P. A. *Ultramicroscopy* **1987**, *21*, 129.

[148] Altomare, A.; Burla, M. C.; Camalli, M.; Cascarano, G. L.; Giacovazzo, C.; Guagliardi, A.; Moliterni, A. G. G.; Polidori, G.; Spagna, R. *J. Appl. Crystallogr.* **1999**, *32*, 115.

[149] *OPUS, Programm zur Auswertung von Schwingungsspektren*; v3.0.2; Bruker Optics GmbH: Karlsruhe, 1996.

[150] Vogel, H. *Phys. Z.* **1921**, *22*, 645.

[151] Fulcher, G. S. *J. Am. Ceram. Soc.* **1925**, *8*, 339.

[152] *TOFSYS, Program for Simulating QENS Spectra*; Forschungszentrum Jülich GmbH: Jülich, Germany.

[153] Davis, J. H.; Jeffrey, K. R.; Bloom, M.; Valic, M. I. *Chem. Phys. Lett.* **1976**, *42*, 390.

[154] Bennett, A. E.; Rienstra, C. M.; Auger, M.; Lakshmi, K. V.; Griffin, R. G. *J. Chem. Phys.* **1995**, *103*, 6951.

[155] Zhang, S.; Wu, X.; Mehring, M. *Chem. Phys. Lett.* **1990**, *173*, 481.

[156] Ishii, Y. *J. Chem. Phys.* **2001**, *114*, 8473.

[157] Press, W. *Single Particle Rotations in Molecular Crystals*, Springer Tracts in Modern Physics, Vol. 92; Springer Verlag: Berlin, 1981.

[158] Bee, M. *Quasielastic Neutron Scattering*; Adam Hilger: Bristol, 1989.

[159] Spiess, H. W.; Sillescu, H. *J. Magn. Reson.* **1981**, *42*, 381.

[160] Böhmer, R.; Diezemann, G.; Hinze, G.; Rössler, E. *Prog. Nucl. Magn. Reson. Spectrosc.* **2001**, *39*, 191.

[161] Senker, J. *Untersuchungen zum Reorientierungsverhalten von Molekül anionen in Alkali- und Erdalkalimetallamiden mit Festkörper-NMR-Spektroskopie und Neutronendiffraktion*, PhD Thesis, Universität Dortmund, **1996**.

[162] Haarmann, F. *Alkalimetallhydrogensulfide - Struktur und Dynamik*, PhD Thesis, Universität Dortmund, **2001**.

[163] Lotsch, B. V. *Untersuchungen zur Struktur und Thermisch Induzierten Reaktivität von Ammonium-Dicyanamid*, Diploma Thesis, Universität München, **2002**.

[164] Squires, G. L. *Introduction to the Theory of Thermal Neutron Scattering*; Cambridge University Press: Cambridge, 1978.

[165] Lovesey, S. W. *Theory of Neutron Scattering from Condensed Matter*; Oxford University Press: Oxford, 1984.

[166] Willis, B. T. M.; Pryor, A. W. *Thermal Vibrations in Crystallography*; Cambridge University Press: Cambridge, 1975.

[167] Müller, M. *Anordnung und Dynamik der  $NH_2^-$ -Ionen in Kalium- und Strontiumamid: Untersuchungen mit Neutronenstreuung*, PhD Thesis, Universität Kiel, **1996**.

[168] van Hove, L. *Phys. Rev.* **1954**, *95*, 249.

[169] Dianoux, A. J.; Volino, F. *Mol. Phys.* **1977**, *34*, 1263.

[170] Raedt, B. D.; Michel, K. H. *Phys. Rev. B* **1979**, *19*, 767.

[171] Prask, H. J.; Trevino, S. F.; Rush, J. J. *J. Chem. Phys.* **1975**, *63*, 4156.

[172] Goyal, P. S.; Dasannacharya, B. A. *J. Chem. Phys.* **1978**, *68*, 2430.

[173] Lechner, R. E.; Badurek, G.; Dianoux, A. J.; Hervet, H.; Volino, F. *J. Chem. Phys.* **1980**, *73*, 934.

[174] Steenbergen, C.; de Graaf, L. A.; Bevaart, L.; Bartolome, J.; de Jongh, L. J. *J. Chem. Phys.* **1979**, *70*, 1450.

[175] Levitt, M. H. *Spin Dynamics. Basics of Nuclear Magnetic Resonance*; John Wiley & Sons, Ltd: Chichester, 2005.

[176] Abragam, A. *Principles of Nuclear Magnetism*, International Series of Monographs on Physics, Vol. 32; Oxford Science Publications: Oxford, 1961.

[177] Slichter, C. P. *Principles of Magnetic Resonance*, Springer Series in Solid-State Sciences, Vol. 1; 3<sup>rd</sup> Ed.; Springer Verlag: Berlin, 1996.

[178] Senker, J. *New Approaches to Structure Determination of Ordered and Disordered Solids by Means of Solid-State NMR*, Habilitation, Universität München, **2005**.

[179] Hoasten, G. L.; Vold, R. L. *<sup>2</sup>H NMR-Spectroscopy of Solids and Liquid Crystals*, in: *NMR: Basic Principles and Progress*, Vol. 32; Diebel, P.; Fluck, E.; Kosfeld, R. (Eds.); Springer Verlag: Berlin, 1994.

[180] Spiess, H. W. *Rotation of Molecules and Nuclear Spin Relaxation*, in: *NMR: Basic Principles and Progress*, Vol. 15; Diebel, P.; Fluck, E.; Kosfeld, R. (Eds.); Springer Verlag: Berlin, 1978.

[181] Greenfiled, M. S.; Ronemus, A. D.; Vold, R. L.; Vold, R. R.; Ellis, P. D.; Rайдy, T. E. *J. Magn. Reson.* **1987**, *72*, 89.

[182] Alderman, D. W.; Solum, M. S.; Grant, D. M. *J. Chem. Phys.* **1986**, *84*, 3717.

[183] Spiess, H. W. *Colloid Polym. Sci.* **1983**, *261*, 193.

[184] Spiess, H. W. *J. Chem. Phys.* **1980**, *72*, 6755.

[185] Haeberlen, U. *High Resolution NMR in Solids; Suppl. 1 to Advances in Magnetic Resonance*; Academic Press: New York, 1976.

[186] Smith, S. A.; Levante, T. O.; Meier, B. H.; Ernst, R. R. *J. Magn. Reson.* **1994**, *106a*, 75.

[187] MATLAB, *The Language of Technical Computing*; MathWorks Inc.: Natick MA, Copyright 1984-1998.

[188] Oppenheim, I.; Schuler, K. E.; Weiss, G. H. *Stochastic Processes in Chemical Physics: The Master Equation*; MIT Press Cambridge: Cambridge, 1977.

[189] Senker, J. *Solid State Nucl. Magn. Reson.* **2004**, *26*, 22.

[190] Bielecki, A.; Kolbert, A. C.; Levitt, M. H. *Chem. Phys. Lett.* **1989**, *155*, 341.

[191] Fu, R.; Tian, C.; Cross, T. A. *J. Magn. Reson.* **2002**, *154*, 130.

[192] Pines, A.; Gibby, M. G.; Waugh, J. S. *J. Chem. Phys.* **1972**, *56*, 1776.

[193] Pines, A.; Gibby, M. G.; Waugh, J. S. *J. Chem. Phys.* **1973**, *59*, 569.

[194] Gervais, C.; Babonneau, F.; Maquet, J.; Bonhomme, C.; Massiot, D.; Framery, E.; Vaultier, M. *Magn. Reson. Chem.* **1998**, *36*, 407.

[195] Sangill, R.; Rastrup-Andersen, N.; Bildsoe, H.; Jakobsen, H. J.; Nielsen, N. C. *J. Magn. Reson. A* **1994**, *107*, 67.

[196] Fayon, F.; King, I. J.; Harris, R. K.; Gover, R. K. B.; Evans, J. S. O.; Massiot, D. *Chem. Mater.* **2003**, *15*, 2234.

[197] Brinkmann, A.; Levitt, M. H. *J. Chem. Phys.* **2001**, *115*, 357.

[198] Bjerring, M.; Nielsen, N. C. *Chem. Phys. Lett.* **2003**, *370*, 496.

[199] Karlsson, T.; Popham, J. M.; Long, J. R.; Oyler, N.; Oyler, G. P. J. *J. Am. Chem. Soc.* **2003**, *125*, 7394.

[200] Edén, M. *Chem. Phys. Lett.* **2003**, *378*, 55.

[201] Lesage, A.; Bardet, M.; Emsley, L. *J. Am. Chem. Soc.* **1999**, *121*, 10987.

[202] Baldus, M.; Meier, B. H. *J. Magn. Reson.* **1997**, *128*, 172.

[203] Sommer, W.; Gottwald, J.; Demco, D. E.; Spiess, H. W. *J. Magn. Reson. A* **1995**, *113*, 131.

[204] Schmedt auf der Günne, J. *J. Magn. Reson. A* **2003**, *165*, 18.

[205] Baldus, M.; Iuliucci, R. J.; Meier, B. H. *J. Am. Chem. Soc.* **1997**, *119*, 1121.

[206] Hong, M.; Griffin, G. *J. Am. Chem. Soc.* **1998**, *120*, 7113.

[207] Saalwächter, K.; Graf, R.; Spiess, H. W. *J. Magn. Reson. A* **2001**, *148*, 398.

[208] Macholl, S.; Sack, I.; Limbach, H.-H.; Pauli, J.; Kelly, M.; Buntkowsky, G. *Magn. Reson. Chem.* **2000**, *38*, 596.

[209] Holland, G. P.; Alam, T. M. *Phys. Chem. Chem. Phys.* **2005**, *7*, 1739.

[210] Ernst, R. R.; Bodenhausen, G.; Wokaun, A. *Principles of Nuclear Magnetic Resonance in One and Two Dimensions*; Clarendon Press: Oxford, 1997.

[211] Massiot, D. *High Resolution Solid State NMR*, in: *High Magnetic Fields: Applications in Condensed Matter Physics and Spectroscopy*, Vol. 595; Berthier, C.; Lévy, L.P.; Martinez, G. (Eds.); Springer Verlag: Berlin, 2002.

[212] van Rossum, B.-J.; Förster, H.; de Groot, H. J. M. *J. Magn. Reson.* **1997**, *124*, 124.

[213] Brinkmann, A.; Schmedt auf der Günne, J.; Levitt, M. H. *J. Magn. Reson.* **2002**, *156*, 79.

[214] Jäger, C.; Hartmann, P.; Witter, R.; Braun, M. *J. Non-Cryst. Solids* **2000**, *263*, 61.

[215] Lesage, A.; Auger, C.; Caldarelli, S.; Emsley, L. *J. Am. Chem. Soc.* **1997**, *119*, 7867.

[216] Lesage, A.; Sakellariou, D.; Steuernagel, S.; Emsley, L. *J. Am. Chem. Soc.* **1998**, *120*, 13194.

[217] Chan, J. C. C.; Brunklaus, G. *Chem. Phys. Lett.* **2001**, *349*, 104.

[218] Hardy, E. H.; Verel, R.; Meier, B. H. *J. Magn. Reson.* **2001**, *148*, 459.

[219] van Wüllen, L.; Jansen, M. *J. Mater. Chem.* **2001**, *11*, 223.

[220] van Wüllen, L.; Müller, U.; Jansen, M. *Chem. Mater.* **2000**, *12*, 2347.

[221] Jansen, M.; Jaeschke, B.; Jaeschke, T. *Struct. Bond.* **2000**, *101*, 137.

[222] Ratai, E.-M.; Jansen, M.; Epping, J. D.; Chan, J. C. C.; Eckert, H. *Phys. Chem. Glasses* **2003**, *44*, 45.

[223] Ishii, Y.; Balbach, J. J.; Tycko, R. *Chem. Phys.* **2001**, *266*, 231.

[224] Bennett, A. E.; Rienstra, C. M.; Griffiths, J. M.; Zhen, W.; Lansbury Jr., P. T.; Griffin, R. G. *J. Chem. Phys.* **1998**, *108*, 9463.

[225] Bennett, A. E.; Ok, J. H.; Griffin, R. G.; Vega, S. *J. Chem. Phys.* **1992**, *96*, 8624.

[226] Wöhler, F. *Ann. Phys. Berlin* **1828**, *12*, 253.

[227] Dunitz, J.; Harris, K. D. M.; Johnston, R. L.; Kariuki, B. M.; MacLean, E. J.; Psallidas, K.; Schweizer, W. B.; Tykwiński, R. R. *J. Am. Chem. Soc.* **1998**, *120*, 13274.

[228] von Liebig, J.; Wöhler, F. *Ann. Phys. Leipzig, Ser. 2* **1830**, *20*, 369.

[229] Grimm, H. G. *Z. Elektrochem.* **1925**, *31*, 474.

[230] Madelung, W.; Kern, E. *Liebigs Ann. Chem.* **1922**, *427*, 1.

[231] Short, W. F. *Chem. News* **1923**, *126*, 100.

[232] Tsipis, C. A.; Karipidis, P. A. *J. Am. Chem. Soc.* **2003**, *125*, 2307.

[233] Schmidt-Rohr, K.; Spiess, H. W. *Multidimensional Solid-State NMR and Polymers*; Academic Press: New York, 1994.

[234] Lusceac, S. A.; Roggatz, I.; Medick, P.; Gmeiner, J.; Rössler, E. A. *J. Chem. Phys.* **2004**, *121*, 4770.

[235] Lusceac, S. A.; Koplin, C.; Medick, P.; Vogel, M.; Brodie-Lindner, N.; LeQuellec, C.; Alba-Simionescu, C.; Rössler, E. A. *J. Phys. Chem.* **2004**, *43*, 16602.

[236] Blochowicz, T.; Karle, C.; Kudlik, A.; Medick, P.; Roggatz, I.; Vogel, M.; Tschirwitz, C.; Wolber, J.; Senker, J.; Rössler, E. A. *J. Phys. Chem. B* **1999**, *103*, 4032.

[237] Senker, J.; Rössler, E. A. *J. Phys. Chem. B* **2002**, *106*, 7592.

[238] Vogel, M.; Rössler, E. A. *J. Chem. Phys.* **2001**, *114*, 5802.

[239] Vogel, M.; Rössler, E. A. *J. Chem. Phys.* **2001**, *115*, 10883.

[240] Jürgens, B. *Molekulare Vorstufen zur Synthese Grafitischen Kohlenstoff(IV)-nitrids - von Dicyanamiden über Tricyanomelamine zu Melem*, PhD Thesis, Universität München, Shaker Verlag: Aachen, **2004**.

[241] Lalowicz, Z. T.; Punkkinen, M.; Olejniczak, Z.; Birczynski, A.; Haeberlen, U. *Solid State Nucl. Magn. Reson.* **2002**, *22*, 373.

[242] Filipek, P.; Lalowicz, Z. T.; Olejniczak, Z.; Birczynski, A. *Chem. Phys. Lett.* **2003**, *367*, 55.

[243] Bonori, M.; Terenzi, M. *Chem. Phys. Lett.* **1974**, *27*, 281.

[244] Prager, M.; Badurch, G. *J. Phys. C: Solid State Phys.* **1986**, *19*, 6105.

[245] Hennel, J. W.; Lalowicz, Z. T. *Proc. XVI Congress Ampere Bucharest, Rumania*, **1997**, 637.

[246] Ylinen, E. E.; Tuohi, J. E.; Niemela, L. K. E. *Chem. Phys. Lett.* **1974**, *24*, 447.

[247] Riehl, J. W.; Wang, R.; Bernard, H. W. *J. Chem. Phys.* **1973**, *58*, 508.

[248] Güttler, W.; von Schültz, J. V. *Chem. Phys. Lett.* **1973**, *20*, 133.

[249] Töpler, J.; Richter, D. R. *J. Chem. Phys.* **1978**, *69*, 3170.

[250] Reynhardt, E. C.; Watton, A.; Petch, H. E. *J. Chem. Phys.* **1979**, *71*, 4421.

[251] Avrami, M. J. *Chem. Phys.* **1939**, *7*, 1103.

[252] Avrami, M. J. *Chem. Phys.* **1940**, *8*, 212.

[253] Avrami, M. J. *Chem. Phys.* **1941**, *9*, 177.

[254] Li, Y. Q.; Zhang, L. *J. Phys.: Condens. Matter* **2003**, *15*, 8081.

[255] Schotte, U.; Schotte, K. D.; Kabs, M.; Dachs, H. *J. Phys.: Condens. Matter* **1992**, *4*, 9283.

[256] Schotte, U.; Schotte, K. D.; Bleif, H.-J.; Kabs, M.; Dachs, H. *J. Phys.: Condens. Matter* **1995**, *7*, 7453.

[257] Anderson, J. E. *Faraday Symp. Chem. Soc.* **1972**, *3*, 82.

[258] *Neutron Scattering at FRJ-2, Experimental Reports 2004*; Forschungszentrum Jülich GmbH: Jülich, Germany, 2004.

[259] Haarmann, F.; Jacobs, H.; Asmussen, B.; Nöldeke, C.; Kearley, G. J.; Combet, J. *J. Chem. Phys.* **2000**, *113*, 8161.

[260] Müller, M.; Asmussen, B.; Press, W.; Senker, J.; Jacobs, H.; Büttner, H.; Schobe, H. *J. Chem. Phys.* **1998**, *109*, 3559.

[261] Brown, C. M.; Manson, J. L. *J. Am. Chem. Soc.* **2002**, *124*, 12600.

[262] Prager, M.; Pawlukojc, A.; Sobczyk, L.; Grech, E.; Grimm, H. *J. Phys.: Condens. Matter* **2005**, *17*, 5725.

[263] Arrighi, V.; Ferguson, R.; Lechner, R. E.; Telling, M.; Triolo, A. *Phys. B* **2001**, *301*, 35.

[264] Frick, B.; Richter, D. *Phys. Rev. B* **1993**, *47*, 14795.

[265] Frick, B.; Fetters, L. J. *Macromolecules* **1994**, *27*, 974.

[266] Arrighi, V.; Batt-Coutrot, D.; C.Zhang.; Telling, M. T. F.; Triolo, A. *J. Chem. Phys.* **2003**, *119*, 1271.

[267] Prager, M.; Heidemann, A. *Rotational Tunnelling and Neutron Spectroscopy: A Compilation*; Forschungszentrum Jülich GmbH: Jülich, Germany, 1995.

[268] Hallwachs, F. *Liebigs Ann. Chem.* **1870**, *153*, 293.

[269] Mushkin, Y. I.; Finkel'shtein, A. I. *Russ. J. Gen. Chem.* **1963**, *33*, 1883.

[270] Blair, J. S.; Smith, G. E. P. *J. Am. Chem. Soc.* **1934**, *56*, 907.

[271] Beyer, H.; Schilling, H. *Z. Chem.* **1965**, *5*, 182.

[272] Beyer, H.; Schilling, H. *Chem. Ber.* **1966**, *99*, 2110.

[273] Britton, D. *Acta Crystallogr. C* **1987**, *43*, 2442.

[274] Magomedova, N. S.; Zvonkova, Z. V. *Zh. Strukt. Khim.* **1974**, *15*, 165.

[275] Iio, K. *Bull. Chem. Soc. Jpn.* **1984**, *57*, 625.

[276] Mushkin, Y. I.; Finkel'shtein, A. I. *Kinet. Katal.* **1966**, *7*, 219.

[277] Mushkin, Y. I.; Finkel'shtein, A. I. *Zh. Org. Khim.* **1967**, *3*, 507.

[278] Lotsch, B. V.; Schnick, W. *Z. Naturforsch.* **2004**, *59b*, 1229.

[279] Beyer, H. *Z. Chem.* **1966**, *6*, 213.

[280] Bieling, H.; Barth, P.; Beyer, H. *Z. Chem.* **1964**, *4*, 146.

[281] Schaber, P. M.; Colson, J.; Higgins, S.; Dietz, E.; Thielen, D.; Anspach, B.; Brauer, J. *American Laboratory* **1999**, *31*, 13.

[282] Lotsch, B. V.; Schnick, W. *Z. Naturforsch.* **2005**, *60b*, 377.

[283] *Cyanoguanylurea*. Ohdo, K.; Ichikawa, E. Japanese Patent, JP 50160220 19751225, **1975**.

[284] Iio, K.; Ichikawa, E.; Odo, K. *Yuki Gosei Kagaku Kyokaishi* **1974**, *32*, 513.

[285] Suyama, T.; Okuno, S.; Ichikawa, E. *Nippon Kagaku Kaishi* **1986**, *9*, 1202.

[286] Cheng, H.; Ma, J.; Zhao, Z.; Qi, L. *Chem. Mater.* **1995**, *7*, 663.

[287] Purdy, A. P.; Jouet, R. J.; George, C. F. *Cryst. Growth Des.* **2002**, *2*, 141.

[288] Schmidt, A.; Glaum, R.; Beck, J. *J. Solid State Chem.* **1996**, *127*, 331.

[289] Ripert, V.; Hubert-Pfalzgraf, L. G.; Papiernik, R.; Belleville, P.; Floch, H. *J. Mater. Chem.* **2001**, *11*, 1880.

[290] M. Emirdag-Eanes, J. A. I. *J. Alloys Compd.* **2003**, *361*, 66.

[291] Hughes, E. W. *J. Am. Chem. Soc.* **1940**, *62*, 1258.

[292] Hirshfield, F. L.; Hope, H. *Acta Crystallogr. B* **1980**, *36*, 406.

[293] Jeremy-Jones, W.; Orville-Thomas, W. J. *Trans. Faraday Soc.* **1959**, *55*, 193.

[294] Cunningham, I. D.; Wan, N. C.; Povey, D. C.; Smith, G. W.; Cox, B. G. *Acta Crystallogr. C* **1997**, *53*, 984.

[295] Cunningham, I. D.; Cox, B. G.; Wan, N. C.; Povey, D. C.; Smith, G. W. *J. Chem. Soc., Perkin Trans. 2* **1999**, 693.

[296] Batsanov, A. S.; Begley, M. J.; Hubberstey, P.; Stroud, J. *J. Chem. Soc., Dalton Trans.* **1996**, 1947.

[297] Pickard, J.; Kuhn, B. *Z. Naturforsch.* **1996**, *51b*, 1469.

[298] Pickard, J.; Kuhn, B. *Z. Kristallogr.* **1995**, *210*, 901.

[299] Mattesini, M.; Matar, S. F.; Etourneau, J. *J. Mater. Chem.* **2000**, *10*, 709.

[300] Komatsu, T. *J. Mater. Chem.* **2001**, *11*, 799.

[301] Kouvretakis, J.; Bandari, A.; Todd, M.; Wilkens, B. *Chem. Mater.* **1994**, *6*, 811.

[302] Jürgens, B.; Milius, W.; Morys, P.; Schnick, W. *Z. Anorg. Allg. Chem.* **1998**, *624*, 91.

[303] Lotsch, B. V.; Schnick, W. *New J. Chem.* **2004**, *28*, 1129.

[304] Burdick, W. L. *J. Am. Chem. Soc.* **1925**, *47*, 1485.

[305] Kuhn, M.; Mecke, R. *Chem. Ber.* **1961**, *94*, 3010.

[306] Bannow, A. *Ber. d. deutsch. chem. Ges.* **1871**, *4*, 253.

[307] Bannow, A. *Ber. d. deutsch. chem. Ges.* **1880**, *13*, 2201.

[308] Shurvell, H. F.; Hyslop, D. W. *J. Chem. Phys.* **1970**, *52*, 881.

[309] Bak, B.; Bang, O.; Nicolaisen, F.; Rump, O. *Spectrochim. Acta, Part A* **1971**, *27*, 1865.

[310] Christe, K. O.; Wilson, W. W.; Sheehy, J. A.; Boatz, J. A. *Angew. Chem.* **1999**, *111*, 2112; *Angew. Chem. Int. Ed.* **1999**, *38*, 2004.

[311] Vij, A.; Wilson, W. W.; Vij, V.; Tham, F. S.; Sheehy, J. A.; Christe, K. O. *J. Am. Chem. Soc.* **2001**, *123*, 6308.

[312] Harcourt, R. D.; Klapötke, T. M. *Z. Naturforsch.* **2002**, *57b*, 983.

[313] Dixon, D. A.; Feller, D.; Christe, K. O.; Wilson, W. W.; Vij, A.; Vij, V.; Jenkins, H. D. B.; Olson, R. M.; Gordon, M. S. *J. Am. Chem. Soc.* **2004**, *126*, 834.

[314] Bernhardi, I.; Drews, T.; Seppelt, K. *Angew. Chem.* **1999**, *111*, 2370; *Angew. Chem. Int. Ed.* **1999**, *38*, 2232.

[315] Bartolomäus, T.; Lentz, D.; Neubert, I.; Röttger, M. *Z. Anorg. Allg. Chem.* **2002**, *628*, 863.

[316] Halpern, J. *Discuss. Faraday Soc.* **1968**, *46*, 7.

[317] Elian, M.; Chen, M. M. L.; Mingos, D. M. P.; Hoffmann, R. *Inorg. Chem.* **1976**, *15*, 1148.

[318] Hoffmann, R. *Angew. Chem.* **1982**, *94*, 725; *Angew. Chem. Int. Ed. Engl.* **1982**, *21*, 711.

[319] Birkenbach, L.; Kellermann, K. *Chem. Ber.* **1925**, *58*, 786.

[320] Birkenbach, L.; Kellermann, K. *Chem. Ber.* **1925**, *58*, 2377.

[321] Perkins, A. J. *Dev. Appl. Spectrosc.* **1962**, *2*, 43.

[322] Köhler, H.; Seifert, B. *J. Organomet. Chem.* **1968**, *12*, 253.

[323] Köhler, H.; Beck, W. *Z. Anorg. Allg. Chem.* **1968**, *359*, 241.

[324] Köhler, H.; Menzel, R.; Mandl, F.; Jäger, L. *Z. Anorg. Allg. Chem.* **1987**, *551*, 173.

[325] Chow, Y. M. *Inorg. Chem.* **1971**, *10*, 1938.

[326] Chow, Y. M.; Britton, D. *Acta Crystallogr. B* **1975**, *31*, 1934.

[327] Purdy, A. P.; House, E.; George, C. F. *Polyhedron* **1997**, *16*, 3671.

[328] Starynowicz, P. *Acta Crystallogr. C* **1991**, *47*, 2198.

[329] Britton, D.; Chow, Y. M. *Acta Crystallogr. B* **1977**, *33*, 697.

[330] Britton, D. *Acta Crystallogr. C* **1990**, *47*, 2297.

[331] Vannerberg, N.-G. *Acta Chem. Scand.* **1962**, *16*, 2263.

[332] Jürgens, B.; Irran, E.; Schnick, W. *J. Solid State Chem.* **2001**, *157*, 241.

[333] Jürgens, B.; Höppe, H. A.; Schnick, W. *Solid State Sci.* **2002**, *4*, 821.

[334] Manson, J. L.; Lee, D. W.; Rheingold, A. L.; Miller, J. S. *Inorg. Chem.* **1998**, *37*, 5966.

[335] Jensen, P.; Batten, S. R.; Fallon, G. D.; Moubaraki, B.; Murray, K. S.; Price, D. J. *Chem. Commun.* **1999**, 177.

[336] Jürgens, B.; Irran, E.; Höppe, H. A.; Schnick, W. *Z. Anorg. Allg. Chem.* **2004**, *630*, 219.

[337] Jürgens, B.; Irran, E.; Schnick, W. *J. Solid State Chem.* **2005**, *178*, 72.

[338] Kurmoo, M.; Kepert, C. J. *New J. Chem.* **1998**, *22*, 1515.

[339] Manson, J. L.; Kmety, C. R.; Huang, Q.-Z.; Lynn, J. W.; Bendele, G. M.; Pagola, S.; Stephens, P. W.; Liable-Sands, L. M.; Rheingold, A. L.; Epstein, A. J.; Miller, J. S. *Chem. Mater.* **1998**, *10*, 2552.

[340] Batten, S. R.; Jensen, P.; Moubaraki, B.; Murray, K. S.; Robson, R. *Chem. Commun.* **1998**, 439.

[341] Manson, J. L.; Kmety, C. R.; Epstein, A. J.; Miller, J. S. *Inorg. Chem.* **1999**, *38*, 2552.

[342] Kurmoo, M.; Kepert, C. J. *Mol. Cryst. Liq. Cryst.* **1999**, *334*, 693.

[343] Kmety, C. R.; Manson, J. L.; Huang, Q.; Lynn, J. W.; Erwin, R. W.; Miller, J. S.; Epstein, A. J. *Phys. Rev. B* **1999**, *60*, 60.

[344] Bordallo, H. N.; Chapon, L. C.; Cook, J. C.; Copley, J. R. D.; Goremychkin, E.; Kern, S.; Lee, S.-H.; Yildirim, T.; Manson, J. L. *Appl. Phys. A* **2002**, *74*, 634.

[345] Jensen, P.; Batten, S. R.; Fallon, G. D.; Hockless, D. C. R.; Moubaraki, B.; Murray, K. S.; Robson, R. *J. Solid State Chem.* **1999**, *145*, 387.

[346] Manson, J. L.; Arif, A. M.; Miller, J. S. *J. Mater. Chem.* **1999**, *9*, 979.

[347] Cho, J.; Lee, U.; Kim, J. C. *Transition Met. Chem.* **2002**, *27*, 429.

[348] Vangdal, B.; Carranza, J.; Lloret, F.; Julve, M.; Sletten, J. *J. Chem. Soc., Dalton Trans.* **2002**, 566.

[349] Moliner, N.; Gaspar, A. B.; Munoz, M.; Niel, V.; Cano, J.; Real, J. A. *Inorg. Chem.* **2001**, *40*, 3686.

[350] van der Werff, P. M.; Batten, S. R.; Jensen, P.; Moubaraki, B.; Murray, K. S. *Inorg. Chem.* **2001**, *40*, 1718.

[351] Marshall, S. R.; Incarvito, C. D.; Manson, J. L.; Rheingold, A. L.; Miller, J. S. *Inorg. Chem.* **2000**, *39*, 1969.

[352] Kini, A. M.; Geiser, U.; Wang, H. H.; Carlson, K. D.; Williams, J. M.; Kwok, W. K.; Vandervoort, K. G.; Thompson, J. E.; Stupka, D. L.; Jung, D.; Whangbo, M.-H. *Inorg. Chem.* **1990**, *29*, 2555.

[353] Frankel, M. B.; Burns, E. A.; Butler, J. C.; Wilson, E. R. *J. Org. Chem.* **1963**, *28*, 2428.

[354] MacFarlane, D.; Golding, J.; Forsyth, S.; Forsyth, M.; Deacon, G. *Chem. Commun.* **2001**, 1430.

[355] Forsyth, S. A.; MacFarlane, D. R.; Thomson, R. J.; von Itzstein, M. *Chem. Commun.* **2002**, 714.

[356] MacFarlane, D.; Forsyth, S.; Golding, J.; Deacon, G. *Green Chem.* **2002**, *4*, 444.

[357] Forsyth, S. A.; Batten, S. R.; Dai, Q.; MacFarlane, D. R. *Aust. J. Chem.* **2004**, *57*, 121.

[358] Gerhard, D.; Alpaslan, S. C.; Gores, H. J.; Uerdingen, M.; Wasserscheid, P. *Chem. Commun.* **2005**, 5080.

[359] Batten, S.; Murray, K. *Coord. Chem. Rev.* **2003**, *246*, 103.

[360] Seeber, A. J.; Forsyth, M.; Forsyth, C. M.; Forsyth, S. A.; Annat, G.; MacFarlane, D. R. *Phys. Chem. Chem. Phys.* **2003**, *5*, 2692.

[361] Hoard, J. L. *J. Am. Chem. Soc.* **1938**, *60*, 1194.

[362] *Nitrogen-Rich Solid Propellant Gas-Generating Formulations with Slag-Trapping Components for Vehicle Airbags*. Gast, E.; Schmid, B.; Semmler, P. International Patent, PTC Int. Appl. WO 9948843 A1, **1999**.

[363] Steiner, T. *Angew. Chem.* **2002**, *114*, 50; *Angew. Chem. Int. Ed.* **2002**, *41*, 48.

[364] Bator, G.; Zeegers-Huyskens, T.; Jakubas, R.; Zaleski, J. *J. Mol. Struct.* **2001**, *570*, 61.

[365] Angell, C. L.; Sheppard, N.; Yamaguchi, A.; Shimanouchi, T.; Miyazawa, T. *Trans. Farad. Soc.* **1957**, *53*, 589.

[366] Szafranski, M. *Phys. Status Solidi B* **1997**, *201*, 343.

[367] Rousseau, D. L.; Baumann, R. P.; Porto, S. P. S. *J. Raman Spect.* **1981**, *10*, 253.

[368] Jakubas, R.; Ciapala, P.; Pietrzaszko, A.; Zaleski, J.; Kusz, J. *J. Phys. Chem. Solids* **1998**, *59*, 1309.

[369] Furukawa, Y.; Terao, H. *Z. Naturforsch.* **2002**, *57a*, 399.

[370] Yamauchi, M.; Ishimaru, S.; Ikeda, R. *Chem. Lett.* **2003**, *32*, 976.

[371] Janczak, J.; Perpetuo, G. J. *Acta Crystallogr. C* **2001**, *57*, 1120.

[372] Janczak, J.; Perpetuo, G. J. *Acta Crystallogr. C* **2002**, *58*, o455.

[373] Janczak, J.; Perpetuo, G. J. *Acta Crystallogr. C* **2001**, *57*, 123.

[374] Janczak, J.; Perpetuo, G. J. *Acta Crystallogr. C* **2001**, *57*, 1431.

[375] Janczak, J.; Perpetuo, G. J. *Acta Crystallogr. C* **2002**, *58*, o339.

[376] Perpetuo, G. J.; Janczak, J. *Acta Crystallogr. C* **2002**, *58*, o112.

[377] Perpetuo, G. J.; Ribeiro, M. A.; Janczak, J. *Acta Crystallogr. E* **2005**, *61*, o1818.

[378] Perpetuo, G. J.; Janczak, J. *Acta Crystallogr. E* **2005**, *61*, o287.

[379] Perpetuo, G. J.; Janczak, J. *Acta Crystallogr. C* **2006**, *62*, o372.

[380] Janczak, J.; Perpetuo, G. J. *Acta Crystallogr. C* **2001**, *57*, 873.

[381] Li, X. M.; Lu, L. P.; Feng, S. S.; Zhang, H. M.; Qin, S. D.; Zhu, M. L. *Acta Crystallogr. E* **2005**, *61*, o811.

[382] Jing, H.; Stroebel, M.; Weisser, M.; Meyer, H.-J. *Z. Anorg. Allg. Chem.* **2003**, *629*, 368.

[383] Marchewka, M. K. *Bull. Korean Chem. Soc.* **2004**, *25*, 466.

[384] Marchewka, M. K. *J. Chem. Res. (S)* **2003**, 518.

[385] Marchewka, M. K.; Baran, J.; Pietraszko, A.; Haznar, A.; Debrus, S.; Ratajczak, H. *Solid State Sci.* **2003**, *5*, 509.

[386] Lakshmi, K. U.; Thamotharan, S.; Ramamurthi, K.; Varghese, B. *Acta Crystallogr. E* **2006**, *62*, o455.

[387] Brodski, V.; Peschar, R.; Schenk, H.; Brinkmann, A.; van Eck, E. R. H.; Kentgens, A. P. M.; Coussens, B.; Braam, A. *J. Phys. Chem. B* **2004**, *108*, 15069.

[388] Choi, C. S.; Venkatraman, R.; Kim, E. H.; Hwang, H. S.; Kang, S. K. *Acta Crystallogr. C* **2004**, *60*, o295.

[389] Colombo, A.; Menabue, I.; Motori, A.; Pellacani, G. C.; Porzio, W.; Sandrolini, F.; Willet, R. D. *Inorg. Chem.* **1985**, *24*, 2900.

[390] Martin, A.; Pinkerton, A. A. *Acta Crystallogr. C* **1995**, *51*, 2174.

[391] Zhang, X. L.; Chen, X. M.; Ng, S. W. *Acta Crystallogr. E* **2005**, *61*, o156.

[392] Karle, I.; Gilardi, R. D.; Rao, C. C.; Muraleedharan, K. M.; Ranganathan, S. *J. Chem. Crystallogr.* **2003**, *33*, 727.

[393] Meier, R. J.; Tiller, A.; Vanhommerig, S. A. M. *J. Phys. Chem.* **1995**, *99*, 5457.

[394] Larkin, P. J.; Makowski, M. P.; Colthoup, N. B. *Spectrochim. Acta A* **1999**, *55*, 1011.

[395] Begley, M. J.; Hubberstey, P.; Martindale, S. P.; Moore, C. H. M.; Price, N. S. *J. Chem. Res.* **1988**, *2*, 101.

[396] Bremner, C. A.; Harrison, W. T. A. *Acta Crystallogr. E* **2002**, *58*, m254.

[397] Harrison, W. T. A.; Rodgers, J. A.; Phillips, M. L. F.; Nenoff, T. M. *Solid State Sci.* **2002**, *4*, 969.

[398] Fischer, G.; Geith, J.; Klapötke, T. M.; Krumm, B. *Z. Naturforsch.* **2002**, *57b*, 19.

[399] *Triazine Derivatives*. D'Alelio, G. F. US Patent, US 2394042, **1946**.

[400] *Carbamoylmelamine*. Odo, K.; Ichikawa, S.; Yamashita, M. Japanese Patent, JP 48064087, **1973**.

[401] *Preparation of 6-Ureido-1,3,5-Triazine-2,4-Diamine*. Garrigue, R.; Lalo, J. French Patent, FR 2625198 A1, **1989**.

[402] *Melamine Purifying Process*. Fingrhut, H.; Canzi, L.; Coufal, G.; Giacomuzzo, S.; Muellner, M. World Patent, WO 9620183, **1996**.

[403] Beyer, H.; Walter, W. *Lehrbuch der Organischen Chemie*; 24. Aufl.; Hirzel Verlag: Stuttgart, 2004.

[404] Streck, R.; Hartig, H. *Chem. Ing. Tech.* **1990**, *62*, 888.

[405] Kosswig, K. *Ullmanns Enzyklopädie der Technischen Chemie*, Vol. 9, 4. Aufl.; WILEY-VCH Verlag GmbH: Weinheim, 1975, 676.

[406] Huthmacher, K.; Hübner, F. *1,3,5-Triazines*, in: *Methods of Organic Chemistry*, Vol. E 9c, 4<sup>th</sup> Ed.; Houben-Weyl: Weinheim, 2001, 667.

[407] Janczak, J.; Sledz, M.; Kubiak, R. *J. Mol. Struct.* **2003**, *659*, 71.

[408] John, E. O.; Shreeve, J. M. *Inorg. Chem.* **1988**, *27*, 3100.

[409] Seifer, G. B. *Russ. J. Coord. Chem.* **2002**, *28*, 301.

[410] Diel, O. *Ber. d. deutsch. chem. Ges.* **1899**, *32*, 692.

[411] Hechenbleikner, I. *J. Am. Chem. Soc.* **1954**, *76*, 3032.

[412] Reilley, W. L.; Brown, H. C. J. *J. Am. Chem. Soc.* **1956**, *78*, 6022.

[413] Reilley, W. L.; Brown, H. C. J. *Org. Chem.* **1957**, *22*, 698.

[414] Bissell, E. R.; Spenger, R. E. *J. Org. Chem.* **1959**, *24*, 1147.

[415] Pakhomova, I. E.; Zhulin, V. M.; Gonikberg, M. G.; Ivanov, V. P. *Russ. Chem. Bull.* **1972**, *21*, 813.

[416] Grundmann, C.; Kreutzberger, A. *J. Am. Chem. Soc.* **1954**, *76*, 632.

[417] Grundmann, C.; Kreutzberger, A. *J. Am. Chem. Soc.* **1954**, *76*, 5646.

[418] Schaefer, F. C.; Hechenbleikner, I.; Peters, G. A. *J. Am. Chem. Soc.* **1958**, *81*, 1466.

[419] Schaefer, F. C.; Peters, G. A. *J. Org. Chem.* **1961**, *26*, 2778.

[420] Brändli, C.; Ward, T. R. *J. Comb. Chem.* **2000**, *2*, 42.

[421] Baxendale, I. R.; Ley, S. V. *J. Comb. Chem.* **2005**, *7*, 483.

[422] Martin, D.; Bauer, M.; Pankratov, V. A. *Russ. Chem. Rev.* **1978**, *47*, 975.

[423] *Gmelins Handbuch der Anorganischen Chemie*, Vol. D1, 8. Aufl.; Gmelin Institut für Anorganische Chemie der Max-Planck-Gesellschaft zur Förderung der Wissenschaft, Verlag Chemie: Weinheim, 1971.

[424] Bann, B.; Miller, S. A. *Chem. Rev.* **1958**, *58*, 131.

[425] Madelung, W.; Kern, E. *Liebigs Ann. Chem.* **1922**, *427*, 26.

[426] Abrahams, B. F.; Egan, S. J.; Hoskins, B. F.; Robson, R. *Chem. Commun.* **1996**, 1099.

[427] Abrahams, B. F.; Egan, S. J.; Hoskins, B. F.; Robson, R. *Acta Crystallogr. C* **1996**, *52*, 2427.

[428] Irran, E.; Jürgens, B.; Schnick, W. *Solid State Sci.* **2002**, *4*, 1305.

[429] Jürgens, B.; Höppe, H. A.; Schnick, W. *Inorg. Chem.* **2004**, *630*, 35.

[430] Grabowski, S. J.; Sokalski, W. A.; Leszczynski, J. *J. Phys. Chem. A* **2005**, *109*, 4331.

[431] Del-Bene, J. E.; Frisch, M. J.; Pople, J. A. *J. Phys. Chem.* **1985**, *89*, 3669.

[432] Song, X.-J.; McDermott, A. E. *Magn. Reson. Chem.* **2001**, *39*, 37.

[433] Allen, F. H.; Kennard, O. *Chem. Des. Autom. News* **1993**, *8*, 31.

[434] Berthold, H. J.; Preibsch, W.; Vonholdt, E. *Angew. Chem.* **1988**, *100*, 1581; *Angew. Chem. Int. Ed. Engl.* **1988**, *27*, 1524.

[435] Berthold, H. J.; Vonholdt, E.; Wartchow, R.; Vogt, T. *Z. Kristallogr.* **1992**, *200*, 225.

[436] Berthold, H. J.; Vonholdt, E.; Wartchow, R.; Vogt, T. *Z. Kristallogr.* **1993**, *203*, 225.

[437] Pfisterer, K.; Korber, N. *Z. Anorg. Allg. Chem.* **2002**, *628*, 762.

[438] Rossmeier, T.; Korber, N. *Z. Naturforsch.* **2003**, *58b*, 672.

[439] Rossmeier, T.; Reil, M.; Korber, N. *Inorg. Chem.* **2004**, *43*, 2206.

[440] Olovsson, I. *Acta Chem. Scand.* **1960**, *14*, 1466.

[441] Scheiner, S.; Harding, L. B. *J. Am. Chem. Soc.* **1981**, *103*, 2169.

[442] Moritani, Y.; Fukunaga, T.; Ishida, H.; Kashino, S. *Acta Crystallogr. C* **2001**, *57*, 1349.

[443] Maurin, J. K.; Pawtowski, M.; Czarnocki, Z. *Acta Crystallogr. C* **2003**, *59*, o656.

[444] Herbison-Evans, D.; Richards, R. E. *Mol. Phys.* **1964**, *8*, 19.

[445] Appleton, T. G.; Hall, J. R.; Ralph, S. F. *Inorg. Chem.* **1988**, *27*, 4435.

[446] Jürgens, B.  $Na_3[C_6N_9]$  und  $Na_3[C_6N_9] \cdot 3H_2O$  – Darstellung, IR- und thermoanalytische Untersuchung und Röntgenstrukturanalyse, Diploma Thesis, Universität Bayreuth, **1996**.

[447] Zerkowski, J. A.; MacDonald, J. C.; Whitesides, G. M. *Chem. Mater.* **1994**, *6*, 1250.

[448] Beatty, A. M. *CrystEngComm* **2001**, *51*, 1.

[449] Russell, K. C.; Lehn, J.-M.; Kyritsakas, N.; DeCianb, A.; Fischer, J. *New J. Chem.* **1998**, *22*, 123.

[450] Yu, Y.-Q.; Lu, C.-Z.; He, X.; Chen, S.-M.; Zhang, Q.-Z.; Chen, L.-J.; Yang, W.-B. *J. Chem. Crystallogr.* **2004**, *34*, 905.

[451] Goodgame, D. M. L.; I.Hussain.; White, A. J. P.; Williams, D. J. *J. Chem. Soc., Dalton Trans.* **1999**, 2899.

[452] Haoguo, Z.; Zhi, Y.; Xiaozheng, Y.; Huaiming, H.; Xiaoying, H. *J. Chem. Crystallogr.* **1999**, *29*, 239.

[453] Guo, Q.; Xie, Y.; Wang, X. J.; Lv, S. C.; Hou, T.; Liu, X. M. *Chem. Phys. Lett.* **2003**, *380*, 84.

[454] Huynh, M. H. V.; Hiskey, M. A.; Archuleta, J. G.; Roemer, E. L. *Angew. Chem.* **2005**, *117*, 747; *Angew. Chem. Int. Ed.* **2005**, *44*, 737.

[455] Huynh, M. H. V.; Hiskey, M. A.; Archuleta, J. G.; Roemer, E. L.; Gilardi, R. *Angew. Chem.* **2004**, *116*, 5776; *Angew. Chem. Int. Ed.* **2004**, *43*, 5658.

[456] von Liebig, J. *Ann. Pharm.* **1834**, *10*, 1.

[457] Voelckel, C. *Ann. Chim. (Phys.)* **1844**, *62*, 90.

[458] Hughes, E. W. *J. Am. Chem. Soc.* **1941**, *63*, 1737.

[459] May, H. *J. Appl. Chem.* **1959**, *9*, 340.

[460] Finkel'shtein, A. I. *Russ. J. Gen. Chem.* **1961**, *31*, 1046.

[461] Costa, L.; Camino, G. *J. Therm. Anal. Calorim.* **1988**, *34*, 423.

[462] Klason, P. *J. Prakt. Chem.* **1886**, *33*, 285.

[463] Finkel'shtein, A. I. *Opt. i Spektr.* **1959**, *6*, 17.

[464] Van der Plaats, G.; Soons, H.; Snellings, R. *Proceedings of the Second European Symposium on Thermal Analysis*; Dollimore, D. (Ed.); Heyden: London, 1981, 215.

[465] Takimoto, M. *Kogyo Kagaku Zasshi* **1964**, *85*, 168.

[466] Takimoto, M. *Kogyo Kagaku Zasshi* **1961**, *64*, 1452.

[467] Schnabel, W. J.; Rätz, R.; Kober, E. *J. Org. Chem.* **1962**, *27*, 2514.

[468] Gal'perin, V. A.; Finkel'shtein, A. I.; Gavrilova, N. K. *Zh. Org. Khim.* **1971**, *7*, 2431.

[469] Costa, L.; Camino, G.; Martinasso, G. *Polym. Prepr. (Am. Chem. Soc., Div. Polym. Chem.)* **1989**, *30*, 531.

[470] Tragl, S.; Gibson, K.; Meyer, H.-J. *Z. Anorg. Allg. Chem.* **2004**, *630*, 2373.

[471] *Flame Retardant Combination*. Schlosser, E.; Nass, B.; Wanzke, W. Eur. Pat. Appl. EP 1386942 A1, **2004**.

[472] *Fire-Resistant Polyester Compositions with Reduced Toxic Gas Generation on Molding and Combustion*. Tojima, T.; Saito, R. Japanese Patent JP 2004217687 A2, **2004**.

[473] *Melam-Based Flame Retardant Polyamide Composition*. Flippo, P.; Tijsse, J.; Sham, C. K.; De Keijzer, A. E. H.; Hulskotte, R. J. M. US Patent US 2001008913 A1, **2001**.

[474] Sattler, A. *Zur Kenntnis von Melem und seinen Verbindungen*, Diploma Thesis, Universität München, **2005**.

[475] Sattler, A.; Schnick, W. *Z. Anorg. Allg. Chem.* **2006**, *632*, 238.

[476] Guo, Q.; Yang, Q.; Zhu, L.; Yi, C.; Zhang, S.; Xie, Y. *Solid State Commun.* **2004**, *132*, 369.

[477] Ghumaan, S.; Kar, S.; Mobin, S. M.; Harish, B.; Puranik, V. G.; Lahiri, G. K. *Inorg. Chem.* **2006**, *45*, 2413.

[478] Dixon, J. K.; Woodberry, N. T. *J. Am. Chem. Soc.* **1947**, *69*, 599.

[479] Finkel'shtein, A. I.; Spiridova, N. V. *Russ. Chem. Rev.* **1964**, *33*, 400.

[480] Nakamoto, K. *Infrared and Raman Spectra of Inorganic and Coordination Compounds*; 4<sup>th</sup> Ed.; John Wiley & Sons, Ltd: New York, 1986.

[481] Scoponi, M.; Polo, E.; Pradella, F.; Bertolasi, V.; Carassiti, V.; Goberti, P. *J. Chem. Soc., Perkin Trans. 2* **1992**, 1172.

[482] Reiser, S.; Brunklaus, G.; Hong, J. H.; Chan, J. C. C.; Eckert, H.; Pfitzner, A. *Chem. Eur. J.* **2002**, *8*, 4228.

[483] von Liebig, J.; Wöhler, F. *Liebigs Ann. Chem.* **1845**, *54*, 371.

[484] Weddige, H. *J. Prakt. Chem.* **1886**, *33*, 85.

[485] Krall, H. *J. Chem. Soc.* **1913**, *103*, 1385.

[486] Ji, S.; Ran, R.; Pittman Jr., C. U. *Polym. Prepr. (Am. Chem. Soc., Div. Polym. Chem.)* **1992**, *33*, 178.

[487] Ji, S.; Crews, G. M.; Pittman Jr., C. U.; Wang, Y.; Ran, R. *J. Polym. Sci., Part A: Polym. Chem.* **1996**, *34*, 2543.

[488] *Flame-Retardant Mixture*. Heinen, W.; Van Tol, M. F. H.; Kierkels, R. H. M.; Van Vliet, G. World Patent, WO 0121698 A1, **2001**.

[489] *Mixture of Additives for Antistatic and Non-Combustible Treatment of the Polymers*. Vasatko, E. CS 218980.B, **1983**.

[490] *Grease Composition*. McCarthy, P. R.; Orem, T. R. US Patent, US 3505224, **1970**.

[491] *Photoresist*. Nishizawa, W. Japanese Patent, JP 58190946 A2, **1983**.

[492] *Photo-Curing Resist Compositions, and Manufacture of Printed Circuit Boards therewith and Printed Circuit Boards*. Imabayashi, S.; Kikuchi, H.; Watabe, M.; Tanaka, I.; Yano, R.; Oka, H.; Taniguchi, Y. Japanese Patent, JP 05194686 A2, **1993**.

[493] Padgett, W. M.; Hammer, W. F. *J. Am. Chem. Soc.* **1958**, *80*, 803.

[494] Wang, Y.; Pittman Jr., C. U.; Saebo, S. *J. Org. Chem.* **1993**, *58*, 3085.

[495] Hantzsch, A. *Ber. d. deutsch. chem. Ges.* **1905**, *38*, 1013.

[496] *Ammeline Salts*. Kaiser, D. W. US Patent, US 2653937, **1953**.

[497] Lotsch, B. V.; Schnick, W. *Z. Anorg. Allg. Chem.* **2006**, *632*, 1457.

[498] Morimoto, G. *Rev. Phys. Chem. Japan* **1967**, *37*, 54.

[499] Sattler, A.; Schnick, W. *Z. Anorg. Allg. Chem.* **2006**, *632*, 1518.

[500] Wagler, J.; El-Gamel, N. A.; Kroke, E. *Z. Naturforsch.* **2006**, *61b*, 975.

[501] Boitsov, E. N.; Finkel'shtein, A. I. *Russ. Chem. Rev.* **1962**, *31*, 712.

[502] Horath-Bordon, E. *Synthese und Eigenschaften von Kohlenstoffnitriden*, PhD Thesis, Technische Universität Darmstadt, **2004**.

[503] Sattler, A.; Schnick, W. *Z. Anorg. Allg. Chem.* **2006**, *632*, 531.

[504] Drozd, M.; Marchewka, M. K. *THEOCHEM* **2005**, *716*, 175.

[505] Scott, B.; Geiser, U.; Willett, R. D.; Patyal, B.; Landee, C. P.; Greeney, R. E.; Manfredini, T.; Pellacani, G. C.; Corradi, A. B.; Battaglia, L. P. *Inorg. Chem.* **1988**, *27*, 2454.

[506] Wang, Y.; Wei, B.; Wang, Q. *J. Cryst. Spectrosc. Res.* **1990**, *20*, 79.

[507] Tanbug, R.; Kirschbaum, K.; Pinkerton, A. A. *J. Chem. Crystallogr.* **1999**, *29*, 45.

[508] Varghese, J. N.; O'Connell, A. M.; Maslen, E. N. *Acta Crystallogr. B* **1977**, *33*, 2102.

[509] von Liebig, J. *Ann. Pharm.* **1834**, *10*, 10.

[510] Kawaguchi, M.; Nozaki, K. *Chem. Mater.* **1995**, *7*, 257.

[511] Zimmermann, J. L.; Williams, R.; Khabashesku, N.; Margrave, J. L. *Nano Lett.* **2001**, *1*, 731.

[512] Todd, M.; Kouvretakis, J.; Groy, T. L.; Chandrasekhar, D.; Smith, D. J.; Deal, P. W. *Chem. Mater.* **1995**, *7*, 1422.

[513] Groenewolt, M.; Antonietti, M. *Adv. Mater.* **2005**, *17*, 1789.

[514] Goettmann, F.; Fischer, A.; Antonietti, M.; Thomas, A. *Angew. Chem.* **2006**, *118*, 4579; *Angew. Chem. Int. Ed.* **2006**, *45*, 4467.

[515] Malkow, T. *Mater. Sci. Eng., A* **2001**, *302*, 311.

[516] dos Santos, M. C.; Alvarez, F. *Phys. Rev. B* **1998**, *58*, 13918.

[517] Komatsu, T. *Macromol. Chem. Phys.* **2001**, *202*, 19.

[518] Miller, D. R.; Swenson, D. C.; Gillan, E. G. *J. Am. Chem. Soc.* **2004**, *126*, 5372.

[519] Miller, D. R.; Wang, J.; Gillan, E. G. *J. Mater. Chem.* **2002**, *12*, 2463.

[520] Zhang, Z. H.; Leinenweber, K.; Bauer, M.; Garvie, L. A. J.; McMillan, P.; Wolf, G. H. *J. Am. Chem. Soc.* **2001**, *123*, 7788.

[521] Shtrempler, G. I.; Murzubraimov, B.; Rysmendeev, K. *Russ. J. Inorg. Chem.* **1982**, *27*, 442.

[522] Nurakhmetov, N. N.; Beremzhanov, B. A.; Tashenov, A.; Erkasov, R. S. *Russ. J. Inorg. Chem.* **1987**, *32*, 6.

[523] Guo, Q.; Xie, Y.; Wang, X. J.; Zhang, S.; Hou, T.; Lv, S. *Chem. Commun.* **2004**, 26.

[524] Montigaud, H.; Tanguy, B.; Demazeau, G.; Alves, I.; Courjault, S. *J. Mater. Sci.* **2000**, *35*, 2547.

[525] Demazeau, G. *J. Mater. Chem.* **1999**, *9*, 15.

[526] Grundmann, C.; Kreutzberger, A. *J. Am. Chem. Soc.* **1955**, *77*, 6559.

[527] Cubicciotti, D. D.; Latimer, W. M. *J. Am. Chem. Soc.* **1948**, *70*, 3509.

[528] Breu, J.; Seidel, W.; Stoll, A. *Z. Anorg. Allg. Chem.* **2003**, *629*, 503.

[529] Sattler, A.; Seyfarth, L.; Senker, J.; Schnick, W. *Z. Anorg. Allg. Chem.* **2005**, *631*, 2545.

[530] Weiss, M. S. *J. Appl. Crystallogr.* **2001**, *34*, 130.

[531] Jiang, J. S.; Li, F. H. *Acta Phys. Sin.* **1984**, *33*, 845.

[532] Dorset, D. L.; Gilmore, C. J. *Acta Crystallogr. A* **2000**, *56*, 62.

[533] Dorset, D. L. *Z. Kristallogr.* **2003**, *218*, 458.

[534] Weirich, T. E.; Zou, X.; Ramlau, R.; Simon, A.; Cascarano, G. L.; Giacovazzo, C.; Hovmöller, S. *Acta Crystallogr. A* **2000**, *56*, 29.

[535] Weirich, T. E.; Portillo, J.; Cox, G.; Hibst, H.; Nicolopoulos, S. *Ultramicroscopy* **2006**, *106*, 164.

[536] Kolb, U.; Matveeva, G. N. *Z. Kristallogr.* **2003**, *218*, 259.

[537] Janiak, C. *J. Chem. Soc., Dalton Trans.* **2000**, 3885.

[538] Hunter, C. A.; Sanders, J. M. *J. Am. Chem. Soc.* **1990**, *112*, 5525.

[539] Weirich, T. E.; Ramlau, R.; Simon, A.; Hovmöller, S.; Zou, X. *Nature* **1996**, *382*, 144.

[540] Stewart, J. J. P. *J. Comput. Chem.* **1989**, *10*, 221.

[541] Frisch, M. J.; Trucks, G. W.; Schlegel, H. B.; Scuseria, G. E.; Robb, M. A.; Cheeseman, J. R.; Montgomery Jr., J. A.; Vreven, T.; Kudin, K. N.; Burant, J. C.; Millam, J. M.; Iyengar, S. S.; Tomasi, J.; Barone, V.; Mennucci, B.; Cossi, M.; Scalmani, G.; Rega, N.; Petersson, G. A.; Nakatsuji, H.; Hada, M.; Ehara, M.; Toyota, K.; Fukuda, R.; Hasegawa, J.; Ishida, M.; Nakajima, T.; Honda, Y.; Kitao, O.; Nakai, H.; Klene, M.; Li, X.; Knox, J. E.; Hratchian, H. P.; Cross, J. B.; Bakken, V.; Adamo, C.; Jaramillo, J.; Gomperts, R.; Stratmann, R. E.; Yazyev, O.; Austin, A. J.; Cammi, R.; Pomelli, C.; Ochterski, J. W.; Ayala, P. Y.; Morokuma, K.; Voth, G. A.; Salvador, P.; Dannenberg, J. J.; Zakrzewski, V. G.; Dapprich, S.; Daniels, A. D.; Strain, M. C.; Farkas, O.; Malick, D. K.; Rabuck, A. D.; Raghavachari, K.; Foresman, J. B.; Ortiz, J. V.; Cui, Q.; Baboul, A. G.; Clifford, S.; Cioslowski, J.; Stefanov, B. B.; Liu, G.; Liashenko, A.; Piskorz, P.; Komaromi, I.; Martin, R. L.; Fox, D. J.; Keith, T.; Al-Laham, M. A.; Peng, C. Y.; Nanayakkara, A.; Challacombe, M.; Gill, P. M. W.; Johnson, B.; Chen, W.; Wong, M. W.; Gonzalez, C.; Pople, J. A. *Gaussian 03, Revision C.02*; Gaussian, Inc.: Wallingford CT, 2004.

[542] Segall, M. D.; Lindan, P. J. D.; Probert, M. J.; Pickard, C. J.; Hasnip, P. J.; Clark, S. J.; Payne, M. C. *J. Phys.: Condens. Matter* **2002**, *14*, 2717.

[543] Mayo, S. L.; Olafson, B. D.; III, W. A. G. *J. Phys. Chem.* **1990**, *94*, 8897.

[544] Delley, B. *J. Chem. Phys.* **1990**, *92*, 508.

[545] Delley, B. *J. Chem. Phys.* **2000**, *113*, 7756.

[546] Lowther, J. E. *Phys. Rev. B* **1999**, *59*, 11683.

[547] Ming, L. C.; Zinin, P.; Meng, Y.; Liu, X. R.; Hong, S. M.; Xie, Y. *J. Appl. Phys.* **2006**, *99*, 033520.

[548] Alvarez, F.; dos Santos, M. C.; Hammer, P. *J. Appl. Phys.* **1999**, *85*, 2642.

[549] Müller, U.; Dehnicke, K. *Angew. Chem.* **1966**, *17*, 825; *Angew. Chem. Int. Ed. Engl.* **1966**, *5*, 841.

[550] Müller, U.; Bärnighausen, H. *Acta Crystallogr. B* **1970**, *26*, 1671.

[551] Müller, U.; Kolitsch, W. *Spectrochim. Acta* **1975**, *31A*, 1455.

[552] Schmidt, A. *Chem. Ber.* **1967**, *100*, 3725.

[553] Kolitsch, W. *Z. Anorg. Allg. Chem.* **1974**, *410*, 21.

[554] Pertrie, M. A.; Sheehy, J. A.; Boatz, J. A.; Rasul, G.; Prakash, G. K. S.; Olah, G. A.; Christe, K. O. *J. Am. Chem. Soc.* **1997**, *119*, 8802.

[555] Subrayan, R. P.; Francis, A. H.; Kampf, J. W.; Rasmussen, P. G. *Chem. Mater.* **1995**, *7*, 2213.

[556] Perera, V. P. S.; Jayaweera, P. V. V.; Pitigala, P. K. D. D. P.; Bandaranayake, P. K. M.; Hastings, G.; Perera, A.; Tennakone, K. *Synth. Met.* **2004**, *143*, 283.

# List of Publications and CSD / CCSD Deposition Numbers

Major results of the this thesis were published in scientific journals by way of the following publications. References of previously published work, as well as oral and poster presentations are included separately below.

## I. Published as Part of this Thesis:

1. **Investigation of Structural and Dynamic Properties of  $\text{NH}_4[\text{N}(\text{CN})_2]$  by Means of X-Ray and Neutron Powder Diffraction as well as Vibrational and Solid-State NMR Spectroscopy,**  
B. V. Lotsch, J. Senker, W. Kockelmann, W. Schnick, *J. Solid State Chem.* **2003**, *176*, 180–191.
2. **Characterization of the Thermally Induced Topochemical Solid-State Transformation of  $\text{NH}_4[\text{N}(\text{CN})_2]$  into  $\text{NCN}=\text{C}(\text{NH}_2)_2$  by Means of X-ray and Neutron Diffraction as well as Raman and Solid-State NMR Spectroscopy,**  
B. V. Lotsch, J. Senker, W. Kockelmann, W. Schnick, *Inorg. Chem.* **2004**, *43*, 895–904.
3. **Towards Novel C-N Materials: Crystal Structures of Two Polymorphs of Guanidinium Dicyanamide and their Thermal Conversion into Melamine,**  
B. V. Lotsch, W. Schnick, *New J. Chem.* **2004**, *28*, 1129–1136.
4. **Crystal Structure and Thermal Solid-State Reactivity of Ammonium Cyanoureate  $\text{NH}_4[\text{H}_2\text{NC}(=\text{O})\text{NCN}]$ ,**  
B. V. Lotsch, W. Schnick, *Z. Naturforsch.* **2004**, *59b*, 1229–1240.

**5. Catalytic Formation and Crystal Structure of Cyanoguanylurea  $\text{H}_2\text{NC}(=\text{O})\text{NHC}(\text{NH}_2)\text{NCN}$ ,**  
B. V. Lotsch, W. Schnick, *Z. Naturforsch.* **2005**, *60b*, 377–382.

**6. Thermal Conversion of Guanylurea Dicyanamide into Graphitic Carbon Nitride via Prototype  $\text{CN}_x$  Precursors,**  
B. V. Lotsch, W. Schnick, *Chem. Mater.* **2005**, *17*, 3976–3982.

**7. Crystal Structure of Guanylurea Sulphate Hydrate  $[\text{H}_2\text{NC}(=\text{O})\text{NHC}(\text{NH}_2)_2]_2\text{SO}_4 \cdot 2\text{H}_2\text{O}$ ,**  
B. V. Lotsch, W. Schnick, *Z. Anorg. Allg. Chem.* **2005**, *631*, 2967–2969.

**8. From Triazines to Heptazines: Novel Nonmetal Tricyanomelamines as Precursors for Graphitic Carbon Nitride Materials,**  
B. V. Lotsch, W. Schnick, *Chem. Mater.* **2006**, *18*, 1891–1900.

**9. Synthesis and Structural Characterization of the Ammelinium Salts  $[\text{C}_3\text{H}_6\text{N}_5\text{O}]\text{Cl}$ ,  $[\text{C}_3\text{H}_6\text{N}_5\text{O}]\text{Br}$ , and  $[\text{C}_3\text{H}_6\text{N}_5\text{O}]\text{NO}_3$ ,**  
B. V. Lotsch, W. Schnick, *Z. Anorg. Allg. Chem.* **2006**, *632*, 1457–1464.

**10. Solid-state NMR Investigation of the Structure of Graphitic Carbon Nitride,**  
B. V. Lotsch, J. Sehnert, L. Seyfarth, J. Senker, W. Schnick, *Abstracts of Papers, 231st ACS National Meeting* **2006**, INOR–665.

**11. Structural Investigation of Graphitic Carbon Nitride,**  
Bettina V. Lotsch, W. Schnick, M. Döblinger, L. Seyfarth, J. Sehnert, J. Senker *Z. Anorg. Allg. Chem.* **2006**, *632*, 2084.

**12. Rare-Earth Ammonium Tricyanomelamines  $[\text{NH}_4]\text{Ln}[\text{HC}_6\text{N}_9]_2[\text{H}_2\text{O}]_7 \cdot \text{H}_2\text{O}$  ( $\text{Ln} = \text{La, Ce, Pr, Nd, Eu, Gd, Tb, Dy}$ ): Structural Investigation, Solid-State NMR Spectroscopy, Thermolysis and Photoluminescence,**  
A. Nag, B. V. Lotsch, J. Schmedt auf der Günne, O. Oeckler, P. J. Schmidt, W. Schnick, *Chem. Eur. J.* **2006**, accepted.

**13. Unmasking Melon by a Complimentary Approach Employing Electron Diffraction, Solid-State NMR and Theoretic Calculations: First Structural Characterization of a Polymeric Carbon Nitride-Type Material,**

B. V. Lotsch, M. Döblinger, J. Sehnert, L. Seyfarth, J. Senker, W. Schnick, *Chem. Eur. J.*, accepted.

**14. New Light on an Old Story: Formation of Melam during Thermal Condensation of Melamine,**

B. V. Lotsch, W. Schnick, *Chem. Eur. J.*, accepted.

**15. Reorientational Dynamics and Solid-Phase Transformation of Ammonium Dicyanamide into Dicyandiamide: A  $^2H$  solid-state NMR Study,**

B. V. Lotsch, W. Schnick, E. Naumann, J. Senker, *J. Phys. Chem. B*, submitted.

## **II. Published Previously (2000 – 2003):**

**16. Separation of Nucleoside Monophosphates using Preferential Anion Exchange Intercalation in Layered Double Hydroxides,**

B. V. Lotsch, F. Millange, R. I. Walton, D. O'Hare, *Solid State Sci.* **2001**, *3*, 883–886.

**17. Method of Separating Nucleoside Phosphates,**

D. M. O'Hare, B. V. Lotsch, *PCT Int. Appl.*, *WO 2002012255 A1 20020214 2001*, 35p.

**18. Cobalt(I)-Catalyzed Neutral Diels-Alder Reactions of Oxygen-Functionalized Acyclic 1,3-Dienes with Alkynes,**

G. Hilt, K. I. Smolko, B. V. Lotsch, *Synlett* **2002**, *7*, 1081–1084.

### III. Presentations:

#### IIIa. Oral

B. V. Lotsch, W. Schnick, *Thermal Solid-State Reactions – Synthetic and Mechanistic Approaches*, 2<sup>nd</sup> Sigma-Aldrich Workshop on Materials Chemistry, Graduate School of Chemistry, University of Münster, Germany, August 24–27, 2004.

B. V. Lotsch, W. Schnick, *From Molecules to Solids: Structure and Properties of Highly Condensed CN<sub>x</sub> Networks and their Molecular Building Blocks*, Postgraduate Research Colloquium of the German National Academic Foundation (Studienstiftung des Deutschen Volkes), Bad Liebenzell, Germany, December 1–14, 2005.

B. V. Lotsch, M. Döblinger, J. Sehnert, L. Seyfarth, J. Senker, W. Schnick, *Solid-state NMR Investigation of the Structure of Graphitic Carbon Nitride*, 231<sup>st</sup> ACS National Meeting 2006, Atlanta (GA), USA, March 24–30, 2006.

B. V. Lotsch, M. Döblinger, J. Sehnert, L. Seyfarth, J. Senker, W. Schnick, *Structural Investigation of Graphitic Carbon Nitride*, Hirschegg-Seminar on Solid-State Chemistry, Hirschegg, Austria, June 15–18, 2006.

B. V. Lotsch, M. Döblinger, J. Sehnert, L. Seyfarth, J. Senker, W. Schnick, *Melon: First Structural Characterization of a Polymeric Carbon Nitride Material*, GDCh-Meeting of the Subsection Solid-State and Materials Chemistry, Aachen, Germany, September 20–22, 2006.

#### IIIb. Posters

B. V. Lotsch, W. Schnick, *Structure and Thermally Induced Reactivity of ND<sub>4</sub>[N(CN)<sub>2</sub>] – Combined Neutron Diffraction, Solid-State NMR and Spectroscopic Investigations*, 11<sup>th</sup> Annual Meeting of the German Society of Crystallography (DGK), Berlin, March 10–13, 2003.

B. V. Lotsch, W. Schnick, *Towards Extended C-N Solids: Crystal Structures and Thermal Solid-State Reactivity of Molecular Precursor Compounds*, 2<sup>nd</sup> Sigma-Aldrich Workshop on Materials Chemistry, Graduate School of Chemistry, University of Münster, Germany, August 24–27, 2004.

B. V. Lotsch, W. Schnick, *Towards Extended C-N Solids: Crystal Structures and Thermal Solid-State Reactivity of Molecular Precursor Compounds*, 2<sup>nd</sup> Wöhler Conference (GDCh-Meeting), Marburg, Germany, September 15–17, 2004.

## IV. CSD and CCSD Reference Numbers:

Crystallographic data were deposited with the Fachinformationszentrum Karlsruhe (76344 Eggenstein-Leopoldshafen, Germany; fax: (+49)7247-808-666; e-mail: crysdata@fiz-karlsruhe.de) or with the Cambridge Crystallographic Data Centre (CCDC, 12 Union Road, Cambridge CB2 1EZ, UK; fax: (+44)1223-336-033; e-mail for inquiry: fileserv@ccdc.cam.ac.uk) and are available on quoting the respective CSD / CCDC reference numbers.

[NH <sub>4</sub> ][N(CN) <sub>2</sub> ]:	CSD-413097
[NH <sub>4</sub> ][H <sub>2</sub> NC(=O)NCN]:	CSD-414279
H <sub>2</sub> NC(=O)NHC(NH <sub>2</sub> )NCN:	CSD-414651
$\beta$ -[C(NH <sub>2</sub> ) <sub>3</sub> ][N(CN) <sub>2</sub> ]:	CCDC-240066
$\alpha$ -[C(NH <sub>2</sub> ) <sub>3</sub> ][N(CN) <sub>2</sub> ]:	CCDC- 240067
[(H <sub>2</sub> N)C(=O)NHC(NH <sub>2</sub> ) <sub>2</sub> ][N(CN) <sub>2</sub> ]:	CCDC-275277
[H <sub>2</sub> NC(=O)NHC(NH <sub>2</sub> ) <sub>2</sub> ] <sub>2</sub> SO <sub>4</sub> · 2 H <sub>2</sub> O:	CCDC-275021
[C <sub>3</sub> H <sub>6</sub> N <sub>5</sub> O]Cl:	CCDC-295005
[C <sub>3</sub> H <sub>6</sub> N <sub>5</sub> O]Br:	CCDC-295006
[C <sub>3</sub> H <sub>6</sub> N <sub>5</sub> O]NO <sub>3</sub> :	CCDC-295007
Zn[C <sub>6</sub> N <sub>11</sub> H <sub>9</sub> ]Cl <sub>2</sub> :	CCDC-618431
[C <sub>6</sub> N <sub>11</sub> H <sub>11</sub> ](ClO <sub>4</sub> ) <sub>2</sub> · 2 H <sub>2</sub> O:	CCDC-618432
C <sub>6</sub> N <sub>11</sub> H <sub>9</sub> :	CCDC-618430
[NH <sub>4</sub> ] <sub>2</sub> [C <sub>6</sub> N <sub>9</sub> H]:	CCDC-287126
[C(NH <sub>2</sub> ) <sub>3</sub> ] <sub>3</sub> [C <sub>6</sub> N <sub>9</sub> ] · 2 H <sub>2</sub> O:	CCDC-287124
[(C <sub>3</sub> N <sub>6</sub> H <sub>7</sub> ) <sub>2</sub> ][C <sub>6</sub> N <sub>9</sub> H] · 2.4 H <sub>2</sub> O:	CCDC-287125

# Curriculum Vitae

## Personal Details

07/09/1977 Born in Frankenthal / Pfalz, Germany, as second child of Dr. Wolfgang Lotsch and Brunhilde Lotsch, nee Weiss;  
Citizenship: German  
Marital status: unmarried

## Education

1984 – 1988 Primary school education at Albrecht – Dürer – Grundschule, Beindersheim

1988 – 1997 High-School education at Karolinen-Gymnasium Frankenthal / Pfalz

1997 Abitur (A–Levels)

1997 – 1999 Undergraduate studies in Chemistry at Ludwig-Maximilians-Universität, München

November 1999 Preliminary Diploma

1999 – 2000 Visiting student at the University of Oxford, Balliol College, practical project in the group of Prof. D. O'Hare, entitled "*Synthesis and Study of Intercalation Compounds*" (advisor: Dr. F. Millange)

2000 – 2002 Graduate Studies in Chemistry at Ludwig-Maximilians-Universität, München

December 2002 Diploma thesis in the group of Prof. W. Schnick (chair of solid-state chemistry) at Ludwig-Maximilians-Universität, München, entitled "*Investigation of the Structure and Thermally Induced Reactivity of Ammonium Dicyanamide*"

since April 2003 Research assistant in the group of Prof. W. Schnick; PhD thesis in inorganic solid-state chemistry, entitled "*From Molecular Building Blocks to Condensed Carbon Nitride Networks: Structure and Reactivity*"